

POLISH SOCIETY OF THEORETICAL AND APPLIED MECHANICS

**JOURNAL OF THEORETICAL
AND APPLIED MECHANICS**

No. 4 • Vol. 56

Quarterly

WARSAW, OCTOBER 2018

JOURNAL OF THEORETICAL AND APPLIED MECHANICS

(until 1997 Mechanika Teoretyczna i Stosowana, ISSN 0079-3701)

Beginning with Vol. 45, No. 1, 2007, *Journal of Theoretical and Applied Mechanics* (JTAM) has been selected for coverage in Thomson Reuters products and custom information services. Now it is indexed and abstracted in the following:

- **Science Citation Index Expanded** (also known as SciSearch®)
- **Journal Citation Reports/Science Edition**

Advisory Board

MICHAŁ KLEIBER (Poland) – Chairman

JORGE A.C. AMBROSIO (Portugal) ★ ANGEL BALTOV (Bulgaria) ★ ROMESH C. BATRA (USA)
★ ALAIN COMBESURE (France) ★ JÜRI ENGELBRECHT (Estonia) ★ WITOLD GUTKOWSKI (Poland)
★ JÓZEF KUBIK (Poland) ★ ZENON MRÓZ (Poland) ★ RYSZARD PARKITNY (Poland)
★ EKKEHARD RAMM (Germany) ★ EUGENIUSZ ŚWITOŃSKI (Poland) ★ HISAAKI TOBUSHI (Japan)
★ ANDRZEJ TYLIKOWSKI (Poland) ★ DIETER WEICHERT (Germany) ★ JOSE E. WESFREID (France)
★ JÓZEF WOJNAROWSKI (Poland) ★ JOSEPH ZARKA (France)
★ VLADIMIR ZEMAN (Czech Republic)

Editorial Board

Editor-in-Chief – **WŁODZIMIERZ KURNIK**

Section Editors: IWONA ADAMIEC-WÓJCIK, PIOTR CUPIAŁ, KRZYSZTOF DEMS,
WITOLD ELSNER, ELŻBIETA JARZĘBOWSKA, OLEKSANDR JEWtusZENKO,
PIOTR KOWALCZYK, ZBIGNIEW KOWALEWSKI, TOMASZ KRZYŻYŃSKI, STANISŁAW KUKLA,
TOMASZ ŁODYGOWSKI, EWA MAJCHRZAK, WIESŁAW NAGÓRKO, JANUSZ NARKIEWICZ,
PIOTR PRZYBYŁOWICZ, BŁAŻEJ SKOCZEŃ, ANDRZEJ STYCZEK,
JACEK SZUMBARSKI, UTZ VON WAGNER (Germany), JERZY WARMIŃSKI

Language Editor – PIOTR PRZYBYŁOWICZ

Technical Editor – EWA KOISAR

Secretary – ELŻBIETA WILANOWSKA



Articles in JTAM are published under Creative Commons Attribution – Non-commercial 3.0. Unported License <http://creativecommons.org/licenses/by-nc/3.0/legalcode>. By submitting an article for publication, the authors consent to the grant of the said license.



Crossref
Similarity Check
Powered by iThenticate

The journal content is indexed in Similarity Check, the Crossref initiative to prevent plagiarism.

* * * * *

Editorial Office

Al. Armii Ludowej 16, room 650

00-637 Warszawa, Poland

phone (+48 22) 825 7180, (+48) 664 099 345, e-mail: biuro@ptmts.org.pl

www.ptmts.org.pl/jtam.html

* * * * *



Ministerstwo Nauki
i Szkolnictwa Wyższego

Publication supported by Ministry of Science and Higher Education of Poland

(Journal of Theoretical and Applied Mechanics: 1) digitalizacja publikacji i monografii naukowych w celu zapewnienia i utrzymania otwartego dostępu do nich przez sieć Internet, 2) stworzenie anglojęzycznych wersji wydawanych publikacji, 3) wdrożenie procedur zabezpieczających oryginalność publikacji naukowych oraz zastosowane techniki zabezpieczeń – są finansowane w ramach umowy 699/P-DUN/2018 ze środków Ministra Nauki i Szkolnictwa Wyższego przeznaczonych na działalność upowszechniającą naukę)

SIMULATION STUDY OF A MISSILE COLD LAUNCH SYSTEM

ROBERT GŁĘBOCKI, MARIUSZ JACEWICZ

Warsaw University of Technology, Institute of Aeronautics and Applied Mechanics, Warsaw, Poland

e-mail: rgleb@meil.pw.edu.pl; mjacewicz@meil.pw.edu.pl

In this paper the missile flight dynamics during the launch phase is studied. The main concept behind this work was to use a vertical cold launch system and the rapid pitch maneuver to achieve longer missile range and better firing coverage. A set of a small pulse rocket engines was used to obtain the desired missile attitude. The physical and mathematical models of the missile are described. The pulse jets control algorithm is presented. The computer program of the missile model has been developed in the Simulink environment. The missile behavior in the low-speed flight envelope has been examined. The results of numerical simulations in the form of the graphs are presented. It has been obtained that there exist several benefits of the cold launch method as increased range and higher target kill probability.

Keywords: guided missile, modeling, simulation

1. Introduction

In this paper, results of the preliminary design phase of a soft launch system for a ground-to-air missile are presented. The main objective of this work is to develop a general physical and mathematical model which may be used for missile flight simulation. The developed model can be used as a baseline for design, analysis and development of guided missiles. The common approach in the field of vertical launch is to use a hot launch technique when the missile main engine is started in the missile container. A potential problem associated with hot vertical launch is range loss due to the turnover maneuver and fuel consumption in the boost phase. This translates into reduced range and increased time to the target. A more sophisticated method is to use a cold launch, which could be complemented with a rapid pitch maneuver over the launcher. In this case, the missile should be equipped with a set of small pulse engines. At the beginning, the missile is ejected vertically upward from a missile canister with an initial velocity between of 15 to 35 meters per second without starting the main engine (Fig. 1).

When the missile is several meters over the ground, the first small engine is used to maintain the pitch angular velocity. Next, the second pulse engine is used to reduce the angular velocity again to zero. Finally, the main rocket engine is started and the object is flying toward the target. At least, two small jet engines are necessary to perform correctly the rapid pitch maneuver. Without using the second jet engine, the missile can rotate freely too much, and when the main engine is fired the missile may fall on the ground. It is desirable to start the main engine when the missile velocity is as low as possible. The missile may be ejected from the launch tube by a piston which can be driven by a compressed gas cylinder or by a pyrotechnic gas generator.

The main benefit of the vertical cold-launch method when compared with the hot-launch is its safety. The lower thermal signature of the launcher is achievable. In this case, there is no hot exhaust of the missile motor interaction with the launcher. The benefits of ejection launching are more and more important as missile size increases. This is the reason why the cold launch method is often used in the case of submarine-launched ballistic missiles. This type of launch can provide full 360 degrees of coverage in all launch sectors. It is possible to achieve longer range

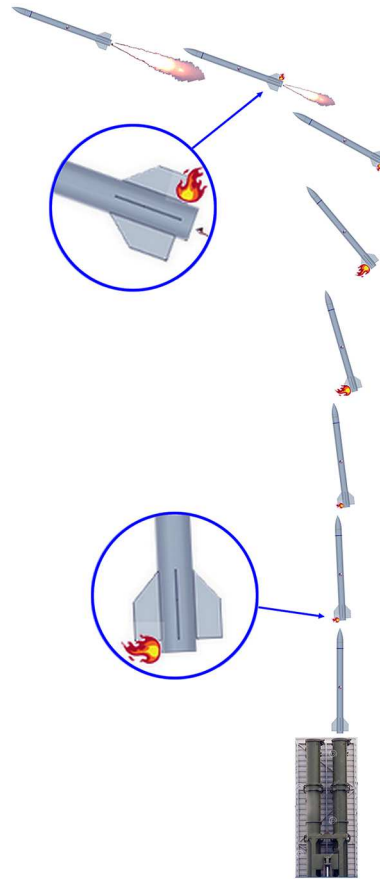


Fig. 1. Cold launch concept

because the main engine is not used in the launch phase and the fuel is consumed only in the midcourse and terminal phases (MBDA Systems, 2014). It offers also improved minimum range capability due to a more direct turnover trajectory that can enable earlier target acquisition. It is able to offer longer maximum range for a given mass when compared with the standard hot vertical launch. Unfortunately, there exist some problems with this type of launch. First of all, immediately after the launch, the missile is in an unstable phase of flight. Because of low velocity, the control surfaces are ineffective so the aerodynamic control at nearly zero speed is practically impossible. The rotational motion is weakly damped, which leads to problems with orienting of the missile in the demanded direction. The engines which control the attitude of the missile should have small delay, because there may appear problems with accuracy. The object after launch may fall on the launcher when the main engine fails. With the lack of a soft launch system there is no possibility of performing manoeuvres like the rapid pitch motion after the launch. There exists a lot of disturbances that can affect the missile trajectory during the launch phase. It is obvious that atmospheric conditions can vary in an unpredictable way. Wind is one of the most important factors which could disturb the missile motion. It is reasonable to assume that in strong wind conditions, the achieved missile pitch angle may be different from the desired one. Another factor that has impact on the launch procedure is the pressure in the missile container and launcher deflection. The reproducibility of the launch may be affected by several factors due to manufacturing inaccuracy (Fleeman, 2006).

2. State of the art

Nowadays, there exist only a few missiles which have both cold and pitch over launcher capabilities. One of the most known examples of this type of missiles is Common Anti-Air Modular

Missile (Fig. 2) which was developed by the MBDA company and demonstrated in May 2011. CAMM has the minimum range under 1 km and the maximum range of about 25 km. CAMM mass is 99 kg, length 3.2 m and diameter 166 mm (MBDA Systems, 2014). The maximum speed of this missile is Mach 3. CAMM has folding tailfins and it is ejected from a compact canister tube by a piston at a height of 30 m. The piston is retained within the tube so there is no launch debris. Next 8 small thrusters are used to point the missile at the target before the main motor fires. Missile turnover is achieved in time less than 1 second. Once turned over, the object is to be held at a selected heading and attitude by lateral thrusters.



Fig. 2. CAMM missile launch (MBDA Systems, 2014)

CAMM is able to provide 360 degree coverage. Small thrusters are able to control the missile in all three planes. CAMM can be fired from the SYLVER and Mark 41 vertical launching systems or from Eurofighter Typhoon aircraft. There also exists CAMM-ER (extended range), and it has an additional booster which increases the missile range up to the value 45 km. CAMM-ER is also bigger: 160 kilograms in weight, 4.2 meters in length, 190 millimeters in diameter. The CAMM launch platform is difficult to detect because of low acoustic, visual and thermal signature. This solution is safer for the ground staff, when compared to hot launch.

The second example of the air defense missile system in which the cold launch method is used is 9K330 Tor (SA-15 Gauntlet) (Fig. 3). The 9M331 missile weight is 167 kg, diameter 235 mm, length 2.9 m, and it carries 15 kg warhead. Tor was developed in 1975 as a new version of Osa (SA-8 Gecko) surface-to-air missile system. Tor was designed for operation from very low to medium altitudes. It entered service with the Soviet Army in 1986, and Russian Army operates 172 of these systems. This system has good performance when used against aircraft (single missile destroy probability 26-75%) and helicopters (50-88%), but can also destroy modern targets like UAVs (85-95%), precision guided munitions or cruise missiles (TOR-M1 9A331, 2012).

The system is mounted on the vehicle which is equipped with 8 missiles, associating radars and fire control systems. The combat vehicle can operate autonomously and the latest version can launch missiles even when the vehicle is on the move. The maximum range is between 5 and 12 km and the maximum altitude is 4-6 km. The missiles have radio command guidance. The system can search for targets while on the move. Tor has reaction time of about 8-12 seconds from target detection to launch. There exist some versions of this system like Tor M, M1, M2K



Fig. 3. Tor missile cold launch (TOR-M1 9A331, 2012)

or M2EK which are improved versions of the system. For example, Tor M1 can track up to 48 targets at the maximum range of 25 km and has higher kill probability.

3. Physical model

To analyze missile dynamics, it is assumed that the missile is a rigid body and has six degrees of freedom. This assumption, though strictly not valid for missiles with a high length-to-diameter ratio, is suitably accurate for describing missile motion during the launch phase. The total mass of the missile is assumed to be equal 58 kg, length 2.3 m, diameter 120 mm and fuel mass 24 kg (Fig. 4). The presented missile is smaller than the missiles presented in the “state of the art” Section. Values of these parameters are limited by the dimensions of the launcher.

It is assumed that the mass and moments of inertia change during the boost-phase. For short range, the flat Earth approximation is used. The vehicle aerodynamics is assumed to be nonlinear and quasi-steady. Moreover, it is assumed that the missile has two geometric and mass symmetry planes and the main motor thrust component passes through the missile center of gravity and is parallel to the missile longitudinal axis of symmetry. The reaction control system (RCS) uses twelve solid propellant pulse engines mounted, which generate the thrust directed normally to the main axis of symmetry of the object. The RCS is located 70 mm from the tail. Each small engine can be fired only once.

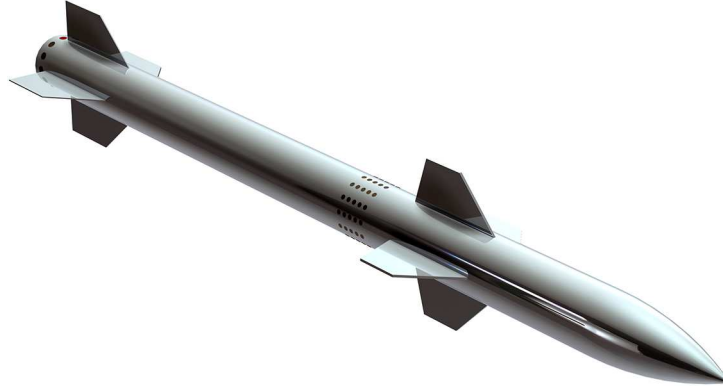


Fig. 4. 3D CAD missile model

4. Mathematical model

In this Section, the missile mathematical model six is derived. The basic frames used in this work are the inertial, body and gravity coordinate systems. The origin O_n of the inertial coordinate system $O_n x_n y_n z_n$ is placed in any selected point on the Earth surface (Fig. 5). The axes $O_n x_n$

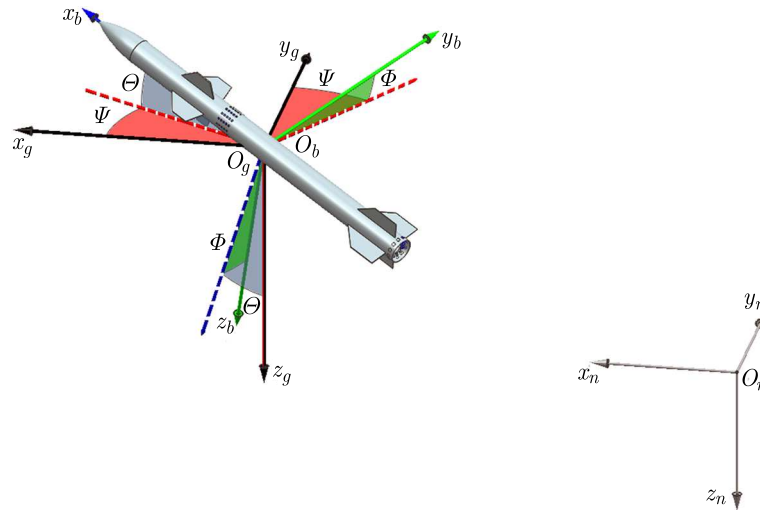


Fig. 5. Coordinate systems which have been used in simulation

and $O_n y_n$ lie in the plane which is perpendicular to the direction of gravity acceleration. The $O_n x_n$ is pointing north, and the $O_n y_n$ axis points east. The $O_n z_n$ axis is pointed vertically, it coincides with the direction of the Earth gravity acceleration. The missile equations of motion are derived in the conventional body coordinate system $O_b x_b y_b z_b$ (Blakelock, 1991). In the general case, the origin O_b of this frame might be not at the center of gravity of the missile and moves forward as the after main engine burnout. In this article, it is assumed that the origin O_b of this frame is coincident with the center of gravity of the missile. In the body coordinate system, the positive $O_b x_b$ axis coincides with the center line of the missile and it is designated as the roll-axis. The positive $O_b y_b$ axis is to the right of the $O_b x_b$ axis in the horizontal plane and it is designated as the pitch axis. The positive $O_b z_b$ axis points downward and it is designated as the yaw axis. The body axis system is fixed with respect to the missile and moves with the missile (Weinacht, 2004). The $O_g x_g y_g z_g$ is the gravity coordinate system. The centre O_g of the gravity system of coordinates coincides with the centre of mass. The axis of the gravity system is parallel to the axis of the ground coordinate system. The mathematical model describing motion of the

missile consists of six rigid-body degrees of freedom. The object orientation is parametrized using quaternions. Yaw, pitch, and roll angles are used only to visualize the results.

The system of six dynamic equations of motion is given by

$$\mathbf{A}\dot{\mathbf{x}} + \mathbf{\Omega A x} = [\mathbf{F}_b \quad \mathbf{M}_b]^T \quad (4.1)$$

where the missile state vector is

$$\mathbf{x} = [U, V, W, P, Q, R]^T \quad (4.2)$$

and

$$\mathbf{F}_b = [X_b, Y_b, Z_b]^T \quad \mathbf{M}_b = [L_b, M_b, N_b]^T \quad (4.3)$$

where U, V, W are linear velocities, P, Q, R – angular velocities, X_b, Y_b, Z_b – axial, side and normal forces along the body axes coordinate system. In a similar way, L_b, M_b, N_b are rolling, pitching and yawing moments. The left-hand side of the equation describes the inertia loads in the missile frame of reference. In the most general case, when the missile centre of mass is not coincident with O_b , the inertia matrix is defined as follows (Żugaj and Głębocki, 2010)

$$\mathbf{A} = \begin{bmatrix} m & 0 & 0 & 0 & S_z & -S_y \\ 0 & m & 0 & -S_z & 0 & S_x \\ 0 & 0 & m & S_y & -S_x & 0 \\ 0 & -S_z & S_y & I_x & -I_{xy} & -I_{xz} \\ S_z & 0 & -S_x & -I_{yx} & I_y & -I_{yz} \\ -S_y & S_x & 0 & -I_{zx} & -I_{zy} & I_z \end{bmatrix} \quad (4.4)$$

and the velocity matrix is

$$\mathbf{\Omega} = \begin{bmatrix} 0 & -R & Q & 0 & 0 & 0 \\ R & 0 & -P & 0 & 0 & 0 \\ -Q & P & 0 & 0 & 0 & 0 \\ 0 & -W & V & 0 & -R & Q \\ W & 0 & -U & R & 0 & -P \\ -V & U & 0 & -Q & P & 0 \end{bmatrix} \quad (4.5)$$

where m is the missile mass, S_x, S_y, S_z – static moments, I_x, I_y, I_z – moments of inertia, I_{xy}, I_{xz}, I_{yz} – products of inertia.

The set of 6 scalar equations describing translational and rotational motion of the missile has the form

$$\begin{aligned} m(\dot{U} + WQ - VR) - S_x(Q^2 + R^2) + S_y(PQ - \dot{R}) + S_z(PR + \dot{Q}) &= X_b \\ m(\dot{V} + UR - WP) + S_x(PQ + \dot{R}) - S_y(P^2 + R^2) + S_z(QR - \dot{P}) &= Y_b \\ m(\dot{W} + VP - UQ) + S_x(PR - \dot{Q}) + S_y(RQ + \dot{P}) - S_z(P^2 + Q^2) &= Z_b \end{aligned} \quad (4.6)$$

and

$$\begin{aligned} I_x \dot{P} - (I_y - I_z)RQ + I_{xy}(PR - \dot{Q}) - I_{xz}(PQ + \dot{R}) + I_{yz}(R^2 - Q^2) \\ + S_y(\dot{W} + VP - UQ) - S_z(\dot{V} + UR - WP) &= L_b \\ I_y \dot{Q} - (I_z - I_x)PR - I_{xy}(QR + \dot{P}) + I_{xz}(P^2 - R^2) + I_{yz}(PQ - \dot{R}) \\ - S_x(\dot{W} + VP - UQ) + S_z(\dot{U} - VR + WQ) &= M_b \\ I_z \dot{R} - (I_x - I_y)PQ - I_{xy}(P^2 - R^2) + I_{xz}(QR - \dot{P}) - I_{yz}(\dot{Q} + PR) \\ + S_x(\dot{V} + UR - WP) - S_z(\dot{U} + WQ - VR) &= N_b \end{aligned} \quad (4.7)$$

However, it is assumed that the origin of the gravity coordinate system $O_gx_gy_gz_g$ is coincident with the origin $O_bx_by_bz_b$ of the body coordinate system so $S_x = S_y = S_z = 0$. The next assumption is that the missile is a body of revolution and has two planes of symmetry. Hence, all products of inertia are zero. The velocity vector of the missile in the $O_nx_ny_nz_n$ can be calculated as (Zipfel, 2007)

$$\begin{bmatrix} \dot{x}_n \\ \dot{y}_n \\ \dot{z}_n \end{bmatrix} = \begin{bmatrix} e_0^2 + e_1^2 - e_2^2 - e_3^2 & 2(e_1e_2 - e_0e_3) & 2(e_0e_2 - e_1e_3) \\ 2(e_0e_3 - e_1e_2) & e_0^2 - e_1^2 + e_2^2 - e_3^2 & 2(e_2e_3 - e_0e_1) \\ 2(e_1e_3 - e_0e_2) & 2(e_0e_1 - e_2e_3) & e_0^2 - e_1^2 - e_2^2 + e_3^2 \end{bmatrix} \begin{bmatrix} U \\ V \\ W \end{bmatrix} \quad (4.8)$$

where e_0, e_1, e_2, e_3 – quaternion elements.

The integration of the rate of change of the quaternion vector is given as follows

$$\begin{bmatrix} \dot{e}_0 \\ \dot{e}_1 \\ \dot{e}_2 \\ \dot{e}_3 \end{bmatrix} = -\frac{1}{2} \begin{bmatrix} 0 & P & Q & R \\ -P & 0 & -R & Q \\ -Q & R & 0 & -P \\ -R & -Q & P & 0 \end{bmatrix} \begin{bmatrix} e_0 \\ e_1 \\ e_2 \\ e_3 \end{bmatrix} - kE \begin{bmatrix} e_0 \\ e_1 \\ e_2 \\ e_3 \end{bmatrix} \quad (4.9)$$

The gain k drives the norm of the quaternion state vector to one. Next, the roll Φ , pitch Θ and yaw Ψ angles are calculated as below (Zipfel, 2007)

$$\begin{aligned} \Phi &= \arctan \frac{2(e_0e_1 + e_2e_3)}{e_0^2 - e_1^2 - e_2^2 + e_3^2} & \Theta &= \arcsin[2(e_0e_2 - e_1e_3)] \\ \Psi &= \arctan \frac{2(e_0e_3 + e_1e_2)}{e_0^2 + e_1^2 - e_2^2 - e_3^2} \end{aligned} \quad (4.10)$$

In missiles, the center of gravity normally shifts due to the burning off of the fuel. Forces \mathbf{F}_b acting on the missile have been obtained by summing up the inertia (left hand side of the equation), gravity \mathbf{F}_G , aerodynamic \mathbf{F}_A , propulsion \mathbf{F}_P , control fins \mathbf{F}_C and control loads from the lateral thrusters \mathbf{F}_T (Yuhang *et al.*, 2006)

$$\mathbf{F}_b = \mathbf{F}_G + \mathbf{F}_A + \mathbf{F}_P + \mathbf{F}_C + \mathbf{F}_T \quad (4.11)$$

In a similar way, the moments and the resultant moment \mathbf{M}_b are calculated as follows

$$\mathbf{M}_b = \mathbf{M}_G + \mathbf{M}_A + \mathbf{M}_P + \mathbf{M}_C + \mathbf{M}_T \quad (4.12)$$

A diagram that shows the forces and moments acting on the missile is illustrated in Fig. 6.

The vector of gravity loads acting on the object is calculated as

$$\mathbf{F}_G = mg[-\sin \Theta, \cos \Theta \sin \Phi, \cos \Theta \cos \Phi]^T \quad \mathbf{M}_G = [0, 0, 0]^T \quad (4.13)$$

The aerodynamic forces and moments in the $O_bx_by_bz_b$ coordinate system are calculated as below

$$\mathbf{F}_A = \frac{1}{2} \rho V_0^2 S [-C_X, C_Y, -C_Z]^T \quad \mathbf{M}_A = \frac{1}{2} \rho V_0^2 S d [-C_L, C_M, -C_N]^T \quad (4.14)$$

where ρ is the air density, V_0 – total flight velocity, S – area of the missile cross section, d – missile diameter and $C_X, C_Y, C_Z, C_L, C_M, C_N$ are force and moment coefficients, respectively. The aerodynamic forces, as given in the above equations, are functions of the aerodynamic coefficients which depend on factors such as the Mach number, the angle of attack, sideslip angle and angular velocities. The table lookup procedure has been used for obtaining the aerodynamic coefficients for various flow angles and the Mach numbers from an offline generated database. Aerodynamic characteristics of the missile have been determined using Arrow Tech PRODAS

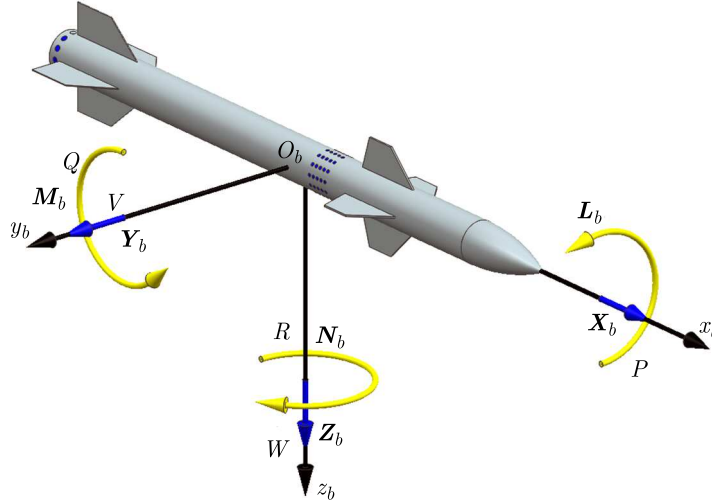


Fig. 6. Forces and moments acting on the missile

software (MAHER, 2002). The coefficients were also checked with the aim of Computational Fluid Dynamics (CFD) methods. Steady-state simulations for angles of attack in range from -15° to 15° and Mach numbers (Ma) from 0.1 to 4 were performed to confirm the values of aerodynamic coefficients

$$\begin{aligned}
 C_X(\alpha, \beta, \text{Ma}) &= C_{X0} + C_{X\alpha 2} \sin^2 \alpha + C_{X\beta 2} \sin^2 \beta \\
 C_Y(\beta, \text{Ma}) &= C_{Y\beta} \sin \beta + C_{Y\beta 3} \sin^3 \beta \\
 C_Z(\alpha, \text{Ma}) &= C_{Z\alpha} \sin \alpha + C_{Z\alpha 3} \sin^3 \alpha & C_L(\text{Ma}) &= C_{LP} \frac{Pd}{2V_0} \\
 C_M(\alpha, \text{Ma}) &= C_{M\alpha} \sin \alpha + \frac{Qd}{2V_0} C_{MQ} & C_N(\beta, \text{Ma}) &= C_{N\beta} \sin \beta + \frac{Rd}{2V_0} C_{NR}
 \end{aligned} \tag{4.15}$$

where C_{LP} is rolling moment coefficient derivative with the roll rate, C_{MQ} – pitching moment coefficient derivative with the pitch rate, C_{NR} – yawing moment coefficient derivative with the yaw rate.

Some of the coefficients are shown in Fig. 7.

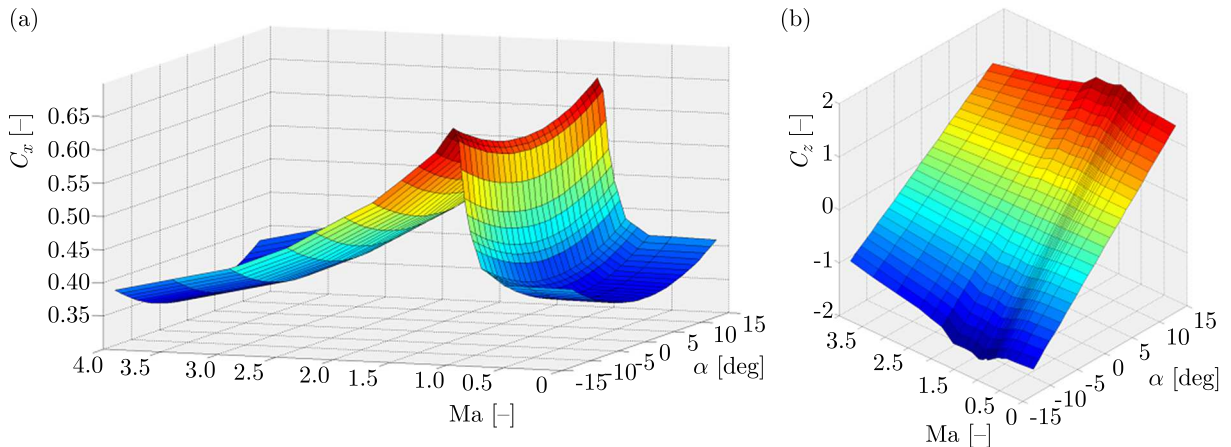


Fig. 7. (a) Axial and (b) normal force coefficients as a function of the Mach number and angle of attack

The International Civil Aviation Organization (ICAO) standard atmosphere model has been used as the flight environment (Zarchan, 2012). Propulsive loads were calculated as follows

$$\mathbf{F}_P = [T(t), 0, 0]^T \quad \mathbf{M}_P = [0, 0, 0]^T \tag{4.16}$$

The thrust profile is a known function of time $T(t)$ and was obtained on the engine test stand. It was assumed that main engine thrust force was parallel to the $O_b x_b$ axis the body coordinate system. Control forces generated by fin deflections are defined as follows

$$\begin{aligned} \mathbf{F}_C &= \frac{1}{2} \rho V_0^2 S \begin{bmatrix} X_{\delta_A} \delta_A + X_{\delta_B} \delta_B + X_{\delta_C} \delta_C + X_{\delta_D} \delta_D \\ Y_{\delta_A} \delta_A + Y_{\delta_B} \delta_B + Y_{\delta_C} \delta_C + Y_{\delta_D} \delta_D \\ Z_{\delta_A} \delta_A + Z_{\delta_B} \delta_B + Z_{\delta_C} \delta_C + Z_{\delta_D} \delta_D \end{bmatrix} \\ \mathbf{M}_C &= \frac{1}{2} \rho V_0^2 S d \begin{bmatrix} L_{\delta_A} \delta_A + L_{\delta_B} \delta_B + L_{\delta_C} \delta_C + L_{\delta_D} \delta_D \\ M_{\delta_A} \delta_A + M_{\delta_B} \delta_B + M_{\delta_C} \delta_C + M_{\delta_D} \delta_D \\ N_{\delta_A} \delta_A + N_{\delta_B} \delta_B + N_{\delta_C} \delta_C + N_{\delta_D} \delta_D \end{bmatrix} \end{aligned} \quad (4.17)$$

where $\delta_A, \delta_B, \delta_C, \delta_D$ are the control surfaces deflection angles. Next, the control forces generated by the reaction control system are calculated (DeSpirito, 2013). The missile has a set of small solid fuel engines placed at the end of the body. It is assumed that there are $N = 12$ jets. It is assumed that nozzles of these engines are perpendicular to the longitudinal axis of symmetry of the missile (Weinacht, 2004). The jets are translated by the vector $\mathbf{r}_{Ti} = [x_{Ti}, y_{Ti}, z_{Ti}]$ from the origin of the $O_b x_b y_b z_b$ coordinate system, where $i = 1, \dots, N$ is the number of the jet engine (Zhen *et al.*, 2012).

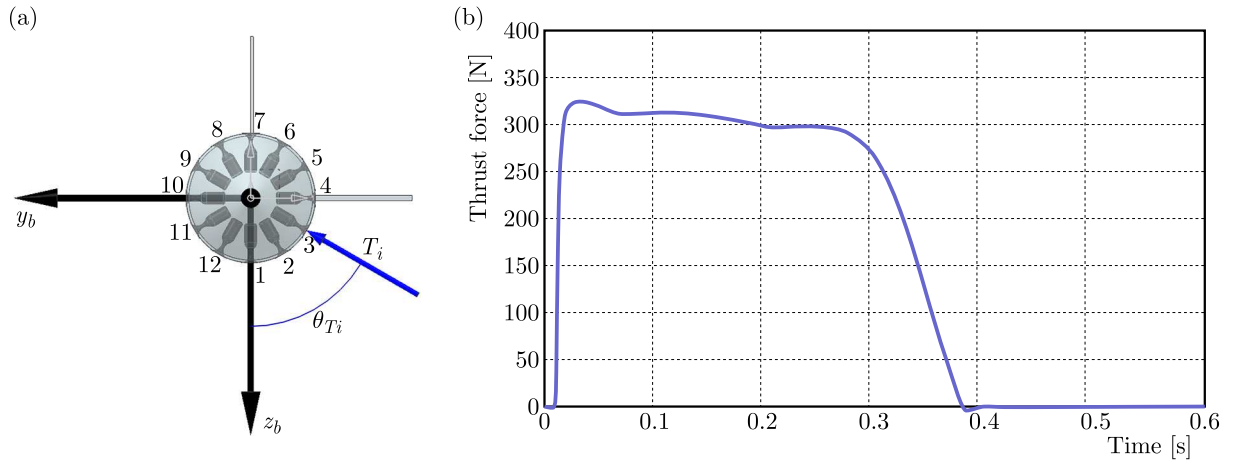


Fig. 8. (a) Reaction control system which is simulated, (b) the jet engine thrust curve

The force from the i -th jet engine in the $O_b x_b y_b z_b$ coordinate system is described as below

$$\mathbf{F}_{Ti} = T_i [0, \sin \theta_{Ti}, -\cos \theta_{Ti}]^T \quad (4.18)$$

The moments generated by this pulse jet are

$$\mathbf{M}_{Ti} = \mathbf{r}_{Ti} \times \mathbf{F}_{Ti} = T_i [-y_{Ti} \cos \theta_{Ti} - z_{Ti} \sin \theta_{Ti}, x_{Ti} \cos \theta_{Ti}, x_{Ti} \sin \theta_{Ti}]^T \quad (4.19)$$

It is assumed that the jet engine thrust force (Fig. 8) is a function of time (Fenghua *et al.*, 2008). The shape of the curve has been designed with the aim of the method which was presented in (Fleeman, 2006). The maximum thrust and jet engine size is limited also by the diameter of the missile. There are defined some time constants which describe delays between subsequent phases of the jet firing logic: τ_1 – start time for the first jet engine, τ_2 – burnout time for the first engine, τ_3 – start time for the second jet engine, τ_4 – burnout time for the second engine, τ_5 – main engine launch time. These time constants are connected with two specific pitch angle values: θ_{τ_2} – pitch angle after the first jet engine burnout, θ_{τ_4} – pitch angle after the first jet engine burnout. These parameters have been calculated offline with the aim of optimisation methods and implemented in the simulation. The methods by which the time constants have

been calculated are out of the scope of this article. The described mathematical model has been implemented in the Matlab software. The inputs to the model are the launch conditions, while the outputs are the missile flight data (velocity, acceleration, etc.).

5. Simulation results

In this part, simulation results are presented. The missile is controlled by twelve small engines mounted at the end of the missile tail. As the missile is launched, one of the engines is ignited to orient the object in the demanded direction. Next, the second pulse engine is used to counteract the pitch motion and, finally, the main missile engine is started. The key goals of the simulation are to find control forces of the lateral jets, time constants and the best height at which the missile should be ejected.

In the first test, the dependency between the τ_3 time constant and the final pitch angle has been analyzed. The second pulse engine was ignited with various delays. In Fig. 9, the missile flight trajectories for various τ_3 time constants are presented. The burntime of the single pulse jet was 0.37 s and the thrust force was assumed constant and equal to 313 N. The missile was ejected vertically (initial pitch angle 90°) with the velocity 25 m/s. Before the launch, the missile was located in the origin of the inertial coordinate system $O_n x_n y_n z_n$.

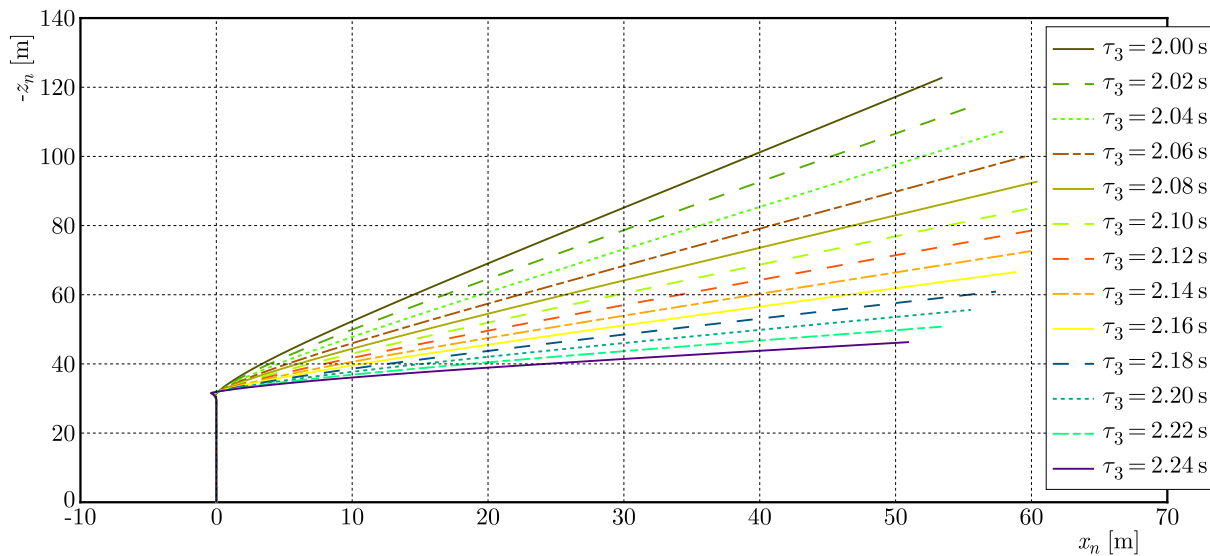


Fig. 9. Trajectories as a function of τ_3 time constants

The time constant τ_3 was varied from 2 s to 2.24 s. For the smallest value of this time constant, the pitch angle was about nearly 60° (for vertically oriented missile pitch angle 90°). It is planned to use the inertial measurement unit to measure the actual pitch angle. For the biggest value of this time constant, the pitch angle is about 10° . The main conclusion from this example is that with using of this time constant it is possible to achieve various pitch angles.

In Fig. 10, the pitch angular velocity and the pitch angle as a function of time and for various time constants which were used during simulations are presented.

The angular velocity does not change until 1.8 s because during this time no pulse jet is used. Next, the first pulse jet is ignited and the missile pitch velocity changes rapidly as expected. Later, the second jet engine is launched and the angular velocity decreases nearly to zero. After 2.3 s there occurs a very small positive singular velocity. It is difficult to drive this small difference to zero because the first and second lateral jet thrust curves are the same. The bigger the τ_3 time constant, the smaller pitch angle is achieved at the end of the simulation.

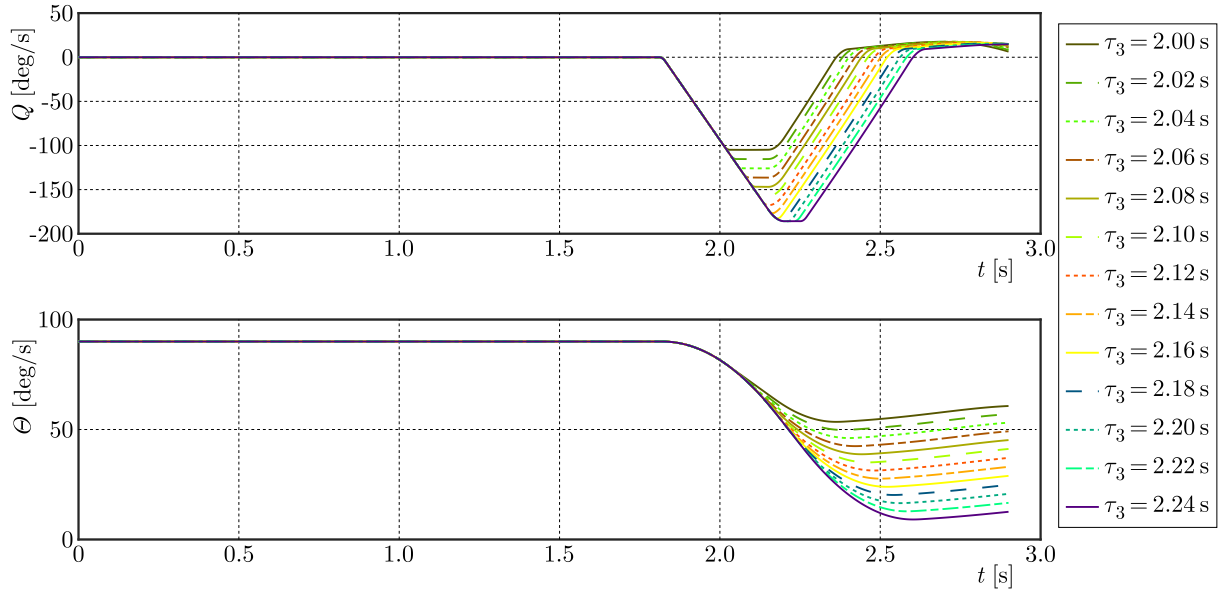


Fig. 10. Pitch velocities and pitch angles for various τ_3 time constants

Next, the influence of τ_1 on the missile altitude has been tested. In Fig. 11, flight paths for various τ_1 are shown. The launch velocity has been assumed to be equal to 27 m/s.

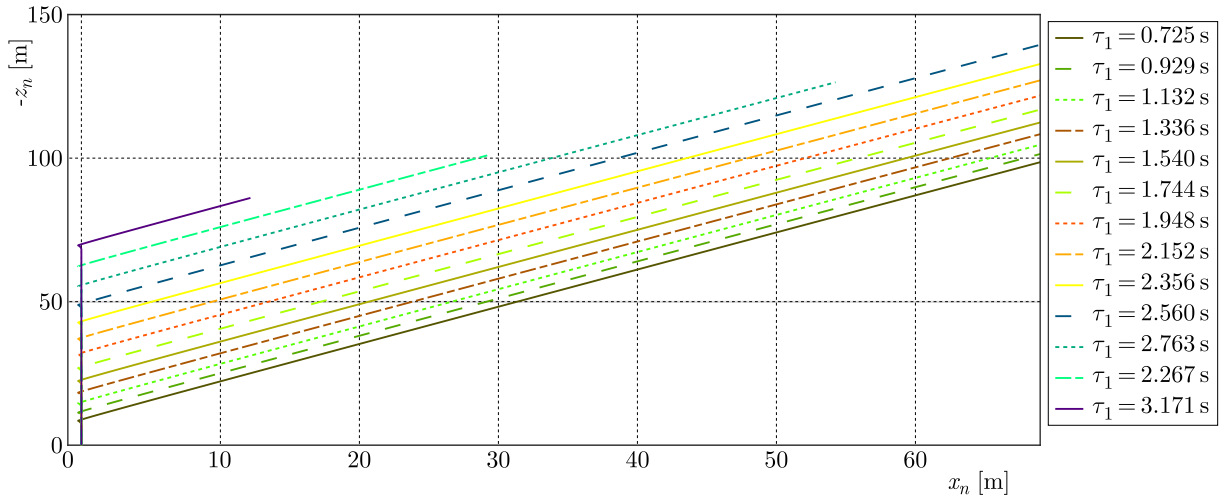


Fig. 11. Flight trajectories for various τ_1 time constants

The time constants τ_2 , τ_3 , τ_4 and τ_5 are connected with the missile launch τ_1 . Satisfactory results of these simulations have been obtained.

In Fig. 12, the pitch angular velocity and the pitch angle as a function of the first delay τ_1 are shown.

At the end of the simulation, the pitch angle is about 53° . The total maneuver time does not exceed 0.6 s, which is quite a small value.

The other goal of the experiments was to compare the simulation results for the object with the aerodynamic control surfaces only and the object with the gasdynamics controls (Fig. 13). In the simulations, two objects are launched vertically and then they are aiming to the same point.

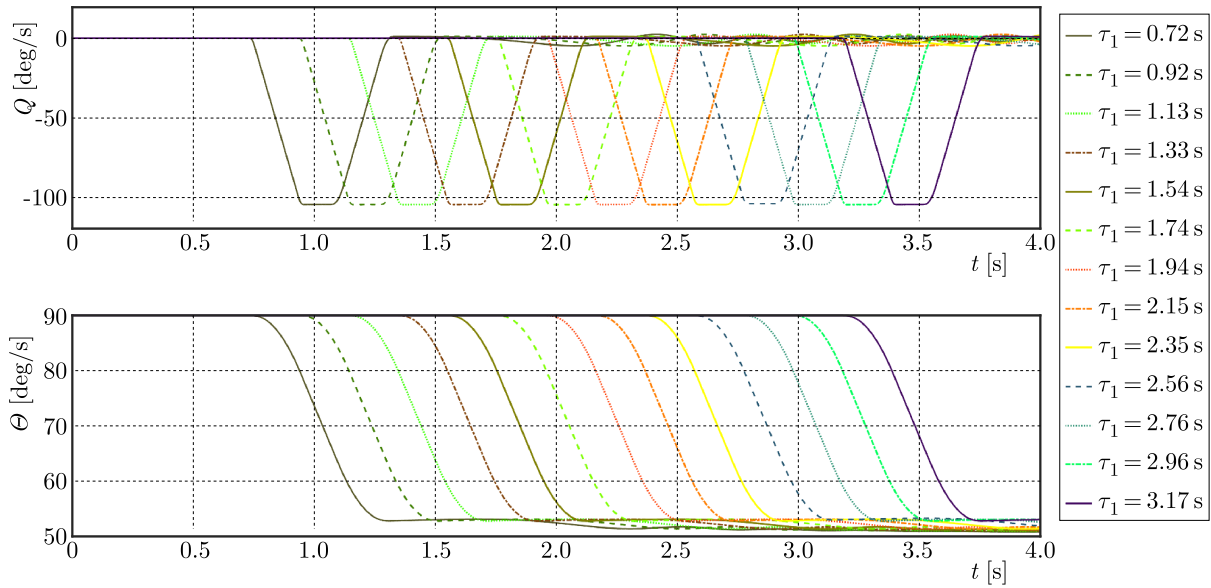


Fig. 12. Missile angular pitch velocity and pitch angle as a function of time

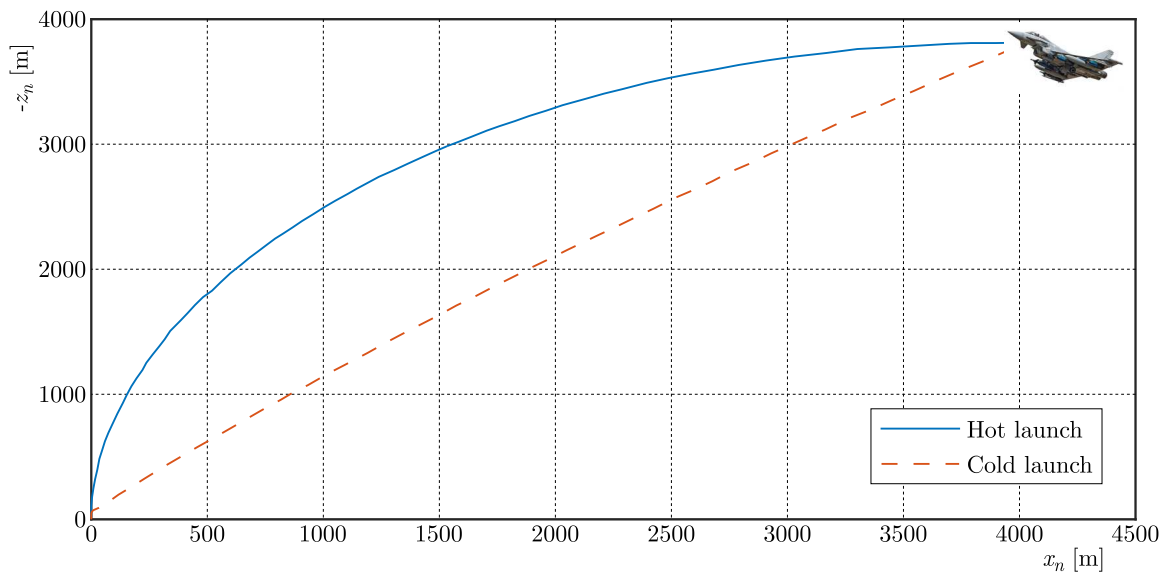


Fig. 13. Comparison of the trajectories for cold and hot launched missiles

There is only motion in the vertical plane, so y distance is zero. There is a significant difference between both curves. The object with gasdynamics control can move along a straight line, which is much more effective than flight along a parabolic curve. The missile with the aerodynamic control has not those capabilities. The missile with the gasdynamics control is able to reach the control point at a different trajectory and also can hit targets which are very low. The missile with the gasdynamic control is able to reach the target in a shorter time than the missile with the classical vertical hot launch system. The presented method is able to save about 14% of fuel. The control system model used in the simulation is adequate to this type of the object and is able to control precisely this object. The object can rotate in the air because there is small damping in the air. When the delay is too big, the object can rotate too much and hits the ground. The simulation results show capabilities of the presented control method.

6. Conclusion

This article investigates the dynamic characteristics of the cold launched missile with the gas-dynamics control. The soft launch ignites the rocket motor after the missile has been launched and directed towards the target. Analysis and simulation have been conducted to investigate the dynamics of the missile. The missile model has been implemented in Simulink software. Numerical experiments have shown some advantages of the proposed method like higher range. It has been obtained that it is possible to use the gasdynamic control to orient the missile objects during the launch phase. It can be concluded that the presented model of the missile launch phase works properly.

References

1. BARANOWSKI L., 2013, Numerical testing of flight stability of spin-stabilized artillery projectiles, *Journal of Theoretical and Applied Mechanics*, **51**, 2, 375-385
2. BLAKELOCK J., 1991, *Automatic Control of Aircraft and Missiles*, New York, NY, John Wiley & Sons, Inc.
3. DESPIRITO J., 2013, *Lateral Reaction Jet Flow Interaction Effects on a Generic Fin-Stabilized Munition in Supersonic Crossflow*, Army Research Laboratory
4. FENGHUA H., KEMAO M., YU Y., 2008, Firing logic optimization design of lateral jets in missile attitude control systems, *17th IEEE International Conference on Control Applications*, San Antonio
5. FLEEMAN E., 2006, *Missile Design and System Engineering*, AIAA Distinguished Lecture
6. MAHER K., 2002, *PRODAS V3 – Technical Manual*, Arrow Tech
7. MBDA Systems, 2014, MBDA – Common Anti-air Modular Missile (CMM), Retrieved from <https://youtu.be/Nnb20mrT1kw>
8. TOR-M1 9A331 (SA-15 Gauntlet) surface-to-air missile, 2012, Retrieved from <https://www.youtube.com/watch?v=qcC0rXxXVNA>
9. WEINACHT P., 2004, *Lateral Control Jet Aerodynamic Predictions for a 2.75-in Rocket Testbed Munition*, Army Research Laboratory
10. YUHAN W., YU Y., KEMAO M., 2006, Lateral thrust and aerodynamics blended control system design based on variable structure model following, *Intelligent Control and Automation*, Dalian, 8183-8186
11. ZARCHAN P., 2012, *Tactical and Strategic Missile Guidance*, American Institute of Aeronautics and Astronautics
12. ZHEN S., WENQIAO M., YUFANG Z., HUICHAO H., 2012, Lateral thrust and aerodynamics compound control system of missile based on adaptive fuzzy control, *Computational Intelligence and Design (ISCID)*, Hangzhou
13. ZIPFEL P., 2007, *Modeling and Simulation for Aerospace Vehicle Dynamics*, American Institute of Aeronautics and Astronautics
14. ŻUGAJ M., GŁĘBOCKI R., 2010, Model of gasodynamic control system for guided bombs, *Journal of Theoretical and Applied Mechanics*, **48**, 1, 27-44

INCLINED SURFACE CRACKS IN A GRADED HALF-PLANE SUBJECTED TO FRICTIONAL SLIDING CONTACT

ONUR ARSLAN

Eskisehir Osmangazi University, Department of Mechanical Engineering, Eskisehir, Turkey

e-mail: oarslan@ogu.edu.tr

Fracture parameters of an inclined surface crack in a graded half-plane subjected to sliding frictional contact are investigated in this study. The problem is modelled via the finite element method (FEM) under the plane strain assumption employing a newly developed displacement boundary condition. The shear modulus of the half-plane is graded exponentially through the thickness direction by means of the homogeneous finite element approach. The augmented Lagrange algorithm is selected as an iterative contact solver. The mixed mode stress intensity factors (SIFs) which are induced by the contact stresses are evaluated utilizing the Displacement Correlation Technique (DCT). The accuracy of the present procedure is ensured comparing the SIF results to those calculated by an analytical method for vertical surface cracks. Additional SIF curves are generated as functions of the crack inclination in order to reveal the effects of non-homogeneity, punch location, crack length and friction coefficient. The prominent conclusion of this study indicates that the crack orientation has profound effects on the behavior of SIF curves, which has not been presented in any study published so far. Hence, consideration of crack inclination is proved essential to successfully predict fracture behavior of a graded medium under frictional contact.

Keywords: inclined surface cracks, crack/contact problems, graded materials, finite element method

1. Introduction

In engineering applications, keeping the structural integrity of a member is the major concern to extend service life. From this point of view, investigation of contact and fracture mechanics problems come into prominence especially for load transfer members. Brittle materials such as ceramics are well suited for load carrying surfaces due to their high wear resistance. However, because of their limited toughness they are prone to surface cracking under frictional contact loadings, which may lead to loss in fatigue strength (Hills *et al.*, 1993). Such destructive effects of contact loadings can be partially tolerated by employing graded materials which consist of spatially varying composition of brittle and ductile materials. For instance, frictional contact and indentation related damages is shown to be mitigated upon introducing material gradation (Suresh, 2001). It is revealed that non-homogeneous ceramics are more damage resistant to loadings induced by spherical indenters (Lawn, 1998). Spatial gradation of Young's modulus is proven to prevent formation of Hertzian cone-cracks on brittle surfaces loaded by spherical stamps (Jitcharoen *et al.*, 1998). Material gradation provides an improvement in damage tolerance of ceramics which are subjected to contact and flexural loadings (Zhang, 2012).

In literature, there are some computational and analytical studies analyzing behavior of cracks in elastic continua which are subjected to contact loadings. Hasebe *et al.* (1989) investigated edge crack problems in an elastic half plane under frictional contact by utilizing a rational mapping function and complex stress functions. Fracture parameters of a surface crack in a

graded medium were evaluated under the action of frictional contact loadings by using the singular integral equation approach (Dag, 2001; Dag and Erdogan, 2002). Embedded horizontal cracks in isotropic (El-Borgi *et al.*, 2004) and orthotropic (El-Borgi *et al.*, 2013) graded coatings subjected to frictional Hertzian contact assumption were examined by means of the singular integral equation approach. An edge crack in a graded coating loaded by a flat rigid stamp was investigated by means of an uncoupled solution procedure based on the singular integral equation approach (Dag *et al.*, 2012). Sarikaya and Dag (2016) analytically calculated fracture parameters of a surface crack in an orthotropic half-plane whose surface was exposed to sliding frictional contact loadings.

In all the aforementioned studies, the cracks are located parallel or perpendicular to the contact surface. However, propagation of the cracks is observed to be slanted in an elastic medium which is subjected to fretting contact (Faanes, 1995; Giner *et al.*, 2014). Moreover, surface cracks may possibly initiate and propagate in any direction through a medium which is under non-symmetrical loading conditions, such as frictional contact loadings. Hence, effects of crack orientation on fracture parameters should be examined to clearly predict critical and sub-critical crack growth. The literature survey revealed that no computational or analytical studies related to inclined surface cracks in a graded medium under frictional contact has been conducted.

In this study, fracture parameters of an inclined surface crack in an elastic graded medium which is subjected to frictional sliding contact are investigated. The medium is modelled on the plane strain assumption by means of a finite element analysis software ANSYS (2013). A newly developed displacement boundary condition is imposed on the model to be able to improve the simulation capability. The shear modulus of the half-plane is graded exponentially through the thickness direction utilizing the homogeneous finite element method. In the solution of the nonlinear contact problem, the augmented Lagrange algorithm is selected. The crack tip SIFs induced from the contact stresses are calculated by using DCT. Comparisons of the results to those generated by the analytical method for vertical surface cracks (Dag, 2001) validate the accuracy of the proposed finite element procedure. Extra SIF curves are depicted as functions of crack inclination for different non-homogeneity parameters, punch location, relative crack length and friction coefficient. The striking outcome of this study indicates that the change in crack inclination have remarkable influence on the mixed mode SIFs. As a result, consideration of crack inclination in crack-contact problems is proved essential to successfully predict fracture behavior of a graded medium under frictional contact loadings.

2. Problem definition and solution method

The geometry of an inclined surface crack in a graded medium which is subjected to frictional sliding contact is depicted in Fig. 1. The surface of the graded medium is loaded by a rigid flat punch whose end points are located at $y = b$ and $y = c$. Coulomb's dry friction is assumed to exist between the rigid punch and the medium surface. Exponential shear modulus gradation is introduced through the thickness direction considering Poisson's ratio as a constant (Dag, 2001; Dag and Erdogan, 2002)

$$\mu(x) = \mu_0 \exp(\gamma x) \quad (2.1)$$

where μ_0 and γ represent the shear modulus at the surface ($x = 0$) and the non-homogeneity parameter, respectively. Thus, constitutive relations for the graded medium can be stated as

$$\varepsilon = \exp(-\gamma x) \mathbf{S} \sigma \quad (2.2)$$

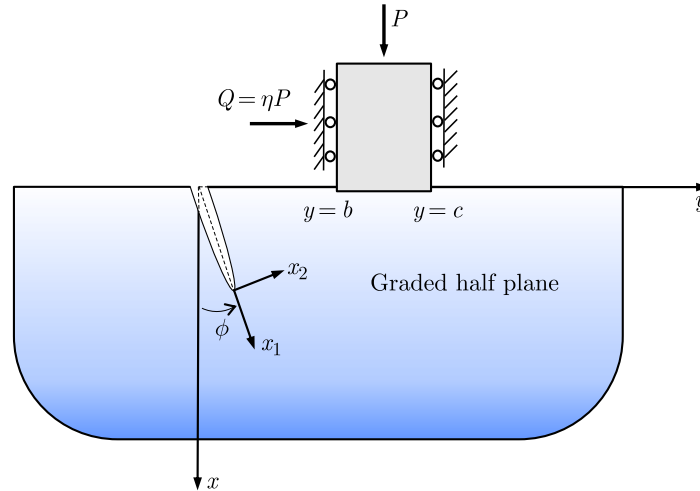


Fig. 1. Problem configuration

where \mathbf{S} , $\boldsymbol{\varepsilon}$ and $\boldsymbol{\sigma}$ respectively stand for the compliance matrix, strain vector and stress vector in the global coordinate system xy . The stress and strain vectors can be written explicitly as

$$\boldsymbol{\varepsilon} = [\varepsilon_{xx}, \varepsilon_{yy}, \varepsilon_{zz}, \varepsilon_{yz}, \varepsilon_{xz}, \varepsilon_{xy}]^T \quad \boldsymbol{\sigma} = [\sigma_{xx}, \sigma_{yy}, \sigma_{zz}, \sigma_{yz}, \sigma_{xz}, \sigma_{xy}]^T \quad (2.3)$$

Isotropic materials have an infinite number of elastic symmetry planes and possess two independent material properties. The compliance matrix in Eq. (2.2) can be expressed in terms of the shear modulus μ_0 and Poisson's ratio ν as follows (Jones, 1998)

$$\mathbf{S} = \begin{bmatrix} C_1 & C_2 & C_2 & 0 & 0 & 0 \\ C_2 & C_1 & C_2 & 0 & 0 & 0 \\ C_2 & C_2 & C_1 & 0 & 0 & 0 \\ 0 & 0 & 0 & C_1 - C_2 & 0 & 0 \\ 0 & 0 & 0 & 0 & C_1 - C_2 & 0 \\ 0 & 0 & 0 & 0 & 0 & C_1 - C_2 \end{bmatrix} \quad (2.4)$$

where

$$C_1 = \frac{1}{2(1+\nu)\mu_0} \quad C_2 = -\frac{\nu}{2(1+\nu)\mu_0}$$

Constitutive relations can be restated for plane elasticity in the local coordinate system x_1x_2 which is defined at the crack tip

$$\begin{Bmatrix} \varepsilon_{11} \\ \varepsilon_{22} \\ 2\varepsilon_{12} \end{Bmatrix} = \exp[-\gamma(x_1 + a) \cos \phi] \begin{bmatrix} s_{11} & s_{12} & s_{16} \\ s_{21} & s_{22} & s_{26} \\ s_{61} & s_{62} & s_{66} \end{bmatrix} \begin{Bmatrix} \sigma_{11} \\ \sigma_{22} \\ \sigma_{12} \end{Bmatrix} \quad (2.5)$$

where a , ϕ and s_{ij} ($i, j = 1, 2, 6$) represent length of the surface crack, crack inclination angle and compliance coefficients, respectively. The compliance coefficients for the plane stress case read

$$\begin{aligned} s_{11} &= s_{22} = C_1 & s_{12} &= C_2 \\ s_{16} &= s_{26} = 0 & s_{66} &= 2(C_1 - C_2) \end{aligned} \quad (2.6)$$

The compliance coefficients for the plane strain case are defined below

$$\begin{aligned} s_{11} &= s_{22} = \frac{C_1^2 - C_2^2}{C_1} & s_{12} &= \frac{C_2(1 - C_2)}{C_1} \\ s_{16} &= s_{26} = 0 & s_{66} &= 2(C_1 - C_2) \end{aligned} \quad (2.7)$$

Analytical expressions of the opening mode (mode I) and the shearing mode (mode II) SIFs are given as follows (Perez, 2004)

$$K_I = \lim_{x_1 \rightarrow 0^+} \sqrt{2\pi(x_1 - a)\sigma_{22}(x_1, 0)} \quad K_{II} = \lim_{x_1 \rightarrow 0^+} \sqrt{2\pi(x_1 - a)\sigma_{12}(x_1, 0)} \quad (2.8)$$

In order to calculate SIFs through Eq. (2.8), one should determine the asymptotic stress expressions by conducting a heavy solution procedure based on the singular integral equation approach (Dag, 2001; Dag and Erdogan, 2002). On the other hand, SIFs can be calculated via DCT with a high level of accuracy within a properly constructed finite element model. DCT utilizes nodal displacements around crack tip which are computed through FEM (Kim and Paulino, 2003)

$$K_I = \frac{1}{8} \sqrt{\frac{2\pi}{\Delta a}} \frac{4V_1 - V_2}{s_{22} \exp[-\gamma a \cos \phi]} \quad K_{II} = \frac{1}{8} \sqrt{\frac{2\pi}{\Delta a}} \frac{4U_1 - U_2}{s_{11} \exp[-\gamma a \cos \phi]} \quad (2.9)$$

where

$$\begin{aligned} U_1 &= u_1(N_1) - u_1(N_3) & U_2 &= u_1(N_2) - u_1(N_4) \\ V_1 &= u_2(N_1) - u_2(N_3) & V_2 &= u_2(N_2) - u_2(N_4) \end{aligned} \quad (2.10)$$

where N_j ($j = 1, \dots, 4$) are the nodes around the crack tip, which are depicted in Fig. 2. Δa represents the characteristic length of the crack tip elements. u_1 and u_2 are the displacement components defined through x_1 and x_2 directions, respectively.

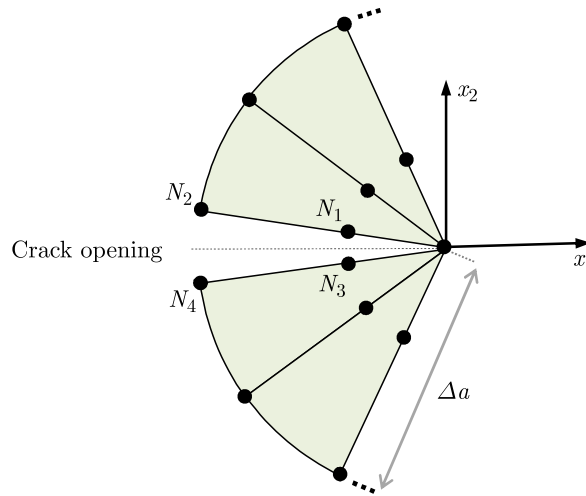


Fig. 2. Nodes on crack tip elements, $\Delta a/a = 1/40000$

The finite element model (as seen in Fig. 3) possesses boundaries on the contrary to the original half-plane problem. B , H and W represent width of the flat punch, height of the model and width of the model, respectively. The ratios B/H and B/W are selected sufficiently small that they do not have any effect on the contact stresses and crack tip parameters.

When the side-lines (lines 1 and 2) of the model are set free, they experience some displacements under the effect of frictional contact stresses leading to incorrect crack tip parameters. These adverse displacement effects are observed to be still active, even if the model is chosen to be very large compared to the crack/contact region. Hence, the effect of side-line displacements on the crack-contact region should be neutralized in order to satisfactorily simulate the half-plane problem. If line 1 and line 2 are forced to undergo the same horizontal displacements under the effect of contact stresses, the behavior of the surface crack can be retrieved from the side-line effects to a certain degree.

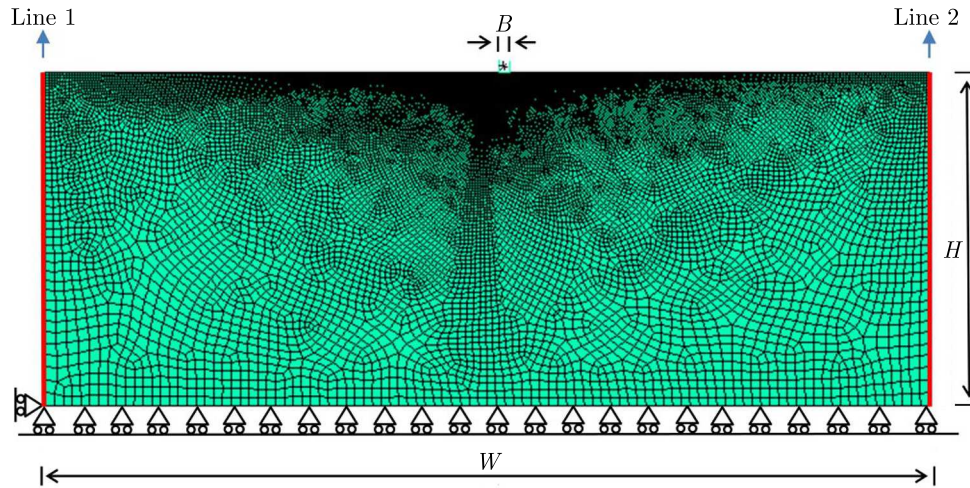


Fig. 3. Finite element model, $B/H = 1/30$, $B/W = 1/80$, $\phi = -30^\circ$

The following displacement boundary condition is imposed on the side-lines of the model which increases the simulation capability of the model

$$v\left(x, -\frac{W}{2}\right) = v\left(x, \frac{W}{2}\right) \quad 0 < x < H \quad (2.11)$$

where $v(x, y)$ stands for the displacement component in the horizontal y -direction. To enable the boundary condition in Eq. (2.11), line 1 and line 2 are discretized with the same degree of mesh refinement. Hence, these lines acquire an equal number of nodes which are exactly at the same x -locations as illustrated in Fig. 4. The y -component displacements of the nodes that locate at the same x -coordinates are equalized by inserting a subroutine into the ANSYS code. Thus Eq. (2.11) is treated in terms of the nodal displacements as

$$v(N_{1k}) = v(N_{2k}) \quad k = 1, 2, 3, \dots, p \quad (2.12)$$

where N_{ik} represents the number of the nodes along line 1 and line 2 as depicted in Fig. 4. p and d_k respectively stand for the total number of the nodes and the vertical distances between consecutive nodes on each of line 1 and line 2.

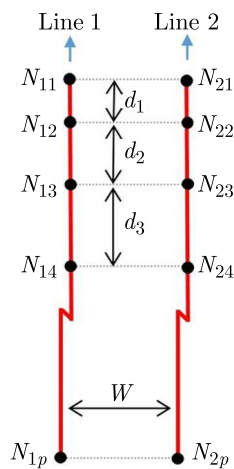


Fig. 4. Nodes on the side lines of the finite element model

As seen in Fig. 3, x -component displacement of the bottom line is restricted to zero, and the node located at the left-bottom corner is entirely fixed.

The plane strain assumption is considered in the model which is meshed by using a total of 219030 8-noded quadrilateral and 6-noded triangular finite elements. Throughout the meshing operation, a 6-noded triangular finite element is obtained by combining 3 nodes of an 8-noded quadrilateral finite element at a single point. The crack tip is discretized by using 48 regularly oriented triangular finite elements as shown in Fig. 5. The mid-side nodes of the crack tip elements (see Fig. 2) are positioned at a quarter of the radius of the crack tip elements. The crack tip SIFs are evaluated by means of Eq. (2.9) which makes use of nodal displacements around the crack tip.

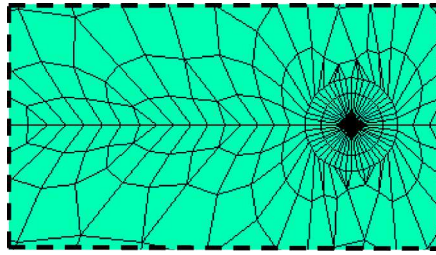


Fig. 5. Finite element mesh of the crack tip

Since contact stresses and contact surfaces are both unknown, contact mechanics problems involve a severe non-linearity. Due to this fact, finite element solutions of frictional contact problems are conducted by using step-by-step iterative procedures. The selected procedure in this study is the augmented Lagrange algorithm, in which consecutive equilibrium iterations are performed per increment of the normal and frictional forces. The details of the algorithm can be seen in the review paper by Mijar and Arora (2004). In the finite element model, three rigid target elements are used to represent rigid surfaces of the flat punch. The contact surface of the elastic medium is finely meshed using 300 contact line elements in order to get sharp variations of the contact stresses. The contact line elements are constructed by the three nodes of underlying solid elements (ANSYS, 2013). The Gauss integration points on the contact line elements are attributed as the contact detection points.

In the previous finite element studies related to graded structures, gradations of material properties through spatial coordinates are provided by using the graded finite element method and the homogeneous finite element method. In the graded finite element method (Santare and Lambros, 2000), the material properties are specified at the Gauss integration points of each finite element. However, in the homogeneous finite element method, the material properties are computed at the centroid. In the theoretical solutions for the contact and fracture mechanics problems of graded structures, utilization of the homogeneous finite element method yields highly accurate results (Dag *et al.*, 2007, 2009; Arslan, 2017). Hence, in this study, the shear modulus gradation through the thickness direction is introduced by using the homogeneous finite element method.

3. Numerical results

In this Section, validity of the present procedure is revealed comparing the results to those generated by an analytical method (Dag, 2001) for a vertical surface crack ($\phi = 0^\circ$). Moreover, some curves of the mixed mode SIFs as functions of the crack inclination ϕ are presented for different problem parameters.

As depicted in Fig. 1, complete frictional contact occurs between the flat rigid stamp and the surface of a graded medium which involves an inclined surface crack. η stands for the Coulomb friction coefficient prevailing between the FGM surface and the flat stamp. The locations $y = b$

and $y = c$ at the contact surface are called the trailing and leading ends of the contact zone, respectively.

Before going through the details of numerical results, it is beneficial to elaborate on the normalizations that are taken into account. The normalized non-homogeneity parameter, relative punch location and relative crack length are represented as γa , b/a , $a/(c-b)$, respectively. Note that the elastic medium is homogeneous when $\gamma a = 0$ and, shear modulus of the elastic medium increases in the positive x -direction when $\gamma a > 0$. In addition, normalizations of mode I (K_I) and mode II (K_{II}) SIFs at the crack tip are defined as

$$K_{In} = \sqrt{\frac{a}{\pi}} \frac{K_I}{P} \quad K_{II n} = \sqrt{\frac{a}{\pi}} \frac{K_{II}}{P} \quad (3.1)$$

Note that negative mode I (K_I) SIF results are not valid, and the negativity reveals that the crack closure occurs. However, these negative results are still useful and applicable in consideration of some problems including remote loading (Dag and Erdogan, 2002). Hence, in literature, negative K_I results have been presented in parametric analysis of crack/contact problem solutions (Dag, 2001; Dag and Erdogan, 2002; Sarikaya and Dag, 2016).

Figure 6 reveals comparisons of the results to those evaluated analytically by Dag (2001) for vertical surface cracks ($\phi = 0^\circ$). The comparisons are depicted for the combinations of two different normalized non-homogeneity parameters γa and four different friction coefficients η . As can be observed in this figure, excellent agreement between the analytical (Dag, 2001) and present results is attained in each case, which indicates the validity and reliability of the present finite element solution.

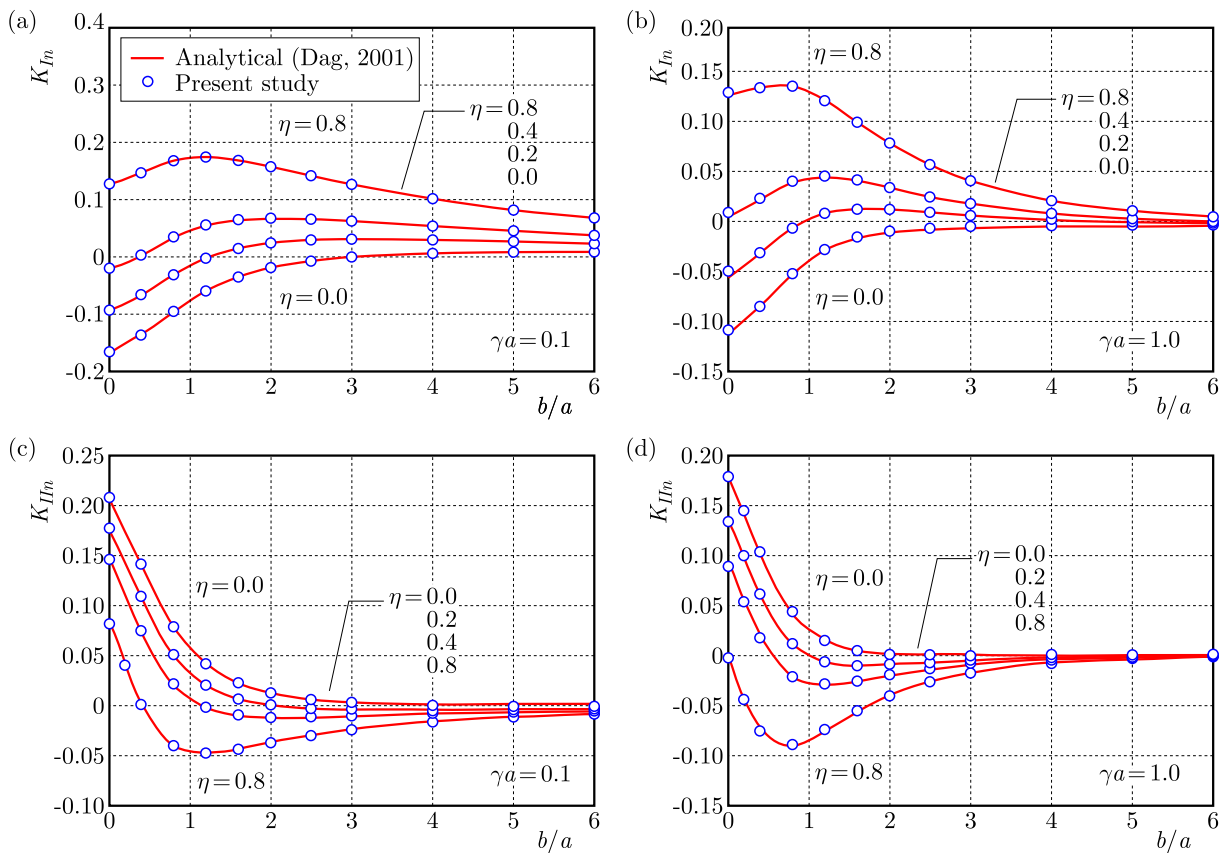


Fig. 6. Comparisons to the analytical results obtained by Dag (2001) for a graded isotropic half plane for $\nu = 0.25$, $a/(c-b) = 1.0$, $\phi = 0^\circ$; (a) K_{In} , $\gamma a = 0.1$, (b) K_{In} , $\gamma a = 1.0$, (c) $K_{II n}$, $\gamma a = 0.1$, (d) $K_{II n}$, $\gamma a = 1.0$

Figure 7 illustrates deformed shape of the graded medium for $a/(c-b) = 1.0$, $b/a = 1.0$, $\phi = -30^\circ$, $\eta = 0.4$, $\nu = 0.25$, and $\gamma a = 1.0$. Mesh densities on the crack-contact region can be seen in this figure, and the surface crack is observed to be opened under the action of frictional contact loading. Figure 8 reveals the effect of normalized non-homogeneity parameter γa on the curves of normalized mixed-mode SIFs versus the inclination angle ϕ . Examining Fig. 8a, when the normalized non-homogeneity parameter γa is increased from 0.1 to 1.0, K_{In} decreases for $\phi < 0^\circ$, however increases for $\phi > 0^\circ$. Note that the crack closure ($K_{In} = 0$) occurs at higher inclination angles ϕ , as γa is increased from 0.1 to 1.0. Observing Fig. 8b, when γa is increased from 0.1 to 1.0, K_{IIIn} has an decreasing trend in the range $-20^\circ < \phi < 60^\circ$. However, this trend is reversed in the range $-60^\circ < \phi < -20^\circ$. Also note that the absolute value of K_{IIIn} is critical in design, not its sign.

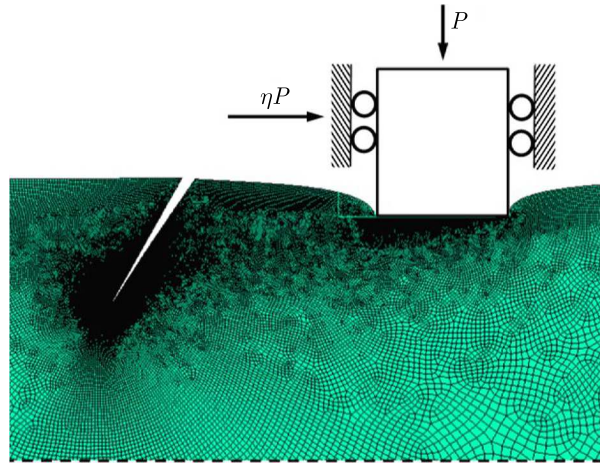


Fig. 7. Deformed shape of the crack-contact region, $\nu = 0.25$, $a/(c-b) = 1.0$, $b/a = 1.0$, $\phi = -30^\circ$, $\eta = 0.4$, $\gamma a = 1.0$

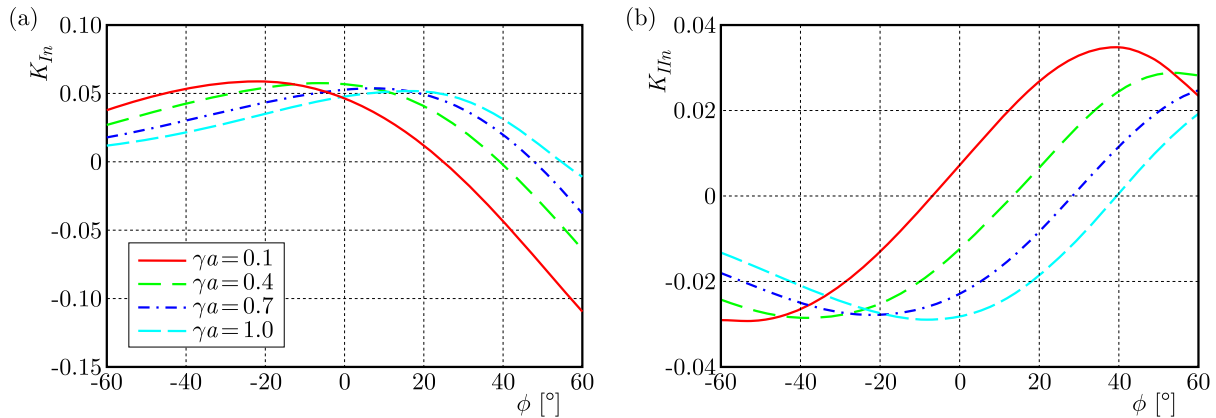


Fig. 8. Effect of normalized non-homogeneity parameter on normalized mode I (a) and mode II (b) SIFs, $\nu = 0.25$, $a/(c-b) = 1.0$, $b/a = 1.0$, $\eta = 0.4$

Figure 9 demonstrates the plots of normalized mixed-mode SIFs at the crack tip versus the inclination angle ϕ for different coefficients of friction η . When the coefficient of friction is increased from 0.0 to 0.8, K_{In} elevates and K_{IIIn} decreases significantly. Note that the crack seems closed for $\eta < 0.2$. In Fig. 10, the normalized mixed-mode SIFs at the crack tip are plotted versus the inclination angle ϕ for different relative crack lengths $a/(c-b)$. As seen in Fig. 10a, K_{In} increases remarkably when $a/(c-b)$ is decreased from 5.0 to 0.66 for $\phi > 0$. When $\phi < 0$, K_{In} is not considerably affected by the change in $a/(c-b)$. Moreover, the crack closure seems to occur at higher inclination angles ϕ , as $a/(c-b)$ is decreased from 5.0 to 0.66. As displayed

in Fig. 10b, when $a/(c-b)$ is decreased from 5.0 to $0.6\bar{6}$, K_{IIIn} decreases for $\phi > 0$ and elevates for $\phi < 0$.

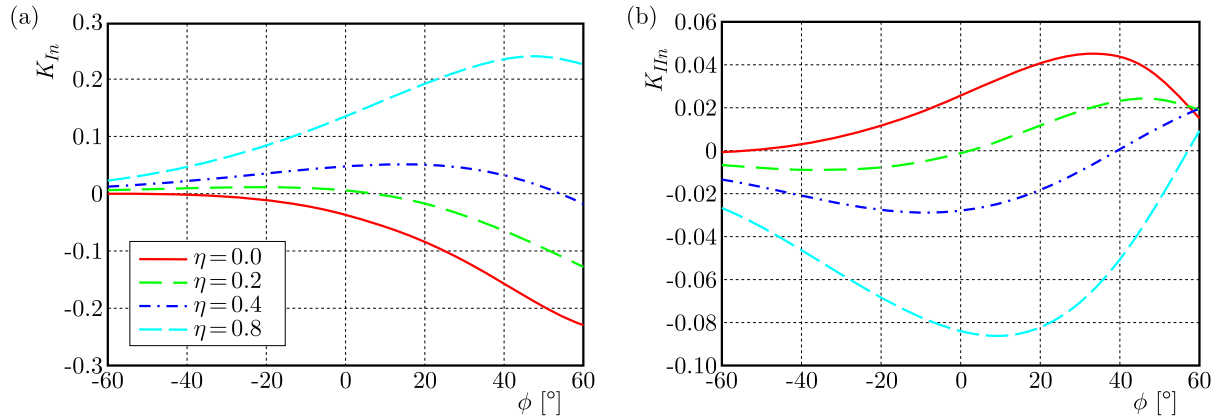


Fig. 9. Effect of friction on normalized mode I (a) and mode II (b) SIFs, $\nu = 0.25$, $a/(c-b) = 1.0$, $b/a = 1.0$, $\gamma a = 1.0$

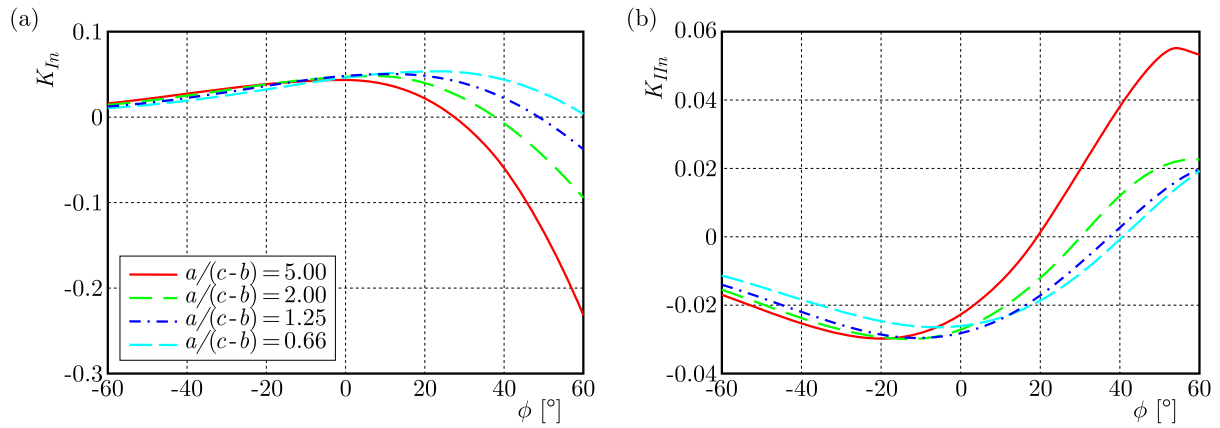


Fig. 10. Effect of relative crack length $a/(c-b)$ on normalized mode I (a) and mode II (b) SIFs, $\nu = 0.25$, $b/a = 1.0$, $\gamma a = 1.0$, $\eta = 0.4$

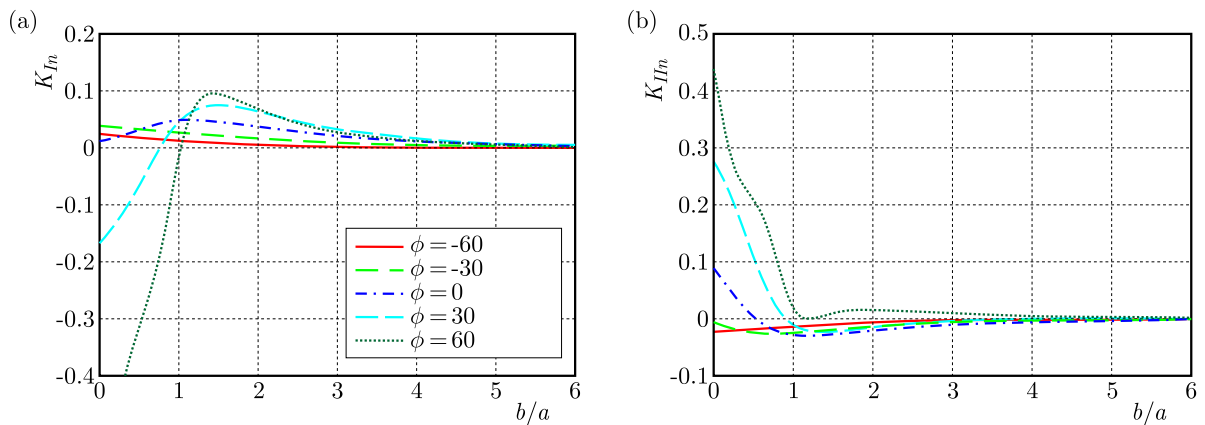


Fig. 11. Variations of normalized mode I (a) and mode II (b) SIFs versus the normalized punch location b/a for different crack inclinations, $\nu = 0.25$, $a/(c-b) = 1.0$, $\gamma a = 1.0$, $\eta = 0.4$

Figure 11 illustrates the plots of normalized mixed-mode SIFs at the crack tip versus the normalized punch location b/a for different crack inclination angles ϕ . As seen in Fig. 11a, K_{In} reaches the local extremum when b/a is between 1.0 and 2.0 for $0 \leq \phi \leq 60$. In this range

of b/a , magnitude of K_{In} elevates significantly when the inclination angle ϕ is increased from -60° to 60° . It can be also inferred from Fig. 11a that the crack is substantially closed ($K_{In} < 0$) for $\phi \geq 30^\circ$ in the range $0 < b/a < 1.0$.

4. Conclusions

In literature, an analytical solution for a vertical surface crack problem in a graded medium subjected to frictional contact is available. In this study, the problem is extended computationally concerning different orientations of the surface crack to investigate fracture behavior of graded continua in a more insightful manner. The graded semi-infinite medium which is loaded by a flat rigid punch is simulated with a finite element model considering a particular displacement boundary condition. The plane strain assumption is taken into account in the model. The solutions of contact and crack problems are managed employing the augmented Lagrange algorithm and DCT, respectively. Comparisons of the results to those evaluated by an analytical technique for a vertical surface crack verify the accuracy of the present finite element approach. Further numerical results enlighten the behavior of the surface cracks for different problem parameters, which can be utilized efficiently in design and optimization. For instance, variation in material gradation has a changing effect on the crack tip parameters as the inclination angle ϕ alters. For the surface cracks possessing negative inclination ($\phi < 0$), the degree of gradation can be increased to suppress mode I type crack propagation. However, for surface cracks having positive inclination ($\phi > 0$), the risk of mode I type failure may arise as the degree of gradation is increased. The risk of mode I failure seems existing especially for $\eta > 0.2$. For the surface cracks having negative inclination ($\phi < 0$), the risks of mode II type failure can be alleviated substantially by increasing the contact length. However, for the surface cracks having positive inclination ($\phi > 0$), the risk of mode I type crack propagation can be mitigated upon decreasing the contact length.

To conclude: effects of the problem parameters on the crack tip SIFs are shown to be altered significantly with the variation in crack orientation ϕ , which is the main outcome of this study. Hence, investigation of the crack tip parameters only for vertical cracks is shown to be insufficient and, therefore, surface crack problems should be examined by taking the crack orientation into account to be able to clearly predict the critical and sub-critical surface crack growth in graded structures subjected to frictional contact loadings. A new displacement boundary condition is also proposed to improve the computational modelling of crack/contact problems.

References

1. ANSYS Inc., 2013, Ansys Basic Analysis Procedures Guide – Release 15, Ansys Inc., Canonsburg
2. ARSLAN O., 2017, Computational contact mechanics analysis of laterally graded orthotropic half-planes, *World Journal of Engineering*, **14**, 145-154
3. DAG S., 2001, Crack and contact problems in graded materials, Ph.D. Thesis, Lehigh University, Bethlehem
4. DAG S., APATAY T., GULER M.A., GULGEC M., 2012, A surface crack in a graded coating subjected to sliding frictional contact, *Engineering Fracture Mechanics*, **80**, 72-91
5. DAG S., ERDOGAN F., 2002, A surface crack in a graded medium loaded by a sliding rigid stamp, *Engineering Fracture Mechanics*, **69**, 1729-1751
6. DAG S., GULER M.A., YILDIRIM B., OZATAG A.C., 2009, Sliding frictional contact between a rigid punch and a laterally graded medium, *International Journal of Solids and Structures*, **46**, 4038-4053

7. DAG S., YILDIRIM B. AND SARIKAYA D., 2007, Mixed-mode fracture analysis of orthotropic functionally graded materials under mechanical and thermal loads, *International Journal of Solids and Structures*, **44**, 7816-40
8. EL-BORGI S., KEER L., WISSEM B.S., 2004, An embedded crack in a functionally graded coating bonded to a homogeneous substrate under frictional Hertzian contact, *Wear*, **257**, 760-776
9. EL-BORGI S., KEER L., WISSEM B.S., 2013, An embedded crack in a functionally graded orthotropic coating bonded to a homogeneous substrate under frictional Hertzian contact, *International Journal of Solids and Structures*, **50**, 3898-3910
10. FAANES S., 1995, Inclined cracks in fretting fatigue, *Engineering Fracture Mechanics*, **80**, 6, 71-82
11. GINER E., SABSABI M., RODENAS J.J., FUENMAYOR F.J., 2014, Direction of crack propagation in a complete contact fretting-fatigue problem, *International Journal of Fatigue*, **58**, 172-180
12. HASEBE N., OKUMURA M., NAKAMURA T., 1989, Frictional punch and crack in plane elasticity, *Journal of Engineering Mechanics*, **115**, 6, 1137-1149
13. HILLS D.A., NOWELL D., SACKFIELD A., 1993, *Mechanics of Elastic Contacts*, Butterworth-Heinemann, London
14. JITCHAROEN J., PADTURE N.P., GIANNAKOPOULOS A.E., SURESH S., 1998, Hertzian-Crack suppression in ceramics with elastic-modulus-graded surfaces, *Journal of the American Ceramic Society*, **81**, 9, 2301-2308
15. JONES R.M., 1998, *Mechanics of Composite Materials*, Taylor & Francis, Philadelphia
16. KIM J-H., PAULINO G.H., 2003, Mixed-mode J-integral formulation and implementation using graded elements for fracture analysis of nonhomogeneous orthotropic materials, *Mechanics of Materials*, **35**, 107-128
17. LAWN B., 1998, Indentation of ceramics with spheres: a century after Hertz, *Journal of the American Ceramic Society*, **81**, 8, 1977-1994
18. MIJAR A.R., ARORA J.S., 2004, An augmented Lagrangian optimization method for contact analysis problems, 1: formulation and algorithm, *Structural Multidisciplinary Optimization*, **28**, 99-112
19. PEREZ N., 2004, *Fracture Mechanics*, Kluwer Academic Publishers, Boston
20. SANTARE M.H., LAMBROS J., 2000), Use of graded finite elements to model behavior of nonhomogeneous materials, *Journal of Applied Mechanics*, **67**, 819-822
21. SARIKAYA D., DAG S., 2016, Surface cracking in an orthotropic medium subjected to frictional contact, *International Journal of Solids and Structures*, **90**, 1-11
22. SURRESH S., 2001, Graded materials for resistance to contact deformation and damage, *Science*, **292**, 5526, 2447-2451
23. ZHANG Y., 2012, Overview: damage resistance of graded ceramic restorative materials, *Journal of the European Ceramic Society*, **32**, 11, 2623-2632

XFEM SIMULATION OF THE INFLUENCE OF CRACKING INTRODUCED BY PRE-LOADING ON THE STRENGTHENING OF A CEMENT TREATED MIXTURE

KAROL BRZEZIŃSKI

*Warsaw University of Technology, Faculty of Civil Engineering, Institute of Roads and Bridges, Warsaw, Poland
e-mail: k.brzezinski@il.pw.edu.pl*

The paper attempts to explain the phenomenon of a static strength increase due to the previous cyclic loading. Finite Element Method simulation of the potential strengthening mechanism is presented. The crack growth is controlled by the energy criterion used in the linear fracture theory. A wedge splitting test has been performed in order to determine the critical energy release rate of the tested mixture G_{IC} . It was observed that the appearance of additional cracks in the material may lead to an increase of its strength. Analysis of the tensile stress distribution allows for a qualitative explanation of the observed phenomenon.

Keywords: fatigue life, cement-treated base layers, strengthening effect, load history, XFEM

1. Introduction

The fatigue strength is an important aspect of estimating durability of many types of structures subjected to cyclic loadings. Particularly, road pavement structures, which are often subject to many millions of load cycles, are designed with regard to their fatigue life. The modern approach to fatigue was initiated by Wöhler (1970). He measured fatigue strength as a feature of the material, so the number of load cycles that the structure can carry depends on the amplitude of the load. This dependency, presented later by his successor in the form of a graph, is known as the “Wöhler curve”. By using such formulas, the number of constant amplitude load cycles causing destruction of the material can be estimated.

Taking into account variable amplitude loads requires additional assumptions about fatigue accumulation. The simplest theory, the so-called linear damage accumulation model, is the Palmgren-Miner hypothesis (Miner, 1945). Based on the assumptions of this theory, the durability of the structure does not depend on the order of the applied load with a variable amplitude. As shown in the literature, the impact of load history can be so significant that we overestimate or underestimate the fatigue life by up to 4 times (Bijak-Żochowski *et al.*, 1999). Accurate assessment of the load amplitude order is the subject of many hypotheses (Brzeziński and Zbiciak, 2014; Fatemi and Yang, 1998; Marco and Starkey, 1954; Xi and Songlin, 2009; Zhao *et al.*, 2014).

In particular, the results of the research conducted by Koba (2000) show that samples of cement-treated soil subjected to a pre-load exhibit a much higher fatigue strength. Furthermore, an increase in the static strength was also observed. Based on the above observations, the fatigue hypothesis has been developed. The hypothesis takes into account the impact of the history on the fatigue of cement-treated soils (Brzeziński and Zbiciak, 2014). In contrast to the previously mentioned criteria, the proposed hypothesis assumes that the static strength also varies due to the cyclic loading. This approach allows for the modeling of strengthening as well as the weakening of fatigue strength, depending on the applied preload. This hypothesis led to the onset of the research concerning changes in static strength of cement-treated mixtures used in road pavement structures (Brzeziński *et al.*, 2017).

This paper attempts to explain the phenomenon of static strength increasing by the previous cyclic loading. The change of the mechanical properties of the loaded sample is undoubtedly related to changes in the structure and microstructure of cementitious materials (e.g. cracks and micro-cracks). An effective method for detecting and locating the cracks within the sample is acoustic detection (Landis and Shah, 1995; Moczko, 1996, Ohtsu, 1996). Formation and merging of micro-cracks usually results in degradation of the material or even destruction of the structure. However, in some cases the increase in density of dislocation may be responsible for an increase in the fracture toughness (Ritchie, 1999). The knowledge of changes in the internal structure of the material allows for a better understanding of the investigated phenomena. However, a quantitative approach requires an appropriate research. In this work, Finite Element Analysis (FEM) analysis is used in order to explain how cracks formed during cyclic loading can cause strengthening of the sample.

2. Microstructure changes under cyclic loads

The change in static strength of a material as a result of the cyclic loading can be explained by transformation of its internal structure. This phenomenon is easier to observe and investigate in more homogeneous materials (e.g. metal alloys). In the case of composite materials, this is a much more difficult task. The internal structure is much more heterogeneous, and mechanical properties depend on characteristics of individual components and the ratio between them.

The polycrystalline grain structure is significantly different from crystal in its ideal form, which is due to numerous defects which significantly affect mechanical properties of the material. The analysis of the influence of dislocations on the mechanical properties of the material is promising. Especially, since dislocations may be introduced into the material by cyclic pre-loading. Due to their presence, the stress required to produce plastic deformation is 10^3 - 10^4 times smaller than that of the ideal crystal (Wawszczuk, 2012). The energy supplied during the cyclic loading may turn into potential energy of misalignment. Furthermore, during long-term operation, the amount of dislocation may increase. Initially, it facilitates slipping. However, when the number of dislocations increases, they block each other, so that their movement (and hence the slip phenomenon) is impeded. In such a situation, strengthening is observed, in the case of metal alloys represented as the increase of the yield point (Moćko and Kowalewski, 2014). In brittle materials, such as cement-treated mixtures, different types of imperfections usually cause strength reduction. However, in some cases, the strengthening effect may occur. The strengthening mechanism at the dislocation level can be explained by the fact that they impede propagation and joining of micro-cracks by cutting the path of their potential development. In this way, they can eliminate critical cracks that would otherwise damage the structure.

The micro-cracks can have a similar influence on the material in the process of static strength changing. The accumulation of micro-cracks in the structure is usually causing weakening of the material because over time it merges into larger cracks and eventually results in destruction of the structure. On the other hand, differently oriented micro-cracks can make propagation of the dominant crack difficult, thus increasing the static or fatigue strength of the structure.

As mentioned above, observing such a phenomenon in the case of cement-bond materials is much more difficult due to heterogeneity of the structure. In addition, the critical element is the cement matrix which is a small part of the material volume. Therefore, the effects observed are much less marked. In spite of this, detection of dislocation motion in cement matrix materials is possible. Studies conducted by Kyriazopoulos *et al.* (2011) showed the possibility of detecting dislocation by recording the flow of small electrical charges generated in the material. Another method of observation of changes occurring inside the materials during load application is the method of acoustic detection (Landis and Shah, 1995; Moczko, 1996, Ohtsu, 1996). The energy

released during micro-cracking or dislocation motion causes a sound wave propagating in the sample. The analysis of the signal recorded from several piezoelectric transducers located on the sample not only allows one to observe the moment of the micro-crack but also allows its localization as well as estimation of the size and direction of the slip plane.

The cracks caused by the cyclic loading may be involved in the mechanisms responsible for improving toughness of the material (Ritchie, 1999). Development of dominant cracks can be prevented if the crack tip encounters several interconnected micro-cracks. Then several crack tips are formed, which reduces the intensity factor of stresses. According to the linear fracture mechanics, based on Griffith's theory (Griffith, 1920; Prokopski, 2008), crack enlargement requires the work of forming a free surface of the crack within the body. Therefore, development of several cracks at the same time can be difficult because it requires more energy.

3. Laboratory tests

3.1. Scope of the research

The main part of the studies consists of the comparison of static strength of not pre-loaded samples and samples subjected to cyclic pre-loading. In these studies, a static change has been observed (even strengthening of the material). The preliminary results are presented in (Brzeziński *et al.*, 2017). However, in this paper, only supplementary laboratory tests related to FEM analysis will be presented. They have been conducted in order to determine the fracture energy (critical energy release rate G_{IC}) of the tested material.

3.2. Materials and preparation of samples

Quartz sand of the standard grain size (PN-EN 196-1:2006) has been used to prepare the mix. The use of this type of aggregate was intended to ensure repeatability of tests and to increase accuracy of the analysis.

The cement used for the preparation was CEM I 42.5 R Portland cement. The mass content of the cement relative to sand was 10%. The cement content in cement-bond soils should be between 4% and 10% (Rafalski, 2007), so the amount of cement used could be considered as typical. In addition, tap water was used in the amount needed to achieve optimum moisture (determined by the Proctor test).

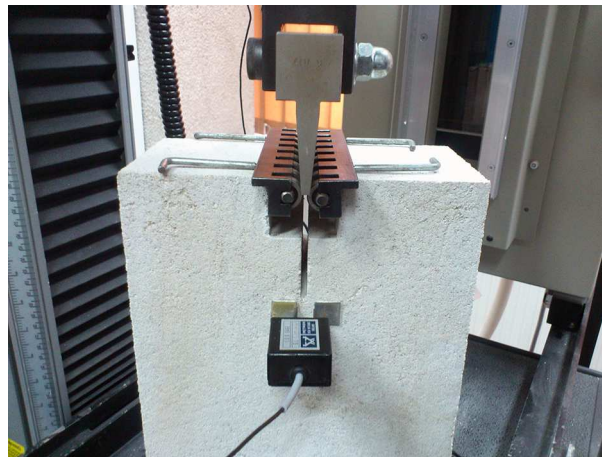


Fig. 1. Sample prepared for the Wedge Splitting Test

The primary objective of the Wedge Splitting Test (WST) is to determine the critical energy release rate G_{IC} (Brühwiler and Wittmann, 1990; Löfgren *et al.*, 2004). This parameter deter-

mines the material susceptibility to cracking and corresponds to the energy dissipated during cracking of the material. The WST is commonly used for brittle materials such as concrete (Sitek *et al.*, 2014). The test stand is shown in Fig. 1.

A sample of $20 \times 20 \text{ cm} \times 10 \text{ cm}$ rectangular shape was prepared with a proper cut allowing installation of a force application mechanism and a notch indicating the origin of the crack. Samples were made of the same mixture as the beams subjected to cyclic tests.

The wedge with an angle of $2\xi = 10^\circ$ was pushed with a constant velocity of 2 mm/s . The load was passed to the specimen via rollers located on the sides of the wedge. Every sample was subjected to a single load until it was destroyed. The vertical force F and the Crack Opening Displacement (COD) were measured during the test.

3.3. Laboratory test results

The test result is usually illustrated as a graph of the dependence of the horizontal force on the COD. The area under the graph defines its work to open the cracks W_F . The critical energy release rate is given by

$$G_{IC} = \frac{W_F}{A} \quad (3.1)$$

where W_F is the work of the force forming the crack [J], A – the area of the created crack surface [m^2].

The test was performed on 3 samples and then the results were averaged. In the FEM simulation, the average value of critical energy release rate $G_{IC} = 50.12 \text{ J/m}^2$ was used.

4. Potential strengthening effect simulation by FEM

The analysis of microstructural mechanisms capable of explaining the changes in strength, in particular the strengthening effect, allows for a more comprehensive analysis and understanding of the phenomena studied. It can improve the effectiveness of the conducted research and also help one to draw additional conclusions useful in determining the future research goals.

The FEM was used in the analysis. The influence of additional cracks in the sample on the propagation delay of the dominant crack was investigated, which might be interpreted as an increase of the static strength. It should be emphasized that the analysis performed can be considered both as simulation of the strengthening or weakening mechanism of the material. In this case, the interpretation of what is strengthening and what is weakening depends on what cracks arrangement is adopted as the reference point. Nevertheless, in order to make the analysis more readable, the reference point is the simplest cracks arrangement (single crack in the middle of the sample), which is also most unfavorable considering the strength of the sample.

4.1. Theoretical assumptions

The FEM simulation has been performed with the Abaqus® program. Advanced modeling techniques such as eXtended Finite Element Method (XFEM) or Virtual Crack Closure Technique (VCCT) were used for this purpose. Therefore, before describing the model, the basic theoretical assumptions of the mentioned techniques and their implementation in the program will be presented.

The first concept of the XFEM application, a method for simulating cracks development independently from the model grid, was presented by Belytschko and Black (1999). In the following years, this method was developed and used in numerous applications (Remmers *et al.*, 2008; Song *et al.*, 2006) and also implemented in commercial software (ABAQUS, 2013). The

idea of the method consists of enriching typical finite elements with additional shape functions that allow for discontinuity modeling and avoiding the singularity problem at the tip of the crack. The analysis is based on the linear fracture mechanics theory, so development of the crack is modeled in such a way that it propagates immediately throughout the finite element. For this reason, the above mentioned problem of singularity does not occur. The detailed description of this technique is given in (Dolbow and Belytschko, 1999).

Description of cohesive properties of the crack is the same as in the classical approach. It is based on the linear fracture theory proposed by Griffith (1920). In the VCCT criterion, deformation energy released during crack propagation by δa is calculated by assuming that it is the same as the work required to close the crack.

The crack propagation occurs when the energy released in the VCCT procedure is greater than the critical value, which can be written as follows

$$f = \frac{G_I}{G_{IC}} > 1.0 \quad (4.1)$$

where f is the condition of crack propagation, G_{IC} – critical energy release rate, G_I – energy release rate (the ratio of the released energy to the additional surface resulting from crack propagation).

When the XFEM elements are used, the crack propagation direction is independent of the mesh. Therefore, the criterion determining the crack propagation direction must be assumed. In this analysis, it is assumed that the crack will propagate perpendicular to the direction of the maximum tensile stress. These criteria require knowledge of the critical value of the energy release rate G_{IC} . It has been determined experimentally in the wedge splitting test.

The XFEM modeling technique is often referred to be as mesh independent. It should be understood that the course of the crack is not determined by the shape of the mesh. However, the solution is sensitive to size of the elements. First of all, this is obviously related to the accuracy of reflecting the state of stress in the structure. Less obvious is the impact resulting from the linear fracture mechanics. In the VCCT technique, which is used in the XFEM, the propagation of the crack occurs abruptly (each time in length determined by the mesh density). Thus, the size of the element corresponds with the characteristic crack length a , which is a component of the crack propagation criterion (Griffith, 1920). Therefore, the specified mesh density is not versatile. However, in the author's opinion, a mesh with a given characteristic density can be used to compare similar models with the same material.

4.2. Geometry and parameters of the FEM model

After conducting tests necessary to obtain characteristic material parameters of the mixture, a proper FEM model has been prepared. A 3-point bending strength test was performed. Geometry of the sample and the static scheme corresponding to the actual test were used. The load was applied in a kinematic manner. In the first simulation, the crack was applied at the bottom of the sample, at the most strained cross section. The load velocity was adjusted so that the result of the strength test simulation was similar to the results obtained in real test. Then, the effect of additional cracks occurrence on the resulting strength was analyzed.

In order to speed up the calculation, a plain stress condition was assumed. The model consisted of a small beam that was freely based on rounded supports, loaded from the top through a rounded loading nose. Geometrical invariability of the static system was ensured by boundary conditions and by defining contact between the elements (Fig. 2).

The loading nose moved in the vertical direction at a speed of 0.2 mm/s. The value of the loading force was calculated on the basis of vertical stresses in the supports. At each stage of simulation, at least one pre-fracture crack was placed at the bottom of the sample, in the most strained section. The enriched elements were used in a limited area because of practical reasons.

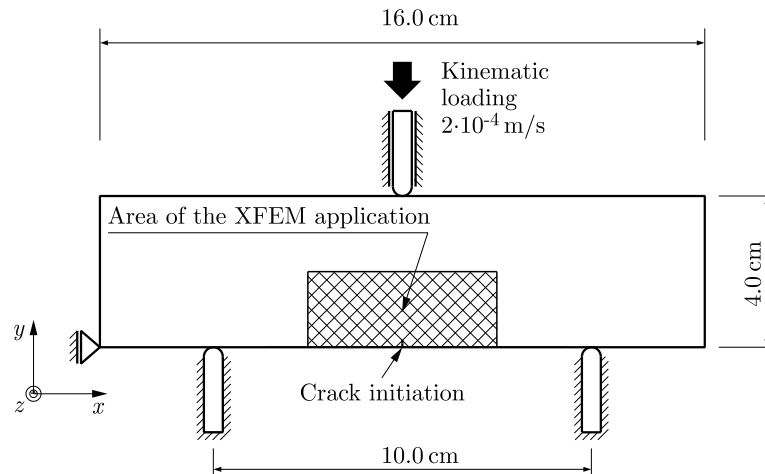


Fig. 2. The static scheme of the FEM model

Various crack configurations were adopted on the basis of the crack development presented in the paper (Landis and Shah, 1995). However, in the model crack configurations were simplified.

The linear elastic material model was applied in order to define constitutive properties of all elements. The applied values of material parameters are summarized in Table 1.

Table 1. Applied parameters of the materials

Element	Young's modulus [GPa]	Poisson's const. [-]	G_{IC} [J/m ²]
Supports and nose	210.00	0.30	–
Beam	3.50	0.25	50.12

4.3. Simulation results

The procedure of the analysis has been as follows. It was assumed that not pre-loaded elements were not cracked, so in the simulation only the initial crack was placed in the material. Therefore, in the strength test, the development of the dominant crack is not disturbed. On the other hand, in the case of pre-loaded samples, cracks and micro-cracks appeared, which might affect the development of the dominant crack. In many cases, the appearance of additional cracks might reduce the observed strength of the sample because destruction progressed easier by merging existing discontinuities. Sometimes, however, the crack propagation of the dominant crack might be difficult due to proximity to other cracks. Accordingly, the simulation of a single-cracked specimen strength test was treated as a benchmark. In the subsequent stages of analysis another crack was placed at the bottom of the sample at a distance of 4.0, 5.0 or 6.0 mm. In addition, the results of triple fracture (two additional cracks symmetrically located at a distance of 6.0 mm from the base fracture) were also compared. Figure 3 shows exemplary results of the 3-point bending tests and the simulation result of this test in the basic variant (single crack).

From Fig. 3 it can be concluded that the first step of the simulation - the strength test modeling, was performed correctly. Both the slope of the pre- and post-destruction graphs, as well as the maximum value of the stress, are very similar. Further simulations were made by adding one or two cracks. The results are shown in Fig. 4. One can see that the strength increased in all cases. The maximum increase in strength was approximately 20% (in the case of an additional crack located at a distance of 4.0 mm).

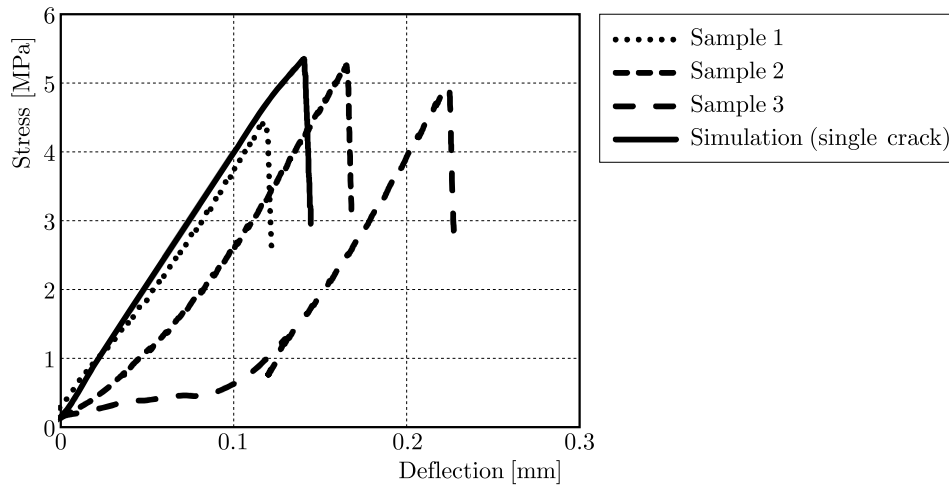


Fig. 3. Comparison of exemplary results of laboratory strength tests and FEM simulation of this test (3-point bending)

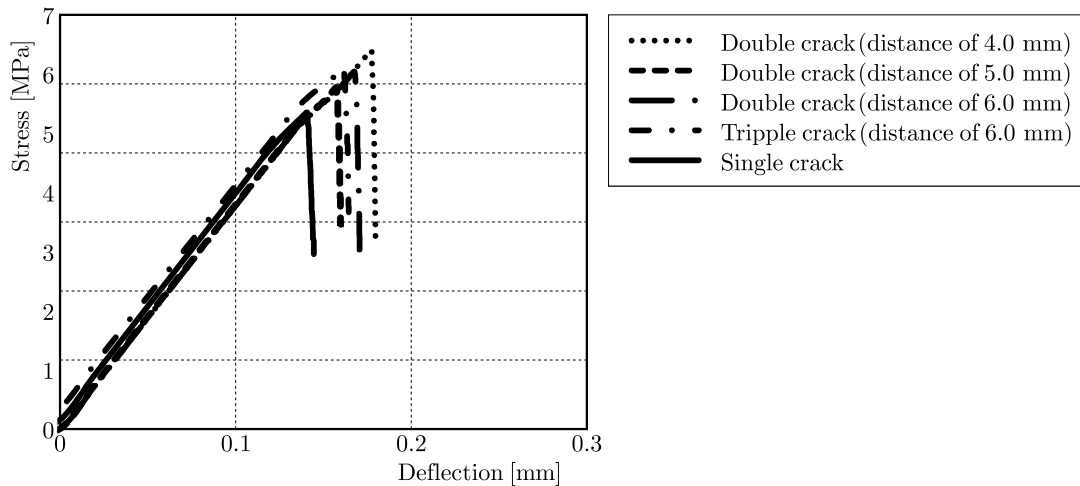


Fig. 4. Comparison of FEM simulation results of a strength test obtained by applying single pre-fracture and additional cracks at a distance of 4.0, 5.0 and 6.0 mm

A more detailed analysis of the stress state in subsequent load phases (illustrated in Figs. 5 and 6) may allow for a better understanding of the observed phenomenon. In the case of the single crack, shown in Fig. 5, general conclusions regarding the effect of crack evolution on the stress distribution in the sample can be drawn. The appearance of the initial crack at a low level of the stress (about 50%) results in reduction of the effective area of the cross-section. Certain stresses are carried between the crack edges until the critical crack mouth opening. It reflects the cohesive zone of interaction at the crack tip (Elfgren and Shah, 1991; Hillerborg, 1989). As the load increases, the gap widens until it stops carrying the stresses at all. It should be noted that the recorded force does not decrease immediately, at the time of initiation of cracks propagation. The crack is 6 mm long at the moment of the maximum stress.

The next figure (Fig. 6) shows a simulation with additional cracks located symmetrically at a distance of 6.0 mm. The introduced cracks lead to redistribution of the internal forces in the loaded sample. The additional crack forms a peculiar “cover” of the dominant crack. This phenomenon reduces tensile stresses near the dominant crack and slows its propagation. Finally, this led to an increase in the measured strength by about 14%. The development of the dominant crack is stopped and destruction is determined by propagation of one of the adjacent cracks. In all analyzed cases, the beneficial effect of the occurrence of additional cracks is observed. This is due to the fact that the reference is the single crack located in the most strained cross section. It

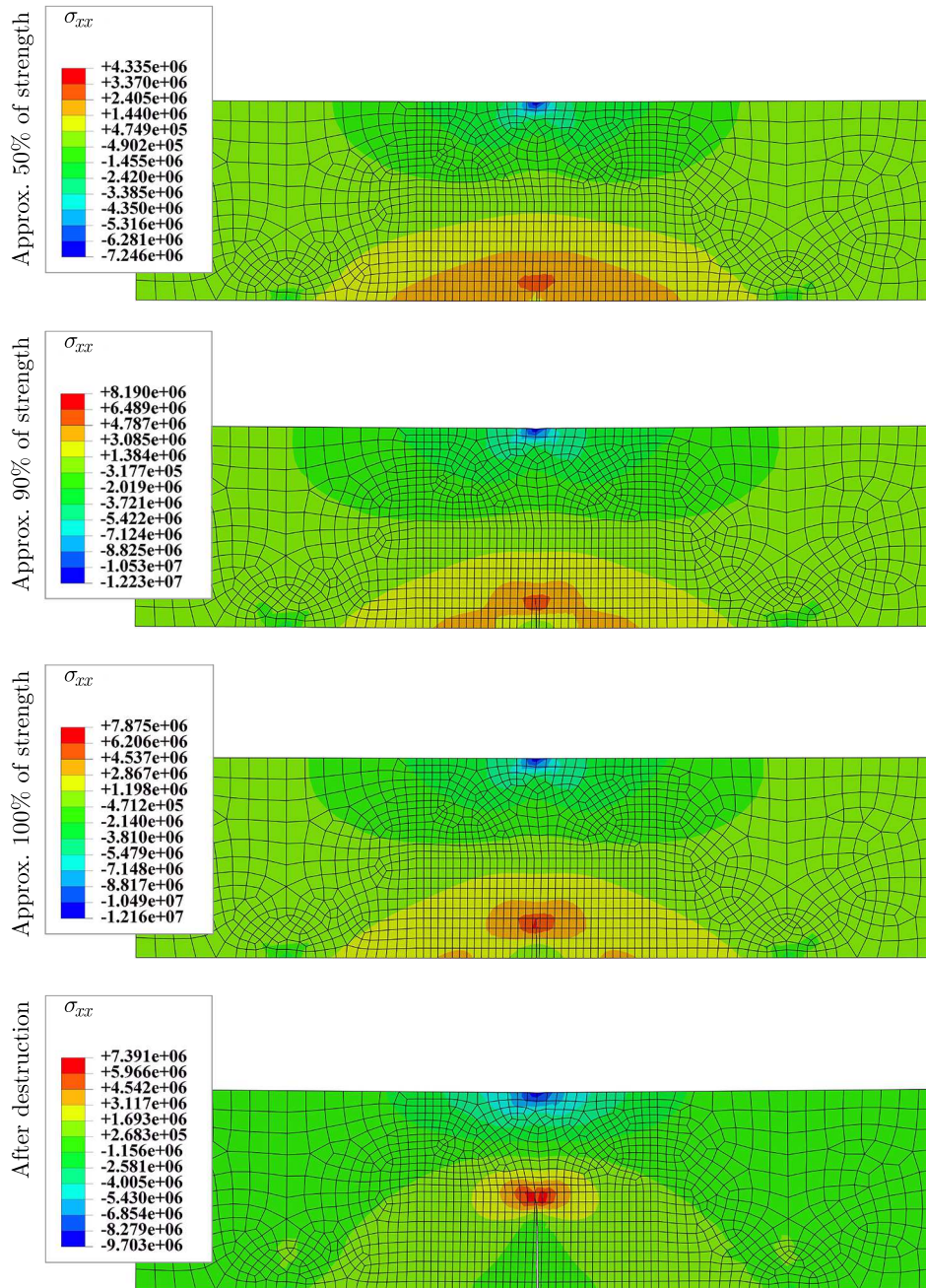


Fig. 5. Development of cracks in subsequent load phases – single cracked sample (displacement scaled 3 times)

should be noted that the maximum strengthening obtained in the simulation is approximately 2 times greater than that presented in (Brzeziński *et al.*, 2017). In fact, some individual samples tested in the laboratory showed even more than 15% increase in strength. The results presented in (Brzeziński *et al.*, 2017) have been already averaged to minimize the impact of random factors.

In order to compare stress rearrangement in different crack configurations, it is summarized in Fig. 7.

At the level of analysis it should be emphasized that the observed change of strength is a characteristic of the structure rather than the material. Nevertheless, in the phenomenological point of view, it manifests as strengthening of the material. In the case of both approaches, it is reasonable to assume that the observed increase in static strength can result into longer fatigue life.

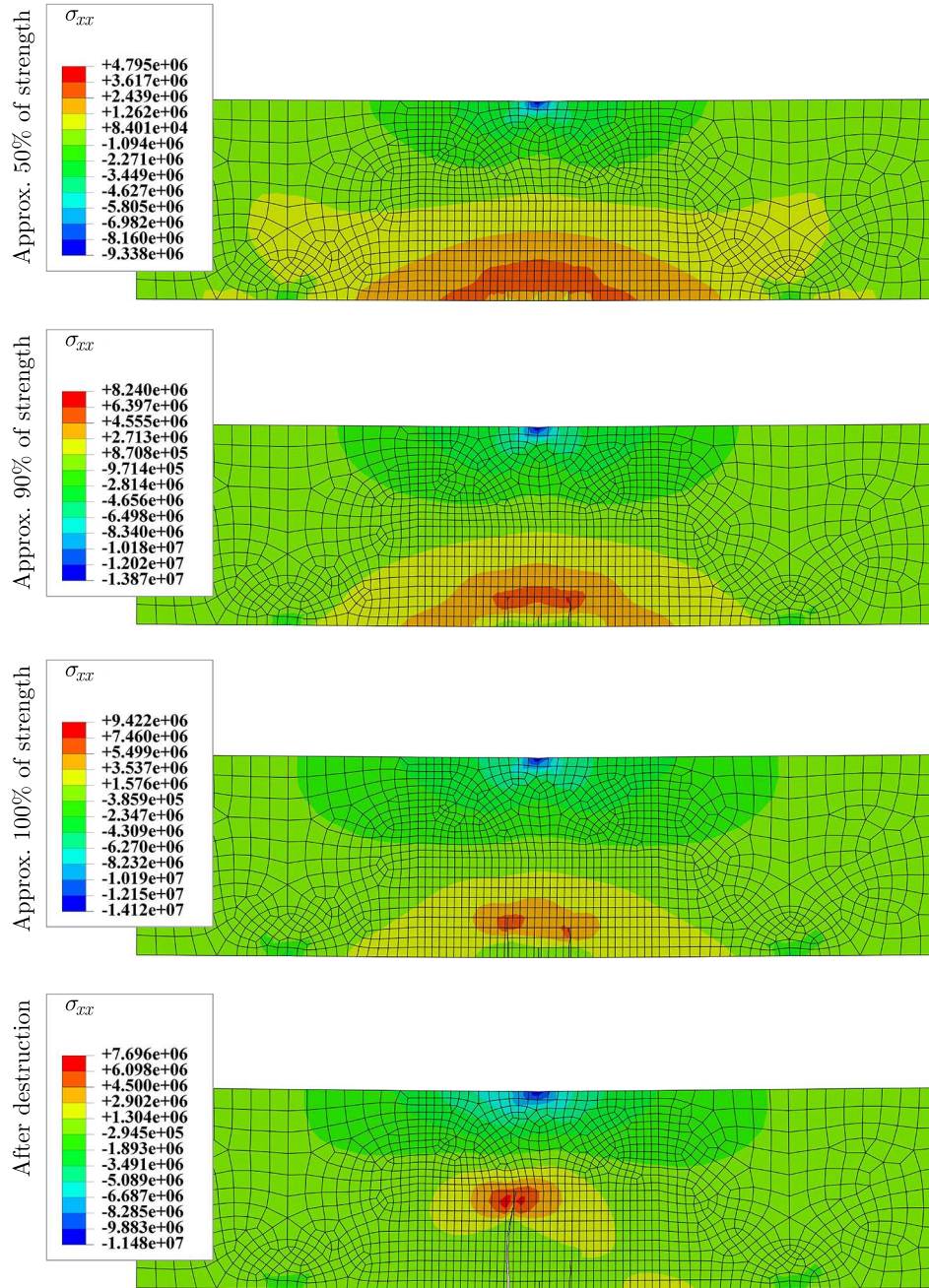


Fig. 6. Development of cracks in subsequent load phases – two additional cracks at a distance of 6.0 mm (displacement scaled 3 times)

5. Conclusions

In this paper, FEM simulation of the potential strengthening mechanism was presented. The analysis is strongly related to the theoretical considerations concerning structural changes of the material. It has been based on the modeling of the 3-point bending test performed in order to determine the strength of the material. The discontinuity modeling XFEM technique was used. The crack growth was controlled by the energy criterion used in the linear fracture theory. The implementation of the criterion in the Abaqus® program was based on the Virtual Crack Closure Technic (VCCT). In order to apply this criterion, it was necessary to know the critical energy release rate of the tested mixture G_{IC} . Therefore, a wedge splitting test (WST) was performed in order to determine the desired property of the material.

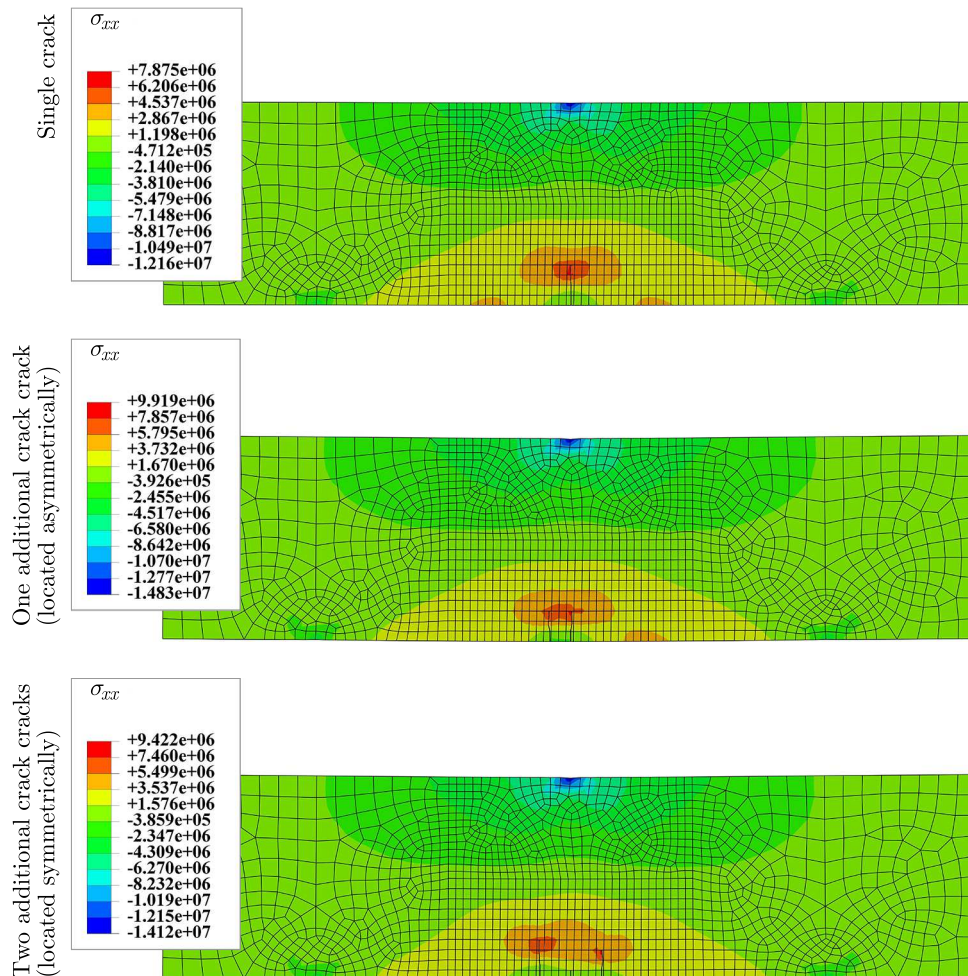


Fig. 7. Stress rearrangement near the crack tip at 100% level of effort in different crack configurations (displacement scaled 3 times)

During the simulation, it was observed that the appearance of additional cracks in the material before the start of the strength test (for example as a result of pre-loading) may lead to an increase in the maximum force required to destroy the sample. Analysis of the tensile stress distribution in the horizontal direction (approximately perpendicular to the crack) allows for a qualitative explanation of the observed strength increase. The additional crack, located outside of the most strained cross section, forms a “cover” of the dominant crack. The reduction of the tensile stress near the dominant crack slows its propagation. It should be emphasized that this is a characteristic of the structure rather than of the material itself. Nevertheless, in phenomenological terms, the result of the simulation, interpreted as a result of the 3-point bending test, indicates strengthening of the material.

References

1. ABAQUS Theory Manual, Ver. 6.13, 2013
2. BELYTSCHKO T., BLACK T., 1999, Elastic crack growth in finite elements with minimal remeshing, *International Journal for Numerical Methods in Engineering*, **45**, 601-620
3. BIJAK-ŻOCHOWSKI M., JAWORSKI A., ZAGRAJEK T., 1999, *Basics of Solid Mechanics* (in Polish), Warsaw, Oficyna Wydawnicza Politechniki Warszawskiej

4. BRÜHWILER E., WITTMANN F.H., 1990, The wedge splitting test, a new method of performing stable fracture mechanics tests, *Engineering Fracture Mechanics*, **35**, 1, 117-125
5. BRZEZIŃSKI K., ADAMCZEWSKI G., TUTKA P., 2017, The influence of cyclic loading on the static strength of cement-bound sand – qualitative analysis, *Roads and Bridges – Drogi i Mosty*, **16**, 1, 37-46, DOI: <http://dx.doi.org/10.7409/rabdim.017.003>
6. BRZEZIŃSKI K., ZBICIAK A., 2014, Influence of load history on fatigue life of cement treated soil (in Polish), *Drogownictwo*, **LXIX**, 9, 288-293
7. DOLBOW J.O.H.N., BELYTSCHKO T., 1999, A finite element method for crack growth without remeshing, *International Journal for Numerical Methods in Engineering*, **46**, 1, 131-150
8. ELFGREN L., SHAH S.P. (EDIT.), 1991, *Analysis of Concrete Structure by Fracture Mechanics*, London, Chapman and Hall
9. FATEMI A., YANG L., 1998, Cumulative fatigue damage and life prediction theories: a survey of the state of the art for homogeneous materials, *International Journal of Fatigue*, **20**, 1, 9-34, ISSN 0142-1123, [http://dx.doi.org/10.1016/S0142-1123\(97\)00081-9](http://dx.doi.org/10.1016/S0142-1123(97)00081-9)
10. GRIFFITH A.A., 1920, The phenomena of rupture and flow in solids, *Philosophical Transactions, Royal Society of London, Series A*, **221**, 163-198
11. HILLERBORG A., 1989, Stability problems in fracture mechanics testing. Fracture of concrete and rock, [In:] *Recent Developments*, S.P. Shah, S.E. Swartz, B. Barr (edit), Amsterdam, Elsevier, 369-378
12. Koba H., 2000, *Durability of Road Pavements with Cement-Bound Sub-Base* (in Polish), Wrocław, Oficyna Wydawnicza Politechniki Wrocławskiej
13. KYRIAZOPOULOS A., ANASTASIADIS C., TRIANTIS D., BROWN C.J., 2011, Non-destructive evaluation of cement-based materials from pressure-stimulated electrical emission – preliminary results, *Construction and Building Materials*, **25**, 4, 1980-1990, DOI: [10.1016/j.conbuildmat.2010.11.053](http://dx.doi.org/10.1016/j.conbuildmat.2010.11.053)
14. LANDIS E.N., SHAH S.P., 1995, Experimental measurements of microfracture in cement-based materials, *Fracture Mechanics of Concrete Structures*, 315-328
15. LÖFGREN I., STANG H., OLESEN J., FORBES O., 2004, Wedge splitting test-A test to determine fracture properties of FRC, [In:] *6th International RILEM Symposium on Fibre Reinforced Concretes*, M. Di Prisco, R. Felicetti, G.A. Plizzari (edit.), RILEM Publications SARL, **1**, 379-388
16. MARCO S.M., STARKEY W.L., 1954, A concept of fatigue damage, *Transactions of ASME*, **76**, 627-632
17. MINER M.A., 1945, Cumulative damage in fatigue, *Journal of Applied Mechanics*, **67A**, 159-164
18. MOĆKO W., KOWALEWSKI Z.L., 2014, Evolution of tensile properties of the TIAL6V4 alloy due to the prior cyclic loading history, *Journal of Theoretical and Applied Mechanics*, **52**, 847-851
19. MOCZKO A., 1996, Acoustic emission in concrete tests (in Polish), *Inżynieria i Budownictwo*, **1**, 42-46
20. OHTSU M., 1996, The history and development of acoustic emission in concrete engineering, *Magazine of Concrete Research*, **48**, 321-330
21. PN-EN 196-1:2006 – Methods Of Testing Cement – Part 1: Determination Of Strength
22. PROKOPSKI G., 2008, *Mechanics of Cement Concretes Cracking* (in Polish), Oficyna Rzeszów, Wydawnicza Politechniki Rzeszowskiej
23. RAFALSKI L., 2007, *Road Subbases* (in Polish), Warszawa, Instytut Badawczy Dróg i Mostów
24. REMMERS J.J.C., DE BORST R., NEEDLEMAN A., 2008, The simulation of dynamic crack propagation using the cohesive segments method, *Journal of the Mechanics and Physics of Solids*, **56**, 70-92

25. RITCHIE R. O., 1999, Mechanisms of fatigue-crack propagation in ductile and brittle solids, *International Journal of Fracture*, **100**, 1, 55-83
26. SITEK M., ADAMCZEWSKI G., SZYSZKO M., MIGACZ B., TUTKA P., NATORFF M., 2014, Numerical Simulations of a Wedge Splitting Test for High-Strength Concrete, *Procedia Engineering*, **91**, 99-104, DOI: 10.1016/j.proeng.2014.12.021
27. SONG J.H., AREIAS P.M.A., BELYTSCHKO T., 2006, A method for dynamic crack and shear band propagation with phantom nodes, *International Journal for Numerical Methods in Engineering*, **67**, 868-893
28. WAWSZCZUK R., 2012, Self-stresses in polycrystalline materials and their variability during thermal processing (in Polish), PhD Thesis, Cracow, Faculty of Physics and Applied Computer Science AGH University of Science and Technology
29. WÖHLER A., 1870, Über die Festigkeitsversuche mit Eisen und Stahl, *Zeitschrift für Bauwesen*, **20**, 73-106
30. XI L. SONGLIN Z., 2009, Strengthening and damaging under low-amplitude loads below fatigue limit, *International Journal of Fatigue*, **31**, 2, 341-345
31. ZHAO L., ZHENG S., FENG J., 2014, Fatigue life prediction under service load considering strengthening effect of loads below fatigue limit, *Chinese Journal of Mechanical Engineering*, **27**, 1178-1185

Manuscript received November 27, 2017; accepted for print February 1, 2018

LOW-VELOCITY IMPACT BEHAVIOUR OF OPEN-CELL FOAMS

REZA HEDAYATI

Department of Mechanical Engineering, Amirkabir University of Technology (Tehran Polytechnic), Hafez Ave, Tehran, Iran, and Faculty of Aerospace Engineering, Delft University of Technology, Delft, Netherlands
e-mail: r.hedayati@tudelft.nl; rezahedayati@gmail.com

MOJTABA SADIGHI

Department of Mechanical Engineering, Amirkabir University of Technology (Tehran Polytechnic), Hafez Ave, Tehran, Iran

Metal foams are cellular solids that show some unique properties which cannot be found in other natural or human-made materials. While the impact characteristics of closed-cell foams under static and impact loadings appear to be well-studied in the literature, the impact behaviour of open-cell foams is not yet well-understood. In this study, open-cell foams with two different densities are impacted by drop weights with different kinetic energies. The effects of foam density, impactor initial height, and impactor weight on the recorded stress-time, stress-strain, and energy-strain curves are investigated. While the stress-strain curve of closed-cell foams under impact loading usually consists of a single bell, the results of the current study showed that both the stress-time and stress-strain curves of most the samples consist of two consecutive bells. By increasing weight of the impacting weight, the number of bells increases which helps in increasing the impact period and keeping the maximum generated stress low. Compared to closed-cell foams, the open-cell foams can therefore better absorb the energy, as long as the impact energy is relatively small. The relatively low stiffness as well as the presence of large hollow space inside the open-cell foams also makes them favorable for being used as biomedical scaffolds.

Keywords: open-cell foam, low-velocity impact, biomaterial, mechanical properties

1. Introduction

Metal foams are a class of cellular materials that show some unique properties which cannot be found in other natural or human-made materials. For example, their specific stiffness and energy absorption capacity are relatively high even for small specific densities (Schüler *et al.*, 2013). Foams are usually categorized into two main groups: open-cell and closed-cell. In closed-cell foams, the cells are completely separated from each other by walls. In open-cell foams, there is no cell wall and the cells are connected to each other by cell edges.

While the energy absorption characteristics of closed-cell foams appear to be well-studied in the literature (Schüler *et al.*, 2013; Fang *et al.*, 2015; Wang *et al.*, 2015; Zhang *et al.*, 2013; Ramachandra *et al.*, 2003; Mukai *et al.*, 2006; Hedayati *et al.*, 2011), the impact behaviour of open-cell foams is not yet well-understood. The main reason can be the difference in the applications that have been considered for decades for the two noted types of foams. Due to higher stiffness and plateau stress levels, closed-cell foams are usually preferred to open-cell foams in energy absorption applications. On the other hand, permeability provided by connectivity of the cells of open-cell foams makes them suitable for applications in which the fluid flow through the foam cells is important, e.g. as heat exchanger or as bone substitute implants. If open-cell foams with small cells are filled by viscous fluids, the expelling of the fluid under a compressive load can also dissipate a great amount of energy (Gibson and Ashby, 1997).

Novel applications found for open-cell foams (such as their use as bone substitute biomaterials) has made understanding of their mechanical properties under different loading conditions important. Depending on their location and person, human bones can have a large range of stiffness from 0.1 GPa to 20 GPa. Particularly, the inner soft and weak tissues of bones, known as cancellous or spongy bones, usually have very small stiffnesses. Solid implants usually remove the load from natural bones around them leading to their resorption. This resorption is followed by detaching the implant from the surrounding bone and, therefore, malfunction of the implant (known as stress shielding). Open-cell foams have low stiffness levels which are comparable to the stiffness levels of bones. Moreover, their hollow space allows for new bone regeneration inside the implant and, therefore, better bone-implant fixation.

Regarding the mechanical properties of open-cell foams, Kashef *et al.* (2008) fabricated open-cell titanium foams using space holder technique and investigated their elastic properties, fracture toughness (Kashef *et al.*, 2010) and fatigue strength (Kashef *et al.*, 2011) for biomedical applications. They found 63% porous foams with 6.5 GPa elastic modulus suitable for dental and orthopaedic applications (Kashef *et al.*, 2008). The elastic mechanical properties of open-cell foams fabricated by directional solidification (Nich *et al.*, 2000), casting (Yamada *et al.*, 2000; Kanahashi *et al.*, 2000) and space-holder (Jiang *et al.*, 2007) techniques have also been investigated in the literature. The effect of the strain rate on the dynamic mechanical properties of different types of open-cell foams have also been studied in several publications (Yi *et al.*, 2001; Wang *et al.*, 2006). However, the mechanical behaviour of open-cell foams under the impact of drop weights has not yet been studied.

Similar to bulk pure copper, copper foams have great corrosion resistance, and they possess excellent electrical and thermal conductivities. Copper foams are excellent candidates for energy absorption applications as well. This is because the possibility of having a large proportion of hollow space inside the open-cell porous structures allows for large plastic deformation of struts (and therefore high energy absorption capacity of the porous structure) until the neighbour struts come into contact with each other. The great ductility properties of copper (compared to other metals) even increases this great toughness capability observed in metal foams.

In this study, open-cell foams with two different densities are impacted by drop weights with different kinetic energies. The effect of foam density and impactor initial energy on the recorded stress-time, stress-strain and energy-strain curves will be investigated. The effect of mass of the drop weight is the other parameter which will be studied.

2. Materials and methods

The open-cell copper foam samples were made by the investment casting process. Two large foam panels (Fig. 1a) were made, which were then cut into several small cubic specimens (Fig. 1b) with dimensions of 22.6 mm×28.2 mm×39.2 mm. The foam samples had two nominal densities of 268.03 kg/m³ and 393.596 kg/m³ (Table 1), respectively named low-density (LD) and high-density (HD) foams in this study. The specimens cut from the edges of the foam panel were not used in order to avoid non-homogeneity in the micro-structure of the foam. To measure density of the foam samples, the weight and dimensions of all the samples were measured and divided. For having the relative density of the foam samples, the density of the foam samples was divided by the density of the bulk material (i.e. 8960 kg/m³). The samples were impacted by drop weights with initial heights between 20 cm and 100 cm. Two drop weights of 1.3 kg and 3.3 kg were considered. The acceleration of the impactor was recorded by an accelerometer installed on it. By two consecutive integration of the acceleration-time diagrams, displacement-time diagrams were also obtained. The force-time diagram was obtained by multiplying the vertical coordinate of the acceleration-time diagram by the mass of the impactor. The specific energy-time diagrams were

measured by calculating the area under the stress-strain curve diagrams. The noises observed in the acceleration diagrams were smoothed using SMOOTH function in MATLAB (Fig. 3).

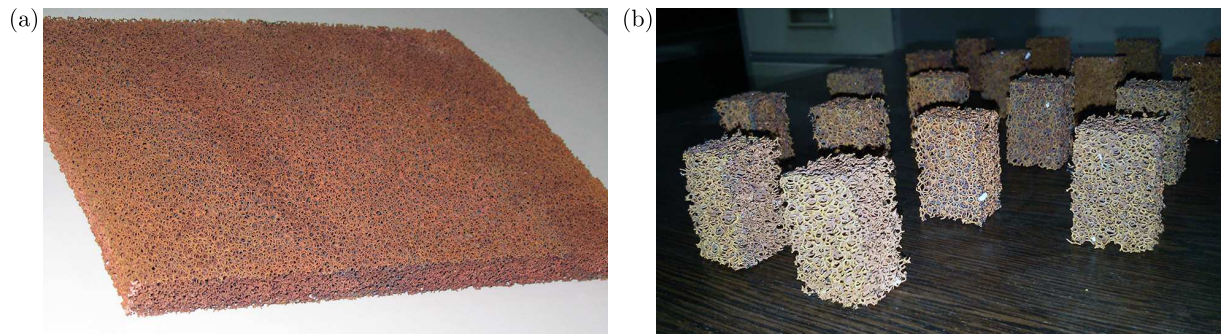


Fig. 1. (a) Foam panel before being cut, (b) samples cut from the foam panel

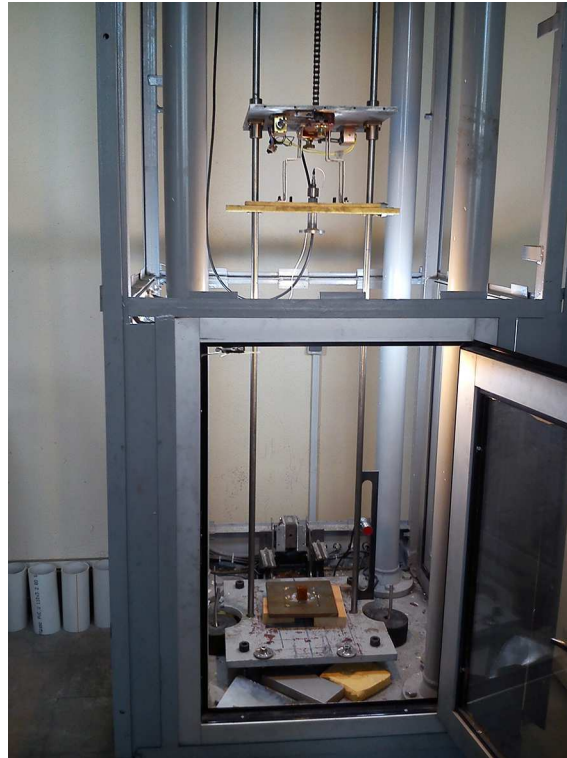


Fig. 2. A copper foam samples in the drop weight testing machine

Table 1. Geometrical properties of low-density and high-density foams

	Density ρ [kg/m ³]	Relative density ρ/ρ_s [%]	Pore size a [mm]
Low-density (LD)	268.03 ± 16.19	2.99 ± 0.169	$2.1 < a < 4.41$
High-density (HD)	393.596 ± 12.82	4.391 ± 0.143	$1.92 < a < 4.22$

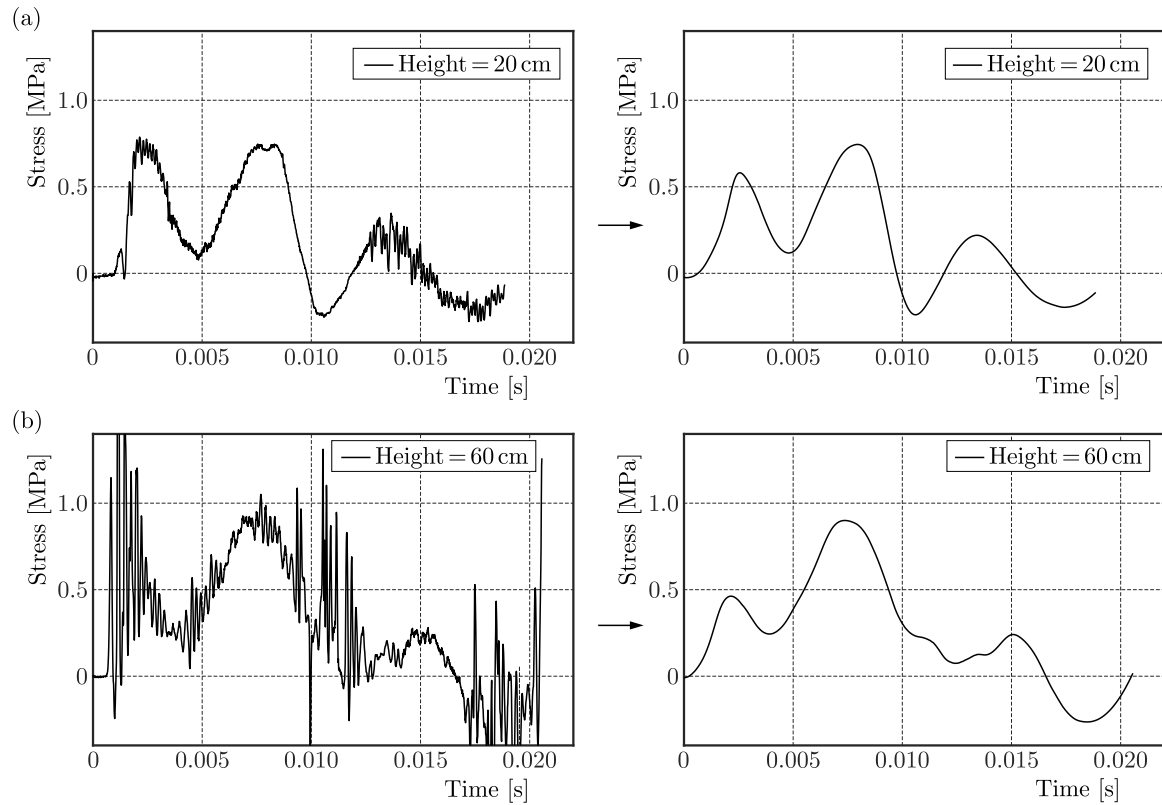


Fig. 3. Smoothing of experimental data curves for two examples of stress-time diagrams

3. Results

The elastic modulus of the high-density foam was almost 1.5 times of that in the low-density foam (Table 2). Both the yield stress and plateau stress of the high-density foam were almost twice of those for the low-density foam (Table 2). Both types of foams demonstrated close densification strains around 0.8 (Fig. 4). The stress-strain curves of both the foams coincided at the strain of 0.9 (Fig. 4).

Table 2. Mechanical properties of low-density and high-density foams

	Elastic modulus E [MPa]	Relative elastic modulus $E/E_s \cdot 10^{-4}$	Yield stress σ_y [kPa]	Plateau stress σ_{pl} [kPa]
LD	20.333 ± 3.78	1.7378 ± 0.323	651.1 ± 131.4	605.47 ± 185.9
HD	30.034 ± 5.919	2.5669 ± 0.506	1316.2 ± 198.6	1512.1 ± 336.7

Due to limitations in the recording period of the accelerometer, the stress of all the samples under the impact loading could be captured up to 20 ms. Both the low-density and high-density foams showed double bell curves in their stress-time diagrams (Fig. 5). In general, increasing the initial height of the impacting weight increased the maximum stress values of both the first and second bells (Fig. 5). There were, however, some exceptions. For example, the maximum stress of the first bell of the test with the initial height of $h = 20$ cm was even larger than that in other tests. The end times of the second bell for low-density foams with different initial heights of the impacting weights were between 10 ms and 14 ms. The end-times of the second bell of all the high-density foams were close and were between 8 ms and 9 ms.

While in low-density foams, the maximum stress of the first bell was always lower than that of the second bell, in high-density foams, the maximum stress of the first and second bells

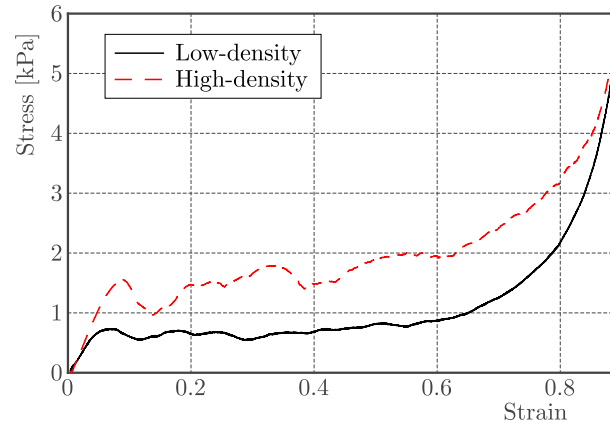


Fig. 4. Stress-strain curve of low-density and high-density foams under quasi-static loading

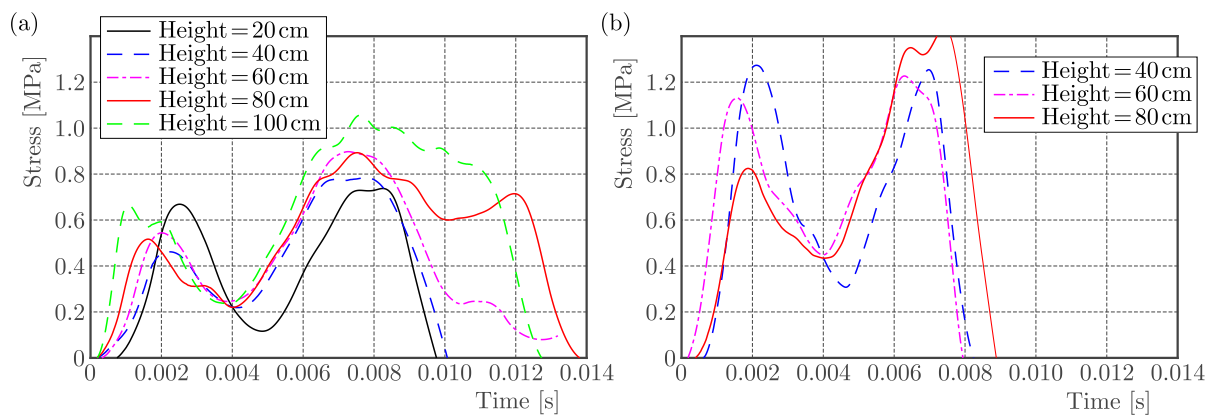


Fig. 5. Stress-time curves of (a) low-density and (b) high-density foams impacted by an impactor with 1.3 kg weight

were close to each other (Fig. 5). As expected, for the same initial height of the impactor, the maximum stress generated in the low-density foam samples were always lower than that in the high-density foam (Fig. 5).

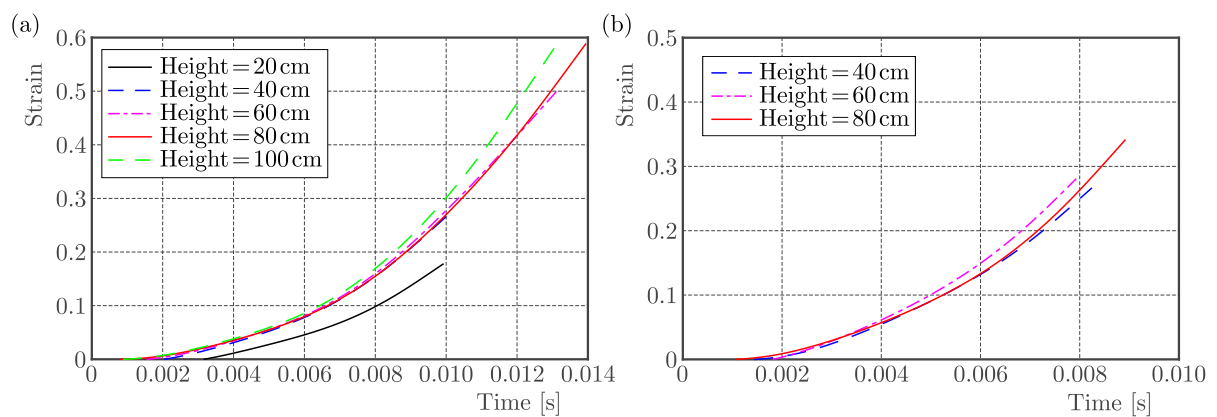


Fig. 6. Strain-time curves of (a) low-density and (b) high-density foams impacted by an impactor with 1.3 kg weight

As expected, increasing the initial height increased the final strain (maximum compaction) of the foam samples (Fig. 6). In low-density samples, the maximum strain in the samples for initial heights of 20 cm, 40 cm, 60 cm, 80 cm, and 100 cm was respectively 18.5%, 28.5%, 50%, 58.8%, and 56% (Fig. 6a). In high-density samples, the maximum strains for initial heights of

40 cm, 60 cm, and 80 cm were respectively 26.6%, 28.1%, and 34.2% (Fig. 6b). As expected, for the same initial height of the impacting weight, the maximum strains of the high-density samples were always lower than those in the low-density samples (compare Fig. 6a and Fig. 6b). While in the stress-time curves (Fig. 5), the span of the second bell was very close to the span of the first bell, in the stress-strain curves (Fig. 7), the span of the first bell was much smaller than the span of the second bell, especially for the low-density foams.

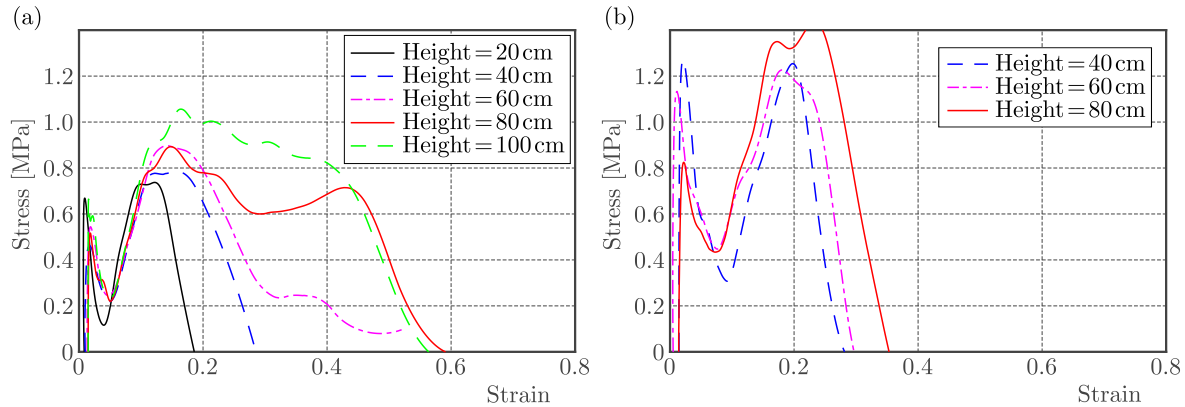


Fig. 7. Stress-strain curves of (a) low-density and (b) high-density foams impacted by an impactor with 1.3 kg weight

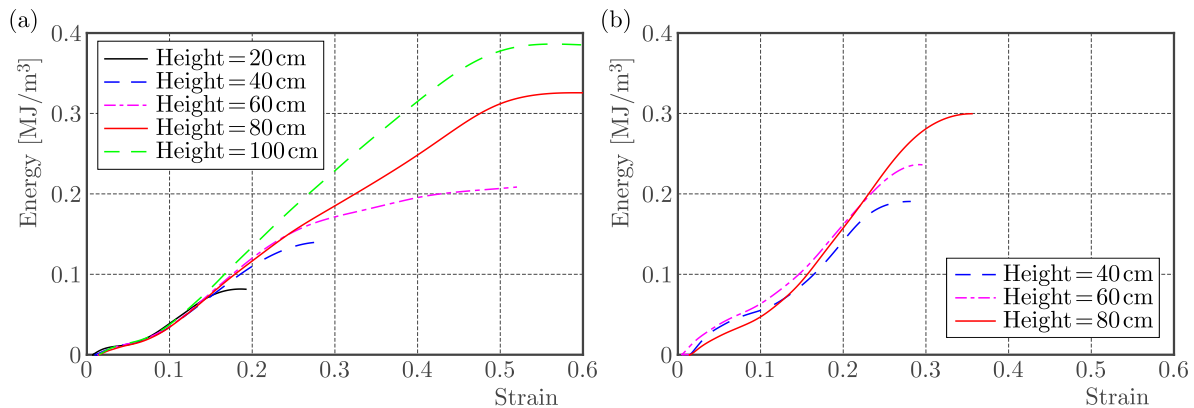


Fig. 8. Absorbed specific energy profiles of (a) low-density and (b) high-density foams impacted by an impactor with 1.3 kg weight

Increasing the initial height of the impactor increased the final energy absorbed by both the low-density and high-density foams (Fig. 8). Plotting the normalized values of the absorbed energy (i.e. the ratio of the absorbed energy by the sample to the initial energy of the impactor) showed that the final absorbed energy in all the foam samples were between 70% and 92% of the initial energy of the impactor (Fig. 9). The highest percentage of the final absorbed energy (about 92%) belonged to the high-density foam under the impact of the weight with the lowest initial height, i.e. 40 cm (Fig. 9b). The normalized energy-strain diagrams of the low-density foams with the impactor initial heights of 80 cm and 100 cm were very close (Fig. 9a).

The effect of impactor weight was investigated on the low-density foam under the impact of weight with the initial height of 40 cm. Increasing the weight of the impactor did not have a significant effect on the maximum stress of the first bell (Fig. 10). Moreover, increasing the impactor weight did not significantly change the time and strain of the maximum stress of the first bell. However, increasing the impactor weight increased the maximum stress of the second bell and decreased its occurrence time (Fig. 10a). More significantly, the stress value of the

sample under the impact of the heavy impactor did not reach zero after the second bell, and a third bell was formed in both the stress-time and stress-strain diagrams (Fig. 10).

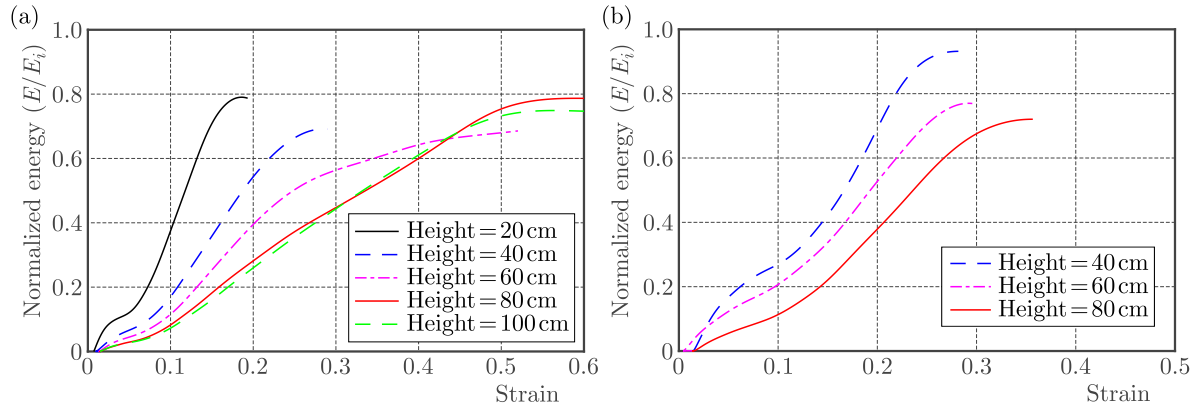


Fig. 9. Normalized absorbed energy profiles of (a) low-density and (b) high-density foams impacted by an impactor with 1.3 kg weight

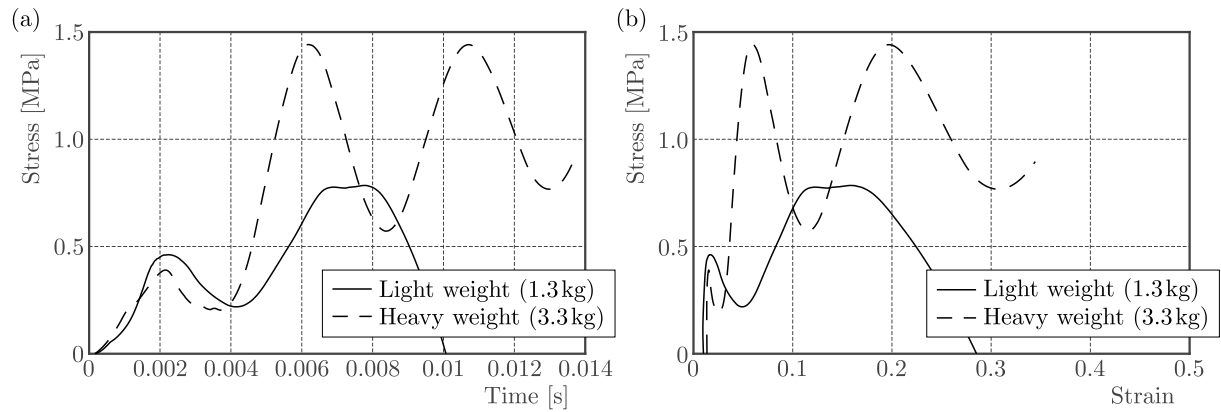


Fig. 10. (a) Stress-time and (b) stress-strain curves of low-density foams under the impact of 1.3 kg and 3.3 kg impactors

4. Discussions

All the stress-time and stress-strain curves consisted of a double bell. Similar bells have also been observed in other experimental and numerical studies on the impact behaviour of closed-cell foams. In some cases, the stress-time curve only consisted of a single bell (Rajendran *et al.*, 2009), while in some cases there was a double bell in the curves, although the span of the first bell was usually very tiny compared to the span of the second bell (Li *et al.*, 2012; Castro *et al.*, 2013; Peroni *et al.*, 2013). The presence of the first bell in the curves can be due to reduction in the stress level in the top face of the specimen after the initial increase in the stress level after the occurrence of the impact.

In the open-cell foams, due to slow propagation of stress waves, the upper part of the specimen initially deforms very easily before the compressive wave is returned from the back plate. Due to fast initial deformation of the upper part of the open-cell foam, the elevated stress level in the interface between the foam sample and the impacting weight decreases fast. After the compressive stress waves have travelled towards and back from the lower parts of the foam and after causing deformation in the foam, the stress level decreases. However, as the impactor moves forward, the stress level increases for a second time.

In the closed-cell foams, the cells are connected to each other by means of cell walls, while in the open-cell foams, the struts connect the cells. In the closed-cell foams, therefore, the initial stress waves can travel to the lower parts of the specimen much faster as compared to the open-cell foams. The deformation of the closed-cell foams can therefore be distributed more uniformly throughout its length. This explains the absence or very little presence of the first bell in the stress-time and stress-strain curves of the closed-cell foams.

The non-uniform deformation of the open-cell foams can increase the impact duration as compared to the closed-cell foams. This increase in the impact duration as well as the weaker nature of open-cell foams decreases the maximum stress in the foam during the impact. Therefore, as compared to the closed-cell foams, the open-cell foams, if used as energy absorbing materials in packaging industry, can better protect delicate goods, since the stress imposed on the package is much lower, as long as the impact energy is relatively small.

After the initial double bell curves, the stress-time curves of the open-cell foams continued in a sine wave shape around zero stress. In all the samples, the accumulation of strain after the second bell was very small, which showed that the sine wave shape of the stress-time curve after the second bell had been caused by vibration of the test machine and specimen rather than the actual displacement of the interface between the specimen and the impacting weight. Therefore, the periodic sine waves after the second bell (in the impacts with light impactor) were omitted from the curves.

The stress value of the sample under the heavy impactor (3.3 kg) did not reach zero after the second bell, and a third bell was formed in both the stress-time and stress-strain diagrams (Fig. 10). Due to limitations in measurement duration, the acceleration could not be measured after the third bell. However, the reason behind the formation of additional bells in the stress-strain curve can be the fact that when the weight of the impactor is increased, the layer-by-layer nature of the deformation of the foam sample increases. This is because in the case of heavier impactors, the foam sample is not tough enough to decrease velocity of the impactor down to zero after the second bell, leading to creation of additional bells in the curves.

After being deformed, none of the samples could absorb all the initial energy of the impacting weight (Fig. 9). The reason behind this can be the dissipation of energy caused by friction between the sample and the impacting weight, friction of the impacting weight with the guiding rail of the testing machine, and conversion of mechanical energy to heat due to plastic deformation during the impact. However, plotting the normalized values of absorbed energy demonstrated that the final absorbed energy in all the foam samples are between 70% and 92% of the initial energy of the impactor, which shows that high percentages of initial energy have been absorbed by the foam samples.

Using open-cell foams for production of bone-replacing implants is becoming more and more common. The open-cell foams manufactured using the traditional methods usually have an irregular morphology. The manufacturing processes that create relatively regular open-cell foams usually lead to a foam unit cell shape believed to have a geometry similar to the ones suggested by Kelvin (Warren and Kraynik, 1997) or Weaire and Phelan (1994). The advent of additive manufacturing techniques has made it possible to create open-cell structures with arbitrary unit cell shape and size. For example, porous open-cell foams with hexagonal (Hedayati *et al.*, 2016c), octagonal (Hedayati *et al.*, 2016b), truncated cube (Hedayati *et al.*, 2018), diamond (Ahmadi *et al.*, 2014; (Hedayati *et al.*, 2017), truncated cuboctahedron (Doig *et al.*, 1999), rhombic dodecahedron (Shulmeister *et al.*, 1998; Babaei *et al.*, 2012; Borleffs, 2012; Amin Yavari *et al.*, 2013; Campoli *et al.*, 2013), tetrakaidecahedrons (Warren and Kraynik, 1997; Zheng *et al.*, 2014) and rhombicuboctahedron (Hedayati *et al.*, 2016a) have been investigated numerically, analytically and experimentally. While additive manufacturing techniques provide good control over the micro-architecture of the porous structure, they result in porous structures with some defects. For example, the additively manufactured porous structures have irregularities in the

strut cross-section diameter. The consecutive fusing of metal powders at neighbour points usually creates very rough surfaces with potentially high stress concentration factors. Moreover, at some points, the strut radius can be very small, which can lead to clustered damage areas. Therefore, the metal foams made by traditional manufacturing techniques still have their advantages over the newly popular additively manufactured porous structures.

5. Conclusions

In this paper, copper open-cell foams with two densities were tested mechanically under static and impact loadings. For the impact loading, two drop-weights with 1.3 kg and 3.3 kg masses were used. The results showed that both the stress-time and stress-strain curves of all the samples consist of two consecutive bells. While in the stress-time curves, the span of the second bell was very close to the span of the first bell, in stress-strain curves, the span of the first bell was much smaller than the span of the second bell, especially in low-density foams. As expected, for the same initial height of the impactor, the maximum stress generated in the low-density foam samples were always lower than that in the high-density foams. The foam samples absorbed between 70% and 92% of the initial energy of the impactor. Increasing the weight of the impactor did not have a significant effect on the maximum stress of the first bell in the stress-time diagram. Moreover, increasing the impactor weight did not change the time of the first maximum stress. However, increasing the impactor weight increased the maximum stress of the second bell and decreased its occurrence time. It can be concluded that as compared to the closed-cell foams, the open-cell foams can better absorb the energy, as long as the impact energy is relatively small. The very small stiffness as well as the presence of large interconnected space inside the open-cell foams also makes them favorable for being used as biomedical scaffolds.

References

1. AHMADI S., CAMPOLI G., AMIN YAVARI S., SAJADI B., WAUTHLÉ R., SCHROOTEN J., WEINANS H., ZADPOOR A.A., 2014, Mechanical behavior of regular open-cell porous biomaterials made of diamond lattice unit cells, *Journal of the Mechanical Behavior of Biomedical Materials*, **34**, 106-115
2. AMIN YAVARI S., WAUTHLÉ R., VAN DER STOK J., RIEMSLAG A., JANSSEN M., MULIER M., KRUTH J.-P., SCHROOTEN J., WEINANS H., ZADPOOR A.A., 2013, Fatigue behavior of porous biomaterials manufactured using selective laser melting, *Materials Science and Engineering: C*, **33**, 8, 4849-4858
3. BABAEE S., JAHROMI B.H., AJDARI A., NAYEB-HASHEMI H., VAZIRI A., 2012, Mechanical properties of open-cell rhombic dodecahedron cellular structures, *Acta Materialia*, **60**, 6, 2873-2885
4. BORLEFFS M., 2012, *Finite Element Modeling to Predict Bulk Mechanical Properties of 3D Printed Metal Foams*, Delft University of Technology
5. CAMPOLI G., BORLEFFS M., AMIN YAVARI S., WAUTHLE R., WEINANS H., ZADPOOR A.A., 2013, Mechanical properties of open-cell metallic biomaterials manufactured using additive manufacturing, *Materials and Design*, **49**, 957-965
6. CASTRO G., NUTT S., WENCHEN X., 2013, Compression and low-velocity impact behavior of aluminum syntactic foam, *Materials Science and Engineering: A*, **578**, 222-229
7. DOIG S., BOAM A., LIVINGSTON A., STUCKEY D., 1999, Mass transfer of hydrophobic solutes in solvent swollen silicone rubber membranes, *Journal of Membrane Science*, **154**, 1, 127-140
8. FANG Q., ZHANG J., ZHANG Y., LIU J., GONG Z., 2015, Mesoscopic investigation of closed-cell aluminum foams on energy absorption capability under impact, *Composite Structures*, **124**, 409-420

9. GIBSON L.J., ASHBY M.F., 1997, *Cellular Solids: Structure and Properties*, Cambridge University Press
10. HEDAYATI R., AHMADI S., LIETAERT K., POURAN B., LI Y., WEINANS H., RANS C., ZADPOOR A., 2018, Isolated and modulated effects of topology and material type on the mechanical properties of additively manufactured porous biomaterials, *Journal of the Mechanical Behavior of Biomedical Materials*, **79**
11. HEDAYATI R., LEEFLANG A., ZADPOOR A., 2017, Additively manufactured metallic pentamode meta-materials, *Applied Physics Letters*, **110**, 9, 091905
12. HEDAYATI R., SADIGHI M., MOHAMMADI-AGHDAM M., ZADPOOR A.A., 2016a, Mechanics of additively manufactured porous biomaterials based on the rhombicuboctahedron unit cell, *Journal of the Mechanical Behavior of Biomedical Materials*, **53**, 272-294
13. HEDAYATI R., SADIGHI M., MOHAMMADI-AGHDAM M., ZADPOOR A.A., 2016b, Mechanical properties of additively manufactured octagonal honeycombs, *Materials Science and Engineering: C*, **69**, 1307-1317
14. HEDAYATI R., SADIGHI M., MOHAMMADI-AGHDAM M., ZADPOOR A.A., 2016c, Mechanical properties of additively manufactured thick honeycombs, *Materials*, **9**, 8, 613
15. HEDAYATI R., ZIAEI-RAD S., 2011, Foam-core effect on the integrity of tailplane leading edge during bird-strike event, *Journal of Aircraft*, **48**, 6, 2080-2089
16. JIANG B., WANG Z., ZHAO N., 2007, Effect of pore size and relative density on the mechanical properties of open cell aluminum foams, *Scripta Materialia*, **56**, 2, 169-172
17. KANAHASHI H., MUKAI T., YAMADA Y., SHIMOJIMA K., MABUCHI M., NIEH T., HIGASHI K., 2000, Dynamic compression of an ultra-low density aluminum foam, *Materials Science and Engineering: A*, **280**, 2, 349-353
18. KASHEF S., LIN J., HODGSON P.D., YAN W., 2008, Mechanical properties of titanium foam for biomedical applications, *International Journal of Modern Physics B*, **22**, 31-32, 6155-6160
19. KASHEF S., ASGARI A., HILDITCH T.B., YAN W., GOEL V.K., HODGSON P.D., 2010, Fracture toughness of titanium foams for medical applications, *Materials Science and Engineering: A*, **527**, 29, 7689-7693
20. KASHEF S., ASGARI A., HILDITCH T.B., YAN W., GOEL V.K., HODGSON P.D., 2011, Fatigue crack growth behavior of titanium foams for medical applications, *Materials Science and Engineering: A*, **528**, 3, 1602-1607
21. LI B., ZHAO G., LU T., 2012, Low strain rate compressive behavior of high porosity closed-cell aluminum foams, *Science China Technological Sciences*, **55**, 2, 451-463
22. MUKAI T., MIYOSHI T., NAKANO S., SOMEKAWA H., HIGASHI K., 2006, Compressive response of a closed-cell aluminum foam at high strain rate, *Scripta Materialia*, **54**, 4, 533-537
23. NIEH T., HIGASHI K., WADSWORTH J., 2000, Effect of cell morphology on the compressive properties of open-cell aluminum foams, *Materials Science and Engineering: A*, **283**, 1, 105-110
24. PERONI M., SOLOMOS G., PIZZINATO V., 2013, Impact behaviour testing of aluminium foam, *International Journal of Impact Engineering*, **53**, 74-83
25. RAJENDRAN R., MOORTHY A., BASU S., 2009, Numerical simulation of drop weight impact behaviour of closed cell aluminium foam, *Materials and Design*, **30**, 8, 2823-2830
26. RAMACHANDRA S., KUMAR P.S., RAMAMURTY U., 2003, Impact energy absorption in an Al foam at low velocities, *Scripta Materialia*, **49**, 8, 741-745
27. SCHÜLER P., FISCHER S.F., BÜHRIG-POLACZEK A., FLECK C., 2013, Deformation and failure behaviour of open cell Al foams under quasistatic and impact loading, *Materials Science and Engineering: A*, **587**, 250-261

28. SHULMEISTER V., VAN DER BURG M., VAN DER GIESSEN E., MARISSEN R., 1998, A numerical study of large deformations of low-density elastomeric open-cell foams, *Mechanics of Materials*, **30**, 2, 125-140
29. WANG P., XU S., LI Z., YANG J., ZHANG C., ZHENG H., HU S., 2015, Experimental investigation on the strain-rate effect and inertia effect of closed-cell aluminum foam subjected to dynamic loading, *Materials Science and Engineering: A*, **620**, 253-261
30. WANG Z., MA H., ZHAO L., YANG G., 2006, Studies on the dynamic compressive properties of open-cell aluminum alloy foams, *Scripta Materialia*, **54**, 1, 83-87
31. WARREN W., KRAYNIK A., 1997, Linear elastic behavior of a low-density Kelvin foam with open cells, *Journal of Applied Mechanics*, **64**, 4, 787-794
32. WEAIRE D., PHELAN R., 1994, A counter-example to Kelvin's conjecture on minimal surfaces, *Philosophical Magazine Letters*, **69**, 2, 107-110
33. YAMADA Y., SHIMOJIMA K., SAKAGUCHI Y., MABUCHI M., NAKAMURA M., ASAHINA T., MUKAI T., KANAHASHI H., HIGASHI K., 2000, Effects of heat treatment on compressive properties of AZ91 Mg and SG91A Al foams with open-cell structure, *Materials Science and Engineering: A*, **280**, 1, 225-228
34. YI F., ZHU Z., ZU F., HU S., YI P., 2001, Strain rate effects on the compressive property and the energy-absorbing capacity of aluminum alloy foams, *Materials Characterization*, **47**, 5, 417-422
35. ZHANG Y., SUN G., XU X., LI G., HUANG X., SHEN J., LI Q., 2013, Identification of material parameters for aluminum foam at high strain rate, *Computational Materials Science*, **74**, 65-74
36. ZHENG X., LEE H., WEISGRABER T.H., SHUSTEFF M., DEOTTE J., DUOSS E.B., KUNTZ J.D., BIENER M.M., GE Q., JACKSON J.A., 2014, Ultralight, ultrastiff mechanical metamaterials, *Science*, **344**, 6190, 1373-1377

Manuscript received February 7, 2017; accepted for print February 2, 2018

MODEL CONSTRUCTION AND EXPERIMENTAL VERIFICATION OF THE EQUIVALENT ELASTIC MODULUS OF A DOUBLE-HELIX WIRE ROPE

HONG YUE CHEN, KUN ZHANG, YANG XI BAI

School of Mechanical Engineering, Liaoning Technical University, Fuxin, China; e-mail: zhangkunliaoning@163.com

YING MA

Coal Mining and Designing Department, Tiandi Science and Technology Co., Ltd., Beijing, China

HAN ZHONG DENG

College of Materials Science and Engineering, Liaoning Technical University, Fuxin, China

To accurately describe mechanical properties of a complex wire rope, a double-helix wire rope is used as an example in this study. According to the spatial structure characteristics of the central helical line of each wire rope, the spatial configuration curve for the double-helix wire rope is obtained by using differential geometry theory. On the basis of this curve, the mathematical model of the equivalent elastic modulus of the wire rope is developed, and the elastic modulus of a $6\times 7+1$ WS wire rope is measured using a universal tensile testing machine. The experimental results are compared with the predicted results to verify correctness of the elastic modulus prediction of the double-helix wire rope.

Keywords: mechanical properties, wire rope, double-helix wire rope, spatial configuration curve, equivalent elastic modulus

1. Introduction

Wire ropes are widely used in material-handling machinery because they possess high strength, are light in weight and provide stable and reliable operation. Their safety and reliability directly affect production efficiency and personnel safety. Since the 1950s, numerous domestic and foreign scholars have conducted research on wire ropes. However, because of the complex spiral structure of a wire rope, the theoretical basis required for accurate prediction of its mechanical performance is not yet completely established. Some existing research studies related to this topic are as follows. Stanova *et al.* (2011) fully considered the spatial spiral structure of a single wire and stranded ropes and developed a parametric mathematical model of the wire rope. Ma *et al.* (2015) deduced a function expression for the central line of a wire rope based on the Serret-Frenet frame theory. Using the differential geometry theory as the theoretical basis, Hobbs and Nabijou (1995) and Nabijou and Hobs (1995) provided a path expression for a wire on a rope sheave based on the mathematical model of a vertical wire rope. Wu and Cao (2016) deduced the equivalent elastic modulus of a wire rope based on the theory of slender elastic rods. Prawoto and Mazlan (2012) studied mechanical properties of a steel wire rope under tensile load by numerical simulation and experimental methods and obtained the microstructure of fracture in the steel wire rope. Stanová (2013) derived mathematical models of oval strand ropes and used Pro/E software to build geometric models of the ropes. Sathikh *et al.* (1996) used the Wempner-Ramsey theory to study the asymmetry of the stiffness matrix in a wire-rope elasticity model under bending and torsional loads and validated the model experimentally. Erdönmez and Erdem Imrak (2009) developed a three-dimensional structural model of a double-helix wire rope that took into account friction and slip between the rope cores. Machida and Durelli (1973) defined an expression for the axial force, bending moment and torsional moment in a helix. Elata *et al.* (2004) proposed a new model

for simulating the mechanical response of wire ropes with individual steel cord cores. The model fully considered the double-helix structure of a single wire in the wound strand and provided the stress in the wire layer to estimate global characteristics of the wire rope. Hu *et al.* (2016) derived initial parameters of different general wire-rope models and developed IWRC6/36WS wire-rope model using MATLAB and Pro/E. The elastic properties of the wire rope under axial tension were analyzed by Abaqus/Explicit. Wang *et al.* (2015) developed a parametric model for arbitrary centerline wire-rope structures and derived a series of recursive formulas for the spatial unwinding equations of wires and strands. Liang *et al.* (2011) calculated the equivalent elastic modulus of a wire rope in different positions based on a linear strengthening model. Bai (2011) derived a mathematical expression for the equivalent elastic modulus of a wire-rope conveyor belt based on pendency. Ma (2014) analyzed the equivalent elastic modulus of a wire-rope using static theory and validated the correctness of the analysis process by using ANSYS and by experimental measurements. Xu *et al.* (2012, 2015) proposed a method for calculating the equivalent elastic modulus of a single-fiber multidirectional winding tube based on the laminated plate theory and a theoretical estimation method for calculating the three-dimensional elastic modulus of a multifiber hybrid multidirectional winding tube considering the mixed effect.

In this study, based on the micromechanical wire-rope model, a theoretical formula for the equivalent elastic modulus of a wire rope is deduced using the differential geometry theory according to spatial characteristics of the central helical lines in the double-helix wire rope. The formula is expected to serve as a theoretical basis for dynamic analysis and optimization of mechanical systems containing wire ropes.

2. Three-dimensional geometrical model of the wire rope

The object of the study is a double-helix wire rope which is shown in Fig. 1. It comprises stranded ropes wound around the central strand helix according to certain rules. Each wire rope is a helical wire bundle with a high load-carrying capacity and consists of multiple wires twisted around the core wire according to a spatial spiral relationship. In this study, the spatial geometry of the wire, whose basic units are strands and ropes, is divided into the following four types: the central strand core wire, central strand side wire, lateral strand core wire, and lateral strand side wire. The central strand core wire is mostly straight or has a simple curve. The central strand side wire and the lateral strand side wire are first-degree spatial helical lines wound around the central strand core wire. The lateral strand side wire is a second-degree spatial helical line with respect to the central strand core wire. The cross section of the double-helix wire rope is shown in Fig. 1b.

To facilitate the analysis, a unit length of the twisted wire rope is intercepted. The central helical lines of the central strand core wire, central strand side wire, lateral strand core wire and the lateral strand side wire are considered separately to establish the Cartesian coordinate system, as shown in Fig. 2.

Consider a random point on the central strand side wire $P_1(x, y, z)$. The projection of this point on the XOY plane is P'_1 , whose coordinates are

$$x = R_1 \cos \theta_1 \quad y = R_1 \sin \theta_1 \quad z = \frac{\theta_1}{2\pi} L_1 \quad (2.1)$$

where R_1 is the twisted circle radius of the central strand side wire ($R_1 = (d_0 + d_1)/2$, where d_0 and d_1 are the radii of the central strand core wire and the central strand side wire, respectively, in millimeters), θ_1 is the polar angle corresponding to P_1 in radians, and L_1 is the twist pitch of the central strand side wire in millimeters.

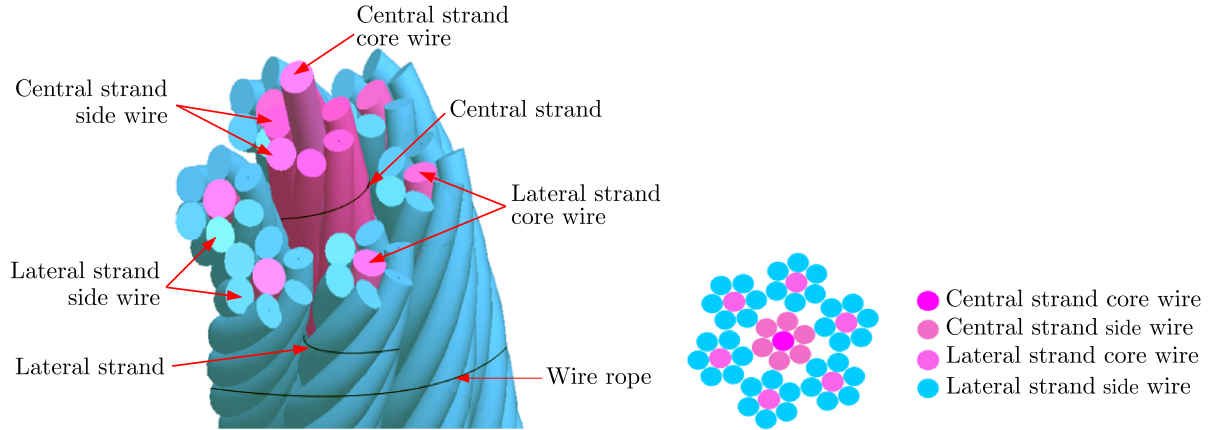


Fig. 1. Schematic diagram of the wire rope; (a) structure diagram of the wire rope, (b) cross section of the wire rope

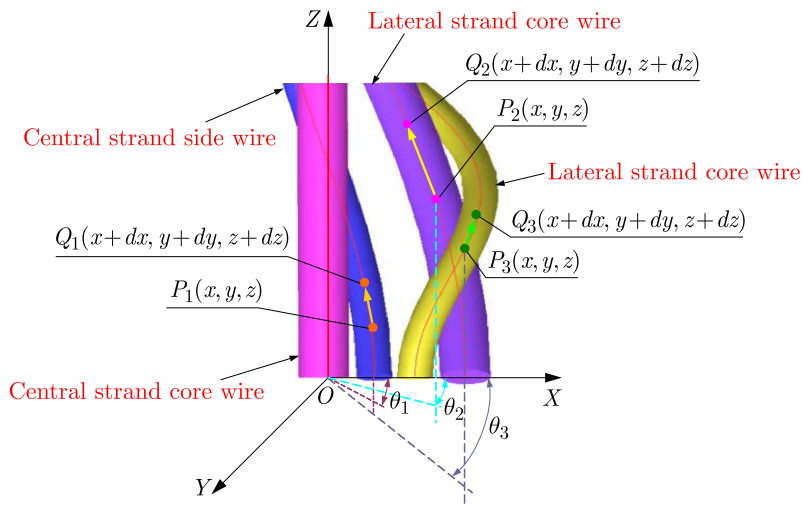


Fig. 2. Spatial coordinate system of the wire rope

Consider a small arc P_1Q_1 with P_1 as the starting point. Then, the coordinates of Q_1 are $(x+dx, y+dy, z+dz)$, and thus

$$dx = -R_1 \sin \theta_1 d\theta_1 \quad dy = R_1 \cos \theta_1 d\theta_1 \quad dz = \frac{L_1}{2\pi} d\theta_1 \quad (2.2)$$

The length of the small arc P_1Q_1 can be obtained from equations (2.1) and (2.2)

$$dS_1 = \sqrt{R_1^2 + \left(\frac{L_1}{2\pi}\right)^2} d\theta_1 \quad (2.3)$$

Thus, the length of the central strand side wire is

$$S_1 = \int_0^{2\pi} \sqrt{R_1^2 + \left(\frac{L_1}{2\pi}\right)^2} d\theta_1 = \sqrt{4\pi^2 R_1^2 + L_1^2} \quad (2.4)$$

The tangent inclination cosine of the small arc P_1Q_1 at P_1 on the central strand side wire is

$$\cos \alpha_1 = \frac{L_1}{\sqrt{4\pi^2 R_1^2 + L_1^2}} = \frac{L_1}{S_1} \quad (2.5)$$

Similarly, consider a random point on the lateral strand core wire $P_2(x, y, z)$. The projection of this point on the XOY plane is P'_2 , whose coordinates are

$$x = R_2 \cos \theta_2 \quad y = R_2 \sin \theta_2 \quad z = \frac{\theta_2}{2\pi} L_2 \quad (2.6)$$

where R_2 is the twisted circle radius of the lateral strand core wire ($R_2 = (d_0 + d_2)/2 + d_1 + d_3$, where d_2 and d_3 are the radii of the lateral strand core wire and the lateral strand side wire, respectively, in millimeters), θ_2 is the polar angle corresponding to P_2 in radians, and L_2 is the twist pitch of the lateral strand core wire in millimeters.

Consider a small arc P_2Q_2 with P_2 as the starting point. Then, the coordinates of Q_2 are $(x + dx, y + dy, z + dz)$, thus

$$dx = -R_2 \sin \theta_2 d\theta_2 \quad dy = R_2 \cos \theta_2 d\theta_2 \quad dz = \frac{L_2}{2\pi} d\theta_2 \quad (2.7)$$

The length of the small arc P_2Q_2 can be obtained from equations (2.6) and (2.7)

$$dS_2 = \sqrt{R_2^2 + \left(\frac{L_2}{2\pi}\right)^2} d\theta_2 \quad (2.8)$$

The length of the lateral strand core wire is

$$S_2 = \int_0^{2\pi} \sqrt{R_2^2 + \left(\frac{L_2}{2\pi}\right)^2} d\theta_2 = \sqrt{4\pi^2 R_2^2 + L_2^2} \quad (2.9)$$

The tangent inclination cosine of the small arc P_2Q_2 at P_2 on the central strand side wire is

$$\cos \alpha_2 = \frac{L_2}{\sqrt{4\pi^2 R_2^2 + L_2^2}} = \frac{L_2}{S_2} \quad (2.10)$$

Consider a random point on the lateral strand side wire $P_3(x, y, z)$. The projection of this point on the XOY plane is P'_3 , whose coordinates are

$$\begin{aligned} x &= R_2 \cos \theta_2 - R_3 \cos \theta_2 \cos \theta_3 + R_3 \sin \beta_2 \sin \theta_2 \sin \theta_3 \\ y &= R_2 \sin \theta_2 - R_3 \sin \theta_2 \cos \theta_3 - R_3 \sin \beta_2 \cos \theta_2 \sin \theta_3 \\ z &= \frac{\theta_2}{2\pi} L_2 + R_3 \cos \beta_2 \sin \theta_3 \end{aligned} \quad (2.11)$$

Consider a small arc P_3Q_3 with P_3 as the starting point. Then, the coordinates of Q_3 are $(x + dx, y + dy, z + dz)$, and thus

$$\begin{aligned} dx &= \left[-\frac{1}{n} R_2 \sin \frac{\theta_3}{n} + \left(\frac{1}{n} + \sin \beta_2 \right) R_3 \sin \frac{\theta_3}{n} \cos \theta_3 + \left(1 + \frac{1}{n} \sin \beta_2 \right) R_3 \cos \frac{\theta_3}{n} \sin \theta_3 \right] d\theta_3 \\ dy &= \left[\frac{1}{n} R_2 \cos \frac{\theta_3}{n} - \left(\frac{1}{n} + \sin \beta_2 \right) R_3 \cos \frac{\theta_3}{n} \cos \theta_3 + \left(1 + \frac{1}{n} \sin \beta_2 \right) R_3 \sin \frac{\theta_3}{n} \sin \theta_3 \right] d\theta_3 \\ dz &= \left(\frac{L_2}{2\pi n} + R_3 \cos \beta_2 \cos \theta_3 \right) d\theta_3 \end{aligned} \quad (2.12)$$

where R_3 is the twisted circle radius of the lateral strand side wire, in millimeters ($R_3 = (d_0 + d_1 + d_3)/2$), θ_3 is the polar angle corresponding to P_3 in radians, β_2 is the helical ascent angle of the lateral strand side wire in radians, and n is the number of twisted rounds of the lateral strand side wires about the lateral strand core wire.

Next, set

$$\begin{aligned} C_1 &= \frac{1}{n}R_2 & C_2 &= \left(\frac{1}{n} + \sin \beta_2\right)R_3 & C_3 &= \left(1 + \frac{1}{n} \sin \beta_2\right)R_3 \\ C_4 &= \frac{L_2}{2\pi n} & C_5 &= R_3 \cos \beta_2 \end{aligned} \quad (2.13)$$

The length of the small arc P_3Q_3 can be obtained from equations (2.11)-(2.13)

$$dS_3 = \sqrt{(C_1 - C_2 \cos \theta_3)^2 + (C_3 \sin \theta_3)^2 + (C_4 + C_5 \cos \theta_3)^2} d\theta_3 \quad (2.14)$$

The length of the lateral strand side wire is

$$S_3 = \int_0^{2\pi} \sqrt{(C_1 - C_2 \cos \theta_3)^2 + (C_3 \sin \theta_3)^2 + (C_4 + C_5 \cos \theta_3)^2} d\theta_3 \quad (2.15)$$

The tangent inclination cosine of the small arc P_3Q_3 at P_3 on the central strand side wire is

$$\cos \alpha_3 = \frac{C_4 + C_5 \cos \theta_3}{\sqrt{(C_1 - C_2 \cos \theta_3)^2 + (C_3 \sin \theta_3)^2 + (C_4 + C_5 \cos \theta_3)^2}} \quad (2.16)$$

Combining equations (2.5), (2.10) and (2.16), the nominal area of the wire rope can be obtained

$$A^* = A_0 + 6\frac{A_1}{\cos \alpha_1} + 6\frac{A_2}{\cos \alpha_2} + 36\frac{A_3}{\cos \alpha_3} \quad (2.17)$$

where A_0 , A_1 , A_2 and A_3 are the cross-sectional areas of the central strand core wire, central strand side wire, lateral strand core wire and lateral strand side wire, respectively.

3. Calculation of the elastic modulus of the wire rope

Because only the equivalent elastic modulus of the double-helix wire rope is calculated in this study, the following assumptions are made: (1) The cross section of the wire is perpendicular to the tangent line corresponding to the central helix. (2) Friction between the wires is negligible. (3) The wires elongate without twisting, and the elongation amount is recorded as ΔL . Tension and elongation of the central strand core wire, central strand side wire, lateral strand core wire and the lateral strand side wire are deduced separately.

Ad. (1) For the central strand core wire, after an elongation of ΔL in the Z -axis direction, the corresponding tensile stress ε and tension T_0 are respectively given as

$$\varepsilon = E \frac{\Delta L}{L_1} \quad T_0 = \varepsilon_0 A_0 = \frac{\pi E d_0^2}{4L_1} \Delta L \quad (3.1)$$

Because materials of the wire rope are mostly nonalloy carbon steels, the elastic modulus is assumed to be $E = 183.9 \text{ GPa}$ (Liu, 2014).

Ad. (2) According to the helical spatial structure of the central strand side wire, the elongation can be deduced by the whole differential as follows

$$\Delta S_1 = \frac{4\pi^2 R_1}{S_1} \Delta R_1 + \frac{L_1}{S_1} \Delta L = \frac{L_1}{S_1} \Delta L \left(1 + \frac{4\pi^2 R_1}{S_1} \frac{\Delta R_1}{\Delta L}\right) \quad (3.2)$$

According to Wang *et al.* (2004)

$$1 + \frac{4\pi^2 R_1}{S_1} \frac{\Delta R_1}{\Delta L} \approx 1 \quad (3.3)$$

Thus

$$\Delta S_1 \approx \frac{L_1}{S_1} \Delta L \quad (3.4)$$

Based on material mechanics, the tension of a single central strand side wire in the Z -axis direction can be expressed as

$$T_1 = E \frac{\Delta S_1}{S_1} A_1 \cos \alpha_1 = \frac{\pi E d_1^2 L_1^2}{4 S_1^3} \Delta L \quad (3.5)$$

Ad. (3) Because the lateral strand core wire has the same spatial structure as the central strand side wire, the same method can be used to obtain expressions for the elongation and tension of the lateral strand core wire. The elongation ΔS_2 can be expressed as

$$\Delta S_2 \approx \frac{L_2}{S_2} \Delta L \quad (3.6)$$

The tension T_2 in the Z -axis direction is

$$T_2 = E \frac{\Delta S_2}{S_2} A_2 \cos \alpha_2 = \frac{\pi E d_2^2 L_2^2}{4 S_2^3} \Delta L \quad (3.7)$$

Ad. (4) The lateral strand side wire is the second-degree spatial helical line with respect to the central strand core wire; thus

$$\Delta S_3 = \frac{\partial S_3}{\partial R_3} + \frac{\partial S_3}{\partial L_3} \quad T_3 = E \frac{\Delta S_3}{S_3} A_3 \cos \alpha_3 = \frac{E A_3 \cos \alpha_3}{S_3} \left(\frac{\partial S_3}{\partial R_3} + \frac{\partial S_3}{\partial L_3} \right) \quad (3.8)$$

According to the above equations, the tension of the wire rope T^* can be expressed as

$$T^* = T_0 + 6T_1 + 6T_2 + 36T_3 \quad (3.9)$$

The elastic modulus of the wire rope can be obtained according to equations (2.17) and (3.9)

$$E^* = \frac{T^*}{A^* X} \quad (3.10)$$

Thus

$$E^* = LE \frac{\frac{d_0^2}{L_1} + \frac{6d_1^2 L_1 \cos \alpha_1}{S_1^2} + \frac{6d_2^2 L_2 \cos \alpha_2}{S_2^2} + \frac{36 \left(\frac{\partial S_3}{\partial R_3} + \frac{\partial S_3}{\partial L_3} \right) d_3^2 \cos \alpha_3}{S_3}}{d_0^2 + \frac{6d_1^2}{\cos \alpha_1} + \frac{6d_2^2}{\cos \alpha_2} + \frac{36d_3^2}{\cos \alpha_3}} \quad (3.11)$$

where $X = \Delta L/L$ (L is length of the wire rope in millimeters), $S_1 = \sqrt{4\pi^2 R_1^2 + L_1^2}$ is length of the central strand side wire in millimeters, $S_2 = \sqrt{4\pi^2 R_2^2 + L_2^2}$ is length of the lateral strand side wire in millimeters, S_3 (see Eq. (2.15)) is length of the lateral strand side wire in millimeters, $\cos \alpha_1 = L_1/S_1$ is tangent inclination cosine of the small arc on the central strand core wire, $\cos \alpha_2 = L_2/S_2$ is tangent inclination cosine of the small arc on the lateral strand core wire, and $\cos \alpha_3$ (see Eq. (2.16)) is tangent inclination cosine of the small arc on the lateral strand side wire. In addition, C_i ($i = 1, \dots, 5$) see Eqs. (2.13).

4. Case analysis and verification

To verify the correctness of the expression for the equivalent elastic modulus predicted by the spatial distribution of the central line of the double-helix wire rope, the 6×7+IWS wire rope is used as an example. The basic structural parameters of this rope are listed in Table 1. According to equation (3.11), the equivalent elastic modulus of the wire rope can be determined. According to the measurement method of the actual elastic modulus of a wire rope given in the national standard GB/T24191-2009, the universal tensile testing machine (Fig. 3) is used to measure the actual equivalent elastic modulus of the wire rope.

Table 1. Structural parameters of 6×7+IWS wire rope

Wire rope diameter [mm]	Twist pitch [mm]	Number of twisted rounds of lateral strand side wires about lateral strand core wire	Wire twist angle [°]	Wire-rope diameter [mm]	
				central strand	lateral strand
4.5	36	3.1416	10.3848	0.6	0.4



Fig. 3. Universal tensile testing machine

In the analysis, 600 mm of the wire rope is intercepted from selected wire-rope samples and placed at a room temperature of 18° for 24 h. Both ends of the sample are mechanically clamped in the universal tensile testing machine. Each end has clamping length of 50 mm. The uniaxial tensile test (Wu *et al.*, 2014) is performed by clamping the wire rope through the jaws of the testing machine.

According to the requirements of the national standard GB/T24191-2009, the elastic modulus of the wire-rope sample in the fully stable state should be 10%-30% of the minimum breaking tension (or nominal breaking load). The loads at 10% and 30% are denoted as $F_{10\%}$ and $F_{30\%}$, respectively. Simultaneously, the elongations of the wire rope at $F_{10\%}$ and $F_{30\%}$ loads are recorded as x_1 and x_2 , respectively. According to the national standard GB8918-2006, the minimum breaking tension of the 6×7+IWS (2006) wire rope is 11.6 kN. According to the above experimental steps, the corresponding displacement-load deformation curve is obtained for the wire rope through measurement of the elastic modulus, as shown in Fig. 4.

According to the actual elastic modulus of the wire rope given in GB/T24191-2009

$$E_{10-30} = l_0 \frac{F_{30\%} - F_{10\%}}{A(x_2 - x_1)} \quad (4.1)$$

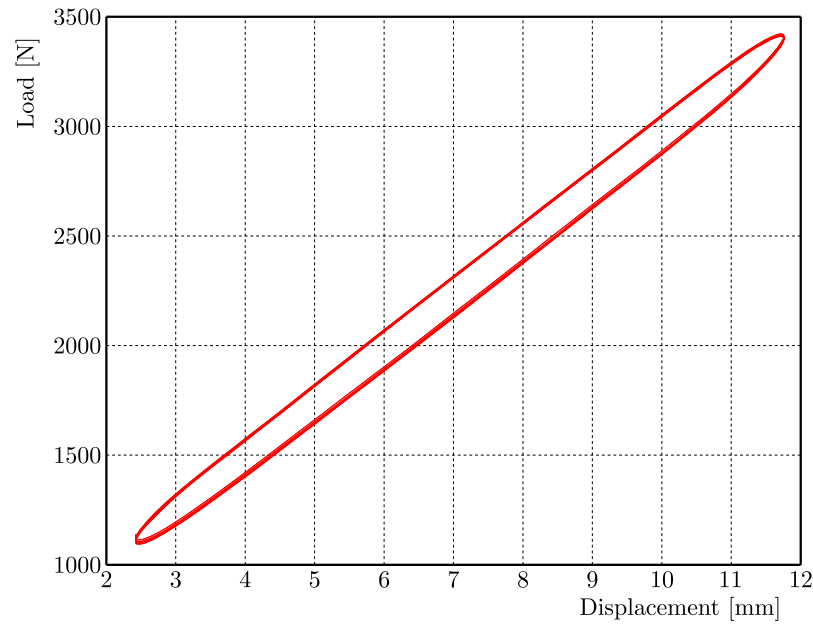


Fig. 4. Displacement-load deformation curve

where E_{10-30} is the actual elastic modulus of the wire rope in gigapascals; l_0 is the initial length of the wire rope in millimeters; $F_{10\%}$ and $F_{30\%}$ are the loads at 10% and 30% of the minimum breaking tension (or nominal breaking load) of the wire-rope sample, respectively, in kilonewtons; A is the cross-sectional area of the wire rope in millimeters (in this study $A = A^*$); and x_1 and x_2 are the elongations of the wire rope at $F_{10\%}$ and $F_{30\%}$ loads, respectively, in millimeters.

According to equation (4.1), the elastic modulus of the 6×7+IWS wire rope is

$$E_{10-30} = 500 \frac{3480 - 1160}{13.52(11.75 - 2.39)} = 9.17 \text{ GPa} \quad (4.2)$$

Compared to the theoretical value of the equivalent elastic modulus of the wire rope $E^* = 8.75 \text{ GPa}$, the error of the calculated is value 4.8%, which is relatively small. The results show that the value calculated using the model can be used to accurately predict the actual elastic modulus of the wire rope.

5. Conclusion

In this study, according to the spatial distribution characteristics of each central line of a double-helix wire rope, the theoretically predicted expression for the equivalent elastic modulus of the wire rope is obtained using the differential geometry theory. The 6×7+IWS wire rope is used as the study object, and an elastic modulus measurement experiment is performed on this rope. The correctness of the theoretical deduction of the equivalent elastic modulus is verified through the comparison and analysis of the experimental value and the theoretically predicted one.

References

1. BAI C.C., 2011, *Simulation and Finite Element Analysis of the Steel-Cord Conveyor Belt on Fragmentation*, Shanghai: East China University of Science and Technology, 16-18
2. ELATA D., ESHKENAZY R., WEISS M.P., 2004, The mechanical behavior of a wire rope with an independent wire rope core, *International Journal of Solids and Structures*, **41**, 5-6, 1157-1172

3. ERDÖNMEZ C., ERDEM IMRAK C., 2009, Modeling and numerical analysis of the wire strand, *Journal of Naval Science and Engineering*, **5**, 1, 30-38
4. GB8918-2006, National Standards of Steel Wire Rope (Steel wire ropes for important purpose)
5. GBT228-2002, National Standards of Metallic materials -Tensile Specimens (Metallic materials – Tensile testing at ambient temperature)
6. GBT24191-2009, Steel wire ropes – determination of the actual modulus of elasticity
7. HOBBS R., NABIJO S., 1995, Changes in wire curvature as a wire rope is bent over a sheave, *Journal of Strain Analysis for Engineering Design*, **30**, 4, 271-281
8. HU Y., HU Z., MA H., YAN P., LIU Y., 2016, Finite element simulation of axial elastic characteristics of wire rope with one round strand layer, *IEEE International Conference on Computer Supported Cooperative Work in Design*, 16-19
9. JOLICOEUR C., CARDOU A., 1991, A numerical comparison of current mathematical models of twisted wire cables under axisymmetric loads, *Journal of Energy Resources and Technology*, **113**, 4, 241-249
10. JOLICOEUR C., CARDOU A., 1996, Semi continuous mathematical for bending of multilayered wire strands, *Journal of Engineering Mechanics*, **122**, 7, 643-650
11. LIANG Q.X., LI C., SUN J., 2011, Numerical simulation of knotted wire rope with finite element method, *Journal of Taiyuan University Science and Technology*, **32**, 3, 232-234
12. LIU Y.H., 2014, *Research on Inherent Properties and Mechanical Performances of Wire Rope*, Shanxi: Taiyuan University of Technology
13. MA Q., 2014, *Performance Analysis of Wire Rope Vibration Absorber*, Beijing: Beijing University of Chemical Technology, 17-27
14. MA W., ZHU Z.C., PENG Y.X., CHEN G.A., 2015, Computer-aided modeling of wire ropes bent over a sheave, *Advance in Engineering Software*, **90**, C, 11-21
15. MACHIDA S., DURELLI A.J., 1973, Response of a strand to axial and torsional displacements, *Journal of Mechanical Engineering Science*, **15**, 4, 241-251
16. NABIJO S., HOBBS R., 1995, Relative movements within wire ropes bent over sheaves, *Journal of Strain Analysis for Engineering Design*, **30**, 2, 155-165
17. PRAWOTO Y., MAZLAN R.B., 2012, Wire ropes: computational, mechanical, and metallurgical properties under tension loading, *Computational Materials Science*, **56**, 174-178
18. SATHIKH S., MOORTHY M., KRISHNAN M., 1996, Symmetric linear elastic model for helical wire strands under axisymmetric loads, *Journal of Strain Analysis for Engineering Design*, **31**, 5, 389-399
19. STANOVÁ E., 2013, Geometric model of the rope created of oval strands, *Transport and Logistics*, 1-7
20. STANOVÁ E., FEDORKO G., FABIAN M., KMET S., 2011, Computer modeling of wire stands and ropes. Part 1: Theory and computer implementation, *Advance in Engineering Software*, **42**, 6, 305-315
21. WANG X.Y., MENG X.B., WANG J.X., SUN Y.H., GAO K., 2015, Mathematical modeling and geometric analysis for wire rope strands, *Applied Mathematical Modelling*, **39**, 3-4, 1019-1032
22. WANG Y.J., LI Z.Q., SONG X.H., 2004, Theoretical computer and analysis affecting factors on stranded wire's elastic module, *Journal of Wuhan University of Technology*, **26**, 4, 80-82
23. WU J., KOU Z.M., LIU Y.H., WU G.X., 2014, Distribution of equivalent stresses and deformations for 6 strand warrington-seale rope with an independent wire rope core, *Journal of China Coal Society*, **39**, 11, 2340-2347
24. WU W.G., CAO X., 2016, Mechanics model and its equation of wire rope based on elastic thin rod theory, *International Journal of Solids and Structures*, **102**, 21-29

25. XU G.L., RUAN W.J., WANG H., YANG Q.P., 2015, Estimation of 3D effective elastic modulus for fiber multidirectional filament-wound tube, *Journal of Materials Science and Engineering*, **31**, 1, 55-59
26. XU G.L., YANG Q.P., RUAN W.J., WANG H., 2012, Estimation and experiment of 3D effective elastic modulus for fiber hybrid tube considering hybrid effects, *Acta Materiae Compositae Sinica*, **29**, 4, 204-209

Manuscript received August 18, 2017; accepted for print February 6, 2018

EFFECTS OF VISCOELASTIC AND POROUS MATERIALS ON SOUND TRANSMISSION OF MULTILAYER SYSTEMS

HADDA FELHI

Laboratory of Mechanics, Modelling and Production (LA2MP), National Engineering School of Sfax, University of Sfax, Sfax, Tunisia, and Faculty of Sciences of Sfax, University of Sfax, Sfax, Tunisia

HASSEN TRABELSI

Laboratory of Mechanics, Modelling and Production (LA2MP), National Engineering School of Sfax, University of Sfax, Sfax, Tunisia

MOHAMED TAKTAK

Laboratory of Mechanics, Modelling and Production (LA2MP), National Engineering School of Sfax, University of Sfax, Sfax, Tunisia, and Faculty of Sciences of Sfax, University of Sfax, Sfax, Tunisia

e-mail: mohamed.taktak@fss.rnu.tn

MABROUK CHAABANE

Faculty of Sciences of Sfax, University of Sfax, Sfax, Tunisia

MOHAMED HADDAR

Laboratory of Mechanics, Modelling and Production (LA2MP), National Engineering School of Sfax, University of Sfax, Sfax, Tunisia

Multilayer structures allow obtaining good performance in acoustic insulation to eliminate unwanted noise in the medium and high frequencies in many applications such as building and transport industry. In this paper, the sound transmission of multilayer systems is studied using the Transfer Matrix Method (TMM). The studied multi-layered panels include elastic, viscoelastic and porous materials. Several configurations of multilayer systems are studied, and their corresponding transmission loss TL is computed. Also, the effects of porous material characteristics are studied to evaluate the impact of each parameter.

Keywords: porous material, multilayer system, transmission loss, transfer matrix

1. Introduction

The control of noise and vibration has become one of the major concerns in several fields of industry (aeronautics, automobile, household appliances...). Indeed, reduction of noise and vibrations avoids material damage and nuisance effects. The use of sandwich systems with a high damping power core is one of ways to reduce elevated noise and vibration levels. This type of structures offers significant technological advantages (low weight, high rigidity, easy automation of manufacturing, etc.). These sandwich panels contain an absorbent porous materials and are widely used in transport and building industries to reduce nuisance noise and improve comfort of individuals.

In order to increase acoustic insulation properties of multilayer panel configurations, elastic, viscoelastic and porous materials were studied by Allard *et al.* (1987), Mueller and Tschudl (1989), Atalla *et al.* (1998), Ghinet *et al.* (2005) and Abid *et al.* (2012). The behavior of panel combinations of materials depends more or less on dimensions and boundary conditions of edges. Nevertheless, interesting results can be obtained by modeling the samples in the form of infinite plates subjected to incident plane waves.

The modeling of the acoustic response of multilayer structures is done using different methods. Tanneau (2004) and Tanneau *et al.* (2006) studied modeling of an aeronautical insulation panel by the finite elements and boundary elements. These methods are applicable in low frequencies. When the frequency domain increases, the implementation of these methods is confronted with an excessive increase of the degrees of freedom associated with fineness of the mesh compatible with wavelengths. The cost of calculations becomes then prohibitive and the results are very sensitive to the least perturbation of geometric and physical parameters. In order to overcome these disadvantages, Thomson (1950), Allard *et al.* (1989), Lee and Xu (2009), Munjal (1993) and Sastry and Munjal (1995) presented an analytical method for the estimation of acoustic indicators of stratified media called the Transfer Matrix Method (TMM). This method is based on the representation of propagation of plane waves in different media in terms of the transfer matrix.

The TMM is applied with an excitation of the air (normal or oblique acoustic wave) and in a diffuse field. The TMM is based on calculation of the transfer matrix of each layer. These matrices are obtained by applying continuity conditions on the interfaces between layers giving a system of equations linking speeds and stresses between the layers. The global transfer matrix is calculated: If the layers are of the same nature, the transfer matrix is made by multiplying the transfer matrix of each layer. If the layers are different, the interface matrix is used. Finally, the transmission loss TL is calculated from the resulting global transfer matrix as presented by Munjal *et al.* (1993).

The aim of the present paper is to predict the acoustic parameters of several multilayer configurations by the Transfer Matrix Method and to study also the effect of replacement of the viscoelastic layer instead of the elastic solid layer. Also, the effects of porous parameters on the behavior of sound transmission of these configurations are studied in order to improve the acoustic insulation of multilayer panels.

The outline of the document is as follows: Section 1 presents description of the TMM for predicting the transfer matrix of a multilayer structure. In Section 2, calculation of the transmission loss from the obtained transfer matrix is presented. Finally, numerical results and a comparison study based on the replacement of the elastic layer by a viscoelastic layer are presented in Section 3. In this Section, a parametric study is carried out to choose the best multilayer configuration.

2. The transfer matrix method

2.1. General formulation

The transfer matrix method is based on the modeling of propagation of plane waves in various layers by the transfer matrix. As presented in Fig. 1, the studied layer is an h thickness layer excited by an oblique wave plane. The geometry of the problem is bidimensional in the incident plane (x_1, x_3) . The lateral dimension of the layer is supposed to be infinite. Various types of waves can propagate in the material according to their nature as studied by Allard and Atalla (2009). The sound propagation in the layer is represented by a transfer matrix \mathbf{T} as follows

$$\mathbf{V}_{M_1} = \mathbf{T}\mathbf{V}_{M_2} \quad (2.1)$$

where M_1 and M_2 are sets close to the forward and backward face of the layer, respectively, and where the components of the vector \mathbf{V}_{M_1} and \mathbf{V}_{M_2} are respectively the variables which describe the acoustic field at the points M_1 and M_2 of the medium. The transfer matrix \mathbf{T} depends on the thickness h and the acoustical properties of each medium.

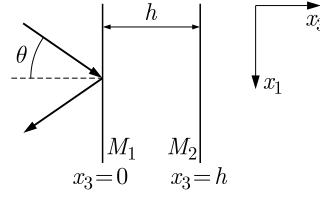


Fig. 1. Layer subjected to an oblique incident wave

2.2. Construction of the transfer matrix

Figure 2 represents a multi-layer structure composed of solid and poroelastic layers. In the following, the computation of the transfer matrix of each medium is presented.

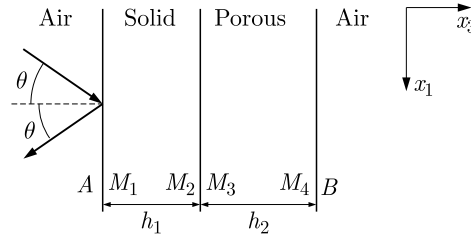


Fig. 2. Multilayered panel

2.2.1. Solid layer

In an elastic solid layer, longitudinal and shear waves propagate into the layer. The acoustic field in the material is described using the amplitudes of the following waves: the incident and reflected longitudinal waves and the incident and reflected shear waves (A_1 , A_2 , A_3 and A_4). The associated displacement potentials can be written as follows

$$\begin{aligned}\phi &= \exp(j\omega t - jk_1x_1)[A_1 \exp(-jk_{13}x_3) + A_2 \exp(jk_{13}x_3)] \\ \psi &= \exp(j\omega t - jk_1x_1)[A_3 \exp(-jk_{33}x_3) + A_4 \exp(jk_{33}x_3)]\end{aligned}\quad (2.2)$$

where the x_3 components k_{13} and k_{33} of the wave number vectors are expressed as follows

$$k_{13} = \sqrt{\delta_1^2 - k_t^2} \quad k_{33} = \sqrt{\delta_3^2 - k_t^2} \quad (2.3)$$

The x_1 component of the wave number k_1 is given by

$$k_1 = k \sin \theta \quad (2.4)$$

δ_1^2 and δ_3^2 are respectively the squares of the wave numbers of the longitudinal and shear waves in the elastic solid layer. They are given by

$$\delta_1^2 = \frac{\omega^2 \rho_s}{\lambda + 2\mu} \quad \delta_3^2 = \frac{\omega^2 \rho_s}{\mu} \quad (2.5)$$

where ρ_s is the surface density of the elastic solid, λ and μ are, respectively, the first and second Lamé coefficients. The acoustic field in the elastic solid layer can be predicted if the amplitudes A_1 , A_2 , A_3 and A_4 are known. Instead of these parameters, four mechanical variables may be known to express sound propagation everywhere in the medium. Following Folds and Loggins (1977) the four chosen quantities are v_1^s and v_3^s being respectively the x_1 and x_3 components

of the velocity at point M_i as well as σ_{33}^s and σ_{13}^s being respectively the normal and tangential stresses at the point M_i . The vector \mathbf{V}^s in this case is expressed as follows

$$\mathbf{V}_{M_i}^s = [\nu_1^s(M_i), \nu_3^s(M_i), \sigma_{33}^s(M_i), \sigma_{13}^s(M_i)]^T \quad i = 1, 2 \quad (2.6)$$

These velocities and stresses are written as follows

$$\begin{aligned} \nu_1^s &= j\omega \left(\frac{\partial \phi}{\partial x_1} - \frac{\partial \psi}{\partial x_3} \right) & \nu_3^s &= j\omega \left(\frac{\partial \phi}{\partial x_3} + \frac{\partial \psi}{\partial x_1} \right) \\ \sigma_{33}^s &= \lambda \left(\frac{\partial^2 \phi}{\partial x_1^2} + \frac{\partial^2 \phi}{\partial x_3^2} \right) + 2\mu \left(\frac{\partial^2 \phi}{\partial x_3^2} + \frac{\partial^2 \psi}{\partial x_1 \partial x_3} \right) & \sigma_{13}^s &= \mu \left(2 \frac{\partial^2 \phi}{\partial x_1 \partial x_3} + \frac{\partial^2 \psi}{\partial x_1^2} - \frac{\partial^2 \psi}{\partial x_3^2} \right) \end{aligned} \quad (2.7)$$

To obtain the transfer matrix \mathbf{T}^s of the elastic solid layer, the vector $\mathbf{V}_{M_1}^s$ is first connected to the amplitudes of different waves propagating in the layer presented by the following vector

$$\mathbf{A} = [(A_1 + A_2), (A_1 - A_2), (A_3 + A_4), (A_3 - A_4)] \quad (2.8)$$

and by the matrix $\mathbf{\Gamma}(x_3)$ such that

$$\mathbf{V}_M^s = \mathbf{\Gamma}(x_3) \mathbf{A} \quad (2.9)$$

If the origin of the x_3 axis is fixed at the point M_i , the vectors $\mathbf{V}_{M_1}^s$ and $\mathbf{V}_{M_2}^s$ are expressed as

$$\mathbf{V}_{M_1}^s = \mathbf{\Gamma}(0) \mathbf{A} \quad \mathbf{V}_{M_2}^s = \mathbf{\Gamma}(h) \mathbf{A} \quad (2.10)$$

Then, the transfer matrix \mathbf{T}^s which relates $\mathbf{V}_{M_1}^s$ and $\mathbf{V}_{M_2}^s$ is equal to

$$\mathbf{T}^s = \mathbf{\Gamma}(0) \mathbf{\Gamma}^{-1}(h) \quad (2.11)$$

2.2.2. Poroelastic layer

In a porous material structure, three elastic waves propagate into the medium: two compression waves and a shear wave (Allard *et al.*, 1987). The displacement potential of the compression ϕ^s and shear ψ^s waves are given by

$$\begin{aligned} \phi_1^s &= \exp(j\omega t - jk_1 x_1) [A_1 \exp(-jk_{13} x_3) + A'_1 \exp(jk_{13} x_3)] \\ \phi_2^s &= \exp(j\omega t - jk_1 x_1) [A_2 \exp(-jk_{23} x_3) + A'_2 \exp(jk_{23} x_3)] \\ \psi_2^s &= \exp(j\omega t - jk_1 x_1) [A_3 \exp(-jk_{33} x_3) + A'_3 \exp(jk_{33} x_3)] \end{aligned} \quad (2.12)$$

The air displacement potentials are related to the layer displacement potentials by

$$\phi_i^f = \mu_i \phi_i^s \quad i = 1, 2 \quad \psi_1^f = \mu_3 \phi_2^s \quad (2.13)$$

with

$$\frac{\phi_i^f}{\phi_i^s} = \frac{P\delta_1^2 - \omega^2 \tilde{\rho}_{11}}{\omega^2 \rho_{12} - Q\delta_i^2} \quad i = 1, 2 \quad \mu_3 = -\frac{\tilde{\rho}_{12}}{\rho_{22}}$$

The ratio μ_i of the velocity of the air over the velocity of the frame is for two compression waves and μ_3 is for the shear wave. The acoustic field in the porous layer can be predicted everywhere if the six amplitudes $A_1, A'_1, A_2, A'_2, A_3, A'_3$ are known. However, instead of these parameters, six independent acoustic quantities can be chosen. Three velocity components and three elements of the stress tensors: two velocity components ν_1^s and ν_3^s of the frame, the velocity component ν_3 of the fluid, two components σ_{33}^s and σ_{13}^s of the stress tensor of the frame and σ_{33}^f in the fluid. If these six quantities are known at the point M_i in the layer, the acoustic field can be predicted

everywhere in the layer. Moreover, the values of these quantities anywhere in the layer depend linearly on the values of these quantities at M_i . So, the vector $\mathbf{V}_{M_i}^p$ can be defined as follows

$$\mathbf{V}_{M_i}^p = [\nu_1^s(M_i), \nu_3^s(M_i), \nu_3^f(M_i), \sigma_{33}^s(M_i), \sigma_{13}^s(M_i), \sigma_{33}^f(M_i)]^T \quad (2.14)$$

$\mathbf{V}_{M_i}^p$ being a column vector. These six quantities are written as

$$\begin{aligned} \nu_1^s &= j\omega \left(\frac{\partial \phi_1^s}{\partial x_1} + \frac{\partial \phi_2^s}{\partial x_1} - \frac{\partial \psi_2^s}{\partial x_3} \right) & \nu_3^k &= j\omega \left(\frac{\partial \phi_1^k}{\partial x_3} + \frac{\partial \phi_2^k}{\partial x_3} - \frac{\partial \psi_2^k}{\partial x_1} \right) & k &= s, f \\ \sigma_{33}^s &= (P - 2N) \left(\frac{\partial^2(\phi_1^s + \phi_2^s)}{\partial x_1^2} + \frac{\partial^2(\phi_1^s + \phi_2^s)}{\partial x_3^2} \right) + Q \left(\frac{\partial^2(\phi_1^f + \phi_2^f)}{\partial x_1^2} + \frac{\partial^2(\phi_1^f + \phi_2^f)}{\partial x_3^2} \right) \\ &\quad + 2N \left(\frac{\partial^2(\phi_1^s + \phi_2^s)}{\partial x_3^2} + \frac{\partial^2 \psi_2^s}{\partial x_1 \partial x_3} \right) \\ \sigma_{13}^s &= N \left(2 \frac{\partial^2(\phi_1^s + \phi_2^s)}{\partial x_1 \partial x_3} + \frac{\partial^2 \psi_2^s}{\partial x_1^2} - \frac{\partial^2 \psi_2^s}{\partial x_3^2} \right) \\ \sigma_{33}^f &= R \left(\frac{\partial^2(\phi_1^f + \phi_2^f)}{\partial x_1^2} + \frac{\partial^2(\phi_1^f + \phi_2^f)}{\partial x_3^2} \right) + Q \left(\frac{\partial^2(\phi_1^s + \phi_2^s)}{\partial x_1^2} + \frac{\partial^2(\phi_1^s + \phi_2^s)}{\partial x_3^2} \right) \end{aligned} \quad (2.15)$$

where N is the shear modulus of the material, and P , Q and R are the elastic coefficients of Biot (Biot, 1956).

The vector $\mathbf{V}_{M_i}^p$ satisfies the relation

$$\mathbf{V}_{M_i}^p = \mathbf{\Gamma}(x_3) \mathbf{A} \quad (2.16)$$

with \mathbf{A} being the column vector defined as

$$\mathbf{A} = [(A_1 + A'_1), (A_1 - A'_1), (A_2 + A'_2), (A_2 - A'_2), (A_3 + A'_3), (A_3 - A'_3)]^T \quad (2.17)$$

and $\mathbf{\Gamma}(x_3)$ is a connectivity matrix which results from system (2.12). As in the case of a solid layer, the transfer matrix between two points is obtained by the same procedure

$$\mathbf{T}^p = \mathbf{\Gamma}(0) \mathbf{\Gamma}(h^{-1}) \quad (2.18)$$

2.2.3. Viscoelastic layer

Mechanical characteristics of viscoelastic materials depend on the excitation frequency. To describe such a material, the complex representation of the Young modulus following (Abid *et al.*, 2012; Szabo, 2000; Soula and Chevalier, 1998) is used

$$E^* = E_0 \frac{1 + j\omega\tau_u}{1 + j\omega\tau} \quad (2.19)$$

and

$$E' = E_0 \frac{1 + \tau\tau_u\omega^2}{1 + \omega^2\tau^2} \quad E'' = E_0 \frac{\omega(\tau_u - \tau)}{1 + \omega^2\tau^2} \quad (2.20)$$

where E' and E'' are respectively the real and imaginary parts of the complex modulus E_0 , τ and τ_u are relaxation times of the viscoelastic material determined experimentally with relaxation and creep tests.

2.3. Continuity relations at the interfaces

The objective of this Section is to examine continuity relations for all possible interfaces. These relations depend on the nature of materials of the adjacent layers (Allard *et al.*, 1989).

2.3.1. Fluid-solid interface

The continuity conditions are given by

$$-p(A) = \sigma_{33}^s(M_1) \quad 0 = \sigma_{13}^s(M_1) \quad \nu_3^f(A) = \nu_3^s(M_1) \quad (2.21)$$

The following equations can be condensed as follows

$$\mathbf{I}_{f,s} \mathbf{V}(A) + \mathbf{J}_{f,s} \mathbf{V}(M_1) = \mathbf{0} \quad (2.22)$$

with

$$\mathbf{I}_{f,s} = \begin{bmatrix} 0 & -1 \\ 1 & 0 \\ 0 & 0 \end{bmatrix} \quad \mathbf{J}_{f,s} = \begin{bmatrix} 0 & 1 & 0 & 0 \\ 0 & 0 & 1 & 0 \\ 0 & 0 & 0 & 1 \end{bmatrix} \quad (2.23)$$

$\mathbf{J}_{f,s}$ and $\mathbf{I}_{f,s}$ must be interchanged for the fluid-solid interface.

2.3.2. Porous-fluid interface

The continuity conditions are given by

$$\begin{aligned} (1 - \phi)\nu_3^s(M_4) + \phi\nu_3^f(M_4) &= \nu_3^f(B) \\ \sigma_{33}^f(M_4) &= -\phi p(B) \quad \sigma_{33}^s(M_4) = -(1 - \phi)p(B) \quad \sigma_{13}^s(M_4) = 0 \end{aligned} \quad (2.24)$$

where ϕ is the porosity of the porous layer. These equations can be rewritten in the form

$$\mathbf{I}_{p,f} \mathbf{V}_{M_4}^p + \mathbf{J}_{p,f} \mathbf{V}_B^f = \mathbf{0} \quad (2.25)$$

with

$$\mathbf{I}_{p,f} = \begin{bmatrix} 0 & 1 - \phi & \phi & 0 & 0 & 0 \\ 0 & 0 & 0 & 1 & 0 & 0 \\ 0 & 0 & 1 & 0 & 1 & 0 \\ 0 & 0 & 0 & 0 & 0 & 1 \end{bmatrix} \quad \mathbf{J}_{p,f} = \begin{bmatrix} 0 & -1 \\ -\phi & 0 \\ 0 & 0 \\ \phi & 0 \end{bmatrix} \quad (2.26)$$

The matrices $\mathbf{I}_{p,f}$ and $\mathbf{J}_{p,f}$ must be interchanged for the fluid-porous interface.

2.3.3. Solid-porous interface

The continuity conditions are given by

$$\begin{aligned} \nu_3^s(M_2) &= \nu_3^s(M_3) = \nu_3^f(M_3) & \nu_1^s(M_2) &= \nu_1^s(M_3) \\ \sigma_{13}^s(M_2) &= \sigma_{13}^s(M_3) & \sigma_{33}^s(M_2) &= \sigma_{33}^f(M_3) + \sigma_{33}^s(M_3) \end{aligned} \quad (2.27)$$

This can be rewritten as follows

$$\mathbf{I}_{s,p} \mathbf{V}_{M_2}^s + \mathbf{J}_{s,p} \mathbf{V}_{M_3}^p = \mathbf{0} \quad (2.28)$$

where

$$\mathbf{I}_{s,p} = \begin{bmatrix} 1 & 0 & 0 & 0 \\ 0 & 1 & 0 & 0 \\ 0 & 1 & 0 & 0 \\ 0 & 0 & 1 & 0 \\ 0 & 0 & 0 & 1 \end{bmatrix} \quad \mathbf{J}_{s,p} = \begin{bmatrix} 1 & 0 & 0 & 0 & 0 & 0 \\ 0 & 1 & 0 & 0 & 0 & 0 \\ 0 & 0 & 1 & 0 & 0 & 0 \\ 0 & 0 & 0 & 1 & 0 & 1 \\ 0 & 0 & 0 & 0 & 1 & 0 \end{bmatrix} \quad (2.29)$$

The matrices $\mathbf{I}_{s,p}$ and $\mathbf{J}_{s,p}$ must be interchanged for the porous-solid interface.

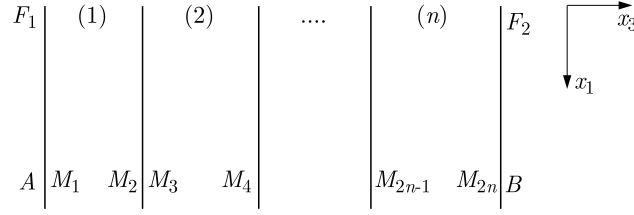


Fig. 3. A multilayer domain

2.4. Computation of the transmission loss TL of the multilayer

Generally way, the expressions of continuity between all layers of the system as presented in Fig. 3, are written by the following intermediate equations

$$\begin{aligned} \mathbf{I}_{f,1} \mathbf{V}_A^f + \mathbf{J}_{f,1} \mathbf{V}_{M_2}^1 &= \mathbf{0} \\ \mathbf{I}_{k,k+1} \mathbf{V}_{M_{2k}}^k + \mathbf{J}_{k,k+1} \mathbf{T}^k \mathbf{V}_{M_{2(k+1)}}^k &= \mathbf{0} \quad k = 1, \dots, n-1 \end{aligned} \quad (2.30)$$

This set of equations can be rewritten as

$$\mathbf{D} \mathbf{V}_0 = \mathbf{0} \quad (2.31)$$

where

$$\begin{aligned} \mathbf{D} &= \begin{bmatrix} \mathbf{I}_{f,1} & \mathbf{J}_{f,1} \mathbf{T}^1 & 0 & 0 & 0 \\ 0 & \mathbf{I}_{1,2} & \mathbf{J}_{1,2} \mathbf{T}^2 & 0 & 0 \\ \dots & \dots & \dots & \dots & \dots \\ 0 & 0 & \mathbf{I}_{(n-2)(n-1)} & \mathbf{J}_{(n-2)} \mathbf{T}^{n-1} & 0 \\ 0 & 0 & 0 & \mathbf{I}_{(n-1)(n)} & \mathbf{J}_{(n-1)(n)} \end{bmatrix} \\ \mathbf{V}_0 &= [V_A^f, V_{M_2}^1, V_{M_1}^2, \dots, V^{(n-1)}(M_{2n-1}), V^{(n)}(M_{2n}), V_B^f]^T \end{aligned} \quad (2.32)$$

Then, \mathbf{D}' and \mathbf{D}'' matrices are defined as follows

$$\mathbf{D}' = \begin{bmatrix} -1 & \dots & \mathbf{D} & \dots & 0 \\ \dots & \dots & \dots & \dots & \dots \\ 0 & \dots & 0 & -1 & Z_B \end{bmatrix} \quad \mathbf{D}'' = \begin{bmatrix} -1 & Z_A & 0 & \dots & 0 \\ \dots & \dots & \mathbf{D} & \dots & \dots \\ 0 & \dots & 0 & -1 & Z_B \end{bmatrix} \quad (2.33)$$

such as

$$\mathbf{D}' \mathbf{V}_0 = \mathbf{0} \quad (2.34)$$

where Z_A and Z_B are, respectively, the impedance of the medium A and B .

The determinant of the matrix \mathbf{D}'' must be equal to zero. Z_A is given by

$$Z_A = -\frac{|\mathbf{D}'|}{|\mathbf{D}'_2|} \quad (2.35)$$

where $|\mathbf{D}'_1|$ is the determinant of the matrix \mathbf{D}' without its first column, $|\mathbf{D}'_2|$ is the determinant of the matrix \mathbf{D}' without its second column.

The reflection coefficient R is related to Z_A by

$$R = \frac{Z_A - \frac{Z_C}{\cos \theta}}{Z_A + \frac{Z_C}{\cos \theta}} \quad (2.36)$$

where Z_C is the characteristic impedance in the air medium

$$Z_C = \rho_{air} C_{air} \quad (2.37)$$

The transmission coefficient T is determined as follows

$$T = (1 + R) \frac{|\mathbf{D}'_{N-1}|}{|\mathbf{D}'_1|} \quad (2.38)$$

where $|\mathbf{D}'_{N-1}|$ is the determinant of \mathbf{D}' without the $(N - 1)$ column.

The TL transmission loss is defined by

$$TL = 10 \log \frac{1}{\tau} \quad (2.39)$$

where τ is the acoustic transparency defined as follows

$$\tau = \frac{P_T}{P_I} \quad (2.40)$$

The symbols P_T , P_I represent, respectively, the transmitted and the incident power waves, and finally

$$TL = 10 \log \frac{P_I}{P_T} = 10 \log \frac{\frac{p_i^2}{2Z_{fluid1}}}{\frac{p_t^2}{2Z_{fluid2}}} \quad (2.41)$$

where p_i , p_t represent, respectively, the amplitude of the incident and the transmitted waves.

3. Numerical results

3.1. Validation of the TMM

The TMM is tested by comparing its results with experimental findings obtained by Tanneau (2004). Two configurations are studied:

- The first is a 2.1 mm thickness plate glued to to 30 mm thick porous material.
- The second is composed by the 30 mm thick porous material glued to two 2.1 mm thick plates on each side. The mechanical proprieties of the used materials are presented in Table 1.

Table 1. Parameters of tested materials

Parameters	Porous	Plate
Porosity φ_p	0.98	–
Tortuosity α_∞	1.03	–
Resistivity σ_p [Ns/m ⁴]	6600	–
Viscous length Λ [μ m]	200	–
Thermal length Λ' [μ m]	380	–
Density ρ [kg/m ³]	11.2	1100
Poisson's coefficient ν	0.3	0.3
Young's modulus E [Pa]	292.8e3	2.62e9
Damping loss factor η	0.0624	0.06

Figures 4a and 4b represent, respectively, a comparison between the computed and the experimental TL obtained in the two studied configurations and for the incident angle $\theta = \pi/4$. A good agreement is observed between the results obtained by the TMM and the experimental results (Tanneau, 2004; Tanneau *et al.*, 2006). In these figures, we can distinguish 3 zones:

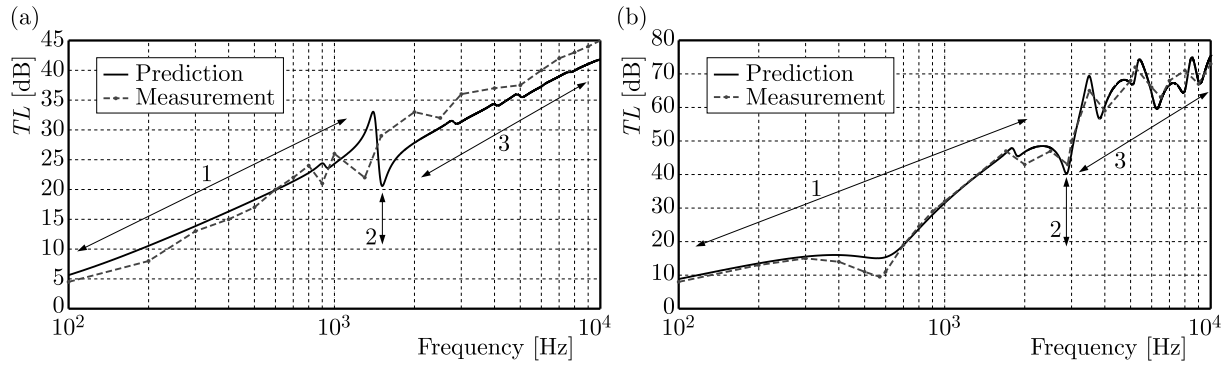


Fig. 4. Theoretical and experimental transmission loss TL of the studied (a) plate-porous configuration and (b) plate-porous-plate configuration

- zone 1: $f < f_{coin}$ – the mass controls the transmission. The wavelength in this frequency range is very large compared to the thickness of the wall. For this, the behavior of the multi-layer wall will be identical to that of a simple wall; therefore, the slope of the transmission will be of 6 dB/octave
- zone 2: $f = f_{coin}$ – the damping plays a significant role
- zone 3: $f > f_{coin}$ – the stiffness controls the transmission.

where f_{coin} is the coincidence frequency. It is the frequency at which the airborne acoustic wavelength matches the plate bending wavelength. It is expressed as follows

$$f_{coin} = \frac{c^2}{2\pi \sin^2 \theta} \sqrt{\frac{12\rho(1 - \nu^2)}{Eh^2}} \quad (3.1)$$

Also, comparison between the coincidence frequencies as presented in Tables 2 and 3 showed a good agreement.

Table 2. Comparison between the theoretical and experimental coincidence frequencies in the case of plate-porous configuration

TMM	Theoretical (London, 1950)	Experimental (Tanneau, 2004)
1643 Hz	1554.7 Hz	1450 Hz

Table 3. Comparison between the theoretical and experimental coincidence frequencies in the case of plate-porous-plate configuration

TMM	Theoretical (London, 1950)	Experimental (Tanneau, 2004)
2987 Hz	3317.8 Hz	3000 Hz

Results presented in Figs. 4a and 4b and Tables 2 and 3 allow validation of the proposed method (TMM).

3.2. Response of multilayer systems

In this part, the TMM is used to compute the TL of several multilayer configurations to find the best arrangement of layers in terms of sound transmission. Two configurations are studied which are:

- First configuration: 1 mm of the elastic layer – 30 mm of the porous layer.
- Second configuration: 0.5 mm of the elastic layer – 30 mm of the porous layer – 0.5 mm of the elastic layer.

The two studied configurations are subjected to an incident wave at $\theta = \pi/4$. The characteristics of the porous and the elastic layers are respectively presented in Table 4.

Table 4. Parameters of the used materials

Parameters	Foam	Steel
Porosity φ_p	0.98	–
Tortuosity α_∞	1.03	–
Resistivity σ_p [Ns/m ⁴]	6600	–
Viscous length Λ [μ m]	200	–
Thermal length Λ' [μ m]	380	–
Density ρ [kg/m ³]	11.2	7850
Poisson's coefficient ν	0.3	0.3
Young's modulus E [Pa]	292.8e3	210e9
Damping loss factor η	0.0624	0.06

The predicted transmission loss TL is presented in Fig. 5. For the first configuration, it is seen that the evaluation of the TL with frequency is progressive but it presents a weak peak at the frequency 1500 Hz.

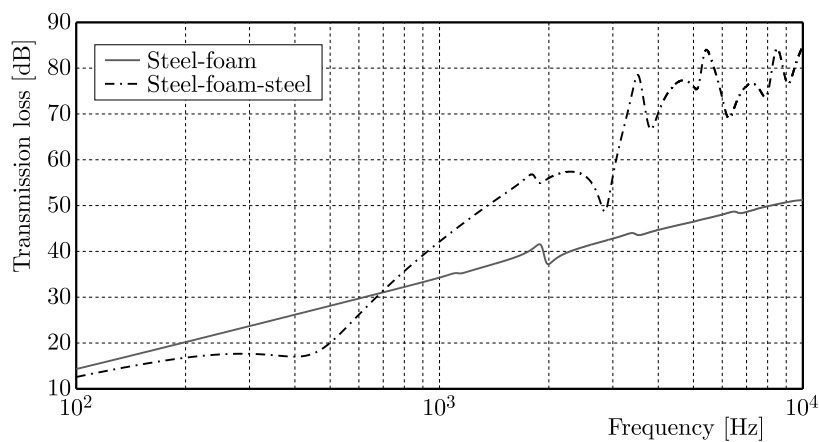


Fig. 5. Comparison of TL versus frequency curves amongst double and triple panel

For the second configuration, the TL is less important for the low frequency up to 450 Hz, then it successively increases with frequency. At high frequencies, the TMM is able to predict the TL with good accuracy. The thickness resonance at 2900 Hz is well predicted. This curve has a high-frequency discontinuous track corresponding to the coincidence zone.

As seen in Fig. 5, the TL value for the first configuration does not exceed 52 dB, on the other hand, for the second configuration, which includes three layers, the TL value reaches 85 dB at high frequencies, which may be explained by the effect of the elastic layer. It is found that the second configuration with triple layers has good insulation behavior, especially in the high frequency range 700 Hz-10000 Hz.

In comparison between the two studied configurations, it seems that the second configuration isolates better than the first configuration.

3.2.1. Effect of replacing the steel layer by a viscoelastic layer

In this Section, the steel layers in the two studied configurations are replaced by viscoelastic layers and conserving the same weight of each configuration to show the effect of this replacement. The mechanical proprieties of the viscoelastic layer are presented in Table 5. To have the same mass after replacing the elastic layer, the dimension of the viscoelastic layer must be changed. In fact, thickness of the viscoelastic layer equivalent to the same mass is

$$e = \frac{7850 \cdot 1}{950} = 8.26 \text{ mm} \quad (3.2)$$

Table 5. Mechanical properties of the viscoelastic layer

E_0 [MPa]	E_∞ [MPa]	f_{carac}	ρ [kg/m ³]	ν
10	100	1000	950	0.49

The viscoelastic material behaves as if it was elastic respectively with the moduli:

- E_∞ : at high frequency
- E_0 : low frequency
- f_{carac} : is the frequency of the maximum of damping.

Figure 6 presents the TL when using the viscoelastic layers. For the double layer structure, the presented results show that in the low frequency region the same behavior is observed. The response is governed by the mass law, although we have the same excitation and mass. It is also noted that the small difference from the frequency 4000 Hz is due to contribution of the viscoelastic layer.

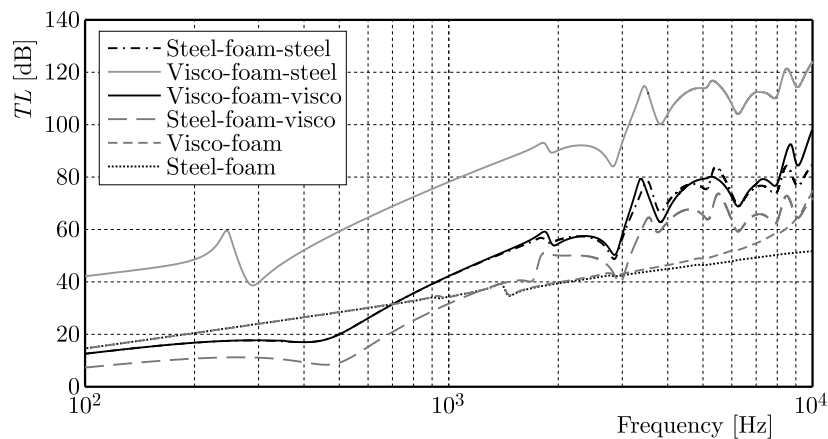


Fig. 6. Comparison between studied configurations

For the 2nd structure, the replacement of the elastic layer by a viscoelastic one generates four cases:

- 1) viscoelastic-porous-elastic
- 2) viscoelastic-porous-viscoelastic
- 3) elastic-porous-elastic
- 4) elastic-porous-viscoelastic

It is observed that adding the viscoelastic layer leads to a clear difference between these four cases: TL significantly changes when the plane wave penetrates the viscoelastic medium. If the incident wave penetrates first the viscoelastic medium it is seen that the sound insulation is very high. Also, it is observed that the peak of the frequency of coincidence moves to the low frequency range.

Finally, these comparisons show an improvement of the sound insulation for three-layer configurations, especially that one which takes the viscoelastic layer and the steel layer to extremity. This is explained by the damping effect of the viscoelastic material.

3.2.2. Effect of angle of incidence

Figure 7 shows the attenuation index TL according to the frequency computed for four angles of incidence. The results show that the acoustic transparency strongly depends on the angle of incidence. It is observed that when the incident angle increases, the TL increases. The coincidence frequencies move to the high frequency range as the angle increases.

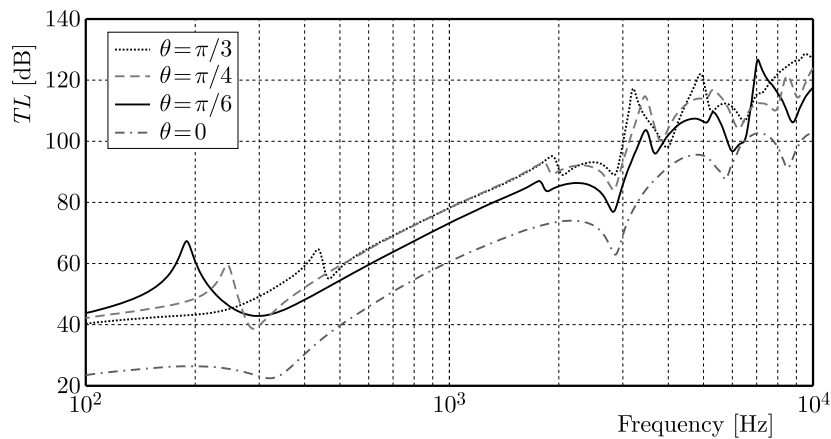


Fig. 7. Effect of the angle of incidence for the configuration (viscoelastic-porous-elastic)

However, we can notice a singular difference at the critical frequency particularly clear for $\theta = 0$.

On the other hand, in Fig. 8, it is clearly observed that the TL is less important if the angle of incidence increases, but the frequency of coincidence retains almost the same position.

As we have seen in the two configurations, the variations in the angle of incidence are not the same. This explains why the viscoelastic layer depends on the angle of excitation.

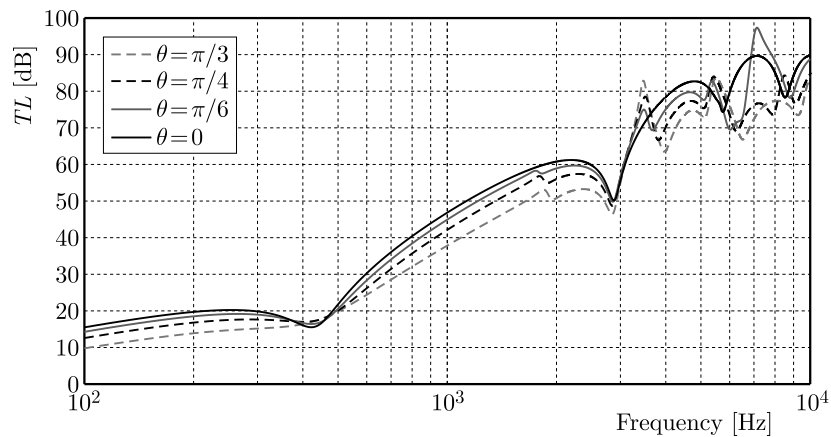


Fig. 8. Effect of the angle of incidence for the configuration (elastic-porous-elastic)

4. Parametric study

In this part, we will choose the configuration which isolates much better than other configurations (viscoelastic-porous-elastic). We are interested in the effect of the porous parameters on the TL of this multilayer structure. The Allard model is used to describe the porous materials. Eight parameters are used: porosity, tortuosity, flux resistivity, viscous lengths and lengths of thermal characteristics, Young's modulus and Poisson's coefficient. The influence of each of these physical parameters on the loss of transmission is studied and discussed in the following Section.

Influence of porosity. Figure 9a presents the effect of porosity – there is no clear influence on the TL of the studied configuration in low frequency band but the higher is porosity, the more absorbent is the material in high frequencies.

Influence of tortuosity. Figure 9b presents the effect of tortuosity – it is seen that an increase in the tortuosity increases the TL just in the high frequency region 1800 Hz-10000 Hz. Tortuosity mainly affects the location of the quarter-wavelength peaks.

Influence of density of the skeleton. As presented in Fig. 10a, if density of the skeleton increases, there will be a shift of the absorption peaks to the low frequency area and the absorption peaks are large. Moreover, density of this material is considered to be an important factor that governs the sound absorption behavior of the material. At the same time, the cost of an acoustical material is directly related to its density.

Influence of Young's modulus. Figure 10b shows that an increase of Young's modulus of the skeleton generates an increase in the rigidity of the skeleton over which the absorption peaks shift to the high frequency area. In our study, we focus on the influence of the porous layer of sound insulation of sandwich plates in the frequency range 100 Hz-10000 Hz, for this reason, we chose Young's modulus for the skeleton of the order of 0.1 MP.

Influence of characteristic length. Figure 11a presents the effect of characteristic length. In the frequency range between 100 Hz-250 Hz, the characteristic length has no effects on the TL . In the frequency range 300 Hz-2500 Hz, the more characteristic length decreases, the more viscous dissipation is important, and TL increases. At high frequencies, characteristic lengths represent no effects on the TL .

Influence of resistivity. The variation of the flow resistivity has no effect on the reduction index as presented in Fig. 11b.

Influence of Poisson's ratio. Figure 12a shows the effect of Poisson's ratio on TL . In the frequency band 100 Hz-220 Hz, an increase in the coefficient occurs at an increase in the transmission loss TL . On the contrary, in the frequency band 220 Hz-5000 Hz, this frequency range shows a drop of TL down to 980 Hz, called the resonance frequency, and in the zone 5000 Hz-10000 Hz, if the Poisson ratio is increased, the transmission loss increases. Then, the more Poisson's ratio increases, the more the shear modulus decreases and the more absorption peaks are shifted towards the high-frequency zone.

Influence of foam thickness. For thickness variation of the order of a few millimeters (Fig. 12b), the greater the thickness, the more the transmission loss coefficient increases in the high frequency zone 180 Hz-10000 Hz and the more the absorption peaks is shifted to the low-frequency area. A greater thickness allows a shock-absorbing effect in the behavior of the multilayer.

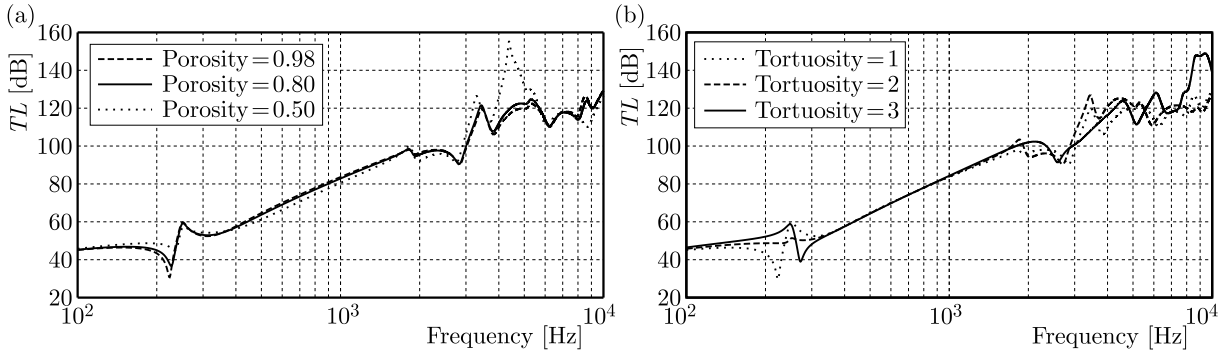


Fig. 9. Influence of (a) porous material porosity and (b) porous material tortuosity on TL of the viscoelastic-porous-elastic configuration

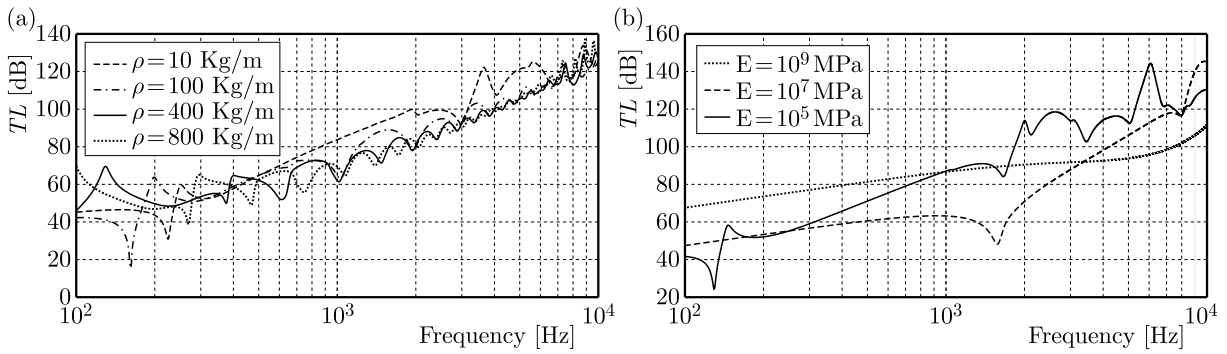


Fig. 10. Influence of (a) porous skeleton density and (b) Young's modulus on TL of the viscoelastic-porous-elastic configuration

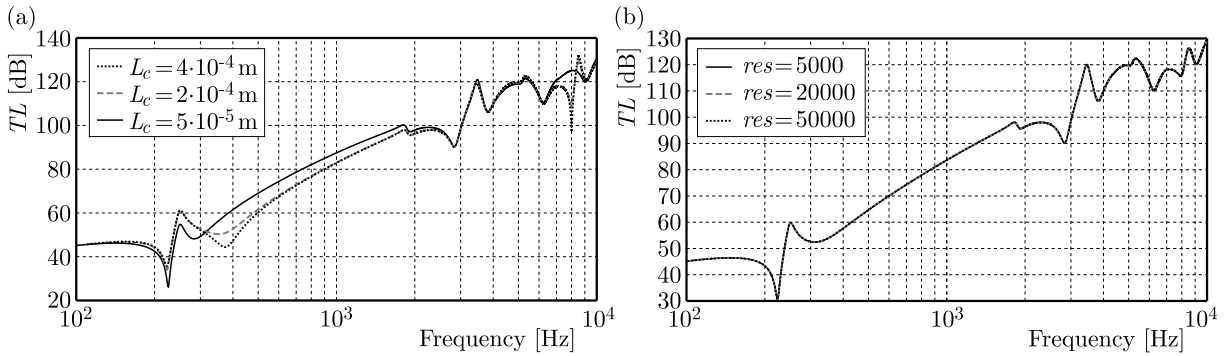


Fig. 11. Influence of (a) porous characteristic length and (b) flow resistivity on TL of the viscoelastic-porous-elastic configuration

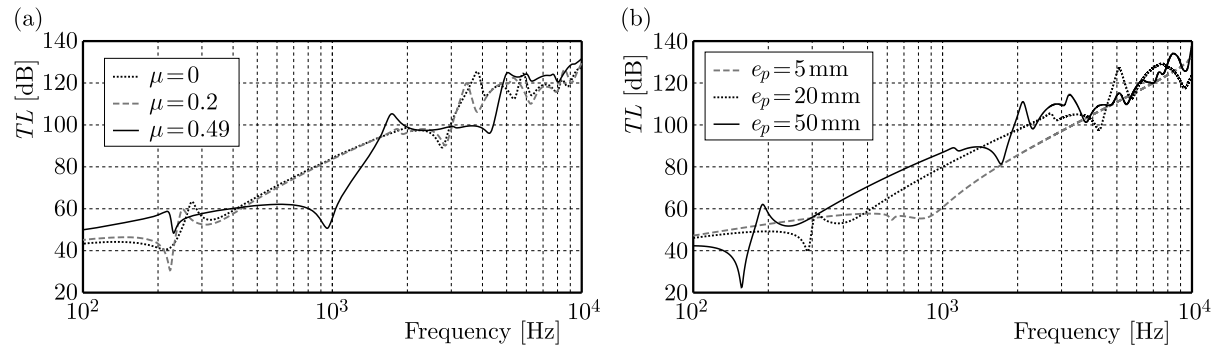


Fig. 12. Influence of (a) porous Poisson's ratio and (b) thickness of the porous material on TL of the viscoelastic-porous-elastic configuration

5. Conclusion

This article investigates the loss of sound transmission in multilayer configurations composed of porous, elastic and viscoelastic materials. A transfer matrix method has been developed to predict the acoustic behavior of a multilayer panel. The results were compared with experiments found in the literature. A comparison was made between all the configurations in order to find the best structure of the multilayer panel in terms of sound insulation. This comparison shows the effect of the damping of the viscoelastic layer which increases the loss of transmission (TL) as a function of the frequency.

Numerical simulations have been carried out to study the effects of porous parameters on the transmission loss for the best chosen configuration (viscoelastic-porous-elastic). This parametric study shows that porous material parameters like Young's modulus, Poisson's ratio and its thickness have a clear influence on the loss by transmission. The observed results are very useful for researchers and developers.

References

1. ABID M., ABBES J.D., CHAZOT L., HAMMAMI M.A., HAMDI, HADDAR M., 2012, Acoustic response of a multilayer panel with viscoelastic material, *International Journal of Acoustics and Vibration*, **17**, 2, 82-89
2. ALLARD J.F., ATALLA N., 2009, *Propagation of Sound in Porous Media. Modeling Sound Absorbing Materials*, Second Edition, John Wiley & Sons
3. ALLARD J.F., CHAMPOUX Y., DEPOLIER C., 1987, Modelization of layered sound absorbing materials with transfer matrices, *Journal of the Acoustical Society of America*, **82**, 1792-1796
4. ALLARD J.F., DEPOLIER C., REBILLARD P., LAURIKS W., COPS A., 1989, Inhomogeneous Biot waves in layered media, *Journal of Applied Physics*, **66**, 2278-2284
5. ATALLA N., PANNETON R., DEBERGUE P., 1998, A mixed displacement pressure formulation for poroelastic materials, *Journal of the Acoustical Society of America*, **104**, 1444-1452
6. BIOT M.A., 1956, The theory of propagation of elastic waves in a fluid saturated porous solid, *Journal of the Acoustical Society of America*, **28**, 68-191
7. FOLDS D.L., LOGGINS D.C., 1977, Transmission and reflection of ultrasonic waves in layered media, *Journal of the Acoustical Society of America*, **62**, 1102-1109
8. GHINET S., ATALLA N., HAISAM O., 2005, The transmission loss of curved laminates and sandwich composite panels, *Journal of the Acoustical Society of America*, **118**, 774
9. LEE C.M., XU Y., 2009, A modified transfer matrix method for prediction of transmission loss of multilayer acoustic materials, *Journal of Sound and Vibration*, **326**, 290-301
10. LONDON A., 1950, Transmission of reverberant sound through double walls, *Journal of the Acoustical Society of America*, 220-270
11. MUNJAL M.L., 1993, Response of a multi-layered infinite plate to an oblique plane wave by means of transfer matrix, *Journal of Sound Vibration*, **162**, 2, 333-343
12. MUELLER P., TSCHUDL H., 1989, Modeling of flat multi-layer acoustic structures with transfer matrices, *SAE Technical Paper*, 111-115
13. SASTRY J.S., MUNJAL M.L., 1995, A transfer matrix approach for evaluation of the response of a multi-layer infinite plate to a two-dimensional pressure excitation, *Journal of Sound and Vibration*, **182**, 1, 109-128
14. SOULA M., CHEVALIER Y., 1998, The fractional derivative in rheology of polymers – application to the elastic and viscoelastic behavior of linear and nonlinear elastomers, *ESAIM Proceedings*, **5**, 87-98

15. SZABO T.L., 2000, A model for longitudinal and shear wave propagation in viscoelastic media, *Journal of the Acoustical Society of America*, **107**, 5, 2437-2446
16. TANNEAU O., 2004, Modélisation de panneaux d'isolation aéronautiques – couplages poroélastique, élastodynamiques et acoustiques par méthodes analytiques, FEM et BEM: Phd Thesis, Université Pierre & Marie Curie, Paris VI
17. TANNEAU O., CASIMIR J.B., LAMARY P., 2006, Optimization of multilayered panels with poroelastic components for an acoustical transmission objective, *Journal of the Acoustical Society of America*, **120**, 3, 1227-1238
18. THOMSON W.T., 1950, Transmission of elastic waves through a stratified solid medium, *Journal of Applied Physics*, **21**, 2, 89-93

Manuscript received April 11, 2017; accepted for print February 28, 2018

ROCKING OF FREESTANDING OBJECTS: THEORETICAL AND EXPERIMENTAL COMPARISONS

ANTONIO GESUALDO, ANTONINO IANNUZZO

University of Naples "Federico II", Department of Structures for Engineering and Architecture, Napoli, Italy
e-mail: gesualdo@ununa.it; antonino.iannuzzo@unina.it

VINCENZO MINUTOLO

University of Campania "Luigi Vanvitelli", Department of Engineering, Aversa (CE), Italy
e-mail: vincenzo.minutolo@unicampania.it

MICHELA MONACO

University of Campania "Luigi Vanvitelli", Department of Architecture and Industrial Design, Aversa (CE), Italy
e-mail: michela.monaco@unicampania.it

The methodical study of safeguard of artistic heritage and other devices subjected to earthquake and, in general, to time-dependent forces has considerably spreaded in the last years, thus increasing researchers' interest in problems concerning motions of rigid objects simply supported on a base plane. The behaviour of piece of equipments, statues, storage tanks, or even tall buildings has been in fact studied as that of rigid bodies with relation to different base excitations. In some cases, the possibility of influencing the quality of motion can be a strong tool to reduce vulnerability, like in the cases in which rocking motion is to be avoided and sliding motion is welcome. This paper focuses the attention on this last problem. This is the same large class of both non-structural and structural elements that can lose their functionality because of earthquake motions. The results of numerical modelling of sliding and rocking motion in presence of both different excitations and mechanical parameters are presented and compared with experimental data performed by the authors. The results developed are in good agreement with the laboratory tests, and this assures the reliability of both the analytical procedure and the determination of the parameters involved.

Keywords: rocking and sliding motion, freestanding rigid body, nonlinear dynamics, experimental testing

1. Introduction

The limitation of excessive motion of rigid bodies under earthquake excitation is a fundamental topic in the seismic protection of art objects in museums (Erdik *et al.*, 2010; Agbabian *et al.*, 1991), medical devices in hospitals (Konstantinidis and Makris, 2009) and goods stored in ships. Since late XIX century, the behaviour of piece of equipments, statues, storage tanks, or even tall buildings has been studied as that of rigid bodies with relation to different base excitations (Cennamo *et al.*, 2017). Six basic conditions (Augusti and Sinopoli, 1992) have been distinguished: rest, slide, rock, slide-rock, impact and free flight (Andreaus and Casini, 1999). Despite its familiarity and apparent simplicity, motions of rigid bodies in response to earthquake excitations pose extremely difficult problems when exact solutions are sought (Voyagaki *et al.*, 2014). A rigid structure placed on a shaking base may enter into rocking motion that occasionally results in overturning (Guadagnuolo and Monaco, 2009). In some cases (small objects and equipments), the protection of the object can be obtained by controlling the overturning through providing an inclination to the support base in order to have a preferential direction toward a safe area (Boroshek and Iruretagoyena, 2006).

Early studies on the rocking response of a rigid block supported on a base undergoing horizontal motion were presented by Housner (1963). To study the problem, it was necessary to first establish equations of motion of the rigid body and solve them accordingly. This was first done just by Housner following the Chilean earthquakes in 1960. Housner first considered the base motion as more irregular time functions modelled by a white noise random process. In the piecewise model by Housner, the block can only rotate around one of the base corners, and the friction coefficient is large enough to prevent any sliding. Shenton (1996) showed that the quality of motion of a rigid object simply supported on an uniformly accelerating rigid plane depended not only on the object shape and the base acceleration, but on the friction coefficient as well. According the author, friction required to initiate a rock mode increased with ground acceleration. It was shown (Monaco *et al.*, 2014) that the range of sliding-rock was larger in the case of a harmonic excitation. The role of friction and its influence in the quality of motion was elsewhere taken into account (Sinopoli, 1997).

Since Housner had already pointed out that the rocking response of a rigid body to base motion was sensitive to the parameters defining the geometry of the body and details of base motion, Yim and Lin (1991) decided that the problem should be examined from a probabilistic point of view. Using a limited number of simulated ground motions, the authors numerically solved the equation of the problem and produced fragility curves giving the probability of the body overturn. Aslam *et al.* (1978, 1980) obtained the rocking response of a rigid body subjected to harmonic shaking as well to simulate earthquake motions both numerically and by laboratory experiments. The work of Aslam essentially confirmed the findings of Housner and Yim *et al.* (1980) about the difficult response prediction. In 1999, Shao and Tung followed the same approach as Yim *et al.* but used two types of base motions: 50 artificial earthquakes simulated in a way identical to that of Yim and 75 real earthquakes. Shao reached the same conclusion as Yim *et al.* but showed that real earthquakes gave less probability of overturning that simulated earthquakes did. In the first studies performed in Japan (Ishiyama, 1982), the computer simulation performed by the author showed that the horizontal velocity as well as the acceleration had to be taken into account as criteria for overturning. In engineering seismology, the rocking problem is of interest from the point of view of characterizing the ground motion level through study of overturned objects, although in many cases this practice is rather misleading and meaningless (Apostolou *et al.*, 2007). The problem becomes simpler in the case of a massless rigid foundation as examined in Sienkiewicz (2009), where only properties of the surrounding ground are considered. The simplest mathematical models that have received notable attention in the past were the planar rocking of rigid rectangular blocks with nonzero mass under harmonic base motions (Spanos and Koh, 1984), although the influence of the ground motion properties have been analyzed since the first paper of Yim *et al.* above mentioned. In the harmonic problem, even in the case of a one-sine pulse (Zhang and Makris, 2001), non-linearity arises not only in the load deflection characteristic but also in dissipation of energy due to impacts (Purvance *et al.*, 2008; Chierchiello *et al.*, 2015).

Some studies on the response of such a system have revealed the presence of a rich variety of non-linear resonances and even the possibility of the response becoming chaotic (Bergamasco *et al.*, 2018). Tackling analytically the equations of motion in the case of real earthquake ground motions is a non trivial task even for very simple waveforms (Konstantinidis and Makris, 2010). A range of idealized ground acceleration pulses expressed by a generalized function controlled by a single shape parameter were considered in Voyagaki *et al.* (2013). The problem was treated analytically by means of linearized equations of motion on the assumption of slender block geometry and rocking without sliding. The peak rocking response and overturning criteria for different waveforms were presented in terms of dimensionless closed-form expressions and graphs. The papers above mentioned (Konstantinidis and Makris, 2009, 2010) reported a series of tests in which the transient rocking response of electrical transformers subjected to horizontal

trigonometric pulses and near source ground motion were investigated in depth. First, it was shown that the solution presented by Housner for the minimum acceleration amplitude of a half-sine pulse that was needed to overturn a rigid block was unconservative. In reality, under a half-sine pulse a block overturns during its free-vibration regime and not at the instant that the pulse expires. Within the limits of linear approximation, the correct expression that yields the minimum acceleration required to overturn a block is derived. Under realistic conditions, the rocking response of a rigid block is affected by additional factors such as the vertical component of the ground acceleration and the additional energy loss due to plastic deformations at the pivot points (Gesualdo and Monaco, 2015). Recent attempts to derive equivalence between a single rocking block and various rocking mechanisms in order to give indication for real structures has been made (Spanos *et al.*, 2001; DeJong and Dimitrakopoulos, 2014). In general, while the rocking response under a deterministic excitation has received considerable attention (Gesualdo *et al.*, 2014, 2018), the corresponding studies on stochastic behaviour are sparse. A significant work on stochastic analysis was carried out by Spanos and Koh (1984). They employed the statistical linearization technique to study stochastic rocking of a rigid rectangular block on Winkler's foundation due to non-stationary shaking. Koh (1986) further studied this problem through a digital simulation technique and estimated the probability of no toppling. The stochastic response of a rigid rectangular block resting on a rigid foundation and acted upon simultaneously by a horizontal and a vertical stationary white-noise excitation was considered. Recent works (Prieto and Lourenço, 2005) have tried to unify the piecewise formulation by Housner with the same hypothesis of a large friction coefficient. The traditional piecewise equations were replaced by a single ordinary differential equation, and damping effects were no longer introduced by means of a coefficient of restitution, but were understood as the presence of impulsive forces. The results are in agreement with the classical formalism, and can be set in the direct analogy with either a two-body central problem in the complex plane or an inverted pendulum through simple variable transformations. Unfortunately, these elegant formulations are unsuitable when rocking motion is to be avoided and sliding motion is welcome.

Recently, the dynamic response of a rocking block subjected to base excitation has been revisited to offer new closed-form solutions and original similarity laws that shed light on the fundamental aspects of the original model by Dimitrakopoulos and DeJong (2012). The focus is on the transient dynamics of the rocking block under finite-duration excitations. In the process, limitations of standard dimensional analysis related to the orientations of the involved physical quantities are revealed. The work shows that the nonlinear and non-smooth rocking response to pulse-type ground motion can be directly determined and need only to be scaled by the intensity and frequency of the excitation. The typology of impulses can in fact reduce or amplify the rocking response. It has been shown that in the case of multiple impulse rocking, the amplification may be significant (DeJong, 2012).

In this work, a comparison between experimental observations and theoretical models for the rocking of rigid bodies has been made. The dynamic tests elsewhere described (Monaco *et al.*, 2014) and performed taking into account the influence of different parameters (Makris and Kampas, 2016) have been used to validate the analytical model and estimate both the restitution coefficient and the dynamic friction coefficient.

2. Theoretical analysis

According to the classical approach, in the response of a rigid block simply supported on a shaking plane base six basic conditions can be distinguished: rest, slide, rock, slide-rock, free flight. The analytical models revised here in the following take into account the first four classes of motion and are identified by comparing their responses with the results obtained from experimental tests on a shaking table.

2.1. Rocking model

In this Section, the pure rocking motion is examined. Reference is made to Fig. 1, in which a rigid block with the aspect ratio b/h , simply supported on a moving plane is shown (Zhang and Makris, 2001).

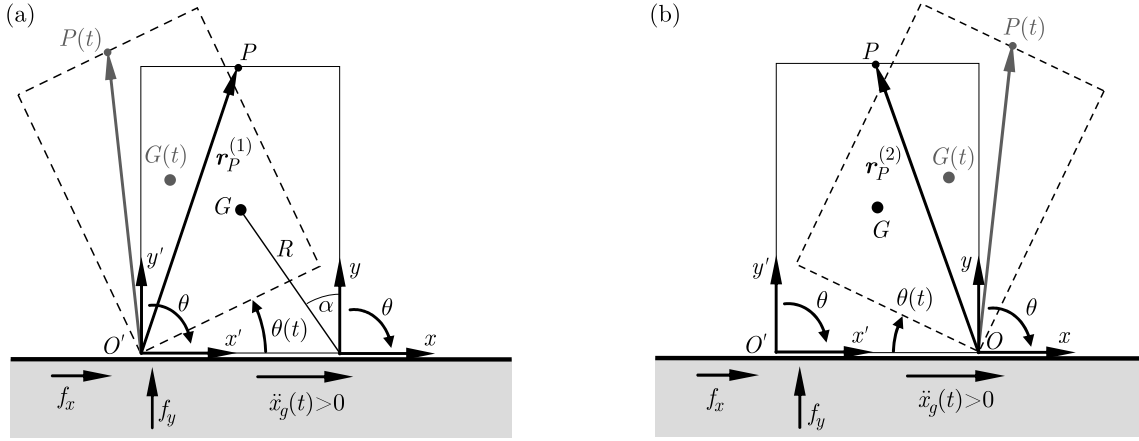


Fig. 1. Reference systems and the single block in rocking for $\theta(t) < 0$ (left) and $\theta(t) > 0$ (right)

The block with base $2b$, height $2h$ and mass m can rotate alternatively around the two base corners O and O' , and energy is lost only during impact, when the angle of rotation $\theta(t)$ reverses. According to the classical approach of the dynamics of the inverted pendulum under impulsive excitations (Lenci and Rega, 2000), the velocity field after a perfect plastic and centered impact is related to the pre-impact field by means of the reduction coefficient e . In particular $e = \sqrt{r}$, being r the restitution coefficient in the Housner sense. The coefficient e can be assumed constant during the motion, so that the angular velocity $\dot{\theta}^+(t)$ of the block after the impact can be given as a function of the angular velocity $\dot{\theta}^-(t)$ before it (Fig. 1)

$$\dot{\theta}^+(t) = e\dot{\theta}^-(t) \quad (2.1)$$

In the case of the perfect plastic impact, conservation of angular momentum about the point O' just before the impact and right after the impact gives

$$(I_o - 2mRb \sin \alpha) \dot{\theta}^-(t) = I_o \dot{\theta}^+(t) \quad (2.2)$$

where I_o is the moment of inertia (defined with respect to O or O'), R is the distance of the center of mass G from the corners O or O' and α is the angle between R and the vertical edge of the block (see Fig. 1). The combination of (2.1) and (2.2) gives for a rectangular block

$$e = 1 - \frac{3}{2} \sin^2 \alpha \quad (2.3)$$

Energy dissipation is involved for $e < 1$. Rocking motion is present when static friction with the base plane prevents sliding. Adopting the notation by Shenton (1996), let f_x and f_y be the horizontal and vertical reactions at the tip O' of the block, at all times it is

$$|f_x| \leq \mu_s f_y \quad (2.4)$$

In other words, starting from an equilibrium configuration of the system, when the angular momentum of inertia forces is greater than that due to the gravity force, rocking motion holds

true with condition (2.4). The rocking motion, according to d'Alembert's principle, is governed by the following relations with clockwise positive rotations

$$\begin{aligned} I_o \ddot{\theta}(t) + mgR \sin(-\alpha - \theta(t)) &= -m\ddot{x}_g(t)R \cos(-\alpha - \theta(t)) & \theta(t) < 0 \\ I_o \ddot{\theta}(t) + mgR \sin(\alpha - \theta(t)) &= -m\ddot{x}_g(t)R \cos(\alpha - \theta(t)) & \theta(t) > 0 \\ \dot{\theta}^+(t) &= e\dot{\theta}^-(t) & \theta(t) = 0 \end{aligned} \quad (2.5)$$

The reference is made to Fig. 1, where $\ddot{x}_g(t)$ is the horizontal base acceleration, I_o is the inertia moment of polar inertia with respect to O and the rocking motion starts when $|\ddot{x}_g(t)| > gb/h$. The angle $\alpha = \arctan b/h$ takes into account slenderness of the block. The resulting system of equations is composed by two ordinary nonlinear differential equations and an algebraic one relative to the impact instant. The system can assume the following simplified form

$$\begin{aligned} \frac{I_o}{mR} \ddot{\theta}(t) + g \operatorname{sgn}(\theta(t)) \sin[\alpha - \operatorname{sgn}(\theta(t))\theta(t)] &= -\ddot{x}_g(t) \cos[\alpha - \operatorname{sgn}(\theta(t))\theta(t)] & \theta(t) \neq 0 \\ \dot{\theta}^+(t) &= e\dot{\theta}^-(t) & \theta(t) = 0 \end{aligned} \quad (2.6)$$

with the signum function given by

$$\operatorname{sgn}(\theta(t)) = \begin{cases} +1 & \theta(t) > 0 \\ -1 & \theta(t) < 0 \end{cases}$$

System (2.6) has been implemented in a routine developed on purpose with the symbolic code Mathematica[©] (Wolfram, 2003) for a generic forcing ground acceleration. As it will be shown in the following paragraph, the experimental data have been obtained placing an accelerometer on top of the block, so that the above system should be rewritten referring to the upper face centre of the specimen. The numerical solution of differential system (2.6) may be put more conveniently in terms of the key point displacement, considering two reference systems with origins in the two rotation points O and O' , namely $R_1 = \{O, x, y\}$ for $\theta(t) > 0$ and $R_2 = \{O', x', y'\}$ for $\theta(t) < 0$. The rotation matrix $R \in SO(2)$, where $SO(2)$ is the orthogonal group of matrices with $\det(R) \geq 1$, for positive clockwise rotation is

$$R(\cdot) = \begin{bmatrix} \cos(\cdot) & \sin(\cdot) \\ -\sin(\cdot) & \cos(\cdot) \end{bmatrix}$$

Let $\theta(t)$ be a rotation function. It is possible to evaluate the position and the acceleration of the point P at the time t in the two reference systems above described as

$$\begin{aligned} OP(t) &= R \cdot \theta(t) \begin{bmatrix} x \\ y \end{bmatrix}_1 & \frac{\partial^2}{\partial t^2} OP(t) &= \frac{d^2}{dt^2} [R \cdot \theta(t)] \begin{bmatrix} x \\ y \end{bmatrix}_1 & \theta(t) > 0 \\ O'P(t) &= R \cdot \theta(t) \begin{bmatrix} x \\ y \end{bmatrix}_2 & \frac{\partial^2}{\partial t^2} O'P(t) &= \frac{d}{dt^2} [R \cdot \theta(t)] \begin{bmatrix} x \\ y \end{bmatrix}_2 & \theta(t) < 0 \end{aligned} \quad (2.7)$$

After some manipulations, the acceleration can be rewritten as follows

$$\begin{aligned} \frac{\partial^2}{\partial t^2} OP &= [\ddot{\theta}(t) \partial R \cdot \theta(t) - \dot{\theta}^2(t) R \cdot \theta(t)] \begin{bmatrix} x \\ y \end{bmatrix}_1 & \theta(t) > 0 \\ \frac{\partial^2}{\partial t^2} O'P &= [\ddot{\theta}(t) \partial R \cdot \theta(t) - \dot{\theta}^2(t) R \cdot \theta(t)] \begin{bmatrix} x \\ y \end{bmatrix}_2 & \theta(t) < 0 \end{aligned} \quad (2.8)$$

where

$$\partial R(\cdot) = \begin{bmatrix} -\sin(\cdot) & \cos(\cdot) \\ -\cos(\cdot) & -\sin(\cdot) \end{bmatrix} \in SO(2)$$

The horizontal component of the relative acceleration can be deduced by (2.8), and is given by

$$\ddot{x}(t) = \begin{cases} -[x_1 \cos(\theta(t)) + y_1 \sin(\theta(t))] \dot{\theta}^2(t) + [-x_1 \sin(\theta(t)) + y_1 \cos(\theta(t))] \ddot{\theta}(t) & \theta(t) > 0 \\ -[x_2 \cos(\theta(t)) + y_2 \sin(\theta(t))] \dot{\theta}^2(t) + [-x_2 \sin(\theta(t)) + y_2 \cos(\theta(t))] \ddot{\theta}(t) & \theta(t) < 0 \end{cases} \quad (2.9)$$

while the absolute acceleration is

$$\ddot{x}_a(t) = \ddot{x}_g(t) + \ddot{x}(t)$$

2.2. Sliding model

The configuration of the block in the case of sliding motion can be characterized by translation of a generic point of the block with respect to the base. The friction force is a function of vertical forces applied to the block and is opposite to the motion.

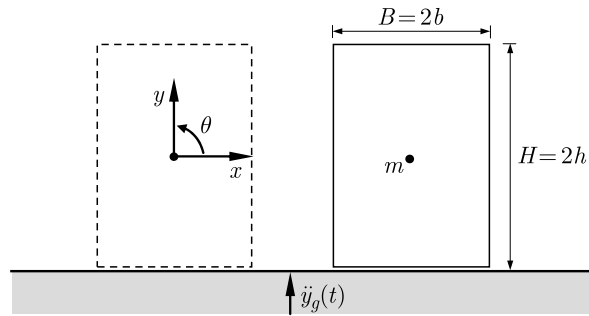


Fig. 2. The rigid block. Sliding motion

Starting from an equilibrium configuration, sliding motion begins when the maximum horizontal force due to the static friction coefficient is attained

$$m|\ddot{x}_g(t)| > m\mu_s[\ddot{y}_g(t) + g] \quad (2.10)$$

The differential equation governing the sliding motion problem is

$$m[\ddot{x}_g(t) + \ddot{x}(t)] = -\operatorname{sgn}(\dot{x}(t))\mu_k m[\ddot{y}_g(t) + g] \quad (2.11)$$

with

$$\operatorname{sgn}(\dot{x}(t)) = \begin{cases} +1 & \dot{x}(t) > 0 \\ -1 & \dot{x}(t) < 0 \end{cases}$$

The numerical procedure has been developed in the general case of nonzero vertical acceleration of the base whose equations are deduced by (2.11) and (2.12) with $\ddot{y}_g(t) = 0$

$$m|\ddot{x}_g(t)| > mg\mu_s \quad m[\ddot{x}_g(t) + \ddot{x}(t)] = -\operatorname{sgn}(\dot{x}(t))mg\mu_k \quad (2.12)$$

Starting from the instant in which the contact force due to static friction is exceeded (2.10), differential equation of sliding (2.11) is integrated until the relative velocity $\dot{x}(t)$ is nonzero. When the velocity becomes null, the block is in relative equilibrium with the base (rest) until the external force attains a value able to reactivate the sliding motion.

3. Experimental tests

The behaviour of prismatic specimens subjected to harmonic shaking is investigated. The results of the above analytical model are compared with experimental tests developed by means of an unidirectional shaking table on prismatic specimens (Monaco *et al.*, 2014). The specimens, prisms with two different aspect ratios, were made of two different materials: cellular concrete and basalt (Fig. 3).

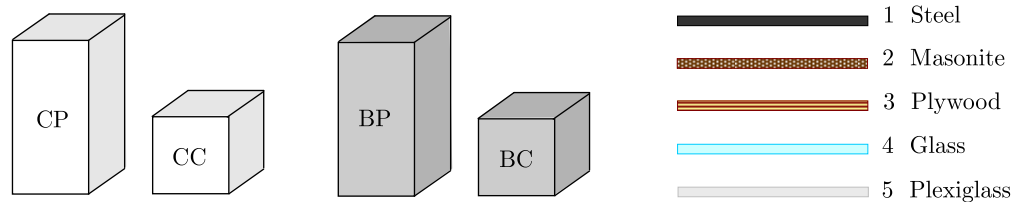


Fig. 3. Specimens respectively made of cellular concrete (C, left) and basalt (B, center), with cubic (C) and prismatic (P) shape and five types of support (right)

On the shaking table plane, five different material supports were arranged, in order to analyze the influence of three different parameters: aspect ratio, friction coefficient and base motion frequency. The shaking table was in fact able to perform a horizontal harmonic excitation with a variable frequency up to 10 Hz and a constant span of 1.5 mm.

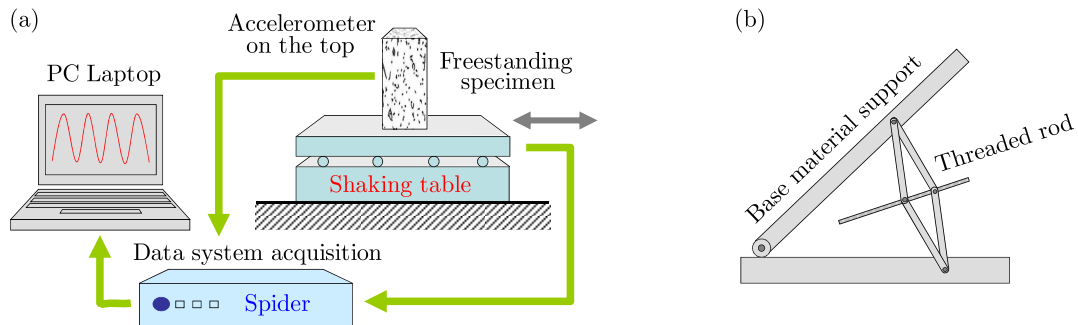


Fig. 4. Shaking table and the acquisition system (left) and the test device for determination of the friction coefficient (right)

As a result, combinations of ten different friction coefficients determined with an on purpose designed test device, and two different aspect ratios ($b/h = 1$ for cubic specimens and $b/h = 0.5$ for prismatic ones), were taken into account.

The friction coefficient has been determined by means of a test device made of a steel structure in which the upper plane could be inclined by means of a worm gear that could be manually controlled. The specimen, equipped with an accelerometer, was placed on the apparatus to which the support material had been previously fixed. The inclination of the support plane was increased slowly until the beginning of specimen sliding (Fig. 4). The values of the friction coefficients so determined were considered as static friction coefficients. They are reported in Table 1 for basalt and cellular concrete specimens, respectively. Shenton (1996) developed simple criteria to evaluate the initial motion of freestanding symmetric objects on a moving base with the acceleration described by a piecewise continuous function ranging from zero (base at rest) to the value A_g (peak value). The author divided the space $A_g - \varphi$ into four regions corresponding to the four possible motions: rest, slide, rocking, slide-rock

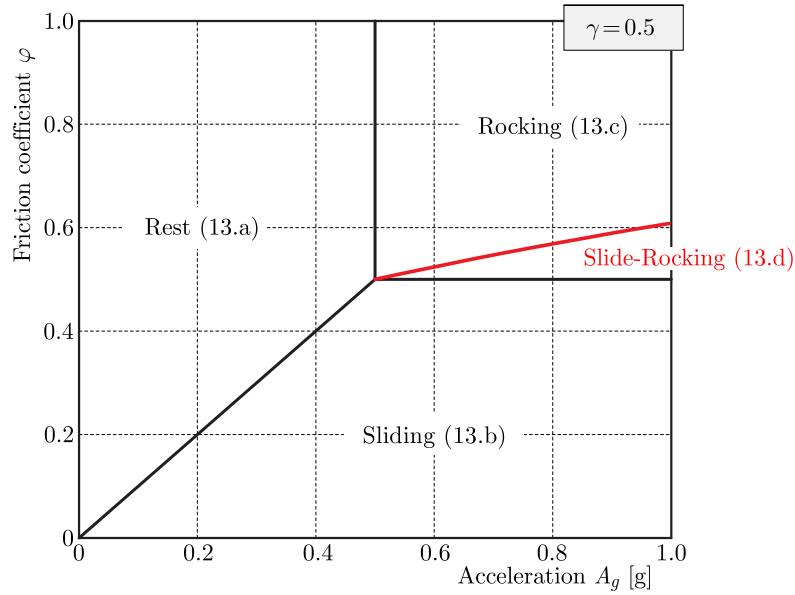


Fig. 5. Four Shenton's regions with the proposed enlargement in the case of the sinusoidal base excitation

$$\left. \begin{array}{l} A_g \leq \varphi \\ A_g \leq \gamma \end{array} \right\} \text{rest} \quad \left. \begin{array}{l} A_g > \gamma \\ A_g \leq \frac{(1 + 4\gamma^2)\varphi - 3\gamma}{(4 + \gamma^2) - 3\gamma\varphi} \end{array} \right\} \text{rocking} \quad (3.1)$$

$$\left. \begin{array}{l} A_g > \varphi \\ \varphi < \gamma \end{array} \right\} \text{slide} \quad \left. \begin{array}{l} \varphi > \gamma \\ A_g > \frac{(1 + 4\gamma^2)\varphi - 3\gamma}{(4 + \gamma^2) - 3\gamma\varphi} \end{array} \right\} \text{slide/rock}$$

where γ is the aspect ratio, $\gamma = b/h$ and A_g is the peak ground acceleration. The criteria, expressed by relations (3.1) are represented in Fig. 5. A tentative description of the variation of the Shenton regions for the sinusoidal base acceleration was proposed in (Monaco *et al.*, 2014). It was shown that in the last case, expansion of the slide-rocking area with respect to that fixed by Shenton was observed (Fig. 5). The expanded slide-rocking area proposed is the following

$$\left. \begin{array}{l} A_g > \gamma \\ A_g > \frac{(1 + 4\gamma^2)\varphi - 3\gamma}{(4 + \gamma^2) - 3\gamma\varphi} \end{array} \right\} \text{slide/rock} \quad (3.2)$$

The results of the experimental tests confirm the expansion of the slide-rocking area for the harmonic base acceleration: Figure 6 represents two different Shenton planes corresponding to the two aspect ratios examined.

It can be noted that, according to the Shenton scheme, for the unitary aspect ratio, the rocking area should be absent, but the experiments have shown the presence of all motion for cubic specimens (rest, sliding and rocking). Similarly, in the case of prismatic specimens, the experiments have shown the presence of all motion (rest, sliding and slide-rocking). The enlargement of the slide-rocking area is reported in Fig. 6 right, where the red line is the boundary of the enlarged area represented by relation (3.2). The experimental results were obtained placing the specimen on the shaking table to which the support material had been previously fixed. An accelerometer was placed on the top of the specimen to evaluate the accelerations registered together with the shaking table data by means of a computer acquisition data system (Fig. 4). The laboratory time histories are discussed and compared with the analytical ones in the following Section.

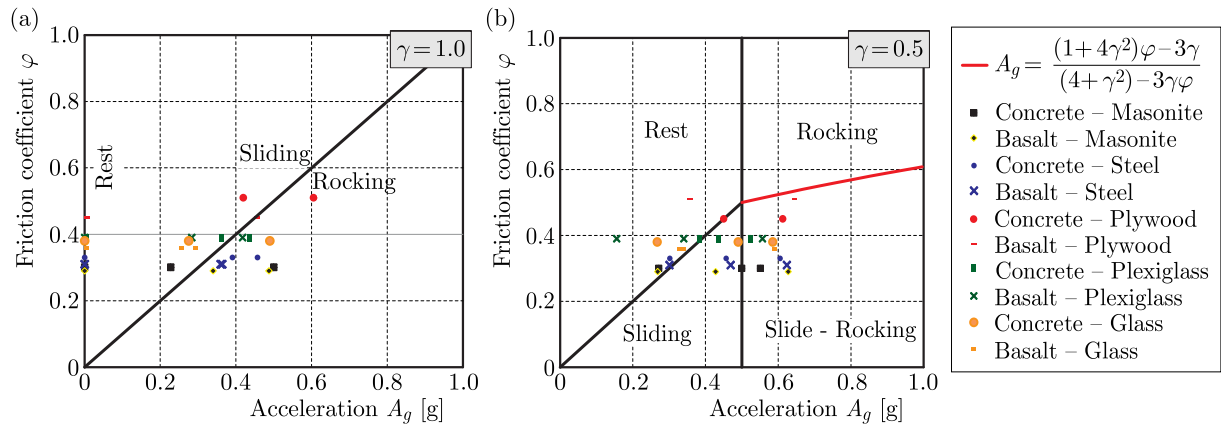


Fig. 6. Friction coefficient vs. peak specimen acceleration for cubic blocks ($\gamma = 1$, left) and prismatic blocks ($\gamma = 0.5$, right)

4. Numerical comparisons

The laboratory test conditions are similar to the real cases of freestanding art objects in museums or laboratory equipments in hospitals, where friction coefficients are of various types due to different quality of support planes (pedestals, shelves, floor). In order to provide a ductile analytical tool for the safeguard of such objects, the numerical procedure previously described in Section 2 has been on purpose implemented in the Mathematica® (2003) routine. Theoretical curves have been obtained by taking into account material parameters evaluated in the experimental tests and reported in Table 1.

Table 1. Static and dynamic friction coefficients, restitution coefficients and frequencies of the examined time histories

Motion type	Specimen type	Support material	Static friction coefficient	Dynamic friction coefficient	Restitution coefficient	Frequency examined
Rocking	BP	1	0.31	–	0.925	9.2
		2	0.29	–	0.925	9.2
		4	0.38	–	0.955	14.3
		5	0.39	–	0.955	14.2
Sliding	CP	1	0.30	0.26	–	6.3
		2	0.29	0.25	–	6.7
		4	0.33	0.29	–	7.2
		5	0.30	0.26	–	7.2
Sliding	BP	1	0.31	0.27	–	7.0
		2	0.29	0.25	–	7.5
		4	0.38	0.33	–	8.3
		5	0.39	0.34	–	7.5
Sliding	CC	1	0.33	0.29	–	9.3
		3	0.45	0.40	–	8.8
		4	0.33	0.29	–	11.0
		5	0.30	0.26	–	8.3
Sliding	BC	1	0.31	0.27	–	10.0
		2	0.29	0.26	–	8.0
		3	0.51	0.45	–	9.0
		4	0.36	0.32	–	8.7

Both restitution and dynamic friction coefficients used in the analytical rocking model are reported. They are satisfactorily in good agreement with the experimental data. In particular, the value of the dynamic friction coefficient used is 88% of the static friction coefficient measured in the laboratory tests, according to the literature, usual values (Bryant, 2016). In Figs. 7-11, time histories obtained in the numerical and experimental campaign are reported: the red line gives the analytical results while the grey one the experimental data. It must be noted that part of the mechanical parameters has been estimated, nevertheless, the numerical model is capable of representing the quality of motion with great accuracy.

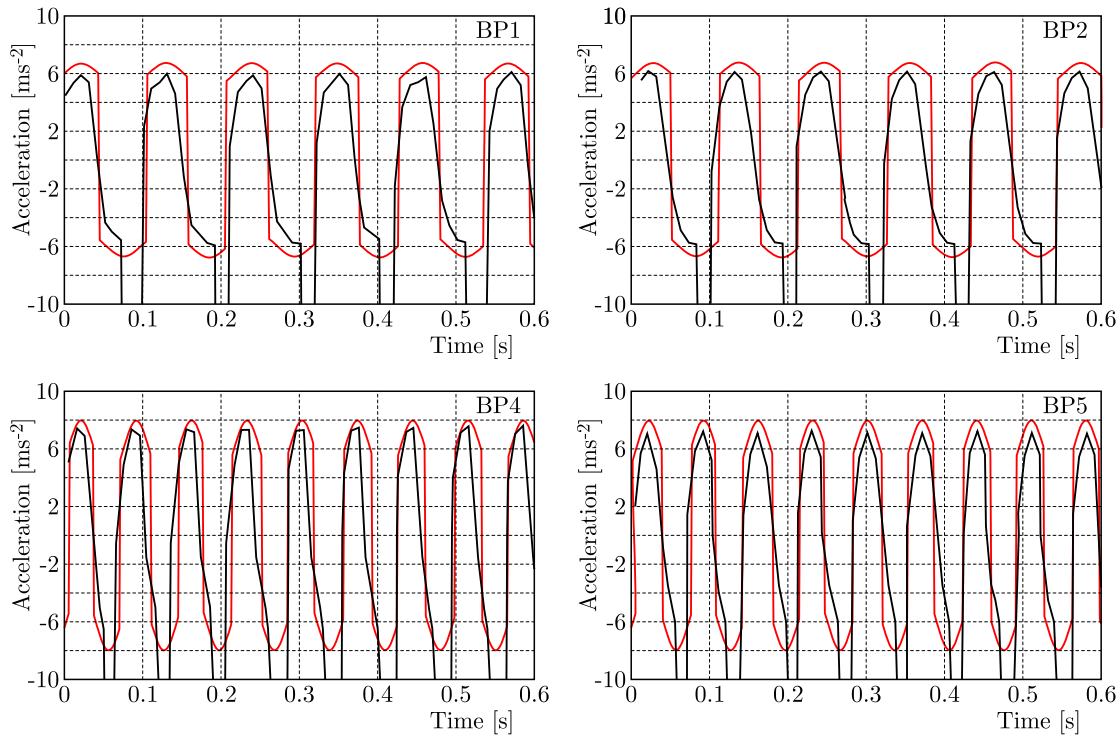


Fig. 7. Rocking motion: analytical (red) and experimental (grey) acceleration time histories

The numerical diagrams obtained are in good agreement with the experimental ones, see for example diagrams BP2 and BP4 in Fig. 8 (basalt prisms) and diagrams BC2 and BC4 (basalt cubes) in Fig. 9 or diagrams CP4 and CP5 in Fig. 10 (concrete prisms) and diagrams CC4 and CC5 (concrete cubes) in Fig. 11. The presence of the accelerometer on the top of the specimen and the acquisition wire gives in general small variation in a single cycle. The analytical curves present small discontinuities due to the structure of the governing equations, but in general the dynamic behaviour is well identified. This confirms that the only estimated parameter, i.e. the dynamic friction coefficient reported in Table 1, has been correctly evaluated. In fact, a reduction of 12% with respect to the static friction coefficient has been experimentally determined. The experimental determination of the dynamic friction coefficient and realization of dynamic tests are somewhat difficult, so that the theoretical model is the starting point for an optimization in the case of safeguard of freestanding objects. It must be considered that, nowadays, it is possible to make surfaces in which the friction coefficient can be previously determined, so that a vulnerable object can be endowed with a specific base surface in order to obtain, in contact with the support plane, a fixed friction coefficient. The motion can in this case be controlled in the case of strong earthquakes and motions that can cause more damage, i.e. rocking ones can be avoided. As expected from the general mechanic statements and verified experimentally, the static friction coefficient is independent of the shape of the specimen and depends only on the contact surfaces. The analysis of experimental diagrams has been taken into account in the

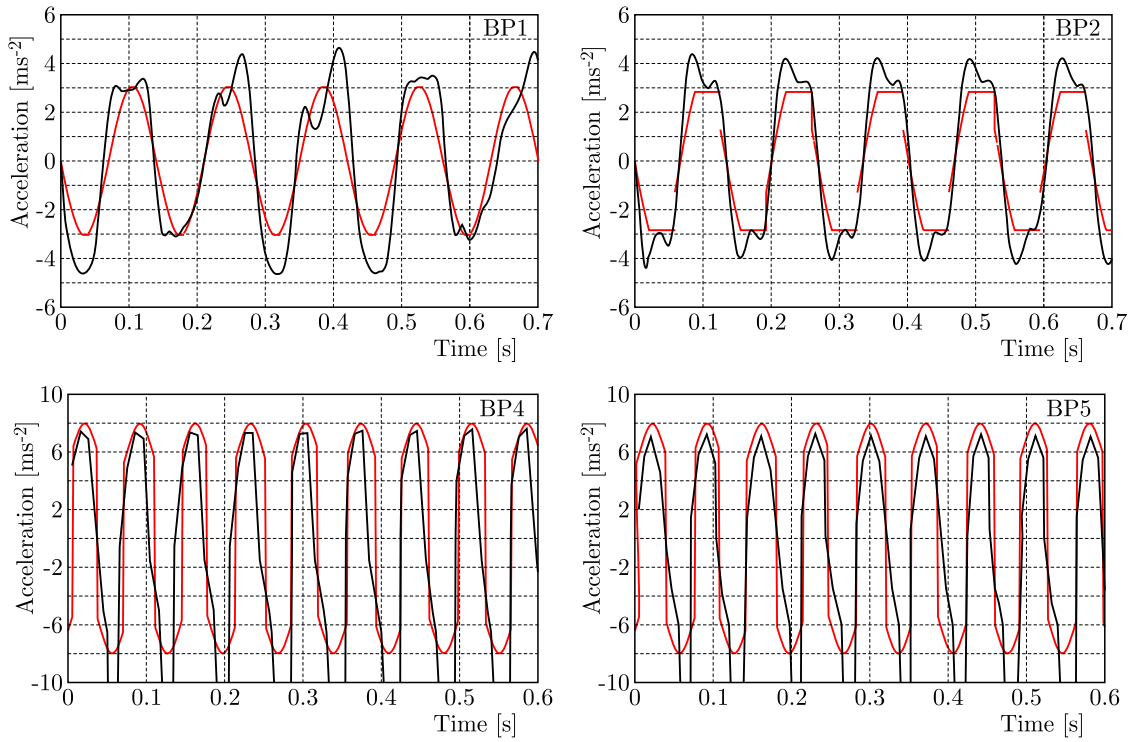


Fig. 8. Sliding motion: analytical (red) and experimental (grey) acceleration time histories

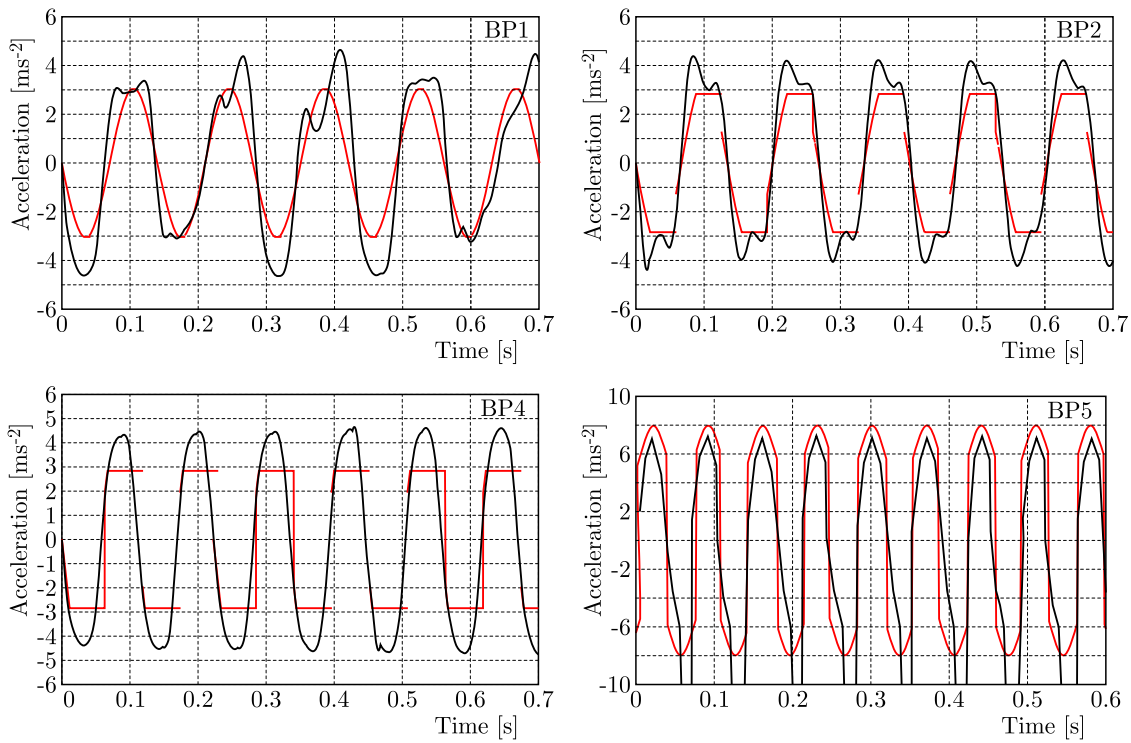


Fig. 9. Sliding motion: analytical (red) and experimental (grey) acceleration time histories

estimation of the dynamic friction coefficient, so that an unique parameter for the aspect ratio has been considered in the numerical procedure. It must be noted that the use of two different values for dynamic and static friction coefficients is the reason of jumps in the analytical curves.

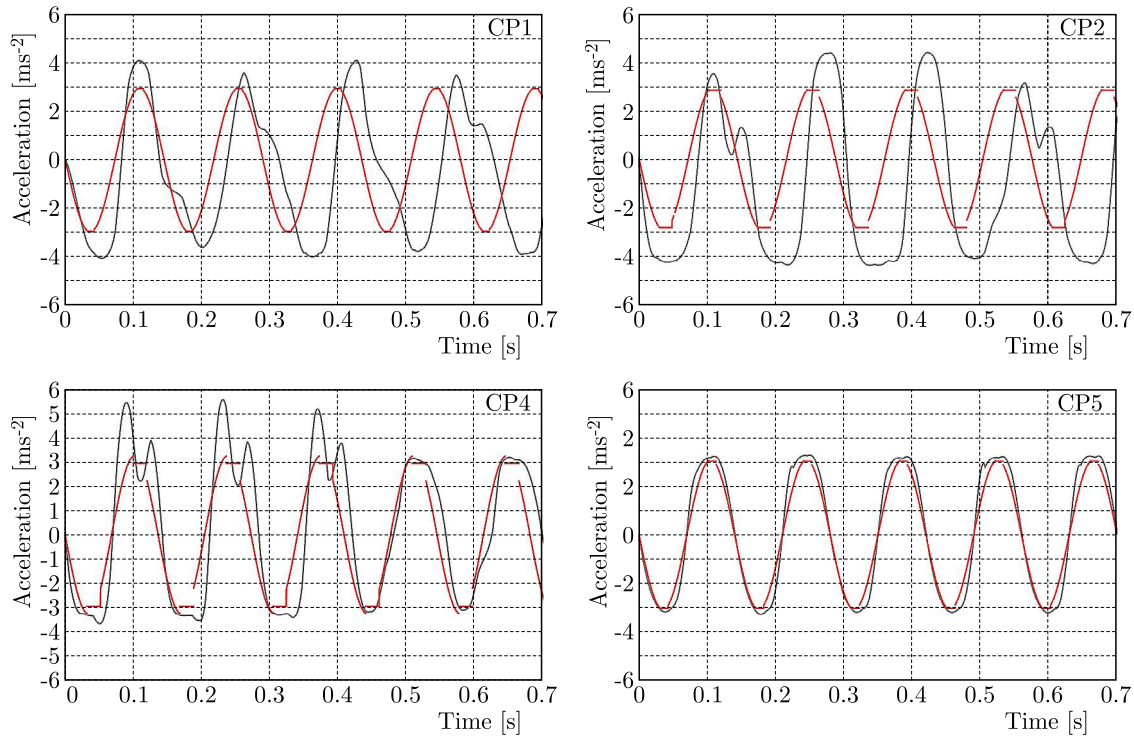


Fig. 10. Sliding motion: analytical (red) and experimental (grey) acceleration time histories

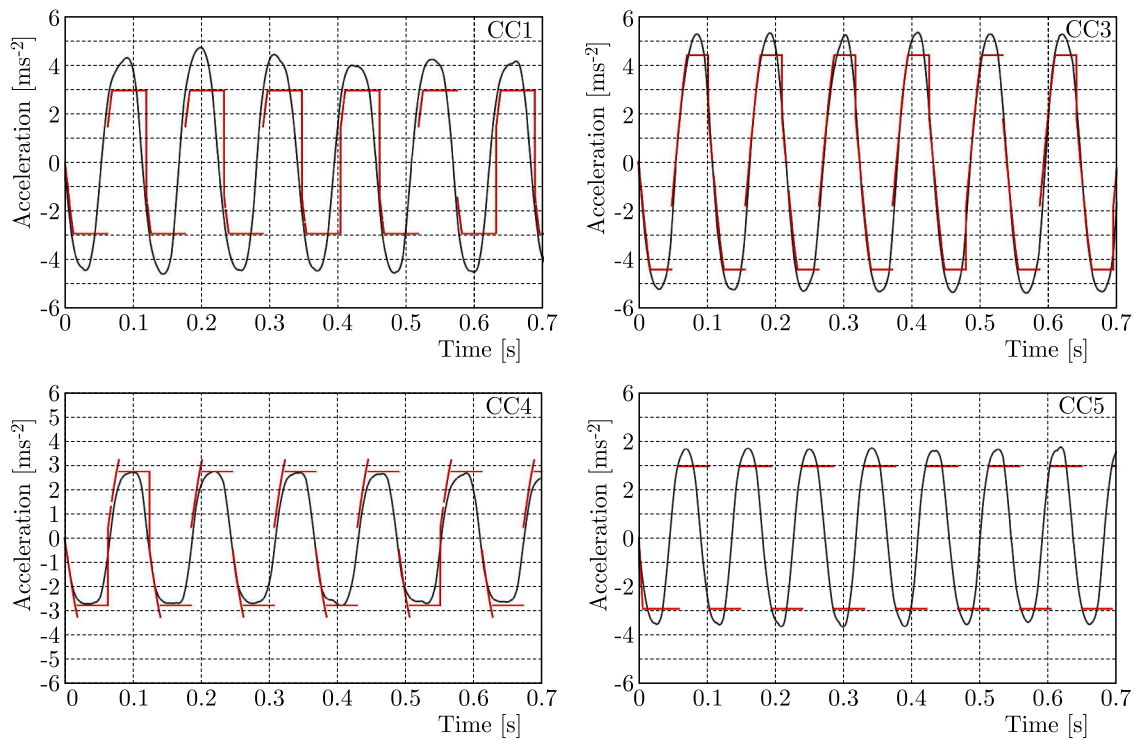


Fig. 11. Sliding motion: analytical (red) and experimental (grey) acceleration time histories

5. Conclusions

The problem of a freestanding rigid object on a moving base has been investigated. The results of numerical modelling of both sliding and rocking motion have been presented and compared with experimental data obtained by the authors on rigid blocks simply supported on a rigid ground

with different friction coefficients between the object and the supporting plane and different aspect ratios of the rigid object. The numerical procedure involves all possible types of motion and takes into account static and dynamic friction coefficients. While the first one has been experimentally derived, the second one has been estimated as a percent of the first, both the values being independent of the shape of the rigid object tested. It has been shown that in the range of frequencies of the laboratory tests performed, a reduction by 12% of the static friction coefficient gives a reliable value of the dynamic one. Laboratory tests and numerical results are in good agreement, which confirms that the theoretical model is the starting point for an optimization in the case of safeguard of freestanding objects. It must be emphasized that, nowadays, it is possible to design surfaces in which the friction coefficient can be previously determined, so that a vulnerable object can be endowed with a specific base surface in order to obtain, in contact with the support plane, a fixed friction coefficient. The motion can in this case be controlled in the case of strong earthquakes and motions that can cause more damage, i.e. rocking ones, can be avoided. Since the experimental tests are often difficult as well as expensive, especially in the case of art objects and ancient artifacts, the development of a reliable analytical procedure and simple determination of mechanical parameters involved in the correct interpretation of the problem is very useful.

References

1. AGBABIAN M.S., GINELL W.S., MASRI F.S., NIGBOR R.L., 1991, Evaluation of earthquake damage mitigation methods for museum objects, *Studies in Conservation*, **36**, 1, 111-120, DOI: 10.1179/sic.1991.36.2.111
2. ANDREAUS U., CASINI P., 1999, On the rocking-uplifting motion of a rigid block in free and forced motion: influence of sliding and bouncing, *Acta Mechanica*, **138**, 3-4, 219-41, DOI: 10.1007/BF01291846
3. APOSTOLOU M., GAZETAS G., GARINI E., 2007, Seismic response of slender rigid structures with foundation uplifting, *Soil Dynamics and Earthquake Engineering*, **27**, 7, 642-654, DOI: 10.1016/j.soildyn.2006.12.002
4. ASLAM M., GODDEN W., SCALISE D., 1978, *Rocking and Overturning Response of Rigid Bodies to Earthquake Motions*, Lawrence Berkeley National Laboratory, University of California, Berkeley, USA
5. ASLAM M., SCALISE D.T., GODDEN W.G., 1980, Earthquake rocking response of rigid bodies, *Journal of the Structural Division ASCE*, **106**, 2, 377-392
6. AUGUSTI G., SINOPOLI A., 1992, Modelling the dynamic of large block structures, *Meccanica*, **27**, 3, 195-211, DOI: 10.1007/BF00430045
7. BERGAMASCO I., GESUALDO A., IANNUZZO A., MONACO M., 2018, An integrated approach to the conservation of the roofing structures in the Pompeian Domus, *Journal of Cultural Heritage*, **31**, 141-151, DOI: 10.1016/j.culher.2017.12.006
8. BOROSHEK R., IRURETAGOYENA A., 2006, Controlled overturning of unanchored rigid bodies, *Earthquake Engineering and Structural Dynamics*, **35**, 6, 695-711, DOI: 10.1002/eqe.554
9. BRYANT M.D., 2016, On constitutive relations for friction from thermodynamics and dynamics, *ASME Journal of Tribology*, **138**, 4, 1215-1223, DOI: 10.1115/1.4032821
10. CENNAMO C., GESUALDO A., MONACO M., 2017, Shear plastic constitutive behaviour for near-fault ground motion, *Journal of Engineering Mechanics ASCE*, **143**, 9, 04017086, DOI: 10.1061/(ASCE)EM.1943-7889.0001300
11. CHIERCHIELLO G., GESUALDO A., IANNUZZO A., MONACO M., SAVINO M.T., 2015, Structural modeling and conservation of single columns in archaeological areas, *Proceedings of XIV International Forum "Le vie dei mercanti"*, Aversa- Capri, Italy, La Scuola di Pitagora Editrice, Napoli, Italy, 2012-2020

12. DEJONG M.J., 2012, Amplification of rocking due to horizontal ground motion, *Earthquake Spectra*, **28**, 4, 1405-1421, DOI: 10.1193/1.4000085
13. DEJONG M.J., DIMITRAKOPOULOS E.G., 2014, Dynamically equivalent rocking structures, *Earthquake Engineering and Structural Dynamics*, **43**, 10, 1543-1564, DOI: 10.1002/eqe.2410
14. DIMITRAKOPOULOS E.G., DEJONG M.J., 2012, Revisiting the rocking block: Closed form solutions and similarity laws, *Proceedings of the Royal Society A*, **468**, 2144, 2294-2318, DOI: 10.1098/rspa.2012.0026
15. ERDIK M., DURUKAL E., ERTÜRK N., SUNGAY B., 2010, Earthquake risk mitigation in Istanbul museums, *Natural Hazards*, **53**, 1, 97-108, DOI: 10.1007/s11069-009-9411-2
16. GESUALDO A., IANNUZZO A., MONACO M., PENTA F., 2018, Rocking of a rigid block freestanding on a flat pedestal, *Journal of Zhejiang University Science A*, **19**, 5, 331-345, DOI: 10.1631/jzus.A1700061
17. GESUALDO A., IANNUZZO A., MONACO M., SAVINO M.T., 2014, Dynamic analysis of freestanding rigid blocks, [In:] *Civil-Comp Proceedings of the Twelfth International Conference on Computational Structures Technology*, B.H.V. Topping and P. Iványi (Eds.), 106, Civil Comp Press, Kippen, Stirlingshire, U.K., DOI: 10.4203/ccp.106.144
18. GESUALDO A., MONACO M., 2015, Constitutive behaviour of quasi-brittle materials with anisotropic friction, *Latin American Journal of Solids and Structures*, **12**, 4, 695-710, DOI: 10.1590/1679-78251345
19. GUADAGNUOLO M., MONACO M., 2009, Out of plane behaviour of unreinforced masonry walls, [In:] *Protection of Historical Buildings*, **2**, 1177-1180, London, New York: CRC Press, Taylor & Francis Group
20. HOUSNER W.G., 1963, The behaviour of inverted pendulum structures during earthquake, *Bulletin of the Seismological Society of America*, **53**, 2, 403-417
21. ISHIYAMA Y., 1982, Motions of rigid bodies and criteria for overtuning by earthquake excitations, *Earthquake Engineering and Structural Dynamics*, **10**, 5, 635-650, DOI: 10.1007/s11069-014-1076-9
22. KOH A.S., 1986, Rocking of rigid bodies on randomly shaking foundations, *Nuclear Engineering and Design*, **97**, 2, 269-276, DOI: 10.1016/0029-5493(86)90114-7
23. KONSTANTINIDIS D., MAKRIS N., 2009, Experimental and analytical studies on the response of freestanding laboratory equipment to earthquake shaking, *Earthquake Engineering and Structural Dynamics*, **38**, 6, 827-848, DOI: 10.1002/eqe.871
24. KONSTANTINIDIS D., MAKRIS N., 2010, Experimental and analytical studies on the response of a 1/4 scale model of freestanding laboratory equipment subjected to strong earthquake shaking, *Bulletin of Earthquake Engineering*, **8**, 6, 1457-1477, DOI: 10.1007/s10518-010-9192-8
25. LENCI S., REGA G., 2000, Periodic solutions and bifurcations in an impact inverted pendulum under impulsive excitation, *Chaos, Solitons and Fractals*, **11**, 5, 2453-2472, DOI: 10.1016/S0960-0779(00)00030-8
26. MAKRIS N., KAMPAS G., 2016, Size versus slenderness: two competing parameters in the seismic stability of free-standing rocking columns, *Bulletin of the Seismological Society of America*, **106**, 1, 104-122, DOI: 10.1785/0120150138
27. MONACO M., GUADAGNUOLO M., GESUALDO A., 2014, The role of friction in the seismic risk mitigation of freestanding art objects, *Natural Hazards*, **73**, 2, 389-402, DOI: 10.1007/s11069-014-1076-9
28. PRIETO F., LOURENÇO P.B., 2005, On the rocking behaviour of rigid objects, *Meccanica*, **40**, 2, 121-133, DOI: 10.1007/s11012-004-5875-z
29. PURVANCE M.D., ABDOLRASOOL A., BRUNE J.N., 2008, Freestanding block overturning fragilities: numerical simulation and experimental validation, *Earthquake Engineering and Structural Dynamics*, **37**, 5, 791-808, DOI: 10.1002/eqe.789

30. SHAO Y., TUNG C.C., 1999, Seismic response of unanchored bodies, *Earthquake Spectra*, **15**, 3, 523-536, DOI: 10.1193/1.1586056
31. SHENTON H.W., 1996, Criteria for initiation of slide, rock, and slide-rock rigid-body modes, *Journal of Engineering Mechanics ASCE*, **122**, 7, 690-693, DOI: 10.1061/(ASCE)0733-9399(1996)122:7(690)
32. SIENKIEWICZ Z., 2009, Local modelling of backfill effects for rigid axisymmetric foundations under dynamic excitation, *Journal of Theoretical and Applied Mechanics*, **47**, 4, 923-942
33. SINOPOLI A., 1997, Unilaterality and dry friction: a geometric formulation for two-dimensional rigid body dynamics, *Nonlinear Dynamics*, **12**, 4, 343-366, DOI: 10.1023/A:1008289716620
34. SPANOS P., KOH A.S., 1984, Rocking of rigid blocks due to harmonic shaking, *Journal of Engineering Mechanics ASCE*, **110**, 11, 1627-1642, DOI: 10.1061/(ASCE)0733-9399(1984)110:11(1627)
35. SPANOS P.D., ROUSSIS P.C., POLITIS N.P.A., 2001, Dynamic analysis of stacked rigid blocks, *Soil Dynamics and Earthquake Engineering*, **21**, 7, 559-578, DOI: 10.1016/S0267-7261(01)00038-0
36. VOYAGAKI E., PSYCHARIS I., MYLONAKIS G., 2013, Rocking response and overturning criteria for free standing rigid blocks to single-lobe pulses, *Soil Dynamics and Earthquake Engineering*, **46**, 85-95, DOI: 10.1016/j.soildyn.2012.11.010
37. VOYAGAKI E., PSYCHARIS I., MYLONAKIS G., 2014, Complex response of a rocking block to a full-cycle pulse, *Journal of Engineering Mechanics ASCE*, **140**, 6, 04014024, DOI: 10.1061/(ASCE)EM.1943-7889.0000712, 04014024
38. WOLFRAM S., 2003, *The Mathematica Book*, Wolfram Media, USA
39. YIM S.C.S., CHOPRA A., PENZIEN J., 1980, Rocking response of rigid blocks to earthquakes, *Earthquake Engineering and Structural Dynamics*, **8**, 6, 565-580, DOI: 10.1002/eqe.4290080606
40. YIM S.C.S., LIN H., 1991, Nonlinear impact and chaotic response of slender rocking objects, *Journal of Engineering Mechanics ASCE*, **117**, 9, 2079-2100, DOI: 10.1061/(ASCE)0733-9399(1991)117:9(2079)
41. ZHANG J., MAKRI N., 2001, Rocking response of free-standing blocks under cycloidal pulses, *Journal of Engineering Mechanics ASCE*, **127**, 5, 473-483, DOI: 10.1061/(ASCE)0733-9399(2001)127:5(473)

MICROSTRUCTURAL CONSIDERATIONS ON SH-WAVE PROPAGATION IN A PIEZOELECTRIC LAYERED STRUCTURE

RICHA GOYAL, SATISH KUMAR

School of Mathematics, Thapar Institute of Engineering and Technology, Patiala, Punjab, India

e-mail: richagoyal705@gmail.com; satishk.sharma@thapar.edu

VIKAS SHARMA

Department of Mathematics, Lovely Professional University, Phagwara, Punjab, India

e-mail: vikassharma10a@yahoo.co.in

Shear wave based acoustic devices are being used in gaseous and liquid environments because of their high-sensitivity. The theoretical study of horizontally polarized shear (SH) waves in a layered structure consisting of a piezoelectric ceramic of $PZT - 5H$ or $BaTiO_3$ material overlying a couple stress substrate is presented in this paper. The considered substrate is supposed to be exhibiting microstructural properties. The closed form expression of dispersion relations are derived analytically for electrically open and short conditions. The effects of internal microstructures of the couple stress substrate, thickness of $PZT - 5H$ or $BaTiO_3$ ceramic, piezoelectric and dielectric constants are illustrated graphically on the phase velocity of the piezoelectric layer under electrically open and short conditions.

Keyword: SH-wave, piezoelectricity, couple stress, characteristic length

1. Introduction

The propagation of surface waves in the layered system consisting of a finite layer having different material properties lying over a semi-infinite solid substrate has been of interest due to its great importance in geophysics, composite materials as well as in non-destructive evaluation. SH-waves refer to the type of surface waves which are horizontally polarized and propagate at the surface of the considered substrate. These waves exist only when a layer of finite thickness is deposited on semi-infinite substrate and the shear wave velocity in the layer is less than that of substrate. The piezoelectric material exhibits the linear coupling between mechanical and electric fields because of the ability of its material to produce an electric charge when subjected to mechanical stress and to produce deformation when subjected to an electric field. A thin film of piezoelectric material bonded over a solid substrate is used to improve the performance of surface acoustic wave (SAW) devices like sensors, transducer, resonators, filters, amplifiers, oscillators, delay lines etc. which are extremely or widely used in navigation, communication and in many other fields (Jakoby and Vellekoop, 1997).

Many researchers have investigated the piezoelectric layered structure to study propagation characteristics of SH-waves. Liu *et al.* (2001) investigated the effect of initial stress on the propagation behavior of Love waves in a layered piezoelectric structure. Wang (2002) examined shear horizontal (SH) wave propagation in a semi-infinite solid medium surface bonded by a layer of a piezoelectric material abutting the vacuum. Liu and He (2010) also illustrated the properties of Love waves for a layered structure with an SiO_2 layer sputtered on an ST-90° X quartz substrate and found the existence of a threshold of normalized layer thickness. Wang *et al.* (2012) examined the dispersion behavior of SH waves propagating in a layered structure consisting of a piezoelectric layer and an elastic cylinder with an imperfect bonding. Wang and

Zhao (2013) studied propagation of the Love wave in two-layered piezoelectric/elastic composite plates with an imperfect interface based on the shear spring model. Wei *et al.* (2009), Ezzin *et al.* (2017) examined the propagation of an SH-guided wave in the piezoelectric/piezomagnetic layered plates. Singh *et al.* (2015) investigated the propagation of a Love-type wave in an irregular piezoelectric layer lying over a piezoelectric half-space. Gupta and Vashishth (2016) studied Bulk wave propagation in a monoclinic porous piezoelectric material.

Though, Love or SH-wave propagation has been examined in detail for a piezoelectric layer overlying a solid substrate but the role of microstructure of the substrate has not been investigated to the full extent. The study of wave propagation in couple stress elastic space is of great interest due to its many applications, e.g. in polymers, cellular solids, composite materials and bones etc. Voigt (1887) proposed the idea of couple stress on the micro sized materials. The relevant mathematical model was presented by Cosserat and Cosserat (1909). Later, many researchers like Mindlin and Tiersten (1962), Koiter (1964), Eringen (1968) proposed different theories to explore this field further. The theories presented by these researchers carry certain drawbacks like indeterminacy of the spherical part of the couple-stress tensor and involvement of separate material length scale parameters. Hadjesfandiari and Dargush (2011) gave consistent couple stress theory which consisted of three material parameters λ , μ and characteristic length (l) which described the effects of inner microstructure of the material. This characteristic length is negligible as compared to the dimensions of the body and is of the order of the average cell size or internal microstructure of the material. The propagation of SH-waves are examined by various researchers under different conditions. Vardoulakis and Georgiadis (1997) examined the existence of SH surface waves in a homogeneous gradient-elastic half space with surface energy. Recently, co-authors Sharma and Kumar (2017) have investigated the propagation of SH waves in a viscoelastic layer bonded imperfectly with a couple stress substrate.

Thus, to enhance the domain of shear wave propagation, we intend to study the SH-wave propagation in a piezoelectric ceramic lying over a couple stress elastic half-space. The substrate is considered to have properties of a microstructure like granular macromorphic rock (Dionysos Marble). Two sets of a piezoelectric layer, i.e. $PZT-5H$ and $BaTiO_3$ materials are considered over a solid substrate. Closed form expressions of the dispersion equation for both the cases of electrically open and electrically short conditions for the propagation of SH-wave are obtained. Numerical computations are preformed for studying the effect of underlying microstructure of substrate, thickness of the layer, piezoelectric and dielectric constants on the phase velocity profiles of the shear wave.

2. Formulation of the problem

Here, we consider a piezoelectric layer of thickness H (where $-H \leq x \leq 0$) lying over a couple stress elastic half-space. The Cartesian coordinate system is considered in such a way that the SH-wave is propagating along the y -axis, and x -axis is pointing positive vertically downward as shown in Fig. 1. Conventionally, the poling direction is assumed along the z -axis.

If $u_i^{(p)} = (u_1, v_1, w_1)$ and $u_i^{(c)} = (u_2, v_2, w_2)$ are the mechanical displacement components due to propagation of the SH-wave in the upper piezoelectric layer and the lower couple stress elastic half-space respectively. As the SH-wave is propagating along the direction of the y -axis, this causes displacement in the z -direction only. We shall suppose that

$$u_i = 0 \quad v_i = 0 \quad w_i = w_i(x, y, t) \quad (i = 1, 2) \quad (2.1)$$

Let us suppose that the electric potential function of the upper piezoelectric layer is

$$\phi = \phi(x, y, t) \quad (2.2)$$

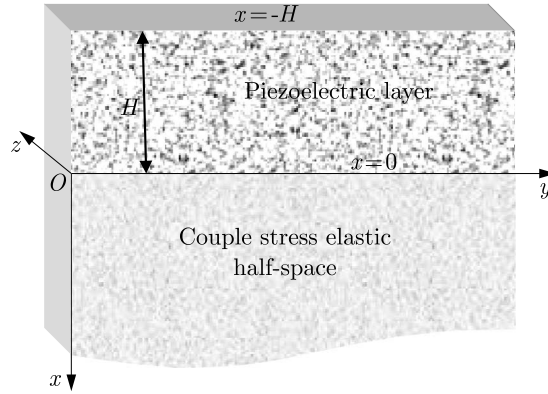


Fig. 1. Geometry of the problem

2.1. Dynamics of the piezoelectric material layer

The equation of motion for a piezoelectric layer, the electric displacement equilibrium equation and the constitutive relations may be written as

$$\sigma_{ij,j}^{(p)} = \rho_1 \frac{\partial^2 u_i^{(p)}}{\partial t^2} \quad D_{i,i} = 0 \quad (2.3)$$

and

$$\sigma_{ij}^{(p)} = c_{ijkl} S_{kl} - e_{kij} E_k \quad D_j = e_{jkl} S_{kl} + \epsilon_{jk} E_k \quad (2.4)$$

where $i, j, k, l = 1, 2, 3$; $\sigma_{ij}^{(p)}$ and S_{kl} are the stress and strain tensors, respectively, c_{ijkl} , e_{kij} and ϵ_{jk} are the elastic, piezoelectric and dielectric coefficients respectively, $u_i^{(p)} = (u_1, v_1, w_1)$ and D_j denotes the mechanical and electric displacement respectively, E_k is the electrical potential field, ρ_1 is the mass density of the piezoelectric layer, the superscript index p is used for the upper piezoelectric layer.

For the transversely isotropic piezoelectric layer, equation (2.4) can be expressed in the component form with the z -axis being the symmetric axis of the material as (Liu *et al.*, 2001)

$$\begin{aligned} \sigma_x^{(p)} &= c_{11} S_x + c_{12} S_y + c_{13} S_z - e_{31} E_z & \sigma_y^{(p)} &= c_{12} S_x + c_{11} S_y + c_{13} S_z - e_{31} E_z \\ \sigma_z^{(p)} &= c_{13} S_x + c_{13} S_y + c_{33} S_z - e_{33} E_z & \sigma_{yz}^{(p)} &= c_{44} S_{yz} - e_{15} E_y \\ \sigma_{zx}^{(p)} &= c_{44} S_{zx} - e_{15} E_x & \sigma_{xy}^{(p)} &= \frac{1}{2}(c_{11} - c_{12}) S_{xy} \\ D_x &= e_{15} S_{zx} + \epsilon_{11} E_x & D_y &= e_{15} S_{yz} + \epsilon_{11} E_y \\ D_z &= e_{31} S_x + e_{31} S_y + e_{33} S_z + \epsilon_{33} E_z \end{aligned} \quad (2.5)$$

where c_{11} , c_{12} , c_{13} , c_{33} , c_{44} are elastic constants, e_{15} , e_{31} , e_{33} are piezoelectric constants and ϵ_{11} , ϵ_{33} are dielectric constants. The relation between the strain components and mechanical displacement components as well as the relation between the electric potential field and the electric potential function as follows

$$S_{ij} = \frac{1}{2}(u_{i,j} + u_{j,i}) \quad i, j = 1, 2, 3 \quad E_k = -\phi_{,i} \quad (2.6)$$

Using equation (2.1) in equation (2.6)₁ and equation (2.2) in equation (2.6)₂, we have

$$\begin{aligned} S_x &= 0 & S_y &= 0 & S_z &= 0 & S_{xy} &= 0 \\ S_{yz} &= \frac{\partial w_1}{\partial y} & S_{zx} &= \frac{\partial w_1}{\partial x} \end{aligned} \quad (2.7)$$

and

$$E_x = -\frac{\partial \phi}{\partial x} \quad E_y = -\frac{\partial \phi}{\partial y} \quad E_z = 0 \quad (2.8)$$

Now, substituting equation (2.7), (2.8) and (2.5), into equation (2.3), we can obtain the governing equations for the piezoelectric layer as

$$c_{44}\nabla^2 w_1 + e_{15}\nabla^2 \phi = \rho_1 \ddot{w}_1 \quad e_{15}\nabla^2 w_1 - \epsilon_{11}\nabla^2 \phi = 0 \quad (2.9)$$

Now, equations (2.9) take the form as

$$\frac{\partial^2 w_1}{\partial x^2} + \frac{\partial^2 w_1}{\partial y^2} = \frac{1}{c_p^2} \frac{\partial^2 w_1}{\partial t^2} \quad \frac{\partial^2 \phi}{\partial x^2} + \frac{\partial^2 \phi}{\partial y^2} = \frac{1}{c_p^2} \left(\frac{e_{15}}{\epsilon_{11}} \right) \frac{\partial^2 w_1}{\partial t^2} \quad (2.10)$$

where $c_p = \sqrt{c_{44}^*/\rho_1}$, $c_{44}^* = c_{44} + e_{15}^2/\epsilon_{11}$ and c_p is the shear wave velocity in the piezoelectric layer.

We assume solutions to equations (2.10) in the form of

$$w_1 = W_1(x)e^{i\xi(y-ct)} \quad \phi = \varphi(x)e^{i\xi(y-ct)} \quad (2.11)$$

where ξ is the wave number and c is the phase velocity. With the help of (2.10) and (2.11), it results in

$$\begin{aligned} \frac{d^2 W_1(x)}{dx^2} + \alpha^2 \xi^2 W_1(x) &= 0 \\ \frac{d^2 \varphi(x)}{dx^2} - \xi^2 \varphi(x) + \frac{\xi^2 c^2}{c_p^2} \frac{e_{15}}{\epsilon_{11}} [A_1 \sin(\alpha \xi x) + A_2 \cos(\alpha \xi x)] &= 0 \end{aligned} \quad (2.12)$$

where $\alpha^2 = (c^2/c_p^2) - 1$.

Using the solutions to equations (2.11) and (2.12), we get solutions to equations (2.12) leads to

$$\begin{aligned} w_1(x, y, t) &= [A_1 \sin(\alpha \xi x) + A_2 \cos(\alpha \xi x)] e^{i\xi(y-ct)} \\ \phi(x, y, t) &= \left(\frac{e_{15}}{\epsilon_{11}} [A_1 \sin(\alpha \xi x) + A_2 \cos(\alpha \xi x)] + A_3 e^{-\xi x} + A_4 e^{\xi x} \right) e^{i\xi(y-ct)} \end{aligned} \quad (2.13)$$

where A_1, A_2, A_3, A_4 are arbitrary constants.

2.2. Dynamics of couple stress elastic half-space

The equation of motion for the couple stress elastic half-space in the absence of body forces and with the constitutive relations (Hadjesfandiari and Dargush, 2011) is

$$\begin{aligned} (\lambda + \mu + \eta \nabla^2) \nabla (\nabla \cdot \mathbf{u}_i^{(c)}) + (\mu - \eta \nabla^2) \nabla^2 \mathbf{u}_i^{(c)} &= \rho_2 \frac{\partial^2 \mathbf{u}_i^{(c)}}{\partial t^2} \\ \sigma_{ji}^{(c)} &= \lambda u_{k,k} \delta_{ij} + \mu (u_{i,j} + u_{j,i}) - \eta \nabla^2 (u_{i,j} - u_{j,i}) \\ \mu_{ji} &= 4\eta (\omega_{i,j} - \omega_{j,i}) \quad \text{where} \quad \omega_i = \frac{1}{2} \epsilon_{ijk} u_{k,j} \end{aligned} \quad (2.14)$$

where $i, j, k = 1, 2, 3$; λ, μ are Cauchy-Lame constants, η is the couple stress coefficient, $\eta = \mu l^2$ where l is characteristic length, $\mathbf{u}_i^{(c)} = [u_2, v_2, w_2]$ is the displacement vector, ρ_2 is the mass density of the couple stress elastic half-space, $\sigma_{ji}^{(c)}$ is the non-symmetric force-stress tensor and

μ_{ji} is the skew-symmetric couple stress tensor, δ_{ij} is Kronecker's delta and ϵ_{ijk} is the alternating tensor, the superscript index c is used for the lower couple stress elastic half-space.

Using equation (2.1) in (2.14)₁, we have

$$\frac{\partial^2 w_2}{\partial x^2} + \frac{\partial^2 w_2}{\partial y^2} - l^2 \left(\frac{\partial^4 w_2}{\partial x^4} + 2 \frac{\partial^4 w_2}{\partial x^2 \partial y^2} + \frac{\partial^4 w_2}{\partial y^4} \right) = \frac{1}{c_1^2} \frac{\partial^2 w_2}{\partial t^2} \quad (2.15)$$

where $c_1^2 = \mu/\rho$ is the shear wave velocity in the couple stress substrate.

We assume the solution to equation (2.15) to be

$$w_2 = W_2(x) e^{i\xi(y-ct)} \quad (2.16)$$

where ξ is the wave number and c is the phase velocity. Using this solution in equation (2.15), we get

$$\frac{d^4 W_2(x)}{dx^4} - S \frac{d^2 W_2(x)}{dx^2} + T W_2(x) = 0 \quad (2.17)$$

where

$$S = 2\xi^2 + \frac{1}{l^2} \quad T = \xi^2 \left[\xi^2 + \frac{1}{l^2} \left(1 - \frac{c^2}{c_1^2} \right) \right]$$

Since the amplitude of waves decreases with an increase in depth in the couple stress elastic half-space, so the solution to differential equation (2.17) becomes

$$w_2(x, y, t) = (A_5 e^{-ax} + A_6 e^{-bx}) e^{i\xi(y-ct)} \quad (2.18)$$

where

$$a = \sqrt{\frac{S + \sqrt{S^2 - 4T}}{2}} \quad b = \sqrt{\frac{S - \sqrt{S^2 - 4T}}{2}}$$

3. Boundary conditions

For propagation of SH-waves in a piezoelectric layer lying over a couple stress elastic half-space, the following boundary conditions are to be satisfied:

(A) Boundary conditions for the traction-free surface of the piezoelectric layer:

1. The mechanical stress-free condition is: $\sigma_{zx}^{(p)} = 0$ at $x = -H$ (3.1)

2. The electrical boundary condition on the traction-free surface is:

- (a) Electrically open condition: $D_x = 0$ at $x = -H$ (3.2)

- (b) Electrically short condition: $\phi_p = 0$ at $x = -H$ (3.3)

(B) Boundary conditions at the common interface of the layer and half-space:

3. Stresses are continuous at the common interface: $\sigma_{zx}^{(p)} = \sigma_{zx}^{(c)}$ at $x = 0$ (3.4)

4. Displacement fields are continuous at the common interface: $w_1 = w_2$ at $x = 0$ (3.5)

5. Electric potential function should vanish at the common interface: $\phi_p = 0$ at $x = 0$ (3.6)

6. Couple stress tensor should vanish at the common interface: $\mu_{xy} = 0$ at $x = 0$ (3.7)

4. Dispersion equations

Using equations (2.13), (2.18) and their corresponding stress and electrical displacement components into boundary equations (3.1)-(3.7), we obtain the following algebraic equations in terms of unknown coefficients A_1, A_2, A_3, A_4, A_5 and A_6

$$\alpha c_{44}^* \cos(\alpha \xi H) A_1 + \alpha c_{44}^* \sin(\alpha \xi H) A_2 - e_{15} \exp(\xi H) A_3 + e_{15} \exp(-\xi H) A_4 = 0 \quad (4.1)$$

$$\exp(\xi H) A_3 - \exp(-\xi H) A_4 = 0 \quad (4.2)$$

$$-\frac{e_{15}}{\epsilon_{11}} \sin(\alpha \xi H) A_1 + \frac{e_{15}}{\epsilon_{11}} \cos(\alpha \xi H) A_2 + \exp(\xi H) A_3 + \exp(-\xi H) A_4 = 0 \quad (4.3)$$

$$\alpha \xi c_{44}^* A_1 - \xi e_{15} A_3 + \xi e_{15} A_4 + \mu a [1 - l^2(\xi^2 - a^2)] A_5 + \mu b [1 - l^2(\xi^2 - b^2)] A_6 = 0 \quad (4.4)$$

$$A_2 - A_5 - A_6 = 0 \quad (4.5)$$

$$\frac{e_{15}}{\epsilon_{11}} A_2 + A_3 + A_4 = 0 \quad (4.6)$$

$$(\xi^2 - a^2) A_5 + (\xi^2 - b^2) A_6 = 0 \quad (4.7)$$

4.1. Dispersion equations for the case of electrically open circuit

The conditions mentioned in equations (4.1), (4.2) and (4.4)-(4.7) constitute six boundary conditions for this case. To obtain a non-trivial solution, the determinant of coefficients of the unknowns A_1, A_2, A_3, A_4, A_5 and A_6 vanishes. The frequency equation for the SH-wave in an electrically open circuit is obtained as

$$\xi(k_a - k_b) \left(\frac{e_{15}^2}{\epsilon_{11}} \tanh(\xi H) + \alpha c_{44}^* \tan(\alpha \xi H) \right) + [\mu a (1 - l^2 k_a) k_b - \mu b (1 - l^2 k_b) k_a] = 0 \quad (4.8)$$

where $k_a = \xi^2 - a^2$ and $k_b = \xi^2 - b^2$.

Equation (4.8) represents dispersion relations of the SH-wave in an electrically open circuit for the piezoelectric layer lying over couple stress elastic half-space.

4.2. Dispersion equations for the case of electrically short circuit

The conditions mentioned in equations (4.1) and (4.3)-(4.7) constitute six boundary conditions for this case. To obtain a non-trivial solution, the determinant of coefficients of the unknowns A_1, A_2, A_3, A_4, A_5 and A_6 vanishes. The frequency equation for the SH-wave in an electrically short circuit is obtained as

$$\begin{aligned} \xi(k_a - k_b) \left[\left(\alpha^2 c_{44}^{*2} - \frac{e_{15}^4}{\epsilon_{11}^2} \right) \tan(\alpha \xi H) \tanh(\xi H) + 2\alpha c_{44}^* \frac{e_{15}^2}{\epsilon_{11}} \left(1 - \frac{\sec(\alpha \xi H)}{\cosh(\xi H)} \right) \right] \\ + [\mu a (1 - l^2 k_a) k_b - \mu b (1 - l^2 k_b) k_a] \left(\alpha c_{44}^* \tanh(\xi H) - \frac{e_{15}^2}{\epsilon_{11}} \tan(\alpha \xi H) \right) = 0 \end{aligned} \quad (4.9)$$

Equation (4.9) represents dispersion relations of the SH-wave in an electrically short circuit for the piezoelectric layer lying over the couple stress elastic half-space.

5. Numerical results

For illustrating the results, we have considered a semi-infinite couple stress substrate which is made of Dionysos Marble having microstructural properties (Vardoulakis and Georgiadis, 1997): $\rho = 2717 \text{ kg/m}^3$, $\mu = 30.5 \cdot 10^9 \text{ N/m}^2$ and $c_p = 3350 \text{ m/s}$.

Piezoelectric layers of $PZT - 5H$ or $BaTiO_3$ are considered (Liu *et al.*, 2001) having properties as given below:

- (a) For $PZT - 5H$ ceramics: $c_{44} = 2.30 \cdot 10^{10} \text{ N/m}^2$, $\rho = 7.50 \cdot 10^3 \text{ kg/m}^3$, $e_{15} = 17.0 \text{ C/m}^2$, $\epsilon_{11} = 277.0 \cdot 10^{-10} \text{ C}^2/\text{Nm}^2$
- (b) For $BaTiO_3$ ceramics: $c_{44} = 4.40 \cdot 10^{10} \text{ N/m}^2$, $\rho = 7.28 \cdot 10^3 \text{ kKg/m}^3$, $e_{15} = 11.0 \text{ C/m}^2$, $\epsilon_{11} = 128.0 \cdot 10^{-10} \text{ C}^2/\text{Nm}^2$

Dispersion curves of SH-type waves propagating in a piezoelectric layer overlying a couple stress medium have been examined in Figs. 2-9. Figures 2, 4, 6, 8 correspond to electrically open conditions and Figs. 3, 5, 7, 9 correspond to electrically short conditions. Phase velocity profiles are highly important for propagation of surface waves in the layered structure for its possible applications in sensors, delay lines, filters etc. One of the common feature of all theses characteristic curves is that the non-dimensional phase velocity c/c_p decreases with an increase in the non-dimensional wave number ξH .

5.1. Effects of microstructure of the substrate

Figures 2 and 3 show variation of the non-dimensional phase speed c/c_p with respect to the non-dimensional wave number ξH for different values of characteristic length $l = 0.00001 \text{ m}$, 0.0001 m , 0.0004 m . Here, the thickness of the piezoelectric layer is taken as $H = 0.002 \text{ m}$. It can be observed that the microstructure of the substrate affects the phase velocity profiles significantly. It can be seen from the profiles that with an increase in characteristic length, the phase velocity increases for both considered layers, i.e. for $PZT - 5H$ material shown in 2(i) and 3(i) under electrically open conditions and for $BaTiO_3$ material shown in 2(ii) and 3(ii) under electrically short conditions, as shown in Figs. 2 and 3, respectively. The characteristic curves clearly demonstrate microstructural effects of the semi-infinite solid substrate that remains ignored in the classical elastic model.

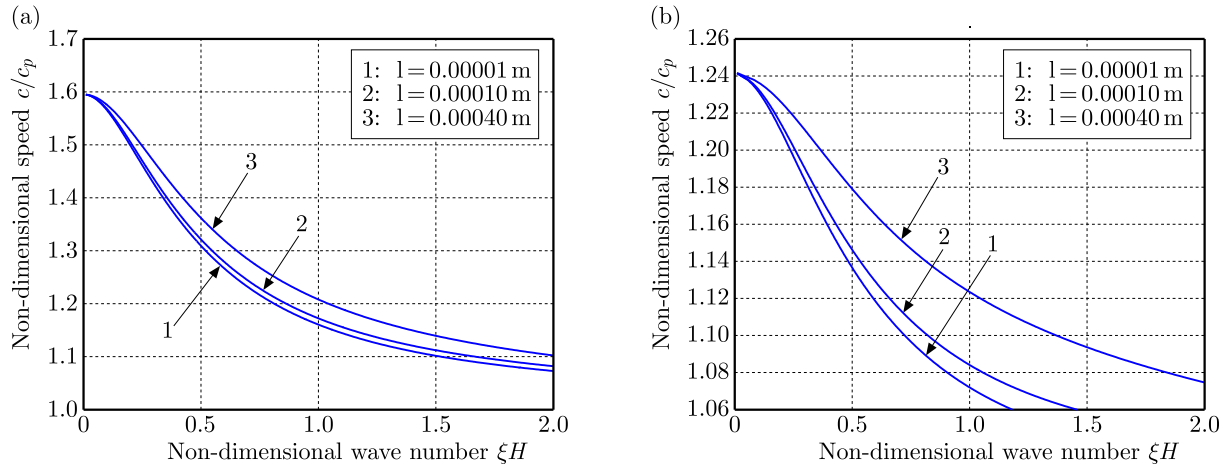


Fig. 2. Variation of the non-dimensional phase velocity against the non-dimensional wave number for different values of characteristic length $l = 0.00001 \text{ m}$, 0.0001 m , 0.0004 m , when $H = 0.002 \text{ m}$ in the case of electrically open conditions; (a) 2(i) for $PZT - 5H$ ceramic, (b) 2(ii) for $BaTiO_3$ ceramic

5.2. Effects of thickness of a piezoelectric layer

To demonstrate the effects of thickness of a layer on the phase velocity profiles of the SH-wave propagating in a layered structure, here in Figs. 4 and 5 we consider different values of the thickness of the layer i.e. $H = 0.0005 \text{ m}$, 0.002 m , 0.05 m , their characteristic length $l = 0.0001 \text{ m}$ is kept constant. It is observed that thickness of the layer has adverse effects on the phase velocities and the phase velocity decreases with an increase in thickness of the layer.

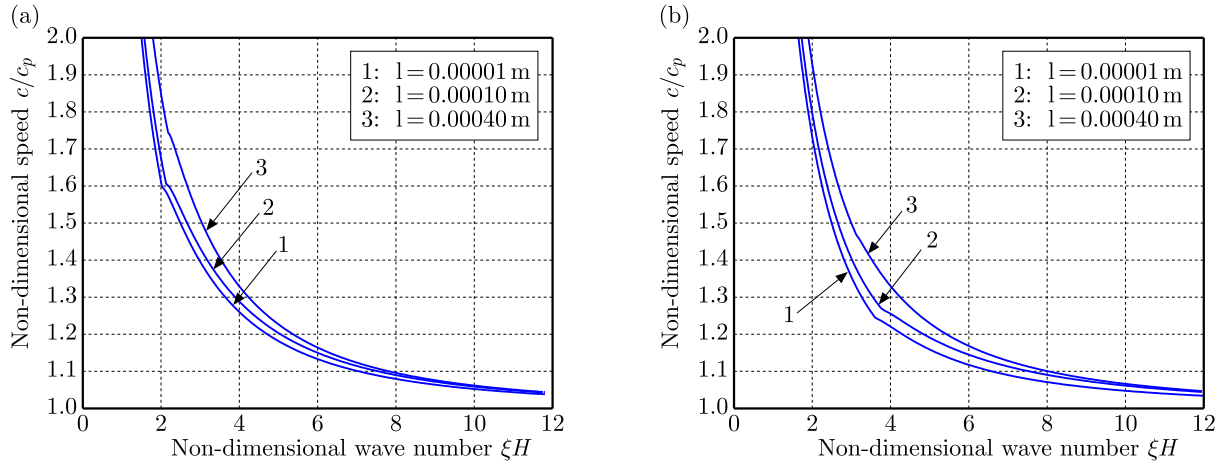


Fig. 3. Variation of the non-dimensional phase velocity against the non-dimensional wave number for different values of characteristic length $l = 0.00001$ m, 0.0001 m, 0.0004 m, when $H = 0.002$ m in the case of electrically short conditions; (a) 3(i) for $PZT - 5H$ ceramic, (b) 3(ii) for $BaTiO_3$ ceramic

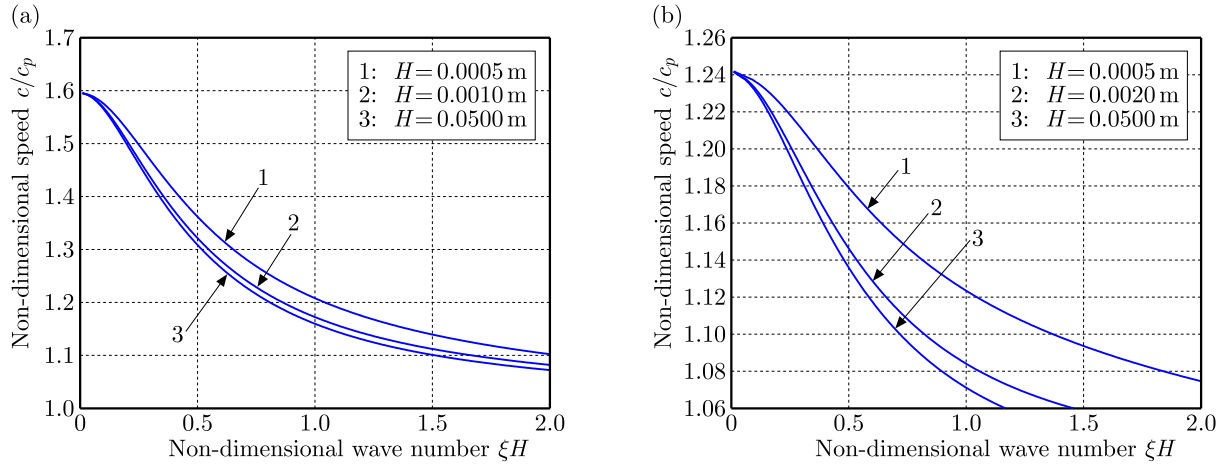


Fig. 4. Variation of the non-dimensional phase velocity against the non-dimensional wave number for different values of width of the piezoelectric layer $H = 0.0005$ m, 0.002 m, 0.05 m, when $l = 0.0001$ m in the case of electrically open conditions; (a) 4(i) for $PZT - 5H$ ceramic, (b) 4(ii) for $BaTiO_3$ ceramic

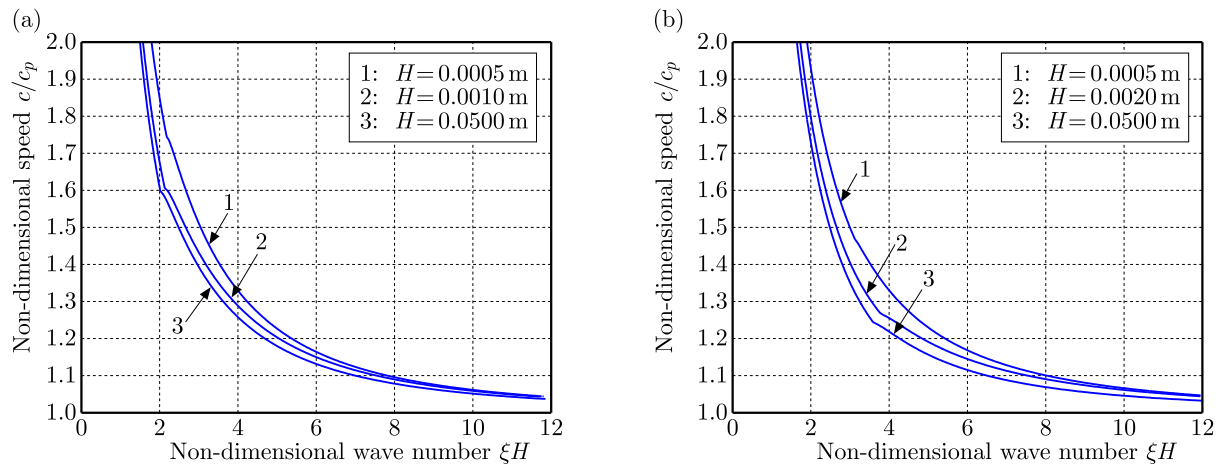


Fig. 5. Variation of the non-dimensional phase velocity against the non-dimensional wave number for different values of width of the piezoelectric layer $H = 0.0005$ m, 0.002 m, 0.05 m, when $l = 0.0001$ m in the case of electrically short conditions; (a) 5(i) for $PZT - 5H$ ceramic, (b) 5(ii) for $BaTiO_3$ ceramic

Characteristic profiles for the corresponding electrically open and short conditions are shown in Figs. 4 and 5, 4(i) and 5(i) correspond to $PZT - 5H$ material and 4(ii) and 5(ii) correspond to $BaTiO_3$ material, respectively.

5.3. Effects of piezoelectric constants

Figures 6 and 7 show variation of the non-dimensional speed c/c_p against the non-dimensional wave number ξH for the SH-wave propagation. The characteristic curves are plotted for different values of the piezoelectric parameter $e_{15} = 17 \text{ C/m}^2$, 21 C/m^2 , 25 C/m^2 for $PZT - 5H$ material shown in 6(i) and 7(i) and $e_{15} = 11 \text{ C/m}^2$, 15 C/m^2 , 19 C/m^2 for $BaTiO_3$ material shown in 6(ii) and 7(ii) for both cases of electrically open and short conditions, respectively. The thickness of the layer $H = 0.002 \text{ m}$ and the characteristic length $l = 0.0001 \text{ m}$ associated with couple stress substrate are kept constant. The piezoelectric constant associated with the piezoelectric layer does not favor the phase velocity profiles of SH-waves. It is observed that an increase in the piezoelectric constant leads in general to a decrease in phase velocity profiles for both cases of electrically open and short conditions.

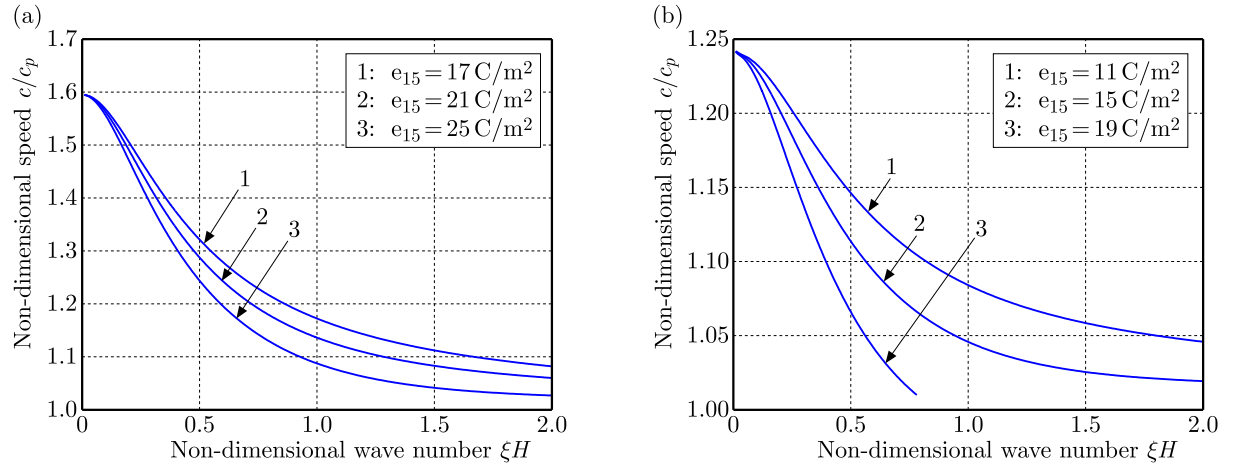


Fig. 6. Variation of the non-dimensional phase velocity against the non-dimensional wave number for different values of piezoelectric constants $e_{15} = 17, 21, 25 \text{ C/m}^2$ in 6(i) and $e_{15} = 11, 15, 19 \text{ C/m}^2$ in 6(ii), for electrically open cases; (a) 6(i) for $PZT - 5H$ ceramic, (b) 6(ii) for $BaTiO_3$ ceramic

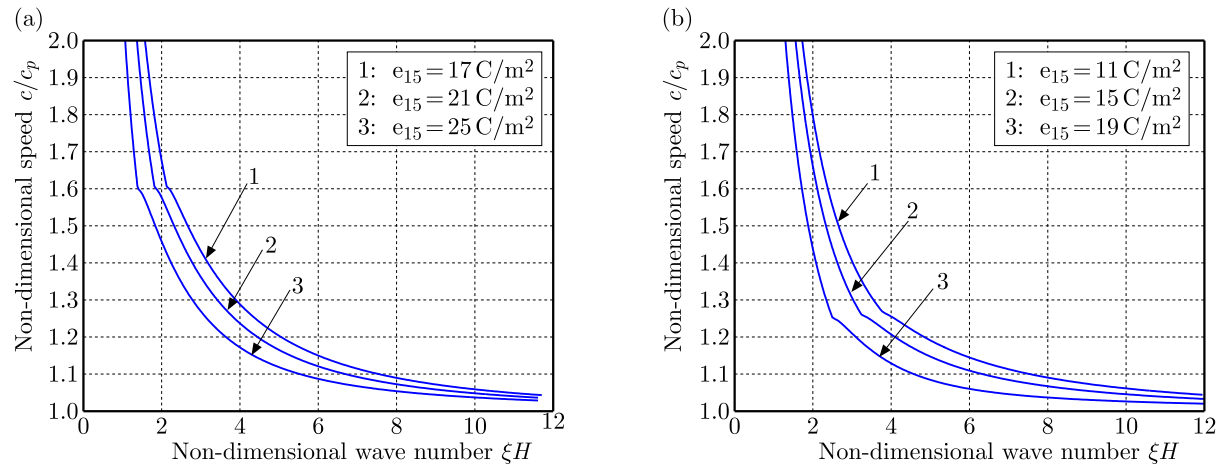


Fig. 7. Variation of the non-dimensional phase velocity against the non-dimensional wave number for different values of piezoelectric constants $e_{15} = 17, 21, 25 \text{ C/m}^2$ in 7(i) and $e_{15} = 11, 15, 19 \text{ C/m}^2$ in 7(ii), for electrically short cases; (a) 7(i) for $PZT - 5H$ ceramic, (b) 7(ii) for $BaTiO_3$ ceramic

5.4. Effects of dielectric constants

Figures 8 and 9 show the trend of the non-dimensional speed c/c_p with respect to the non-dimensional wave number ξH on the SH-type wave propagation for different values of dielectric constants $\epsilon_{11} = 77 \text{ C}^2/\text{Nm}^2$, $177 \text{ C}^2/\text{Nm}^2$, $277 \text{ C}^2/\text{Nm}^2$ for $PZT - 5H$ material shown in 8(i) and 9(i) for electrically open conditions and $\epsilon_{11} = 98 \text{ C}^2/\text{Nm}^2$, $128 \text{ C}^2/\text{Nm}^2$, $158 \text{ C}^2/\text{Nm}^2$ for $BaTiO_3$ material shown in 8(ii) and 9(ii) for electrically short conditions. Here, we have taken the material characteristic length parameter $l = 0.0001 \text{ m}$ and the thickness of the piezoelectric layer $H = 0.002 \text{ m}$. Dielectric constants of the piezoelectric layer overlying couple stress substrate affect the phase velocity profiles significantly. It is observed that the phase velocity of SH-waves increases with an increase in the dielectric constant for both considered materials of the piezoelectric layer i.e. $PZT - 5H$ and $BaTiO_3$ materials for both the cases of electrically open and short conditions.

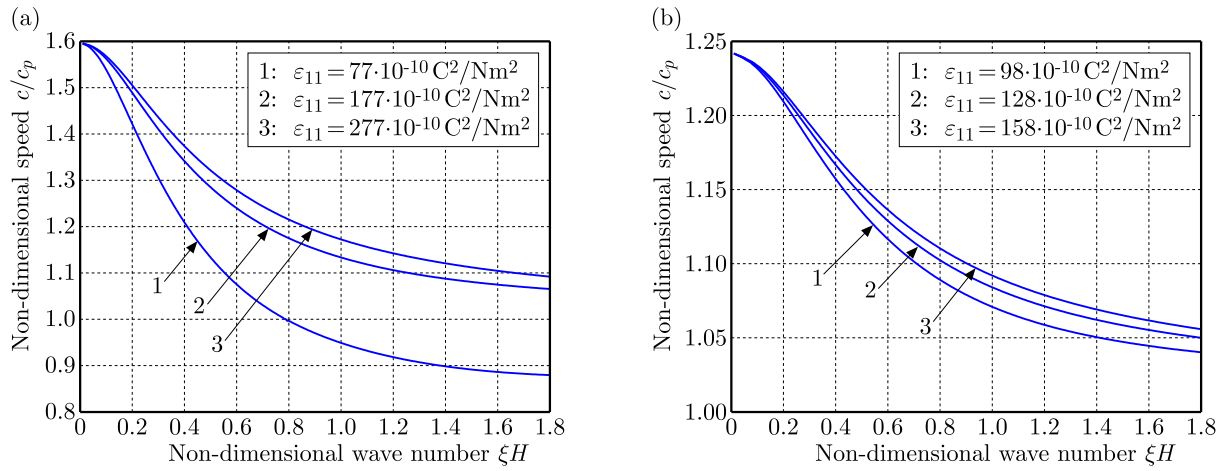


Fig. 8. Variation of the non-dimensional phase velocity against the non-dimensional wave number for different values of dielectric constants $\epsilon_{11} = 77, 177, 277 \text{ C}^2/\text{Nm}^2$ in 8(i), $\epsilon_{11} = 98, 128, 158 \text{ C}^2/\text{Nm}^2$ in 8(ii), for electrically open cases; (a) 8(i) for $PZT - 5H$ ceramic, (b) 8(ii) for $BaTiO_3$ ceramic

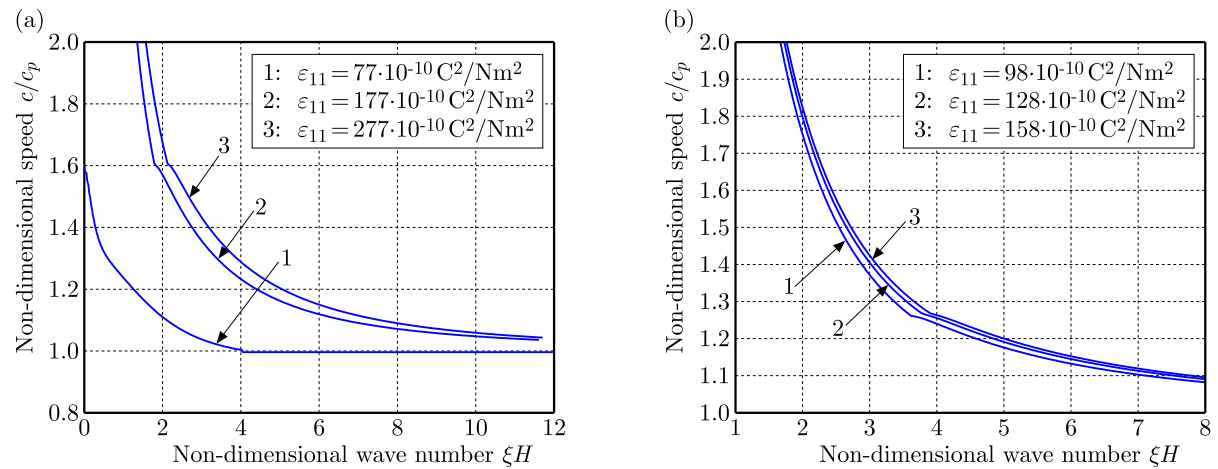


Fig. 9. Variation of the non-dimensional phase velocity against the non-dimensional wave number for different values of dielectric constants $\epsilon_{11} = 77, 177, 277 \text{ C}^2/\text{Nm}^2$ in 9(i), $\epsilon_{11} = 98, 128, 158 \text{ C}^2/\text{Nm}^2$ in 9(ii), for electrically short case; (a) 9(i) for $PZT - 5H$ ceramic, (b) 9(ii) for $BaTiO_3$ ceramic

6. Conclusion

Dispersion equations (4.8) and (4.9) provide implicit relations between the phase velocity of SH-wave and different characteristic parameters associated with the layer and substrate. The phase velocity profiles are affected with variation in the associated parameters of the considered layered structure. The major conclusions of the study may be pointed out as follows:

- (i) The wave number affects the phase velocity profiles of SH-waves significantly. The non-dimensional phase velocity decreases with an increase in the non-dimensional wave number in each case of electrically open and short circuits for both considered materials of the piezoelectric layer.
- (ii) Internal microstructure of the couple stress substrate affects the phase velocity profiles significantly. It is observed that the phase velocity of SH-waves increases with an increase in the characteristic length l . This effect justifies consideration of microstructural properties of the semi-infinite substrate.
- (iii) Thickness of the piezoelectric layer shows an adverse effect on phase velocity profiles of SH-waves. It is observed that the phase velocity of SH-waves decreases with an increase in the thickness parameter associated with the piezoelectric layer.
- (iv) The piezoelectric constant affects the phase velocity profiles of SH-wave substantially. Specifically, an increase in the piezoelectric parameter leads to a decrease in the phase velocity of SH-waves propagation in the piezoelectric layer overlying the couple stress elastic half-space.
- (v) Dielectric constants associated with the piezoelectric layer favor the phase velocity profiles of SH-waves. It is observed that with an increase in the dielectric parameter, the phase velocity increases.

The findings obtained in the paper through theoretical and numerical demonstrations could help the development of more efficient and high performance Love wave based devices.

Acknowledgement

The authors gratefully acknowledge the support of the Indian government research agency: DST (Department of Science and Technology) via Grant No. EMR/2016/002601.

References

1. COSSERAT E., COSSERAT F., 1909, *Theory of Deformable Bodies* (in French), A Hermann et Fils, Paris
2. ERINGEN A.C., 1968, Theory of micropolar elasticity, [In:] *Fracture*, H. Liebowitz (Edit.), Academic Press New York, **2**, 662-729
3. EZZIN H., AMOR M.B., GHOZLEN M.H.B., 2017, Propagation behavior of SH waves in layered piezoelectric/piezomagnetic plates, *Acta Mechanica*, **228**, 3, 1071-1081
4. GUPTA V., VASHISHTH A.K., 2016, Effects of piezoelectricity on bulk waves in monoclinic poro-elastic materials, *Journal of Theoretical and Applied Mechanics*, **54**, 2, 571-577
5. HADJESFANDIARI A.R., DARGUSH G.F., 2011, Couple stress theory for solids, *International Journal of Solids and Structures*, **48**, 2496-2510
6. JAKOBY B., VELLEKOOP M.J., 1997, Properties of Love waves: Applications in sensors, *Smart Materials and Structures*, **6**, 668-679
7. KOITER W., 1964, Couple stresses in the theory of elasticity – I and II, *Proceedings of the Koninklijke Nederlandse Akademie Van Wetenschappen*, **67**, 17-44

8. LIU H., WANG Z.K., WANG T.J., 2001, Effect of initial stress on the propagation behavior of Love waves in a layered piezoelectric structure, *International Journal of Solids and Structures*, **38**, 1, 37-51
9. LIU J., HE S., 2010, Properties of Love waves in layered piezoelectric structures, *International Journal of Solids and Structures*, **47**, 2, 169-174
10. MINDLIN R.D., TIERSTEN H.F., 1962, Effects of couple-stresses in linear elasticity, *Archive for Rational Mechanics and Analysis*, **11**, 415-448
11. SHARMA V., KUMAR S., 2017, Dispersion of SH waves in a viscoelastic layer imperfectly bonded with a couple stress substrate, *Journal of Theoretical and Applied Mechanics*, **55**, 2, 535-546
12. SINGH A.K., KUMAR S., CHATTOPADHYAY A., 2015, Love-type wave propagation in a piezoelectric structure with irregularity, *International Journal of Engineering Science*, **89**, 35-60
13. VARDOULAKIS I., GEORGIADIS H.G., 1997, SH surface waves in a homogeneous gradient-elastic half-space with surface energy, *Journal of Elasticity*, **47**, 2, 147-165
14. VOIGT W., 1887, *Theoretical Studies on the Elasticity Relationships of Crystals* (in German), Abhandlungen der Gesellschaft der Wissenschaften zu Gttingen, 34
15. WANG H.M., ZHAO Z.C., 2013, Love waves in a two-layered piezoelectric/elastic composite plate with an imperfect interface, *Archive of Applied Mechanics*, **83**, 1, 43-51
16. WANG Q., 2002, Wave propagation in a piezoelectric coupled solid medium, *Journal of Applied Mechanics*, **69**, 6, 819-824
17. WANG Y., WANG M., LIU J., 2012, Propagation behaviors of SH waves in piezoelectric layer/elastic cylinder with an imperfect interface, *Applied Mechanics and Materials*, **151**, 130-134
18. WEI W., LIU J., FANG D., 2009, Shear horizontal surface waves in a piezoelectric-piezomagnetic coupled layered half-space, *International Journal of Nonlinear Sciences and Numerical Simulation*, **10**, 6, 767-778

Manuscript received November 9, 2017; accepted for print February 8, 2018

INVESTIGATION OF INLET DISTORTION EFFECTS ON AXIAL COMPRESSOR PERFORMANCE BASED ON STREAMLINE CURVATURE METHOD

SARALLAH ABBASI

Department of Mechanical Engineering, Arak University of Technology, Arak, Iran
e-mail: s_abbasi@arakut.ac.ir

ALIREZA PIRNIA

Department of Mechanical Engineering, Clarkson University, New York, USA

REZA TAGHAVI-ZENOUEH

Department of Mechanical Engineering, Iran University of Science and Technology, Tehran, Iran

In this paper, the effects of inlet flow distortion on performance maps and details of the flow field are investigated using the Streamline Curvature Method. The results are presented for both design and off-design conditions and compared with experimental data, which shows good agreement. The effects of inlet flow distortion are investigated by inlet total pressure variation in three different cases in the way that the average total pressure remains constant and equal to the design value. The results show that a relative increase in the total pressure at tip causes an increase in the pressure ratio and efficiency as well as a better performance in the choking region. Alternatively, a relative increase in the total pressure in hub causes opposite behavior and a better performance at the surging region.

Keywords: axial compressor, performance map, inlet distortion, surge margin, streamline curvature

1. Introduction

The compressor is one of the most important parts of jet engines which must have a stable operation in all flight maneuvers or atmospheric conditions. One of the most appropriate assumptions in the normal approach to compressor and fan design is undistorted flow at the inlet in which flow properties are assumed to be uniform and the flow direction to be axial. But under a variety of conditions in military and commercial aircraft engines, a highly distorted flow at the compressor inlet is produced, which is commonly referred to as “inlet distortion”. Non uniform flow at the inlet of the fan stage may be originated from atmospheric turbulence, boundary layer growth, flow distortions induced by the shape of the intake duct and boundary layer ingesting engines in the modern high efficient airframe.

Many performance problems and engine failures in aircraft including rotating stall and surge were observed due to inlet distortion. Therefore, it is important to explore the behavior of the engine compressor towards inlet distortion. There are many ways to investigate the flow field in an axial compressor or fan with inlet distortion. In prior research investigations, models of the response to distortion have been developed which utilize clean compressor performance or stage characteristics to anticipate the compressor behavior with distortion (Chue *et al.*, 1989; Day, 1993; Greitzer, 1980).

With rapid development of computer technology, Computational Fluid Dynamics (CFD) methods have been employed extensively to study the flow field in a compressor with inlet flow distortion. Zhang and Hou (2017) explored stall inception in a low-speed axial compressor under

rotating distorted inflow conditions using full annulus, unsteady, three dimensional computational fluid dynamics (CFD). The results indicated that under co-rotating inflow distortion, close to the tip region the flow incidence angle is increased and the axial flow coefficient decreased. It has an important role on the stall inception process. Liu *et al.* (2016) investigated the effect of inlet distortion on the performance of an axial transonic contra-rotating compressor by means of full-annulus simulation. Results revealed that the inlet distortion leads to reduction of the pressure ratio and efficiency. The interaction between the detached shockwave and the tip leakage flow leads to blockage of the blades passage. It is one important of reasons for the compressor stall. Naseri and Boroomand (2016) using CFD approach evaluated the effect of inlet distortion in forms of inlet swirl and total pressure distortion on compressor performance and stability. Results indicated that hub and tip radial distortions change the stability range of the compressor.

Review of the literature shows that most of the researches were employed experimentally and by numerical methods (CFD method) to explore the effects of inlet distortion on axial compressor performance. In experimental tests, limitations of instruments and cost make this method difficult to investigate. Also, application of CFD analysis, which is associated with solving complete flow and energy equations in a very complex geometry like a compressor or fan, takes long period of time and is not reasonable.

Due to difficulties in experimental and CFD analysis, various methods with some simplifications are presented for design purposes and flow analysis. Some researchers such as Kim *et al.* (1996) used a simple integral method which rendered the multistage analysis as a natural part instead of solving a detailed flow field problem. By using this method, they calculated the qualitative trend of distorted performance of an axial compressor successfully. Most of researchers and designers prefer working on meridional plane of a turbomachine (Lakshminarayana, 1996). Governing equations on hub to tip through the flow surface (referred to as S2-surface) can be solved on the meridional plane using streamline curvature (SCM). This method is mostly used because of its rapid convergence and accurate results. Final results based on this method are comparable with those obtained through CFD methods, which consume usually extreme time and expenses (Pachidis and Pilidis, 2006). This method has been employed by Hearsey (1986), Pachidis and Pilidis (2006), Hu *et al.* (2011) and Gong *et al.* (2016) to design and analyze different kinds of turbomachines.

Based on the above mentioned subjects, it can be realized that the effects of inlet distortion on the compressor performance are investigated, but details of characteristics of flow fields such as flow angles, velocity and pressure field are still under question. In this paper, the streamline curvature method, as a rapid and accurate method, is used to investigate the effects of inlet total pressure distortion on flow field details, performance characteristics and surge/choke margins.

2. Streamline Curvature Method and verification

2.1. Streamline Curvature Method

Governing equations for viscous compressible flows through compressors are highly nonlinear. Therefore, most of methods that have been presented so far utilize some simplifications. One effective approach is to divide the flow field into a series of blade to blade surfaces (so-called S1-surface) and some surfaces extended from hub to tip (so-called S2-surface). Based on the experiences, working only on the through-flow surface, i.e., the S2-surface, which is extended from the hub to tip in the radial and mean flow directions, can provide the final geometry of blades with an acceptable accuracy. The Streamline Curvature Method (SCM) is widely used for quasi three-dimensional design of axial compressor blades. This method which was presented

by Novak (1967) is based on successive refinement of streamlines to satisfy the balance between centrifugal and pressure forces while ensuring the given mass flow rate.

SCM utilizes primarily an inviscid flow. In fact, it offers a flexible method of determining the Euler solution of axisymmetric flow through a turbomachine. Then, a discrete increase of entropy, which is determined from loss correlations, is imposed to represent viscous effects. It is obvious that accuracy of results highly depends on the validity of loss correlations. The governing main system of equations consists of linear momentum and continuity equations. Then, combined with the thermodynamic equation of state, the resultant equation is mapped into the meridional plane of the flow passage. As a consequence of the assumptions made in this method, and mapping into the meridional plane, the final form of the governing equation can be presented as Eq. (2.1). Some of the parameters appeared in this equation are introduced in Fig. 1, showing the coordinate axes and angles necessary for formulation in SCM. Fundamentals of this method including its precise concept and more details on the governing equations and necessary correlations can be found in Hearsey (1986)

$$V_m \frac{dV_m}{dl} = \sin(\varphi - \gamma) \left(V_m \frac{\partial V_m}{\partial m} - F_m \right) + \cos(\varphi - \gamma) \left(\frac{V_m^2}{r_c} - F_n \right) + \frac{dh_0}{dl} - T \frac{ds}{dl} - \frac{V_\theta}{r} \frac{d(rV_\theta)}{dl} \quad (2.1)$$

where V_m and V_θ are, respectively, the meridional and swirl velocity, F_m and F_n are blade forces (meridional blade force and normal blade force), l and m are, respectively, the quasi-orthogonal and meridional direction, r and r_c is the radial direction and streamline curvature radius, h_0 is stagnation enthalpy, s is entropy and T is static temperature. φ and γ are deflection and sweep angles.

Equation (2.1) is solved as an ordinary first order differential equation. In this respect, a computerized program is developed which consists of two main parts. The first part is mainly attributed to obtain three dimensional geometry of blades, and the next part produces performance curves of the turbomachine. The computer code utilizes empirical correlations for calculations of various kinds of loss accompanied by axial compressors. Obviously, reliability of final results depends highly on the degree of precision of these correlations.

2.2. Loss and angle correlations

In order to implement viscous effects in governing equations, empirical correlations must be used for the loss coefficient, incidence and deviation angles. The loss coefficient is divided into four parts; profile loss, shock loss, secondary flow loss and tip clearance loss. The profile loss coefficient is calculated from Koch and Smith's correlation (1976), shock loss coefficient from Swan's correlation (1958), secondary flow loss coefficient from Griepentrog's correlation (1970) and tip clearance loss coefficient from Storer and Cumpsty's correlation (1994). These coefficients are based on the minimum loss condition (design condition). Therefore, summation of these four coefficients is multiplied by a factor which includes off-design effects in the total loss coefficient. This factor is based on the difference between design and off-design incidence angles. Equation (2.2) shows the total loss coefficient for each blade row

$$\omega = (\omega_p + \omega_{sh} + \omega_{sec} + \omega_{tip,cl}) \frac{i - i_{des}}{W^2} \quad (2.2)$$

where ω_p is the blade profile loss factor, ω_{sh} is the blade shock wave loss factor, ω_{sec} is the secondary loss factor, and $\omega_{tip,cl}$ is the tip clearance loss factor. In this equation, i_{des} and i are the design and off design incidences, respectively. An increment in the loss of actual incidence (off-design) and Mach number is originally accounted for through the parabolic term in brackets in Eq. (2.2). W in Eq. (2.2) is "width" which specifies the working range of the section. This is a common approach taken in streamline curvature methods to achieve a more realistic loss

“bucket” shape (Cetin *et al.*, 1987). Other parameters which are computed via empirical correlations are incidence and deviation angles. Lieblein’s popular correlations are used for obtaining these parameters (Cumpsty, 1989).

2.3. Surge and choking criteria

In order to obtain the mass flow rate in which surge or choking occurs in each speed line, some criteria must be defined. One suitable criterion for surge or stall occurrence, which is used in the current research, belongs to Aungier (2003). In his method, the aerodynamic velocity ratio across each blade row (W_{aero}) and the equivalent geometric velocity ratio (W_{geom}), which are calculated from equation (2.3), are compared (Aungier, 2003)

$$W_{aero} = \sqrt{\frac{P_{0,2} - P_2}{P_{0,1} - P_1}} \quad W_{geom} = \frac{\frac{0.15+11\frac{t_{max}}{c}}{0.25+10\frac{t_{max}}{c}}}{1 + 0.4\left(\frac{\theta\sigma}{2\sin\frac{\theta}{2}\cos\gamma}\right)^{0.65}} \quad (2.3)$$

where t_{max} represents the maximum thickness, c is the chord length, γ is the stagger angle, σ is the solidity, θ is the momentum thickness, $P_{0,2}$ and $P_{0,1}$ are the total pressures downstream and upstream the blade row, respectively. Also, P_2 and P_1 are the static pressures downstream and upstream the blade row, respectively. W_{geom} is just a function of geometric parameters and, therefore, remains constant for varying mass flow rate while W_{aero} increases as the flow rate decreases. Aungier (2003) suggested that as long as the aerodynamic velocity ratio remains higher than the geometric velocity ratio, the compressor is un-stalled, or surge has not occurred. In order to predict choking in the compressor, a decrease in the rate of Mach number variation is considered as the beginning of choking.

2.4. Experimental validation

In the design of an axial fan or compressor by the streamline curvature method, several input parameters such as meridional geometry, inlet condition, radial distribution of some parameters, and etc. are required. Also, to validate SCM results, experimental results in forms of radial distribution of parameters, performance maps and flow fields (meridional velocity and etc.) are required. To validate results in design and off-design conditions, Urasek *et al.* (1979) employed experimental data. Although that paper (Urasek’s fan) is a very old one, but it is one of the best papers that provides all required data for design of an axial fan by SCM. These data refer to a two-stage axial fan with a pressure ratio of 2.4. A view of its blades in the meridional plane along with the computational grid is shown in Fig. 1.

Overall characteristics of this fan are also shown in Table 1. Also, the estimated errors of the experimental data based on inherent accuracies of the instrumentation and recording system are provided in the paper (Urasek *et al.*, 1979) and added to Table 1.

Table 1. Overall characteristics of Urasek’s two-stage fan (Urasek *et al.*, 1979)

Inlet total pressure [kPa]	101.325 ± 0.7
Inlet total temperature [K]	288 ± 0.6
Mass flow rate [kg/s]	33.2 ± 0.3
Rotational velocity [r/min]	16042 ± 30
Overall pressure ratio	2.4
Number of stages	2
First rotor aspect ratio	1.56
Aerodynamic efficiency [%]	84.9

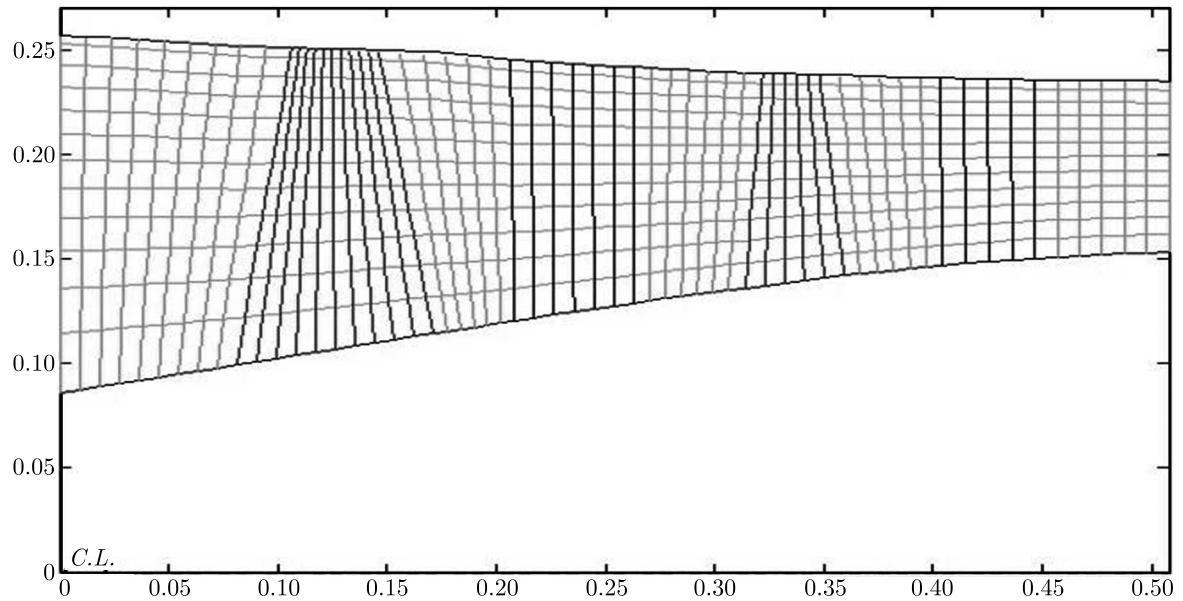


Fig. 1. Computational grid in the meridional plane

Analyzing the results of design conditions is not in the scope of this paper. But in Fig. 2, as an example, the meridional velocity distribution (as the most important result of SCM) for the first rotor is compared with the experimental one. In this figure, the difference between the obtained results with the experimental ones is about 8%.

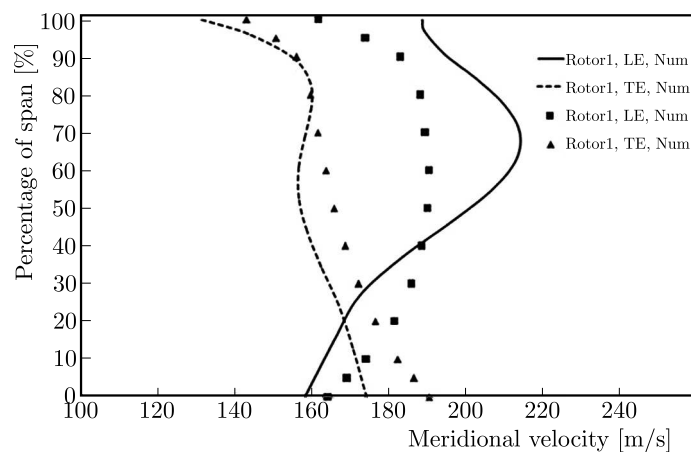


Fig. 2. Experimental validation of the first rotor meridional velocity in the design condition

The performance characteristics taken from the presented research work against the experimental ones are shown in Figs. 3 and 4. Figure 3 shows the variation of pressure ratio in 100 to 50 percent speed lines. The chance of choking occurrence is increased with increasing rotational speed. As shown in Fig. 3a, the maximum discrepancy between the SCM result and experimental data is lower than 7% in each speed line. Referring to Fig. 3b, good agreement is observed between SCM results and experimental data, and the maximum discrepancy is about 5% in 100% speed line.

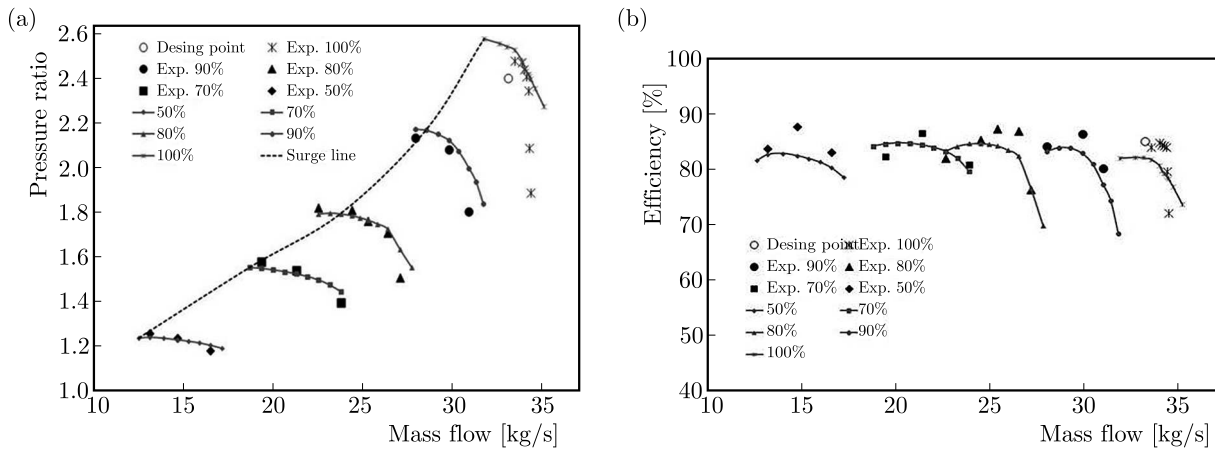


Fig. 3. Experimental validation of (a) fan pressure ratio and (b) fan efficiency in the off-design condition

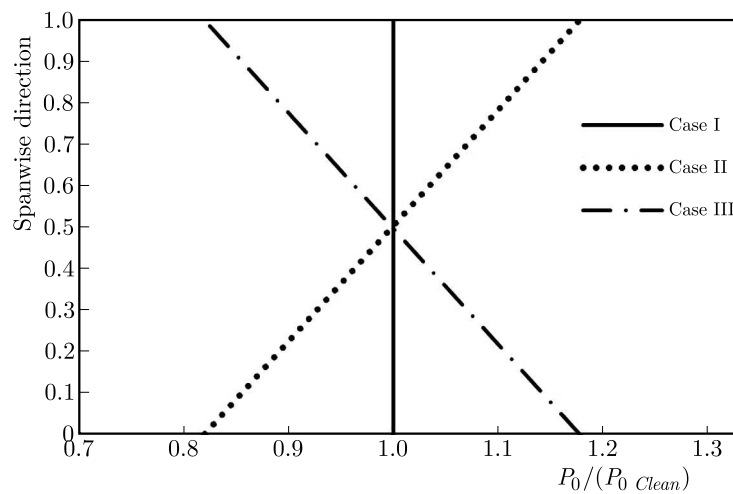


Fig. 4. All cases of disturbance patterns

3. Results and discussion

During flights, the inlet total pressure distortion due to rapid maneuvering or bumping into strong cross-winds causes destabilization of aircraft engines. The aerodynamic stability problems of compressors become increasingly critical while the loads of modern compressors are ceaselessly increasing. Conventional, good prediction of the performance of a whole engine can be achieved by a low-fidelity gas turbine performance simulation tool. But it is incapable of both precisely exploring the performance of individual engine components and grasping complex physical phenomena such as inlet flow distortion. On the other hand, CFD tools can study the performance of individual engine components appropriately, but application of CFD analysis, which is associated with solving complete flow and energy equations in very complex geometry typical for compressors or fans, takes a long period of time and is not reasonable. Also, experimental tests, due to limitations of measurement instruments and cost make this method difficult for investigation. Therefore, in the present work, the streamline curvature method (SCM) has been used to model inlet flow distortion due to fast convergence, precision results and the absence of the above constraints. As shown above, the presented results are comparable with those obtained from experimental tests.

Occurrence of distortion patterns in the incoming flow is applied in simulations by defining proper boundary conditions at the inlet. In the current research, the inlet flow with total pressure distortion is studied. Radial variations are in a way that the average total pressure

remains constant and equal to design value. Accordingly, a parameter named “distortion index” is introduced as follows (Aungier, 2003)

$$I = \frac{P_{0,max} - P_{0,min}}{P_{0,max}} \quad (3.1)$$

where $P_{0,max}$ and $P_{0,min}$ are the maximum and minimum total pressures. All considered cases are shown in Fig. 4. Case I has the design condition with a uniform inlet total pressure. Case II has linear variation of the inlet total pressure with the maximum at the tip and the minimum in the hub. Case III is opposite to the second case. The distortion index in the second and third cases is equal to 0.3. But in this regard, other researchers behaved differently. For example, Naseri and Boroomand (2016) used a CFD approach to investigate the effect of radial total pressure disturbances but the average total pressure was not the same in different cases. In another research, Liu *et al.* (2016) using commercial CFD software investigated the effects of circumferential total pressure inlet distortion on the performance and flow field of the axial counter-rotating compressor but the radial disturbance was not studied.

As can be seen in Fig. 5, the total pressure increase at the tip (case II) aims at blade loading and is more successful in controlling the loss in this region than in other cases. This fact leads to an increase in the pressure ratio and efficiency. Also, in this case, a lower total pressure in the hub make the Mach numbers lower at this region, which produces choking at higher mass flow rates.

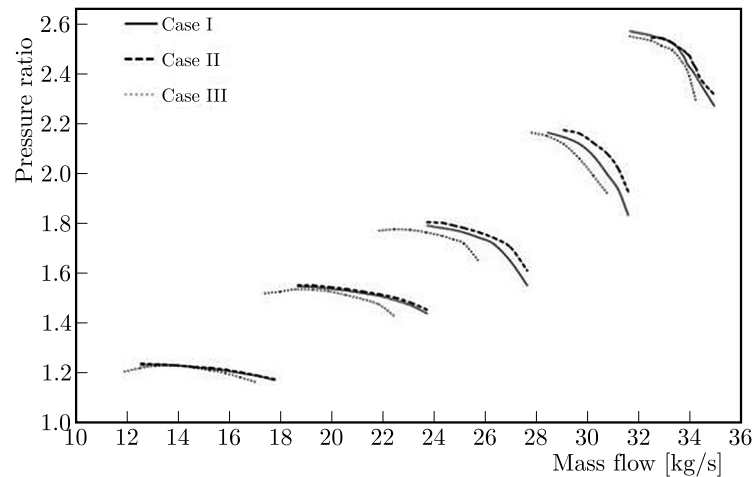


Fig. 5. Effect of inlet distortion on the pressure ratio

In Fig. 6, the incidence angle related to the second stator at a mid-range mass flow rate is visible in 90% of speed lines, which shows its increase in case II. In case III, with the decreasing total pressure at the tip and increasing in the hub, totally different behavior is observed in Fig. 5. Surge and choking occur at lower mass flow rates and the surge margin is higher. One could say that the total pressure increase at the tip shifts pressure ratio curves to the right and its decrease shifts the curves to the left (compared to uniform inlet total pressure). The surge margin (as defined by Urasek *et al.* (1979)) is 11.7% in the design case (case I), 7.7% in case II with a greater total pressure at the tip and 12.9% in case III with a higher total pressure in the hub.

In the research conducted by Naseri and Boroomand (2016), the authors employed tip radial and hub radial patterns to model total-pressure distortion. They approached a tip radial distortion pattern by assuming its value in the blade hub area equal to the total pressure of clean inlet and its decreasing to a lower value at the blade tip area linearly. Alternatively, in the hub radial pattern, they set the total pressure in the blade tip area equal to the clean value and the

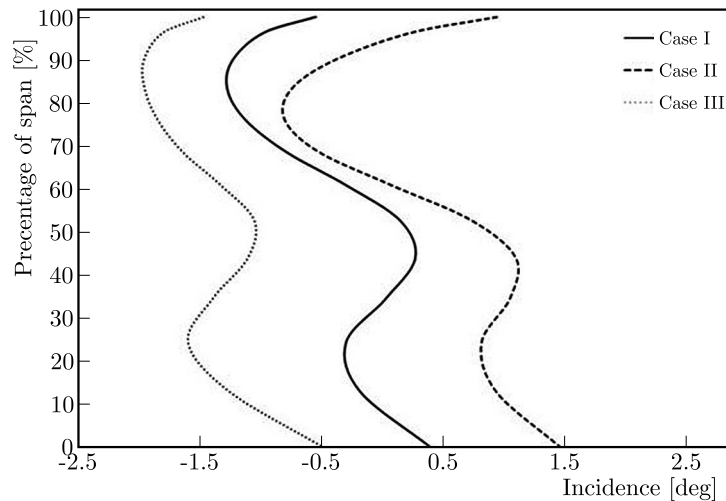


Fig. 6. Effect of inlet distortion on the incidence angle (mass flow = 29.9 kg/s , $N = 0.9N_{des}$, 2nd stator)

low pressure side in the hub area. Their results indicated that hub radial distortion improves the operability range of the compressor. Therefore, the stall mass flow is reduced and the mass flow range between stall and choking conditions widened. The stall pressure ratio is also slightly reduced. Conversely, tip radial distortion reduces the operability range of the compressor. The mass flow range between choking and stall conditions is considerably reduced by increasing the intensity of tip radial distortion. Considering different definitions of radial distortion in Naseri's research, which leads to reduced averaged total pressure in different cases, their results confirmed the presented research findings. It should also be noted that with the decreasing rotational speed, lower absolute or relative Mach numbers are created. It can reduce the opportunity of surge and choking. Therefore, it is visible in Fig. 5 that the difference between the curves (three investigated cases) is higher at higher rotational speeds (except for 100% speed line in which SCM has higher computational errors). It is worth to mention that the prior research such as Liu *et al.* (2016), Naseri and Boroomand (2016), mainly focused on a specific rotational speed, and no study has been conducted for different revolution.

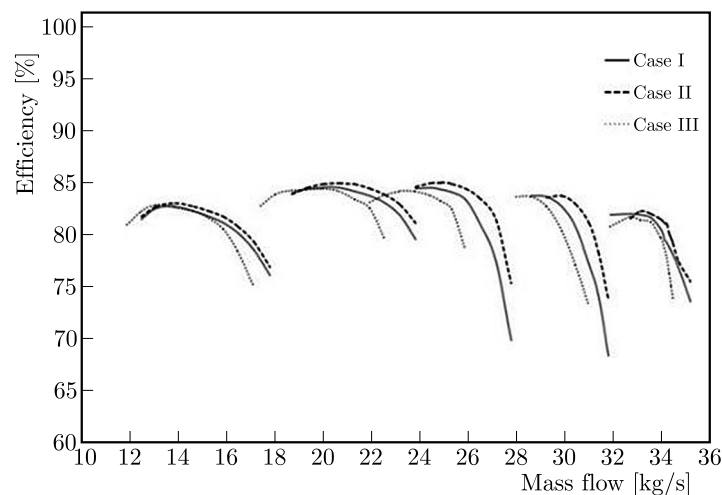


Fig. 7. Effect of inlet distortion on efficiency

Effects of inlet distortion on fan efficiency are also shown in Fig. 7 for the three cases. The previous statement about shifts in curves to the right or left due to distortions is also presented in Fig. 7. The results of the previous study (Naseri and Boroomand, 2016) just focused on the

effects of distortion on the pressure ratio and its effect on the efficiency was not presented. The total pressure increase at the tip and a decrease in the hub (case II) produces higher efficiencies and the inverse case (case III) has opposite results. Also it could be seen that distortion effects are more significant in higher speed lines (except for 100% speed line in which SCM has higher computational errors).

3.1. Effects of inlet distortion on surge and choking

In order to have a deeper understanding on the effects of inlet distortion on the compressor performance, some flow details are investigated. In this Section, the Mach number and the diffusion factor distribution for each case are presented in near surge condition. But, in similar studies, such results have not been extracted.

The diffusion factor can be considered as a criterion for the beginning of surge and stall. Therefore, in Fig. 8, a comparison between diffusion factors of different cases is carried out. The diffusion factor is plotted for the second stator at 90% speed line and the mass flow rate of surge beginning in the uniform flow case. A shift of the curves due to inlet distortions is also visible in Fig. 8. The total pressure increase at the tip and a decrease in the hub (case II), as stated in the previous Section, has weaker performance in the surge region. This behavior appears as the diffusion factor increases. This increase is higher in the hub and at the tip and is less in the mid-height, but there are higher diffusion factors in the whole blade height than in other cases. It can be seen that the case with a total pressure decrease in the hub and an increase at the tip (case III) has smallest diffusion factors and, therefore, better performance in the surge region.

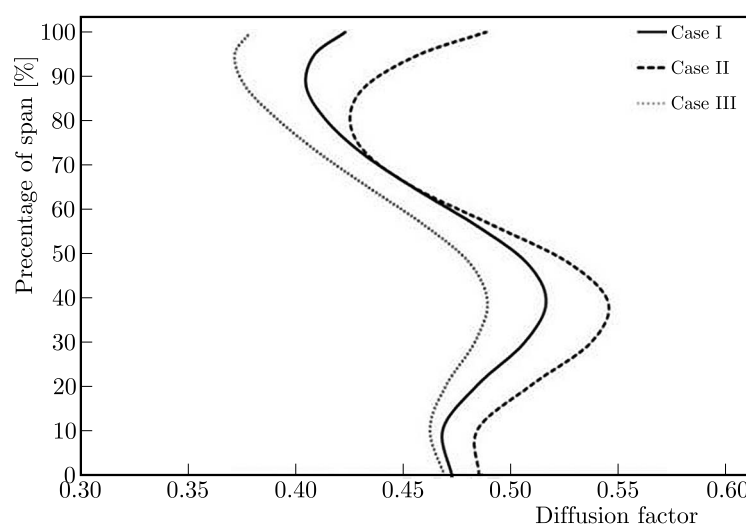


Fig. 8. Effect of inlet distortion on the diffusion factor (mass flow = 28 kg/s, $N = 0.9N_{des}$, 2nd stator)

Since, the Mach number is a criterion for choking prediction, a comparison between the Mach number for different investigated cases has been illustrated in Fig. 9. This figure compares the Mach number at the first stator inlet (with the highest inlet Mach numbers) at 90% speed line and the mass flow rate at the beginning of choking in the uniform flow case. Referring to Fig. 9, the difference between the curves is small. It can be seen that the total pressure increase in the hub and a decrease at the tip (case III) creates higher Mach numbers in the total height of blade and, consequently, shows a weaker performance in the choking region. In this case, the Mach number in the hub of the first stator inlet is about 0.86. So, it is a critical value that may increase to 1 in the blade throat and cause choking.

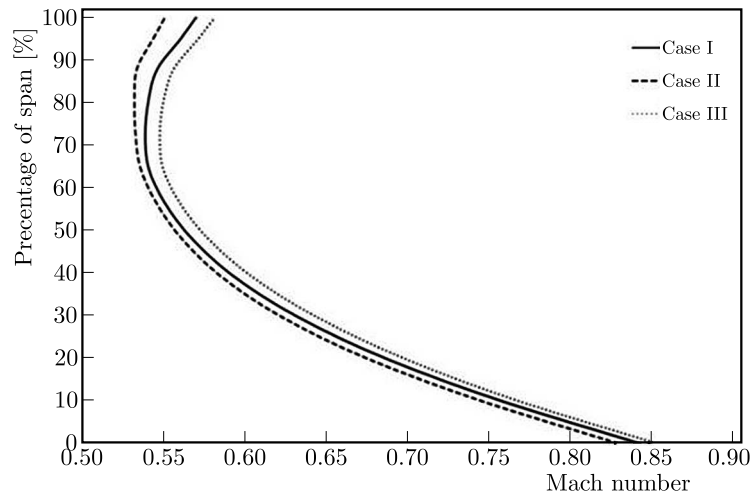


Fig. 9. Effect of inlet distortion on the Mach number (mass flow = 31.4 kg/s, $N = 0.9N_{des}$, 1st stator)

4. Conclusion

Under a variety of conditions in military and commercial aircraft engines, inlet flow distortion produces many performance problems and engine failures including rotating stall and surge. Therefore, it is important to explore the behavior of the engine compressor towards inlet distortion. In this paper, the streamline curvature method (SCM) has been used to explore effects of inlet flow distortion on performance maps and change of surge/choke margins. This method compared with numerical (CFD) and experimental methods, can help avoiding costly and time consuming problems and indicates good accuracy and fast convergence. In order to achieve the purpose of the paper, radial variations of the total pressure set in a way that the average total pressure remains constant and equal to the design value. While, in a similar research, the average total pressure is not the same in different cases. The results show that the total pressure increase at the tip can shift performance curves to the right, increase the pressure ratio and efficiency, whereas its decrease shifts the curves to the left. The former case could lead to better performance in choking regions but reduces the surge margin. Conversely, the second case with the decreased total pressure at the tip and increased in the hub improved the surge margin. The research studies conducted to date are limited and mainly focus on the effect of distortion on the pressure ratio for a specific rotational speed and no study has been conducted in terms of both efficiency and different revolution speeds. Besides the aforementioned limitations, details of characteristics of the flow field such as flow angles, Mach number and the diffusion factor distribution have not been extracted from prior researches. But in the present research, these characteristics for each case are presented in a near surge condition under inlet total pressure distortion. The results indicated that variations of the second stator incidence and diffusion factor has only presented a weaker performance of the former case in surge regions. But variation of the first stator inlet Mach number has proved a weaker performance of the second case in choking regions.

References

1. AUNGIER R.H., 2003, *Axial-Flow Compressors: a Strategy for Aerodynamic Design and Analysis*, ASME Press, New York
2. CETIN M., UECER A.S., HIRSCH C., SEROVY G.K., 1987, *Application of Modified Loss and Deviation Correlations to Transonic Axial Compressors*, Defense Technical Information Center, ADA191187

3. CHUE R., HYNES T.P., GREITZER E.M., TAN C.S., LONGLEY J.P., 1989, Calculations of inlet distortion induced compressor flow field instability, *International Journal of Heat and Fluid Flow*, **10**, 3, 211-223
4. CUMPSTY, 1989, *Compressor Aerodynamics*, John Wiley & Sons, New York
5. DAY I.J., 1993, Active suppression of rotating stall and surge in axial compressors, *Journal of Turbomachinery*, **115**, 1, 40-47
6. GONG W.Q., WU R.K., ZHANG B., 2016, A new finite difference method to solve the velocity gradient equation in streamline curvature method, *Advances in Mechanical Engineering*, **8**, 9, 1-13
7. GREITZER E.M., 1980, Review: axial compressor stall phenomena, *Journal of Fluids Engineering*, **102**, 2, 134-151
8. GRIEPENTROG H.R., 1970, Secondary flow losses in axial compressors, *AGARD Lecture Series*, **39**
9. HEARSEY R.M., 1986, Practical compressor aerodynamic design, *Advanced Topics in Turbomachinery Technology, Principal Lecture Series*, **2**, Concepts ETI
10. HU J.F., OU-YANG H., ZHU X. CH., QIANG X.Q., DU Z., 2011, An improved streamline curvature approach for transonic axial compressor performance prediction, *Journal of Aerospace Engineering*, **225**, 5, 575-584
11. KIM J.H., MARBLE F.E., KIM C.J., 1996, Distorted inlet flow propagation in axial compressors, *Proceedings of 6th International Symposium Transport Phenomena and Dynamics of Rotating Machinery*, **2**, 123-130
12. KOCH C.C., SMITH L.H., 1976, Loss sources and magnitudes in axial flow compressors, *Journal of Engineering for Gas Turbines and Power*, **98**, 3, 411-424
13. LAKSHMINARAYANA B., 1996, *Fluid Dynamics and Heat Transfer of Turbomachinery*, John Wiley & Sons, New York
14. LIU H., WANG Y., XIAN S., HU W., 2016, Effect of inlet distortion on the performance of axial transonic contra-rotating compressor, *Journal of Aerospace Engineering*, **10**, 3, 1-13
15. NASERI M., BOROOMAND S., 2016, Numerical investigation of effect of inlet swirl and total-pressure distortion on performance and stability of an axial transonic compressor, *Journal of Thermal Science*, **25**, 6, 501-510
16. NOVAK R.A., 1967, Streamline curvature computing procedures for fluid-flow problems, *Journal of Engineering for Power*, **89**, 4, 478-490
17. PACHIDIS V., PILIDIS P., 2006, Prediction of engine performance under compressor inlet flow distortion using streamline curvature, *Journal of Engineering for Gas Turbines and Power*, **129**, 1, 97-103
18. STORER J.A., CUMPSTY N.A., 1994, An approximation analysis and prediction method for tip clearance loss in axial compressors, *Journal of Turbomachinery*, **116**, 4, 648-656
19. SWAN W.C., 1958, A practical method of predicting transonic compressor performance, *Journal of Engineering for Gas Turbines and Power*, **83**, 3, 322-330
20. URASEK D.C., GORRELL W.T., CUNNAN W.S., 1979, Performance of a two stage fan having low aspect ratio first stage rotor blading, *NASA Technical Paper*, Report No. 1493
21. ZHANG M., HOU A., 2017, Investigation on stall inception of axial compressor under inlet rotating distortion, *Journal of Mechanical Engineering Science*, **231**, 10, 1859-1870

ANALYTICAL MODEL FOR INVESTIGATION OF THE EFFECT OF FRICTION POWER ON THERMAL STRESSES IN FRICTION ELEMENTS OF BRAKES

KATARZYNA TOPCZEWSKA

Białystok University of Technology, Faculty of Mechanical Engineering, Białystok, Poland
e-mail: k.topczewska@doktoranci.pb.edu.pl

The influence of the change with time of friction power on thermal stresses in a friction element of a brake system is investigated. For this purpose, a list of ten different temporal profiles of specific friction power is used, which has been experimentally established for a single braking process. The corresponding profiles of transient temperature fields in the considered element are applied as input parameters to find quasi-static thermal stresses. Numerical analysis concerned with spatio-temporal distributions of the stresses and their evolutions on the heated surface is presented.

Keywords: frictional heating, temperature, specific power of friction, braking, thermal stresses

1. Introduction

One of the efficient and quick methods to preliminary estimate temperature and thermal stresses in a designed friction pair of a brake system is usage of analytical models. Generally, there are one-dimensional thermal problems of friction for bodies with canonical shape (i.e. semi-space, strip, circular disc), heated on its working surface by the heat flux with intensity proportional to the specific power of friction (Fazekas, 1953; Carslaw and Jaeger, 1959; Newcomb and Spurr, 1967). The last mentioned is defined as a product of the friction coefficient, contact pressure and relative sliding speed between the pad and the brake rotor (Blok, 1955; Ling, 1973). Experimental research shows that, in the real braking processes, the friction momentum (and hence the force of friction) vary with time, and the nature of this change depends on thermophysical properties of materials of the friction pair elements, working conditions and construction of the brake (Chichinadze *et al.*, 1979; Balakin and Sergienko, 1999). As a result, the power of friction may have a complicated time profile. Most exact analytical solutions to the thermal problem of friction were obtained for constant or linearly decreasing with time specific power of friction (Yevtushenko and Kuciej, 2012; Kuciej, 2012; Jewtuszenko *et al.*, 2015). Those solutions describe non-stationary fields of temperature in friction elements during braking with an invariable friction force and constant velocity or constant retardation. Distributions of thermal stresses initiated by such temperatures in a semi-space were investigated by Evtushenko and Kutsei (2006), and in a strip applied on the foundation analyzed by Yevtushenko *et al.* (2011), Yevtushenko and Kuciej (2010).

The list of different temporal profiles of the specific friction power, established by means of experimental research of frictional heating during single braking, was presented in the monograph by Chichinadze (1967). Exact, analytical solutions to boundary-value problems of heat conduction for a semi-space, heated on its surface by the frictional heat flux with intensity proportional to the specific friction power, placed on the above-mentioned list, were obtained in the articles by Topczewska (2017a) and Yevtushenko *et al.* (2017a).

The aim of this paper is to investigate the influence of time profiles of the specific friction power on distributions of thermal stresses generated due to frictional heating in a friction element during single braking. Some results of the investigations were presented at the 9th International Conference Balttrib'2017 (Yevtushenko *et al.*, 2017b).

2. Temperature

Temporal profiles of the specific friction power during single braking have the following forms (Chichinadze, 1967)

$$q_i(t) = q_0 q_i^*(t) \quad q_0 = \frac{w_0}{t_s} \quad 0 \leq t \leq t_s \quad i = 1, 2, \dots, 10 \quad (2.1)$$

where t_s is the braking time, q_0 and w_0 are nominal values of the specific friction power and friction work, respectively

$$\begin{aligned} q_1^*(t) &= 2(1 - t^*) & q_2^*(t) &= 2t^* & q_3^*(t) &= 1.5\sqrt{1 - t^*} \\ q_4^*(t) &= 1.5\sqrt{t^*} & q_5^*(t) &= 3(1 - t^*)^2 & q_6^*(t) &= 3t^{*2} \\ q_7^*(t) &= 6t^*(1 - t^*) & q_8^*(t) &= 1.2(1 - t^*)(1 + 2t^*) \\ q_9^*(t) &= 1.2t^*(3 - 2t^*) & q_{10}^*(t) &= 6\sqrt{t^*}(1 - \sqrt{t^*}) & t^* &= \frac{t}{t_s} \end{aligned} \quad (2.2)$$

where

$$w_0 = \int_0^{t_s} q_i(t) dt \quad i = 1, 2, \dots, 10 \quad (2.3)$$

is constant for all cases, at the end of braking $t = t_s$.

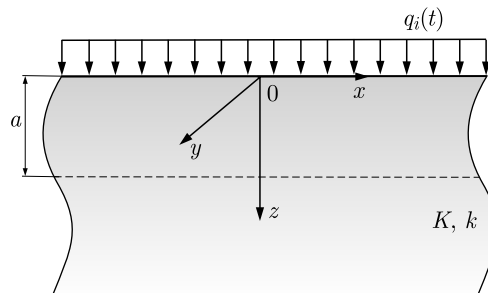


Fig. 1. Scheme of the problem

Temperature fields $T_i(z, t)$, $z \geq 0$, $0 \leq t \leq t_s$, $i = 1, 2, \dots, 10$ in a friction element (pad, disc, etc.) caused by heating its working surface (Fig. 1) by the heat flux with intensities $q_i(t)$, $i = 1, 2, \dots, 10$ (2.1)-(2.3) are found from exact solutions to the proper thermal problem of friction for a semi-space $z \geq 0$ in dimensionless forms (Topczewska, 2017a; Yevtushenko *et al.*, 2017a)

$$\begin{aligned}
T_1^*(\zeta, \tau) &= \frac{4}{3}\sqrt{\tau}\tau^* \left\{ \left[\frac{3}{\tau^*} - 2(1 + Z^2) \right] \text{ierfc } Z + Z \text{erfc } Z \right\} \\
T_2^*(\zeta, \tau) &= \frac{4}{3}\sqrt{\tau}\tau^* [2(1 + Z^2) \text{ierfc } Z - Z \text{erfc } Z] \\
T_3^*(\zeta, \tau) &= 3\sqrt{\tau} \text{ierfc } Z - \frac{1}{2}\sqrt{\tau}\tau^* [2(1 + Z^2) \text{ierfc } Z - Z \text{erfc } Z] \\
&\quad - \frac{1}{40}\sqrt{\tau}\tau^{*2} [(8 + 18Z^2 + 4Z^4) \text{ierfc } Z - Z(7 + 2Z^2) \text{erfc } Z] \\
&\quad - \frac{1}{560}\sqrt{\tau}\tau^{*3} [(48 + 174Z^2 + 80Z^4 + 8Z^6) \text{ierfc } Z - Z(57 + 36Z^2 + 4Z^4) \text{erfc } Z] \\
T_4^*(\zeta, \tau) &= \frac{3}{4}\sqrt{\pi\tau_s}\tau^* [\text{erfc } Z - 2Z \text{ierfc } Z] \\
T_5^*(\zeta, \tau) &= 2\sqrt{\tau} \{ 3 \text{ierfc } Z - 2\tau^* [2(1 + Z^2) \text{ierfc } Z - Z \text{erfc } Z] \\
&\quad + \frac{1}{5}\tau^{*2} [(8 + 18Z^2 + 4Z^4) \text{ierfc } Z - Z(7 + 2Z^2) \text{erfc } Z] \} \\
T_6^*(\zeta, \tau) &= \frac{2}{5}\sqrt{\tau}\tau^{*2} [(8 + 18Z^2 + 4Z^4) \text{ierfc } Z - Z(7 + 2Z^2) \text{erfc } Z] \\
T_7^*(\zeta, \tau) &= 4\sqrt{\tau}\tau^* \{ [2(1 + Z^2) \text{ierfc } Z - Z \text{erfc } Z] \\
&\quad - \frac{1}{5}\tau^* [(8 + 18Z^2 + 4Z^4) \text{ierfc } Z - Z(7 + 2Z^2) \text{erfc } Z] \} \\
T_8^*(\zeta, \tau) &= \frac{4}{5}\sqrt{\tau} \{ 3 \text{ierfc } Z + \tau^* [2(1 + Z^2) \text{ierfc } Z - Z \text{erfc } Z] \\
&\quad - \frac{2}{5}\tau^{*2} [(8 + 18Z^2 + 4Z^4) \text{ierfc } Z - Z(7 + 2Z^2) \text{erfc } Z] \} \\
T_9^*(\zeta, \tau) &= \frac{4}{5}\sqrt{\tau}\tau^* \{ 3[2(1 + Z^2) \text{ierfc } Z - Z \text{erfc } Z] \\
&\quad - \frac{2}{5}\tau^* [(8 + 18Z^2 + 4Z^4) \text{ierfc } Z - Z(7 + 2Z^2) \text{erfc } Z] \} \\
T_{10}^*(\zeta, \tau) &= \tau^* \{ 3\sqrt{\pi\tau_s} (\text{erfc } Z - 2Z \text{ierfc } Z) - 4\sqrt{\tau} [2(1 + Z^2) \text{ierfc } Z - Z \text{erfc } Z] \}
\end{aligned} \tag{2.4}$$

where the function $\text{erf}(x)$ is error function, $\text{erfc}(x) = 1 - \text{erf}(x)$, $\text{ierfc}(x) = \exp(-x^2)/\sqrt{\pi} - x \text{erfc}(x)$, and the dimensionless parameters are determined by the following relations

$$\begin{aligned}
\zeta &= \frac{z}{a} & \tau &= \frac{kt}{a^2} & \tau_s &= \frac{kt_s}{a^2} & \tau^* &= \frac{\tau}{\tau_s} \\
Z &= \frac{\zeta}{2\sqrt{\tau}} & T_0 &= \frac{q_0 a}{K} & T_i^* &= \frac{T_i - T_a}{T_0}
\end{aligned} \tag{2.5}$$

and $a = \sqrt{3kt_s}$ – effective depth of heat penetration (Chichinadze *et al.*, 1979), K – thermal conductivity [W/(Km)]; k – thermal diffusivity [m²/s]; T_a – ambient temperature [K].

3. Thermal stresses

Thermal stresses corresponding to the fields of temperature $T_i^*(\zeta, \tau)$, Eqs. (2.4) and (2.5), are found based on the model of thermal bending of a thick plate with unfixed ends. In accordance with this model, $\sigma_{i,x}(z, t) = \sigma_{i,y}(z, t) \equiv \sigma_i(z, t)$, $\sigma_{i,z}(z, t) = 0$, where the transverse normal component of the stress tensor σ_i ($i = 1, 2, \dots, 10$) (Noda *et al.*, 2000)

$$\sigma_i(z, t) = \sigma_0 \sigma_i^*(\zeta, \tau) \quad \sigma_0 = \frac{\alpha_t E T_0}{1 - \nu} \quad 0 \leq z \leq a \quad 0 \leq t \leq t_s \tag{3.1}$$

where the material properties are E – Young's modulus [MPa], α_t – coefficient of linear thermal expansion [K^{-1}], ν – Poisson's ratio

$$\begin{aligned}\sigma_i^*(\zeta, \tau) &= \varepsilon_i^*(\zeta, \tau) - T_i^*(\zeta, \tau) & 0 \leq \zeta \leq 1 & \quad 0 \leq \tau \leq \tau_s \\ \varepsilon_i^*(\zeta, \tau) &= (4 - 6\zeta)N_i(\tau) + 6(2\zeta - 1)M_i(\tau)\end{aligned}\quad (3.2)$$

and

$$N_i(\tau) = \int_0^1 T_i^*(\zeta, \tau) d\zeta \quad M_i(\tau) = \int_0^1 \zeta T_i^*(\zeta, \tau) d\zeta \quad (3.3)$$

Substituting the dimensionless temperatures $T_i^*(\zeta, \tau)$, Eq. (2.4) to equations (3.3), the following are determined

$$\begin{aligned}N_1(\tau) &= \frac{8}{3}\tau\tau^* \left[\left(\frac{3}{\tau^*} - 2 \right) I_0(\tau) - 2I_2(\tau) + J_1(\tau) \right] \\ M_1(\tau) &= \frac{16}{3}\tau\sqrt{\tau}\tau^* \left[\left(\frac{3}{\tau^*} - 2 \right) I_1(\tau) - 2I_3(\tau) + J_2(\tau) \right] \\ N_2(\tau) &= \frac{8}{3}\tau\tau^* \{ 2[I_0(\tau) + I_2(\tau)] - J_1(\tau) \} \\ M_2(\tau) &= \frac{16}{3}\tau\sqrt{\tau}\tau^* \{ 2[I_1(\tau) + I_3(\tau)] - J_2(\tau) \} \\ N_3(\tau) &= 6\tau I_0(\tau) - \tau\tau^* \{ 2[I_0(\tau) + I_2(\tau)] - J_1(\tau) \} \\ &\quad - \frac{1}{20}\tau\tau^{*2} [8I_0(\tau) + 18I_2(\tau) + 4I_4(\tau) - 7J_1(\tau) - 2J_3(\tau)] \\ &\quad - \frac{1}{280}\tau\tau^{*3} [48I_0(\tau) + 174I_2(\tau) + 80I_4(\tau) + 8I_6(\tau) - 57J_1(\tau) - 36J_3(\tau) - 4J_5(\tau)] \\ M_3(\tau) &= 12\tau\sqrt{\tau}I_1(\tau) - 2\tau\sqrt{\tau}\tau^* \{ 2[I_1(\tau) + I_3(\tau)] - J_2(\tau) \} \\ &\quad - \frac{1}{10}\tau\sqrt{\tau}\tau^{*2} [8I_1(\tau) + 18I_3(\tau) + 4I_5(\tau) - 7J_2(\tau) - 2J_4(\tau)] \\ &\quad - \frac{1}{140}\tau\sqrt{\tau}\tau^{*3} [48I_1(\tau) + 174I_3(\tau) + 80I_5(\tau) + 8I_7(\tau) - 57J_2(\tau) - 36J_4(\tau) - 4J_6(\tau)] \\ N_4(\tau) &= \frac{3}{2}\sqrt{\pi\tau\tau_s}\tau^* [J_0(\tau) - 2I_1(\tau)] & M_4(\tau) &= 3\tau\sqrt{\pi\tau_s}\tau^* [J_1(\tau) - 2I_2(\tau)] \\ N_5(\tau) &= 4\tau \{ 3I_0(\tau) - 2\tau^* [2I_0(\tau) + 2I_2(\tau) - J_1(\tau)] \\ &\quad + \frac{1}{5}\tau^{*2} [8I_0(\tau) + 18I_2(\tau) + 4I_4(\tau) - 7J_1(\tau) - 2J_3(\tau)] \} \\ M_5(\tau) &= 8\tau\sqrt{\tau} \{ 3I_1(\tau) - 2\tau^* [2I_1(\tau) + 2I_3(\tau) - J_2(\tau)] \\ &\quad + \frac{1}{5}\tau^{*2} [8I_1(\tau) + 18I_3(\tau) + 4I_5(\tau) - 7J_2(\tau) - 2J_4(\tau)] \} \\ N_6(\tau) &= \frac{4}{5}\tau\tau^{*2} [8I_0(\tau) + 18I_2(\tau) + 4I_4(\tau) - 7J_1(\tau) - 2J_3(\tau)] \\ M_6(\tau) &= \frac{8}{5}\tau\sqrt{\tau}\tau^{*2} [8I_1(\tau) + 18I_3(\tau) + 4I_5(\tau) - 7J_2(\tau) - 2J_4(\tau)] \\ N_7(\tau) &= 8\tau\tau^* \{ 2I_0(\tau) + 2I_2(\tau) - J_1(\tau) \\ &\quad - 0.2\tau^* [8I_0(\tau) + 18I_2(\tau) + 4I_4(\tau) - 7J_1(\tau) - 2J_3(\tau)] \} \\ M_7(\tau) &= 16\tau\sqrt{\tau}\tau^* \{ 2I_1(\tau) + 2I_3(\tau) - J_2(\tau) \\ &\quad - \frac{1}{5}\tau^* [8I_1(\tau) + 18I_3(\tau) + 4I_5(\tau) - 7J_2(\tau) - 2J_4(\tau)] \}\end{aligned}\quad (3.4)$$

$$\begin{aligned}
N_8(\tau) &= \frac{8}{5}\tau\{3I_0(\tau) + \tau^*[2I_0(\tau) + 2I_2(\tau) - J_1(\tau)] \\
&\quad - \frac{2}{5}\tau^2[8I_0(\tau) + 18I_2(\tau) + 4I_4(\tau) - 7J_1(\tau) - 2J_3(\tau)]\} \\
M_8(\tau) &= \frac{16}{5}\tau\sqrt{\tau}\{3I_1(\tau) + \tau^*[2I_1(\tau) + 2I_3(\tau) - J_2(\tau)] \\
&\quad - \frac{2}{5}\tau^2[8I_1(\tau) + 18I_3(\tau) + 4I_5(\tau) - 7J_2(\tau) - 2J_4(\tau)]\} \\
N_9(\tau) &= \frac{8}{5}\tau\tau^*\{3[2I_0(\tau) + 2I_2(\tau) - J_1(\tau)] \\
&\quad - \frac{2}{5}\tau^*[8I_0(\tau) + 18I_2(\tau) + 4I_4(\tau) - 7J_1(\tau) - 2J_3(\tau)]\} \\
M_9(\tau) &= \frac{1}{5}\tau\sqrt{\tau}\tau^*\{3[2I_1(\tau) + 2I_3(\tau) - J_2(\tau)] \\
&\quad - \frac{2}{5}\tau^*[8I_1(\tau) + 18I_3(\tau) + 4I_5(\tau) - 7J_2(\tau) - 2J_4(\tau)]\} \\
N_{10}(\tau) &= 2\sqrt{\tau}\tau^*\left\{3\sqrt{\pi\tau_s}[J_0(\tau) - 2I_1(\tau)] - 8\sqrt{\tau}\left[I_0(\tau) + I_2(\tau) - \frac{1}{2}J_1(\tau)\right]\right\} \\
M_{10}(\tau) &= 4\tau\tau^*\left\{3\sqrt{\pi\tau_s}[J_1(\tau) - 2I_2(\tau)] - 8\sqrt{\tau}\left[I_1(\tau) + I_3(\tau) - \frac{1}{2}J_2(\tau)\right]\right\}
\end{aligned}$$

where

$$\begin{aligned}
I_k(\tau) &= \int_0^X Z^k \operatorname{ierfc} Z \, dZ = \frac{1}{\sqrt{\pi}} L_k(\tau) - J_{k+1}(\tau) \quad k = 0, 1, \dots, 7 \\
L_k(\tau) &= \int_0^X Z^k e^{-Z^2} \, dZ \quad J_k(\tau) = \int_0^X Z^k \operatorname{erfc} Z \, dZ \quad X = \frac{1}{2\sqrt{\tau}}
\end{aligned} \tag{3.5}$$

and the variable Z has the form of Eq. (2.5).

Using the recursive formulas (Prudnikov *et al.*, 1986, 1998), $k = 2, 3, \dots$

$$\begin{aligned}
L_k(\tau) &= \frac{1}{2}[(k-1)L_{k-2}(\tau) - X^{k-1}e^{-X^2}] \\
J_k(\tau) &= \frac{1}{k+1}\left[\frac{1}{2}k(k-1)J_{k-2}(\tau) + \left(X^2 - \frac{1}{2}k\right)X^{k-1}\operatorname{erfc} X - \frac{1}{\sqrt{\pi}}X^k e^{-X^2}\right]
\end{aligned} \tag{3.6}$$

and taking into account that

$$\begin{aligned}
L_0(\tau) &= \frac{1}{2}\sqrt{\pi}(1 - \operatorname{erfc} X) & L_1(\tau) &= \frac{1}{2}(1 - e^{-X^2}) \\
J_0(\tau) &= \frac{1}{\sqrt{\pi}} - \operatorname{ierfc} X & J_1(\tau) &= \frac{1}{4}\operatorname{erf} X - \frac{1}{2}X \operatorname{ierfc} X
\end{aligned} \tag{3.7}$$

integrals (3.5)₂ are computed as

$$\begin{aligned}
L_2(\tau) &= \frac{1}{4}\sqrt{\pi}\operatorname{erf} X - \frac{1}{2}Xe^{-X^2} & L_3(\tau) &= \frac{1}{2}[1 - (1 + X^2)e^{-X^2}] \\
L_4(\tau) &= 0.375\sqrt{\pi}\operatorname{erf} X - \frac{1}{2}X\left(X^2 + \frac{3}{2}\right)e^{-X^2} \\
L_5(\tau) &= 1 - \left(\frac{1}{2}X^4 + X^2 + 1\right)e^{-X^2} \\
L_6(\tau) &= 0.9375\sqrt{\pi}\operatorname{erf} X - X(0.5X^4 + 1.25X^2 + 1.875)e^{-X^2} \\
L_7(\tau) &= 3 - \left(\frac{1}{2}X^6 + \frac{3}{2}X^4 + 3X^2 + 3\right)e^{-X^2}
\end{aligned} \tag{3.8}$$

and

$$\begin{aligned}
J_2(\tau) &= \frac{1}{3} \left\{ X^3 \operatorname{erfc} X + \frac{1}{\sqrt{\pi}} [1 - (X^2 + 1)e^{-X^2}] \right\} \\
J_3(\tau) &= \frac{1}{4} \left[X^4 \operatorname{erfc} X + \frac{3}{4} \operatorname{erf} X - \frac{1}{\sqrt{\pi}} X \left(X^2 + \frac{3}{2} \right) e^{-X^2} \right] \\
J_4(\tau) &= \frac{1}{5} \left\{ X^5 \operatorname{erfc} X + \frac{1}{\sqrt{\pi}} [2 - (X^4 + 2X^2 + 2)e^{-X^2}] \right\} \\
J_5(\tau) &= \frac{1}{6} \left[X^6 \operatorname{erfc} X + 1.875 \operatorname{erf} X - \frac{1}{\sqrt{\pi}} X (X^4 + 2.5X^2 + 3.75) e^{-X^2} \right] \\
J_6(\tau) &= \frac{1}{7} \left\{ X^7 \operatorname{erfc} X + \frac{1}{\sqrt{\pi}} [6 - (X^6 + 3X^4 + 6X^2 + 6)e^{-X^2}] \right\} \\
J_7(\tau) &= \frac{1}{8} \left[X^8 \operatorname{erfc} X + 6.5625 \operatorname{erf} X - \frac{1}{\sqrt{\pi}} X (X^6 + 3.5X^4 + 8.75X^2 + 13.125) e^{-X^2} \right] \\
J_8(\tau) &= \frac{1}{9} \left\{ X^9 \operatorname{erfc} X + \frac{1}{\sqrt{\pi}} [24 - (X^8 + 4X^6 + 12X^4 + 24X^2 + 24)e^{-X^2}] \right\}
\end{aligned} \tag{3.9}$$

With account of relations (3.7)-(3.9), in the right side of equation (3.5)₁, the following expressions are obtained

$$\begin{aligned}
I_0(\tau) &= \frac{1}{2\sqrt{\pi}} X e^{-X^2} + \frac{1}{4} \operatorname{erf} X - \frac{1}{2} X^2 \operatorname{erfc} X \\
I_1(\tau) &= \frac{1}{6} \left\{ \frac{1}{\sqrt{\pi}} [1 + (2X^2 - 1)e^{-X^2}] - 2X^3 \operatorname{erfc} X \right\} \\
I_2(\tau) &= \frac{1}{8} \left[X(2X^2 - 1)e^{-X^2} \sqrt{\pi} + \frac{1}{2} \operatorname{erf} X - 2X^4 \operatorname{erfc} X \right] \\
I_3(\tau) &= \frac{1}{5} \left\{ \frac{1}{2\sqrt{\pi}} [1 + (2X^4 - X^2 - 1)e^{-X^2}] - X^5 \operatorname{erfc} X \right\} \\
I_4(\tau) &= \frac{1}{6} \left[\frac{1}{4\sqrt{\pi}} X(4X^4 - 2X^2 - 3)e^{-X^2} + 0.375 \operatorname{erf} X - X^6 \operatorname{erfc} X \right] \\
I_5(\tau) &= \frac{1}{7} \left\{ \frac{1}{\sqrt{\pi}} \left[1 + \left(X^6 - \frac{1}{2} X^4 - X^2 - 1 \right) e^{-X^2} \right] - X^7 \operatorname{erfc} X \right\} \\
I_6(\tau) &= \frac{1}{8} \left\{ \frac{1}{\sqrt{\pi}} X(X^6 - 0.5X^4 - 1.25X^2 - 1.875)e^{-X^2} + 0.9375 \operatorname{erf} X - X^8 \operatorname{erfc} X \right\} \\
I_7(\tau) &= \frac{1}{9} \left\{ \frac{1}{\sqrt{\pi}} \left[3 + \left(X^8 - \frac{1}{2} X^6 - \frac{3}{2} X^4 - 3X^2 - 3 \right) e^{-X^2} \right] - X^9 \operatorname{erfc} X \right\}
\end{aligned} \tag{3.10}$$

Substituting functions $J_k(\tau)$, $I_k(\tau)$, $k = 0, 1, \dots, 7$, Eqs. (3.7)₂, (3.9) and (3.10) to Eqs. (3.4), temporal profiles of temperature $N_i(\tau)$ averaged over the plate thickness and the temperature momentum $M_i(\tau)$, $i = 1, 2, \dots, 10$, Eqs. (3.3), and next, dimensionless stresses $\sigma_i^*(\zeta, \tau)$, Eqs. (3.2), have been determined.

It should be noted that distributions of the thermal stresses corresponding to the profiles of the specific friction power $q_i^*(t)$, $i = 5, 7, 10$, Eqs. (2.2), were studied in the article by Topczewska (2017b), too.

4. Numerical analysis

Influence of the temporal profiles of the specific friction power $q_i^*(t)$, $i = 1, 2, \dots, 10$, Eqs. (2.2) on the dimensionless temperature $T_i^*(\zeta, \tau)$ (2.4) was detailed investigated in the article by Yevtushenko *et al.* (2017a). Therefore, in this paper, the effect of this factor on the quasi-static normal thermal stresses $\sigma_i^*(\zeta, \tau)$, $i = 1, 2, \dots, 10$ Eqs. (3.1) and (3.2), initiated by the

temperature, have been determined. Isolines of these stresses are shown in Figs. 2 and 3. The presented data can be divided into two specific groups. The first one consists of the results obtained for $i=1,3,8$ and $i=5,7,10$ (Topczewska, 2017b). These cases are characterized by the fact that with the onset of the braking process, along with a rapid increase of temperature, in the region $0 \leq \zeta \leq 0.2$ under the friction surface, compressive stresses ($\sigma_i^* < 0$) appear. Absolute values of the stresses in this zone decrease with time, achieving zero at the particular time moment, then change the sign and become tensile stresses ($\sigma_i^* > 0$). The time of change of the stress sing (compressive into tensile) is strongly dependent on the time of achieving the maximum temperature on the friction surface of the heated element. The faster temperature reaches the maximum value, the earlier this transition occurs and the tensile stress achieves a higher value on the outer surface at the moment of standstill. The second region $0.75 \leq \zeta \leq 1$ of the compressive stresses occurs adjacent to the unheated, bottom surface of the element. Evolution of the stresses in this region is similar, as in the previous – at the initial stage

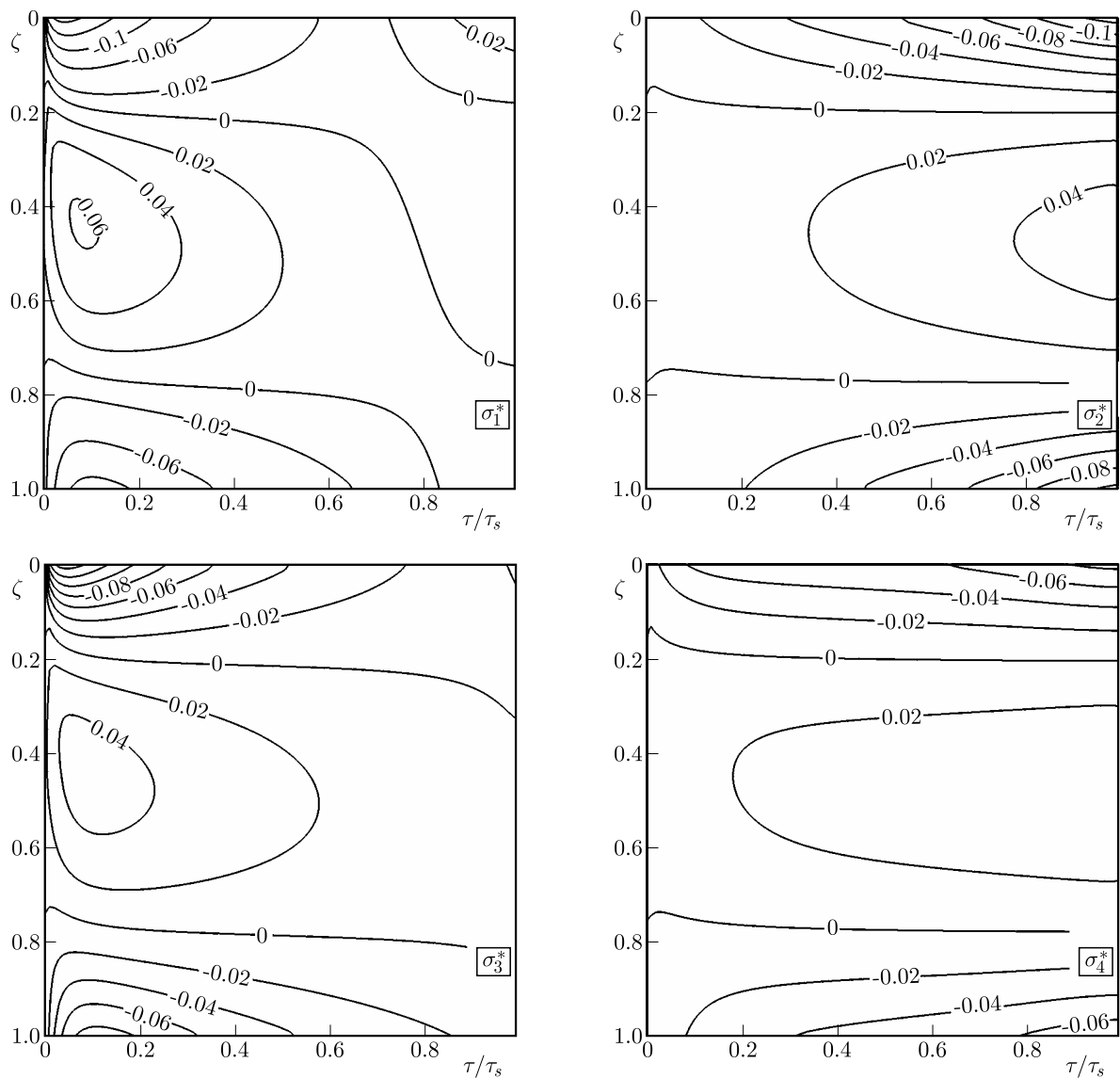


Fig. 2. Isolines of the dimensionless normal transverse stresses σ_i^* , $i = 1, 2, 3, 4$

of braking the compressive stresses appear, then change their sign with approaching to the stop moment. Between these zones of tensile stresses, there is a region of compressive stresses, which rapidly increase at the initial stage of braking, achieving their maximum values after

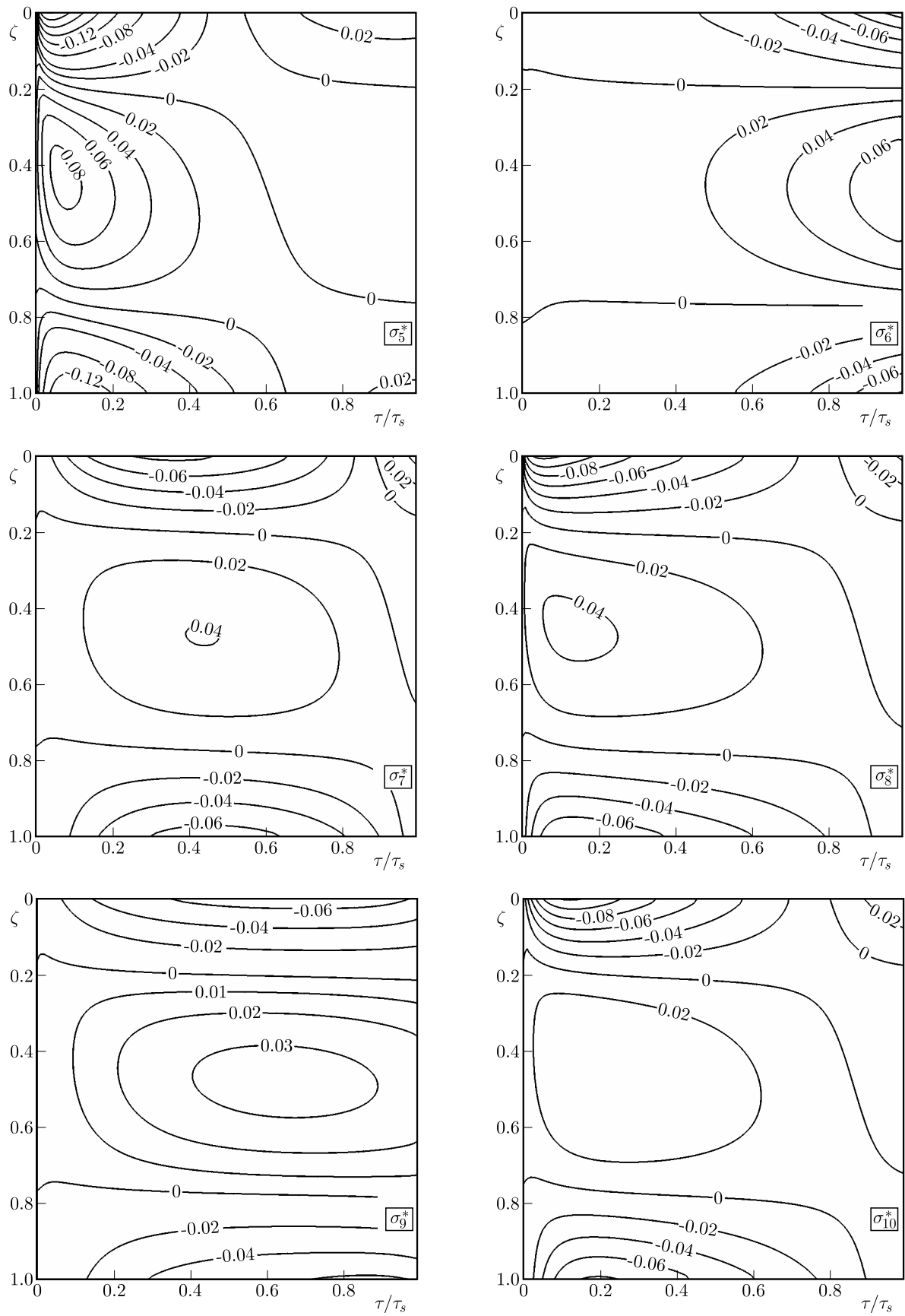


Fig. 3. Isolines of the dimensionless normal transverse stresses σ_i^* , $i = 5, 6, 7, 8, 9, 10$

a relatively short time. Subsequently, these stresses decrease with time, disappearing near the moment of standstill. Values and evolutions of the stresses in the all above-mentioned regions are interdependent. The higher values of tensile stresses on the surface occurs, the higher values of the compressive stresses are achieved. The time of occurrence of the maximum tensile stresses inside the friction element is almost equal to the time of appearance of the greatest values of compressive stresses on its heated surface.

Stresses isolines $\sigma_i^*(\zeta, \tau)$, $i = 2, 4, 6, 9$, from the second group, reflect a monotonical increase of the corresponding temperatures $T_i^*(\zeta, \tau)$ during braking with set distance from the heated surface ζ (Yevtushenko *et al.*, 2017a). In contrast to the first group, in the considered regions of the greatest concentration of compressive stresses, adjacent to the upper and lower edge of the friction element, the maxima are located closer to the end of the braking process, and the maximum absolute values on the friction surface $\zeta = 0$ are achieved at the stop moment $\tau = \tau_s$. In this second group, between the lines of zero stresses, which remain during the whole braking process at depths $\zeta \approx 0.2$ and $\zeta \approx 0.75$, also the region of tensile stresses occurs. These stresses monotonically increase with time, reaching the maximum value at the stop moment.

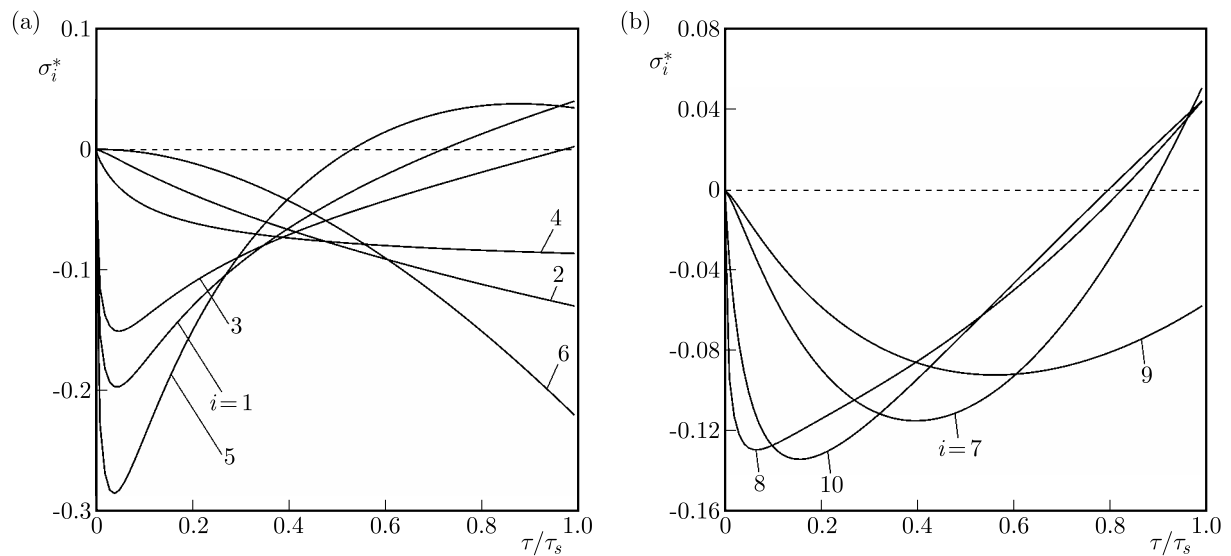


Fig. 4. Evolutions of the dimensionless normal transverse stresses σ_i^* on the surface of friction $\zeta = 0$: (a) $i = 1, 2, \dots, 6$; (b) $i = 7, 8, 9, 10$

Changes of the dimensionless thermal stresses $\sigma_i^*(0, \tau)$, $i = 1, 2, \dots, 10$ with time on the friction surface of the element are presented in Fig. 4. As shown in the article by Yevtushenko *et al.* (2017a), temporal profiles of the specific friction power $q_i^*(\tau)$, $i = 1, 2, \dots, 10$ (2.1)-(2.3) can be classified into one of three specific groups. The first group includes functions $q_i^*(t)$, $i = 1, 3, 5$, which reach the maximum value at the initial moment of braking, and then monotonically decrease to zero at the standstill moment. The corresponding stresses on the heated surface, after start of the process are compressive, and their absolute values rapidly increase, reaching the maximum values 0.2, 0.15 and 0.29 at moments $0.04\tau_s$, $0.05\tau_s$ and $0.04\tau_s$ for $i = 1, 3, 5$, accordingly (Fig. 4a). Then, the compressive stresses on the heated surface disappear with time, and at the moments $0.72\tau_s$ ($i = 1$), $0.97\tau_s$ ($i = 3$) and $0.53\tau_s$ ($i = 5$) change the sign of stresses, and the tensile stresses appear.

The second group contains the functions $q_i^*(t)$, $i = 2, 4, 6$ (2.1) and (2.2), which monotonically increase from zero at the initial moment of the braking process to the maximum value at the stop moment. In a similar way, the evolutions of the corresponding dimensionless temperatures T_i^* , $i = 2, 4, 6$ are calculated on the friction surface $\zeta = 0$ from equations (2.4)₂, (2.4)₄ and (2.4)₆,

respectively. Dimensionless thermal stresses σ_i^* , $i = 2, 4, 6$ on the heated surface are compressed during the whole braking, and their absolute values monotonically increase with time from zero at the start moment to the maximum values 0.13 ($i = 2$), 0.09 ($i = 4$), 0.22 ($i = 6$), at the standstill (Fig. 4a).

The last one of the three highlighted groups consists of four time profiles of the specific friction power $q_i^*(t)$, $i = 7, 8, 9, 10$, which have a local maximum within the time braking interval. Profiles of these functions affect the evolution of the corresponding stresses. At the initial stage of braking, the absolute values of compressive stresses decrease, reaching a local minimum -0.16 at $\tau = 0.4\tau_s$ ($i = 7$), -0.13 at $\tau = 0.07\tau_s$ ($i = 8$), -0.09 at $\tau = 0.56\tau_s$ ($i = 9$) and -0.13 at $\tau = 0.16\tau_s$ ($i = 10$) (Fig. 4b). Stresses σ_i^* , $i = 7, 8, 10$ at the moments $\tau = 0.88$, $\tau = 0.82$ and $\tau = 0.8$, accordingly, change the sign, and their highest values 0.05, 0.044 and 0.044 are achieved at the stop moment. In the case $i = 9$, stresses on the friction surface of the element compress the material during the whole braking process.

5. Conclusions

It is known that the sum of the intensities of heat fluxes generated due to friction on the contact surface of the friction pair (which are directed along the normal to the inside of the friction elements) are equal to the specific friction power (Ling, 1973). Changes of friction power with time can be different, and their typical cases were classified in the monograph by Chichinadze *et al.* (1967). Using this classification, in the articles by Topczewska (2017a) and Yevtushenko *et al.* (2017a) it has been established that the temporal profile of the specific friction power has crucial influence on the distribution of temperature in the pad and the brake disk, and the maximum value of temperature on the contact surface of these elements. In this paper, based on exact analytical solutions to the boundary-value problem of heat conduction for a semi-space heated on its surface by the heat flux with intensity equal to the specific power of friction, the exact solution of the boundary quasi-static problems of thermoelasticity has been received. This allows one to conduct numerical analysis and to investigate the influence of the time profile of friction power on the state of thermal stresses in a selected element of the friction pair. As a result, it has been established that the values and distribution of the thermal stresses initiated by frictional heating depends mainly on the temporal profile of a specific friction power. If the friction power monotonically increases during braking ($i = 2, 4, 6$) or its maximum value is reached near the moment of standstill ($i = 9$), on the friction surface of the element there occur merely compressive normal stresses. However, when the maximum values of the friction power and also temperature are achieved earlier during the braking process ($i = 1, 3, 5, 7, 8, 10$), then due to relative cooling of the surface, before the standstill moment, the stresses change the sign and tensile stresses appear. In the case of exceeding the ultimate strength of the friction material by the value of this stress, initiation of the superficial thermal cracks may appear (Evtushenko and Kutsei, 2006; Yevtushenko *et al.*, 2011).

It has been established that the relationship between the maximum values of specific friction power and the normal transverse stresses is directly proportional. However, the moment of thermal stresses change of sign on the friction surface (transition from compressive to tensile stresses) mainly depend on the time of achieving the maximum temperature. The most rational modes of frictional heating from the “stresses” point of view corresponds the following temporal profiles $q_i^*(t)$, $i = 2, 4$ and 9. For the same brake work, evolutions of the stresses corresponding to these time profiles are the most uniform and the change of their sign does not occur. Their extreme values are the lowest in comparison with other cases.

References

1. BALAKIN V. A., SERGIENKO V. P., 1999, *Heat Calculations of Brakes and Friction Units* (in Russian), MPRI of NASB, Gomel,
2. BLOK H., 1955, The dissipation of friction heat, *Applied Scientific Research*, **A 2-3**, 151-181
3. CARSLAW H.S., JAEGER J.C., 1959, *Conduction of Heat in Solids*, 2nd ed., Clarendon Press, Oxford
4. CHICHINADZE A.V., 1967, *Calculation and Study of External Friction During Braking* (in Russian), Nauka, Moscow
5. CHICHINADZE A.V., BRAUN E.D., GINSBURG A.G., IGNAT'eva Z.V., 1979, *Calculation, Test and Selection of Frictional Couples* (in Russian), Nauka, Moscow
6. EVTUSHENKO A., KUTSEI M., 2006, Initiating of thermal cracking of materials by frictional heating, *Journal of Friction and Wear*, **27**, 2, 9-16
7. FAZEKAS G.A.G., 1953, Temperature gradients and heat stresses in brake drums, *SAE Transactions*, **61**, 279-284
8. JEWTUSZENKO O., KUCIEJ M., TOLSTOJ-SIENKIEWICZ J., 2015, *Transients and Quasi-Stationary Friction Temperature Fields* (in Polish), Publ. Office of Bialystok Technical University, Bialystok
9. KUCIEJ M., 2012, *Analytical Models of Transient Frictional Heating* (in Polish), Publ. Office of Bialystok Technical University, Bialystok
10. LING F.F., 1973, *Surface Mechanics*, New York, John Wiley
11. NEWCOMB T.P., SPURR R.T., 1967, *Braking of Road Vehicles*, Chapman and Hall, London
12. NODA N., HETNARSKI R.B., TANIGAWA Y., 2000, *Thermal Stresses*, Lastran Corp., Rochester, NY, USA
13. PRUDNIKOV A.P., BRYCHKOV YU.A., MARICHEV O.I., 1986, *Integrals and Series, Vol. 1. Elementary Functions*, Gordon and Breach, New York
14. PRUDNIKOV A.P., BRYCHKOV YU.A., MARICHEV O.I., 1998, *Integrals and Series, Vol. 2. Special Functions*, Taylor and Francis, New York
15. TOPCZEWSKA K., 2017a, Frictional heating with time dependent specific power of friction, *Acta Mechanica et Automatica*, **11**, N2, 111-115
16. TOPCZEWSKA K., 2017b, Thermal stresses due to frictional heating with time-dependent specific power of friction, *Acta Mechanica et Automatica*, **11**, 4, 280-284
17. YEVTUSHENKO A., KUCIEJ M., 2010, Two calculation schemes for determination of the thermal stresses due to frictional heating during braking, *Journal of Theoretical and Applied Mechanics*, **48**, 3, 605-621
18. YEVTUSHENKO A., KUCIEJ M., 2012, One-dimensional thermal problem of friction during braking: The history of development and actual state, *International Journal of Heat and Mass Transfer*, **55**, 4118-4153
19. YEVTUSHENKO A.A., KUCIEJ M., TOPCZEWSKA K., 2017a, Analytical model for investigation of the effect of friction power on temperature in the disk brake, *Advances in Mechanical Engineering*, **9**, 1-12
20. YEVTUSHENKO A.A., KUCIEJ M., TOPCZEWSKA K., 2017b, Effect of the temporal profile of the friction power on thermal stresses during braking, *Proceedings of the 9th International Scientific Conference "BALTTTRIB 2017"*, Kaunas, Lithuania 123-128, <https://doi.org/10.15544/balttrib.2017.23>
21. YEVTUSHENKO A.A., KUCIEJ M., YEVTUSHENKO O.O., 2011, Temperature and thermal stresses in material of a pad during braking, *Archive of Applied Mechanics*, **81**, 6, 715-726

THERMOELASTIC STRESSES IN FUNCTIONALLY GRADED ROTATING ANNULAR DISKS WITH VARIABLE THICKNESS

MOHAMMED N.M. ALLAM

Mansoura University, Faculty of Science, Department of Mathematics, Mansoura

RANIA TANTAWY

Damietta University, Faculty of Science, Department of Mathematics, Damietta, Egypt

ASHRAF M. ZENKOUR

King Abdulaziz University, Faculty of Science, Department of Mathematics, Jeddah, Saudi Arabia, and

Kafrelsheikh University, Faculty of Science, Department of Mathematics, Kafrelsheikh, Egypt

e-mail: zenkour@kau.edu.sa; zenkour@kaf-sci.edu.eg

This article presents semi-analytical solutions for stress distributions in exponentially and functionally graded rotating annular disks with arbitrary thickness variations. The disk is under pressure on its boundary surfaces and exposed to temperature distribution varying linearly across thickness. Material properties are supposed to be graded in the radial direction of the disk and obeying to two different forms of distribution of volume fraction of constituents. Different conditions at boundaries for stresses and displacement are discussed. Accurate and efficient solutions for displacement and stresses in rotating annular disks are determined using infinitesimal theory. Numerical results are carried out and discussed for different cases. It can be deduced that the gradient of material properties and thickness variation as well as the change of temperature sources have a specific effect in modern applications.

Keywords: functionally graded, variable thickness, semi-analytical approach, rotating, thermal effect

1. Introduction

Stress analyses of rotating circular disks have long been an important topic in engineering applications. Disks made of homogeneous materials have been discussed extensively with constant and thickness variation (Hartog, 1952). Cavallaro (1965) presented variable-thickness disks, symmetrical with respect to both their axes and their mid-planes, under the effect of centrifugal and thermal loadings. Wu and Ramsey (1966) presented solutions for stresses in rotating, symmetrical, three-layer circular disks. Murthy and Sherbourne (1970) presented rotating anisotropic variable-thickness disks under centrifugal loading. Yella Reddy and Srinath (1974) derived closed-form solutions for the bending response of rotating variable-thickness and variable-density disks. Sherbourne and Murthy (1974) presented a dynamic relaxation technique to study stresses and displacements of rotating variable-thickness disks with different boundary conditions.

An extension to rotating solid and annular disks with variable profiles made of viscoelastic materials has been investigated. Feng (1985) presented governing equations of rotating disks subjected to large elastic and viscoelastic deformations. Allam *et al.* (2008) presented a circular variable-thickness elastic disk under the effect of steady coaxial current and bearing coaxial viscoelastic coating. Zenkour and Allam (2006) presented an analytical solution for displacement and stresses in rotating fiber-reinforced viscoelastic variable-thickness disks. Allam *et al.* (2007) presented analytical solutions for inhomogeneous rotating variable-thickness viscoelastic disks.

Recently, the research on rotating circular disks has become more and more active after changing the material model, especially in the case of functionally graded materials (FGMs) (Argeso, 2012; Das *et al.*, 2012; Hassani *et al.*, 2012; Peng and Li, 2012a,b; Golmakani, 2013; Kadhodayan and Golmakani, 2014; Zenkour, 2014; Dai and Dai, 2015; Leu and Chien, 2015; Sahni and Sahni, 2015; Hosseini *et al.*, 2016; Zhenga *et al.*, 2016; Entezari *et al.*, 2017; Essa and Argeso, 2017; Tutuncu and Temel, 2013). Allam and Zenkour (2005) presented viscoelastic rotating disks of made of an exponentially graded (EG) varying thickness and fiber-reinforced viscoelastic material. Zenkour (2005) obtained accurate elastic solutions for EG rotating annular disks with different conditions. You *et al.* (2007) obtained closed-form solutions of FG rotating circular disks under uniform angular velocity and uniform temperature change taking into consideration that material properties were functions of the radial coordinate. Bayat *et al.* (2008), Asghari and Ghafoori (2010) and Ghorbanpour Arani *et al.* (2010) used a semi-analytical method to present elastic and magneto-thermo-elastic solutions for FG rotating disks with a variable profile. Vullo and Vivio (2008) obtained elastic stresses and strains in rotating variable-thickness solid and annular disks under thermal load with density variation along the radial coordinate. Bayat *et al.* (2009a,b) used the first-order shear deformation theory to discuss elastic and thermoelastic bending responses of rotating disks with graded material properties. Bayat *et al.* (2009c) derived thermoelastic responses for axisymmetric FG rotating variable-thickness disks with temperature-dependent material properties. Zenkour (2009) presented two models of sandwich rotating solid disks with the EG core with free or clamped-edge conditions. The finite difference, finite element and semi-exact elastic solutions of thermoelastic analysis of FG rotating disks were presented by Afsar and Go (2010), Hassani *et al.* (2011), Sharma (2013), Zafarmand and Hassani (2014), Arnab *et al.* (2014), and Entezari *et al.* (2017).

An additional extension to thermo-piezo-magneto-mechanical stresses analyses of FG rotating disks was presented by Ghorbanpour Arani (2010a, b). Dai *et al.* (2017) presented temperature, moisture, displacement and stress distributions of an exponentially graded piezoelectric (EGP) rotating disk. Dai and Dai (2017) presented a rotating disk with variable thickness in thermal environment made of an FG magneto-electro-elastic material (MEEM). In this article, the problem of stresses and deformation of a rotating variable-thickness inhomogeneous and FG annular disk is presented. Numerical results are investigated according to different profiles of the annular disk. Two specific thickness variations namely power and exponential laws for thickness variation are considered. A comparison between different cases is made and some conclusions are presented.

2. Formulation of the problem

Here, the basic equations of elasticity are used (Mashat and Zenkour, 2014). The constitutive equations are represented as

$$\begin{aligned}\sigma_r &= \frac{E}{1-\nu^2} \left(\nu \frac{u}{r} + \frac{du}{dr} \right) - \frac{E}{1-\nu} \alpha T \\ \sigma_\theta &= \frac{E}{1-\nu^2} \left(\frac{u}{r} + \nu \frac{du}{dr} \right) - \frac{E}{1-\nu} \alpha T\end{aligned}\tag{2.1}$$

where u represents the radial displacement, σ_r and σ_θ denote radial and hoop stresses, T is temperature distribution, E denotes Young's modulus, ν denotes Poisson's ratio and α represents the thermal expansion coefficient. It is considered that thickness is a function of the radial coordinate, that is $h(r)$ represents variable-thickness of the rotating disk. So, the dynamic equation of a rotating variable-thickness disk may be represented by

$$\frac{d}{dr}(hr\sigma_r) - h\sigma_\theta + h\rho\omega^2 r^2 = 0\tag{2.2}$$

where ω represents angular velocity and ρ denotes material density. Assume that the material of the rotating disk is isotropic with uniform Poisson's ratio while the elastic modulus, density, and thermal coefficient are all radially varying. Equation (2.2) with the help of Eq. (2.1) yields

$$\begin{aligned} \frac{d^2u}{dr^2} + \left(\frac{1}{r} + \frac{1}{E} \frac{dE}{dr} + \frac{1}{h} \frac{dh}{dr} \right) \frac{du}{dr} + \left[\frac{\nu}{r} \left(\frac{1}{E} \frac{dE}{dr} + \frac{1}{h} \frac{dh}{dr} \right) - \frac{1}{r^2} \right] u \\ + (\nu + 1) \left[\frac{\omega^2 \rho r}{E} (1 - \nu) - \alpha \frac{dT}{dr} + \left(\frac{d\alpha}{dr} + \alpha \frac{1}{E} \frac{dE}{dr} + \alpha \frac{1}{h} \frac{dh}{dr} \right) T \right] = 0 \end{aligned} \quad (2.3)$$

3. Various disk profiles

3.1. Thickness profiles

The present rotating disk is annular and made of a variable-thickness, single-layer of functionally or exponentially graded material with the inner radius a and the outer one b . Two thickness disk profiles are supposed here. In the first one, the thickness is varied with radius of the disk according to the following power-law form

$$h(r) = h_0 \left[1 - n \left(\frac{r}{b} \right) \right]^k \quad (3.1)$$

where h_0 denotes the thickness at the axis of the disk and n and k are dimensionless parameters. The parameter n defines thickness at edge of the disk relative to h_0 while the parameter k defines the shape of the disk profile. The uniform-thickness disk is deduced when either $n = 0$ or $k = 0$ while linearly-decreasing thickness is deduced if $k = 1$. In addition, if $k < 1$ the disk profile is convex while if $k > 1$ it is concave. Figure 1 illustrates the case of a convex disk with $n = 0.415196$ and $k = 3$. The dimensionless thickness $\bar{h} = h(r)/h_0$ is displayed in terms of dimensionless radius $\bar{r} = r/b$ for $a = 0.2$ m.

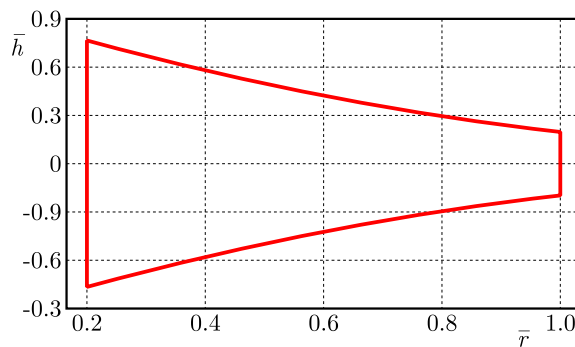


Fig. 1. Power disk profiles, $n = 0.415196$ and $k = 3$

The second thickness of the disk profile is considered to vary radially according to this exponential form

$$h(r) = h_0 \exp \left[-n \left(\frac{r}{b} \right)^k \right] \quad (3.2)$$

Also, in this case n defines thickness at edge of the disk and k determines the shape of the disk profile. Figure 2 shows two plots of this disk profile in two cases: (a) $n = 2$ and $k = 0.5$ while (b) $n = 0.415196$ and $k = 3$ for the same inner radius a .

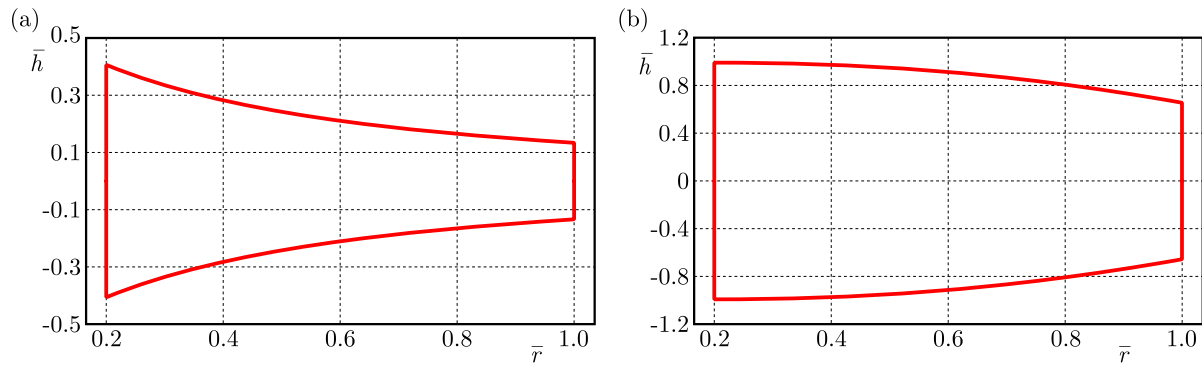


Fig. 2. Exponential disk profiles: (a) $n = 2$, $k = 0.5$, (b) $n = 0.415196$, $k = 3$

3.2. Material properties profiles

The material properties of the annular disk are considered to vary across the radial direction. Young's modulus E , thermal expansion coefficient α , and material density ρ are assumed to vary according to the following simple power law

$$P(r) = P_0 \left(\frac{r}{b} \right)^\beta \quad (3.3)$$

where P_0 is the material property (E_0 , α_0 and ρ_0) at the outer surface of the disk and β denotes the inhomogeneity parameter. The above formula means that the annular disk is inhomogeneous with respect to its coefficients ρ , α , and E .

For the functionally graded (FG) annular disk, the property variation $P(r)$ of the thermal coefficient, density and modulus of elasticity across the radial direction is considered as (Ruhi *et al.*, 2005)

$$P(r) = P_a + (P_b - P_a) \left(\frac{r - a}{b - a} \right)^\beta \quad (3.4)$$

where P_a and P_b denote the corresponding properties of the inner and outer surfaces of the rotating disk. The grading index parameter $\beta \geq 0$ represents the volume fraction exponent. The above power law reflects a simple rule of mixture in terms of volume fraction of constituents, and it is widely admitted form of property variation.

3.3. Temperature profiles

The temperature distribution across the radial direction is derived from heat conduction equation

$$\kappa \nabla^2 T(r) + q(r) = 0 \quad (3.5)$$

where $\nabla^2 = (d^2/dr^2) + (1/r)(d/dr)$, κ denotes thermal conductivity, and q represents the heat generation function. The temperature satisfies the following boundary conditions

$$T(r)|_{r=a} = T_0 \quad \frac{dT(r)}{dr} \Big|_{r=b} = 0 \quad (3.6)$$

in which T_0 denotes the reference temperature. The internal energy generation within both surfaces is given by the heat generating function

$$q(r) = -Q \left(\frac{r - a}{a} \right) \left(\frac{r - b}{b} \right) \quad a \leq r \leq b \quad (3.7)$$

where Q represents a uniform rate of internal energy generation. So, Eq. (3.5) gets the solution

$$T(r) = \frac{Qr^2}{144\kappa ab}[9(r^2 + 4ab) - 16r(a + b)] + c_1 \ln(r) + c_2 \quad (3.8)$$

in which c_1 and c_2 represent arbitrary integration constants obtained from conditions appeared in Eq. (3.6) as

$$\begin{aligned} c_1 &= \frac{Qb^2}{12\kappa a}(b - 2a) \\ c_2 &= \frac{Q}{144\kappa ab}[a^3(7a - 20b) - 12b^3 \ln(a)(b - 2a)] + T_0 \end{aligned} \quad (3.9)$$

In addition to Eq. (3.8), one can use another simple and efficient form of temperature. That is

$$T(r) = T_a + \frac{T_b - T_a}{\ln \frac{b}{a}}(\ln r - \ln a) \quad (3.10)$$

4. Solution of the problem

It is known that it is difficult to get a general solution of the second-order differential equation with variable coefficients as Eq. (2.3). A semi-analytical approach is presented here for this purpose. The radial domain will be divided into some virtual sub-domains with thickness $s^{(m)}$ as illustrated in Fig. 3. Evaluating the coefficients of Eq. (2.3) at $r = r^{(m)}$, which is said to be

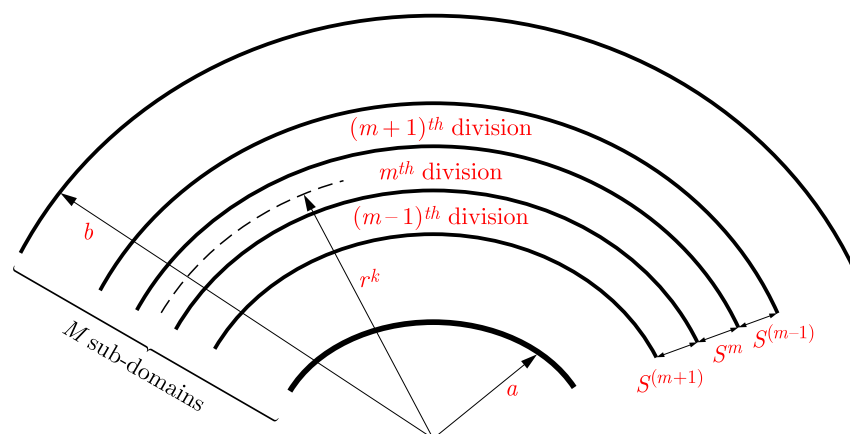


Fig. 3. Dividing radial domain into some finite sub-domains

the mean radius of m -th division, and using them instead of variable coefficients one obtains

$$\frac{d^2 u^{(m)}}{dr^2} + N_1^{(m)} \frac{du^{(m)}}{dr} + N_2^{(m)} u^{(m)} - N_3^{(m)} = 0 \quad (4.1)$$

where

$$\begin{aligned}
 N_1^{(m)} &= \frac{1}{r^{(m)}} + \frac{1}{E(r^{(m)})} \frac{dE}{dr} \bigg|_{r=r^{(m)}} + \frac{1}{h(r^{(m)})} \frac{dh}{dr} \bigg|_{r=r^{(m)}} \\
 N_2^{(m)} &= \frac{\nu}{r^{(m)}} \left(\frac{1}{E(r^{(m)})} \frac{dE}{dr} \bigg|_{r=r^{(m)}} + \frac{1}{h(r^{(m)})} \frac{dh}{dr} \bigg|_{r=r^{(m)}} \right) - \frac{1}{(r^{(m)})^2} \\
 N_3^{(m)} &= (\nu + 1) \left[\frac{\omega^2 \rho(r^{(m)}) r^{(m)}}{E(r^{(m)})} (\nu - 1) + \alpha(r^{(m)}) \frac{dT}{dr} \bigg|_{r=r^{(m)}} \right. \\
 &\quad \left. + \left(\frac{d\alpha}{dr} \bigg|_{r=r^{(m)}} + \frac{\alpha(r^{(m)})}{E(r^{(m)})} \frac{dE}{dr} \bigg|_{r=r^{(m)}} + \frac{\alpha(r^{(m)})}{h(r^{(m)})} \frac{dh}{dr} \bigg|_{r=r^{(m)}} \right) T(r^{(m)}) \right]
 \end{aligned} \tag{4.2}$$

Now, Eq. (4.1) becomes a system of M -equations. So, it is easy to obtain the solution of Eq. (4.1) as

$$u^{(m)} = B_1^{(m)} e^{\beta_1 r} + B_2^{(m)} e^{\beta_2 r} + \frac{N_3^{(m)}}{N_2^{(m)}} \tag{4.3}$$

where m represents the number of virtual sub-domains, and β_1 and β_2 denote roots of $\beta^2 + N_1^{(m)}\beta + N_2^{(m)} = 0$, and $B_1^{(m)}$ and $B_2^{(m)}$ denote uncharted constants for the m -th sub-domain. Indeed, the above solution is valid for

$$r^{(m)} - \frac{s^{(m)}}{2} \leq r \leq r^{(m)} + \frac{s^{(m)}}{2} \tag{4.4}$$

where $r^{(m)}$ and $s^{(m)}$ represent the mean radius and radial width of m -th sub-domain, respectively. The uncharted $B_1^{(m)}$ and $B_2^{(m)}$ can be derived by applying necessary conditions between each two adjacent sub-domains. The continuity conditions at the interfaces may be expressed as

$$\begin{aligned}
 u^{(m)} \big|_{r=r^{(m)} + \frac{s^{(m)}}{2}} &= u^{(m+1)} \big|_{r=r^{(m+1)} - \frac{s^{(m+1)}}{2}} \\
 \sigma_r^{(m)} \big|_{r=r^{(m)} + \frac{s^{(m)}}{2}} &= \sigma_r^{(m+1)} \big|_{r=r^{(m+1)} - \frac{s^{(m+1)}}{2}}
 \end{aligned} \tag{4.5}$$

The continuity and boundary conditions yield a set of linear algebraic equations in $B_1^{(m)}$ and $B_2^{(m)}$ ($m = 1, 2, \dots, M$). After getting $B_1^{(m)}$ and $B_2^{(m)}$ and using them in Eqs. (4.3), $u^{(m)}$ are completely determined. The accuracy of the results improves if the number of divisions is increasing.

5. Numerical results and discussion

Many examples for the analysis of inhomogeneous or FG rotating annular disks are illustrated to discuss radial and hoop stresses, temperature and radial displacement. The following non-dimensional variables are fixed through numerical examples

$$\{\bar{r}, \bar{u}\} = \frac{1}{b} \{r, u\} \quad \bar{T} = \frac{T}{T_0} \tag{5.1}$$

while other non-dimensional forms of stresses will be given according to the case studied. Now, we will discuss four examples to cover all the presented cases. In all cases studied, one can use some values for the parameters as $a = 0.2$ m, $b = 1$ m, and $\omega = 100 \text{ s}^{-1}$.

5.1. Example 1

In this case, thickness, material properties, and temperature profiles are given according to Eqs. (3.1), (3.3) and (3.10), respectively. For the thickness profile, the geometric parameters are given by $n = 0.415196$ and $k = 3$. The mechanical boundary conditions are represented as

$$u|_{r=a} = 0 \quad \sigma_r|_{r=b} = -p \quad (5.2)$$

where p is the outer pressure. In this case, the dimensionless stresses are given by

$$\bar{\sigma}_i = \frac{\sigma_i}{p} \quad i = r, \theta \quad (5.3)$$

The elastic and thermal constants are assumed as: $E_0 = 390 \text{ GNm}^{-2}$, $\rho_0 = 3.9 \text{ Mgm}^{-3}$, $\nu = 0.25$, $\alpha_0 = 7 \cdot 10^{-6} \text{ K}^{-1}$, $T_a = 373 \text{ K}$, $T_b = 273 \text{ K}$.

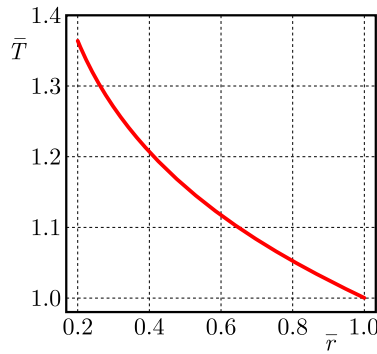


Fig. 4. Temperature distribution in an inhomogeneous rotating annular disk

The distribution of temperature is given in Fig. 4. The temperature, as expected, decreases as the radial direction increases. The radial stress $\bar{\sigma}_r$, hoop stress $\bar{\sigma}_\theta$ and radial displacement \bar{u} are plotted in Figs. 5a,b,c. Different values of the inhomogeneity parameter β are considered. Figure 5a shows that $\bar{\sigma}_r$ for different values of β at $\bar{r} = 1$ is equal to -1 , which satisfies the second part of conditions appeared in Eq. (5.2). The radial stress $\bar{\sigma}_r$ increases as β decreases while it is decreasing along the radial direction. Figure 5b plots the hoop stress $\bar{\sigma}_\theta$ across the radial direction

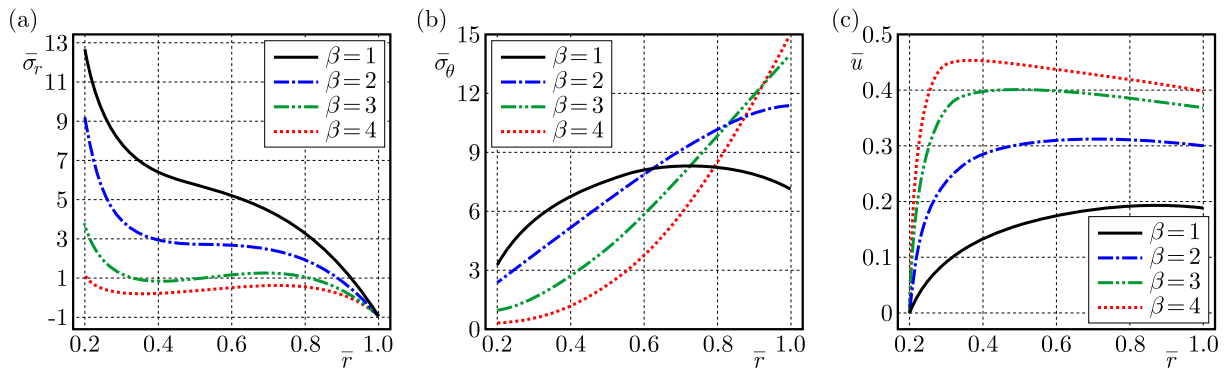


Fig. 5. (a) Radial stress, (b) hoop stress and (c) radial displacement distribution of the inhomogeneous rotating annular disk for different values of β

of the inhomogeneous annular disk. It is directly increasing to obtain its absolute maximum at the outer edge of the disk except for $\beta = 1$. The value of $\beta = 4$ yields the smallest hoop stress at the inner edge and greatest one at the outer edge. However, the value of $\beta = 1$ yields the greatest hoop stress at the inner surface and the smallest one at the outer surface. Figure 5c plots the

radial displacement distribution along the radial direction of the inhomogeneous annular disk. The radial displacement \bar{u} for different values of β at $\bar{r} = 0.2$ is equal to zero, which satisfies the first part of the boundary conditions given in Eq. (5.2). The radial displacement \bar{u} increases along the radial direction. Its maximum occurs at the outer edge for $\beta = 1$ only. However, this position of its maximum may be moved to be nearer to the inner surface as β increases.

5.2. Example 2

Here, thickness, material properties, and temperature profiles are given according to Eqs. (3.2), (3.3) and (3.10), respectively. The geometric parameters are taken as $n = 0.415196$ and $k = 3$. However, the mechanical conditions at boundaries are represented as

$$\sigma_r|_{r=a} = -p \quad \sigma_r|_{r=b} = 0 \quad (5.4)$$

The results for such an inhomogeneous disk are illustrated in Figs. 6a,b,c. The non-dimensional forms for radial and hoop stresses appeared in Eq. (5.3) are repeated here. Figure 6a shows that $\bar{\sigma}_r$ for different values of β at $\bar{r} = 0.2$ is equal to -1 and at $\bar{r} = 1$ is equal to 0 according to conditions in Eq. (5.4). The differences between radial stresses $\bar{\sigma}_r$ increase at $r/b = 0.5$ with the occurrence of the absolute maximum value of $\bar{\sigma}_r$. Figure 6b shows that $\bar{\sigma}_\theta$ is directly increasing to get its absolute maximum at the outer surface of the inhomogeneous disk, except for $\beta = 1$. The value of $\beta = 4$ yields the smallest hoop stress at the inner edge and the greatest hoop stress at the outer edge. However, $\beta = 1$ yields the greatest hoop stress at the outer edge and the smallest hoop stress at the outer surface of disk. Figure 6c shows that \bar{u} is decreasing to assume its absolute minimum at the outer edge for $\beta > 1$. However, it increases to get its absolute maximum at outer edge of the inhomogeneous disk.

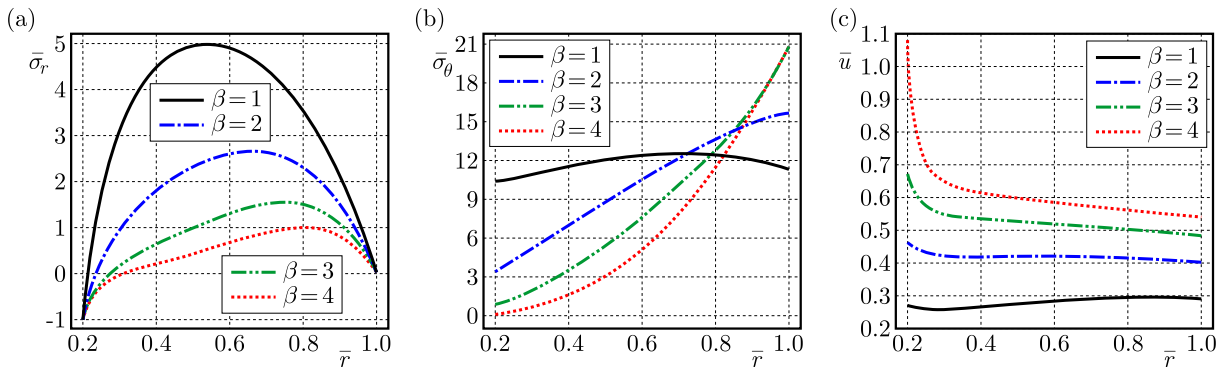


Fig. 6. (a) Radial stress, (b) hoop stress and (c) radial displacement distribution in the inhomogeneous rotating annular disk for different values of β

5.3. Example 3

The inner surface of the FG rotating annular disk is traction free while the outer one is under constant pressure. The mechanical boundary conditions are given in the form

$$\sigma_r|_{r=a} = 0 \quad \sigma_r|_{r=b} = -p \quad (5.5)$$

where p is the outer pressure. The dimensionless stresses are also given as in Eq. (5.3). The thickness profile is given according to Eq. (3.2) with geometric parameters $n = 2$ and $k = 0.5$. The material properties profile is given according to Eq. (3.4) with $\nu = 0.3$ and $E_a = 390 \text{ GNm}^{-2}$, $E_b = 200 \text{ GNm}^{-2}$, $\rho_a = 3.9 \text{ Mgm}^{-3}$, $\rho_b = 7.7 \text{ Mgm}^{-3}$, $\alpha_a = 7 \cdot 10^{-6} \text{ K}^{-1}$, $\alpha_b = 11 \cdot 10^{-6} \text{ K}^{-1}$.

The temperature profile is also given according to Eq. (3.10) with $T_a = 373 \text{ K}$ and $T_b = 273 \text{ K}$. The stresses and radial displacement are illustrated in Figs. 7a,b,c. From these figures, all stresses

and displacement increase with the decrease of the gradient parameter β . Figure 7a plots the radial stress distribution along the radial direction of the FG rotating disk. It is shown that $\bar{\sigma}_r$ for various values of β at $\bar{r} = 0.2$ is equal to 0 and at $\bar{r} = 1$ is equal to -1 according to conditions presented in Eq. (5.5). The differences between radial stresses $\bar{\sigma}_r$ increase near to the middle plane (far from internal and external boundaries). Figure 7b plots hoop stress $\bar{\sigma}_\theta$ along the radial direction. It is directly decreasing from its absolute maximum at the inner edge to get its absolute minimum at outer edge of the disk. Figure 7c shows that \bar{u} is no longer decreasing and has its absolute minimum near the inner surface of the disk. Then, the radial displacement \bar{u} is directly increasing to get its absolute maximum near the outer edge of the FG rotating annular disk.

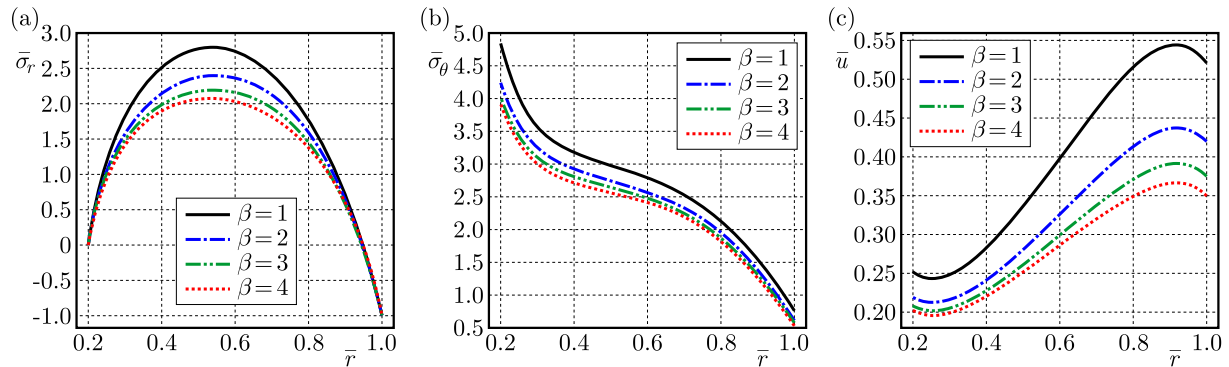


Fig. 7. (a) Radial stress, (b) hoop stress and (c) radial displacement distribution in the FG rotating annular disk for different values of β

5.4. Example 4

In this case, we take the same assumption of Example 3 except for temperature. It is given according to Eq. (3.8) with the help of Eq. (3.9). The uniform rate of internal energy generation Q , the thermal conductivity κ and the reference initial temperature T_0 are given, respectively, by $Q = 12 \text{ Wm}^{-3}$, $\kappa = 0.35 \text{ W(Km)}^{-1}$, $T_a = 273 \text{ K}$.

The mechanical boundary conditions are given by

$$\sigma_r|_{r=a} = -p_1 \quad \sigma_r|_{r=b} = -p_2 \quad (5.6)$$

where p_2 and $p_1 = 0.6p_2$ are outer and inner pressures, respectively. The dimensionless stresses are given by

$$\bar{\sigma}_i = \frac{\sigma_i}{p_2} \quad i = r, \theta \quad (5.7)$$

The dimensionless temperature distribution is plotted in Fig. 8. In addition, the radial and hoop stresses and radial displacement are illustrated in Figs. 9a,b,c. Figure 9a shows the radial stress distribution along the radial direction of the FG rotating disk. It is obvious that $\bar{\sigma}_r$ for various values of β at $\bar{r} = 0.2$ is equal to -0.6 and at $\bar{r} = 1$ is equal to -1 , according to the conditions in Eq. (5.6). The radial stress $\bar{\sigma}_r$ has its absolute maximum value near the middle plane (far from internal and external boundaries). Figure 9b plots hoop stress $\bar{\sigma}_\theta$ along the radial direction. It is directly decreasing from its absolute maximum at the inner edge to get its absolute minimum at the outer edge of the disk. Figure 9c shows that \bar{u} is no longer decreasing and has its absolute minimum near the inner edge of the disk. Then, it is directly increasing to get its absolute maximum near the outer surface. It is to be noted that all stresses and displacement increase as the gradient parameter β decreases.

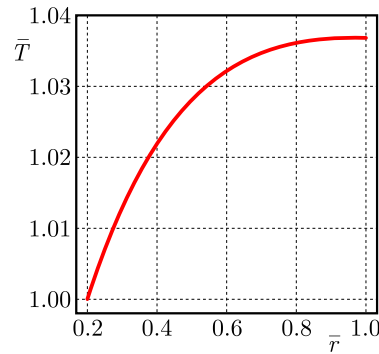


Fig. 8. Temperature distribution in the FG rotating annular disk

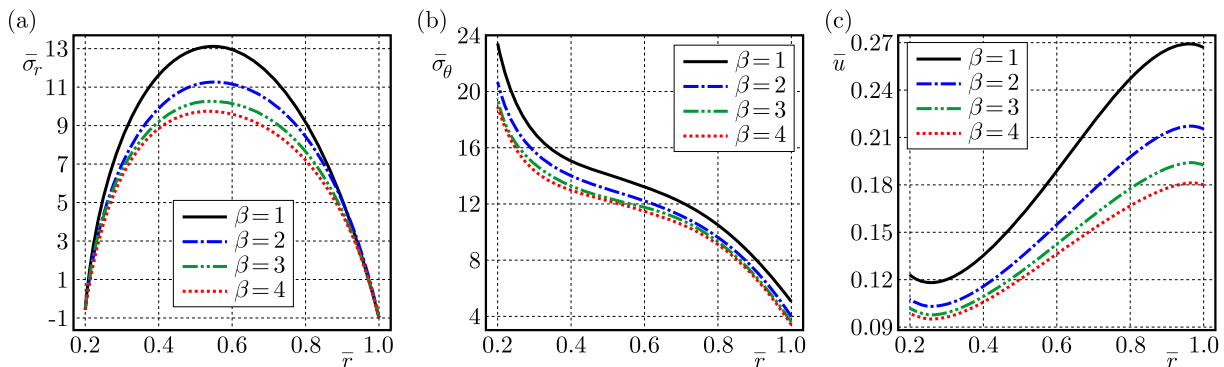


Fig. 9. (a) Radial stress, (b) hoop stress and (c) radial displacement distribution in the FG rotating annular disk for different values of β

6. Concluding remarks

- In this article, semi-analytical solutions for stress distributions in inhomogeneous and FG variable-thickness rotating annular disks are investigated.
- The semi-analytical method is improved for the thermomechanical problem where stresses are produced based on different mechanical loading conditions.
- A selection of proper values of the graded index β and suitable loads helps engineers to design FG rotating disks that can meet some special requirements.
- The main conclusion is that the semi-analytical solution is an accurate and reliable, and the method is simple and effective.

References

1. AFSAR A.M., GO J., 2010, Finite element analysis of thermoelastic field in a rotating FGM circular disk, *Applied Mathematical Modelling*, **34**, 3309-3320
2. ALLAM M.N.M., BADR R.E., TANTAWY R., 2008, Stresses of a rotating circular disk of variable thickness carrying a current and bearing a coaxial viscoelastic coating, *Applied Mathematical Modelling*, **32**, 1643-1656
3. ALLAM M.N.M., ZENKOUR A.M., 2005, On the rotating fiber-reinforced viscoelastic composite solid and annular disks of variable thickness, *International Journal for Computational Methods in Engineering Science and Mechanics*, **7**, 1-11
4. ALLAM M.N.M., ZENKOUR A.M., EL-AZAB T.M.A., 2007, Viscoelastic deformation of the rotating inhomogeneous variable thickness solid and annular disks, *International Journal for Computational Methods in Engineering Science and Mechanics*, **8**, 5, 313-322

5. ARGESO H., 2012, Analytical solutions to variable thickness and variable material property rotating disks for a new three-parameter variation function, *Mechanics Based Design of Structures and Machines*, **40**, 2, 133-152
6. ARNAB B., ISLAM S.M.R., KAHLAK A.A., AFSAR A.M., 2014, Finite difference solution to thermoelastic field in a thin circular FGM disk with a concentric hole, *Procedia Engineering*, **90**, 193-198
7. ASGHARI M., GHAFOORI E., 2010, A three-dimensional elasticity solution for functionally graded rotating disks, *Composite Structures*, **92**, 1092-1099
8. BAYAT M., SAHARI B.B., SALEEM M., ALI A., WONG S.V., 2009a, Bending analysis of a functionally graded rotating disk based on the first order shear deformation theory, *Applied Mathematical Modelling*, **33**, 4215-4230
9. BAYAT M., SAHARI B.B., SALEEM M., ALI A., WONG S.V., 2009b, Thermoelastic solution of a functionally graded variable thickness rotating disk with bending based on the first-order shear deformation theory, *Thin-Walled Structures*, **47**, 568-582
10. BAYAT M., SAHARI B.B., SALEEM M., HAMOUDA A.M.S., REDDY J.N., 2009c, Thermoelastic analysis of functionally graded rotating disks with temperature-dependent material properties: uniform and variable thickness, *International Journal of Mechanics and Material Design*, **5**, 263-279
11. BAYAT M., SALEEM M., SAHARI B.B., HAMOUDA A.M.S., MAHDI E., 2008, Analysis of functionally graded rotating disks with variable thickness, *Mechanics Research Communications*, **35**, 283-309
12. CAVALLARO L., 1965, Stress analysis of rotating disks, *Nuclear Structural Engineering*, **2**, 271-281
13. DAI H.-L., ZHENG, Z.-Q., DAI T., 2017, Investigation on a rotating FGPM circular disk under a coupled hygrothermal field, *Applied Mathematical Modelling*, **46**, 28-47
14. DAI T., DAI H.-L., 2015, Investigation of mechanical behavior for a rotating FGM circular disk with a variable angular speed, *Journal of Mechanical Science and Technology*, **29**, 9, 3779-3787
15. DAI T., DAI H.-L., 2017, Analysis of a rotating FGME circular disk with variable thickness under thermal environment, *Applied Mathematical Modelling*, **45**, 900-924
16. DAS D., SAHOO P., SAHA K., 2012, Dynamic analysis of rotating annular disk of variable thickness under uniform axial pressure, *International Journal for Computational Methods in Engineering Science and Mechanics*, **13**, 1, 37-59
17. ENTEZARI A., FILIPPI M., CARRERA E., 2017, On dynamic analysis of variable thickness disks and complex rotors subjected to thermal and mechanical prestresses, *Journal of Sound and Vibration*, **405**, 68-85
18. ENTEZARI A., KOUCHAKZADEH M.A., CARRERA E., FILIPPI M., 2017, A refined finite element method for stress analysis of rotors and rotating disks with variable thickness, *Acta Mechanica*, **228**, 575-594
19. ESSA S., ARGESO H., 2017, Elastic analysis of variable profile and polar orthotropic FGM rotating disks for a variation function with three parameters, *Acta Mechanica*, **228**, 3877-3899
20. FENG W.W., 1985, On finite deformation of viscoelastic rotating disks, *International Journal of Nonlinear Mechanics*, **20**, 1, 21-26
21. GHORBANPOUR ARANI A., KHODDAMI MARAGHI Z., MOZDIANFARD M.R., SHAJARI A.R., 2010a, Thermo-piezo-magneto-mechanical stresses analysis of FGPM hollow rotating thin disk, *International Journal of Mechanics and Material Design*, **6**, 341-349
22. GHORBANPOUR ARANI A., LOGHMAN A., SHAJARI A.R., AMIR S., 2010b, Semi-analytical solution of magneto-thermo-elastic stresses for functionally graded variable thickness rotating disks, *Journal of Mechanical Science and Technology*, **24**, 10, 2107-2117

23. GOLMAKANI M.E., 2013, Large deflection thermoelastic analysis of shear deformable functionally graded variable thickness rotating disk, *Composites: Part B*, **45**, 1143-1155
24. HARTOG D., 1952, *Advanced Strength of Materials*, New York, McGraw-Hill
25. HASSANI A., HOJJATI M.H., FARRAHI G., ALASHTI R.A., 2011, Semi-exact elastic solutions for thermo-mechanical analysis of functionally graded rotating disks, *Composite Structures*, **93**, 3239-3251
26. HASSANI A., HOJJATI M.H., MAHDAVI E., ALASHTI R.A., FARRAHI G., 2012, Thermo-mechanical analysis of rotating disks with non-uniform thickness and material properties, *International Journal of Pressure Vessels and Piping*, **98**, 95-101
27. HOSSEINI M., SHISHESAZ M., TAHAN K.N., HADI A., 2016, Stress analysis of rotating nano-disks of variable thickness made of functionally graded materials, *International Journal of Engineering Science*, **109**, 29-53
28. KADKHODAYAN M., GOLMAKANI M.E., 2014, Non-linear bending analysis of shear deformable functionally graded rotating disk, *International Journal of Non-Linear Mechanics*, **58**, 41-56
29. LEU S.-Y., CHIEN L.-C., 2015, Thermoelastic analysis of functionally graded rotating disks with variable thickness involving non-uniform heat source, *Journal of Thermal Stresses*, **38**, 415-426
30. MASHAT D.S., ZENKOUR A.M., 2014, Hygrothermal bending analysis of a sector-shaped annular plate with variable radial thickness, *Composite Structures*, **113**, 446-458
31. MURTHY D.N.S., SHERBOURNE A.N., 1970, Elastic stresses in anisotropic disks of variable thickness, *International Journal of Mechanical Sciences*, **12**, 827-840
32. PENG X.-L., LI X.-F., 2012, Elastic analysis of rotating functionally graded polar orthotropic disks, *International Journal of Mechanical Sciences*, **60**, 84-91
33. PENG X.-L., LI X.-F., 2012, Effects of gradient on stress distribution in rotating functionally graded solid disks, *Journal of Mechanical Science and Technology*, **26**, 1483-1492
34. RUHI M., ANGOSHTARI A., NAGHDABADI, R., 2005, Thermoelastic analysis of thick-walled finite-length cylinders of functionally graded materials, *Journal of Thermal Stresses*, **28**, 391-408
35. SAHNI M., SAHNI R., 2015, Rotating functionally graded disc with variable thickness profile and external pressure, *Procedia Computer Science*, **57**, 1249-1254
36. SHARMA J.N., SHARMA D., KUMAR S., 2013, Vibration analysis of a rotating FGM thermoelastic axisymmetric circular disk using FEM, *International Journal for Computational Methods in Engineering Science and Mechanics*, **14**, 262-270
37. SHERBOURNE A.N., MURTHY D.N.S., 1974, Stresses in disks with variable profile, *International Journal of Mechanical Sciences*, **16**, 449-459
38. TUTUNCU N., TEMEL B., 2013, An efficient unified method for thermoelastic analysis of functionally graded rotating disks of variable thickness, *Mechanics of Advanced Materials and Structures*, **20**, 38-46
39. VULLO V., VIVIO, F., 2008, Elastic stress analysis of non-linear variable thickness rotating disks subjected to thermal load and having variable density along the radius, *International Journal of Solids and Structures*, **45**, 5337-5355
40. WU N.-G., RAMSEY J.H., 1966, Stresses in a layered rotating disk, *International Journal of Mechanical Sciences*, **8**, 629-639
41. YELLA REDDY T., SRINATH H., 1974, Elastic stresses in a rotating anisotropic annular disk of variable thickness and variable density, *International Journal of Mechanical Sciences*, **16**, 85-89
42. YOU L.H., YOU X.Y., ZHANG J.J., LI J., 2007, On rotating circular disks with varying material properties, *Zeitschrift für angewandte Mathematik und Physik*, **58**, 1068-1084
43. ZAFARMAND H., HASSANI B., 2014, Analysis of two-dimensional functionally graded rotating thick disks with variable thickness, *Acta Mechanica*, **225**, 453-464

44. ZENKOUR A.M., 2005, Analytical solution for rotating exponentially-graded annular disks with various boundary conditions, *International Journal of Structural Stability and Dynamics*, **5**, 557-577
45. ZENKOUR A.M., 2009, Stress distribution in rotating composite structures of functionally graded solid disks, *Journal of Materials Processing Technology*, **209**, 3511-3517
46. ZENKOUR A.M., 2014, On the magneto-thermo-elastic responses of FG annular sandwich disks, *International Journal of Engineering Science*, **75**, 54-66
47. ZENKOUR A.M., ALLAM, M.N.M., 2006, On the rotating fiber-reinforced viscoelastic composite solid and annular disks of variable thickness, *International Journal for Computational Methods in Engineering Science and Mechanics*, **7**, 21-31
48. ZHENG Y., BAHALOOA H., MOUSANEZHADA D., MAHDIB E., VAZIRIA A., NAYEB-HASHEMI, H., 2016, Stress analysis in functionally graded rotating disks with non-uniform thickness and variable angular velocity, *International Journal of Mechanical Sciences*, **119**, 283-293

Manuscript received January 29, 2017; accepted for print February 27, 2018

ASSESSMENT OF THE STRENGTH REDUCTION FACTOR IN PREDICTING THE FLEXURAL STRENGTH

SEMA ALACALI, GURAY ARSLAN

Yildiz Technical University, Department of Civil Engineering, Istanbul, Turkey

e-mail: semanoyal@gmail.com; aguray@yildiz.edu.tr

In the design of flexural strength, the strength reduction factor ϕ decreases from tension-controlled sections to compression-controlled sections to increase safety with decreasing ductility. This paper presents how to determine the reduction factor for flexural strength of reinforced concrete beams according to ACI code. In the reliability-based design, the reliable prediction of the flexural strength of reinforced concrete members is assured by the use of reduction factors corresponding to different target reliability index β . In this study, for different β and coefficients of variation of the flexural strength parameters, the flexural strength reduction factor has been investigated by using experimental studies available in the literature. In the reliability analysis part of the study, the first-order second moment approach (FOSM) has been used to determine the reduction factor. It has also been assumed that the random variables are statistically independent.

Keywords: reinforced concrete, beam, flexure strength, reduction factor, target reliability

1. Introduction

In the design of flexural strength, tension-controlled sections are desirable for their ductile behavior for giving sufficient warning prior to failure. Hence, reinforced concrete (RC) elements are designed to behave in a ductile manner, whenever possible. This behavior can be ensured by limiting the amount of reinforcement such that tension reinforcement yields prior to concrete crushing. In ACI 318 codes (1995, 1999, 2002, 2005, 2008, 2011, 2014), a lower strength reduction (ϕ) factor is used for compression-controlled sections compared to the one for tension-controlled sections because the compression-controlled sections are less ductile. Naaman (2004) noted that changes made from the ACI 318 (1999) to the ACI 318 (2002) codes relocated the limits for tension and compression controlled sections and added a transition region between the two. The flaw lies in this definition for these regional boundaries.

In the codes, it is intended to provide the target failure probability by means of safety factors that are load factors and strength reduction factors (Arslan *et al.*, 2017). Safety factors depend on the selected target reliability index β , which is established in terms of the acceptable probability of failure varying with the considered loading condition, type of failure mode and material (Arslan *et al.*, 2016). According to Du and Au (2005), the reliability indexes based on the requirements of the strength limit state for bridge girders are 3.9-4.4, 5.2-5.3 and 3.4-3.5 according to AASHTO (1998), the Chinese Code (1991) and the Hong Kong Code (2002), respectively. Nowak *et al.* (2001) compared the reliability levels of prestressed concrete girders designed using Spanish Code (1998), Eurocode ENV 1991-3 (1994), and AASHTO (1998), and indicated that the reliability indexes varied considerably for the three codes. The reliability indexes for bridge girders were 7.0-8.0, 5.1-6.8 and 4.5-4.9 according to Eurocode ENV 1991-3 (1994), the Spanish Code (1998) and AASHTO (1998), respectively. In this study, the change in the strength reduction factor considered in predicting the flexural strength of tension-controlled

sections according to ACI 318 (2014) is investigated and compared for different reliability indexes and coefficients of variation of the flexural strength parameters.

2. Design of RC beams for flexure

According to ACI 318 (2014), the nominal flexural strength M_n of a beam section is computed from internal forces at the ultimate strain profile when the extreme compressive fiber strain is equal to 0.003. Sections in flexure exhibit different modes of failure depending on the strain level in the extreme tension reinforcement. According to Section 21.2 of ACI 318 (2014), these modes are defined as tension-controlled sections, compression-controlled sections and a transition region between the tension- and compression-controlled sections. Tension-controlled sections have the net tensile strain in the extreme tension steel either equal to or greater than 0.005. Compression-controlled sections have the net tensile strain in the extreme tension reinforcement either equal to or less than the compression-controlled strain limit when the concrete in compression reaches the strain limit of 0.003. The compression-controlled strain limit is the net tensile strain in the reinforcement at balanced strain conditions. Compression-controlled sections have strains equal to or less than the yield strain, which is equal to 0.002 for Grade 420 reinforcement. There exists a transition region between the tension- and compression-controlled sections.

The nominal flexural strength of a rectangular section with tension reinforcement is computed from the internal force couple for tension failure by the yielding of the reinforcement. The nominal flexural strength of the beams M_n can be calculated as

$$M_n = A_s f_y d - 0.59 \frac{A_s^2 f_y^2}{b f_c} \quad (2.1)$$

in which A_s is the area of the flexural reinforcement, f_y is the yield strength of the reinforcement, f_c is the compressive strength of concrete, d and b are the effective depth and beam width, respectively.

The governing equation given by ACI 318 (2014) states that the reduced (design) strength ϕM_n must exceed the ultimate (factored) moment M_u , and the safety criteria for flexural design of the RC beams can be defined as

$$\phi M_n \geq M_u \quad (2.2)$$

in which ϕ is the strength reduction factor for flexure. According to ACI 318 (2014), the ϕ for an element depends on parameters such as the ductility and the importance of the element in terms of the reliability of the entire structure. For tension-controlled sections, a ϕ of 0.90 is used. Compression-controlled sections are defined as having strain limit at the nominal strength at or below the yield strain of the reinforcement. For compression-controlled sections, the ϕ is either 0.65 or 0.75 depending on the nature of the lateral confinement reinforcement. For sections with reinforcement strains between the aforementioned two limits, the strength reduction factor ϕ is determined by a linear interpolation between the value of ϕ for tension- and compression-controlled sections.

3. Reliability analysis

In reliability analysis, the main objective of engineering planning and design is to insure the performance of an engineering system. Under conditions of uncertainty, the assurance of the performance is possible with the use of safety factors. The reliability assessment requires knowledge of the performance function to define the safety factors (Ang and Tang, 1984). The performance

function, $Z = g(X_1, X_2, \dots, X_n)$, can be determined in terms of many random variables as load components, resistance parameters, material properties. In this equation, X_i are basic random variables influencing the limit state. The failure surface can be defined as $Z = 0$. The safety or reliability is defined by $Z > 0$, and the failure state is $Z < 0$. In the reliability based design, the problem is to determine the partial safety factors of the variables according to the target reliability index β . In this study, the first-order second moment approach (FOSM) is used and the design points $\gamma_i m_{X_i}$ corresponding to the target reliability index β are obtained. In the space of reduced variates, β being a measure of reliability is defined as the shortest distance from the failure surface to the origin.

The limit state function can be defined with Eq. (3.1) by multiplying the safety factor γ_i with each of the basic design variables

$$g(\gamma_1 m_{X_1}, \gamma_2 m_{X_2}, \dots, \gamma_i m_{X_i}) = 0 \quad i = 1, 2, \dots, n \quad (3.1)$$

$x_i^* (= \gamma_i m_{X_i})$ is the most probable failure point on the failure surface, and the determination of x_i^* requires an iterative solution. In the space of reduced variates, the most probable failure point is $x_i'^* = -\alpha_i^* \beta$. The sensitivity coefficient α_i^* is defined by

$$\alpha_i^* = \frac{\partial g}{\partial X_i'} / \sqrt{\sum_{i=1}^n \left(\frac{\partial g}{\partial X_i'} \right)^2} \quad (3.2)$$

The partial safety factors required for the given β are defined as $\gamma_i (= x_i^* / m_{X_i})$. The original variates are given by $x_i^* = m_{X_i} (1 - \alpha_i^* \beta V_{X_i})$, in which m_{X_i} and V_{X_i} are the mean value and the variance coefficient of the original variable X_i with normal distribution, respectively. V_{X_i} is the ratio of standard deviation σ_{X_i} to the mean value m_{X_i} . The partial safety factors are calculated as (Nowak and Collins, 2000)

$$\gamma_i = 1 - \alpha_i^* \beta V_{X_i} \quad (3.3)$$

In this study, the distributions of random variables in the performance function are given in Table 1. In lognormal and extreme type I distributions, m_{X_i} and σ_{X_i} are replaced by the equivalent normal mean $m_{X_i}^N$ and standard deviation $\sigma_{X_i}^N$. In addition, it is also assumed that the random variables are statistically independent.

3.1. Establishment of performance function

According to ACI 318 (2014), the strength reduction factor for flexure ranges from 0.70 to 0.90 depending on the nature of the lateral confinement reinforcement and the strain level in the extreme tension reinforcement. The reduction factors for RC beams have been investigated by considering the reliability indexes β (5.2, 4.75, 4.27, 3.72, 3.5, 3.09 and 2.33) corresponding to various failure probabilities p_F (10^{-7} , 10^{-6} , 10^{-5} , 10^{-4} , $2.33 \cdot 10^{-4}$, 10^{-3} and 10^{-2}). The performance function used in the calculations is given by

$$g(X) = \gamma_1 M_n - \gamma_2 M_u \quad (3.4)$$

in which M_u is the ultimate (factored) moment at the RC beam section that can be taken as the test result and M_n is the nominal flexural strength of the beam defined in ACI 318 (2014). γ_1 and γ_2 are the strength reduction factors for the corresponding variables.

3.2. Coefficients of variation of design parameters

The ultimate (factored) and nominal flexural strength of the beams obtained through experiments and equation have been modeled as random variables to perform a probability-based analysis. In modeling of those parameters as random variables, the values of coefficients of variations have been determined based on the studies available in the literature and codes. They are summarized in Table 1. In the literature review (Table 1), it has been observed that the coefficient of variation of the concrete compressive strength V_{f_c} varies between 0.10 and 0.21, depending on the construction quality (Arslan *et al.*, 2015). By taking advantage of studies in the literature and codes, it is assumed that V_{f_c} is 0.05, 0.10 and 0.15, respectively, in this study.

Table 1. Coefficients of variation of the variables

Cases	Coefficients of variation					
	f_y	f_c	A_s	b	d	M_u
Case 1	0.03	0.05	0.04	0.03	0.03	0.04
Case 2		0.10				
Case 3		0.15				
Case 4	0.05	0.05				
Case 5		0.10				
Case 6		0.15				
Case 7	0.07	0.05				
Case 8		0.10				
Case 9		0.15				
Case 10	0.10	0.05				
Case 11		0.10				
Case 12		0.15				
Distribution type	Log-normal	Log-normal	Normal	Normal	Normal	Extreme type I

The coefficient of variation of the reinforcement yield strength V_{f_y} has also been reported by many researchers, and V_{f_y} ranges from 0.05 to 0.15 (Arslan *et al.*, 2016). V_{f_y} was taken as 0.03 by Nowak *et al.* (2005), 0.05 by JCSS (2000), 0.06 by Soares *et al.* (2002), 0.07 by Akiyama *et al.* (2012), 0.08 by Val *et al.* (1997), Hosseinneshad *et al.* (2000) and Low and Hao (2001), 0.08-0.11 by Ostlund (1991), 0.12 by Enright and Frangopol (1998), 0.15 by Mirza (1996). In the present study, model variations of f_y are taken as 0.03, 0.05, 0.07 and 0.10, respectively.

The coefficients of variation of the effective depth V_d , width V_b and tensile reinforcement area V_{A_s} of beams have also been reported by many researchers. V_d was taken as 0.02 by Lu *et al.* (1994), 0.03 by Wiegand and Atadero (2011), 0.04 by Nowak and Szerszen (2003) and Szerszen *et al.* (2005). V_b was taken as 0.04 by Nowak and Szerszen (2003) and Szerszen *et al.* (2005). It is assumed that the V_d , V_b and V_{A_s} are 0.03, 0.03 and 0.04, respectively, in this study.

To carry out the reliability analysis of RC beam specimens, a meaningful probability distribution for the nominal flexural strength parameters and ultimate flexural strength is also necessary. In the present study, randomness of the applied load is described using Extreme type I distribution. In the studies by Hognestad (1951) and Mirza (1996), it was assumed that the coefficient of variation of strength due to test procedure was 0.04, which is the value used in this study.

3.3. Properties of beams

In the determination of the flexural strength reduction factors, 84 beams with flexural failure collected from 3 different researches (Johnson and Cox, 1939; Ashour, 2000; Pam *et al.*, 2001)

have been evaluated. The number of beams produced from normal-strength concrete (NSC) and high-strength concrete (HSC) with $f_c \geq 55$ MPa are 52 and 32, respectively. The beams have a broad range of design parameters: $22.0 \leq f_c \leq 48.6$ MPa, $0.17 \leq \rho \leq 2.37\%$, $200 \leq b \leq 305$ mm and $215 \leq d \leq 305$ mm for NSC beams and $57.1 \leq f_c \leq 107.1$ MPa, $1.03 \leq \rho \leq 4.04\%$, $120 \leq b \leq 200$ mm and $208 \leq d \leq 260$ mm for HSC beams.

4. Investigating the strength reduction

The ACI 318 code imposes a ϕ factor of 0.65 when the strain in the tension reinforcement equals 0.002 for Grade 420 reinforcement. The ϕ increases linearly to the maximum value of 0.90 as the tension strain increases from 0.002 to 0.005. A tension-controlled section is defined as a cross section in which the tensile strain in the extreme tension reinforcement at the nominal strength is greater than or equal to 0.005. Tension-controlled sections are desirable for their ductile behavior, which allows redistribution of the stresses and sufficient warning against an imminent failure. It is always a good practice to design RC elements to behave in a ductile manner, whenever possible. For tension-controlled sections, a ϕ factor of 0.9 has been used.

In the design of RC beams, to apply a higher resistance factor ϕ of 0.9, the member should exhibit desirable behavior. In this study, ϕ factors of the ACI 318 code are investigated for tension-controlled beam sections. For different V_{fc} and V_{fy} , the value of ϕ corresponding to β (2.33, 3.09, 3.50, 3.72, 4.27, 4.75 and 5.20) and different V_{fc} and V_{fy} are summarized for NSC, HSC and all beams (NSC and HSC) in Table 2. For a given β and different V_{fc} and V_{fy} , the value of ϕ for HSC beams is found to be smaller than the one for NSC beams, so it can be inferred that ϕ for NSC beams is more safe than that for HSC beams.

Saatcioglu (2014) indicated that the ACI 318 (2005) adopted strength reduction factors that were compatible with ASCE7-02 (2002) load combinations, except for the tension controlled section for which the ϕ was increased from 0.80 to 0.90.

In this study, it is founded that 0.80 value of ϕ corresponds to the target values of $\beta = 3.5$, $V_{fc} = 0.05$ and $V_{fy} = 0.10$ in all analyzed beams. In ACI 318 (2014), ϕ considered in predicting flexural strength of beams is updated as 0.90, which corresponds to the target values of $\beta = 3.5$, $V_{fy} = 0.05$ and $V_{fc} = 0.05$, in all analyzed beams. It is observed that this value is conservative for β in the range from 2.33 to 5.20 for $V_{fy} = 0.05$ and $V_{fc} \leq 0.15$ in NSC beams, and it can also be noted that it is conservative for β in the range from 2.33 to 5.20 for $V_{fy} = 0.03$ and $V_{fc} \leq 0.15$ in HSC beams.

The values of ϕ obtained from the analyses which have been performed by considering different V_{fc} (0.05, 0.10 and 0.15), V_{fy} (0.03, 0.05, 0.07 and 0.10) and β (5.2, 4.75, 4.27, 3.72, 3.50, 3.09 and 2.33) values of the beam sections are shown in Fig. 1.

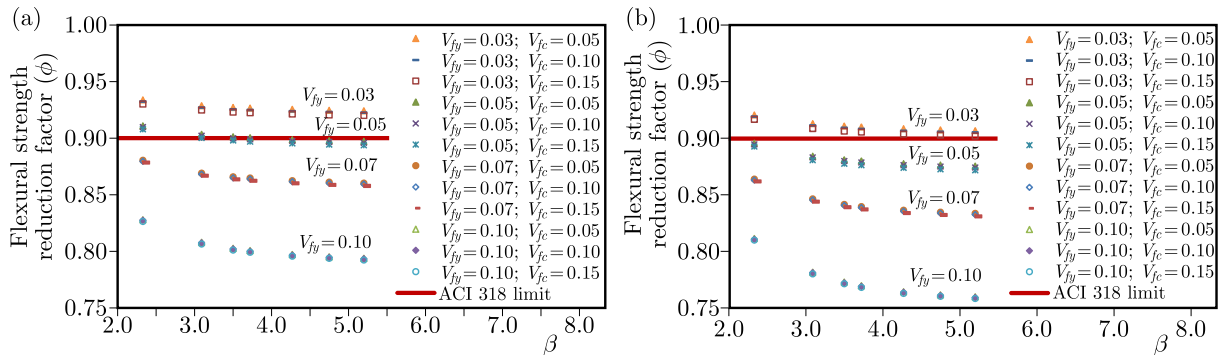


Fig. 1. Effect of variation in the β on ϕ ; (a) NSC, (b) HSC

Table 2. Average ϕ for different values of COV and β values

Beams	Coefficients of variation		β						
			2.33	3.09	3.50	3.72	4.27	4.75	5.20
NSC	$V_{f_y} = 0.03$	$V_{f_c} = 0.05$	0.934	0.929	0.927	0.926	0.925	0.925	0.924
		$V_{f_c} = 0.10$	0.932	0.927	0.926	0.925	0.924	0.923	0.923
		$V_{f_c} = 0.15$	0.930	0.925	0.923	0.922	0.921	0.921	0.920
	$V_{f_y} = 0.05$	$V_{f_c} = 0.05$	0.911	0.903	0.901	0.900	0.899	0.898	0.897
		$V_{f_c} = 0.10$	0.910	0.902	0.900	0.899	0.898	0.897	0.896
		$V_{f_c} = 0.15$	0.908	0.900	0.898	0.897	0.895	0.894	0.894
	$V_{f_y} = 0.07$	$V_{f_c} = 0.05$	0.880	0.869	0.866	0.865	0.862	0.861	0.860
		$V_{f_c} = 0.10$	0.880	0.868	0.865	0.864	0.862	0.860	0.859
		$V_{f_c} = 0.15$	0.878	0.867	0.863	0.862	0.860	0.859	0.858
	$V_{f_y} = 0.10$	$V_{f_c} = 0.05$	0.828	0.808	0.803	0.801	0.797	0.795	0.794
		$V_{f_c} = 0.10$	0.827	0.807	0.802	0.800	0.797	0.795	0.793
		$V_{f_c} = 0.15$	0.826	0.806	0.801	0.799	0.796	0.794	0.792
HSC	$V_{f_y} = 0.03$	$V_{f_c} = 0.05$	0.921	0.913	0.911	0.910	0.909	0.908	0.907
		$V_{f_c} = 0.10$	0.920	0.912	0.910	0.909	0.907	0.906	0.906
		$V_{f_c} = 0.15$	0.917	0.909	0.907	0.906	0.904	0.903	0.902
	$V_{f_y} = 0.05$	$V_{f_c} = 0.05$	0.896	0.885	0.881	0.880	0.878	0.877	0.876
		$V_{f_c} = 0.10$	0.895	0.883	0.880	0.879	0.877	0.875	0.874
		$V_{f_c} = 0.15$	0.893	0.881	0.878	0.877	0.874	0.873	0.872
	$V_{f_y} = 0.07$	$V_{f_c} = 0.05$	0.864	0.847	0.842	0.840	0.837	0.835	0.834
		$V_{f_c} = 0.10$	0.863	0.846	0.841	0.839	0.836	0.834	0.833
		$V_{f_c} = 0.15$	0.862	0.844	0.839	0.837	0.834	0.832	0.831
	$V_{f_y} = 0.10$	$V_{f_c} = 0.05$	0.812	0.782	0.773	0.770	0.764	0.762	0.760
		$V_{f_c} = 0.10$	0.811	0.781	0.772	0.769	0.764	0.761	0.759
		$V_{f_c} = 0.15$	0.810	0.780	0.771	0.768	0.763	0.760	0.758
NSC + HSC	$V_{f_y} = 0.03$	$V_{f_c} = 0.05$	0.929	0.923	0.921	0.920	0.919	0.918	0.918
		$V_{f_c} = 0.10$	0.928	0.921	0.920	0.919	0.918	0.917	0.916
		$V_{f_c} = 0.15$	0.925	0.919	0.917	0.916	0.915	0.914	0.913
	$V_{f_y} = 0.05$	$V_{f_c} = 0.05$	0.905	0.896	0.894	0.893	0.891	0.890	0.889
		$V_{f_c} = 0.10$	0.904	0.895	0.892	0.891	0.890	0.889	0.888
		$V_{f_c} = 0.15$	0.902	0.893	0.890	0.889	0.887	0.886	0.885
	$V_{f_y} = 0.07$	$V_{f_c} = 0.05$	0.874	0.860	0.857	0.855	0.853	0.851	0.850
		$V_{f_c} = 0.10$	0.873	0.860	0.856	0.854	0.852	0.850	0.849
		$V_{f_c} = 0.15$	0.872	0.858	0.854	0.853	0.850	0.849	0.848
	$V_{f_y} = 0.10$	$V_{f_c} = 0.05$	0.822	0.798	0.791	0.789	0.785	0.782	0.781
		$V_{f_c} = 0.10$	0.821	0.797	0.791	0.788	0.784	0.782	0.780
		$V_{f_c} = 0.15$	0.820	0.796	0.790	0.787	0.783	0.781	0.779

It is seen that ϕ decreases with an increase in the value of V_{f_y} . The rate of increasing in the value of ϕ for low values of β is higher than that for high values of β . When β becomes higher, the variation of ϕ versus β almost becomes a smooth curve for NSC and HSC beams. For given V_{f_y} and β , ϕ for HSC beams are found to be smaller than the one for NSC beams, so it can be inferred that ϕ for NSC beams is more safe than that for HSC beams. For the same V_{f_y} , V_b , V_d , V_{A_s} and β values, it can also be said that ϕ values for NSC, HSC and all beams (NSC and HSC) are very close to each other for different V_{f_c} .

For some experimental beams, the effects of variations of the tensile strain in the tension reinforcement ε_s , the compressive strength of concrete f_c , the ratio of tensile strain to yield

strain in the tension reinforcement $\varepsilon_s/\varepsilon_y$, the ratio of percentage of tension reinforcement to the percentage of balanced reinforcement ρ/ρ_b , the ratio of neutral axis depth to the effective depth x/d , and effective depth of the beam d on the ϕ are plotted in Fig. 2 for $\beta = 3.5$, $V_{fy} = 0.05$, $V_{fc} = 0.05$, $V_b = 0.03$, $V_d = 0.03$ and $V_{As} = 0.04$.

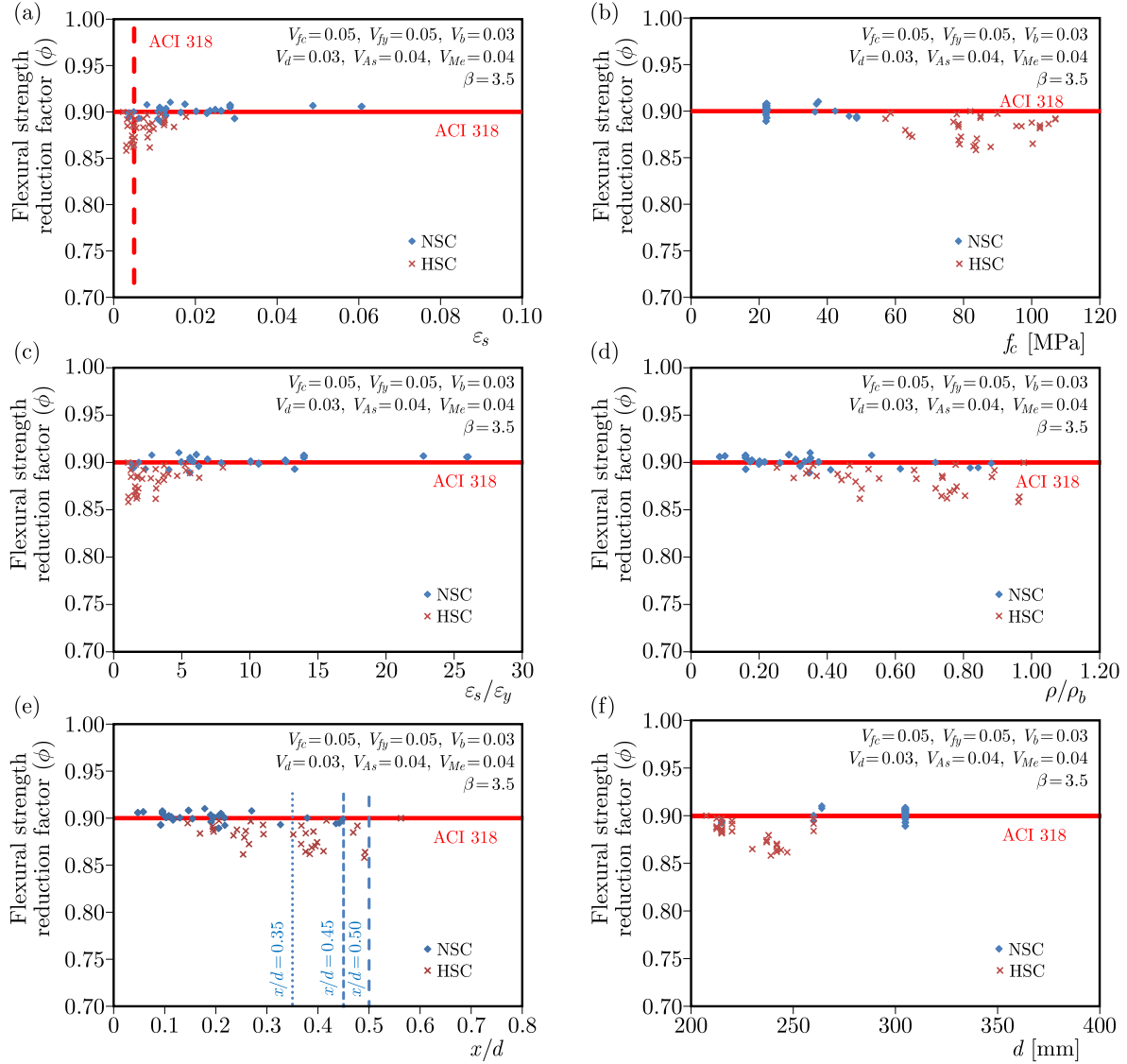


Fig. 2. Effect of variation in ε_s , f_c , $\varepsilon_s/\varepsilon_y$, ρ/ρ_b , x/d and d on ϕ

The relationship of ϕ and ε_s at the nominal strength for the analyzed beams is shown in Fig. 2a. According to ACI 318, if the reinforcement strain at the nominal strength is greater than 0.005, ϕ equals to 0.90 for the desirable behavior of beam sections. 20% of the tests (4 for NSC and 12 for HSC of 84 tests) delivered relatively low ε_s values $\varepsilon_s \leq 0.005$, where the corresponding strength reduction factors are mostly less than 0.90 for $\beta = 3.5$, $V_{fy} = 0.05$ and $V_{fc} = 0.05$. It is observed that the ϕ factor increases with ε_s for NSC and HSC beams. Based on the results of analyses, ACI 318 provisions are non-conservative for $\varepsilon_s \leq 0.02$. The ϕ factor for the existing test data yields a large scatter in the results, especially for beams with $\varepsilon_s \leq 0.02$.

Figure 2b shows the ϕ - f_c for the analyzed beams. Based on the studies of the stress-strain behavior of NSC and HSC, it is shown that concrete becomes increasingly more brittle as its compressive strength is increased. Despite HSC being a more brittle material compared with NSC, the x/d values of HSC sections are smaller than those of the NSC sections for a given ρ .

Hence, HSC flexural members exhibit greater ductility owing to lower neutral axis depths (Arslan and Cihanli, 2010). Based on the results of analyses, ACI 318 provisions are non-conservative for HSC flexural beams. The ϕ factor for the existing test data yields a large scatter in the results, especially for HSC beams with $f_c > 75$ MPa.

The ϕ - $\varepsilon_s/\varepsilon_y$ for the analyzed beams are shown in Fig. 2c. According to ACI 318, if ε_s is at least 2.5 times the yield strain ($\varepsilon_y \cong 0.002 = f_y/E_s$), then the maximum value of $\phi = 0.90$ can be used. 32% of the tests (10 for NSC and 17 for HSC of 84 tests) delivered relatively low $\varepsilon_s/\varepsilon_y$ values ($\varepsilon_s/\varepsilon_y \leq 5$), where the corresponding strength reduction factors are mostly less than 0.90 for $\beta = 3.5$, $V_{fy} = 0.05$ and $V_{fc} = 0.05$. It is observed that the ϕ factor increases with $\varepsilon_s/\varepsilon_y$ for the beams. The ϕ factor for the existing test data yields a large scatter in the results, especially for HSC beams with $\varepsilon_s/\varepsilon_y \leq 5$.

The effect of ρ/ρ_b on ϕ is illustrated in Fig. 2d. The ACI 318 (1999) and previous codes limit the tension reinforcement ratio ρ to no more than 75% of the ratio ($0.75\rho_b$) that would produce balanced strain conditions. The ACI 318 (2002) limits the net tensile strain ε_t of the extreme tension steel at the nominal strength to be not less than 0.004. Meanwhile, when the net tensile strain in the extreme tension steel is sufficiently large (equal to or greater than 0.005), the section is defined as tension-controlled where ample warning of failure with excessive deflection and cracking may be expected. The effect of this limitation is to restrict ρ in RC beams to about the same ratio as in editions of the code prior to 2002. 69% of the tests (26 for NSC and 32 for HSC of 84 tests) delivered relatively high ρ/ρ_b values ($\rho/\rho_b \geq 0.25$), where the corresponding strength reduction factors are mostly less than 0.90 for $\beta = 3.5$, $V_{fy} = 0.05$ and $V_{fc} = 0.05$. The results of the ϕ factor of beams with $\rho/\rho_b < 0.25$ are limited for all the beams (6 for NSC of 84 tests).

Figure 2e shows the ϕ - x/d for the analyzed beams. The design codes BS8110, EC 2 and GBJ 11 limit the neutral axis depth x to no more than a certain fraction of the effective depth d . It can be noted that in the design of beams, using the simplified stress block BS 8110 (1997) limits x to $0.5d$ for all concrete with $f_{cu} \leq 100$ MPa to ensure that the section is under-reinforced and the strain in the longitudinal reinforcement is not less than 0.0035. EC 2-1 (1992) limits the x to no more than $0.45d$ when $f_{cu} < 50$ MPa or $0.35d$ when $f_{cu} \geq 50$ MPa. GBJ 11 (1989) requires x to be smaller than $0.35d$ for all concrete grades. The values of ϕ decrease significantly as x/d increases from 0.2 to 0.5. The corresponding ϕ of HSC beams are smaller than 0.90 for $\beta = 3.5$, $V_{fy} = 0.05$, $V_{fc} = 0.05$, $V_b = 0.03$, $V_d = 0.03$ and $V_{As} = 0.04$. Based on the results of analyses, the ϕ factor for $x/d > 0.30$ is non-conservative for 22 flexural beams (5 for NSC and 17 for HSC of 84 tests). The ϕ factor for the existing test data yields a large scatter in the results, especially for $x/d \geq 0.20$.

The ϕ - d for the analyzed beams are shown in Fig. 2f. 6% of the NSC beam tests (3 of 52 tests) have been conducted for $d < 250$ mm and only 9% of the HSC beam tests (3 of 32 tests) have been conducted for $d \geq 250$ mm. The ϕ factor for the existing test data yields a large scatter in the results, especially for HSC beams with $d < 250$ mm.

5. Conclusion

The change in the strength reduction factor for flexure according to the ACI 318 is investigated for different coefficients of variation and β values. The following conclusions can be drawn from the results of this study.

- It is found that ϕ of 0.90, which is a value recommended by the ACI 318 (2002) and ACI 318 (2011), corresponds to the target values of $\beta = 3.5$, $V_{fy} = 0.03$ and $V_{fc} = 0.05$ in all analyzed beams. It is observed that this value is conservative for β in the range from 2.33 to 5.20 for $V_{fy} = 0.05$ and $V_{fc} \leq 0.15$ in NSC beams, and it can also be noted that it

is conservative for β in the range from 2.33 to 5.20 for $V_{fy} = 0.03$ and $V_{fc} \leq 0.15$ in HSC beams.

- For the given $\beta = 3.5$, $V_{fy} = 0.05$, $V_{fc} = 0.05$, $V_b = 0.03$, $V_d = 0.03$ and $V_{As} = 0.04$, ϕ for the HSC beams are found to be smaller than those for the NSC beams, so it can be inferred that ϕ for the HSC beams is more non-conservative than that for the NSC beams.
- According to ACI 318, if ε_s is at least 2.5 times the yield strain ($\varepsilon_y \cong 0.002 = f_y/E_s$), then the maximum value of $\phi = 0.90$ can be used. 32% of the tests (10 for NSC and 17 for HSC of 84 tests) delivered relatively low $\varepsilon_s/\varepsilon_y$ values ($\varepsilon_s/\varepsilon_y \leq 5$), where the corresponding strength reduction factors are mostly less than 0.90 for $\beta = 3.5$, $V_{fy} = 0.05$ and $V_{fc} = 0.05$. It is observed that the ϕ factor increases with $\varepsilon_s/\varepsilon_y$ for beams. The ϕ factor for the existing test data yields a large scatter in the results, especially for HSC beams with $\varepsilon_s/\varepsilon_y \leq 5$.
- The values of ϕ decrease significantly as x/d increases from 0.2 to 0.5. The corresponding ϕ of HSC beams are smaller than 0.90 for $\beta = 3.5$, $V_{fy} = 0.05$, $V_{fc} = 0.05$, $V_b = 0.03$, $V_d = 0.03$ and $V_{As} = 0.04$. Based on the results of analyses, the ϕ factor for $x/d > 0.30$ is non-conservative for 22 flexural beams (5 for NSC and 17 for HSC of 84 tests). The ϕ factor for the existing test data yields a large scatter in the results, especially for $x/d \geq 0.20$.

In order to make a more reliable evaluation, the determination of the reduction factor for flexural strength of RC beams for a greater number of beams with different material and geometric properties should be realized.

References

1. AASHTO LRFD: Bridge Design Specifications, 1998, American Association of State Highway and Transportation Officials, Washington, DC
2. ACI, 1995, ACI 318M-95: *Building Code Requirements for Structural Concrete and Commentary*, ACI, Farmington Hills, MI, USA
3. ACI, 1999, ACI 318M-99: *Building Code Requirements for Structural Concrete and Commentary*, ACI, Farmington Hills, MI, USA
4. ACI, 2002, ACI 318R-02: *Building Code Requirements for Structural Concrete and Commentary*, ACI, Farmington Hills, MI, USA
5. ACI, 2005, ACI 318R-05: *Building Code Requirements for Structural Concrete and Commentary*, ACI, Farmington Hills, MI, USA
6. ACI, 2008, ACI 318R-08: *Building Code Requirements for Structural Concrete and Commentary*, ACI, Farmington Hills, MI, USA
7. ACI, 2011, ACI 318R-11: *Building Code Requirements for Structural Concrete and Commentary*, ACI, Farmington Hills, MI, USA
8. ACI, 2014, ACI 318-14: *Building Code Requirements for Structural Concrete and Commentary*, ACI, Farmington Hills, MI, USA
9. AKIYAMA M., MATSUZAKI H., DANG H.T., SUZUKI M., 2012, Reliability-based capacity design for reinforced concrete bridge structures, *Structure and Infrastructure Engineering*, Maintenance, Management, Life-Cycle Design and Performance, **8**, 12, 1096-1107
10. ANG A.H.S., TANG W.H., 1984, *Probability Concepts in Engineering Planning and Design. Vol. II, Decision, Risk, and Reliability*, Wiley, New York, NY, USA
11. ARSLAN G., ALACALI S., SAGIROGLU A., 2016a, Assessing reduction in concrete shear strength contribution, *Proceedings of the Institution of Civil Engineers, Structures and Building*, **169**, 4, 237-244

12. ARSLAN G., ALACALI S.N., SAGIROGLU A., 2016, The investigation of the strength reduction factor in predicting the shear strength, *Journal of Theoretical and Applied Mechanics*, **53**, 2, 371-381
13. ARSLAN G., ALACALI S.N., SAGIROGLU A., 2017, Determining the reduction factor in predicting the contribution of concrete to shear strength by using a probabilistic method, *International Journal of Civil Engineering (IJCE) Transaction A: Civil Engineering*, in reviewer
14. ARSLAN G., CIHANLI E., 2010, Curvature ductility prediction of reinforced high-strength concrete beam sections, *Journal of Civil Engineering and Management (JCEM)*, **16**, 4, 462-470
15. ASHOUR S.A., 2000, Effect of compressive strength and tensile reinforcement ratio on flexural behavior of high-strength concrete beams, *Engineering Structures*, **22**, 5, 413-423
16. British Standards Institution – Part 1, 1997, Structural Use of Concrete: *Code of Practice for Design and Construction*, BSI, London, BS 8110
17. Chinese Design Code for Highway Bridges-Beijing, 1991, People's Communication Press
18. DU J.S., AU F.T.K., 2005, Deterministic and reliability analysis of prestressed concrete bridge girders: comparison of the Chinese, Hong Kong and AASHTO LRFD Codes; *Structural Safety*, **27**, 230-245
19. ENRIGHT, M.P., FRANGOPOL, D.M., 1998, Probabilistic analysis of resistance degradation of reinforced concrete bridge beams under corrosion, *Engineering Structures*, **20**, 960-971
20. Eurocode ENV 1991-3. Eurocode 1, 1994, Basis of Design and Actions on Structures. Part 3, *Traffic Loads on Bridges*, Final draft, August
21. European Committee for Standardisation, Design of Concrete Structures, Part 1, 1992, *General Rules and Rules for Buildings*, European Committee for Standardisation, Brussels, EC 2
22. HOGNESTAD E., 1951, A study of combined bending and axial load in reinforced concrete members, *Engineering Experiment Station Bulletin*, **399**, University of Illinois, Urbana, IL, USA
23. HOSSEINNEZHAD A., POURZEYNALI S., RAZZAGHI J., 2000, Application of first-order second moment level 2 reliability analysis of prestressed concrete bridges, *7th International Congress on Civil Engineering*
24. JCSS 2000, *Probabilistic model code – Part III*, Joint Committee on Structural Safety
25. JOHNSON B., COX K.C., 1939, High yield-point steel as tension reinforcement in beams, *ACI Journal Proceedings*, **36**, 1, 65-80
26. LOW H.Y., HAO H., 2001, Reliability analysis of reinforced concrete slabs under explosive loading, *Structural Safety*, **23**, 2, 157-178
27. LU R.H., LUO Y.H., CONTE J.P., 1994, Reliability evaluation of reinforced concrete beams, *Structural Safety*, **14**, 4, 277-298
28. Minimum Design Loads for Buildings and Other Structures (SEI/ASCE 7-02), 2002, American Society of Civil Engineers, <http://dx.doi.org/10.1061/9780784406243>.
29. MIRZA S.A., 1996, Reliability-based design of reinforced concrete columns, *Structural Safety*, **18**, 2/3, 179-194
30. NAAMAN A.E., 2004, Limits of reinforcement in 2002 ACI code, transition, flaws, and solution, *ACI Structural Journal*, **101**, 2, 209-218
31. National Standard of the People's Republic of China, 1989, *Code for Seismic Design of Buildings*, GBJ11-89 (in Chinese)
32. NOWAK A.S., COLLINS K.R., 2000, *Reliability of Structures*, McGraw Hill, Boston, MA, USA
33. NOWAK A.S., PARK C.H., CASAS J.R., 2001, Reliability analysis of prestressed concrete bridge girders: comparison of Eurocode, Spanish Norma IAP and AASHTO LRFD, *Structural Safety*, **23**, 331-344

34. NOWAK A.S., SZERSZEN M.M., 2003, Calibration of design code for buildings (ACI 318), Part 1 – Statistical models for resistance, *ACI Structural Journal*, **100**, 3, 377-382
35. NOWAK A.S., SZERSZEN M.M., SZWED S.A., PODHORECKI P.J., 2005, *Reliability-Based Calibration for Structural Concrete*, Report No. UNCLE 05-03, University of Nebraska
36. OSTLUND L., 1991, An estimation of T-values, [In:] *Reliability of Concrete Structures. CEB Bulletin d'Information*, **202**, Lausanne, Switzerland
37. PAM J.H., KWAN A.K.H., ISLAM M.S., 2001, Flexural strength and ductility of reinforced normal- and high-strength concrete beams, *Structure and Buildings*, **4**, 381-389
38. SAATCIOGLU M., 2014, *Chapter 1 – Design for Flexure*, Published by Albert Path on Sep. 14
39. SOARES R.C., MOHAMMED A., VENTURINI W.S., LEMAIRE M., 2002, Reliability analysis of nonlinear reinforced concrete frames using the response surface method, *Reliability Engineering and System Safety*, **75**, 1-16
40. Spanish Norma IAP-98, 1998, Actions in highway bridges, Road Directorate, Spanish Ministry of Public Works, Madrid
41. Structures Design Manual for Highways and Railways, 1997, Highways Department, Government of the Hong Kong Special Administrative Region, 2nd ed., with Amendment No. 1/2002, Hong Kong
42. SZERSZEN M.M., SZWED A., NOWAK A.S., 2005, Reliability analysis for eccentrically loaded columns, *ACI Structural Journal*, **102**, 5, 676-688
43. VAL D., BLJUGER F., YANKELEVSKY D., 1997, Reliability evaluation in nonlinear analysis of reinforced concrete structures, *Structural Safety*, **19**, 2, 203-217
44. WIEGHAUS K.T., ATADERO R.A., 2011, Effect of existing structure and FRP uncertainties on the reliability of FRP-based repair, *Journal of Composites for Construction*, **15**, 4, 635-643

Manuscript received June 29, 2017; accepted for print March 2, 2018

MONOTONIC BEHAVIOUR OF TYPICAL AL-CU-MG ALLOY PRE-STRAINED AT ELEVATED TEMPERATURE

ADAM TOMCZYK, ANDRZEJ SEWERYN, MICHAŁ DOROSZKO

Białystok University of Technology, Faculty of Mechanical Engineering, Białystok, Poland

e-mail: a.tomczyk@pb.edu.pl; a.seweryn@pb.edu.pl; m.doroszko@pb.edu.pl

This paper presents results of monotonic tensile and creep tests conducted on typical Al-Cu-Mg alloy (commercial 2024) specimens. Tensile tests carried out at room (20°C) and elevated (100°C, 200°C, 300°C) temperatures made it possible to determine strength properties of the material (Young's modulus, yield stress, ultimate tensile strength). Creep tests were performed at elevated temperature (100°C, 200°C and 300°C) with a constant force. In order to obtain material creep characteristics, creep-rupture tests were carried out. Then creep tests were conducted with two different strain values: one corresponding to the beginning of the secondary creep and the other corresponding to a certain value of the tertiary creep. After preliminary creep deformation at two various strain levels, specimens were cooled at ambient temperature and then subjected to monotonic tensile tests. The characteristics of the material were obtained for pre-strained specimens at different temperatures. Specimens fracture surfaces obtained as a result of tensile (at elevated and room temperature), creep and combined tests were analyzed.

Keywords: creep and tensile tests, metals and alloys, scanning electron microscopy, numerical calculations, mechanical properties

1. Introduction

EN-AW 2024 aluminum alloy finds widespread applications in mechanical engineering and, particularly, in aviation. It is commonly used in the aerospace industry, e.g. as a structural element of a wing or fuselage. At high cruising speeds, temperature of these components can rise to 120°C (Chakherlou *et al.*, 2010). For riveted joints and earlier cold expansion, elevated temperatures may cause creep and stress relaxation. Aluminum alloys are widely used as housings for coreless low-speed wind turbine generators. The operating temperature of generators, when the maximum power is reached, may exceed 250°C (Karakas and Szusta, 2016). As a result of speed of rotation, centrifugal forces may cause creep. After cooling to ambient temperature, the material is already different from the original.

Numerous studies concerning mechanical properties of 2024 aluminum alloy, particularly strength and durability, are conducted. Considering the criterion of the type of load acting on structural elements, studies can be divided into several groups related to loadings: monotonic, including elements with notches (e.g. Derpinski and Seweryn, 2011; Haigen *et al.* 2017), fatigue (e.g. Kowalewski *et al.*, 2014; Szusta and Seweryn, 2017), dynamic (e.g. Kumar *et al.*, 2011; Wang *et al.*, 2013), creep (and relaxation) (e.g. Lumley *et al.*, 2002; Lin *et al.* 2013a).

Studies of Zhao *et al.* (2013) and Naimi *et al.* (2013) presented results of investigations of the effect of high, cold plastic deformation succeeded by aging at elevated temperature on the strength parameters of alloy 2024. The effect of creep time, temperature and preliminary loadings on hardness and yield point was the subject of many other studies (Ro *et al.*, 2006; Li *et al.*, 2010; Guo *et al.*, 2013). Results of such tests, conducted on alloy 7B04-T7451, were presented by Li *et al.* (2010). There, a significant change of the yield point was obtained, depending

on aging conditions. Increasing preliminary load and aging time (with constant temperature 150°C) caused the yield point (σ_y) to increase at an aging time up to 5 hours. After that time was exceeded, the value of σ_y was reduced, and that reduction was higher when higher loadings were applied during aging. Guo *et al.* (2013) compared hardness of alloy 7075 subjected to prior purely thermal loadings with the hardness of alloy subjected to thermo-mechanical loadings. Lower hardnesses were obtained for thermal aging at temperatures lower than 140°C. Above that temperature, specimens previously subjected to thermo-mechanical loadings exhibited greater hardness. The paper by Ro *et al.* (2006) presented test results relating to the effect of aging at the same temperature but for different times on the plastic properties and hardness of alloy 2024. They showed a decrease of the yield point for short aging times, an increase for medium times, and a decrease once again for long times. The effect of pre-deformation at various temperatures on the value of the yield point, ultimate tensile strength and elongation of the same alloy was presented by Lin *et al.* (2014). A decrease of the yield point and ultimate tensile strength was observed for pre-deformation of 185-225 MPa at a temperature of 200°C while for lower stress values, that difference was greater. In turn, preliminary loading at 150°C and 170°C improved the value of both the yield point and ultimate tensile strength. The effect was reversed for elongation: pre-deformation at 200°C increased elongation, and at lower temperatures – reduced elongation. Wang *et al.* (2016) described results of investigations on the effect of preliminary compressive strains (3% and 5%) during aging of alloy 2219 at a temperature of 175°C on its mechanical properties. A significant increase of both the yield point and tensile strength was obtained relative to the material subjected only to thermal aging. Chen *et al.* (2012) presented test results for alloy 7050 concerning thermal (160°C) and thermo-mechanical loadings for different aging times. Different values of strength parameters were obtained depending on the share of mechanical loads (age-formed) or lack thereof (stress-free aging) in the preliminary ageing process. The yield point decreased as a result of the action of external loadings during the ageing process, while tensile strength generally increased. The longest aging time (24 h) was the exception, leading to a reduction of tensile strength. The material elongation decreased significantly when preliminary loadings occurred. Papers by Yang *et al.* (2016, 2017) concerned tests of alloy 2219. The influence of creep pre-deformation at a constant temperature (165°C) at different load levels and for different aging times on the material yield point value was analyzed in those papers. Compared to the material without pre-deformation, i.e. subjected only to the action of temperature, the yield point of the material with pre-deformation increased nearly two-fold for short aging times. That difference decreased as aging time increased. The highest differences were obtained for the lowest preliminary tensile loads, i.e. 120 MPa. A model was also proposed allowing for determination of the yield point of the material previously subjected to thermo-mechanical loadings, among other things. A proposal of a model accounting for the effects of pre-deformation at elevated temperatures was also presented by Zhang *et al.* (2013). It was verified successfully on alloy 2124. Similar models have been verified experimentally for several 7XXX series alloys (Ho *et al.*, 2004; Zhan *et al.*, 2011; Singh *et al.*, 2016).

The fundamental goal of the tests presented in this paper is to investigate the effect of creep pre-deformation of specimens made of EN AW-2024 (T3511) aluminum alloy on strength properties at room temperature. The results of monotonic tensile tests conducted on specimens at room temperature and at elevated temperature (100°C, 200°C, 300°C) are presented here. These results made it possible to determine basic material characteristics of the studied alloy. The next part concerns tests of preliminary material creep at elevated temperature (100°C, 200°C, 300°C) and at various strain levels. The stage after that consists of monotonic tensile tests conducted on specimens subjected to preliminary creep at room temperature, enabling determination of strength parameters of the material with pre-deformation. Most of papers in this field focus on the effect of initial creep carried out at temperatures of 150-200°C on properties of the analyzed alloy (Ro *et al.*, 2006; Lin *et al.*, 2013b, 2014). The research presented in this paper

concerns pre-deformation realized at both 200°C temperature and 100°C and above all – at 300°C temperature. It should also be noted that in the case of low creep temperature (100°C), high load values are used. Thus, here the dominant effect deciding on the later properties of the material is not the temperature effect but the mechanical one. The most important results concern pre-deformation at 300°C. Initial creep carried out at this level and its effect on monotonic properties of alloy 2024 still remains not fully investigated.

2. Test stand and specimens

EN AW-2024 aluminum alloy in form T3511 was used in the tests. Bars with length of 3 m and diameter of 16 mm were prefabricated for making axisymmetric specimens. According to attestation, the material was hardened AlCu₄Mg, and the rod was manufactured by extrusion. The material chemical composition was: Si (0.13%), Fe (0.25%), Cu (4.4%), Mn (0.62%), Mg (1.7%), Cr (0.01%), Zn (0.08%), Ti (0.05%).

Specimens applied in monotonic tensile and creep tests were characterized by identical shape and dimensions. Gauge length and diameter dimensions were 13 mm and 6.5 mm, respectively. The gripped part of specimens was threaded, as dictated by the design of the creep testing machine (threaded pull rods).

Monotonic tensile tests and creep tests were conducted on a 4-column Kappa 100 SS creep testing machine from the Zwick/Roell with an electro-mechanical drive. An electric Maytec furnace with three heating zones, with a temperature range up to 900°C, controlled by universal Zwick/Roell controller was used for tests at elevated temperature. A device specially designed and made for measuring deformations was used (Tomczyk and Koniuszewski, 2017). This device allowed for measurement of specimen deformations at elevated temperature by means of any gauge (e.g. extensometer) serving for measurement of strains at room temperature. Axial extensometer (Epsilon 3542050M-50-ST) with a variable measuring base of 25/50 mm and a range of +25 mm and –5 mm was used in cooperation with the grip described above.

3. Results of tests

3.1. Monotonic tensile and creep-rupture tests for the material with no pre-deformation

In order to determine basic strength parameters of the material at elevated temperature (100°C, 200°C, 300°C) and room temperature (20°C), monotonic tensile tests were conducted on a series of three specimens at each temperature according to EN ISO 6892-1 (2016) and EN ISO 6892-2 (2011). Results in the form of averaged nominal (engineering) tensile curves and true curves $\sigma_1 = \sigma_1(\varepsilon_1)$ and $\sigma_{eq} = \sigma_{eq}(\varepsilon_{eq})$ are given in Fig. 1.

It should be added that true stress-strain curves were obtained on the basis of numerical calculations using the finite element method, since the average experimental relation between load and displacement of the gauge length was known. The MSC.Marc software package was used for simulations, while the procedure of curve determination was similar to the procedure described by Derpenski and Seweryn (2011). The elastic-plastic material model with isotropic hardening and the Huber-von Mises yield criterion was applied in that procedure. This made it possible to obtain principal stress and strain (σ_1, ε_1) as well as equivalent stress and strain ($\sigma_{eq}, \varepsilon_{eq}$) according to the Huber-von Mises hypothesis.

Average values of basic parameters, such as Young's modulus E , yield point σ_y , ultimate tensile strength σ_u , strain ε_u (corresponding to σ_u), strain at break ε_B are presented in Table 1. It should be noted that values σ_c and ε_c correspond to the maximum values of principal true stress σ_1 and strain ε_1 were obtained based on the true stress-strain curves.

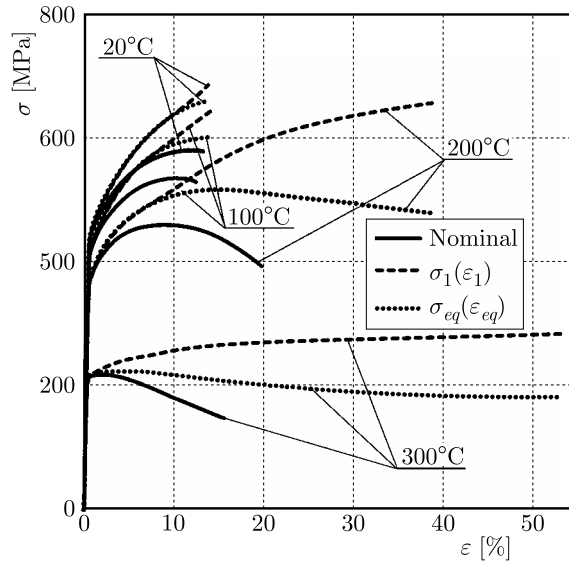


Fig. 1. Nominal (continuous line), actual $\sigma_1 = \sigma_1(\varepsilon_1)$ (dashed line) and $\sigma_{eq} = \sigma_{eq}(\varepsilon_{eq})$ (dotted line) monotonic tensile curves obtained at different temperatures for specimens without creep pre-deformation

Table 1. Values of strength parameters at various temperatures (based on nominal tensile curves) as well as the critical stress and strain value σ_c, ε_c (based on the true curve $\sigma_1 = \sigma_1(\varepsilon_1)$)

T [°C]	E [GPa]	σ_y [MPa]	σ_u [MPa]	σ_c [MPa]	ε_u [%]	ε_B [%]	ε_c [%]
20	74	447	580	686	12.1	13.3	13.8
100	71	418	536	647	10.3	12.7	14.5
200	70	372	460	657	9.1	19.8	38.7
300	56	214	219	283	2.1	17.0	52.9

Fracture surfaces of specimens subjected to tension at temperatures of 20°C and 100°C are essentially similar in nature (Fig. 2). Nevertheless, it is clearly visible that the fracture plane angle of orientation relative to the specimen axis is close to 45°, which suggests that shear stress has the main influence on the failure process. The fracture surface is smooth (with low roughness), however, at the highest magnification, remnants left behind by growing micro-voids and sheared bridges between them are visible. Damage initiation took place as a result of the maximum principal stress σ_1 occurrence exactly on the specimen axis.

Further, sudden development of damage based on final shearing of the bridges between voids was dictated by the action of the maximum shear stress. Numerous, unevenly distributed precipitates can be observed in dimples, and they are significantly responsible for the material hardening. The damage initiation process usually begins at the boundary between the matrix and the coarse precipitate (e.g. Li *et al.*, 2013).

Specimen fractures obtained in monotonic tensile tests at temperatures of 200°C and 300°C are completely different in nature (Fig. 3a). Here, two fracture planes are clearly visible. In the central part, the plane is perpendicular to the specimen axis and has a fibrous character with clearly visible dimples, which are remnants after voids that grew in the loading direction and were ruptured. This fracture plane is distinguished by high roughness. In the case of the fracture surface obtained at 200°C, this roughness is clearly lower than on the surface of the fracture obtained at 300°C. The second plane of failure is oriented at an angle of 45°-50° relative to the specimen axis, and its surface is visibly smoother than the previous surface. It links the central plane, corresponding to ductile fracture, with the free exterior surface of the specimen.

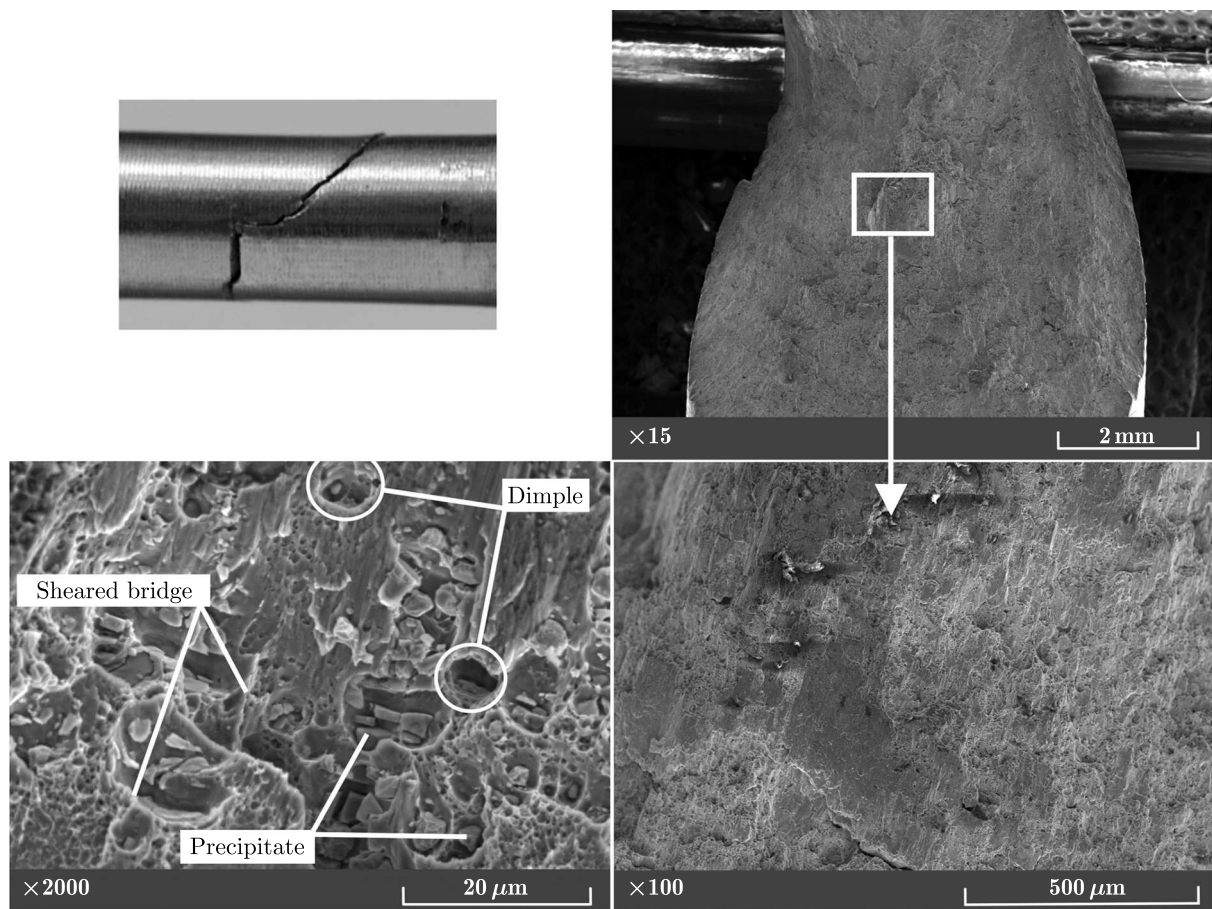


Fig. 2. Specimen fracture obtained in the monotonic tensile test at temperature 20°C

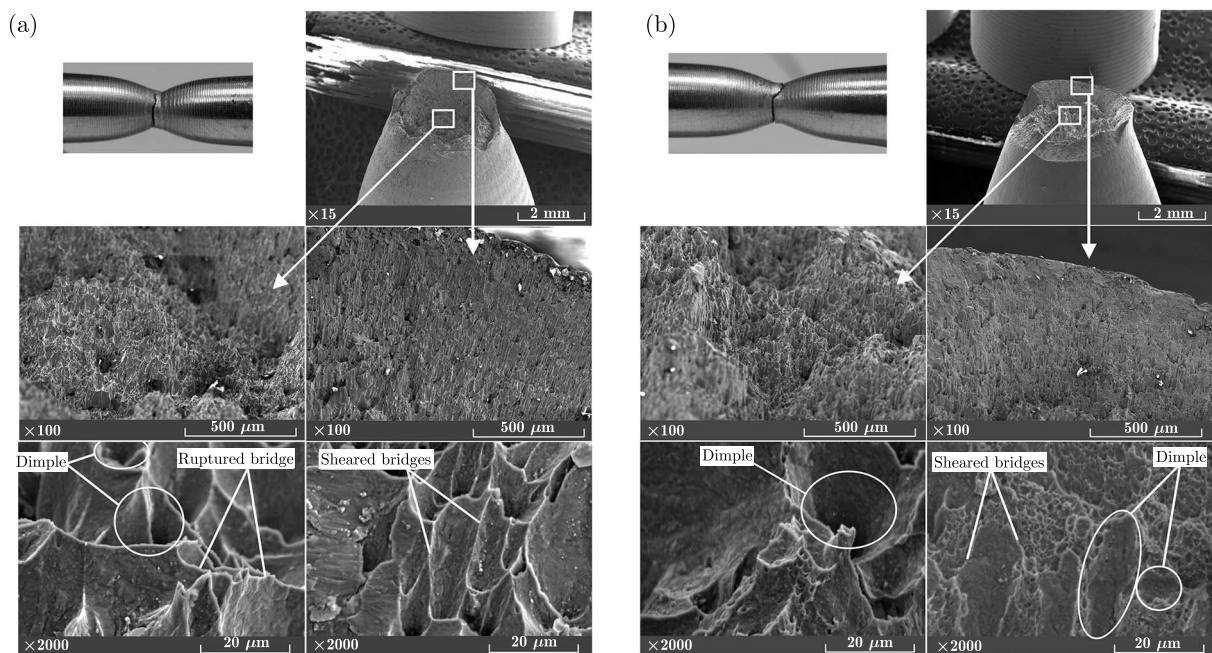


Fig. 3. Specimen fracture surfaces obtained in: (a) monotonic tensile test at a temperature of 300°C, (b) creep-rupture test at $T = 300^{\circ}\text{C}$ and with constant load $F = 3.06 \text{ kN}$

It occupies a much smaller area of the fracture surface than in the case of tension at 300°C. The fracture mechanism here was fundamentally different than in the case of temperatures of 20°C and 100°C. As a result of necking, the stress state changed from uniaxial to tri-axial with the maximum principal stress σ_1 clearly dominant on the specimen axis. That stress caused crack initiation on the plane perpendicular to the axis in the central part of the specimen cross section. Smaller voids were gradually joined and clearly deformed in the direction of σ_1 . Void deformations indicate that higher temperature produced greater deformation.

At the time at which the stress reached the critical value, successive bridges between the voids were ruptured. After this process, the material was suddenly sheared along planes of the maximum shear stress, ultimately causing formation of a fracture. The presence of fine precipitates can be observed at the bottom of pores.

The results obtained over the course of monotonic tensile tests made it possible to estimate loadings in creep tests at different elevated temperatures. At the temperature of 100°C a constant loading $F = 17.55$ kN was applied. At 200°C and 300°C, loadings $F = 9.26$ kN and $F = 3.06$ kN were applied respectively. The creep tests were conducted according to EN ISO 204 (2009). The tests were conducted for a series of four specimens at each temperature after which the results of these tests in the form of creep-rupture curves were averaged relative to time.

The fracture surface corresponding to creep-rupture tests at 200°C and 300°C (Fig. 3b) has a bi-planar nature, similarly as in the case of monotonic tension. However, the part of the surface perpendicular to the specimen axis, mainly related to normal plastic strain, occupies a much larger area in comparison to the shear plane. The fracture mechanism was similar to that observed in Fig. 3a, i.e. material rupturing first took place in the central area of the cross section followed by sudden shearing. The progression of the pore deformation process under the action of constant loading was much slower in comparison to monotonic tension at the same temperature. The much more deformed remnants (dimples) in the direction of the axis left behind after ruptured or sheared bridges between the pores, particularly visible in Fig. 3b, are indicative of this. The nature of fracture in Fig. 3b exhibit similarity to the post-creep fractures obtained by Li *et al.* (2013) for 2124 alloy. However, it must be noted that, in the cited paper, the creep tests were conducted at a temperature of 260°C and tensile stress of 120, 130 and 140 MPa. The fractures presented in this paper were obtained for 275 MPa and 200°C as well as 90 MPa and 300°C (Fig. 3b). The growth of voids due to the increase of loading during creep at constant temperature was demonstrated here. However, a similar effect can be achieved by e.g. increasing temperature in the creep process.

3.2. Monotonic tensile test for the material with pre-deformation

The level of strain for creep pre-deformation was determined on the basis of averaged creep-rupture curves. It was decided to adopt two different strain levels corresponding to the beginning of the secondary creep ε_s and a certain tertiary creep ε_t . This means that the process of preliminary creep in one series of specimens, at a given temperature and under a given loading, lasted until the strain ε_s was reached, and in the second series – until strain ε_t was reached. Unloading of the measuring base of specimens, after the set strain levels were reached, took place at a rate of 2 mm/min. The specimens were cooled at room temperature. ε_s and ε_t strain values could differ depending on temperature at which tests were conducted. In the case of creep at 100°C, $\varepsilon_s = 10\%$ and $\varepsilon_t = 15\%$ strain levels were applied. At 200°C and 300°C, levels $\varepsilon_s = 0.6\%$, $\varepsilon_t = 2.3\%$ and $\varepsilon_s = 0.4\%$, $\varepsilon_t = 2.3\%$ were applied respectively. Ultimately, two series of specimens pre-deformed in the creep process at a set temperature were obtained, and each series consisted of 3 specimens. They were subjected to monotonic tensile tests at room temperature in order to determine basic strength parameters. The values of basic strength parameters obtained on the basis of the nominal curves and the critical stress and strain values σ_c

and ε_c corresponding to the maximum σ_1 and ε_1 are given in Table 2. Figure 4 presents nominal (engineering) monotonic stress-strain curves obtained at room temperature for the specimens previously subjected to pre-deformation at different temperatures and for two different strain levels, as well as the true $\sigma_1 = \sigma_1(\varepsilon_1)$ and $\sigma_{eq} = \sigma_{eq}(\varepsilon_{eq})$ curves corresponding to them.

Table 2. Strength parameters obtained for each specimen subjected to preliminary creep and average values for both strain levels (based on the nominal tensile curves) as well as the critical stress and strain values σ_c , ε_c (based on the true curve $\sigma_1 = \sigma_1(\varepsilon_1)$)

T [°C]	ε_s [%]	ε_t [%]	E [GPa]	σ_y [MPa]	σ_u [MPa]	σ_c [MPa]	ε_u [%]	ε_B [%]	ε_c [%]
100	10	–	71.6	598	610	680	4.6	5.3	7.1
	–	15	72.1	635	640	673	2.7	2.7	3.5
200	0.6	–	74.1	475	550	716	7.9	13.9	20.8
	–	2.3	74.1	443	490	642	4.9	13.1	25.3
300	0.4	–	71.2	255	363	518	7.1	17.9	36.5
	–	2.3	72.6	186	316	380	8.7	13.1	15.2

Let us note that creep at 200°C and 300°C took place under lower loading than that corresponding to the yield point, and at 100°C – under a higher loading. Therefore, in the latter case, the hardening process related to crossing of the yield point and unloading of the specimen mostly dictated the material properties after the creep pre-deformation process. Thus, the significant increase of the offset yield stress compared to the original material can be observed, with a simultaneous decrease of total elongation (Fig. 4a). We can observe an interesting situation in the case of pre-deformation $\varepsilon_s = 0.6\%$ at a temperature of 200°C. The creep process, up to the aforementioned, with a relatively low strain value, caused hardening of the material in comparison to the original material, despite the high temperature. The offset yield point increased with simultaneous reduction of the ultimate tensile strength.

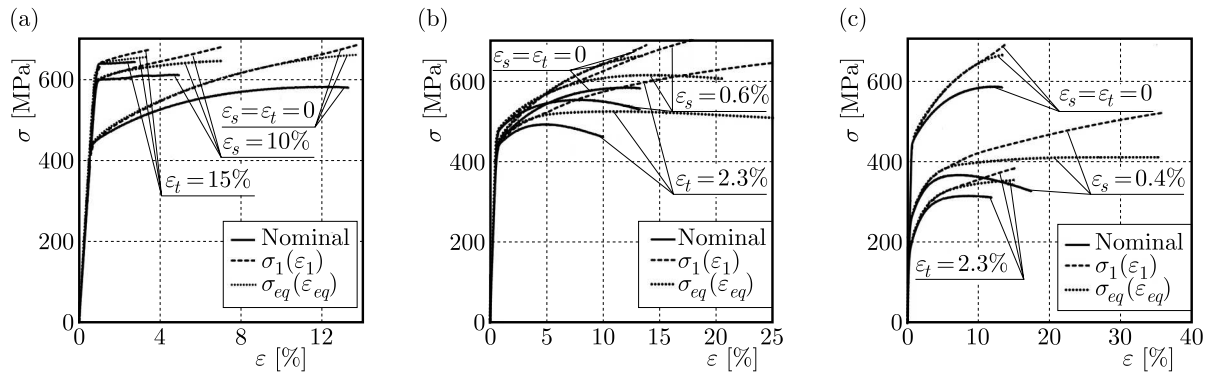


Fig. 4. Nominal (continuous line), actual $\sigma_1 = \sigma_1(\varepsilon_1)$ (dashed line) and $\sigma_{eq} = \sigma_{eq}(\varepsilon_{eq})$ (dotted line) monotonic tensile curves obtained for specimens subjected to creep pre-deformation at different temperatures and strain levels against the background of the tensile curve for specimens without pre-deformation at room temperature: (a) 100°C, (b) 200°C, (c) 300°C

The results of numerical simulations in the form of principal and equivalent stress and strain distributions in the specimen transverse plane of symmetry are presented in Fig. 5. They correspond to the situation at the instant at which the specimen ruptured and at which the critical stress and strain values were reached. Due to symmetry, distributions are presented for half of the tested specimen, i.e. for radius r changing from the axis to the exterior surface of the measuring base. In all cases, failure was determined by the principal stress and strain σ_1 and ε_1 , the value of which always exceeds the equivalent stress and strain in the central area of the cross section, which indicates the presence of a tri-axial stress and strain state. The principal stress

reaches its maximum values exactly on the specimen axis, while the equivalent stress reaches its minimum on the axis. It should be noted that the equivalent values reach their maximum earlier – before σ_1 and ε_1 reach the critical values.

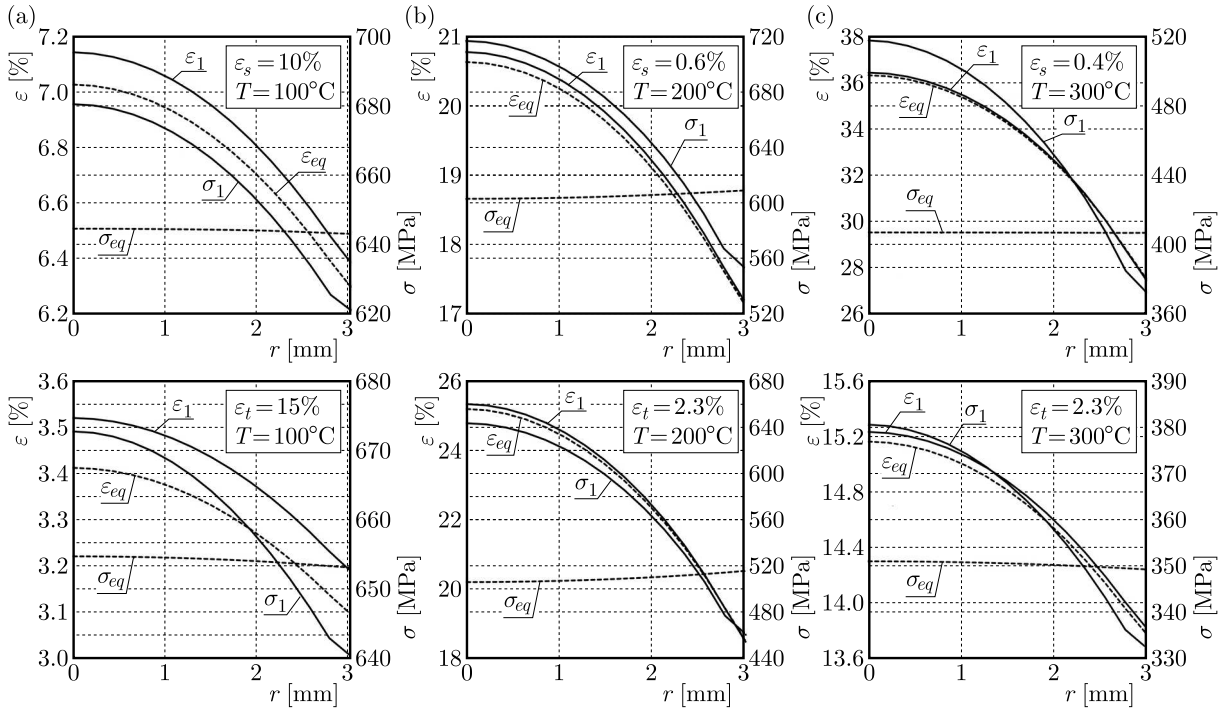


Fig. 5. Distributions of the equivalent stress and strain (dashed line) and the maximum principal stress and strain (continuous line) along the specimen transverse plane of symmetry obtained on the basis of numerical simulations of tensile tests of the material at room temperature with pre-deformation at temperatures: (a) 100°C, (b) 200°C, (c) 300°C

In the case of the fracture surface obtained in the creep-rupture test at 100°C, its clear similarity to fracture obtained in the monotonic tensile test at the same temperature can be observed. However, it must be noted that the above mentioned fracture surfaces are characterized by much greater roughness, which is mainly caused by the long-acting load exceeding the material yield point at the set temperature. The maximum shear stress ultimately caused fracture, as indicated by the orientation of the fracture plane. However, the damage was first initiated on the specimen axis as a result of the action of the principal stress. Numerous precipitates found in the remnants left behind after ruptured bridges between the pores in the central part of the cross section are indicative of this. They are not hidden as a result of closure of these remnants by sheared material.

Figures 6 and 7 present examples of fracture surfaces obtained in monotonic tensile tests of specimens (at room temperature) subjected to creep pre-deformation at different temperatures and under different levels of strain. The essential differences between fractures corresponding to tension with creep pre-deformation at 100°C (Fig. 6) and fractures of specimens without pre-deformation (Fig. 2) pertain to specimens with pre-deformation $\varepsilon_t = 15\%$, which is linked to significant hardening of the material. Here, the fracture surface is made up of two planes, where both are inclined at an identical angle to the specimen vertical axis of symmetry. The temperature at which the pre-deformation took place was too low to enable significant plastic deformation. This is indicated by the remnants left behind by ruptured bridges between the pores in the form of rather small dimples (Fig. 6). The area occupied by these dimples is very small, and in the case of pre-deformation at a level of $\varepsilon_s = 10\%$ – almost not visible.

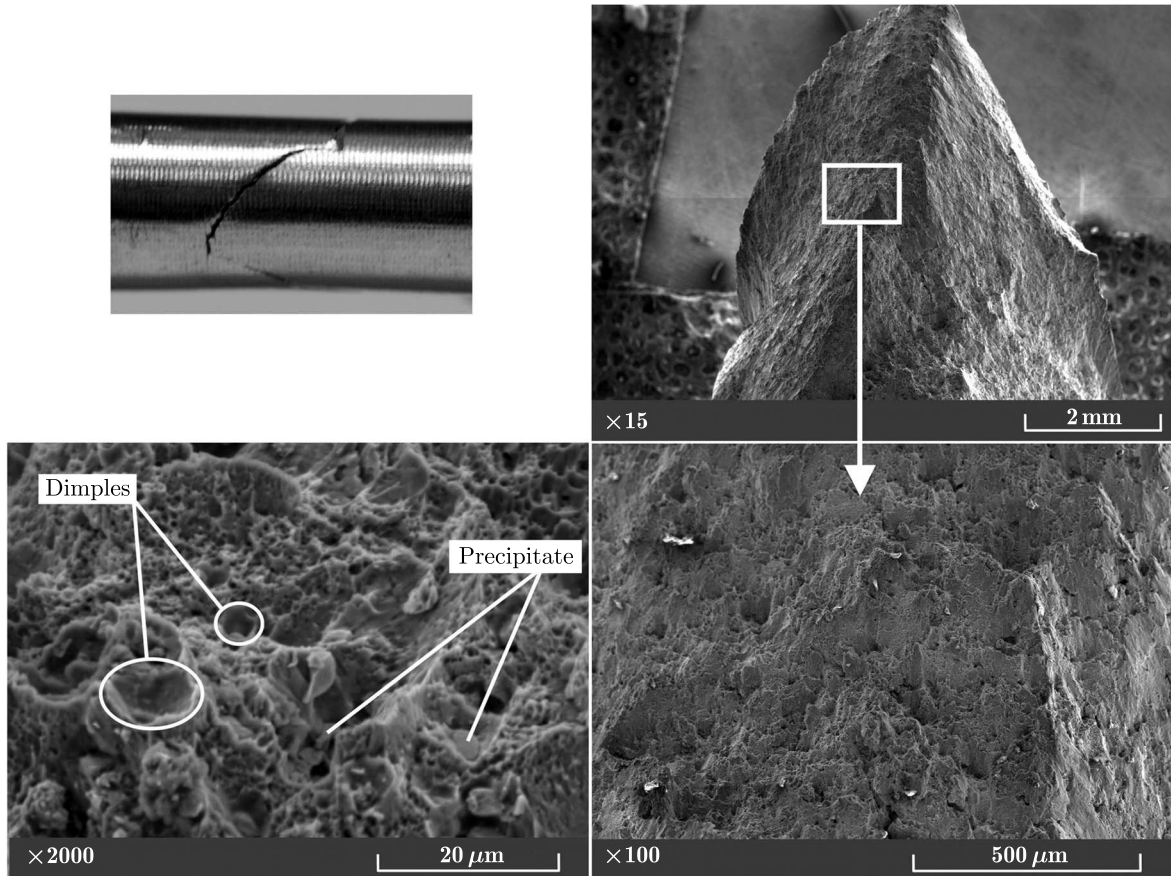


Fig. 6. Example of a fracture surface of the specimen with creep pre-deformation ($T=100^{\circ}\text{C}$, $F = 17.55\text{ kN}$, $\varepsilon_t = 15\%$) subjected to monotonic tension at room temperature

This may indicate that, in the case of high pre-deformations ($\varepsilon_t = 15\%$), the fracture process in the monotonic tensile test was initiated in the central part, after which sudden shearing of the material occurred immediately.

There are no significant differences between the fracture surfaces for the material with pre-deformation $\varepsilon_s = 0.4\%$ and $\varepsilon_t = 2.3\%$ at 300°C . There exist two planes: the first plane of crack initiation perpendicular to the axis of the specimen and the second plane of shearing (Fig. 7b). The share of the first plane in the fracture surface is much lower here than in the case of tension at 300°C (Fig. 3a). For both levels of strain, the voids were joined and clearly deformed in the direction of creep axial loading in the central part of the cross section. After unloading, the voids that were not ruptured took on a spherical shape once again and were ruptured during tension at room temperature, and so, without such strong strains.

The fracture process in the central part of the cross section preceded ultimate shearing of the specimen material. Pre-deformation $\varepsilon_s = 0.4\%$ caused a significant decrease in the yield stress and the critical stress, but a strong increase in strain at the moment of the specimen rupture (Fig. 4c). Pre-deformation $\varepsilon_t = 2.3\%$ at the same temperature resulted in an even stronger decrease in the yield stress and the critical stress. However, it induced significantly a less increase in strain at the moment of the specimen rupture – the material was thus significantly damaged.

For specimens with pre-deformation at 200°C , the level of pre-deformation decides about the character of fracture. Let us note that, for pre-deformation $\varepsilon_s = 0.6\%$, material hardening occurred first (compared to material without pre-deformation) and softening occurred later (Fig. 4b). No significant material deformation occurred during pre-deformation $\varepsilon_s = 0.6\%$ –

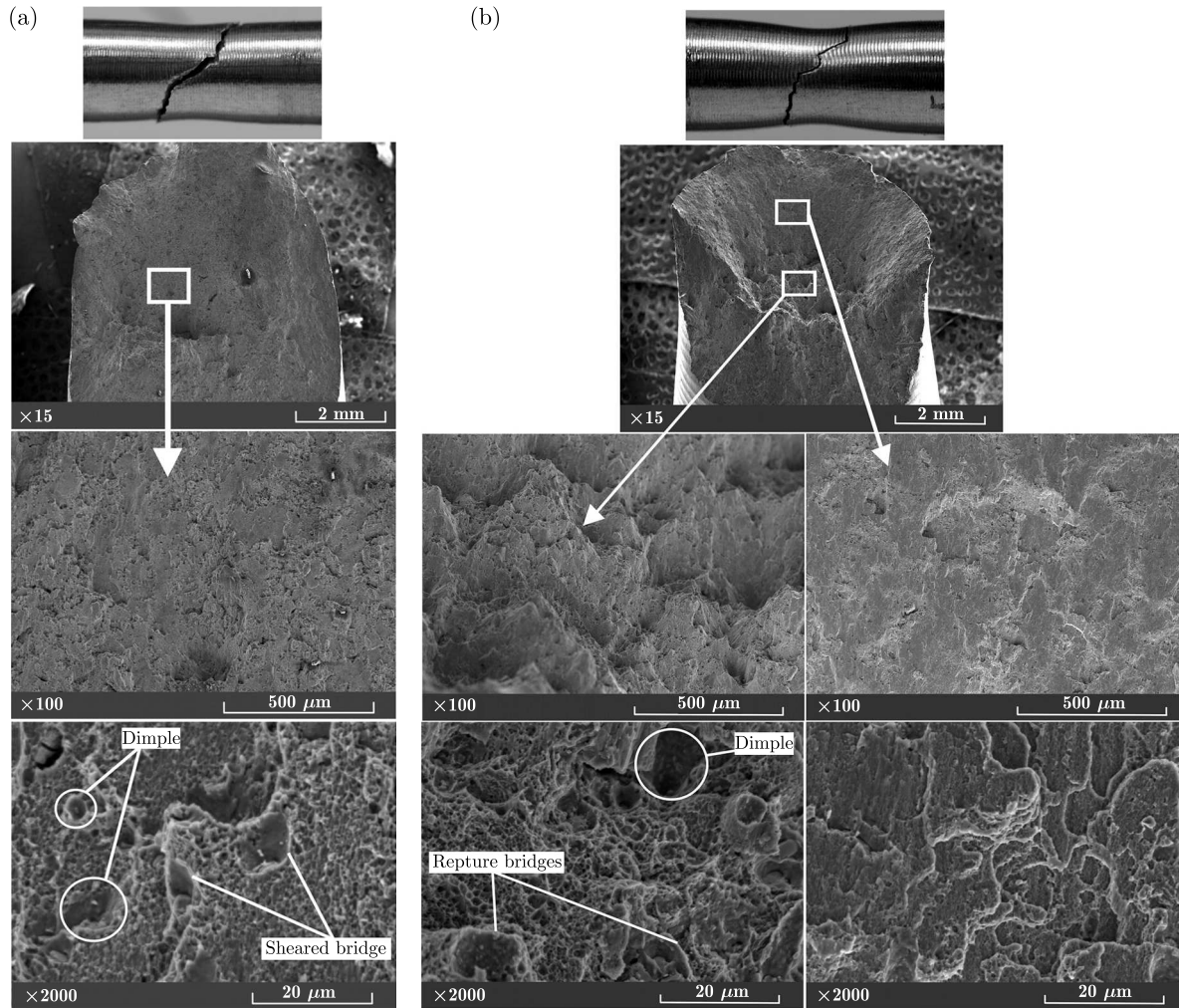


Fig. 7. Example of a fracture surface of the specimen with creep pre-deformation at: (a) $T = 200^{\circ}\text{C}$, $F = 9.26\text{ kN}$, $\varepsilon_s = 0.6\%$, (b) $T = 300^{\circ}\text{C}$, $F = 3.06\text{ kN}$, $\varepsilon_t = 2.3\%$ subjected to monotonic tension at room temperature

there were not many large voids, and their visibly sheared remnants had a spherical character (rather than longitudinal). Sparse precipitates could be observed. The absence of a large number of deep voids after pre-deformation caused the yield point to increase during the monotonic tension process. However, the later growth of these voids caused the material to be incapable of carrying shear stress, resulting in their easy and sudden shearing, which might caused reduction of the ultimate tensile strength. The fracture character was similar here to the fracture obtained in the tensile test of the material with no pre-deformation (Fig. 2).

It is worth emphasizing that the time for which the material is held at elevated temperature is very significant, and this time has also a significant impact on the values of strength parameters (see e.g. Ro *et al.*, 2006; Li *et al.*, 2010; Guo *et al.*, 2013). In the case of pre-deformation at 200°C , the time was differed significantly for $\varepsilon_s = 0.6\%$ (approx. 30 min) and $\varepsilon_t = 2.3\%$ (approx. 300 min). For higher pre-deformation ($\varepsilon_t = 2.3\%$) the fracture mechanism was very similar to the mechanism in specimens pre-deformed at 300°C .

It should be pointed out that fractures obtained for specimens with lower pre-deformation ε_s at 100°C and 200°C are characterized by the presence of a large number of small dimples – remnants left behind after small pores. In the case of greater pre-deformation ε_t at the same temperatures, smaller dimples occupy a significantly lesser area. A similar effect was observed in

the study by Lin *et al.* (2013b) when temperature was increased at the same stress or when the stress was increased at the same temperature over the course of pre-deformation of alloy 2024. A similar effect of the pore growth due to rise of stress in creep-rupture tests of alloy 2124 at a temperature of 260°C was also obtained by Li *et al.* (2013). The character of fracture in the case of specimens with pre-deformation at a temperature of 300°C does not exhibit significant differences in terms of the value of this pre-deformation. The plane of crack initiation perpendicular to the specimen axis and shear plane is clearly visible here. The share of the shear plane in the entire area of the fracture is significantly less than, e.g. in the case of tension at 300°C (Fig. 3a).

4. Summary

This paper presents results of monotonic tensile tests conducted at room temperature and elevated temperature as well as of creep tests conducted at elevated temperature on aluminum alloy EN-AW 2024. It also contains a comparison between monotonic tensile curves obtained for specimens without pre-deformation and with pre-deformation. Specimen fracture surfaces obtained in monotonic tensile and creep tests were also compared, and fundamental differences between them were indicated.

A clear decrease in basic strength parameters, such as Young's modulus, yield point and ultimate tensile strength, was observed with a temperature increase. While this reduction is slight at 100°C, the parameters drop significantly at 300°C. The offset yield point and ultimate tensile strength are reduced two-fold compared to the values corresponding to the room temperature. Specimen fracture surfaces obtained in tensile tests at elevated temperature clearly demonstrate that the material plastic properties increase with temperature growth.

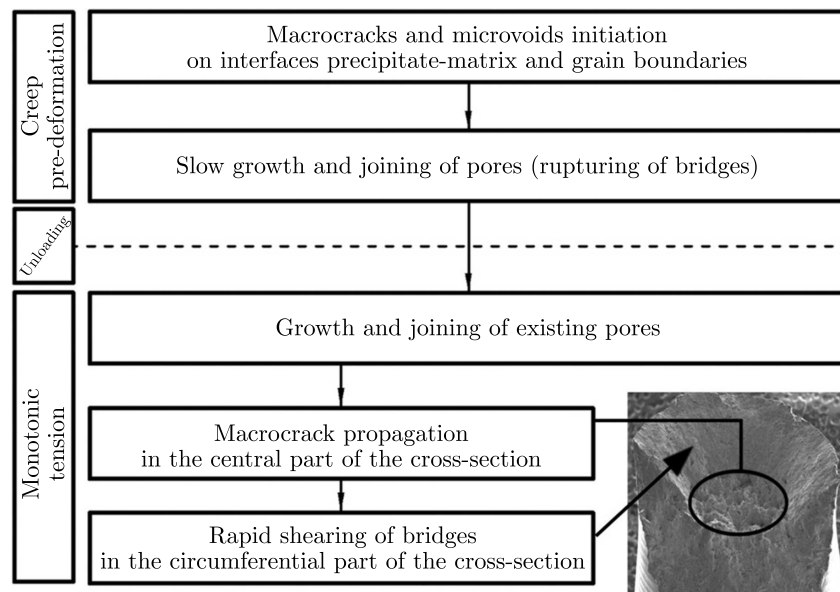


Fig. 8. Schematic representation of damage evolution and failure of the material

Fractographic analysis of the fracture surfaces proves that the following stages can be distinguished in the failure process (Fig. 8):

1. Damage initiation exactly on the specimen axis as a result of the action of maximum principal plastic stress or strain (or both simultaneously) during monotonic tensile or creep tests. This initiation occurs on the boundary between the matrix and precipitate, particularly when the latter has a coarse character. The precipitates visible in fracture surfaces prove this.

2. Growth and deformation of pores (damage).
3. Joining of pores together by rupturing bridges between them in the central part of the cross section (close to the axis of symmetry). The size of this area depends mostly on temperature and loading, but also on the duration of its action (during creep process).
4. Rapid shearing of the material close to the lateral surface of the specimen along the planes of maximum shear stress. On these planes, the precipitates may be hidden due to closure of the remnants (dimples) left behind after sheared bridges between the pores.

Analysis of the results allows one to observe two antagonistic processes. On the one hand, there occurs material hardening as a result of large plastic deformation and the migration and blocking of dislocations on grain boundaries associated with it. On the other hand, the material is weakened due to nucleation and growth of micro-voids as well as rupturing and shearing of bridges between them. Both mechanisms can be found in problems related to low speed wind turbine generators (see Introduction).

Strong pre-deformations at low temperatures result in a significant increase in the yield strength σ_y with a slight change in the critical stress σ_c . At the same time, the ductility of the material decreases, which is evidenced by a significant drop in the value of deformations at the moment of sample rupturing. Minor changes in σ_y and σ_c are observed at both values of strain (ε_s and ε_t) for the material with pre-deformation at higher temperature. There is also a strong increase in strain at the moment of specimen rupture. Low creep pre-deformation ε_s at high temperature 300°C causes a significant decrease in σ_y and σ_c with a simultaneous increase in strain at the moment of sample rupturing. On the other hand, significant pre-deformation ε_t at the same temperature causes an even greater decrease in σ_y and σ_c . The increase in deformation at the moment of rupture is significantly smaller, which indicates strong earlier damage of the material. Young's modulus does not change significantly due to pre-deformation at elevated temperature.

Creep pre-deformation performed at different temperatures makes it possible to shape the material strength properties. Selection of the proper parameters of this pre-deformation, such as temperature, stress and strain, provides the possibility of improving material characteristics.

Acknowledgement

The present paper was financially supported by the Ministry of Science and Higher Education of Poland (research project No. S/WM/4/2017) and realized at Bialystok University of Technology.

References

1. CHAKHERLOU T.N., AGHDAM A.B., AKBARI A., SAEEDI K., 2010, Analysis of cold expanded fastener holes subjected to short time creep: Finite element modelling and fatigue tests, *Materials and Design*, **31**, 2858-2866
2. CHEN J.F., ZHEN L., JIANG J.T., YANG L., SHAO W.Z., ZHANG B.Y., 2012, Microstructures and mechanical properties of age-formed 7050 aluminum alloy, *Materials Science and Engineering: A*, **539**, 115-123
3. DERPENSKI L., SEWERYN A., 2011, Experimental research into fracture of EN-AW 2024 and EN-AW 2007 aluminum alloy specimens with notches subjected to tension, *Experimental Mechanics*, **51**, 1075-1094
4. EN ISO 204, 2009, Metallic materials, uniaxial creep testing in tension: Method of test
5. EN ISO 6892-1, 2016, Metallic materials, tensile testing -Part 1: Method of test at room temperature
6. EN ISO 6892-2, 2011, Metallic materials, tensile testing -Part 2: Method of test at elevated temperature

7. GUO W., YANG M., ZHENG Y., ZHANG X., LI H., WEN X., ZHANG J., 2013, Influence of elastic tensile stress on aging process in an Al-Zn-Mg-Cu alloy, *Materials Letters*, **106**, 14-17
8. HAIGEN W., FUZHONG X., MINGPU W., 2017, Effect of ingot grain refinement on the tensile properties of 2024 Al alloy sheets, *Materials Science and Engineering: A*, **682**, 1-11
9. HO K.C., LIN J., DEAN T.A., 2004, Constitutive modelling of primary creep for age forming an aluminium alloy, *Journal of Materials Processing Technology*, **153-154**, 122-127
10. KARAKAŞ Ö., SZUSTA J., 2016, Monotonic and low cycle fatigue behaviour of 2024-T3 aluminium alloy between room temperature and 300°C for designing VAWT components, *Fatigue and Fracture of Engineering Materials and Structure*, **39**, 95-109
11. KOWALEWSKI Z.L., SZYMCZAK T., MACIEJEWSKI J., 2014, Material effects during monotonic-cyclic loading, *International Journal of Solids and Structures*, **51**, 740-753
12. KUMAR P., LEBLANC J., SHUKLA A., 2011, Effect of curvature on shock loading response of aluminum panels, [In:] *Dynamic Behavior of Materials*, Proulx T. (Ed.), Vol. 1, Springer, 369-374
13. LI C., WAN M., WU X.-D., HUANG L., 2010, Constitutive equations in creep of 7B04 aluminum alloys, *Materials Science and Engineering: A*, **527**, 3623-3629
14. LI L.-T., LIN Y.C., ZHOU H.-M., JIANG Y.-Q., 2013, Modeling the high temperature creep behaviors of 7075 and 2124 aluminum alloys by continuum damage mechanics model, *Computational Materials Science*, **73**, 72-78
15. LIN Y.C., JIANG Y.-Q., XIA Y.-C., ZHANG X.-C., ZHOU H.-M., DENG J., 2014, Effects of creep-aging processing on the corrosion resistance and mechanical properties of an Al-Cu-Mg alloy, *Materials Science and Engineering: A*, **605**, 192-202
16. LIN Y.C., XIA Y.-C., CHEN M.-S., JIANG Y.-Q., LI L.-T., 2013a, Modeling the creep behavior of 2024-T3 Al alloy, *Computational Materials Science*, **67**, 243-248
17. LIN Y.C., XIA Y.-C., JIANG Y.-Q., ZHOU H.-M., LI L.-T., 2013b, Precipitation hardening of 2024-T3 aluminum alloy during creep aging, *Materials Science and Engineering: A*, **565**, 420-429
18. LUMLEY R.N., MORTON A.J., POLMEAR I.J., 2002, Enhanced creep performance in an Al-Cu-Mg-Ag alloy through underageing, *Acta Materialia*, **50**, 3597-3608
19. NAIMI A., YOUSFI H., TRARI M., 2013, Influence of cold rolling degree and ageing treatments on the precipitation hardening of 2024 and 7075 alloys, *Mechanics of Time-Dependent Materials*, **17**, 285-296
20. RO Y.J., BEGLEY M.R., GANGLOFF R.P., AGNEW S.R., 2006, Effect of aging on scale-dependent plasticity in aluminum alloy 2024, *Materials Science and Engineering: A*, **435-436**, 333-342
21. SINGH A.K., GHOSH S., MULA S., 2016, Simultaneous improvement of strength, ductility and corrosion resistance of Al2024 alloy processed by cryoforging followed by ageing, *Materials Science and Engineering: A*, **651**, 774-785
22. SZUSTA J., SEWERYN A., 2017, Experimental study of the low-cycle fatigue life under multiaxial loading of aluminum alloy EN AW-2024-T3 at elevated temperatures, *International Journal of Fatigue*, **96**, 28-42
23. TOMCZYK A., KONIUSZEWSKI R., 2017, *Construction of a System for Measuring Sample Elongations at Elevated Temperatures Using Devices Intended for Work at Room Temperature* (in Polish), Patent No. PL 68955 Y1
24. WANG H., YI Y., HUANG S., 2016, Influence of pre-deformation and subsequent ageing on the hardening behavior and microstructure of 2219 aluminum alloy forgings, *Journal of Alloys and Compounds*, **685**, 941-948
25. WANG Y.G., JIANG Z.G., WANG L.L., 2013, Dynamic tensile fracture behaviours of selected aluminum alloys under various loading conditions, *Strain*, **49**, 335-347

26. YANG Y., ZHAN L., MA Q., FENG J., LI X., 2016, Effect of pre-deformation on creep age forming of AA2219 plate: Springback, microstructures and mechanical properties, *Journal of Materials Processing Technology*, **229**, 697-702
27. YANG Y., ZHAN L., SHENA R., YIN X., LI X., LI W., HUANG M., HE D., 2017, Effect of pre-deformation on creep age forming of 2219 aluminum alloy: Experimental and constitutive modeling, *Materials Science and Engineering: A*, **683**, 227-235
28. ZHAN L., LIN J., DEAN T.A., HUANG M., 2011, Experimental studies and constitutive modelling of the hardening of aluminium alloy 7055 under creep age forming conditions, *International Journal of Mechanical Sciences*, **53**, 595-605
29. ZHANG J., DENG Y., ZHANG X., 2013, Constitutive modeling for creep age forming of heat-treatable strengthening aluminum alloys containing plate or rod shaped precipitates, *Materials Science and Engineering: A*, **563**, 8-15
30. ZHAO Y.L., YANG Z.Q., ZHANG Z., SU G.Y., MA X.L., 2013, Double-peak age strengthening of cold-worked 2024 aluminum alloy, *Acta Materialia*, **61**, 1624-1638

Manuscript received January 29, 2018; accepted for print March 6, 2018

FREE VIBRATIONAL ANALYSIS OF RECTANGULAR DUCTS WITH DIFFERENT JOINT CONDITIONS

NAGARAJA JADE, B. VENKATESHAM

Indian Institute of Technology Hyderabad, Department of Mechanical and Aerospace Engineering, Telangana, India
e-mail: me12p1002@iith.ac.in; venkatesham@iith.ac.in

Rectangular ducts are fabricated using thin sheets of a metal with different joint conditions. Due to the presence of these joints, ducts deviate from their assumptive ideal shapes. The objective of the present work is to study the effect of different joint conditions and wall thickness on dynamic characteristics of the ducts. Experimental Modal Analysis (EMA) is performed on three rectangular ducts of different joint types. Numerical Modal Analysis (NMA) is also performed by considering that the ducts are of ideal rectangular shape (without joint condition). Correlation analysis is performed between EMA and NMA in terms of Modal Assurance Criteria (MAC), Relative Frequency Difference (RFD) plots and auto-MAC. It is observed that natural frequencies are in good agreement but there is a discrepancy in mode shapes.

Keywords: rectangular duct, duct joint, experimental modal analysis, modal assurance criteria

1. Introduction

Dynamic characteristics such as natural frequencies, mode shapes and damping factors of an engineering structure are determined by modal analysis, either analytically, numerically or experimentally (Ewins, 2000a). Finite Element Analysis (FEA) is a quick and easy way to know dynamic characteristics of any structure, but determination of its damping parameters is difficult. Another method is using the analytical technique for solving mathematical models which represent the actual structure. Experimental Modal Analysis (EMA) is most common and effective method to determine, improve and optimize dynamic characteristics of an engineering structure (Ewins, 2000a). The analytical and FEA models can be verified using EMA. Kennedy and Pancu (1947) first proposed the most significant method of EMA before Fast Fourier Transforms (FFT) was invented. Fu and He (2001) provided a detailed theory of analytical and experimental modal analysis to characterize the dynamic behavior of any structure. Significant advances in experimental techniques enhanced the modeling of a structure and determining its dynamic properties. Experimental results can be used as reference (i) to modify the existing structure and to optimize the structure design by an iteration process, (ii) validate analytical models in order to refine future designs (Maia, 1988).

Prior to the actual modal test, it is essential to identify the optimal number, locations of excitation and the response measurement points to acquire all the modes excited within the interested frequency range. In the literature, few researchers proposed techniques for calculating the optimum number and position of measurements for the modal test based on Frequency Response Functions (FRF) (Schwarz *et al.*, 2002) and finite element analysis (Linehan and Napolitano, 2012). Similarly, it is important to choose an apt excitation method, as the influence of each mode on the overall response of the structure depends on the type of the excitation. Shaker and impact hammer are the most common types of excitations. Dynamic characteristics are extracted from the measured FRF's using curve fitting methods. Selection of the curve fitting techniques

is important in extracting dynamic characteristics from the measured time domain or frequency domain data (Maia, 1988; Ibrahim, 1999). In this regard, different algorithms are developed, which are based on Single-Degree of Freedom (SDOF) and Multi-Degree of Freedom (MDOF) methods (Brandon and Cowley, 1983; Maia and Silva, 1997). The modal vectors obtained from experimental measurements are compared using numerical modal vectors by correlation analysis, in terms of the Modal Assurance Criteria (MAC) plot. Allemang (1999) and Ewins (2000b) discussed various existing methods to perform systematic comparison and correlation between two sets of vibration data, namely numerical and experimental data.

Different analytical methods are proposed in the literature for calculating natural frequencies and mode shapes of rectangular and circular ducts with different axial boundary conditions (Blevins, 1979; Lee, 1993; Chavan and Venkatesham, 2015). Majorly in the literature, an ideal rectangular duct geometry is considered in analytical and numerical studies. However, practical ducts are fabricated with different joint conditions. Hence, it is important to study the effect of these joints on dynamic characteristics. Xiao *et al.* (2011) studied the effect of variation in geometry, boundary conditions and material properties on the vibration characteristics of the cylinder. Zaman *et al.* (2013) discussed the effect of bolted joints on dynamic characteristics of the beam and frame structures. They showed that natural frequencies are varied due to the presence of joints. Adequate literature is unavailable to show the joint effect and geometric distortion on the dynamic characteristics.

The current paper discusses the effect of joint conditions (used for fabrication) and wall thickness on dynamic characteristics of a duct, experimentally. To understand the effect of these parameters, the present study considers three different ducts which differ mainly by the type of joints (such as Pittsburgh lock joint, welded joint and adhesive joint) used in fabrication. Ducts with different wall thickness are considered to study the modal density effect. In the present paper, Section 2 describes theoretical background for estimating the dynamic characteristics and correlation analysis. Pre-test analysis, the experimental test setup, modal test procedure and numerical modal analysis are explained in Section 3. In Section 4, experimental and numerical modal analysis results are discussed while in Section 5 conclusions are presented.

2. Theoretical background

This Section provides a brief theoretical explanation about the estimation of dynamic characteristics such as natural frequencies and mode shapes of a structure. It also outlines the available techniques to perform the correlation of experimental and numerical results after modal analysis. Here, dynamic characteristics can also be referred as modal parameters.

2.1. Natural frequencies and mode shapes

The conventional hypothesis for calculating dynamic characteristics of a structure is using the equation of motion. For free vibration analysis of a multi-degree freedom system, this is written in terms of mass, stiffness and damping matrices as follows (Blevins, 1979)

$$\mathbf{M}_{N \times N} \ddot{\mathbf{x}}_{N \times 1} + \mathbf{C}_{N \times N} \dot{\mathbf{x}}_{N \times 1} + \mathbf{K}_{N \times N} \mathbf{x}_{N \times 1} = \mathbf{0} \quad (2.1)$$

where N is the number of degrees of freedom (DOF) in the system, \mathbf{M} , \mathbf{C} and \mathbf{K} designate the matrices of mass, damping, and stiffness respectively. $\ddot{\mathbf{x}}$, $\dot{\mathbf{x}}$ and \mathbf{x} are the second, first and zeroth derivatives of system displacements. Solving Eq. (2.1), which is similar to the general eigenvalue problem, results in N eigenvalues (natural frequencies) and N eigenvectors (mode shapes)

$$\lambda_i = -\xi_i \omega_i + j \omega_i \sqrt{1 - \xi_i^2} \quad (2.2)$$

where λ_i is the i -th pole of the FRF, ω_i is the i -th circular natural frequency of the system and ξ_i is the damping ratio for the i -th natural frequency of the system.

2.1.1. Numerical modal analysis (NMA) approach

Equation (2.1) can be solved using an analytical and FEA method. Calculation of the mass and stiffness matrix for simple geometry is straightforward, but for complex geometries, FEA is an appropriate method. In this method, continuous geometry is discretized with the finite number of elements. So, it is an approximation to infinite degrees of freedom system with finite degrees. This assumption leads to discretized equations which can be solved using different numerical methods for eigenvalues and eigenvectors. For this numerical analysis, convergence study is required for accurate result predictions. This methodology is well established in the literature and a good number of commercial softwares are available in the market. The prediction analysis can be referred to as numerical modal analysis in this paper.

2.1.2. Experimental modal analysis (EMA) approach

In the EMA approach, dynamic characteristics of a structure are estimated using measured frequency response functions (FRF). These FRFs can be obtained by exciting the structure and measuring the system inputs and outputs at various positions on the structure. There are mainly three important steps involved for performing EMA, namely, establishing the measurement set-up, acquiring the data and extracting the modal parameters. The detailed procedure for the experimental test setup and extraction of natural frequencies and mode shapes is given in Section 3.

2.2. Modal assurance criteria

There are different methods available for performing the correlation analysis of EMA and NMA results (FEA analysis). The frequently used method is the modal assurance criterion (MAC) plot. It compares the EMA vector and FEA vector. MAC is a scalar quantity and it varies between 0 and 1. If two vectors are the same, then MAC value is 1. Generally, MAC value of 0.6 and above is considered as acceptable (Vacher *et al.*, 2010).

If Φ_i^{EMA} is the modal vector from EMA and Φ_j^{FEM} is from FEA, then MAC is defined as

$$MAC_{ij} = \frac{|\Phi_i^{EMA} \Phi_j^{FEM}|^2}{(\Phi_i^{EMA} \Phi_i^{EMA})(\Phi_j^{FEM} \Phi_j^{FEM})} \quad (2.3)$$

where Φ is the modal vector, i and j are the mode numbers of the experimental and numerical results, respectively.

2.3. Relative frequency difference

Relative Frequency Difference (RFD) is a simple plot which calculates the RFD between two different natural frequency sets. RFD values should be as low as possible, typically, an error of 10% is acceptable. Higher values are observed while moving away from the diagonal elements (Ewins, 2000b). The acceptable error may vary for different types of test structures and testing methods.

If f_e^i is the experimental natural frequency of i -th mode and f_n^j is the numerical natural frequency of j -th mode, then RFD is given as

$$RFD_{ij} = \frac{f_n^j - f_e^i}{f_e^i} \quad (2.4)$$

2.4. Drive point residue

Drive Point Residue (DPR) can be specified as equivalent to modal participation factors, and DPR measures how well each mode is excited or its participation in the overall response of the structure at a chosen driving point. The definition of DPR for mode k and mode i is given by Allemang (1999)

$$DPR_k(i) = \frac{\Phi_{ik}^2}{2m_k\omega_k} \quad (2.5)$$

where Φ is the mode shape (modal vector), ω is the circular natural frequency, m is the modal mass. The degrees of freedom (DOF) with the maximum average DPR for chosen mode shapes are considered to be a better excitation DOFs for the interesting set of target modes.

3. Experimental setup and numerical analysis

The present Section discusses the pre-test analysis, setup and procedure for experimental and numerical modal analysis. Firstly, specifications such as dimensions, type of the joint for the fabrication and material properties of the different ducts are discussed. Three different types of rectangular ducts are considered in the analysis as shown in Fig. 1 are as follows:

Case 1. Duct with Pittsburgh lock joint (Duct 1)

In this configuration, the rectangular sheet of mild steel is bent at three corners, and the edges are joined using Pittsburgh locking mechanism. Dimensions of the duct is: $0.3\text{ m} \times 0.4\text{ m} \times 1.2\text{ m}$ with 20 gauge ($\sim 1\text{ mm}$). Material properties are: Young's modulus E is 200 GPa, Poisson's ratio μ is 0.3 and density is 7850 kg/m^3 .

Case 2. Duct with welded joints at four edges (Duct 2)

The duct is fabricated by welding joints at four right angle corners of individual plates. The arc welding technique is used for fabrication. Two pairs of plates with dimensions $0.3\text{ m} \times 1.5\text{ m}$ and $0.4\text{ m} \times 1.5\text{ m}$ are used. The overall dimensions of the duct are: $0.3\text{ m} \times 0.4\text{ m} \times 1.5\text{ m}$ with 10 gauge ($\sim 3\text{ mm}$). Duct material properties are: Young's modulus E is 200 GPa, Poisson's ratio μ is 0.3 and density is 7850 kg/m^3 .

Case 3. Duct with adhesive joint (Duct 3)

In this configuration, to fabricate a duct closer to an ideal rectangular shape, an acrylic sheet with the smooth plane surface is used. The individual plates are joined by an adhesive joint. Cyanoacrylate adhesive is used which establishes strong bond and smooth connectivity between the plates. The overall dimensions of the duct are: $0.206\text{ m} \times 0.258\text{ m} \times 0.9\text{ m}$ with 4 gauge ($\sim 5\text{ mm}$). The material properties are: Young's modulus E is 3.2 GPa. Poisson's ratio μ is 0.4, and density is 1100 kg/m^3 .

3.1. Numerical modal analysis

Numerical modal analysis is performed on all duct cases using commercial software (ANSYS) to calculate natural frequencies and mode shapes of the ducts. However, the description is provided for Case 1 only since a similar procedure applies to all cases. Rectangular duct of dimensions $0.3\text{ m} \times 0.4\text{ m} \times 1.2\text{ m}$ with wall thickness of 1 mm is modelled (as ideal duct i.e. without joint condition) and meshed using SHELL 63 elements. An element size of 0.005 m is chosen for meshing based on convergence study. The simply supported boundary condition is applied at

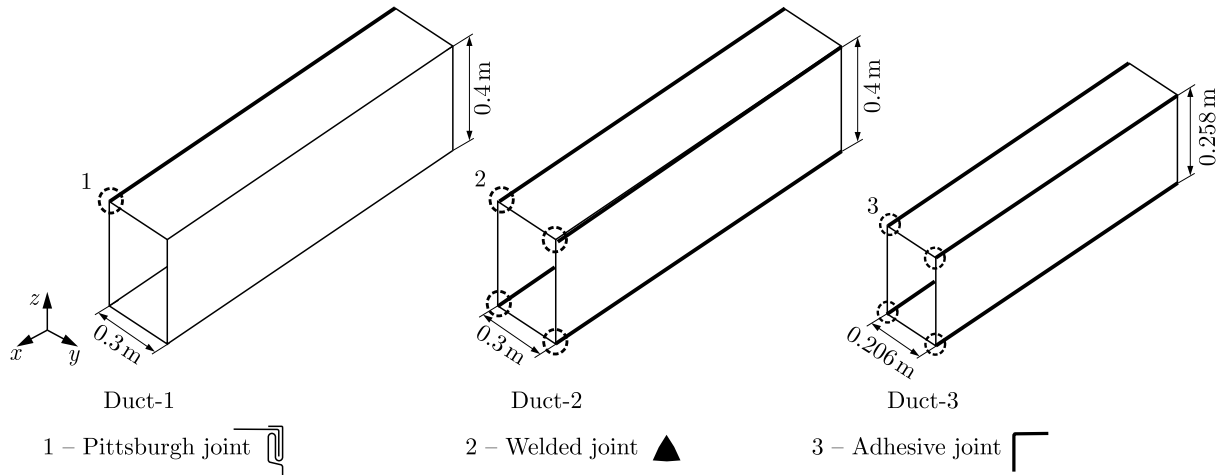


Fig. 1. Duct configurations with different joint conditions used in the experimental modal analysis

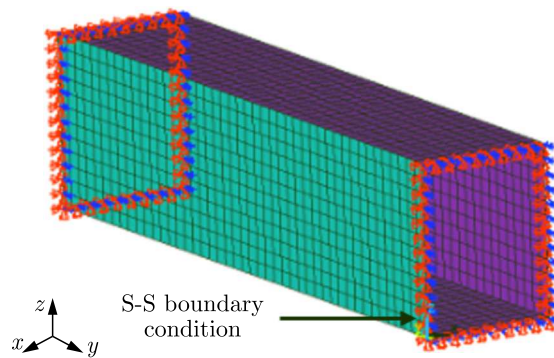


Fig. 2. Finite Element Model of a rectangular duct with simply supported boundary conditions

both ends of the duct. Figure 2 shows the meshed model with boundary conditions of the duct structure.

Mild steel properties such as: Young's modulus 200 GPa, density 7850 kg/m³, Poisson's ratio 0.3 and structural damping ratio of 0.01 are applied to the duct structure. Numerical modal analysis is performed to calculate the modal parameters up to 200 Hz frequencies. These parameters are used for pre-test analysis and also for correlation with EMA results.

3.2. Pre-test analysis

Preceding to the EMA, a pre-test is performed to find an appropriate reference point and response locations to mount the accelerometers. Thus, accurate structural modal parameters can be captured from modal test. This analysis is done for all cases within the interested frequency range of 10-200 Hz. The results are given for Case 1 only, as shown in Fig. 3, which indicates the location, number of excitations and response measurement points. Figure 3a shows that nodal point numbers, 128 with $+x$ -direction and 84 with $+z$ -direction are suitable DOFs for excitation in the experimental modal test. The locations of these points are $(x = 0.3, y = 0.1, z = 0.24)$ and $(x = 0.18, y = 0.5, z = 0.4)$ as shown in Fig. 3b. Here, due to closely spaced modes, 160 response measurement points are considered to efficiently characterize individual mode shapes as shown in Fig. 3c.

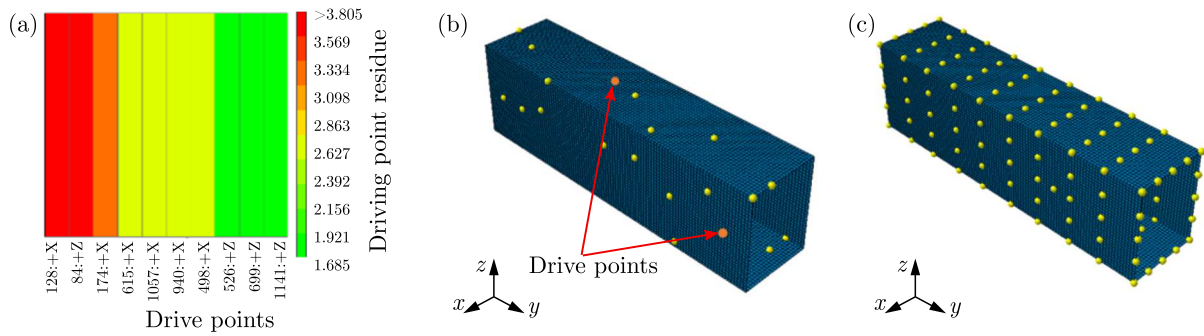


Fig. 3. Pre-test analysis: (a) drive point residue, (b) drive points to excite the structure, (c) response measurement points highlighted with dots

3.3. Experimental test setup

Preparation of measurement set-up involves preparation of boundary conditions, selection of the excitation method, type of transducers and measurement locations. EMA is performed on ducts in Case 1 and Case 2 with simply supported (S-S) boundary condition (BC) and Case 3 with free-free (F-F) BC as shown in Fig. 4. The S-S condition is achieved by making the contact point with duct walls at the front and rear portion of the duct. Steel balls are inserted into the rectangular frames to make them as a point of contact with the duct at the front and rear cross sections. The F-F boundary condition is achieved by suspending the duct with flexible bungee ropes.

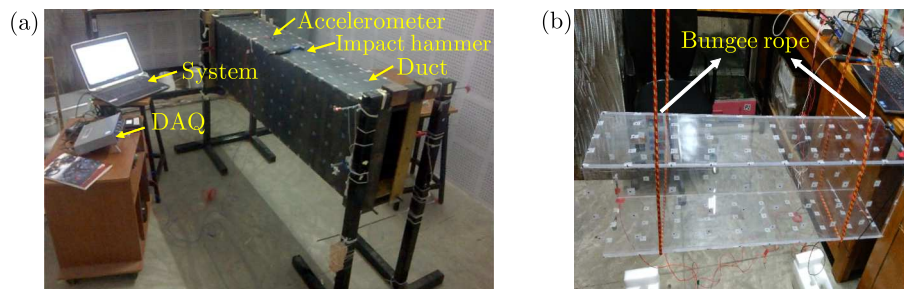


Fig. 4. EMA test setup: (a) simply supported boundary conditions, (b) free-free boundary condition

The modal test is performed by the roving hammer method. As the reciprocity principle holds good, the drive points obtained from pre-test analysis are used as response points. High sensitivity, lightweight tri-axial and uni-axial accelerometers of IEPE type are used to capture the vibration response. Weight of tri- and uni-axial sensors are 3 and 10 grams, respectively. An impact hammer of IEPE type with 100 gram head weight is used for excitation in order to induce vibrations in the structure. Once the measurement set-up is established, FRFs are measured with appropriate settings such as sampling frequency, bandwidth, number of samples and windowing function. It is important to verify the quality of acquiring data to ensure consistent measurements by observing the input excitation, coherence and FRFs. The measured FRFs are used to extract modal parameters of the duct. There are several methods to extract modal parameters in both the time domain and frequency domain as mentioned in Section 1. Multivariate Mode Indicator Function (MvMIF) is used for extracting modal parameters. Selection of poles is verified by comparing the measured drive point FRF and synthesized MvMIF curve. Figure 5 shows the stability diagram for multi-degree of freedom (MDOF) analysis to select poles and vectors. Selected stabilized poles are indicated by solid squares.

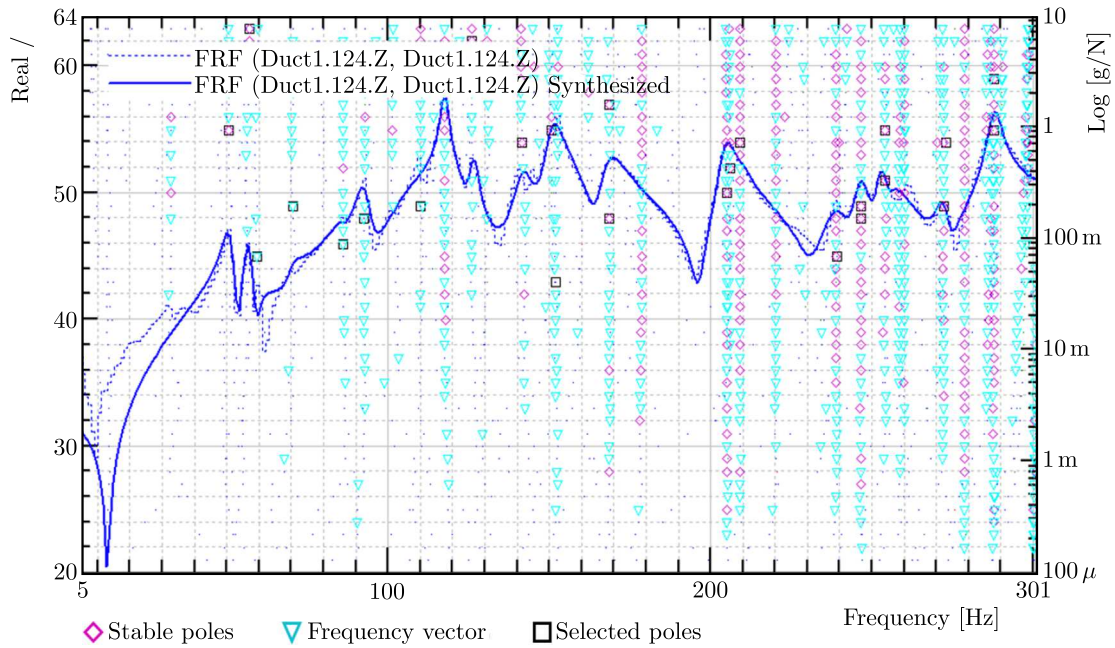


Fig. 5. Stability diagram for MDOF analysis of the duct as a function of frequency

4. Results and discussion

Experimental and numerical modal analysis results corresponding to all three ducts cases are discussed here. As a primary step, auto-MAC analysis is performed. Natural frequencies obtained from the experimental and numerical analysis are compared in the form of tables and RFD plots. Next, mode shapes are compared by visual inspection and correlation analysis in terms of MAC values.

4.1. Auto-MAC correlation

Auto-correlation analysis is performed for experimental mode shapes to (i) verify that a sufficient number and location of measurements are chosen for performing the model test and (ii) determine the correlation of individual modes with other modes within the interested frequency range (Linehan and Napolitano, 2012). Auto-MAC plots are shown in Fig. 6 for three cases (Ducts 1-3). The auto-MAC matrix is almost diagonal because the individual modal vector is orthogonal to other modal vectors.

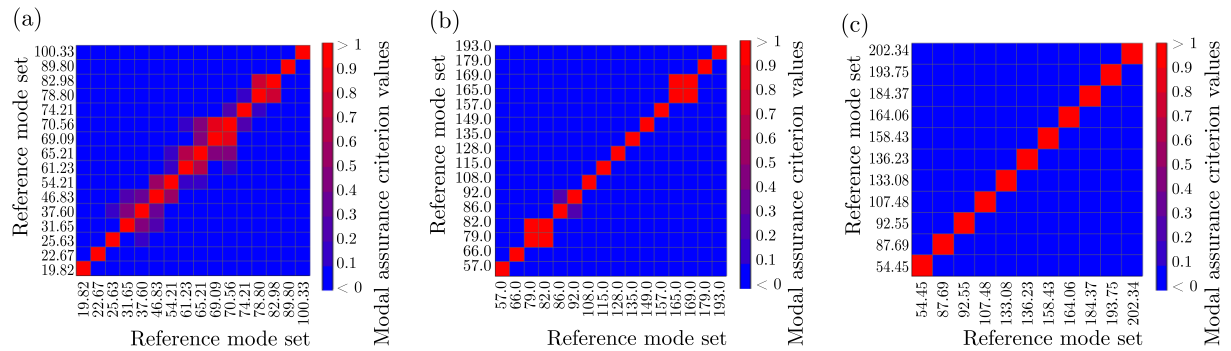


Fig. 6. Auto-MAC plots of experimental modal analysis results for all three ducts cases

From the auto-MAC plot of Case 1, it is observed that some individual modes are correlated with multiple modes. This is due to close spacing of modes, which leads to poor MAC values.

For example, mode 4 is correlated with modes 5, 6 and mode 10 with modes 9, 11. In Case 2, most of the off-diagonal MAC values are very low except for modes 3, 4 and modes 14, 15. This is due to symmetric modes and existence of welded joints. Auto-MAC plot in Case 3 is perfectly diagonal.

4.2. Comparison of natural frequencies

Analytical natural frequencies for Duct 1 and Duct 2 are calculated using the analytical models available in literature (Chavan *et al.*, 2015). Comparison of experimental, numerical and analytical natural frequencies for Duct 1 and Duct 2 is shown in Table 1. It is observed that analytical and numerical results are in good agreement and match well with experimental results with less than a 10% error. However, in Duct 1, modes 5, 8 and 10 are not captured in EMA due to higher modal density and the symmetric condition of duct geometry (as the repeated modes are difficult to be obtained from an experiment). Similarly, mode 9 in Duct 2 case.

Table 1. Comparison of natural frequencies for Duct 1 and Duct 2

Mode No.	Duct 1 Natural frequencies [Hz]			Duct 2 Natural frequencies [Hz]		
	Experimental	Numerical	Analytical	Experimental	Numerical	Analytical
1	19.82	20.64	20.69	57.00	58.71	58.79
2	22.67	25.52	25.58	66.00	67.77	67.91
3	25.63	26.85	27.07	79.00	76.96	77.87
4	31.65	30.70	30.91	82.00	83.05	83.27
5	–	33.77	33.85	86.00	84.12	84.84
6	37.6	37.75	37.97	92.00	96.66	97.40
7	41.12	40.03	40.24	108.00	104.66	105.00
8	–	44.53	44.74	115.00	115.08	116.10
9	46.83	45.44	45.54	–	115.53	116.37
10	–	48.39	48.62	128.00	123.71	124.45

Table 2 shows a comparison of natural frequencies obtained from the experimental modal test and predicted by numerical analysis for Duct 3. It shows that the predicted frequencies are well captured by the experimental modal test with less than a 5% error.

Table 2. Comparison of natural frequencies for Duct 3

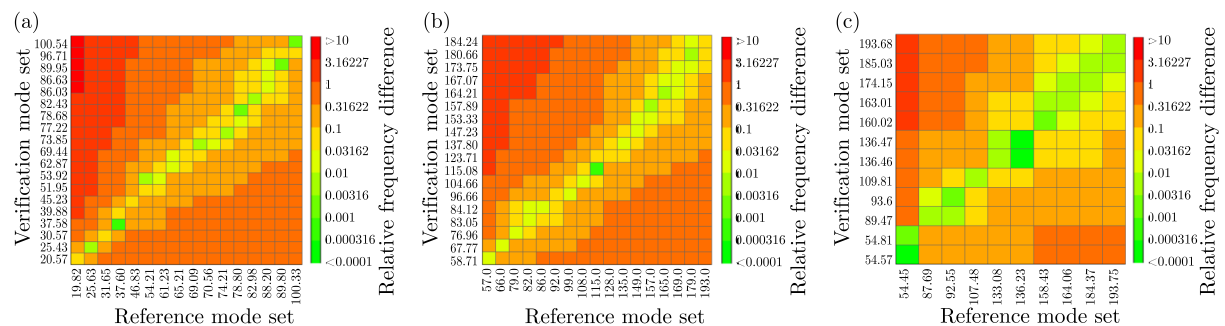
Mode No.	Natural frequencies [Hz]		Mode No.	Natural frequencies [Hz]	
	Experimental	Numerical		Experimental	Numerical
1	54.45	54.57	6	133.08	136.46
2	–	54.81	7	136.23	136.47
3	87.69	89.47	8	158.43	160.02
4	92.55	93.60	9	159.37	160.79
5	107.48	109.81	10	164.06	163.01

Numerical modal analysis is performed for Duct 1 with different thickness and compared with the experimental results as shown in Table 3. It is observed that the experimental results are close to the numerical results of duct with 1 mm thickness. It can be noticed (from Table 3) that as thickness of the duct wall increases (from 1 mm to 3 mm), the natural frequency also increases. It indicates that the modes are well separated. The similar behaviour is observed between Duct 1 and 2.

Table 3. Comparison of natural frequencies of experimental and numerical analysis with different thickness for Duct 1

Mode No.	Natural frequencies [Hz]					
	Experimental	Numerical				
	1 mm	1 mm	1.5 mm	2 mm	2.5 mm	3 mm
1	19.82	20.64	30.97	41.29	51.61	61.93
2	22.67	25.52	38.29	51.05	63.81	76.57
3	25.63	26.85	40.25	53.61	66.94	80.21
4	31.65	30.70	46.04	61.37	76.70	92.02
5	–	33.77	50.65	67.54	84.42	101.30
6	37.6	37.75	56.62	75.49	94.35	113.20
7	41.12	40.03	60.01	79.94	99.80	119.58
8	–	44.53	66.78	89.03	111.26	133.48
9	46.83	45.44	68.15	90.87	113.58	136.29
10	–	48.39	72.59	96.78	120.96	145.14

RFD plots can also be used to check the relation between measured and predicted natural frequencies. Minimum RFD value indicates that two-mode sets are close to each other. The RFD plot for all cases is shown in Fig. 7. It is observed that RFD values are minimum along the diagonal, and it is clear that both measured and predicted frequencies are in good agreement. Thus it is interpreted that material properties used in numerical simulations are appropriate (Ewins, 2000b). The RFD of experimental and numerical results is less than 10% for all the cases. It is clear from the RFD plot that experimental and numerical natural frequencies are matched well.

**Fig. 7.** Relative frequency difference plot between experimental and numerical modal analysis results for all ducts

4.3. Mode shape comparison

One of the quick ways to compare experimental and numerical results is the visual inspection of mode shapes. For easiness of visual observation of mode shapes, the colour bar is maintained the same in both experimental and numerical results. Figure 8 shows comparison of numerically predicted and experimentally measured mode shapes for the first four modes of Duct 1 and Duct 2. In the case of Duct 1, it is observed that there is a poor agreement between experimental and numerical mode shapes. For example, the modal displacement is not significant on the side plate for modes 1, 2 and 4 due to the joint between the top and side plate. Modal strain energy is not transferring from one plate to another due to high stiffness and irregularity of the joint. In Duct 2 case, it is observed that experimental mode shapes reasonably resemble the numerical mode shapes.

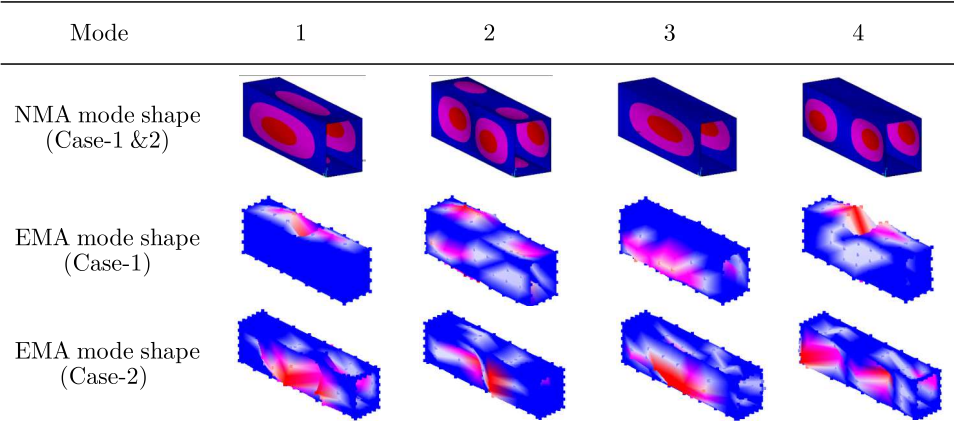


Fig. 8. Comparison of the first four mode shapes for Duct 1 (Pittsburgh lock joint) and Duct 2 (welded joints)

Figure 9 shows a comparison of the measured and predicted mode shapes for Duct 3. It is observed that experimental mode shapes are matched very well with numerical mode shapes except for the first mode, since it is difficult to capture twisted modes in EMA. The extent of correlations between these mode pairs can be verified by MAC values which are shown in the next Section.

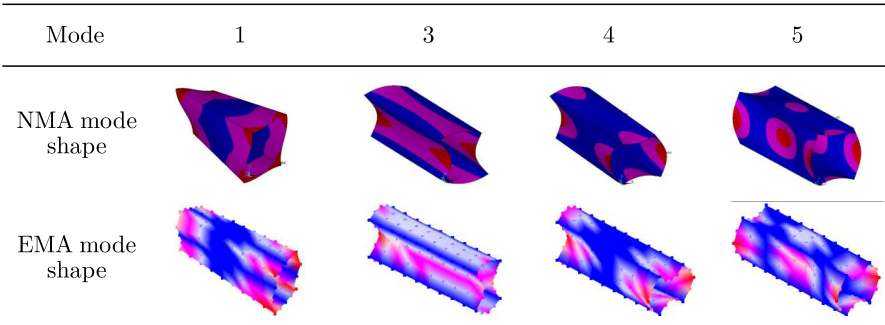


Fig. 9. Comparison of experimental and numerical mode shapes for Duct 3 (adhesive joint)

4.4. Modal assurance criteria

Correlated modes are calculated in terms of MAC values, which vary from 0 to 1. Generally, the reasonable MAC value 0.6 is acceptable, but for good correlation of experimental and numerical results, MAC values should be greater than 0.9 (Vacher *et al.*, 2010). The MAC plot for all the cases is shown in Fig. 10. In Duct 1, it is observed that only two mode pairs have MAC values greater than or equal to 0.6 and the remaining modes have a poor correlation. It clearly shows that the first numerical mode shape is correlated with the second experimental mode (MAC is 0.59). One of the higher mode pairs such as FE mode 13 and experimental mode 11 have MAC values greater than 0.8.

The MAC plot for sixteen experimental modes and twenty-one FEA modes are calculated and plotted for Duct 2 (Fig. 10b). Few off-diagonal mode pairs display that MAC values are greater than 0.5 which indicates that one mode has a correlation with multiple modes. This is due to the presence of welded joints, which makes the structure stiffer at the joints and each wall of the duct behaves as an individual plate constrained at the edges. Experimental modes 2-4, 8 and 10 have MAC values greater than 0.6.

The effect of thickness is also observed between Case 1 and Case 2. It shows that modal density is high in Case 1 when compared to Case 2.

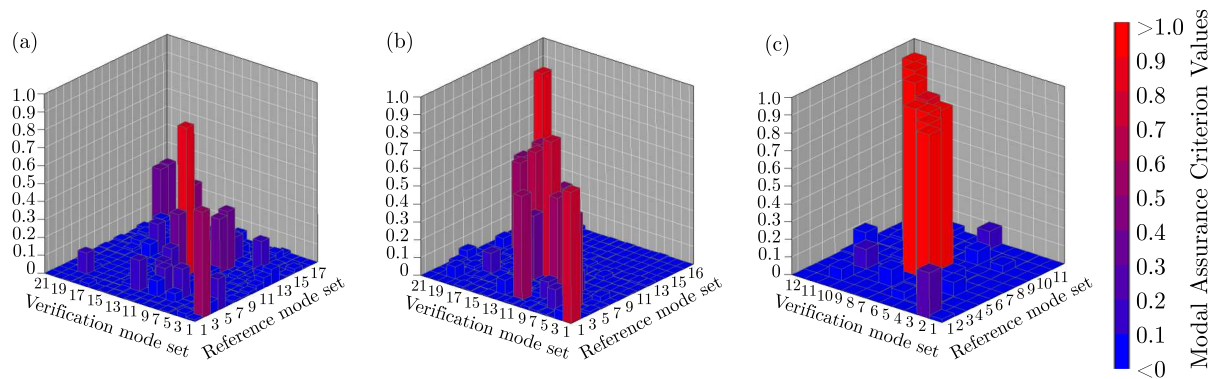


Fig. 10. Comparison of mode shapes for EMA and NMA results in terms of the Modal Assurance Criteria plot

In Duct 3, correlation analysis is done for eleven experimental modes with twelve FEA modes. From the MAC plot shown in Fig. 10c, it is observed a good agreement between the predicted and measured mode shapes except for two fundamental modes (as these are two rotated modes). However, there exists a cross-correlation between modes 7 and 8 (as they are symmetric modes) which can be corrected by updating the FEA modal model. A mode pair table for correlated mode pairs with MAC values greater than or equal to 0.9 is shown in Table 4. It is observed that modes 3, 4 and 5 have excellent correlation with the MAC value equal to 0.99. The results of Duct 3 (acrylic), which is close to an ideal rectangular shape without any joint problem show good correlation with MAC value of 0.99.

Table 4. Mode pair table with MAC values for Duct 3

Experimental natural frequencies [Hz]	Numerical natural frequencies [Hz]	MAC Value
87.7	89.5	0.981
92.5	93.6	0.985
107.5	109.8	0.992
133.1	136.5	0.935
158.4	160.0	0.894
169.3	174.2	0.914
179.8	185.0	0.928
190.1	193.7	0.922
87.7	89.5	0.981
92.5	93.6	0.985
107.5	109.8	0.992

As the rectangular ducts are axisymmetric in structure, repeated roots (symmetrical modes) exist. It is difficult to capture these symmetrical modes in the experimental modal test. This can be observed from natural frequency comparison tables (for ducts of Case 1-3), where few modes are missing (Tables 1 and 2).

4.5. Effect of boundary condition

To study the effect of the boundary condition on mode shapes of a duct with the joint condition, EMA is performed on Duct 2 with free-free BC along with simply supported BC. Experimental and numerical natural frequencies are in a good agreement with less than a 10% error. The experimental mode shapes are compared with the numerical mode shapes, and the corresponding MAC plot is shown in Fig. 11. It can be observed that a single mode is correlated with multiple modes, and MAC values are low. Similar behaviour is also observed in the MAC plot of Duct 2 with S-S BC (Fig. 10b). So, it is clearly observed that the presence of joint conditions plays a critical role than the boundary conditions.

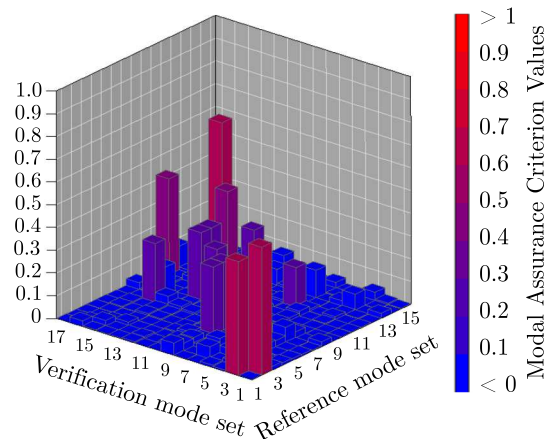


Fig. 11. Modal Assurance Criteria plot for Duct 2 with free-free boundary condition

5. Conclusions

Experimental modal analysis is performed for three different rectangular ducts to study the effect of joint conditions on dynamic characteristics of the duct. An ideal rectangular duct shape is considered for numerical calculation. Frequency and RFD plots are used to compare predicted and measured natural frequencies. It is observed from all the cases that experimental modal frequencies are in good agreement with numerical natural frequencies with less than the 10% error. Mode shapes of predicted and measured results are compared in terms of visual inspection, MAC plot and mode pair table. Low MAC values are observed for Duct 1 and Duct 2 when compared to Duct 3. However, the effect of boundary conditions is also studied on Duct 2 considering free and simply supported boundary conditions. So, based on the observation of all the results, it is concluded that joint conditions play a critical role in mode shape behavior and have a less influence on natural frequency estimation. Further studies are required to incorporate joint stiffness effects in analytical and numerical models to predict dynamic characteristics of rectangular ducts.

References

1. ALLEMANG R.J., 1999, The Modal Assurance Criterion (MAC): Twenty Years of Use and Abuse, #309, *Proceedings Spie, The International Society for Optical Engineering*, **1**, 397-405
2. BLEVINS R.D., 1979, *Formulas for Natural Frequency and Mode Shape*, Kreiger Publ. Comp., New York
3. BRANDON J.A., COWLEY A., 1983, A weighted least squares method for circle fitting to frequency response data, *Journal of Sound and Vibration*, **89**, 419-424

4. CHAVAN P.N., VENKATESHAM B., 2015, Free vibration analysis of a rectangular duct with different axial boundary conditions, *International Journal of Acoustics and Vibration*, **20**, 1, 10-14
5. EWINS D.J., 2000a, *Modal Testing: Theory and Practice*, Letchworth: Research Studies Press, Baldock, Hertfordshire, England
6. EWINS D.J., 2000b, Model validation: correlation for updating, *Sadhana*, **25**, 3, 221-234
7. FU Z.F., HE J., 2001, *Modal Analysis*, Butterworth-Heinemann, Great Britain
8. IBRAHIM S.R., 1999, Fundamentals of time domain modal identification, [In:] *Modal Analysis and Testing*, Montalvão e Silva J.M., Maia N.M.M. (Eds.), Springer Netherlands, 241-250
9. LEE H.P., 1993, Natural frequencies and modes of cylindrical polygonal ducts, *Journal of Sound and Vibration*, **164**, 1, 182-187
10. LINEHAN D., NAPOLITANO K., 2012, Accelerometer selection methods for modal pre-test analysis, *Sound and Vibration Magazine*, **46**, 2, 5-8
11. KENNEDY C.C., PANCU C.D., 1947, Use of vectors in vibration measurement and analysis, *Journal of the Aeronautical Sciences*, **14**, 603-625
12. MAIA N.M.M., 1988, Extraction of valid modal properties from measured data in structural vibrations, Doctoral dissertation, Imperial College London (University of London)
13. MAIA N.M.M., SILVA J.M.M., 1997, *Theoretical and Experimental Modal Analysis*, Research Studies Press, Taunton
14. SCHWARZ B., RICHARDSON M., AVITABILE P., 2002, Locating optimal references for modal testing, *Proceedings of the 20th International Modal Analysis Conference*, Los Angeles
15. VACHER P., JACQUIER B., BUCHARLES A., 2010, Extensions of the MAC criterion to complex modes, *Proceedings of the International Conference on Noise and Vibration Engineering*, 2713-2726
16. XIAO H., PAN J., SHENG M., 2011, Vibration characteristics of a cylinder with asymmetries, *Proceedings of Acoustics*, Australia
17. ZAMAN I., KHALID A., MANSHOOR B., ARABY S., GHAZALI M.I., 2013, The effects of bolted joints on dynamic response of structures, *IOP Conference Series: Materials Science and Engineering*, IOP Publishing

NUMERICAL LOSS ANALYSIS IN A COMPRESSOR CASCADE WITH LEADING EDGE TUBERCLES

TAN ZHENG, XIAO-QING QIANG, JIN-FANG TENG, JIN-ZHANG FENG

School of Aeronautics and Astronautics, Shanghai Jiao Tong University, Shanghai, China

e-mail: qiangxiaoqing@sjtu.edu.cn

A numerical analysis of loss has been carried out to explore the loss mechanism of leading edge tubercles in a high speed compressor cascade. Taking the lead from flippers of the humpback whale, tubercles are passive structures of a blade for flow control. Evaluation of the overall performance in terms of entropy increase shows that the loss reduction is achieved both at high negative and high positive incidence angles, while a rise in the loss is obtained near the design point. And a smaller wave number as well as a smaller amplitude results in lower additional losses at the design point. Spanwise and streamwise distributions of pitchwise-averaged entropy increase combined with flow details have been presented to survey the loss development and, subsequently, to interpret the loss mechanism. The tubercle geometry results in the deflection flow and the consequent spanwise pressure gradient. This pressure gradient induces formation of counter-rotating streamwise vortices, transports away the low-momentum fluid near wall from crests towards troughs and leads to local high loss regions behind troughs as well as loss reduction behind the crests in comparison to the baseline. The interaction between these vortices and flow separation by momentum transfer leads to separation delay and the consequent loss reduction at the outlet.

Keywords: compressor cascade, flow separation, passive flow control, leading edge tubercles, streamwise vortices, loss analysis

Nomenclature

c, c_z	–	blade and axial blade chord [mm]
H, t, l	–	blade span, pitch and camber length, respectively [mm]
β, γ	–	flow angle and stagger angle with respect to axial direction [°]
$\Delta\beta$	–	deflection angle [°]
ω	–	total pressure loss coefficient [–]
Δs	–	specific entropy increase relative to incoming flow [J/(kg·K)]
Δs_{ref}	–	reference specific entropy increase [J/(kg·K)]
p, p_t	–	static and total pressure [Pa]
C_p	–	pressure coefficient [–]
M	–	Mach number [–]
i	–	incidence angle [°]
A, W	–	amplitude and wavelength of leading edge tubercles [mm]
N	–	wave number of leading edge tubercles [–]
X, Y, Z	–	spanwise, pitchwise and axial direction
S	–	camber length direction
ξ_z	–	streamwise vorticity [s ^{–1}]
V	–	velocity [m/s]
LE, TE	–	leading edge and trailing edge [–]

1. Introduction

Flow separation is a common phenomenon in the axial compressors that occurs near the blades. Severe separation contributes greatly to passage blockage and to aerodynamic losses. Worse yet, compressor stall may be induced, which subsequently leads to a sharp decrease in the aerodynamic performance.

Studies of active and passive flow control have been carried out with the aim of depressing flow separation. An overview of possible flow control methods in gas turbine engines is given by several researchers (Lord *et al.*, 2000). Active flow control techniques have the advantage of being suitable for a wide range of operation conditions. Due to their increased complexity, however, gas turbine manufacturers are not fond of them as much as passive flow control techniques such as bowed stators (Fischer *et al.*, 2003), non-axisymmetric profiled endwalls (Dorfner *et al.*, 2011), vortex generators (Hergt *et al.*, 2013). Another way for passive flow control is application of leading edge tubercles. This method is inspired by previous works on the morphology of humpback whale flippers by marine biologists (Fish and Battle, 1995).

A number of previous experimental and numerical works have been performed to explore the effects of leading edge tubercles on the performance of humpback whale flippers and isolated airfoils. A numerical study for the NACA 634-021 wing with and without tubercles shows that large streamwise vortices are formed in the regions posterior to the troughs between tubercles (Fish and Lauder, 2006). Johari *et al.* (2007) also take the NACA 634-021 airfoil as the baseline and carry out an experimental investigation comparing the effect of varying the wavelength and amplitude of sinusoidal tubercles on airfoil performance. Miklosovic *et al.* (2004) constructed two idealized scale models of a humpback pectoral flipper with and without leading edge tubercles and conducted wind-tunnel tests on them at $Re = 505\,000$ – $520\,000$. The results showed that tubercles delayed the stall angle by approximately 40% while decreasing drag and increasing lift in the post-stall regime. Pedro and Kobayashi (2008) performed a numerical simulation of the setup used for the experimental studies (Miklosovic *et al.*, 2004) with the detached eddy turbulence model. They indicated that the higher aerodynamic performance for the scalloped flipper results from the presence of streamwise vortices originated by the tubercles (Pedro and Kobayashi, 2008).

Also, leading edge tubercles have been applied in cascades. An experimental investigation (Keerthi *et al.*, 2014) was carried out to quantify aerodynamic benefits of sinusoidal tubercles in a linear compressor cascade with different tubercle configurations at low Reynolds numbers ($Re = 130\,000$). The results indicated that the performance of the cascade had substantially improved due to the effect of tubercles in terms of delaying the stall angle.

In consideration of the fact that the application of leading edge tubercles is not widespread in turbomachinery, the present work is committed to clarifying the effects of leading edge tubercles on the performance of a high-speed linear compressor cascade and elaborating the underlying loss mechanism of tubercle structures. The overall performance in terms of entropy increase is evaluated over the operating range of the cascade with different tubercle configurations. Span-wise and streamwise entropy distributions are utilized to investigate the difference in the loss development between the cascades with and without leading edge tubercles. Entropy distributions with flow visualizations on several axial cross-sections are examined in detail to interpret the loss development procedure.

2. Numerical setup

2.1. Baseline cascade

A high-speed linear compressor cascade is used in this study. The blade profile of the baseline cascade is modified from an airfoil of a high loading stator of a compressor. The airfoil is suitable

to be used in axial compressors with a subsonic inlet flow over the full blade span. The blade profile and geometrical definitions are shown in Fig. 1.

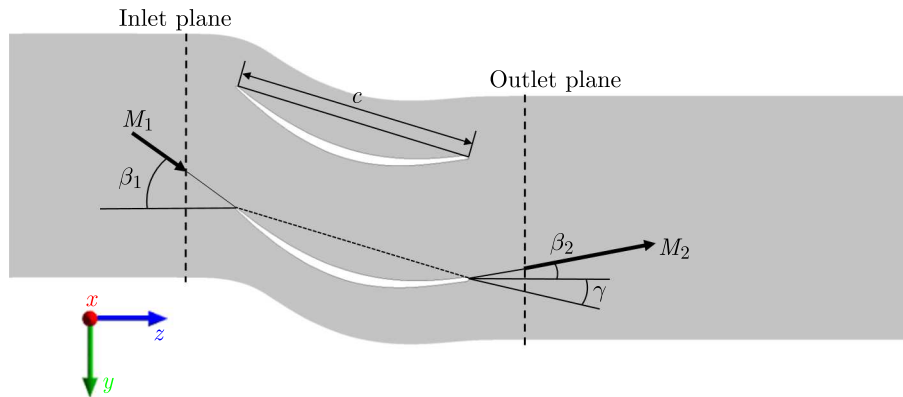


Fig. 1. Blade profile and geometrical definitions

The general design parameters of the cascade are listed in Table 1. The cascade is built with a blade aspect ratio of 0.48 and a design inlet Mach number of 0.64. This aspect ratio is selected in order to study the effects of leading edge tubercles in a certain blade span of about 50% chord length. Furthermore, this value is also related to the number and wavelength of tubercles. Based on the design inflow angle ($\beta_1 = 42^\circ$), numerical simulations are performed in a wide operation range of incidence angles from -16° to 16° .

Table 1. General design parameters of the cascade

M_1	β_1	β_2	γ	$\Delta\beta$	H	c	l	H/c	c/t
0.64	42°	-9°	16.9°	51°	24.5 mm	51 mm	53.2 mm	0.48	2

2.2. Leading edge tubercles

The structure of tubercles is built by using a sinusoidal-like curve as the leading edge. The characteristic geometry definitions of tubercles are shown in Fig. 2a. What calls for special attention is that the horizontal axis S represents the camber length direction and the longitudinal axis X means the spanwise direction. The amplitude A and wavelength W , characteristic dimen-

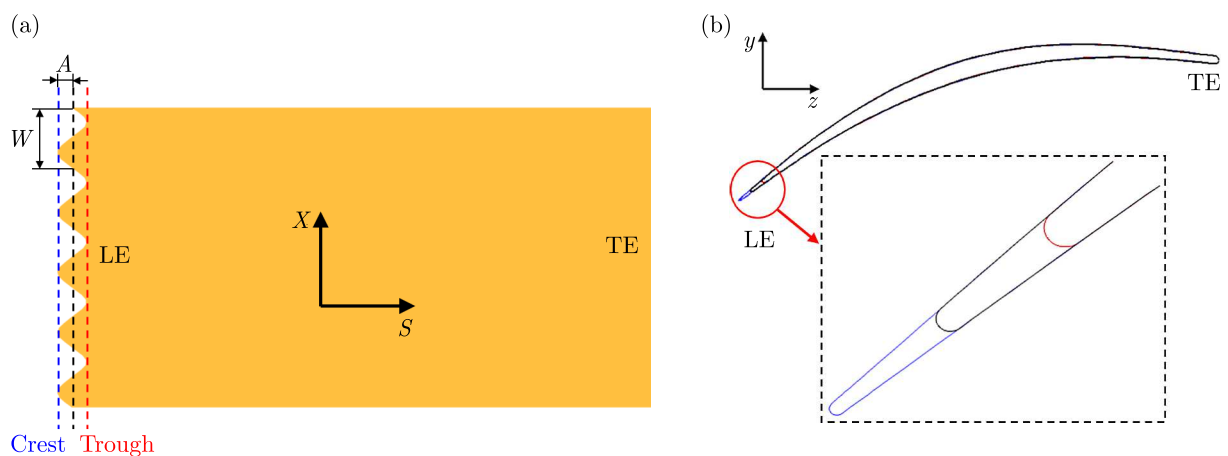


Fig. 2. (a) Characteristic geometry definitions of tubercles. (b) A sketch of profiles for the crest, middle and trough cross-sections

sions of the sinusoidal-like curve are selected to study their effects on the compressor cascade performance.

In order to have a distinct comparison of the baseline geometry and two modified ones, a sketch of three blade profiles is shown in Fig. 2b. They have the same shape despite the difference in the leading edge.

Different computational cascade models are constructed covering variations in the amplitude and wavelength (or wave number). Different amplitudes of $A = 0.02l$, $0.03l$ and $0.04l$ (named as A_2 , A_3 and A_4) combined with several wavelengths of $W = 0.16c$, $0.12c$ and $0.096c$ (or several wave numbers of $N = 3$, 4 and 5) are systematically investigated in this work. These parameter values are selected according to the suggestions given by studies of pioneering researchers (Johari *et al.*, 2007; Hansen *et al.*, 2011). Table 2 shows notations of various configurations. According to the table, nine cascades are named by combining A_2 - A_4 with N_3 - N_5 . Besides, ORI represents the baseline cascade.

Table 2. Notations of different configurations

Notations	A_2	A_3	A_4	N_3	N_4	N_5
Amplitude	0.02l	0.03l	0.04l	—	—	—
Wavelength	—	—	—	0.16c	0.12c	0.096c
Wave Number	—	—	—	3	4	5

2.3. Numerical method

ANSYS-CFX software package has been used to perform RANS simulations on the baseline cascade and on the cascade with different leading edge tubercles. The overall performance of these cascades was investigated with the S-A turbulence model. As one of the most prominent turbulence models, the S-A model is widely used in turbomachinery due to its numerical efficiency and robustness. The Reynolds number based on the characteristic chord length and inlet velocity was about $7.9 \cdot 10^5$.

In the simulations of these cascades, fine multiblock structured grids with an H-O-H topology were constructed. The grid consisted of 3.1 million nodes with 97 pitchwise and 69 spanwise. Thus, the blade boundary layer was sufficiently resolved, where $y^+ \approx 1$ was realized.

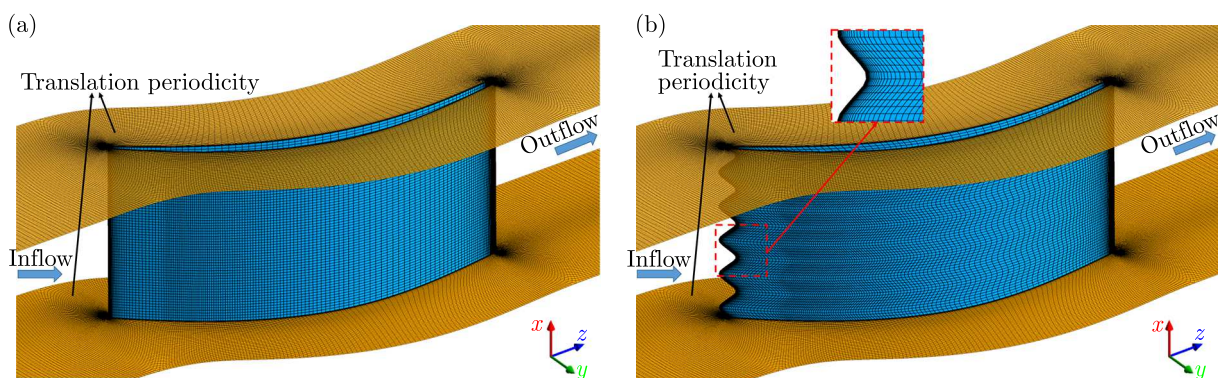


Fig. 3. Schematic diagram of cascade grids with and without leading edge tubercles;
(a) baseline cascade, (b) cascade with tubercles

Figure 3 shows a schematic diagram of the baseline cascade and the cascade with leading edge tubercles. At the inlet of the domain, boundary conditions consisted of uniform total pressure, total temperature and flow direction. The turbulence intensity of 5% was selected. At the outlet boundary, an average static pressure of 101325 Pa was imposed. Solid boundaries were applied

at the blade surfaces with no slip and impermeability conditions. The side boundaries of the passage were modeled with matching translational periodicity. At the passage endwalls, the translational periodicity was also used so as to obtain an “infinite blade cascade”.

A linear cascade constructed with the controlled diffusion airfoil (Steinert *et al.*, 1991) was simulated to validate the numerical method mentioned above. The loading and flow phenomenon in this cascade was similar to the investigated cascade in the paper. Figure 4 shows experimental and numerical results of Mach number characteristics at the design point. The parameter $\bar{\omega}$ is calculated by following equations

$$\bar{p}_t = \frac{\sum \dot{m} p_t}{\sum \dot{m}} \quad \bar{\omega} = \frac{\bar{p}_{t1} - \bar{p}_{t2}}{\bar{p}_{t1} - \bar{p}_1} \quad (2.1)$$

where \bar{p}_t means the mass flow averaged total pressure in a local plane. The predicted results reasonably agree with the experimental data. This gives some confidence on the CFD model used in the following study.

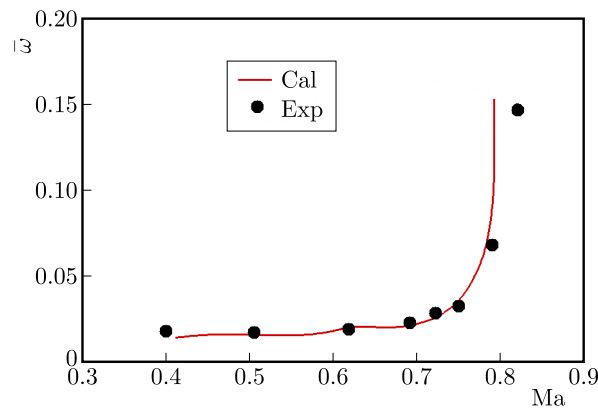


Fig. 4. Comparison of Mach number characteristics of experimental and numerical results

3. Results and discussion

3.1. Overall loss characteristics

For adiabatic flow through a stationary blade row, the total temperature is constant, and so entropy changes depend only on total pressure. Hence, for stator blades and cascade flows, total pressure losses can be taken to be synonymous with specific entropy increase (Denton, 1993).

In order to compare the overall loss characteristics of cascades with and without leading edge tubercles, the variation of the mass flow averaged specific entropy increase relative to incoming flow Δs in the outlet plane is described for different wave numbers and amplitudes. The entropy increase is calculated and normalized with the reference value Δs_{ref} , the entropy value in the outlet plane at the incidence angle of $i = 0^\circ$.

In Fig. 5, the normalized entropy increase $\Delta s / \Delta s_{ref}$ in the outlet plane is plotted against incidence angles for all the cascades. It is seen that the normalized entropy increase for the baseline cascade equals to 1 at the incidence angle of 0° . The minimum entropy increase of the baseline cascade is obtained at the incidence angle of -4° . All the modified cascades have the same minimum loss incidence angle. Figure 5a shows the loss characteristics for cascades with a wave amplitude of 0.021 and different wave numbers of 3, 4 and 5. For A_2N_3 , A_2N_4 and A_2N_5 cascades, it is observed that the loss reduction is achieved in the range from -16° to -8° and from 8° to 16° , compared to the baseline. However, in the operation conditions from -8° to 4° incidence angles, the leading edge tubercles result in no loss reduction. In high negative incidence angles ranged from -16° to -8° , the loss reduction gets larger as the wave number increases.

And yet in high positive incidence angles ranged from 8° to 16° , no definite trend in the loss reduction is observed as the wave number increases. Figure 5b shows the loss characteristics for A_2N_5 , A_3N_5 and A_4N_5 cascades, with a wave number of 5 and different wave amplitudes of 0.02l, 0.03l and 0.04l. In high negative incidence angles of -16° and -12° , it is shown that the loss reduction, compared to the baseline, gets larger as the wave amplitude increases. The same relation between the loss reduction and wave amplitude is observed in the high positive incidence angles of 12° and 16° . However, A_2N_5 , A_3N_5 and A_4N_5 cascades show similar loss reductions as the wave amplitude increases at the incidence angle of $i = 8^\circ$.

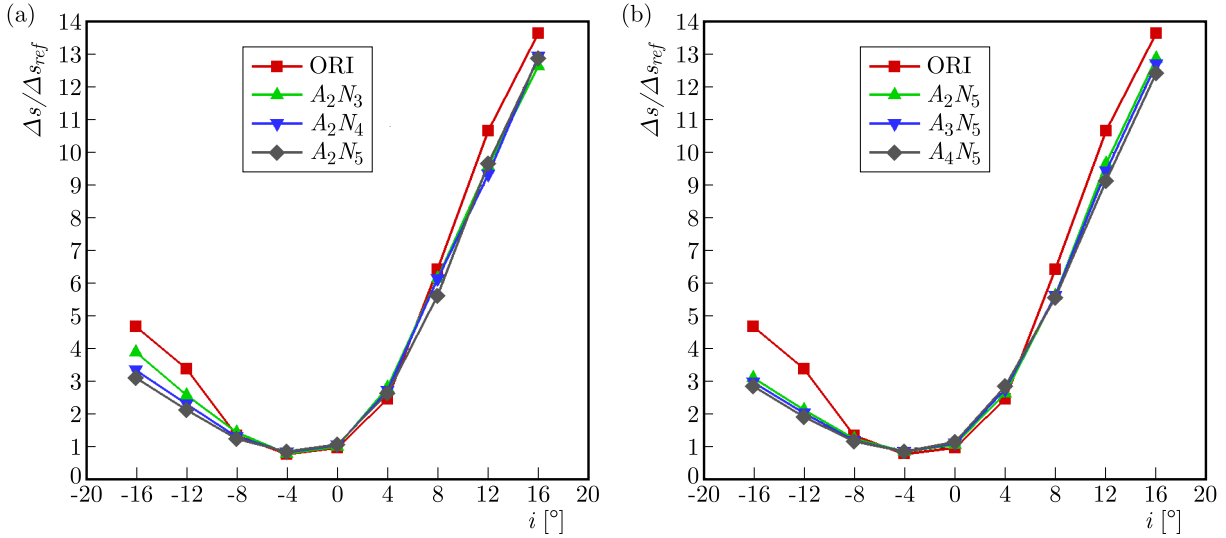


Fig. 5. Normalized entropy increase variation with incidence angle: (a) different wave numbers, (b) different wave amplitudes

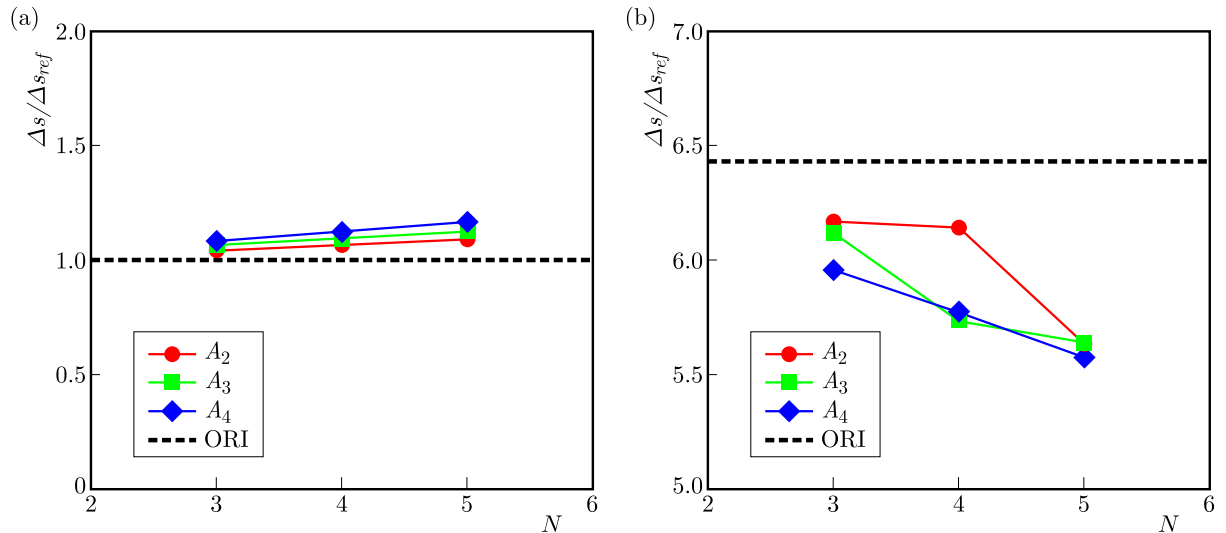


Fig. 6. Cascade loss characteristics for different wave numbers and amplitudes: (a) $i = 0^\circ$, (b) $i = 8^\circ$

In order to further explore the influence of tubercles on losses, Fig. 6 shows the results of normalized entropy increase predicted at two incidence angles of $i = 0^\circ$ and 8° for all the cascades. Compared to the baseline, a rise in the entropy increase is observed for all the tubercle configurations at $i = 0^\circ$, just as shown in Fig. 6a. A smaller amplitude is shown to result in lower additional losses. It means that among all these amplitude configurations, the A_2 configuration with an amplitude of 0.02l produces the least negative influence on the cascade performance.

Also, there exists a positive relation between the loss and wave number, which indicates a higher loss for a larger wave number, namely a smaller wavelength. For A_2N_5 , A_3N_5 and A_4N_5 configurations, the losses respectively rise by 4.2%, 6.7% and 8.3% compared to the baseline. Figure 6b shows that all cascades with leading edge tubercles obtain a decrease in the loss at $i = 8^\circ$. And the loss reduction gets larger as the wave number increases. The normalized entropy increase equals to 6.4333 in the baseline configuration. The loss reductions for A_2N_5 , A_3N_5 and A_4N_5 configurations, respectively, equal to 12.4%, 12.3% and 13.3% in contrast to the baseline. These values are close to each other.

3.2. Spanwise and streamwise entropy distributions

In this Section, spanwise and streamwise distributions of pitchwise-averaged entropy increase are analyzed to survey the loss development in the baseline and A_2N_5 cascades.

Spanwise distributions of the normalized entropy increase at axial positions of $z/c_z = 30\%$, 90% and 150% are shown in Fig. 7. It is noted that the axial positions of $z/c_z = 0\%$, 100% and 150% represent the leading edge, trailing edge and outlet. Three wave periods are included in the range from 20% to 80% span for A_2N_5 . It is shown that the normalized entropy increase has little change along the span for ORI both at $i = 0^\circ$ and 8° . For A_2N_5 , a periodical variation of the entropy increase along the span is observed at both operating incidence angles. We focus on one of the periods in the range from 40% to 60% span for further analysis. The locations of M_0 , trough, middle and crest sections are shown in Fig. 8. In Fig. 7a, a rise in the loss is observed in the range from 52% to 58% span for A_2N_5 compared to ORI at the axial position of $z/c_z = 30\%$, and the maximum rise of loss locates at the trough section. At $z/c_z = 90\%$, the loss reduction is almost not observed over the full span for A_2N_5 . At $z/c_z = 150\%$, there exists loss reduction merely in a small range from 54% to 56% for A_2N_5 , and the maximum loss reduction also locates at the trough section. In Fig. 7b, it is shown that there exists a reduction in the loss between 43% and 47% span at $z/c_z = 30\%$ for A_2N_5 , compared to ORI. And the maximum loss reduction locates at the crest section at $i = 8^\circ$. At $z/c_z = 90\%$, no loss reduction is achieved over the whole span for A_2N_5 . However, at $z/c_z = 150\%$, the loss reduction is achieved over the whole span. It is seen that the spanwise variance of Δs tends to be smaller along the streamwise direction for A_2N_5 and, finally, an approximately uniform distribution of Δs is achieved.

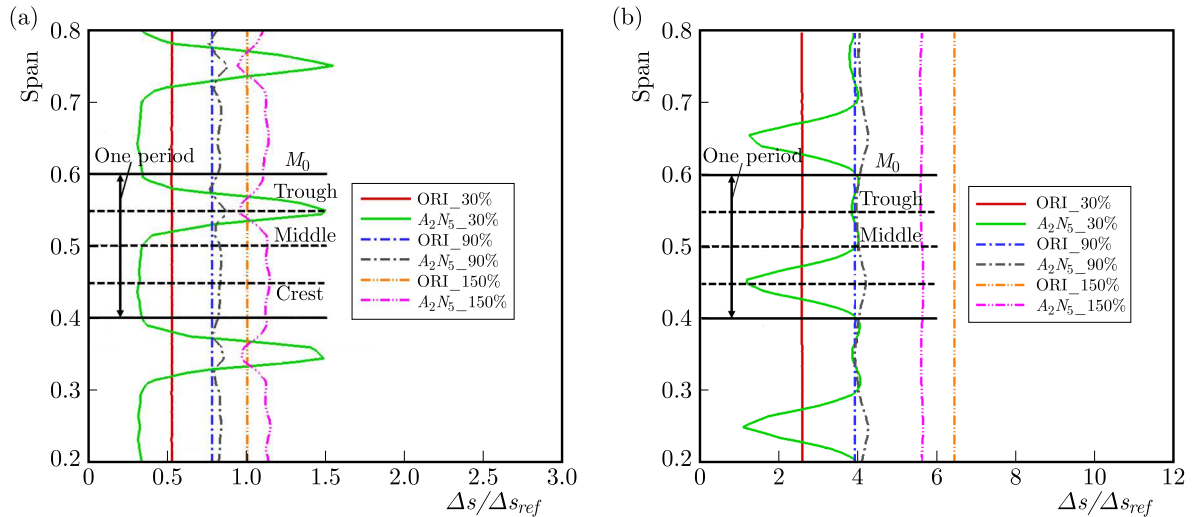
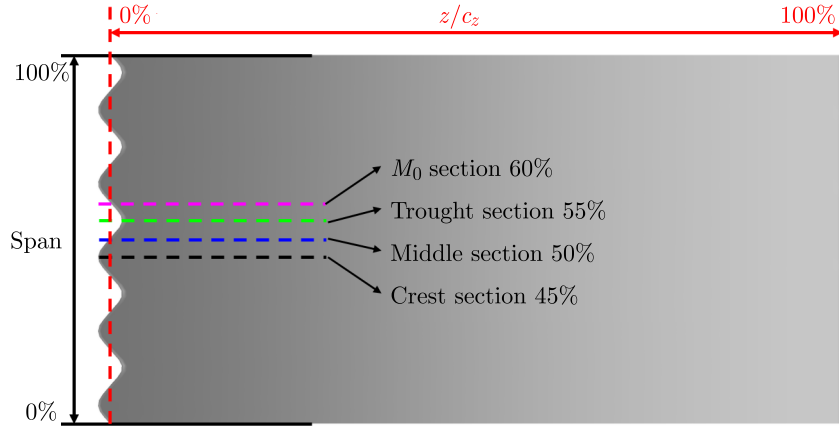
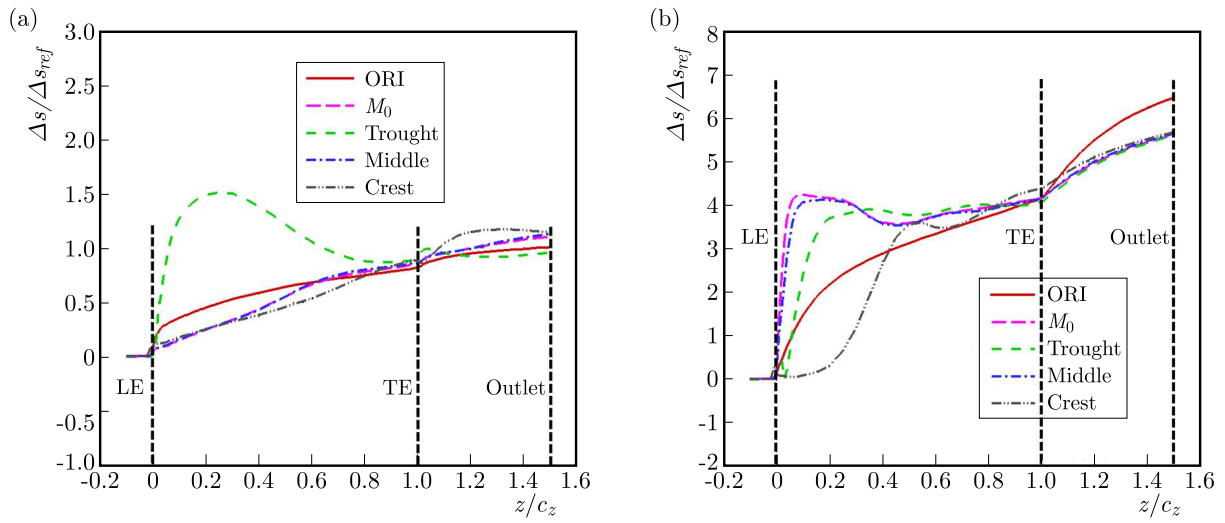


Fig. 7. Spanwise distributions of normalized entropy increase for baseline and A_2N_5 cascades:
(a) $i = 0^\circ$, (b) $i = 8^\circ$

Streamwise distributions of the normalized entropy increase at several spans for the baseline and A_2N_5 cascades are presented in Fig. 9. For A_2N_5 , the M_0 , trough, middle and crest respec-

Fig. 8. Locations of M_0 , trough, middle and crest sectionsFig. 9. Streamwise distributions of normalized entropy increase for baseline and A_2N_5 cascades:
(a) $i = 0^\circ$, (b) $i = 8^\circ$

tively correspond to 60%, 55%, 50% and 45% spans shown in Fig. 8. For the baseline cascade, ORI represents the middle section of 50% span. Actually, the entropy distributions at these four spans have little difference between one another.

In Fig. 9a, Δs of ORI rises gradually downstream LE at $i = 0^\circ$, and the value of normalized entropy increase equals to 1 at the outlet. As for the M_0 section, Δs also shows a gradual rise downstream LE, and the growing rate is larger than that of ORI. The loss reduction is observed from LE to 60% z/c_z compared to ORI. The Δs curve at the middle section is almost the same as that at the M_0 section. At the trough section, a rapid increase of Δs from LE is followed by a decrease till 90% z/c_z . The maximum value is reached at 25% z/c_z . At the crest section, Δs shows the similar trend to that at the M_0 section despite a slight difference downstream TE. From LE to 80% z/c_z , the loss reduction is observed compared to ORI. Among all four sections for A_2N_5 , only Δs of the trough section is smaller than that of ORI at the outlet.

In Fig. 9b, Δs of ORI shows a rapid rise downstream LE at $i = 8^\circ$, and the value of normalized entropy increase equals to 6.5 at the outlet. At the M_0 and middle sections, a sharp increase of Δs is seen from LE to 20% z/c_z , followed by a tender decrease till 46% z/c_z and a subsequent sustained growth till the outlet. As for the trough section, the trend of Δs downstream LE is similar to that at the M_0 and middle sections. A local peak value of the entropy increase lies in the 36% z/c_z . At the crest section, an upward trend of Δs is observed between LE and 50% z/c_z .

Differently, the loss reduction is achieved from LE to 42% z/c_z at the crest compared to ORI. It is worth nothing that the normalized entropy increases at the M_0 , trough, middle and crest sections come to the same value of 5.6 at the outlet, which is smaller than that for the baseline. The streamwise entropy results are in good consistence with the spanwise distributions of Δs .

From the above analysis of spanwise and streamwise entropy distributions, it is concluded that the loss reduction at the outlet is merely obtained at the trough section for A_2N_5 in contrast to ORI at $i = 0^\circ$, while the loss reduction is achieved over the whole span at $i = 8^\circ$. The introduction of leading edge tubercles turns the uniform spanwise distribution of Δs into a nonuniform one and leads to local high loss regions in the fore part of the blade. Also, it is indicated that there exists a spanwise fluid migration downstream LE for A_2N_5 , which narrows the gap of Δs among the M_0 , trough, middle and crest sections and accounts for the loss decrease from 25% to 90% z/c_z behind the trough. It is inferred that entropy variations are induced by an altered flow field by leading edge tubercles. The following Section combines the loss development process with flow visualizations, making further efforts to interpret the loss mechanisms.

3.3. Discussion of loss mechanism

This Section gives a discussion of the loss development process along the streamwise direction as well as flow visualizations, making further efforts to interpret the loss mechanisms with A_2N_5 .

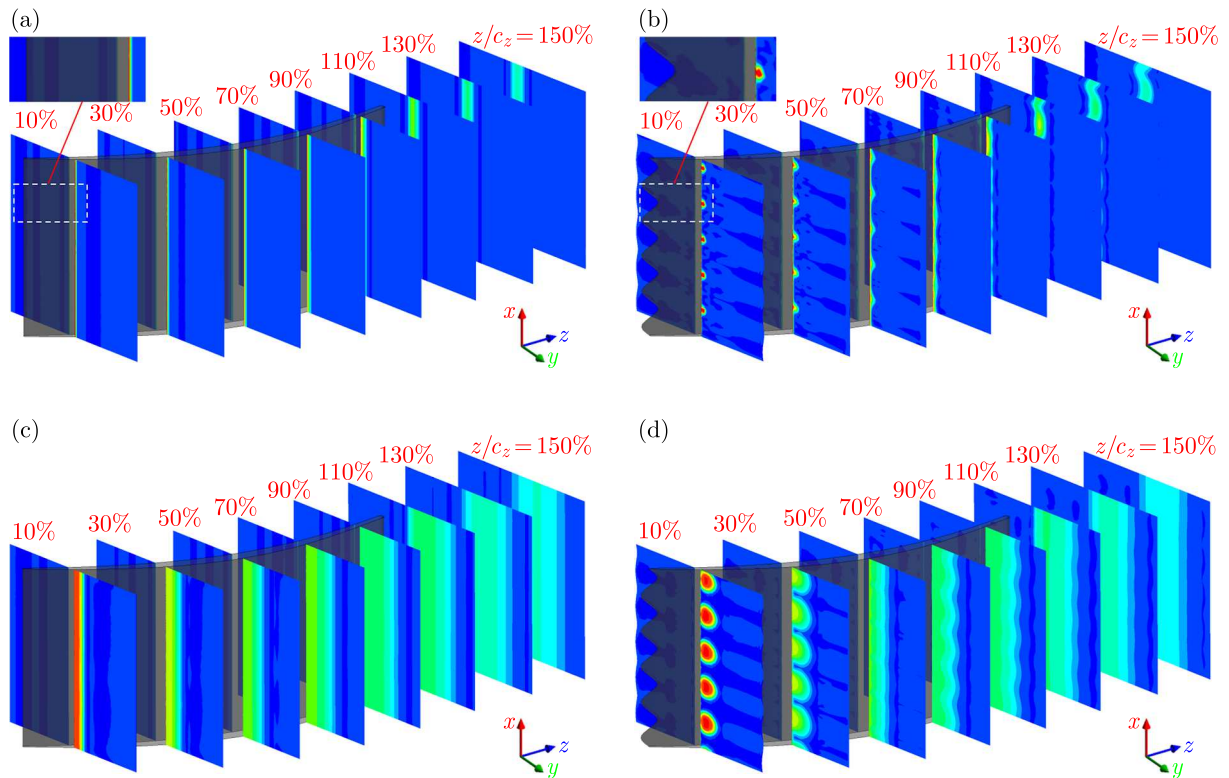


Fig. 10. Distributions of the normalized entropy increase on different axial cross-sections: (a) ORI, $i = 0^\circ$, (b) A_2N_5 , $i = 0^\circ$, (c) ORI, $i = 8^\circ$, (d) A_2N_5 , $i = 8^\circ$

In Fig. 10, distributions of the normalized entropy increase at $i = 0^\circ$ and 8° on different axial cross-sections are shown. The ORI configuration, representing the baseline cascade, shows an almost uniform loss distribution along the blade span in Fig. 10a and 10c. High loss regions are mainly distributed near the blade suction side at $i = 8^\circ$, see Fig. 10c. From Fig. 10b and 10d, it is observed that the introduction of the leading edge tubercles results in the redistribution of the entropy increase along the span. In the A_2N_5 cascade, high losses accumulate in several

rounded areas near the blade suction side at 10% z/c_z rather than long narrow strips in the baseline. It is found that high loss regions are in the downstream location of the wave troughs. And the number of high loss regions is equal to the wave number. Without doubt, high loss regions at $i = 0^\circ$ are much smaller than those at $i = 8^\circ$. Figure 10d also shows an evidence of the spanwise fluid migration near the blade suction side, which results in the uniform spanwise distribution of Δs downstream TE.

Figure 11 shows an isosurface of zero streamwise velocity at $i = 8^\circ$, which is indicative of the size of the separated region. The baseline case is also presented for comparison. It is apparent from the figure that the size of the recirculation region for A_2N_5 is dramatically reduced, and that separation is delayed relative to the baseline. It can also be seen from the figure that the flow separation is delayed behind crests to a greater extent than behind the troughs. The reduced size of the separation region explains the improved aerodynamic performance. However, separation bubbles are still observed behind the troughs, which correspond with the high loss regions shown in Fig. 10d.

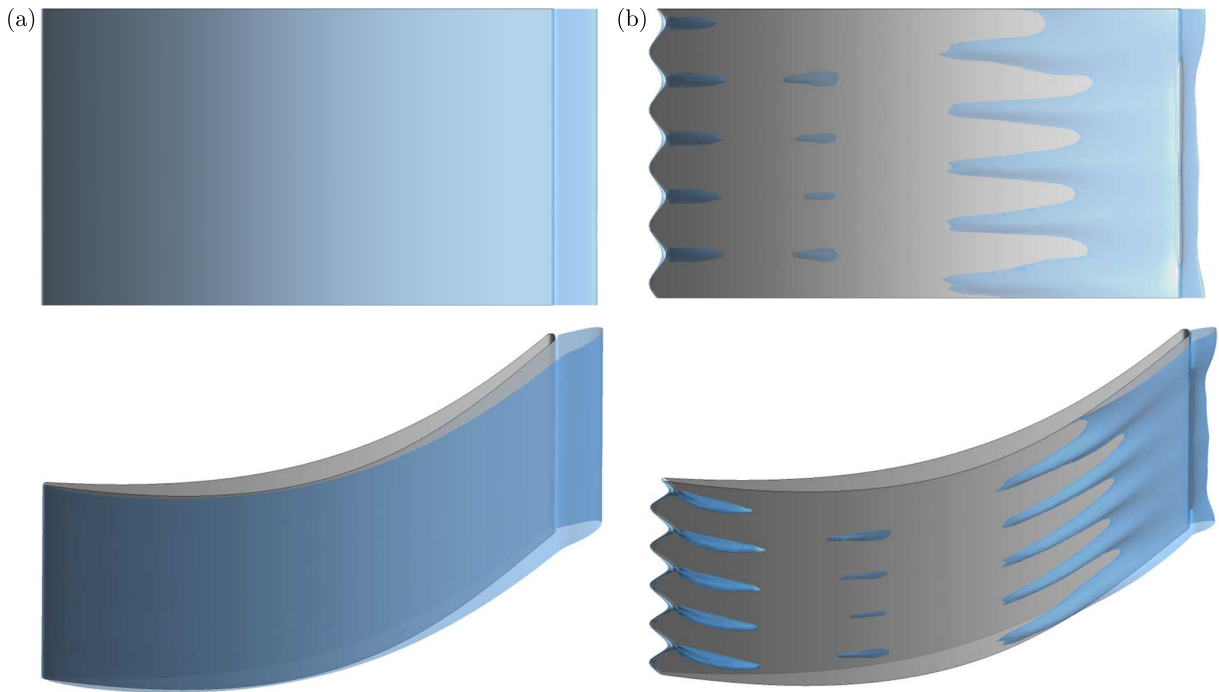


Fig. 11. Isosurface of zero streamwise velocity at $i = 8^\circ$: (a) ORI, (b) A_2N_5

Slices of streamwise vorticity plotted in Fig. 12 provide insight into the locality where the normalized entropy increase is greater than 1 at $i = 0^\circ$ and 8° and indicate the development of counter-rotating vortices along the streamwise direction.

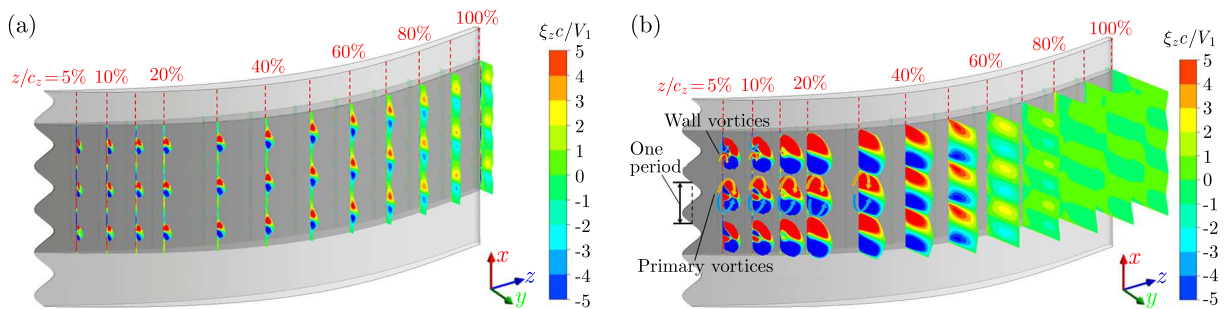


Fig. 12. Slices of streamwise vorticity for A_2N_5 : (a) $i = 0^\circ$, (b) $i = 8^\circ$

In Fig. 12a, pairs of counter-rotating streamwise vortices are induced by leading edge tubercles and located behind the troughs. The vorticity generally expands in area and declines in strength along the streamlines. And the vortical structure is still visible at 100% z/c_z . As a kind of secondary flow, the induced vortices may raise the entropy increase and account for a relatively high loss between LE and TE at the trough section shown in Fig. 9a. It is apparent from Fig. 12b that two different pairs of counter-rotating streamwise vortices are produced behind the wave trough. The wall vortices are adjacent to the primary vortices and have an opposite sense of rotation. The wall vortices gradually disappear along the streamlines and there are only primary vortices visible downstream 15% z/c_z . The strength of primary vortices declines along the streamlines and there are almost no vortical structures visible downstream 70% z/c_z . It indicates that streamwise vortices feed into the separated flow region and sufficiently interact with flow separation by transfer of the momentum. The interaction significantly delays the flow separation near the blade suction side shown in Fig. 11. It should be noted that there is no flow separation at $i = 0^\circ$ and this explains the visible vortical structure at 100% z/c_z . The wall vortices with primary vortices may be related to the loss increase upstream TE at the trough section and the sharp rise of Δs at the M_0 and middle sections between LE and 20% z/c_z in comparison to the baseline. Another observation that the counter-rotating primary vortices in a pair go away from each other along the streamlines indicates the spanwise movement of vortices, which transports momentum in the spanwise direction.

Figure 13 shows distributions of the pressure coefficient on the suction surface and 3D streamlines at $i = 0^\circ$ and $i = 8^\circ$. The pressure coefficient is defined as

$$C_p = \frac{p - \bar{p}_1}{\bar{p}_{t1} - \bar{p}_1} \quad (3.1)$$

where \bar{p}_{t1} and \bar{p}_1 mean the reference total pressure and static pressure in the inlet plane. It is observed in Fig. 13 that the incoming flow is deflected by tubercle geometry such that the bulk of the flow is redirected behind the trough. The deflection results in the spanwise pressure gradient, which transports away the low-momentum fluid near the wall from the crests towards troughs. This pressure gradient also accounts for the production of counter-rotating streamwise vortices.

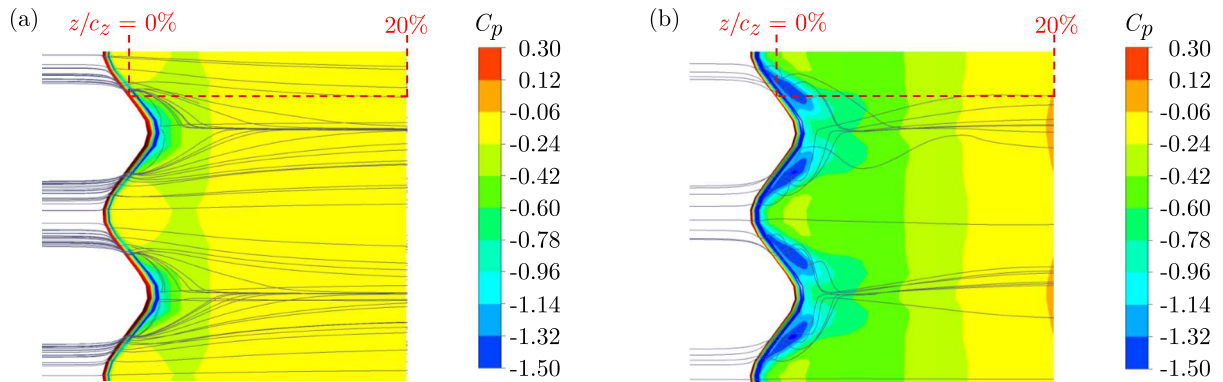


Fig. 13. Distributions of the pressure coefficient on the suction surface and 3D streamlines for A_2N_5 :
(a) $i = 0^\circ$, (b) $i = 8^\circ$

From the above analysis, loss development procedures along the streamwise direction for ORI and A_2N_5 cascades are clarified. Loss generations for ORI at $i = 0^\circ$ are primarily ascribed to the viscous boundary-layer near the blade suction side. At a more critical condition of $i = 8^\circ$, the flow separation and consequent recirculation flow occupies the major part of the high loss. For A_2N_5 , the deflection flow resulted from the tubercle geometry leads to the spanwise pressure gradient which transports away the low-momentum fluid near the wall from crests towards the troughs.

The loss increase at the trough section and loss reduction at the crest section are ascribed to the low-momentum fluid migration in the fore part of the blade. The resulted from the spanwise pressure gradient, two different pairs of counter-rotating streamwise vortices, wall vortices and primary vortices locate behind the troughs and extend to the M_0 and middle sections in the spanwise direction at $i = 8^\circ$. The interaction between these vortices and the flow separation by the momentum transfer leads to separation delay and consequent loss reduction at the outlet.

4. Conclusions

Taking the lead from humpback whale flippers, leading edge tubercles are applied in a high speed compressor cascade. This paper clarifies the influence of tubercles on loss distributions and elaborate the underlying loss mechanism. Several conclusions are drawn as follows:

- For all configurations of leading edge tubercles investigated in this work, the loss reduction is achieved both at high negative and high positive incidence angles, while a rise in the loss is obtained near the design point. A smaller wave number or a smaller wave amplitude results in lower additional losses at $i = 0^\circ$, while a larger wave number brings about a greater loss reduction. There is no linear relation between the amplitude and loss at $i = 8^\circ$.
- Loss generations for ORI at $i = 0^\circ$ are primarily ascribed to the viscous boundary-layer near the blade suction side. At a more critical condition of $i = 8^\circ$, the flow separation occupies the major part of the high loss. For A_2N_5 , the introduction of leading edge tubercles turns the uniform spanwise loss distribution into a nonuniform one and leads to local high loss regions behind the troughs in the fore part of the blade, both at $i = 0^\circ$ and 8° . The flow separation is delayed behind the crests to a greater extent than behind the troughs, and the loss reduction is achieved over the whole span in the outlet plane at $i = 8^\circ$.
- The loss mechanism of tubercle structures by which the size of the flow separation region is reduced has been explored. The tubercle geometry results in the deflection flow and the consequent spanwise pressure gradient. This pressure gradient transports away the low-momentum fluid near the wall from crests towards troughs and also accounts for the formation of counter-rotating streamwise vortices, including wall vortices and primary vortices. The interaction between these vortices and flow separation by the momentum transfer leads to separation delay and consequent loss reduction.

Acknowledgements

This work has been supported by the National Natural Science Foundation of China (No. 51406115), the “2011 Aero-Engine collaborative Innovation Plan”.

References

1. DENTON J.D., 1993, Loss mechanisms in turbomachines, *Journal of Turbomachinery*, **115**, 4, 621-656
2. DORFNER C., HERGT A., NICKE E., MOENIG R., 2011, Advanced nonaxisymmetric endwall contouring for axial compressors by generating an aerodynamic separator-part i: principal cascade design and compressor application, *Journal of Turbomachinery*, **133**, 2, 021026
3. FISCHER A., RIESS W., SEUME J.R., 2003, Performance of strongly bowed stators in a 4-stage high speed compressor, *ASME Proceedings*, **GT2003-38392**, 429-435

4. FISH F.E., BATTLE J.M., 1995, Hydrodynamic design of the humpback whale flipper, *Journal of Morphology*, **225**, 1, 51-60
5. FISH F.E., LAUDER G.V., 2006, Passive and active flow control by swimming fishes and mammals, *Annual Review of Fluid Mechanics*, **38**, 193-224
6. HANSEN K.L., KELSO R.M., DALLY B.B., 2011, Performance variations of leading-edge tubercles for distinct airfoil profiles, *AIAA Journal*, **49**, 1, 185-194
7. HERGT A., MEYER R., ENGEL K., 2013, Effects of vortex generator application on the performance of a compressor cascade, *Journal of Turbomachinery*, **135**, 2, 021026
8. JOHARI H., HENOC H., CUSTODIO D., LEVSHIN A., 2007, Effects of leading-edge protuberances on airfoil performance, *AIAA Journal*, **45**, 11, 2634-2642
9. KEERTHI M. C., KUSHARI A., DE A., KUMAR A., 2014, Experimental investigation of effects of leading-edge tubercles on compressor cascade performance, *ASME Proceedings*, **GT2014-26242**
10. LORD W.K., MACMARTIN D.G., TILLMAN T. G., 2000, Flow control opportunities in gas turbine engines, *Proceedings of AIAA*, **AIAA 2000-2234**
11. MIKLOSOVIC D.S., MURRAY M.M., HOWLE L.E., FISH F.E., 2004, Leading-edge tubercles delay stall on humpback whale (*Megaptera novaeangliae*) flippers, *Physics of Fluids*, **16**, 5, L39-L42
12. PEDRO H.T.C., KOBAYASHI M.H., 2008, Numerical study of stall delay on humpback whale flippers, *Proceedings of AIAA*, **AIAA 2008-0584**
13. STEINERT W., EISENBERG B., STARKEN H., 1991, Design and testing of a controlled diffusion airfoil cascade for industrial axial flow compressor application, *Journal of Turbomachinery*, **113**, 4, 583-590

Manuscript received January 24, 2018; accepted for print March 12, 2018

FINITE ELEMENT STUDY ON THERMAL BUCKLING OF FUNCTIONALLY GRADED PIEZOELECTRIC BEAMS CONSIDERING INVERSE EFFECTS

REZA NASIRZADEH, BASHIR BEHJAT, MAHSA KHARAZI

Mechanical Engineering Faculty, Sahand University of Technology, Tabriz, Iran

e-mail: behjat@sut.ac.ir

In this article, the buckling behavior and bifurcation point of Functionally Graded Piezoelectric (FGP) beams are investigated based on Euler-Bernoulli beam theory. The finite element method is employed to model the beam in thermal environment. The material properties of the beam are considered to vary gradually in the thickness direction and the beam is subjected to electrical and thermal loading. In this paper, direct and inverse piezoelectric effects are considered and buckling of the beam in the sensor state is investigated. By solving the eigenvalue problem, the buckling load of the FGP beam is obtained and the effect of various parameters such as power law index, temperature, applied voltage and beam aspect ratio on the buckling load are investigated. The results show that the boundary conditions are the main factor that affects the buckling load of the FGP beam.

Keywords: FGPM beam, buckling load, inverse piezoelectric effect, thermal environment

1. Introduction

In the recent years, smart materials have found more applications as sensors and actuators in structures. Piezoelectric materials are the most significant materials that are used in structures for the purpose of monitoring and controlling as sensors and actuators. They are used in electromechanical, medical and aerospace industries (Takagi *et al.*, 2003). Also Functionally Graded Materials (FGMs) have received more attention in the recent decades because of their especial behavior in thermal environments. These materials can endure high thermal stresses and thermal shocks because of smooth distributions of the materials through thickness. New functionally graded piezoelectric materials are introduced by combining the concept of so called piezoelectric materials and FGMs. There are many reports on related topics that have been presented in the last years and some of them are mentioned here. Kapuria and Alam (2004) introduced an efficient coupled one-dimensional nonlinear zigzag theory for buckling analysis of hybrid piezoelectric beams under electromechanical loading. They used an analytical solution for buckling of simply supported beams. Li *et al.* (2006) investigated thermal post-buckling of FGM Timoshenko beams subjected to a transversely non-uniform temperature rise. They used the shooting method to solve the problem, and the thermal buckling and post-buckling response of FGM Timoshenko beams with fixed-fixed edges were obtained. Jerome and Ganesan (2010) used a generalized plane strain finite element formulation for the buckling analysis of piezocomposite beams. They used a 2D finite element formulation to improve accuracy in prediction of the buckling load of the piezocomposite. Kiani and Eslami (2010) investigated the buckling load of functionally graded Euler-Bernoulli beams in thermal environments. In this work, the effect of three types of thermal loading was investigated on the critical buckling load of FGM beams. Wattanasakulpong *et al.* (2011) investigated thermal buckling of FGM beams using third-order shear deformation beam theory. The Ritz method was adopted to obtain the eigenvalue problem of thermal buckling in various types of immovable boundary conditions. Kiani *et al.* (2011) investigated thermo-electrical buckling of piezoelectric functionally graded beams based on Timoshenko theory. The

electric field in the piezoelectric layer was assumed constant through the thickness. The results were obtained for three types of thermal loading. Fallah and Aghdam (2011) suggested a simple analytical expression for large amplitude free vibration and a post-buckling analysis of functionally graded beams resting on elastic foundation. Euler-Bernoulli assumptions with von Karman type nonlinear strain-displacement relations were used to derive the governing equation of motion. Komijani *et al.* (2012) investigated non-linear thermo-electrical stability of an FGPM beam using Timoshenko beam theory. All of thermo-electro-mechanical properties were assumed to vary in the thickness direction and expressed by a power law distribution. The Ritz finite element method was used to solve the governing equation. Fu *et al.* (2012) analyzed buckling and free vibration of the FGM beam with two clamped ends and surface-bonded piezoelectric actuators in thermal environments. The governing equation was derived by Hamilton's principle. Rahimi *et al.* (2013) studied the free vibration and post-buckling behavior of functionally graded beams using Timoshenko beam theory. They investigated the post-buckling behavior of the FGM beams and obtained an exact solution based on the applied axial load. Li and Batra (2013) achieved an analytical relations between the critical buckling load of a FGM Timoshenko beam and the corresponding homogeneous Euler-Bernoulli beam subjected to axial and compressive load for various boundary conditions. Rafiee *et al.* (2013) investigated nonlinear thermal buckling of carbon nanotube reinforced composite beams with surface-bonded piezoelectric layers. The governing equations of the beam were obtained based on the Euler-Bernoulli beam theory and considering von Karman type geometric nonlinearity. The critical temperature at which buckling occurred was obtained in that article. Esfahani *et al.* (2013) studied thermal buckling and post-buckling analysis of FGM Timoshenko beams resting on the non-linear elastic foundation. Different types of boundary conditions such as clamped, simply supported and roller edges were considered, and the generalized differential quadrature method was employed to solve the problem. Komijani *et al.* (2014) analyzed buckling, post-buckling and small amplitude vibrations of functionally graded beams resting on a nonlinear elastic foundation and subjected to in-plane thermal loads. The microstructural length scale based on the modified couple stress theory was used to derive the governing nonlinear equilibrium equations of the FGM beam. Nasirzadeh *et al.* (2014) used an exact solution to investigate the stability of FGP beams based on the Euler-Bernoulli beam theory. Ghiasian *et al.* (2015) studied dynamic buckling of the FGM Timoshenko beam subjected to sudden uniform temperature rise considering imperfection. The analysis was performed with an assumption of temperature dependency of each thermo-mechanical property of the FGM beam. The obtained non-linear algebraic equations were solved via the Newton-Raphson iterative scheme. Li and Qiao (2015) studied buckling and post-buckling behavior of shear deformable anisotropic laminated composite beams with initial imperfection subjected to axial compression. The governing equations were based on the higher order shear deformation beam theory with a von Karmann type nonlinearity. In that paper, composite beams with the fixed-fixed, fixed-hinged, and hinged-hinged boundary conditions were considered. The results were obtained by combining Newton's iterative method and Galerkin's method. Chen *et al.* (2015) investigated the elastic buckling and static bending of shear deformable functionally graded (FG) porous beams based on the Timoshenko beam theory. The partial differential equation was derived based on Hamilton's principle, and the Ritz method was employed to obtain the critical buckling load of porous beams.

In this paper, the buckling analysis of FGP beam is investigated considering the inverse piezoelectric effect. The finite element method is employed to model the beam. The effect of two different types of thermal loading on the buckling load of the beam is investigated. The main aim of the study is to evaluate the influence of functional grading of the properties on the buckling behavior of the beams in thermal environments. Various numerical results are presented in graphical forms to give an insight into the influence of material composition, loading type and boundary condition on the buckling load and bifurcation point of the FGP beam.

2. Theoretical formulation

2.1. Geometry and material definition

The beam has length l , height and width h and b , respectively, which is shown in Fig. 1. The coordinate system of the FGPM beam oriented in such a way that the x -axis is in the longitudinal direction in the middle of the beam and the z -axis and y -axis are in the thickness of the beam up to the plate and perpendicular to it, respectively (Fig. 1).

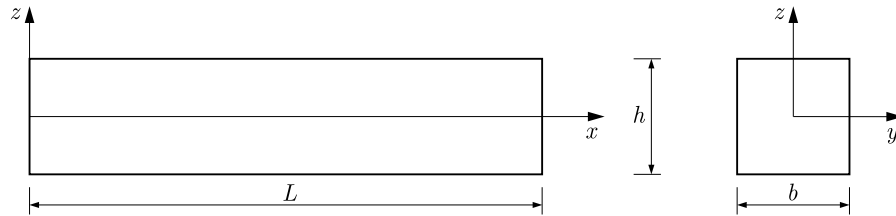


Fig. 1. Definition of geometry and coordinate system of the FGP beam

With regard to gradual changes in the material properties through the thickness of the beam, on the basis of the power distribution law, the effective properties of material can be defined as follows

$$P(z) = P_L + P_{UL} \left(\frac{1}{2} + \frac{z}{h} \right) \quad (2.1)$$

where $P_{UL} = P_U - P_L$ and P_L , P_U are the properties in the bottom and upper surface of the FGP beam, respectively.

2.2. Kinematic and constitutive relations

In this study, considering Euler-Bernoulli beam assumptions, the displacement field is presented as follows (Bathe, 1996)

$$\hat{u}(x, z) = u(x) - zw_{,x} \quad \hat{w}(x, z) = w(x) \quad (2.2)$$

where $\hat{w}(x)$, $\hat{u}(x)$ are beam displacements in the z and x coordinates in a general point, and $w(x)$, $u(x)$ show the displacement of the beam in mid-plane, and $w_{,x}$ is the beam slope. The displacement field based on Euler-Bernoulli beam theory allows only the axial component of the strain component ε_x and the other components to be zero. The strain-displacement relations considering non-linear von Karman strain can be defined for the normal strain as

$$\varepsilon_x = u_{,x} + \frac{1}{2}(w_{,x})^2 - zw_{,xx} \quad (2.3)$$

The characteristic equation of the FGP beam under thermal, electrical and mechanical forces in matrix form is expressed as follows

$$\boldsymbol{\sigma} = \mathbf{Q}\boldsymbol{\varepsilon} - \mathbf{e}^T \mathbf{E} - \mathbf{Q}\boldsymbol{\alpha}\Delta\theta \quad \mathbf{D} = \mathbf{e}\boldsymbol{\varepsilon} + \mathbf{k}\mathbf{E} + \mathbf{P}\Delta\theta \quad (2.4)$$

in which \mathbf{D} , \mathbf{E} , $\boldsymbol{\sigma}$ represent vectors of electric displacement, electric field and stress, respectively. Also the matrices \mathbf{P} , \mathbf{k} , \mathbf{e} , \mathbf{Q} and $\boldsymbol{\alpha}$ represents the pyroelectric vector, dielectric matrix, piezoelectric matrix, elastic stiffness matrix and thermal expansion vector.

2.3. Thermal and electrical loading

In this paper, the effect of two different types of thermal loading (uniform temperature rise and linear temperature rise) on the buckling load of the beam is studied. In the first case, the total volume of the beam is subjected to the temperature rise of $\Delta\theta = \theta - \theta_0$ where θ_0 is the reference temperature. In the second case, the upper layer of the beam is subjected to temperature rise but the lower surface remains in the reference temperature. In this case, by using the narrow beam assumptions, the heat transfer equation can be solved as follows (Kiani *et al.*, 2011)

$$\theta = \theta_L + \theta_{UL} \left(\frac{1}{2} + \frac{z}{h} \right) \quad \theta_{UL} = \theta_U - \theta_L \quad \Delta\theta = \theta - \theta_0 \quad (2.5)$$

where θ_L and θ_U are the lower and upper surface temperature of the beam, respectively.

Considering both the direct and reverse piezoelectric effect, the electrical potential function can be assumed as (Komijani *et al.*, 2013)

$$V(x, z) = \cos(\beta z) \varphi(x) + \frac{V_0 z}{h} \quad (2.6)$$

here V_0 is the applied electrical potential to the beam, which is a constant value, and $\varphi(x)$ shows variation of the electric potential in the axial direction and $\beta = \pi/h$. The electric field is described as follows

$$E_x = -\cos(\beta z) \varphi_{,x} \quad E_y = 0 \quad E_z = \beta \sin(\beta z) \varphi(x) - E_0 \quad (2.7)$$

where

$$E_0 = \frac{V_0}{h} \quad (2.8)$$

2.4. Governing equations

The governing equation of the beam considering the reverse effect under mechanical, thermal and electrical loads will be derived by using the principle of minimum potential. Accordingly, it can be written as

$$\delta\Pi = \delta U + \delta W_{ext} = 0 \quad (2.9)$$

where U is the total potential energy of the beam and W_{ext} is the work of external forces. The total potential energy of the piezoelectric beam can be defined as follows

$$\delta U = \iiint_V [\delta \boldsymbol{\varepsilon}^T \boldsymbol{\sigma} - \delta \mathbf{E}^T \mathbf{D} - \delta \theta S] dV \quad (2.10)$$

It is obvious that

$$\delta\theta = 0 \quad (2.11)$$

The electric field variation by considering Eq. (2.7) can be obtained as

$$\delta E_x = -\cos(\beta z) \delta \varphi_{,x} \quad \delta E_y = 0 \quad \delta E_z = \beta \sin(\beta z) \delta \varphi \quad (2.12)$$

The linear part of the strain and the nonlinear part of it can be written as

$$\boldsymbol{\varepsilon} = \boldsymbol{\varepsilon}_L \quad \delta \boldsymbol{\varepsilon} = \delta \boldsymbol{\varepsilon}_L + \delta \boldsymbol{\varepsilon}_{NL} \quad (2.13)$$

where

$$\delta \varepsilon_L = [(\delta u_{,x} - z \delta w_{,xx}), 0, 0, 0, 0, 0]^T \quad \delta \varepsilon_{NL} = [w_{,x} \delta w_{,x}, 0, 0, 0, 0, 0]^T \quad (2.14)$$

By replacing relations (2.11) to (2.14) in relation (2.10), the total potential energy can be divided into two types of elastic potential energy and geometrical potential energy in tension. These equations can be written as

$$\begin{aligned} \delta U_{ela} &= \iiint_V [\delta \varepsilon_L^T (\mathbf{Q} \varepsilon_L - \mathbf{e}^T \mathbf{E} - \mathbf{Q} \alpha \Delta \theta)] dV + \iiint_V [-\delta \mathbf{E}^T (\mathbf{e} \varepsilon_L + \mathbf{k} \mathbf{E} + \mathbf{P} \Delta \theta)] dV \\ \delta U_{geo} &= \iiint_V [\delta \varepsilon_{NL}^T (\mathbf{Q} \varepsilon_L - \mathbf{e}^T \mathbf{E} - \mathbf{Q} \alpha \Delta \theta)] dV \end{aligned} \quad (2.15)$$

The work done by external forces acting on the beam can be written as follows

$$\delta W_{ex} = -\delta \bar{u}^T \left(f_p + \int_A f_S dA \right) - \delta \bar{\varphi}^T \int_A q_A dA \quad (2.16)$$

In which q_A , f_S , f_p represents charge density, surface forces and concentrated load, respectively. By replacing relations (2.15) and (2.16) in the principle of minimum potential energy (Eq. (2.9)), the total potential energy will be achieved as

$$\begin{aligned} \delta \mp &= \iiint_V [\delta \varepsilon_L^T (\mathbf{Q} \varepsilon_L - \mathbf{e}^T \mathbf{E} - \mathbf{Q} \alpha \Delta \theta)] dV + \iiint_V [-\delta \mathbf{E}^T (\mathbf{e} \varepsilon_L + \mathbf{k} \mathbf{E} + \mathbf{P} \Delta \theta)] dV \\ &+ \iiint_V [\delta \varepsilon_{NL}^T (\mathbf{Q} \varepsilon_L - \mathbf{e}^T \mathbf{E} - \mathbf{Q} \alpha \Delta \theta)] dV - \delta \bar{u}^T \left(f_p + \int_A f_S dA \right) - \delta \bar{\varphi}^T \int_A q_A dA \end{aligned} \quad (2.17)$$

2.5. Finite element formulation

To investigate stability behavior of the FGP beam, a two-node beam element is used (Fig. 2) to model the beam. Each node in the element has 4 degrees of freedom as φ , $w_{0,x}$, w_0 , u_0 which represent the electric potential, slope, deflection and axial displacement of the beam and as nodal variables.

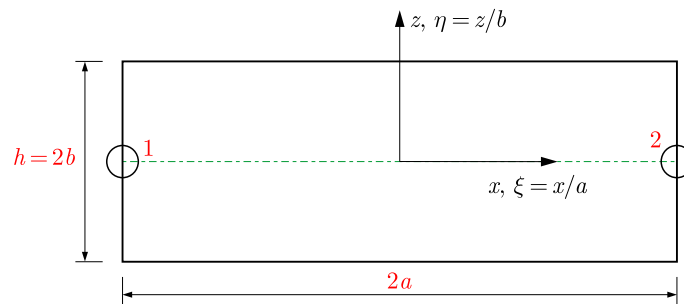


Fig. 2. Definition of the 2-node beam element

Dimensionless variables instead of the coordinate variable are used as follows

$$\xi = \frac{x}{a} \quad \eta = \frac{z}{b} \quad (2.18)$$

By using the Hermite and Lagrange interpolation functions, the axial displacement, vertical deflection and electrical potential in the beam can be written as

$$u_0 = \sum_{i=1}^2 \psi_i u_{0i}^e \quad w_0 = \sum_{i=1}^4 \bar{\psi}_i \Phi_i^e \quad \varphi_0 = \sum_{i=1}^2 \psi_i \varphi_{0i}^e \quad (2.19)$$

in which ψ_i and $\bar{\psi}_i$ denote the Lagrange and Hermite interpolation functions, respectively (Bathe, 1996).

Based on the above relationships, the linear and nonlinear strain vector and the electric field vector are expressed based on nodal variables as follows

$$\boldsymbol{\varepsilon}_L = \mathbf{B}_L \mathbf{u}^e \quad \boldsymbol{\varepsilon}'_{NL} = \mathbf{B}_{NL} \mathbf{u}^e \quad \mathbf{E} = \mathbf{B}_\varphi \boldsymbol{\varphi}^e + \mathbf{E}_0 \quad (2.20)$$

where

$$\begin{aligned} \mathbf{E}_0 &= \begin{Bmatrix} 0 \\ 0 \\ -E_0 \end{Bmatrix} \quad \mathbf{E} = \begin{Bmatrix} -\cos(\beta z)\varphi_{,x} \\ 0 \\ \beta \sin(\beta z)\varphi(x) \end{Bmatrix} + \begin{Bmatrix} 0 \\ 0 \\ -E_0 \end{Bmatrix} \\ \mathbf{B}_L &= \begin{bmatrix} \psi_{1,x} & z\bar{\psi}_{1,xx} & z\bar{\psi}_{2,xx} & \psi_{2,x} & z\bar{\psi}_{3,xx} & z\bar{\psi}_{4,xx} \\ 0 & 0 & 0 & 0 & 0 & 0 \\ 0 & 0 & 0 & 0 & 0 & 0 \\ 0 & 0 & 0 & 0 & 0 & 0 \\ 0 & 0 & 0 & 0 & 0 & 0 \\ 0 & 0 & 0 & 0 & 0 & 0 \end{bmatrix} \\ \mathbf{B}_{NL} &= \begin{bmatrix} 0 & \bar{\psi}_{1,x} & \bar{\psi}_{2,x} & 0 & \bar{\psi}_{3,x} & \bar{\psi}_{4,x} \\ 0 & 0 & 0 & 0 & 0 & 0 \\ 0 & 0 & 0 & 0 & 0 & 0 \\ 0 & 0 & 0 & 0 & 0 & 0 \\ 0 & 0 & 0 & 0 & 0 & 0 \\ 0 & 0 & 0 & 0 & 0 & 0 \end{bmatrix} \\ \mathbf{B}_\varphi &= \begin{bmatrix} -\cos(\beta z)\psi_{1,x} & -\cos(\beta z)\psi_{2,x} \\ 0 & 0 \\ \beta \sin(\beta z)\psi_1 & \beta \sin(\beta z)\psi_2 \end{bmatrix} \end{aligned} \quad (2.21)$$

By using relation (2.20) and replacing it in equation (2.17), the final relation of the FGP beam in matrix form can be obtained as

$$\begin{aligned} (\mathbf{K}_{uu} - \sigma_0 \mathbf{K}_{Guu}) \mathbf{u}_t^e - \mathbf{K}_{u\varphi} \boldsymbol{\varphi}_t^e &= \mathbf{F}_m + \mathbf{F}_{u\theta} \\ \mathbf{K}_{\varphi u} \mathbf{u}_t^e + \mathbf{K}_{\varphi\varphi} \boldsymbol{\varphi}_t^e &= \mathbf{F}_\varphi + \mathbf{F}_{\varphi\theta} \end{aligned} \quad (2.22)$$

in which σ_0 represents the negative pre-stress in the beam and $\mathbf{K}_{u\varphi}$, \mathbf{K}_{Guu} , \mathbf{K}_{uu} and $\mathbf{K}_{\varphi\varphi}$ show the piezoelectric stiffness, geometric stiffness, elastic stiffness matrix and dielectric permittivity matrix. $\mathbf{F}_{u\theta}$, \mathbf{F}_φ , \mathbf{F}_m and $\mathbf{F}_{\varphi\theta}$ are the thermal expansion, electrical, mechanical and pyro-electric load vectors in the local coordinate system. They can be defined as below

$$\begin{aligned} \mathbf{K}_{uu} &= \iiint_V \mathbf{B}_L^T \mathbf{Q} \mathbf{B}_L dV = b \sum_{element} \int_{-1}^1 \int_{-1}^1 \mathbf{B}_L^T \mathbf{Q} \mathbf{B}_L |\mathbf{J}| d\xi d\eta \\ \mathbf{K}_{Guu} &= \iiint_V \mathbf{B}_{NL}^T \bar{\boldsymbol{\sigma}}_0 \mathbf{B}_{NL} dV = b \sum_{element} \int_{-1}^1 \int_{-1}^1 \mathbf{B}_{NL}^T \bar{\boldsymbol{\sigma}}_0 \mathbf{B}_{NL} |\mathbf{J}| d\xi d\eta \\ \mathbf{K}_{\varphi u} &= \iiint_V \mathbf{B}_\varphi^T \mathbf{e} \mathbf{B}_L dV = b \sum_{element} \int_{-1}^1 \int_{-1}^1 \mathbf{B}_\varphi^T \mathbf{e} \mathbf{B}_L |\mathbf{J}| d\xi d\eta \end{aligned}$$

$$\begin{aligned}
\mathbf{K}_{\varphi\varphi} &= \iiint_V \mathbf{B}_\varphi^T \mathbf{k} \mathbf{B}_\varphi dV = b \sum_{element} \int_{-1}^1 \int_{-1}^1 \mathbf{B}_\varphi^T \mathbf{k} \mathbf{B}_\varphi |\mathbf{J}| d\xi d\eta \\
\mathbf{F}_m &= \sum_{i=1}^N \mathbf{N}_u^T \mathbf{H}^T f_{pi} + \int_A \mathbf{N}_u^T \mathbf{H}^T f_S dA \\
\mathbf{F}_{u\theta} &= \iiint_V \mathbf{B}_L^T \mathbf{Q} \boldsymbol{\alpha} \Delta\theta dV & \mathbf{F}_\varphi &= \int_A \mathbf{N}_\varphi^T q_A dA \\
\mathbf{F}_{\varphi\theta} &= \iiint_V -\mathbf{B}_\varphi^T \mathbf{P} \Delta\theta dV & \mathbf{F}_{\varphi\varphi} &= \iiint_V -\mathbf{B}_\varphi^T \mathbf{k} \mathbf{E}_0 dV
\end{aligned} \tag{2.23}$$

By simplifying relation (2.21)₃ based on the electrical potential and combining with Eq. (2.21)₂, the final equation of the FGP beam will be achieved as

$$(\mathbf{K}_{uu} + \mathbf{K}_{u\varphi} \mathbf{K}_{\varphi\varphi}^{-1} \mathbf{K}_{\varphi u} - \mathbf{K}_{Guu}) \mathbf{u}_t^e = \mathbf{F}_m + \mathbf{F}_{u\theta} + \mathbf{K}_{u\varphi} \mathbf{K}_{\varphi\varphi}^{-1} (\mathbf{F}_\varphi + \mathbf{F}_{\varphi\theta}) \tag{2.24}$$

The above equation expresses the final governing relation of the FGP beam using the finite element model based on the Euler-Bernoulli theory under thermo-electro-mechanical loading. It is obvious that based on homogenous and nonhomogeneous equations, the behavior of the beam will be changed and this is affected by the boundary condition of the beam. It means that if the boundary condition is in such a way that the problem change to the eigen-value problem, the beam will buckle, which can be found by solving the eigenvalue problem. Otherwise, if Eq. (2.24) has a non-zero value on the right hand side of the relation, it will be an ordinary equation and represent only the bending problem.

3. Results and discussion

3.1. Comparison studies

In this Section, to verify the solution procedure, the results obtained in this paper are compared with data reported in the literature. The buckling load of the FGP beam is listed in Table 1 and the results are compared with the values reported by Komijani *et al.* (2013). The boundary condition of the beam is clamped in both ends and there is no electrical and thermal loading on the beam. The eigenvalue problem of Eq. (2.24) is solved and the results are shown in Table 1. As it is seen from this table, the values of the buckling load of the FGP beam are in good agreement with the data reported by Komijani *et al.* (2013).

Table 1. Buckling load of the FGP beam for various power law indexes, $L/h = 60$, $\Delta\theta = 0$, $V_0 = 0$

	Power law index			
	0	0.2	2	10
Komijani <i>et al.</i> (2013)	6.892e+4	7.171e+4	7.919e+4	8.317e+4
Present study	6.603e+4	7.067e+4	8.010e+4	8.319e+4

3.2. Parametric studies

In this Section, the stability and buckling load of FGP beams will be investigated. The effect of parameters such as temperature and electrical fields, power law index and aspect ratio of the beam will be discussed.

Figure 3 depicts the buckling load of the beam considering the direct and revers piezoelectric effects based on different power law indexes in various aspect ratios. It is seen that the buckling load increases with a decrease in the aspect ratio. On the other hand, the critical axial load increases versus the power law index. This is explained as that the beam is stiffer for higher power law indexes considering the elastic modulus. Also the sensor-actuator state has a greater buckling load than the actuator state. This can be explained by considering the sensor stiffness terms in Eq. (2.21)₁.

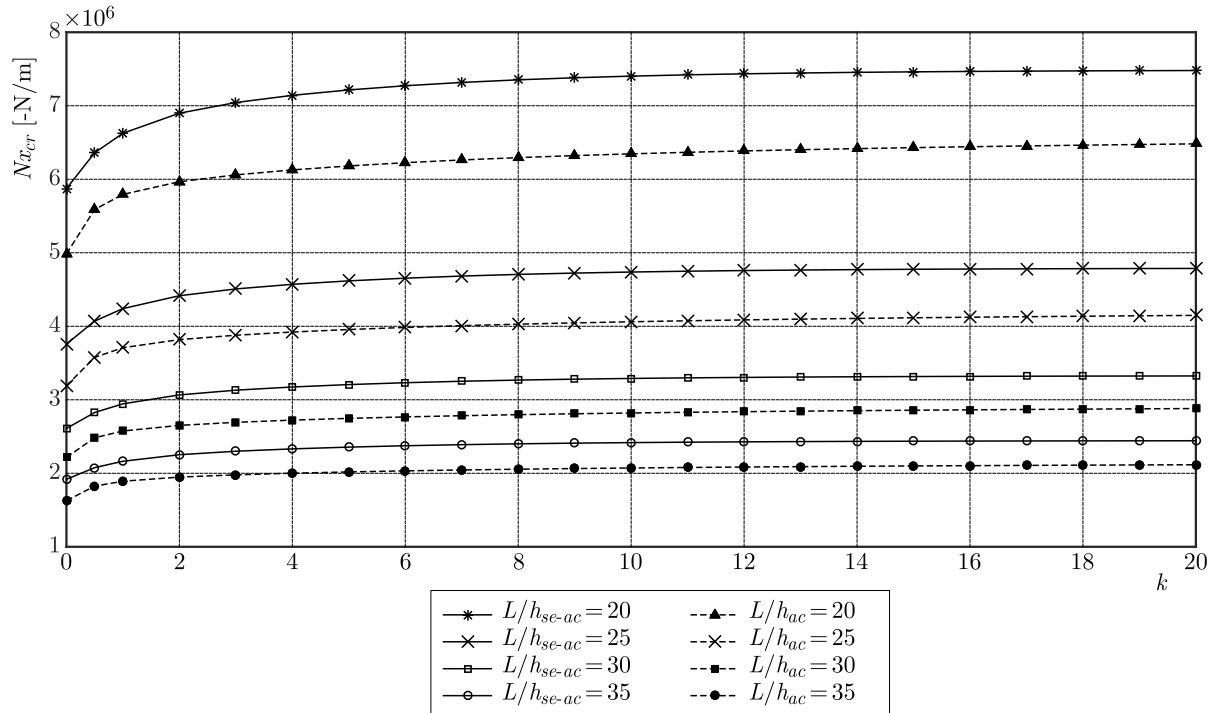


Fig. 3. The critical buckling load of the FGP beam in sensor-actuator and sensor states versus the power law index, $\Delta\theta = 0$, $V_0 = 0(v)$

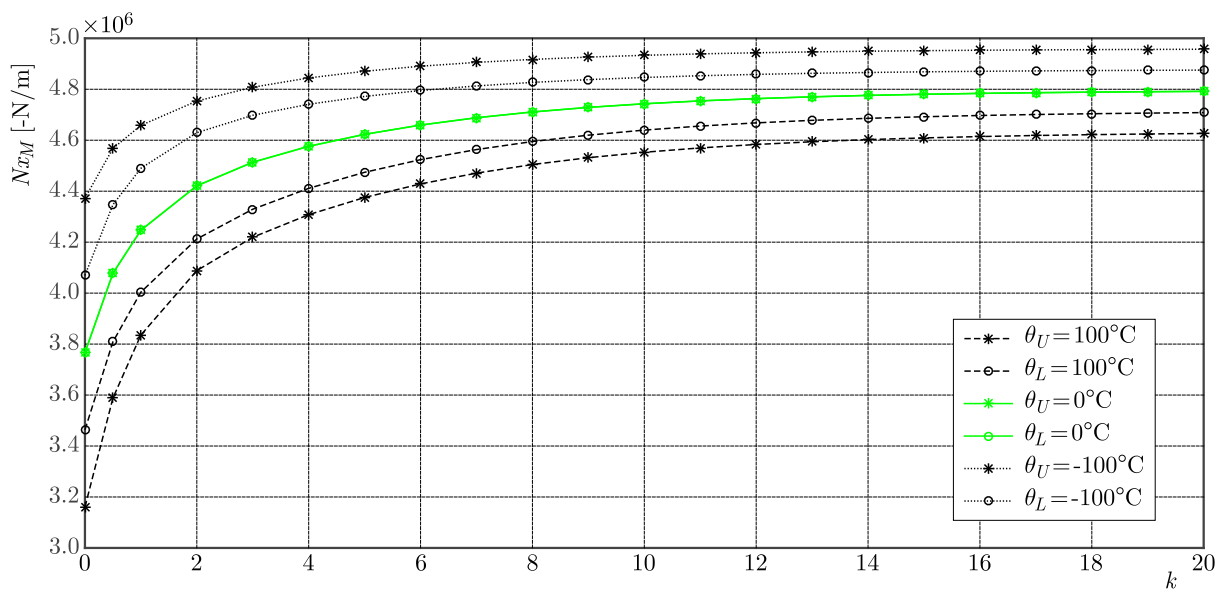


Fig. 4. Buckling load of the beam versus the power law index for various constant and linear temperature rise, $L/h = 25$, $V_0 = 500(v)$

Figure 4 compares the effect of uniform and linear temperature fields on the buckling load versus the power law index. The beam has a clamped-clamped boundary condition and is under electrical loading ($L/h = 25$, $V_0 = 500(v)$). This figure shows that by increasing the temperature, the buckling load rises. Also, by increasing the power law index, the buckling load of the beam increases. This is explained by the difference in the elastic modulus and thermal expansion coefficient of the beam materials, here PZT-4 and PZT-5H. It is worth to note that the buckling load in thermal environment depends on the aspect ratio, elastic and thermal expansion coefficients.

In the next figures, the parameters k_{UT} and k_{LT} mean the power law index for uniform temperature rise, linear temperature rise, and k means the power law index under electrical loading.

Figure 5 compares the effect of uniform and linear temperature changes on the buckling load of the clamped-clamped beam. The beam has a constant aspect ratio and is under electrical loading ($L/h = 25$, $V_0 = 500(v)$). This figure shows that by increasing the power law index, the buckling load decreases. Also, for a constant power law index, the uniform temperature rise has a greater effect on the buckling load than the linear one. This is explained by considering the temperature distribution through thickness of the beam.

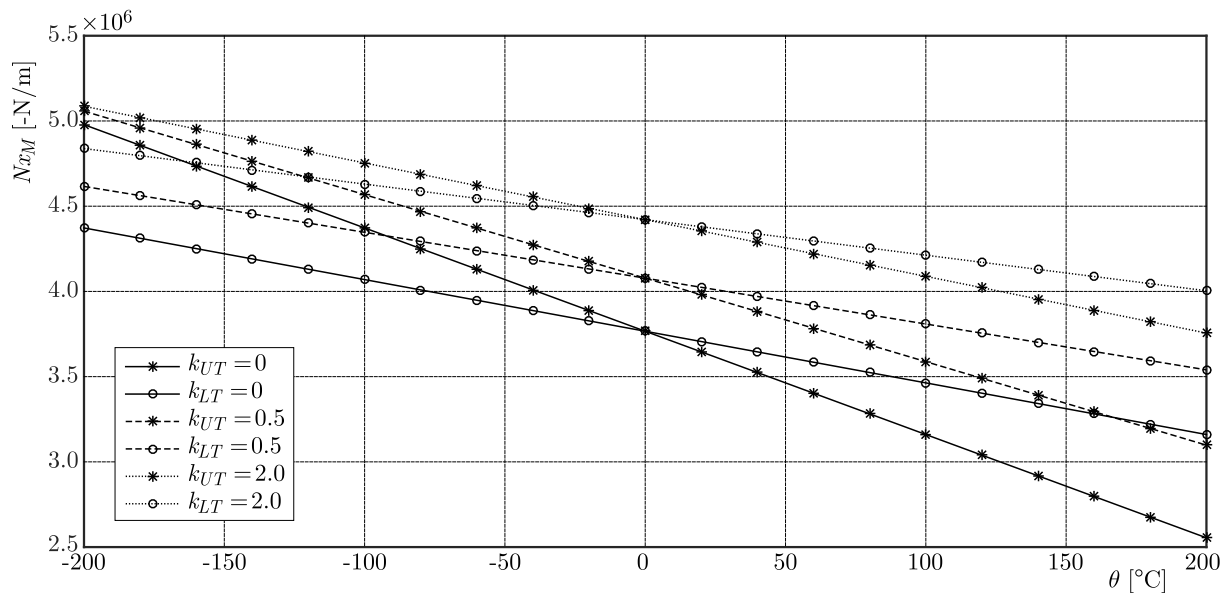


Fig. 5. The effect of uniform and linear temperature changes on the buckling load of the beam

Figure 6 depicts the buckling load of the beam versus the power law index under electrical loading. The beam has an aspect ratio $L/h = 25$ and is under uniform and linear thermal loading. It is inferred from this figure that the applied voltage has not a considerable effect on the buckling load. However, these results show that by increasing the power law index, the buckling load decreases because of a lower elastic modulus.

Figure 7 shows the deflection of the mid-plane of the beam for various power law indexes and different aspect ratios. The behavior of the beam is very similar to the buckling analysis, and the axial force in the bifurcation point increases with an increase in the power law index and decreases with an increase in the aspect ratio.

Figures 8 and 9 show the bifurcation point of the beam for simply-clamped boundary conditions. These figures show that the bifurcation point for the simply-clamped boundary conditions takes a larger axial load than the simply-roller one.

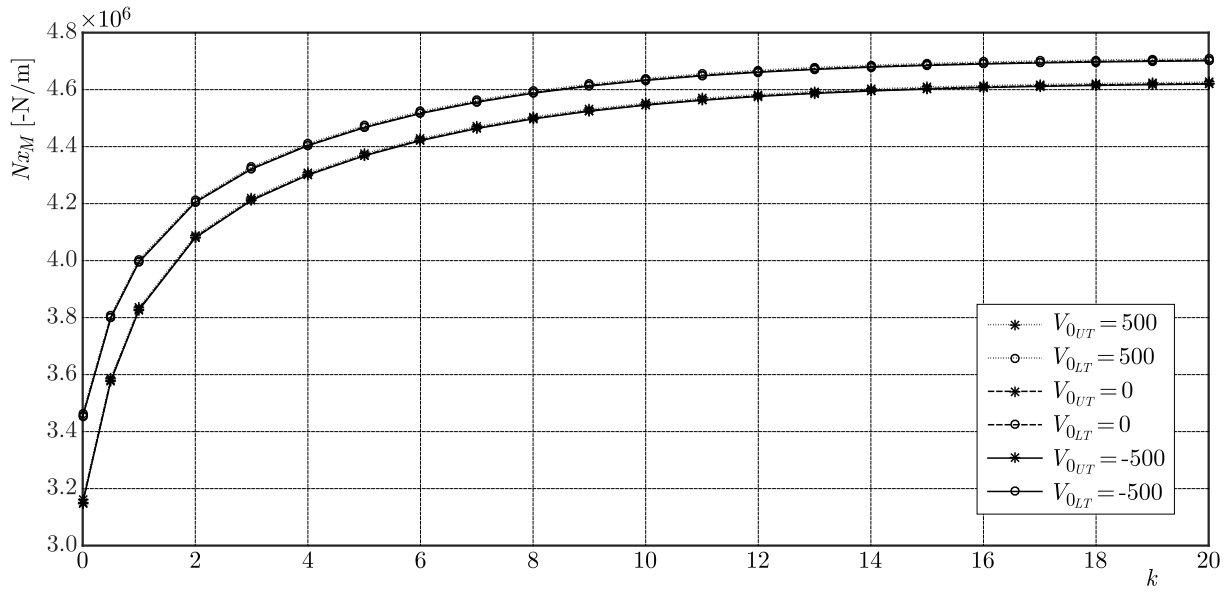


Fig. 6. The buckling load of the beam versus power law index for various electrical loadings

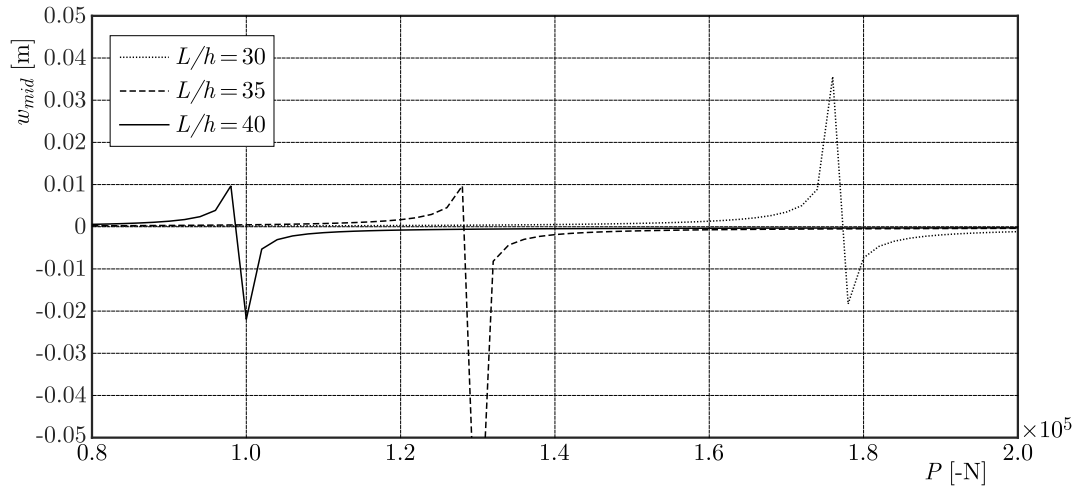


Fig. 7. Deflection of the FGP beam versus axial load for aspect ratios and simply-roller boundary conditions, $\Delta\theta = 0$, $V_0 = 0(v)$, $k = 0.5$

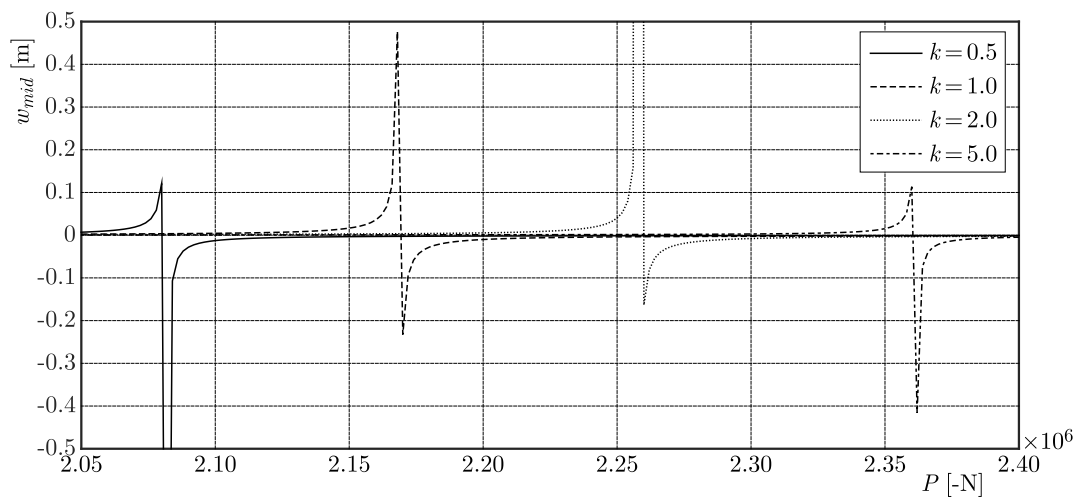


Fig. 8. Deflection of the FGP beam versus axial load for various power law indexes and simply-clamped boundary conditions, $\Delta\theta = 0$, $V_0 = 0(v)$, $L/h = 25$

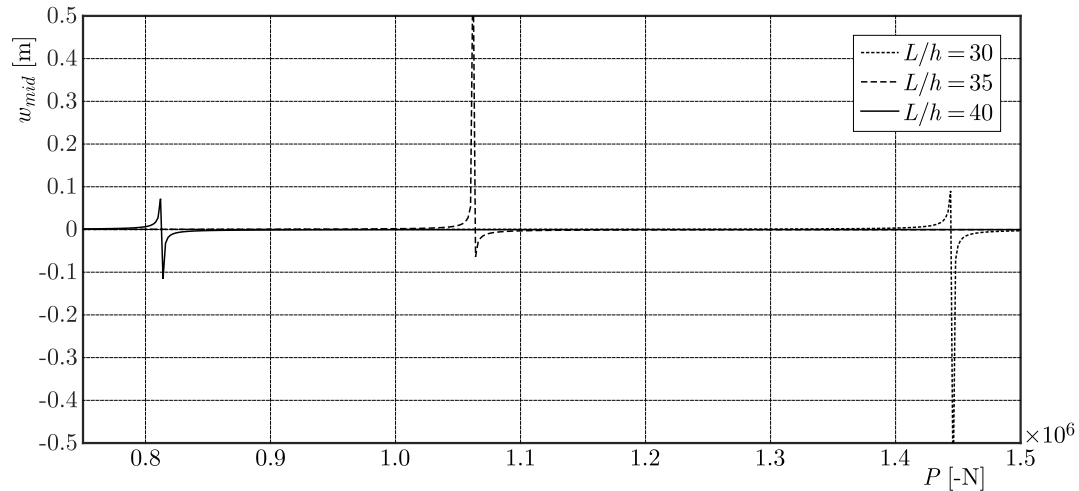


Fig. 9. Deflection of the FGP beam versus axial load for aspect ratios and simply-clamped boundary conditions, $\Delta\theta = 0$, $V_0 = 0(v)$, $k = 0.5$

4. Conclusions

In this paper, buckling and bifurcation point of the Functionally Graded Piezoelectric (FGP) beams are investigated based on the Euler-Bernoulli beam theory in a thermal environment by using the finite element method. All mechanical and electrical properties of the beam are considered to change gradually in the thickness direction of the beam, and the inverse piezoelectric behavior of the beam is investigated. In addition, the effects of various parameters of the beam such as the power law index, temperature, applied voltage and the aspect ratio on the buckling and bifurcation point of the beam are investigated. The results show that because of the coupled electro-mechanical nature of the FGP beams, some boundary conditions have stable behavior while some others are unstable in thermal environments. Also, considering the inverse effect of the piezoelectricity increases the buckling load of the FGP beam.

References

1. BATHE K.J., 1996, *Finite Element Procedures*, Prentice Hall, New York
2. CHEN D., YANG J., KITIPORNCHAI S., 2015, Elastic buckling and static bending of shear deformable functionally graded porous beam, *Composite Structures*, **133**, 54-61
3. ESFAHANI S.E., KIANI Y., ESLAMI M.R., 2013, Non-linear thermal stability analysis of temperature dependent FGM beams supported on non-linear hardening elastic foundations, *International Journal of Mechanical Sciences*, **69**, 10-20
4. FALLAH A., AGHDAM M.M., 2011, Nonlinear free vibration and post-buckling analysis of functionally graded beams on nonlinear elastic foundation, *European Journal of Mechanics-A/Solids*, **30**, 571-583
5. FU Y., WANG J., MAO Y., 2012, Nonlinear analysis of buckling, free vibration and dynamic stability for the piezoelectric functionally graded beams in thermal environment, *Applied Mathematical Modelling*, **36**, 4324-4340
6. GHIASIAN S.E., KIANI Y., ESLAMI M.R., 2015, Nonlinear thermal dynamic buckling of FGM beams, *European Journal of Mechanics A/Solids*, **54**, 232-242
7. JEROME R., GANESAN N., 2010, New generalized plane strain FE formulation for the buckling analysis of piezocomposite beam, *Finite Elements in Analysis and Design*, **46**, 896-904

8. KAPURIA S., ALAM N., 2004, Zigzag theory for buckling of hybrid piezoelectric beams under electromechanical loads, *International Journal of Mechanical Sciences*, **46**, 1-25
9. KIANI Y., ESLAMI M., 2010, Thermal buckling analysis of functionally graded material beams, *International Journal of Mechanics and Materials in Design*, **6**, 229-238
10. KIANI Y., REZAEI M., TAHERI S., ESLAMI M., 2011, Thermo-electrical buckling of piezoelectric functionally graded material Timoshenko beams, *International Journal of Mechanics and Materials in Design*, **7**, 185-197
11. KOMIJANI M., ESFAHANI S.E., REDDY J.N., LIU Y.P., ESLAMI M.R., 2014, Nonlinear thermal stability and vibration of pre/post-buckled temperature- and microstructure-dependent functionally graded beams resting on elastic foundation, *Composite Structures*, **112**, 292-307
12. KOMIJANI M., KIANI Y., ESLAMI M., 2012, Non-linear thermoelectrical stability analysis of functionally graded piezoelectric material beams, *Journal of Intelligent Material Systems and Structures*, **24**, 399-410
13. KOMIJANI M., REDDY J.N., FERREIRA A.J.M., 2013, Nonlinear stability and vibration of pre/post-buckled microstructure-dependent FGPM actuators, *Meccanica*, **49**, 1-17
14. LI S.R., BATRA R.C., 2013, Relations between buckling loads of functionally graded Timoshenko and homogeneous Euler-Bernoulli beams, *Composite Structures*, **95**, 5-9
15. LI S.-R., ZHANG J.-H., ZHAO Y.-G., 2006, Thermal post-buckling of functionally graded material Timoshenko beams, *Applied Mathematics and Mechanics* (English Edition), **27**, 803-810
16. LI Z.-M., QIAO P., 2015, Buckling and postbuckling behavior of shear deformable anisotropic laminated beams with initial geometric imperfections subjected to axial compression, *Engineering Structures*, **85**, 277-292
17. NASIRZADEH R., BEHJAT B., KHARAZI M., 2014, Stability of FGP beams under thermo-electromechanical loading, *International Journal of Material Science Innovations*, **2**, 164-177
18. RAFIEE M., YANG J., KITIPORNCHAI S., 2013, Thermal bifurcation buckling of piezoelectric carbon nanotube reinforced composite beams, *Computers and Mathematics with Applications*, **66**, 1147-1160
19. RAHIMI G., GAZOR M., HEMMATNEZHAD M., TOORANI H., 2013, On the postbuckling and free vibrations of FG Timoshenko beams, *Composite Structures*, **95**, 247-253
20. TAKAGI K., LI J.F., YOKOYAMA S., WATANABE R., 2003, Fabrication and evaluation of PZT/PT piezoelectric composites and functionally graded actuators, *Journal of the European Ceramic Society*, **23**, 1577-1583
21. WATTANASAKULPONG N., GANGADHARA PRUSTY B., KELLY D.W., 2011, Thermal buckling and elastic vibration of third-order shear deformable functionally graded beams, *International Journal of Mechanical Sciences*, **53**, 734-743

Manuscript received June 13, 2017; accepted for print April 7, 2018

LIFE PREDICTION FOR LY12CZ NOTCHED PLATE BASED ON THE CONTINUUM DAMAGE MECHANICS AND THE GENETIC ALGORITHM AND RADIAL BASIS FUNCTION METHOD

JIAYING GAO, PENG LI

School of Aeronautics Science and Engineering, Beihang University, Beijing, China

e-mail: gaojiaying_1988@163.com; lpeng210@sina.com (corresponding author)

In this paper, a new method based on the Continuum Damage Mechanics (CDM) and the Genetic Algorithm and Radial Basis Function neural network method (GARBF) is proposed to predict fatigue life of LY12CZ notched plate. Firstly, the multiaxial fatigue damage evolution equation is derived, and the fatigue life of the notched specimen is predicted based on the CDM method. Secondly, the RBF method is introduced to modify the relative deviation between the theoretical result and actual life. According to the drawbacks of the RBF method, the GA is adopted to optimize network parameters to effectively improve the model quality and reduce the training error. Then, the verification test indicates that the combined method of CDM and GARBF is able to reduce the average relative error of the results of fatigue life prediction to about 7%, which shows that the new method to predict the fatigue life is more reliable. At last, compared with the predicted results of the traditional Back Propagation (BP) neural network, the GARBF model proposed in this paper has a better optimization effect and the result is more stable. This research provides a feasible way to predict the fatigue lives of the notched plate based on the CDM and GARBF method.

Keywords: life prediction, CDM, LY12CZ, notched plate, GARBF

1. Introduction

In practical applications, many engineering structures are subject to cyclic loads, and fatigue damage is a common form of failure (Schijve, 2001; Zhan *et al.*, 2013). Fatigue damage is a progressive and localized material behavior which occurs when a structure component is subjected to cyclic loading. Fatigue cracks are prone to initiate at the positions of notches and geometrical irregularity due to stress concentration. The notch is considered as one of the most important problems in the design of structure components. Different from the uniaxial fatigue problem, the fatigue damage of a notched component involves multiaxial stress and strain states. So, it is important to present a method for fatigue life prediction of notched plates.

In the past decades, many researchers have been focused on the fatigue experiment and statistic analysis (Suresh, 1998), which is a general method of fatigue life prediction in engineering. However, this method takes too much time and sometimes the result is not satisfactory. So, it is necessary to find an easy and reliable method. The critical plane approach (Karolczuk and Macha, 2005) and stress invariant approaches (Li *et al.*, 2000) have been widely used in researches and applications. However, these approaches often fail to capture the fatigue damage evolution such as material degradation due to damage. Fatigue accumulation damage theory (Lemaitre and Chaboche, 1990; Zhan *et al.*, 2015b, 2016, 2017c) is considered to be one of the most effective methods for fatigue life prediction. The Continuum Damage Mechanics (CDM) provides an effective method to describe degradation of mechanical properties of materials, which take into account damage evolution using the concept of effective stress and has been widely used in

recent years (Movaghghar and Lvov, 2012; Upadhyaya and Sridhara, 2012; Zhang *et al.*, 2015a, 2017a,b).

While the methods based on the damage law are carried out, such problems also attract some researchers engaged in the machine learning field. They attempt to take the advantages of machine learning theories in complex system modeling to enhance the accuracy of fatigue life prediction. Pujol and Pinto (2011) proposed a novel method based on neural network to predict the fatigue life. Guo *et al.* (2014) introduced the support vector machine (SVM) method to predict the life of the packaging EMC material. Liu and Xuan (2008) adopted the rough sets theory to analyze important affecting parameters on low cycle fatigue life. The fatigue life prediction is a complicated problem. There is a large amount of non-linear and non-smooth factors that rapidly influence the actual material life. Compared to traditional theoretical methods, the artificial neural network (ANN) method can better overcome these difficulties (Gao *et al.*, 2015, 2016; Monteiro *et al.*, 2016; Nagarajan and Jonkman, 2013; Reid *et al.*, 2013). Introducing the ANN method into the solution of fatigue life prediction has several advantages: (1) ANN is able to approximate any non-linear and non-smooth function with any accuracy; (2) ANN has strong anti-interference ability and good robustness; (3) The ANN structure is suitable for parallel data processing, and the computation is efficient and fast; (4) ANN has good generalization ability. In this paper, the Radial Basis Function (RBF) neural network method is adopted to predict the fatigue life for LY12CZ notched plate. Some researches have shown that the RBF neural network has better optimal approximation ability than the traditional Back Propagation neural network (BPNN). Compared to BPNN, the RBF model has fewer parameters to be learnt. The RBF neural network is composed of 3 layers: an input layer, a hidden layer and an output layer. After suitable data pre-processing, the data will be imported into the hidden layer. The hidden layer consists of several neurons, and each neuron can be regarded as a cluster center which is able to generate the local response by the inputs. When the distance between the inputs and the cluster center are close enough, the hidden neuron will make a non-zero response. The final output of the RBF network is equal to a linear combination of all hidden layer neuron responses.

There are also some defects in the use of the RBF method. The RBF is not good at global searching and is easy to fall into the local minimum. In this paper, the Genetic Algorithm (GA) is adopted to optimize the training process of the RBF model. The GA is developed based on the biological evolution process. Several biological concepts such as reproduction, crossover, mutation, competition are introduced into the GA algorithm. The GA will adjust and improve a series of feasible solutions in the process of evolution, and finally find the optimum solution in the whole multi-dimensional space. The GA is a global optimization algorithm, so it can effectively overcome the drawbacks of traditional methods (Camacho-Vallejo *et al.*, 2015; Goldberg and Samtani, 2015; Zhan *et al.*, 2015c).

In this paper, the continuum damage mechanics (CDM) and an optimization model composed of the Genetic Algorithm and Radial Basis Function neural network method (GARBF) are proposed to conduct the fatigue life prediction for LY12CZ notched plate in the case of cyclic loading using the framework is shown in Fig. 1. Firstly, the multiaxial fatigue damage evolution equation is derived. Secondly, according to the fatigue experimental data, the material parameters in the damage evolution equation are identified. Then the fatigue life prediction of the notched specimen is conducted. On the basis of the CDM method, the Radial Basis Function (RBF) method is introduced to modify the relative deviation between the theoretical result and actual life. In addition, the Genetic Algorithm (GA) is adopted to improve the RBF training effect in order to obtain a more reliable optimization model (GARBF). Finally, the verification test indicates that the combined method of CDM and GARBF is able to reduce the average relative error of fatigue life prediction to about 7%, and the life prediction result is more reliable. Compared to the traditional backpropagation (BP) neural network, the GARBF model proposed in this paper has a better optimization effect and the result is more stable.

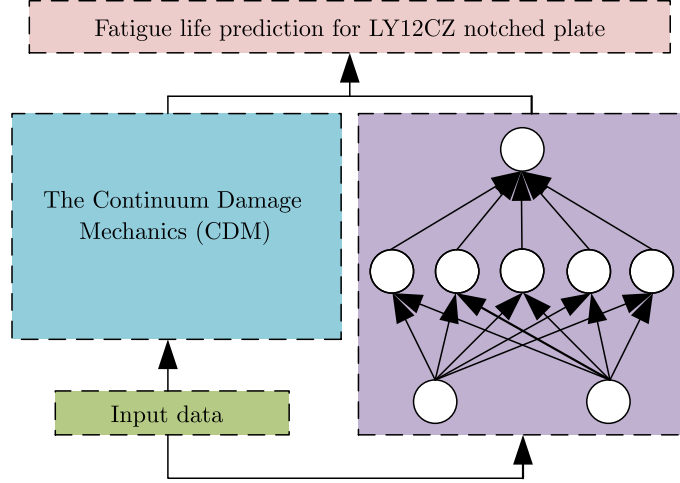


Fig. 1. The framework of the methodology

2. The fatigue damage evolution model

In uniaxial cycle loading, based on the remaining life and continuum damage concepts, the fatigue cumulative damage model can be illustrated as (Zhan *et al.*, 2015c)

$$\dot{D} = \frac{dD}{dN} = [1 - (1 - D)^{\beta+1}]^{\alpha(\sigma_{max}, \sigma_m)} \left[\frac{\sigma_{max} - \sigma_m}{M(\sigma_m)(1 - D)} \right]^{\beta} \quad (2.1)$$

where D is the damage scalar variable and N is the number of cycles. σ_{max} and σ_m are, respectively, the maximum and mean applied stress. β is a material parameter. The expression of $\alpha(\sigma_{max}, \sigma_m)$ is defined as

$$\alpha(\sigma_{max}, \sigma_m) = 1 - a \left\langle \frac{\sigma_{max} - \sigma_f(\sigma_m)}{\sigma_u - \sigma_{max}} \right\rangle \quad (2.2)$$

where σ_u is the ultimate tensile stress, σ_{l0} is the fatigue limit for fully reversed conditions. a and b_1 are material parameters. The expression of $M(\sigma_m)$ is defined as

$$M(\sigma_m) = M_0(1 - b_2\sigma_m) \quad (2.3)$$

where M_0 and b_2 are material parameters. The number of cycles to failure N_F for a constant stress condition is obtained by integrating Eq. (2.1) from $D = 0$ to $D = 1$, leading to

$$N_F = \frac{1}{1 + \beta} \frac{1}{a M_0^{-\beta}} \frac{\langle \sigma_u - \sigma_{max} \rangle}{\langle \sigma_{max} - \sigma_f(\sigma_m) \rangle} \left(\frac{\sigma_a}{1 - b_2\sigma_m} \right)^{-\beta} \quad (2.4)$$

where σ_a is the stress amplitude during one loading cycle.

In the practical engineering application, the stress and strain are always multiaxial. The damage evolution law in the case of multiaxial loading is given as follows

$$\dot{D} = \frac{dD}{dN} = [1 - (1 - D)^{\beta+1}]^{\alpha} \left(\frac{A_{II}}{M_0(1 - 3b_2\sigma_{H,m})(1 - D)} \right)^{\beta} \quad (2.5)$$

where A_{II} is the amplitude of octahedral shear stress and $\sigma_{H,m}$ is the mean hydrostatic stress. The parameter α is defined by

$$\alpha = 1 - a \left\langle \frac{A_{II} - A_{II}^*}{\sigma_u - \sigma_{e,max}} \right\rangle \quad (2.6)$$

where $\sigma_{e,max}$ is the maximum equivalent stress which is calculated by maximising the von Mises stress over a loading cycle. The Sines fatigue limit criterion A_{II}^* in this model is formulated by

$$A_{II}^* = \sigma_{l0}(1 - 3b_1\sigma_{H,m}) \quad (2.7)$$

By integrating of Eq. (2.5) from $D = 0$ to $D = 1$ for a constant stress condition, the number of cycles to failure N_F is

$$N_F = \frac{1}{1 + \beta} \frac{1}{aM_0^{-\beta}} \frac{\langle \sigma_u - \sigma_{e,max} \rangle}{\langle A_{II} - A_{II}^* \rangle} \left(\frac{A_{II}}{1 - b_2\sigma_{H,m}} \right)^{-\beta} \quad (2.8)$$

3. The material parameters identification

The static properties of LY12CZ aluminium alloy and fatigue experiment results can be consulted from a handbook (Wu, 1996), and the static mechanics properties are presented in Table 1. In the modified damage evolution law, there are five parameters in the damage evolution equation. The four material parameters (β, M_0, b_1, b_2) can be determined by fatigue experimental data of smooth specimens. For smooth specimens under conditions of uniaxial fatigue loading, an S-N curve has been derived. When fatigue tests are carried out at a fixed stress ratio, the relation between the number of cycles to failure N_F and the maximum stress σ_{max} can be obtained. Parameters β and $1/[(1 + \beta)aM_0^{-\beta}]$ come from stress-controlled ($R = -1$) fatigue tests stress-life data. With the least square method, parameters b_1 and b_2 can be obtained from the fatigue tests data at other different stress ratios. Then the independent parameters β and $aM_0^{-\beta}$ will be used in the incremental damage formulation (Zhan *et al.*, 2017d), and a is identified numerically by using the fully reversed fatigue test data for the notched specimens. Finally, the identified damage evolution parameters are listed in Table 2.

Table 1. Static properties of LY12CZ aluminium alloy

E [GPa]	ν [-]	σ_b [MPa]	σ_s [MPa]
73	0.3	466	343

Table 2. Material parameters in the fatigue damage evolution equation

a	β	M_0	b_1	b_2
0.62	1.76	712398	0.0001	0.0002

4. Fatigue life prediction for LY12CZ notched plate

Two kinds of the LY12CZ notched specimen are used and geometric profiles of which are shown in Fig. 2. The corresponding stress concentration factors K_T are 2 and 4, respectively. The fatigue load, stress ratio and the predicted fatigue lives under different stress levels are shown in Table 3.

5. Introduction of an RBF neural network model

The establishment of a theoretical model (CDM) provides an important basis and foundation for the solution of notched specimen fatigue life prediction. As shown in Table 3, there is about 20%

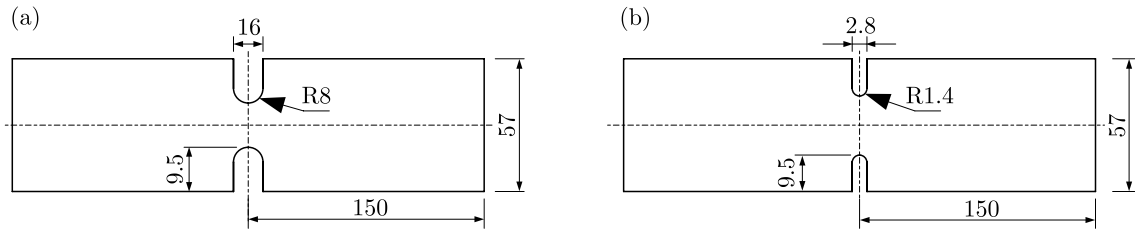


Fig. 2. The geometric profile of the notched specimen (dimensions in mm): (a) $K_T = 2$, (b) $K_T = 4$

Table 3. Comparisons between experimental lives and predicted results

	Stress ratio	σ_{max} [MPa]	Experimental life	Numerical results	Error [%]
$K_T = 2$	-0.2	175	34160	26370	22.80
	-0.09	155	114000	90450	20.66
	0.02	137	217200	238000	9.58
	0.25	112	1094000	1354000	23.77
	0.4	100	9490000	8035000	15.33
	0.4	300	85390	74300	12.98
	0.60	262	226100	288900	27.77
	0.68	250	778600	881350	13.20
	0.75	240	2037000	1672000	17.92
	0.79	235	2445000	1906000	22.04
$K_T = 4$	0.02	137	45350	35700	21.28
	0.25	112	180900	157500	12.93
	0.4	100	646000	803200	24.33
	0.55	90	2458000	2079000	15.42
	0.60	87	3319000	2885000	13.08
	0.60	262	45320	36500	19.46
	0.68	250	64200	78300	21.96
	0.75	240	190400	174000	8.61
	0.83	230	753200	845400	12.24
	0.91	220	1483000	1727000	16.45

deviation between the actual fatigue life and the results calculated by CDM. The deviation is mainly due to several factors: (1) some parameters in the theoretical model are not accurate; (2) there are structural defects in the theoretical model; (3) experimental environment and hardware conditions lead to certain system errors. In a word, the deviation is appeared by complicated reasons. It is difficult to develop a theoretical approach to calculate. Therefore, the RBF neural network method is adopted to modify the CDM model to obtain a more reliable fatigue life prediction result.

The RBF neural network model is composed of 3 layers: an input layer, a hidden layer and an output layer. Its topological structure is shown in Fig. 3. There are two neurons in the input layer, one stands for the stress ratio R and another represents the ultimate stress σ_{max} . In order to enhance the training efficiency and speed up the convergence rate, the input data will be standardized $(\bar{\sigma}_{max}, \bar{R})$ before imported into the hidden layer. Each weight from the input layer to the hidden layer is equal to 1. The neuron number in the hidden layer is set as h , and each neuron represents a cluster center which is corresponding to the basis vector. The Gauss function is selected as the radial basis function. The input sample in the training set is denoted as: $\mathbf{X} = [x_1, x_2, \dots, x_i, \dots, x_p]^T$, and each sample contains 2 dimension data: $x_i = (\bar{\sigma}_{max}, \bar{R})$. The

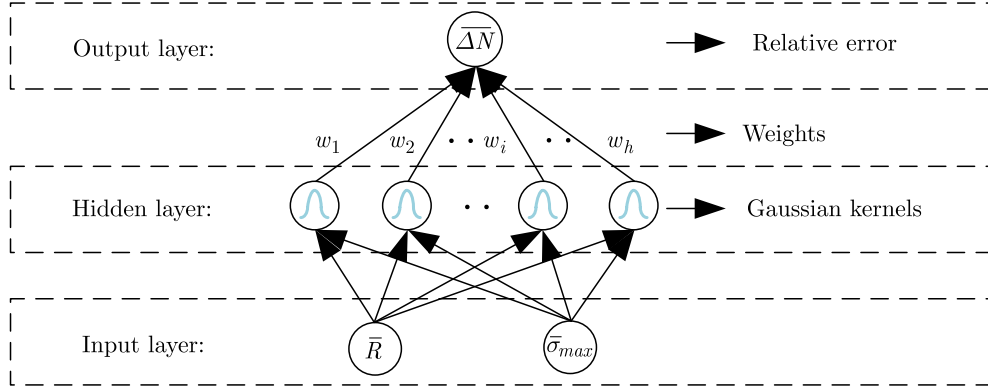


Fig. 3. The topological structure for an RBR neural network model

output label $\overline{\Delta N} = [\overline{\Delta N}_1, \overline{\Delta N}_2, \dots, \overline{\Delta N}_i, \dots, \overline{\Delta N}_p]^T$ is the relative deviation percent between the actual life N_A and the theoretical result N_F , expressed as: $\overline{\Delta N}_i = (N_A - N_F)/N_F$. p is the total sample number in the train set. The response output O_{1ij} from the i -th sample to the j -th neuron in the hidden layer can be calculated by Eq. (5.1), in which σ is the variance of the Gauss function, c_j stands for the j -th cluster center, $\|\mathbf{x}_i - \mathbf{c}_j\|$ represents the Euclidean distance between the input vector \mathbf{x}_i and \mathbf{c}_j

$$O_{1ij} = \exp\left(-\frac{1}{2\sigma^2}\|\mathbf{x}_i - \mathbf{c}_j\|^2\right) \quad (5.1)$$

The final output \overline{N} of the RBF model is the relative deviation percent between the actual life and the theoretical result. The output is calculated by a linear combination of all Gaussian function outputs in the hidden layer. w_j is the weight from the j -th neuron in the hidden layer to the output. Then, the final output for the i -th sample can be calculated as

$$O_{2i} = \sum_{j=1}^h w_j O_{1ij} = \sum_{j=1}^h w_j \exp\left(-\frac{1}{2\sigma^2}\|\mathbf{x}_i - \mathbf{c}_j\|^2\right) \quad (5.2)$$

6. The learning process for the RBF neural network model

The learning process for the RBF model is divided into the unsupervised learning stage and the supervised learning stage.

6.1. Unsupervised learning stage

In the unsupervised learning stage, the K -means method is used to automatically cluster the sample data and locate the center of each Gaussian kernel function. The iteration step is shown as below.

Step 1. Initialization: h points are random selected as the initial cluster center

$$c_1(\overline{\sigma}_1, \overline{R}_1), c_2(\overline{\sigma}_2, \overline{R}_2), \dots, c_i(\overline{\sigma}_i, \overline{R}_i), \dots, c_h(\overline{\sigma}_h, \overline{R}_h)$$

Step 2. Clustering: Each point is sorted out into the corresponding cluster by the principle of proximity.

Step 3. Adjustment of the clustering center: The new position of each clustering center is updated by calculating the average value of sample points. If all the clustering centers are not changed any more, then the current centers will be regarded as the Gaussian kernel function centers in the hidden layer of the RBF model, the iteration ends; Else, back to Step 2.

6.2. Supervised learning stage

On the basis of the K -means clustering result in the unsupervised learning stage, the variance of the Gaussian kernel function in the hidden layer can be obtained by Eq. (6.1), in which d_{max} represents the maximum distance between the clustering centers

$$\sigma = \frac{d_{max}}{\sqrt{2h}} \quad (6.1)$$

After the determination of the clustering centers $c = (c_1, c_2, c_3, \dots, c_i, \dots, c_h)$ and the variance σ , the weight matrix can be calculated by solving the linear system in Eq. (6.2) with the least squares method

$$\begin{bmatrix} w_{11} & w_{12} & \cdots & w_{1h} \\ w_{21} & w_{12} & \cdots & w_{2h} \\ w_{31} & w_{12} & \cdots & w_{3h} \end{bmatrix} \begin{bmatrix} O_{11} \\ O_{12} \\ \vdots \\ O_{1h} \end{bmatrix} = \begin{bmatrix} y_1 \\ y_2 \\ y_3 \end{bmatrix} \quad (6.2)$$

7. Optimization of the RBF model based on a GA algorithm

The selection of the Gaussian kernel center is the core element of the RBF neural network design. In order to improve the neural network quality and reduce the training error, a Genetic Algorithm is adopted to optimize the initial position of each Gaussian kernel center. Chromosome encoding, fitness function selection and definition of the genetic operator are 3 parts of the GA algorithm design.

7.1. Chromosome encoding

When a GA is used to solve a numerical optimization problem, the binary code cannot achieve very good results. Therefore, the real number chromosome encoding is adopted, as shown in Fig. 4. Each chromosome is composed of several gene segments, and each segment represents a certain Gaussian kernel center position $c_i(\bar{\sigma}_i, \bar{R}_i)$.



The gene segment corresponding to the i -th Gaussian kernel

Fig. 4. A sample of chromosome encoding

7.2. The fitness function and the roulette selection probability

The fitness function is used to evaluate the accuracy of calculated results. According to the previous discussion, the objective function of RBF training is expressed as Eq. (7.1)₁, and the definition of the fitness function is shown in Eq.(7.1)₂

$$E = \frac{1}{2} \sum_{i=1}^{i=p} (O_{2i} - y_i)^2 \quad \text{Fitness} = \frac{1}{E} \quad P_k = \frac{\text{Fitness}_k}{\sum_{i=1}^{i=Pop} \text{Fitness}_i} \quad (7.1)$$

For the k -th individuals in the population, its probability of being chosen for evolution is calculated by the individual fitness and the total fitness, as shown in Eq. (7.1)₃. The selection process is carried out by the roulette mode, as shown in Fig. 5. The whole disc area represents the total fitness of the population, and the fitness of each individual is corresponding to a certain sector area. The area the pointer finally stays determines which individual is selected. In this way, a higher individual fitness means a greater possibility of being chosen, while a lower fitness also has a little possibility to evolve.

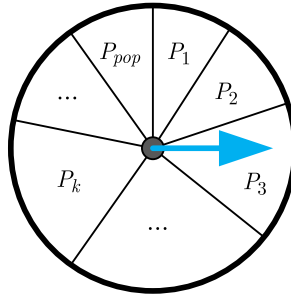


Fig. 5. The roulette choosing mode

7.3. Genetic operator: crossover and mutation

The purpose of the genetic operator is to preserve good chromosomes into the next generation. Assuming the crossover operator is happening on the k -th gene segment of the parent chromosome $ch^i = \{ch_1^i, ch_2^i, \dots, ch_k^i, \dots, ch_m^i\}$ and $ch^j = \{ch_1^j, ch_2^j, \dots, ch_k^j, \dots, ch_m^j\}$, then the real numbers of the k -th gene segment in the two new chromosome (ch^{is}, ch^{js}) are calculated by Eq. (7.2), where ψ is the crossover possibility and set as 80%.

$$ch_k^{is} = \psi ch_k^i + (1 - \psi) ch_k^j \quad ch_k^{js} = \psi ch_k^j + (1 - \psi) ch_k^i \quad (7.2)$$

Each gene segment is composed of 2 normalized data: the stress ratio and the ultimate stress. Therefore, the crossover process between the parents is equivalent to calculation of two symmetric definite proportionate inserted points in a straight line defined by $(\bar{\sigma}_k^i, \bar{R}_k^i)$ and $(\bar{\sigma}_k^j, \bar{R}_k^j)$, as shown in Fig. 6.

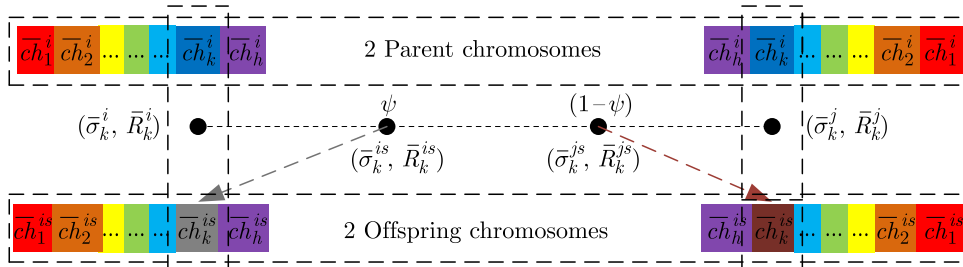


Fig. 6. The crossover process between 2 parent chromosomes

Different from binary coding, the mutation operator of real number encoding is to add a random bias d to the selected gene segment, denoted as: $ch_k^{is} = ch_k^i + d$. The mutation operator ensures diversity of population, and its probability is set as 3%.

7.4. The training process of the GARBF model

The GA algorithm is adopted to optimize the Gaussian kernel center positions in the hidden layer during the RBF training process, and the iteration step is shown as below.

- Step 1.** Randomly initialize the population (random selection of the clustering center position in the hidden layer), and encode the chromosomes.
- Step 2.** Calculate the fitness of each individual in the population, and select the optimal individual.
- Step 3.** If the number of generation reaches the maximum or the optimal individual satisfies the requirements of training accuracy, go to Step4; Else, the next generation of population will be produced by the 3 genetic operator: mutation, crossover and selection, then go to Step 2.
- Step 4.** The chromosomes are anti-encoding and the initial clustering center positions c_1, c_2, \dots, c_h in the hidden layer are obtained.
- Step 5.** The parameters of the RBF model are trained by the supervised learning method, the iteration ends.

All the experimental data are divided into two parts, 80% for training and 20% for the verification test. There is no intersection between the training set and the test set. The training error descent curve by the GARBF and RBF method are shown in Fig. 6. When the iteration epoch is less than 30, the optimization effect of the GA is not obvious, just as the red circle region shown in Fig. 7; As the iteration epoch is increasing, it is indicated that the GARBF method is superior to simple use of the RBF method in both the convergence rate and training error aspect. After about 430 epochs, the training error is reduced and converged to 0.0017.

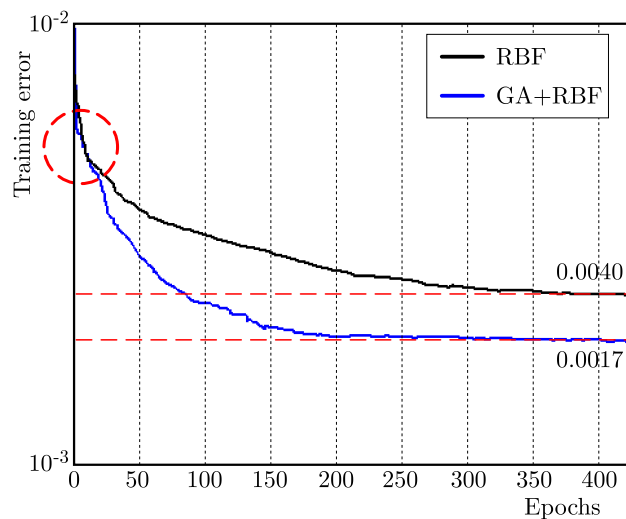


Fig. 7. The training error descent curve of GARBF and RBF models

8. The combined method of CDM and GARBF

The CDM and GARBF method are combined to accurately predict the fatigue life for LY12CZ notched plate. On the basis of the establishment of the CDM model, the trained GARBF model is adopted to modify the theoretical result and obtain the prediction life. In the verification

test, N_F represents the theoretical result calculated by the CDM model, and N_{GARBF} stands for the result after being modified by the trained GARBF model, N_A actual life measured in the experiment. The relative error percent between N_F and N_A is denoted as e_{FA} , and the relative error percent between N_{GARBF} and N_A is denoted as e_{GARBF} . e_{FA} and e_{GARBF} can be calculated by Eq. (8.1). Under the two conditions of $K_T = 2$ and $K_T = 4$, the distributions of e_{FA} and e_{GARBF} are shown in Fig. 8, in which X and Y label respectively mean the input value of σ_{max} and R . The red circles mean the relative error exceed 20%, while the blue ones mean that the relative error is less than 5%. The distribution of the relative error indicates that the prediction results modified by the trained GARBF will be closer to the actual life in the whole. The combined method of CDM and GARBF proposed in this paper is effective and reliable

$$e_F = \frac{N_F - N_A}{N_F} \cdot 100.0\% \quad e_{GARBF} = \frac{N_{GARBF} - N_A}{N_{GARBF}} \cdot 100.0\% \quad (8.1)$$

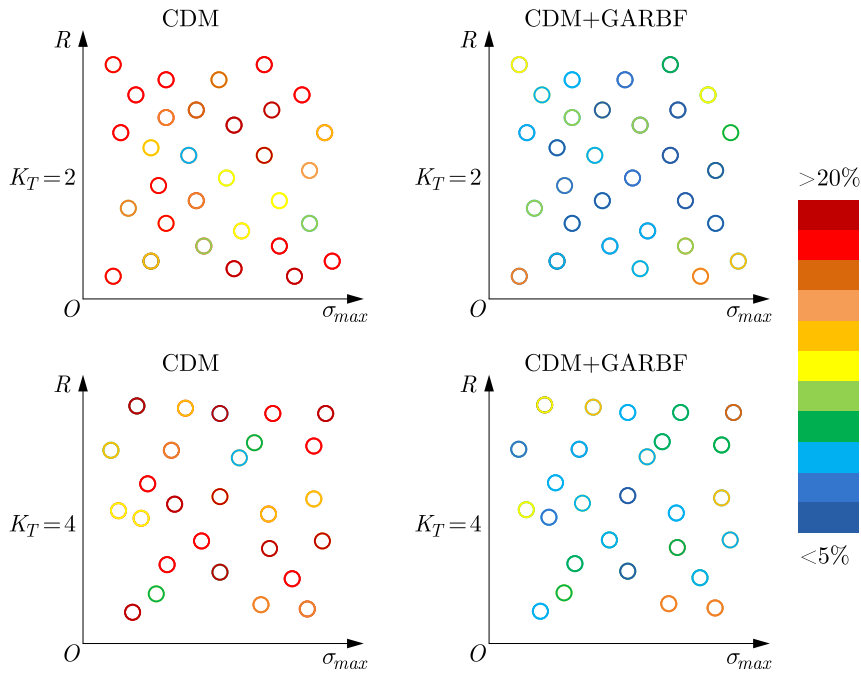


Fig. 8. The distribution of relative error calculated by CDM and CDM + GARBF

The combination method proposed in this paper is composed of a theoretical model (CDM) and an optimization model (GARBF). Actually, the selection of optimization model is not unique. In order to compare the effects of different optimization models, Table 4 respectively presents the optimization performances by traditional BPNN and GARBF models under the same verification test data. The statistic results indicate the average relative error of GARBF is 6.85%, and the average relative error calculated by BPNN is 7.2%. The two methods have a similar optimization effect of the average relative error. However, the GARBF model is much better than the BPNN model when comparing the variance of the relative error ($D_{BP} = 6.0, D_{GARBF} = 2.49$). Figure 9 shows the relative error optimized after BPNN and GARBF under a fixed value of K_T and R . The distribution of the relative error indicates that the optimization effect of GARBF is more stable in the whole, while some calculations of BPNN seem to fluctuate significantly. The GARBF method adopts Gaussian kernel as the activation function that means the response will close to 0 when the input data is far from the cluster centers. The BPNN method uses the sigmoid function which has a large output region. Therefore, when the input data is a set of “strange

data” that has not been trained, the output of the BPNN maybe seriously far from the true one, while the GARBF model will output a relative small value and choose to believe the results calculated by CDM theory. In a word, the optimization effect of GARBF is more reliable and stable.

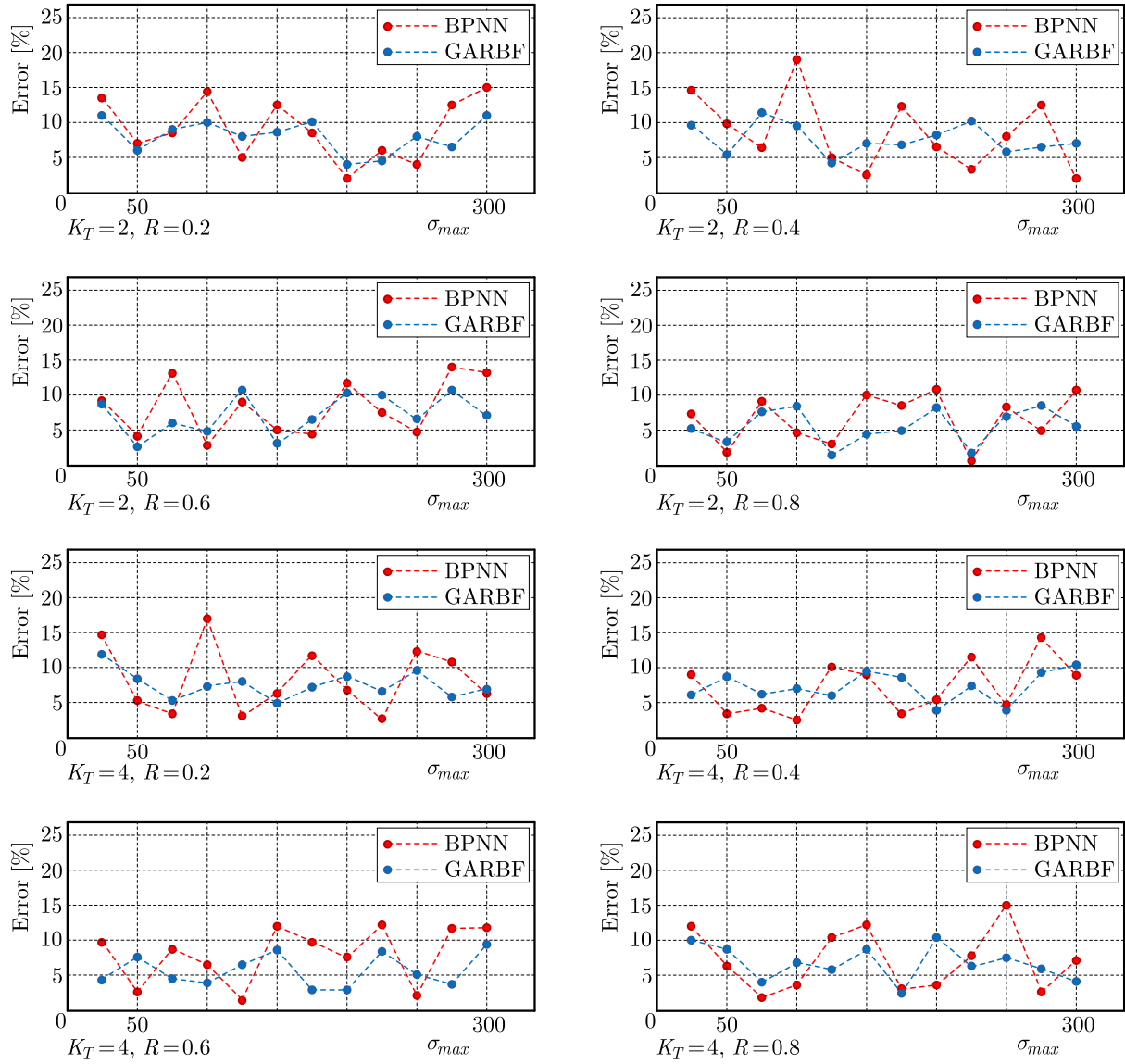


Fig. 9. The error distribution optimized by BPNN and GARBF under a fixed value of K_T and R

9. Conclusions remarks

In this paper, a new method based on the CDM and GARBF neural network method is proposed to predict the fatigue life of LY12CZ notched plate. Some important conclusions are summarized as follows:

- The multiaxial fatigue damage evolution equation is derived and the theoretical model for fatigue life prediction of LY12CZ notched plate is established. The predicted results based on the CDM method tally with the fatigue experimental results.

Table 4. Optimization effect comparisons between the BPNN and GARBF model

	Stress ratio	σ_{max} [MPa]	Relative error of BPNN [%]	Relative error of GARBF [%]
$K_T = 2$	-0.2	175	14.78	9.07
	-0.09	155	5.09	5.64
	0.02	137	0.84	4.04
	0.25	112	14.73	10.69
	0.4	100	17.79	8.79
	0.4	300	2.44	7.06
	0.60	262	2.09	6.27
	0.68	250	15.16	7.16
	0.75	240	2.14	3.05
	0.79	235	1.76	2.88
$K_T = 4$	0.02	137	10.85	12.03
	0.25	112	16.48	8.48
	0.4	100	3.47	7.66
	0.55	90	2.85	5.64
	0.60	87	6.93	3.95
	0.60	262	2.87	5.41
	0.68	250	3.98	3.83
	0.75	240	15.54	8.54
	0.83	230	1.6	7.55
	0.91	220	2.65	9.27
Mean relative error [%]: $e_{BP} = 7.2$, $e_{GARBF} = 6.85$				
Variance of relative error [% ²]: $D_{BP} = 6.0$, $D_{GARBF} = 2.49$				

- The RBF method is introduced to modify the relative deviation between the theoretical result and the actual life. The verification test indicates the combined method of CDM and GARBF is able to reduce the average relative error of the results of fatigue life prediction to about 7%, which shows that the new method to predict the fatigue life is more reliable.
- Compared to the traditional BPNN model, the GARBF model proposed in this paper has a better optimization effect and the result is more stable. When the input is a set of “strange data” that has not been trained, the output of the BPNN may be seriously far from the true output in some local region, while the GARBF model will output a relative small value and choose to believe the results calculated by CDM theory.

References

1. CAMACHO-VALLEJO J.-F., MAR-ORTIZ J., LÓPEZ-RAMOS F., RODRÍGUEZ R.P., 2015, A genetic algorithm for the bi-level topological design of local area networks, *Plos One*, **10**, 6, 1-21
2. GAO J., HE Q., ZHAN Z., GAO X., 2016, Dynamic modeling based on fuzzy Neural Network for a billiard robot, *IEEE, 13th International Conference on Networking, Sensing and Control*
3. GAO J., ZHU M., LIANG H., GUO X., HE Q., 2015, Design of the multiple Neural Network compensator for a billiard robot, *IEEE, International Conference on Networking, Sensing and Control*, 17-22
4. GOLDBERG D.E., SAMTANI M.P., 2015, Engineering optimization via genetic algorithm, *Proceedings of 9th Conference Electronic Computation, ASCE*, 471-482

5. GUO H., YIN J., ZHAO J., HUANG Z., PAN Y., 2014, Prediction of fatigue life of packaging EMC material based on RBF-SVM, *International Journal of Materials and Product Technology*, **49**, 1, 5-17
6. KAROLCZUK A., MACHA E., 2005, A review of critical plane orientations in multiaxial fatigue failure criteria of metallic materials, *International Journal of Fracture*, **134**, 3-4, 267-304
7. LEMAITRE J., CHABOCHE J.L., 1990, *Mechanics of Solid Materials*, Cambridge University Press
8. LI B., SANTOS J.L.T., FREITAS M., 2000, A unified numerical approach for multiaxial fatigue limit evaluation, *Mechanics of Structures and Machines*, **28**, 1, 85-103
9. LIU C.H., XUAN F.Z., 2008, A determination method of important affecting parameters on low circle fatigue life, *Materials for Mechanical Engineering*, **32**, 12, 22-24
10. MONTEIRO R.L.S., CARNEIRO T.K.G., FONTOURA J.R.A., DA SILVA V.L., MORET M.A., PEREIRA H.B., 2016, A model for improving the learning curves of artificial neural networks, *Plos One*, **11**, 2
11. MOVAGHGHAR A., LVOV G.I., 2012, A method of estimating wind turbine blade fatigue life and damage using continuum damage mechanics, *International Journal of Damage Mechanics*, **21**, 6, 810-821
12. NAGARAJAN R., JONKMAN J.N., 2013, A neural network model to translate brain developmental events across mammalian species, *Plos One*, **8**, 1
13. PUJOL J.C.F., PINTO J.M.A., 2011, A neural network approach to fatigue life prediction, *International Journal of Fatigue*, **33**, 3, 313-322
14. REID D., HUSSAIN A.J., TAWFIK H., 2013, Financial time series prediction using spiking neural networks, *Plos One*, **9**, 8, e103656-e103656
15. SCHIJVE J., 2001, *Fatigue of Structures and Materials*, Springer
16. SURESH S., 1998, *Fatigue of Materials*, Cambridge (UK), Cambridge University Press
17. UPADHYAYA Y.S., SRIDHARA B.K., 2012, Fatigue life prediction: a continuum damage mechanics and fracture mechanics approach, *Materials and Design*, **35**, 220-224
18. WU X., 1996, *Handbook of Mechanical Properties of Aircraft Structural Metals*, China Aviation Industry Press, Beijing
19. ZHAN Z., HU W., LI B., ZHANG Y., MENG Q., 2017a, Continuum damage mechanics combined with the extended finite element method for the total life prediction of a metallic component, *International Journal of Mechanical Sciences*, **124**, 48-58
20. ZHAN Z., HU W., MENG Q., GUAN Z., 2017b, Fatigue life and defect tolerance calculation for specimens with foreign object impact and scratch damage, *Archive of Applied Mechanics*, **88**, 3, 373-390
21. ZHAN Z., HU W., MENG Q., SHI S., 2016, Continuum damage mechanics-based approach to the fatigue life prediction for 7050-T7451 aluminum alloy with impact pit, *International Journal of Damage Mechanics*, **25**, 7, 943-966
22. ZHAN Z., HU W., SHEN F., MENG Q., PU J., GUAN Z., 2017c, Fatigue life calculation for a specimen with an impact pit considering impact damage, residual stress relaxation and elastic-plastic fatigue damage, *International Journal of Fatigue*, **96**, 208-223
23. ZHAN Z., HU W., ZHANG M., MENG Q., 2015a, A study on the effect of surface defect on the fatigue performance of metal component based on damage mechanics, *Mechanics*, **21**, 1, 5-10
24. ZHAN Z., HU W., ZHANG M., MENG Q., 2015b, Revised damage evolution equation for high cycle fatigue life prediction of aluminum alloy LC4 under uniaxial loading, *Applied Mathematics and Mechanics*, **36**, 9, 1185-1196
25. ZHAN Z., HU W., ZHANG M., MENG Q., 2015c, The fatigue life prediction for structure with surface scratch considering cutting residual stress, initial plasticity damage and fatigue damage, *International Journal of Fatigue*, **74**, 173-182

26. ZHAN Z., HU W., ZHANG M., ZHU Y., MENG Q., 2013, Experimental method for and theoretical research on defect tolerance of fixed plate based on damage mechanics, *Chinese Journal of Aeronautics*, **26**, 5, 1195-1201
27. ZHAN Z., MENG Q., HU W., SUN Y., SHEN F., ZHANG Y., 2017d, Continuum damage mechanics based approach to study the effects of the scarf angle, surface friction and clamping force over the fatigue life of scarf bolted joints, *International Journal of Fatigue*, **102**, 59-78

Manuscript received January 14, 2018; accepted for print April 10, 2018

AN EFFICIENT ANALYSIS OF STEADY-STATE HEAT CONDUCTION INVOLVING CURVED LINE/SURFACE HEAT SOURCES IN TWO/THREE-DIMENSIONAL ISOTROPIC MEDIA

MEHRDAD MOHAMMADI

Department of Mechanical Engineering, Shiraz Branch, Islamic Azad University, Shiraz, Iran

MOHAMMAD R. HEMATIYAN

Department of Mechanical Engineering, Shiraz University, Shiraz, Iran

YUICHUIN C. SHIAH

Department of Aeronautics and Astronautics, National Cheng Kung University, Tainan, Taiwan, R.O.C.

e-mail: ycsiah@mail.ncku.edu.tw

In this paper, a new formulation based on the method of fundamental solutions for two/three-dimensional steady-state heat conduction problems involving internal curved line/surface heat sources is presented. Arbitrary shapes and non-uniform intensities of the curved heat sources can be modeled by an assemblage of several parts with quadratic variations. The presented mesh-free modeling does not require any internal points as in domain methods. Four numerical examples are studied to verify the validity and efficiency of the proposed method. Our analyses have shown that the presented mesh-free formulation is very efficient in comparison with conventional boundary or domain solution techniques.

Keywords: heat conduction, concentrated heat source, curved heat source, mesh-free method

1. Introduction

Heat conduction and thermoelasticity involving boundary or domain heat sources have been subject of many studies in the last years, and they are still active areas of researches (e.g. Rogowski, 2016; Hidayat *et al.*, 2017). In real applications, it is quite often to have internal heat sources concentrated on points, lines or curved paths due to electrical heating or some other heat sources like laser beams. As examples, we can mention infrared heating, a method of electric heating that is frequently used in the metallurgy and textile industries, laser beam heating/welding that is used in automotive and aerospace industries, and friction heating for material processing and joining. Despite several analytical solutions for simple problems involving concentrated heat sources (e.g. Chao and Tan, 2000; Han and Hasebe, 2002), practical problems with complicated conditions still need to resort to numerical tools. The accuracy analysis of the domain solution methods such as the finite element method (FEM) depends on the mesh density especially near the concentrated heat source. As powerful alternative approaches, the boundary methods such as the boundary element method (BEM) and the method of fundamental solutions (MFS) only require boundary discretization.

To date, the BEM has been effectively used to solve direct and inverse problems containing concentrated sources of heat generation. Le Niliot (1998) proposed a boundary element formulation for identification of the intensity of point heat sources in diffusive systems. In another work, Le Niliot and Lefèvre (2001) proposed a BEM to identify the location and strength of multiple point heat sources in a transient heat conduction problem. Karami and Hematiyan (2000a,b) proposed a formulation based on the BEM for direct and inverse analyses of heat

conduction problems containing concentrated sources of heat generation. They presented an exact implementation of a source of heat generation concentrated on a point or a line in the BEM formulation. Shiah *et al.* (2005) analyzed two-dimensional thermo-mechanical problems containing point sources using the BEM. They could solve the problem with boundary-only discretization. In another research, Shiah *et al.* (2006) used the direct domain mapping (DDM) technique to analyze 2D and 3D heat conduction problems in composites consisting of multiple anisotropic media with embedded point heat sources. Hematiyan *et al.* (2011) presented a formulation based on the BEM for analysis of two and three dimensional thermo-elastic problems involving point, line and area heat sources. They only employed boundary discretization in their formulation. However, their proposed formulation considered only straight line and flat surface heat sources with a linear variation of the heat source intensity. Mohammadi *et al.* (2016) used the BEM for analysis of two- and three-dimensional thermo-elastic problems involving arbitrary curved line heat sources. They effectively solved the problem without considering any internal points/cells; but they did not consider curved surface heat sources.

The present work uses the MFS to analyze problems of 2D/3D heat conduction involving internal concentrated heat sources. In this paper, the MFS, a widely applied meshless method, is shown to be very efficient for the analysis on account of which the benefit is that no internal points/nodes are required for the modeling. Similar to the BEM, the MFS is applicable when a fundamental solution of the problem is known. However, the important advantage of the MFS over the BEM is that the MFS is an integration-free method and it can be easily implemented for problems especially in three-dimensional and irregular domains. The basic idea of the MFS is to approximate the solution as a linear combination of fundamental solutions. The singularities (sources) of the fundamental solutions are located outside the physical domain of the problem. The MFS solutions exactly satisfy governing equations of the problem and approximately satisfy boundary conditions. In the study carried out by Fairweather and Karageorghis (1998), the development of the MFS in the past three decades was explained.

The equation governing steady-state heat conduction in a medium with a heat source is the standard Poisson equation. To solve Poisson's equation using the MFS, a particular solution corresponding to the heat source term in addition to a homogeneous solution of the Laplace equation should be found. Two important methods proposed to calculate this particular solution are the Atkinson method (1985) and the dual reciprocity method (DRM) (Partridge *et al.*, 1992). In Atkinson's method, the particular solution is taken to be a Newton potential and is obtained by evaluating a domain integral. Poulikkas *et al.* (1998) used this method for solving inhomogeneous harmonic and biharmonic problems. In the DRM, the particular solution is approximated by a series of basis solutions. As an example, Golberg (1995) used this method to solve Poisson's equation without a boundary or domain discretization.

In this work, the MFS is formulated for 2D/3D problems of heat conduction involving internal heat sources concentrated on curved lines/surfaces. Although the MFS has been widely used for analysis of heat conduction problems in different conditions (e.g. Ahmadabadi *et al.*, 2009; Kołodziej *et al.*, 2010; Mierzwiczak and Kołodziej, 2012); however, to the authors' knowledge, the MFS formulation for analysis of internal curve line/surface heat sources has not been presented yet. The method presented here can be simply employed without considering any internal points/nodes and, therefore, it preserves the attractiveness of the MFS as a boundary-type mesh-free method. Several two- and three-dimensional numerical examples are presented at the end to show that the proposed formulation is very efficient to yield accurate results in comparison with the BEM and FEM.

2. MFS formulation for steady-state heat conduction in a domain including heat sources

Consider an isotropic medium Ω with its boundary Γ (Fig. 1). In the presence of heat sources, the governing equation of steady-state heat conduction can be expressed as follows

$$\nabla^2 \tau(\mathbf{x}) = -\frac{s(\mathbf{x})}{k} \quad \mathbf{x} \in \Omega \quad (2.1)$$

where ∇^2 represents the Laplace operator, τ is temperature, k is thermal conductivity, and $s(\mathbf{x})$ is a known function describing the heat source distribution.

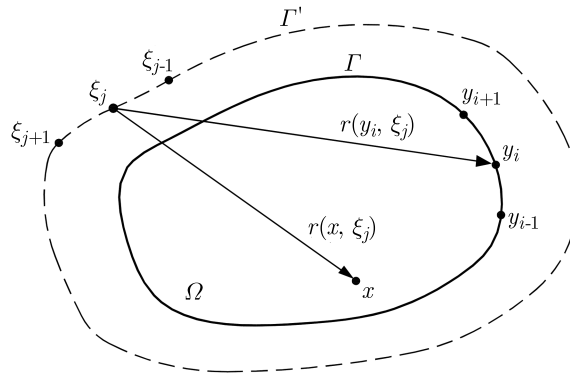


Fig. 1. Domain Ω , boundary Γ and pseudo boundary Γ'

Boundary condition in a generalized form can be written as follows

$$f_1 \tau + f_2 \frac{\partial \tau}{\partial n} = f_3 \quad \text{on } \Gamma \quad (2.2)$$

where f_1 , f_2 and f_3 are given functions on the boundary and n is the normal direction.

In the MFS, the solution to Poisson equation (2.1) is approximated by a linear combination of fundamental solutions of the Laplace equation and a particular solution

$$\tau(\mathbf{x}) = \sum_{j=1}^N a_j \tau^*(\mathbf{x}, \xi_j) + \tau_p(\mathbf{x}) \quad (2.3)$$

where ξ_j and a_j are the known location and unknown intensity of the j -th source located on the pseudo-boundary Γ' (Fig. 1), respectively. \mathbf{x} is a point in the domain or on the boundary of the solution domain, and N is the number of sources. τ^* represents the fundamental solution to the Laplace operator that is given as follows

$$\tau^*(\mathbf{x}, \xi_j) = \begin{cases} \frac{-1}{2\pi} \ln(r(\mathbf{x}, \xi_j)) & \text{for } 2D \\ \frac{1}{4\pi r(\mathbf{x}, \xi_j)} & \text{for } 3D \end{cases} \quad (2.4)$$

where $r(\mathbf{x}, \xi_j)$ is the distance between the field point \mathbf{x} and the source point ξ_j . $\tau_p(\mathbf{x})$ is the particular solution to equation (2.1) associated to the heat source function $s(\mathbf{x})$ that can be concentrated on a part of the domain or distributed over the entire domain. The particular solution can be obtained by constructing the associated Newton potential in the following domain integral form

$$\tau_p(\mathbf{x}) = \frac{1}{k} \int_{\Omega} s(\xi) \tau^*(\mathbf{x}, \xi) dV(\xi) \quad (2.5)$$

Efficient evaluation of this domain integral is very important in the MFS to maintain the attractiveness of the method. If one can evaluate the domain integral in Eq. (2.5) without considering any internal cells/points, the attractiveness of the MFS is preserved.

The constants a_j (with the unit m°C in the SI system) are unknown intensities of the sources and they have to be found. To find these unknowns, we consider N boundary points $\mathbf{y}_1, \mathbf{y}_2, \dots, \mathbf{y}_N$ that are a priori located on Γ and collocate the corresponding boundary condition at these points. From Eqs. (2.2) and (2.3), the following equation is obtained

$$\sum_{j=1}^N a_j \left[f_1(\mathbf{y}_i) \tau^*(\mathbf{y}_i, \boldsymbol{\xi}_j) + f_2(\mathbf{y}_i) \frac{\partial \tau^*(\mathbf{y}_i, \boldsymbol{\xi}_j)}{\partial n} \right] = f_3(\mathbf{y}_i) - \left[f_1(\mathbf{y}_i) \tau_p(\mathbf{y}_i) + f_2(\mathbf{y}_i) \frac{\partial \tau_p(\mathbf{y}_i)}{\partial n} \right] \quad i = 1, 2, \dots, N \quad (2.6)$$

which represents a system of N linear equations with N unknowns. In general, one can write system (2.6) as follows

$$\mathbf{A}\mathbf{X} = \mathbf{F} \quad (2.7)$$

where the components of the matrix $\mathbf{A} \in \mathcal{R}^{N \times N}$ and the vectors $\mathbf{F} \in \mathcal{R}^N$ and $\mathbf{X} \in \mathcal{R}^N$ are expressed as follows

$$A_{ij} = f_1(\mathbf{y}_i) \tau^*(\mathbf{y}_i, \boldsymbol{\xi}_j) + f_2(\mathbf{y}_i) \frac{\partial \tau^*(\mathbf{y}_i, \boldsymbol{\xi}_j)}{\partial n} \quad F_i = f_3(\mathbf{y}_i) - \left[f_1(\mathbf{y}_i) \tau_p(\mathbf{y}_i) + f_2(\mathbf{y}_i) \frac{\partial \tau_p(\mathbf{y}_i)}{\partial n} \right] \quad X_i = a_i \quad (2.8)$$

By selecting a suitable configuration for boundary and source points, Eq. (2.7) can be solved by standard methods such as the Gaussian elimination method.

In the next Section, the method for computation of the particular solution $\tau_p(\mathbf{x})$ using Eq. (2.5) for the special case of heat sources concentrated on a curved line/surface is described.

3. Formulations for heat sources concentrated on a curved line/surface

In this Section, particular solutions associated to curved line/surface heat sources in the MFS are presented. For the 2D case, curved line sources, while for the 3D case, both curved line and curved surface sources are considered.

3.1. Curved line heat source in 2D problems

At first, the formulation for a curved line heat source with a quadratic shape is presented. It is also assumed that the intensity of the source has a quadratic variation along the heat source. An arbitrary curved line heat source can be modeled by several quadratic heat sources. A domain including a general curved line heat source and a part of the source modeled as a quadratic line heat source is illustrated in Fig. 2. Each quadratic line heat source is discretized by three points. The intensity per unit length of the source at the starting point (x_1, y_1) , middle point (x_2, y_2) , and end point (x_3, y_3) are represented by g_1, g_2, g_3 , respectively.

Assuming a quadratic variation for the intensity of the heat source, $s(\mathbf{x})$ can be given as follows

$$s(\eta) = N_1 g_1 + N_2 g_2 + N_3 g_3 \quad (3.1)$$

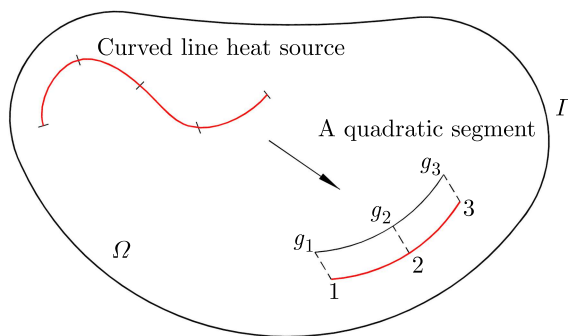


Fig. 2. An arbitrary curved line heat source modeled as several quadratic line heat sources

where the quadratic shape functions N_i are

$$N_1 = \frac{1}{2}\eta(\eta - 1) \quad N_2 = -(\eta + 1)(\eta - 1) \quad N_3 = \frac{1}{2}\eta(\eta + 1) \quad (3.2)$$

where η is a dimensionless local coordinate aligned with the quadratic segment that varies from -1 to 1 .

Domain integral (2.5) for the quadratic line heat source can be expressed as follows

$$\tau_p(\mathbf{x}) = \int_L \frac{s(\boldsymbol{\xi})}{k} \tau^*(\mathbf{x}, \boldsymbol{\xi}) dl \quad (3.3)$$

where dl is an infinitesimal element along the quadratic line heat source. Substituting τ^* in the 2D case from Eq. (2.4) into Eq. (3.3) results in

$$\tau_p(\mathbf{x}) = \frac{-1}{2\pi k} \int_l s(\boldsymbol{\xi}) \ln[r(\mathbf{x}, \boldsymbol{\xi})] dl \quad (3.4)$$

where $r(\mathbf{x}, \boldsymbol{\xi}) = \sqrt{(x - x_s)^2 + (y - y_s)^2}$ is the distance between the field point $\mathbf{x} = (x, y)$ and the source points $\boldsymbol{\xi} = (x_s, y_s)$ on the quadratic line heat source. x_s and y_s can be expressed in terms of the three points of the quadratic line heat source as follows

$$x_s = (N_1x_1 + N_2x_2 + N_3x_3) \quad y_s = (N_1y_1 + N_2y_2 + N_3y_3) \quad (3.5)$$

Using Eqs. (3.5), the infinitesimal element dl in Eq. (3.4) can be expressed as

$$dl = \sqrt{dx_s^2 + dy_s^2} = J d\eta \quad (3.6)$$

where J is Jacobian which can be expressed as

$$J = \sqrt{\left(x_1 \frac{dN_1}{d\eta} + x_2 \frac{dN_2}{d\eta} + x_3 \frac{dN_3}{d\eta}\right)^2 + \left(y_1 \frac{dN_1}{d\eta} + y_2 \frac{dN_2}{d\eta} + y_3 \frac{dN_3}{d\eta}\right)^2} \quad (3.7)$$

Substituting Eqs. (3.1) and (3.6) into Eq. (3.4) results in

$$\tau_p(\mathbf{x}) = \frac{-1}{2\pi k} \int_{-1}^1 (N_1g_1 + N_2g_2 + N_3g_3) \ln[r(\eta)] J d\eta \quad (3.8)$$

The integral in Eq. (3.8) can be calculated using conventional numerical integration methods such as the Gaussian quadrature method (GQM). It should be noted that if the field point

$\mathbf{x} = (x, y)$ is exactly on the line source, the integral in Eq. (3.8) will be weakly singular with a finite value. In other words, in the two-dimensional case, the temperature has a finite value at points exactly on the curved line heat source. In this case, the integral in Eq. (3.8) can be calculated by various methods such as the weighted Gaussian integration (Stroud and Secrest, 1996), transformation of variable (Telles, 1987) and subtraction of singularity (Aliabadi 2002) method. In this research, the weighted Gaussian integration method is used.

3.2. Curved line heat source in three-dimensional problems

Similar to 2D, the intensity per unit length of the quadratic line heat source at the starting point (x_1, y_1, z_1) , middle point (x_2, y_2, z_2) and end point (x_3, y_3, z_3) are assumed g_1 , g_2 and g_3 , respectively.

Substituting τ^* in the 3D case from Eq. (2.4) into Eq. (3.3) results in

$$\tau_p(\mathbf{x}) = \frac{1}{4\pi k} \int_L \frac{s(\boldsymbol{\xi})}{r(\mathbf{x}, \boldsymbol{\xi})} dl \quad (3.9)$$

where $r(\mathbf{x}, \boldsymbol{\xi}) = \sqrt{(x - x_s)^2 + (y - y_s)^2 + (z - z_s)^2}$ is the distance between the field point $\mathbf{x} = (x, y, z)$ and the source point $\boldsymbol{\xi} = (x_s, y_s, z_s)$ on the line heat source. x_s , y_s , and z_s can be expressed as follows

$$\begin{aligned} x_s &= (N_1x_1 + N_2x_2 + N_3x_3) & y_s &= (N_1y_1 + N_2y_2 + N_3y_3) \\ z_s &= (N_1z_1 + N_2z_2 + N_3z_3) \end{aligned} \quad (3.10)$$

The infinitesimal element dl in Eq. (3.9) can be expressed as

$$dl = \sqrt{dx_s^2 + dy_s^2 + dz_s^2} = Jd\eta \quad (3.11)$$

where

$$J = \sqrt{\left(\sum_{j=1}^3 x_j \frac{dN_j}{d\eta}\right)^2 + \left(\sum_{j=1}^3 y_j \frac{dN_j}{d\eta}\right)^2 + \left(\sum_{j=1}^3 z_j \frac{dN_j}{d\eta}\right)^2} \quad (3.12)$$

Therefore, Eq. (3.9) can be written as follows

$$\tau_p(\mathbf{x}) = \frac{1}{4\pi k} \int_{-1}^1 \frac{N_1g_1 + N_2g_2 + N_3g_3}{r(\eta)} J d\eta \quad (3.13)$$

Similar to the 2D case, the integral in equation (3.13) can be evaluated using standard numerical integration methods such as the GQM. According to the integral in equation (3.13), it is clear that if the field point $\mathbf{x} = (x, y, z)$ is exactly on the curved line source, the integral in Eq. (3.13) will be a strongly singular integral without any finite value. In other words, in the 3D case, the temperature at points on the curved line source does not have a finite value.

3.3. Curved surface heat source in 3D problems

We consider a heat source distributed over a curved surface in a 3D domain. The shape of the surface source and its intensity function are assumed arbitrarily and sufficiently complicated. The surface of the heat source is discretized by several quadrilateral surfaces. Each quadrilateral surface heat source has a quadratic shape with a quadratic variation of the intensity over it.

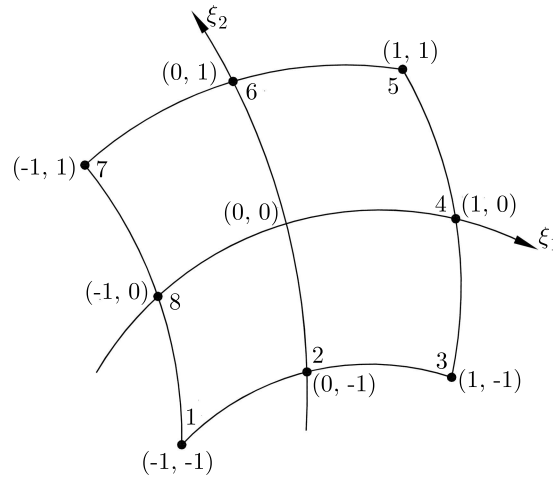


Fig. 3. A quadratic surface heat source

In this part, the formulation for treatment of a quadratic surface heat source is presented. A quadratic surface heat source, which is described by 8 points, is shown in Fig. 3.

The intensity per unit area of the quadratic surface heat source is written as follows

$$s(\xi_1, \xi_2) = \sum_{i=1}^8 N_i(\xi_1, \xi_2) g_i \quad (3.14)$$

where g_1, g_2, \dots, g_8 are the intensities per unit area at 8 points of the source, ξ_1 and ξ_2 are local coordinates which have a variation between -1 and 1 in the source. The shape functions N_i in terms of ξ_1 and ξ_2 are expressed as follows (Becker, 1992)

$$\begin{aligned} N_1 &= \frac{-1}{4}(1 - \xi_1)(1 - \xi_2)(1 + \xi_1 + \xi_2) & N_2 &= \frac{1}{2}(1 - \xi_1^2)(1 - \xi_2) \\ N_3 &= \frac{-1}{4}(1 + \xi_1)(1 - \xi_2)(1 - \xi_1 + \xi_2) & N_4 &= \frac{1}{2}(1 + \xi_1)(1 - \xi_2^2) \\ N_5 &= \frac{-1}{4}(1 + \xi_1)(1 + \xi_2)(1 - \xi_1 - \xi_2) & N_6 &= \frac{1}{2}(1 - \xi_1^2)(1 + \xi_2) \\ N_7 &= \frac{-1}{4}(1 - \xi_1)(1 + \xi_2)(1 + \xi_1 - \xi_2) & N_8 &= \frac{1}{2}(1 - \xi_1)(1 - \xi_2^2) \end{aligned} \quad (3.15)$$

The domain integral in Eq. (2.5) associated to the quadratic surface heat source is given as follows

$$\tau_p(\mathbf{x}) = \int_A \frac{s(\boldsymbol{\xi})}{k} \tau^*(\mathbf{x}, \boldsymbol{\xi}) dA \quad (3.16)$$

where dA is an infinitesimal area element on the quadratic surface heat source. Substituting τ^* in the 3D case from Eq. (2.4) into Eq. (3.16) results in

$$\tau_p(\mathbf{x}) = \frac{1}{4\pi k} \int_A \frac{s(\boldsymbol{\xi})}{r(\mathbf{x}, \boldsymbol{\xi})} dA \quad (3.17)$$

where $r(\mathbf{x}, \boldsymbol{\xi})$ is the distance between the field point $\mathbf{x} = (x, y, z)$ and the source points $\boldsymbol{\xi} = (x_s, y_s, z_s)$ on the quadratic surface heat source. x_s , y_s and z_s can be expressed in terms of the 8 shape functions as follows

$$\begin{aligned}
 x_s(\xi_1, \xi_2) &= \sum_{i=1}^8 N_i(\xi_1, \xi_2) x_i & y_s(\xi_1, \xi_2) &= \sum_{i=1}^8 N_i(\xi_1, \xi_2) y_i \\
 z_s(\xi_1, \xi_2) &= \sum_{i=1}^8 N_i(\xi_1, \xi_2) z_i
 \end{aligned} \tag{3.18}$$

The infinitesimal area element dA can be written as follows (Becker, 1992)

$$dA = J(\xi_1, \xi_2) d\xi_1 d\xi_2 \tag{3.19}$$

where

$$J = \sqrt{(J_x)^2 + (J_y)^2 + (J_z)^2} \tag{3.20}$$

and

$$\begin{aligned}
 J_x &= \frac{\partial y_s}{\partial \xi_1} \frac{\partial z_s}{\partial \xi_2} - \frac{\partial z_s}{\partial \xi_1} \frac{\partial y_s}{\partial \xi_2} & J_y &= \frac{\partial z_s}{\partial \xi_1} \frac{\partial x_s}{\partial \xi_2} - \frac{\partial x_s}{\partial \xi_1} \frac{\partial z_s}{\partial \xi_2} & J_z &= \frac{\partial x_s}{\partial \xi_1} \frac{\partial y_s}{\partial \xi_2} - \frac{\partial y_s}{\partial \xi_1} \frac{\partial x_s}{\partial \xi_2}
 \end{aligned} \tag{3.21}$$

Substituting Eqs. (3.19) and (3.14) into Eq. (3.17) results in

$$\tau_p(\mathbf{x}) = \frac{1}{4\pi k} \int_{-1}^1 \int_{-1}^1 \frac{\sum_{i=1}^8 N_i(\xi_1, \xi_2) g_i}{r(\xi_1, \xi_2)} J(\xi_1, \xi_2) d\xi_1 d\xi_2 \tag{3.22}$$

The integral in Eq. (3.22) can be calculated using standard 2D numerical integration methods such as the GQM.

In the case that the field point \mathbf{x} is exactly on the surface of the heat source, the integral in Eq. (3.22) will be weakly singular with a finite value. In other words, in the three-dimensional case, temperatures at points on a surface heat source have finite values. In this case, the integral in Eq. (3.22), which is weakly singular, can be calculated by various methods such as the transformation of variable and subtraction of singularity method (Aliabadi, 2002). In this research, the method of transformation of the variable is used for these cases.

4. Numerical examples

In this Section, two 2D and two 3D examples containing different kinds of curved heat sources are presented. In each example, the results computed by the presented MFS in comparison with the BEM and FEM are presented. Source codes are developed in MATLAB software for analysis of the examples using the MFS and BEM. ANSYS package is used for analysis of the examples using the FEM. The computations are implemented on a laptop with an Intel(R) (Intel, Inc., Santa Clara, CA, USA) Core(TM) i7-2670QM CPU of 2.20 GHz, on 64-bit Windows operating system with 8.00 GB RAM. In all examples, the thermal conductivity is $k = 60 \text{ W}/(\text{m}^\circ\text{C})$.

4.1. A circular domain including a circular heat source

In this example, according to Fig. 4, a circular domain with $R = 0.5$ is considered. This problem is analyzed under the Dirichlet boundary condition with $\tau_B = 10^\circ\text{C}$. A curved heat source which is distributed over a circle with the radius $r = 0.25 \text{ m}$ is considered. The strength of the heat source is considered to be constant over the circle and equal to $s = 4000 \text{ W/m}$. The pseudo boundary Γ' is considered to be a circle with radius $R' = 2.5 \text{ m}$ (5 times of R). Only

4 sources are considered on this pseudo-boundary. The circular heat source is modeled by only four quadratic line heat sources. The obtained results by the proposed MFS are compared with those of the BEM (32 linear boundary elements) and FEM (9461 quadratic elements) presented in (Mohammadi *et al.*, 2016). The temperature results along the vertical diameter of the circle are shown in Fig. 5. As can be seen, the presented MFS formulation yields very accurate results.

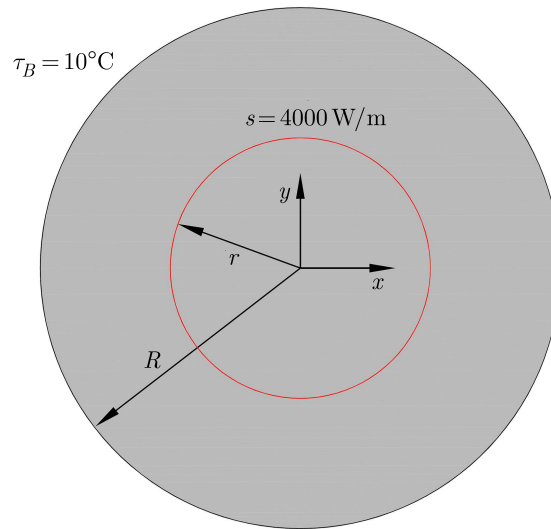


Fig. 4. A circular domain including a circular heat source

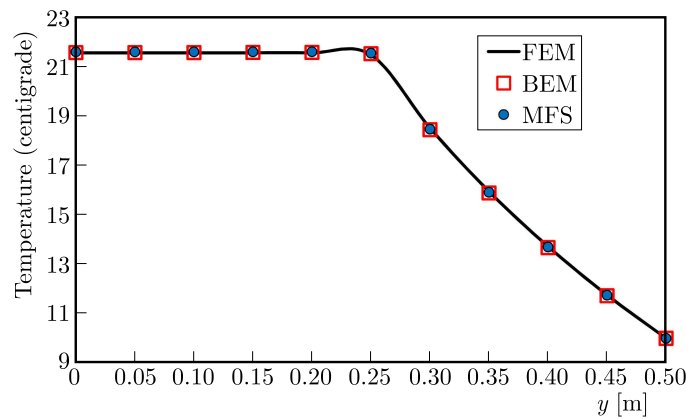


Fig. 5. Temperature on the vertical diameter (y -axis) of the circle obtained by the FEM, BEM and MFS

4.2. A rectangular domain including a heat source with an elliptical shape and non-uniform intensity

In this example, a heat conduction problem over a 0.15×0.3 m rectangle containing a curved heat source is considered. Figure 6a shows the geometry and thermal boundary conditions of the problem.

An elliptical curved line heat source centered at $(0.085, 0.065)$ is considered in the domain. The lengths of the horizontal and vertical radii of the ellipse are $r_1 = 0.04$ m and $r_2 = 0.02$ m, respectively. The heat source intensity is considered to be a function of $\beta \in [0, 2\pi]$ as follows

$$s = 40000(1 + \cos \beta) \text{ W/m} \quad (4.1)$$

where β is the angular coordinate on the heat source measured from a horizontal axis passing through the center of the ellipse (Fig. 6a).

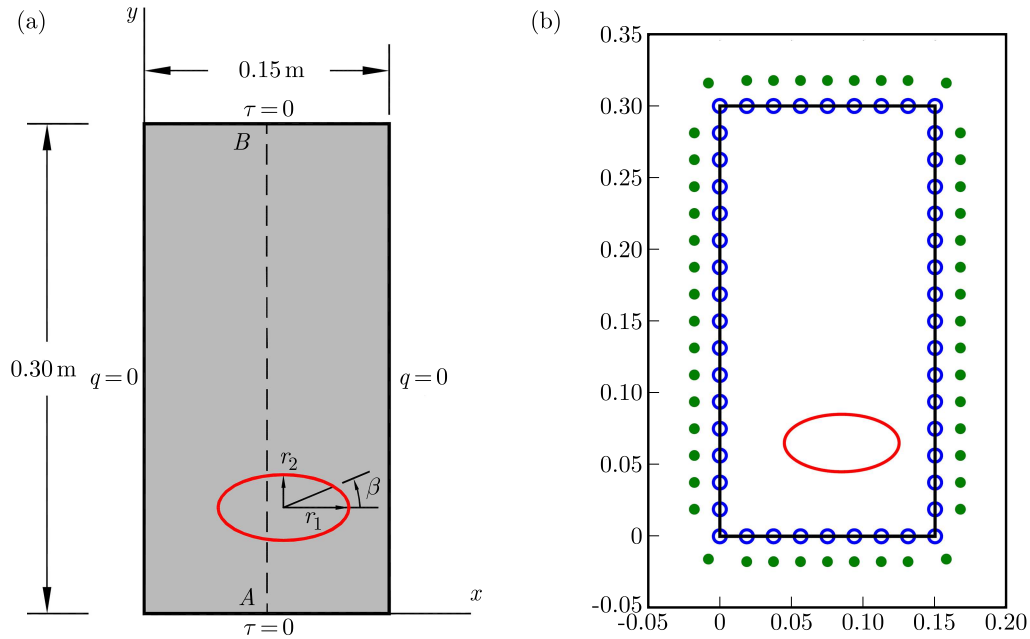


Fig. 6. A rectangle with an elliptical heat source: (a) geometry and boundary conditions, (b) configuration of collocation and source points

In the proposed MFS, the elliptical heat source is modeled by only eight quadratic heat sources. 48 source points and 48 collocation points are considered for the MFS analysis. The configuration of collocation and source points is depicted in Fig. 6b. The locations of source points are determined according to the method suggested by Hematiyan *et al.* (2018). The ratio of the distance from the source point to its corresponding collocation point to the distance from the same source point to the neighboring collocation point is 0.85. By this configuration, a solution without undesired oscillation is obtained (Hematiyan *et al.*, 2018).

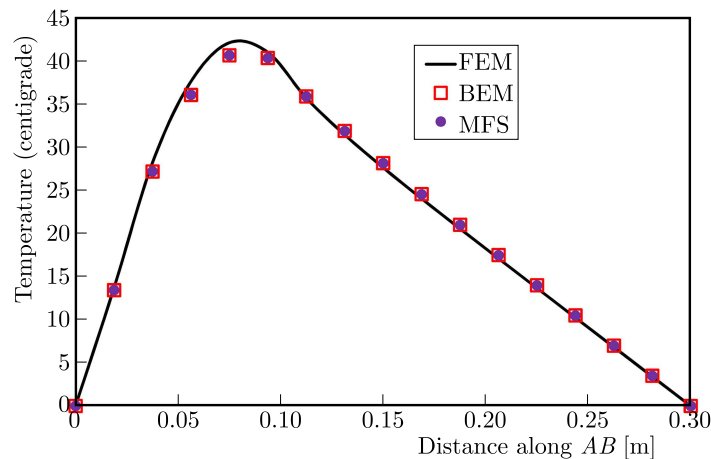


Fig. 7. The FEM, BEM and MFS results for temperature along the line AB of the rectangle with an elliptical heat source

The temperature results along the line AB (Fig. 6a) are depicted in Fig. 7. In this figure, the results based on the presented formulation are compared with those of the BEM (48 linear boundary elements) and FEM (4356 quadratic elements) presented in (Mohammadi *et al.*, 2016). As it can be seen, the presented MFS and the BEM yield accurate results. The computational times (in seconds) for solving this problem using the proposed MFS and the BEM based on

(Mohammadi *et al.*, 2016) have been 2.11 and 6.24, respectively. The reported results indicate that the proposed MFS is more efficient than the BEM for analysis of this example.

4.3. A cubic domain including two circular heat sources with non-uniform intensity

In this example, as shown in Fig. 8, a cube with edges of $L = 10$ m, including two circular heat sources, is considered. All faces are kept at $\tau = 0^\circ\text{C}$. The radius of both circular heat sources is $r = 2.5$ m.

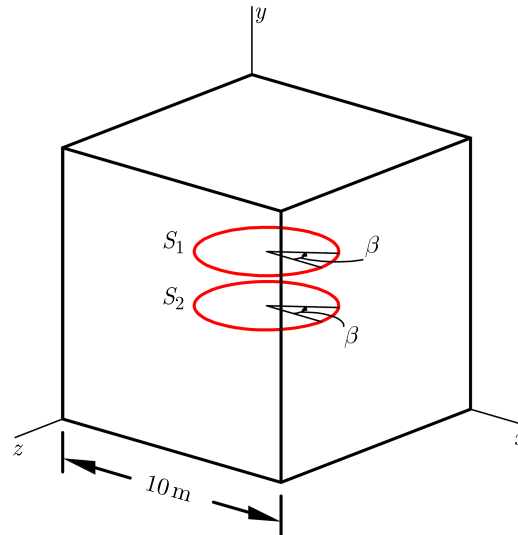


Fig. 8. A cube with two circular heat sources

The first circular heat source is centered at $(5, 6, 5)$ and the second one is centered at $(5, 4, 5)$. The strengths of the sources are considered to be functions of $\beta \in [0, 2\pi]$ with the following forms

$$s_1 = 10000(1 + \cos \beta) \text{ W/m} \quad s_2 = 20000(1 + \cos \beta) \text{ W/m} \quad (4.2)$$

where β is the angular coordinate on the heat sources as shown in Fig. 8.

In the proposed MFS, each circular heat source is modeled by only four quadratic line heat sources. 100 collocation points are considered on each face of the cube. Therefore, 600 collocation points with 600 corresponding source points which are located on the cube with edges of $L' = 14$ m are considered. The configuration of the collocation points and their corresponding source points on a face of the cube is shown in Fig. 9.

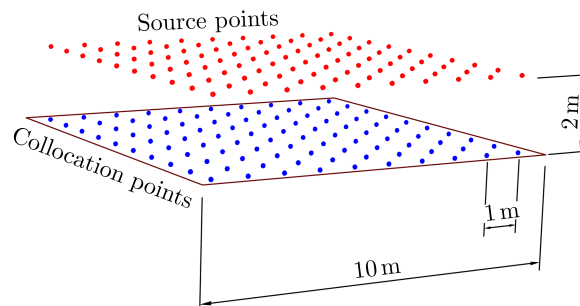


Fig. 9. The configuration of collocation and source points on a face of the cube

The temperature results along the line $x = z = 5$ and the line $x = y = 5$ are shown in Fig. 10. In this figure, the obtained results by the proposed MFS are compared with those of the BEM (600 constant elements) and FEM (56669 3D quadratic elements) presented in

(Mohammadi *et al.*, 2016). As it can be seen, the presented MFS and the BEM formulation yield very accurate results. However, the running CPU time for the BEM is almost 1.8 times the MFS. The computations take 48.1 s for the presented MFS while they take 87.0 s for the BEM.

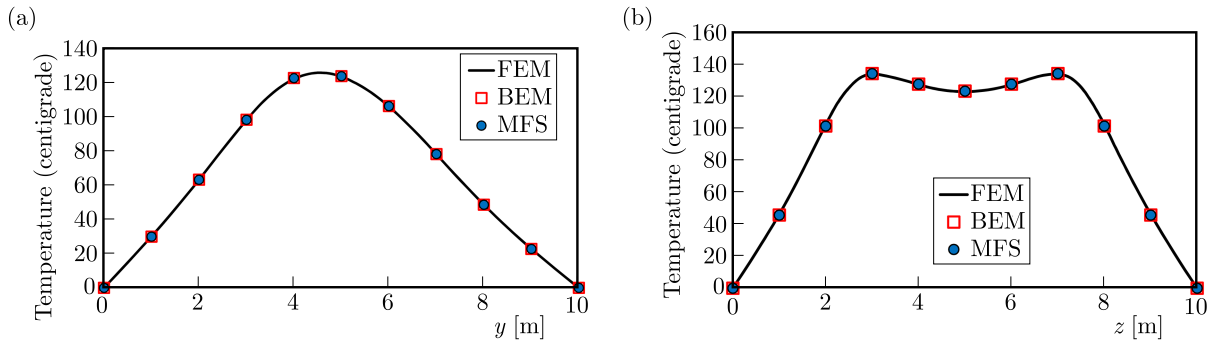


Fig. 10. Temperature on the line (a) $x = z = 5$ and (b) $x = y = 5$ of the cube with circular heat sources obtained by the FEM, BEM and MFS

4.4. A spherical domain including a cylindrical heat source with a non-uniform intensity

In the last example, a spherical domain with the radius $R = 1$ m, centered at $(0, 0, 0)$ is considered. The surface of the sphere is kept at $\tau = 0^\circ\text{C}$. A surface heat source with a cylindrical shape is included in the domain. The radius, center of the base, and the height of the cylindrical heat source are 0.2 m, $(0, 0, 0)$, and 0.8 m, respectively. A cut-out part of the spherical domain and the cylindrical heat source is shown in Fig. 11a. The intensity per unit area of the source is considered to be a function of $\beta \in [0, 2\pi]$ (angular coordinate on the heat source, measured from the x -axis) and the y -coordinate with the following form

$$s = 20000y(1 + \cos \beta) \text{ W/m}^2 \quad (4.3)$$

In the proposed MFS, the cylindrical heat source is modeled by only eight quadrilateral quadratic heat sources. The pseudo boundary Γ' is considered to be a sphere with the radius $R' = 1.4$ m. 98 collocation points and 98 sources are considered for the MFS analysis of the problem. The configuration of collocation and source points are shown in Fig. 11b.

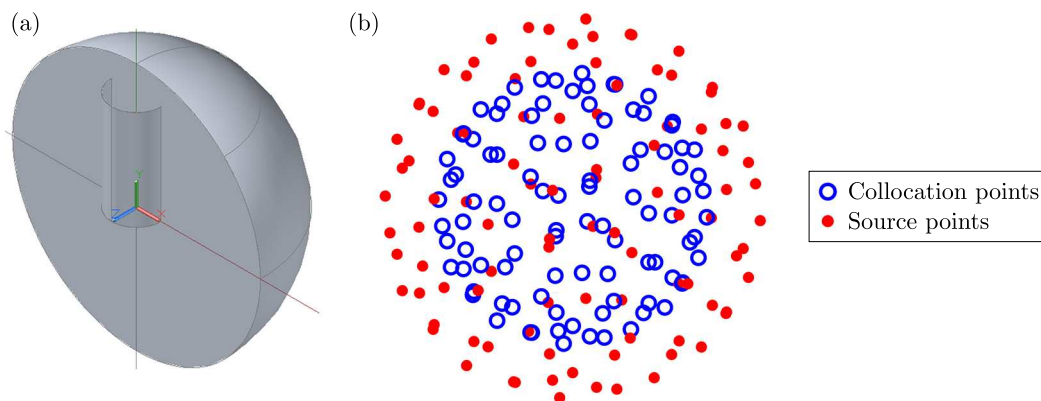


Fig. 11. The spherical domain including a cylindrical heat source: (a) a cut-out part of the domain, (b) the configuration of collocation and source points

So far, this kind of problem has not been solved by the BEM. The obtained results by the presented MFS are compared with those of the FEM. The commercial software package, ANSYS, is employed for the FE analysis. In the FE analysis, the heat source which is concentrated over

a cylindrical surface should be modeled as a cylindrical volume with a small thickness. The inner and outer radius of this cylindrical volume are considered as $r_i = 0.18$ m and $r_o = 0.22$ m, respectively. The finite element discretization of the domain with 3D quadratic elements is shown in Fig. 12. The whole domain is discretized with 48 178 elements and 64 869 nodes. In order to visualize the position of the curved surface heat source inside the domain, only a cut-out part of the FE mesh is shown in Fig. 12a. The nodal arrangement of the mesh is depicted in Fig. 12b.

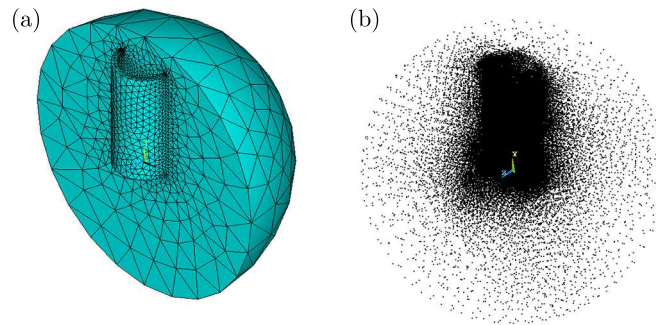


Fig. 12. The finite element discretization of the sphere with a cylindrical heat source:
(a) 48 178 elements, (b) 64 869 nodes

The temperature results on the y - and z -axes are depicted in Fig. 13. As it can be observed, the MFS results are in an excellent agreement with the FEM solutions. noteworthy is the fact that the modeling of the problem in the proposed MFS is much simpler than in the FEM.

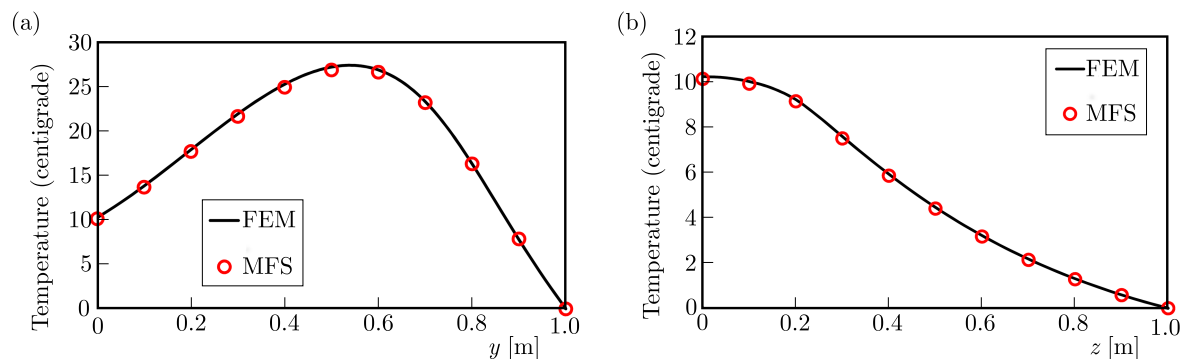


Fig. 13. The FEM, and MFS results for temperature along (a) the y -axis and (b) the z -axis in the sphere with a cylindrical heat source

5. Conclusions

A formulation based on the MFS for analysis of 2D and 3D heat conduction problems in isotropic media containing heat sources concentrated on arbitrary curved lines/surfaces has been presented. The shape and the variation of the intensity of the sources can be arbitrarily and sufficiently complicated.

For 2D problems, curved line heat sources while for 3D problems, curved surface heat sources have been considered. The equations derived for 2D curved line heat sources showed that temperature at points exactly on the source had a finite value. The formulation for 3D curved line heat sources showed that the temperature at points exactly on those sources had an infinite value but the temperature had a finite value at points on the curved surface heat source.

For reliable modeling of a concentrated heat source in the FEM, the source should be modeled as a separated region with a small thickness. Moreover, a large number of internal elements and

nodes should also be considered for the modeling of the source. However, these sources can be effectively modeled in the BEM as well as the proposed MFS without considering any internal cells or points. To show the performance of the presented MFS formulation, four numerical examples have been given. It was observed that the proposed method gave accurate results even with a small number of source points and it was found that the computational cost of the presented method was much smaller than the BEM.

Some modified/improved versions of the MFS such as the singular boundary method (Gu *et al.*, 2012) have been presented too. The proposed formulation for the implementation of curved heat sources can be employed for these methods too.

References

1. AHMADABADI M.N., ARAB M., GHAINI F.M., 2009, The method of fundamental solutions for the inverse space-dependent heat source problem, *Engineering Analysis with Boundary Elements*, **33**, 10, 1231-1235
2. ALIABADI M.H., 2002, *The Boundary Element Method, Volume 2, Applications in Solids and Structures*, John Wiley & Sons
3. ATKINSON K.E., 1985, The numerical evaluation of particular solutions for Poisson's equation, *IMA Journal of Numerical Analysis*, **5**, 3, 319-338
4. BECKER A.A., 1992, *The Boundary Element Method in Engineering: A Complete Course*, McGraw-Hill Book Company
5. CHAO C.K., TAN C.J., 2000, On the general solutions for annular problems with a point heat source, *Journal of Applied Mechanical*, **67**, 3, 511-518
6. FAIRWEATHER G., KARAGEORGHIS A., 1998, The method of fundamental solutions for elliptic boundary value problems, *Advances in Computational Mathematics*, **9**, 1-2, 69-95
7. GOLBERG M.A., 1995, The method of fundamental solutions for Poisson's equation, *Engineering Analysis with Boundary Elements*, **16**, 3, 205-213
8. GU Y., CHEN W., HE X.Q., 2012, Singular boundary method for steady-state heat conduction in three dimensional general anisotropic media, *International Journal of Heat and Mass Transfer*, **55**, 17, 4837-4848
9. HAN J.J., HASEBE N., 2002, Green's functions of point heat source in various thermoelastic boundary value problems, *Journal of Thermal Stresses*, **25**, 2, 153-167
10. HEMATIYAN M.R., HAGHIGHI A., KHOSRAVIFARD A., 2018, A two-constrained method for appropriate determination of the configuration of source and collocation points in the method of fundamental solutions for 2D Laplace equation, *Advances in Applied Mathematics and Mechanics*, **10**, 3, 554-580
11. HEMATIYAN M.R., MOHAMMADI M., ALIABADI M.H., 2011, Boundary element analysis of two- and three-dimensional thermo-elastic problems with various concentrated heat sources, *Journal of Strain Analysis for Engineering Design*, **46**, 3, 227-242
12. HIDAYAT M.I.P., ARIWAHOEDI B., PARMAN S., RAO, T.V.V.L., 2017, Meshless local B-spline collocation method for two-dimensional heat conduction problems with nonhomogenous and time-dependent heat sources, *Journal of Heat Transfer*, **139**, 7, 071302
13. KARAMI G., HEMATIYAN M.R., 2000a, A boundary element method of inverse non-linear heat conduction analysis with point and line heat sources, *International Journal for Numerical Methods in Biomedical Engineering*, **16**, 3, 191-203
14. KARAMI G., HEMATIYAN M.R., 2000b, Accurate implementation of line and distributed sources in heat conduction problems by the boundary-element method, *Numerical Heat Transfer, Part B*, **38**, 4, 423-447

15. KOŁODZIEJ J.A., MIERZWICZAK M., CIAŁKOWSKI M., 2010, Application of the method of fundamental solutions and radial basis functions for inverse heat source problem in case of steady-state, *International Communications in Heat and Mass Transfer*, **37**, 2, 121-124
16. LE NILIOT C., 1998, The boundary element method for the time varying strength estimation of point heat sources: Application to a two dimensional diffusion system, *Numerical Heat Transfer, Part B*, **33**, 3, 301-321
17. LE NILIOT C., LEFÈVRE F., 2001, Multiple transient point heat sources identification in heat diffusion: Application to numerical two- and three-dimensional problems, *Numerical Heat Transfer, Part B*, **39**, 3, 277-301
18. MIERZWICZAK M., KOŁODZIEJ J.A., 2012, Application of the method of fundamental solutions with the Laplace transformation for the inverse transient heat source problem, *Journal of Theoretical and Applied Mechanics*, **50**, 4, 1011-1023
19. MOHAMMADI M., HEMATIYAN M.R., KHOSRAVIFARD A., 2016, Boundary element analysis of 2D and 3D thermoelastic problems containing curved line heat sources, *European Journal of Computational Mechanics*, **25**, 1-2, 147-164
20. PARTRIDGE P.W., BREBBIA C.A., WROBEL, L.C., 1992, *The Dual Reciprocity Boundary Element Method*, Southampton, Computational Mechanics Publications
21. POULLIKKAS A., KARAGEORGHIS A., GEORGIU G., 1998, The method of fundamental solutions for inhomogeneous elliptic problems, *Computational Mechanics*, **22**, 1, 100-107
22. ROGOWSKI, B., 2016, Green's function for a multifield material with a heat source, *Journal of Theoretical and Applied Mechanics*, **54**, 3, 743-755
23. SHIAH Y.C., GUAO T.L., TAN C.L., 2005, Two-dimensional BEM thermoelastic analysis of anisotropic media with concentrated heat sources, *Computer Modeling in Engineering and Sciences*, **7**, 3, 321-338
24. SHIAH Y.C., HWANG P.W., YANG R.B., 2006, Heat conduction in multiply adjoined anisotropic media with embedded point heat sources, *Journal of Heat Transfer*, **128**, 2, 207-214
25. STROUD A.H., SECREST D., 1966, *Gaussian Quadrature Formulas*, New York, Prentice-Hall
26. TELLES J.C.F., 1987, A self-adaptive coordinate transformation for efficient numerical evaluation of general boundary element integrals, *International Journal for Numerical Methods in Engineering*, **24**, 5, 959-973

STRUCTURAL RESPONSE OF MULTILAYERED ALUMINUM AND STEEL SPECIMENS SUBJECTED TO HIGH STRAIN RATE LOADING CONDITIONS

DANISH IQBAL, VIKRANT TIWARI

Indian Institute of Technology Delhi, Department of Applied Mechanics, New Delhi, India

e-mail: amz128262@iitd.ac.in; tiwariv@am.iitd.ac.in

Series of experiments and a detailed computational analysis has been performed to investigate the high strain rate behaviour of homostacked Al 6063-T6 and IS 1570 alloys. Split Hopkinson pressure bar technique was utilized to study the effect of high rate loading on the stress strain relationship of single, double, tri and quad layered/stacked specimens. Three different specimen aspect ratios 1, 0.75 and 0.5 were also evaluated for different strain rates. A 2 mm thick pulse shaper was employed in achieving dynamic stress equilibrium, a near constant strain rate and a high rise time as per requirements. After analyzing the results from the experiments it was observed that single and halved specimens showed a close match in both the elastic and plastic regions for aluminium alloy as well as for steel. In the case of Al 6063-T6, a nearly bi-linear nature of the constitutive curve was observed for single and halved specimens, which transformed into near tri-linear nature for tri and quad stacked specimens. The dynamic numerical analysis showed a good agreement between the numerical and experimental results for a single and halved specimen in the case of Al alloy. For steel, a close correlation was observed for all the four cases.

Keywords: dynamic stress strain behaviour, multilayering, pulse shaper, finite element simulation

1. Introduction

Safety of a structure and its economics plays an important role in its designing process. Multilayer stacking and sandwiched structures are commonly used in structural applications where the required strength and material properties can be achieved at low financial cost. Such multilayered structures can be commonly classified in two categories: First is homo-stacking where all constituent layers are made up of the same material of the same or different thickness. In the second category, constituent layers are made up of two or more different materials of the same or different thickness and can be called as hetero-stacked structures. Both these categories provides an important economical option of replacing a damaged layer instead of replacing the whole structure.

Some of the applications of multilayered stacking includes, but not limited to, thin walled compound cylinders, air-frames and layered armors. Such structures are commonly utilized in defence and space industries where they can be subjected to high rate loading applications, as in the case of vehicle crash or projectile impact/shock loading. Thus, it is warranted that dynamic mechanical response of such structures should be correctly evaluated and the effect of multilayering is clearly understood. In the related research literature many specialized experimental setups are reported to test materials under such high rate loading conditions. One such an important technique is the Split Hopkinson Pressure Bar (SHPB) or the Kolsky bar which is also used in this work for the stated purpose.

The split Hopkinson bar technique was initially developed by Kolsky (1949) to evaluate the material response at high strain rates. Since then SHPB and different numerical models have been utilized in dynamic characterization of a wide range of materials like metals, alloys, composites, ceramics etc. In one such an attempt, Jeng and Sheu (1994) investigated the dynamic response of Al 6061-O using SHPB and numerical modelling. They found that dynamic yield stress can be nearly 45% greater when compared with quasi-static conditions. In another study, Khan and Huang (1992) evaluated the dynamic response of Al 1100 alloy for a strain rate range of 10^2 - 10^4 s⁻¹. It was suggested that dislocation movements was the main reason behind the plastic flow of metals and was primarily responsible for the strain rate sensitivity.

With the advancements in technology, it is getting easier to conduct SHPB experiments. However, in most of the SHPB related studies researchers have expressed that maintaining the mandatory condition of force/stress equilibrium is a difficult task and needs to be verified. Wu and Gorham (1997) studied these requirements in detail and found factors that can adversely affect this equilibrium. Their results showed that inertia and wave propagation effects can cause a significant force difference between the two ends of the specimen.

In order to achieve force equilibrium and a near constant strain rate in the specimen, a technique called pulse shaping is commonly utilized. It requires a thin disc of metal to be placed at the impact end of the incident bar. Ellwood *et al.* (1982) modified the conventional SHPB setup by using a pre-loading bar and a dummy specimen as the pulse shaper. They suggested that the actual test specimen would be the best material to use as the pulse shaper. A substantially less variation in the strain rate was observed in the pulse shaped experiment.

Another important aspect that has been studied quite frequently is the geometrical effect or the effect of specimen dimensions on its dynamic response. In one such a study, graphite/epoxy composite specimens with varying l/d ratios having square and rectangular cross sections were tested at high strain rates by Woldesenbet and Vinson (1999). They did not find any significant effect of either the aspect ratio or the specimen geometry on the stress-strain response of the material. However, in another similar study by Pankow *et al.* (2009) on the effect of specimen aspect ratio (L/D ratio) and shape (cylindrical and square) on the stress-strain response of a material, it was observed that for some softer materials like aluminium, a smaller aspect ratio is advantageous. The study on the specimen cross section revealed that the stress-strain response did not differ much, although the plastic deformation in the case of cylindrical specimen was higher. Apart from the aspect ratio, interfacial friction between the specimen bar interfaces also influences the stress-strain response. Jankowiak *et al.* (2011) studied the effects of parameters like friction, inertia and elastic wave dispersion in many quasi-static and dynamic compression experiments. They used a friction correction and suggested that prior knowledge of the limiting value of friction was necessary for a correct numerical prediction. Li *et al.* (2009) observed that for Al 2024 alloys the effect of specimen geometry and lubrication was in the same order of magnitude as strain rate sensitivity. The specimen aspect ratio can also trigger the formation of adiabatic shear bands in materials which show little or no effect of geometry on the stress strain response (Walley *et al.*, 2006).

Highlighting the application of homolayered structures as protective barriers, many researchers (Corran *et al.*, 1983; Radin and Goldsmith, 1988; Nia and Hoseini, 2011; Flores-Johnson *et al.*, 2011) have conducted a series of investigations on different aluminium and steel alloys. They have evaluated the ballistic performance of a monolithic layer viz. different sequence of the homostacked configurations. These articles provide valuable insight into failure mechanisms and applicability of such structures. However, studies related to dynamic response characterization of such homostacked configurations are rare to find. In this article, an effort has been made to investigate the effect of high strain rate loading on homo-stacked specimens for two different materials, namely Al 6063-T6 and IS 5170 (mild steel). The specimens are evaluated at three different strain rates, and their true stress versus strain curves are analyzed and discussed. It

should be noted that all experiments have been repeated at least three times for validating the repeatability of the specimen response. Numerical simulations using non-linear finite element software ABAQUS have also been carried out and their results are compared with the corresponding experiments.

2. Experimental procedure

2.1. Split Hopkinson pressure bar

The dynamic compressive experiments were performed on the split Hopkinson pressure bar apparatus based on the design provided by Engineers and Builders (2015). A schematic of the experimental setup is shown in Fig. 1.

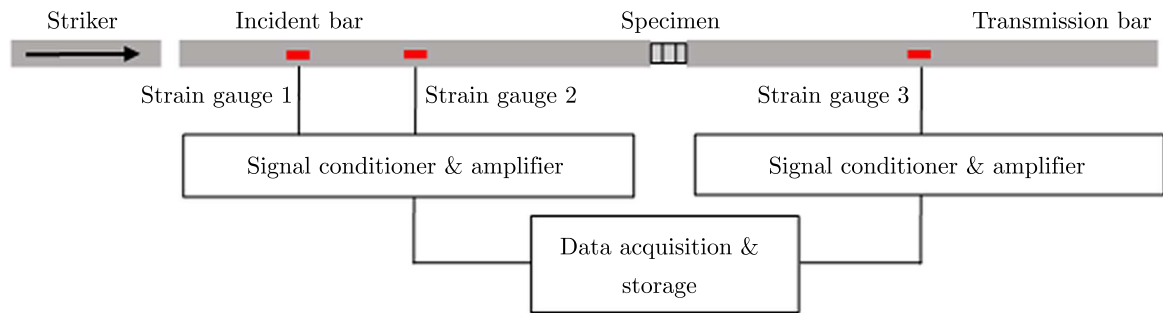


Fig. 1. Schematic of the split Hopkinson bar setup

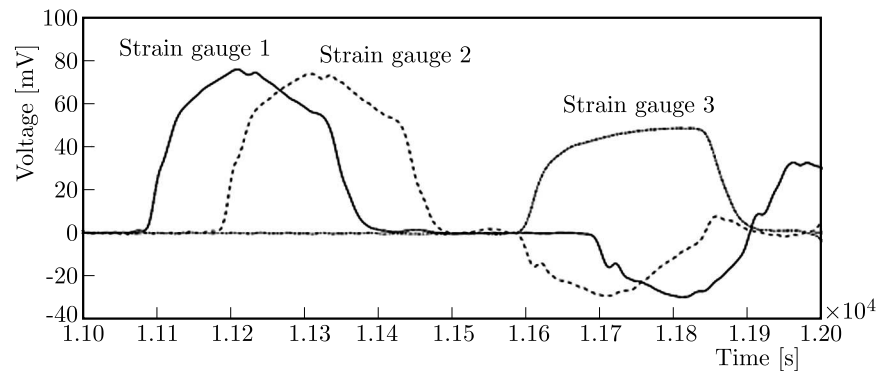


Fig. 2. A typical voltage signal obtained in SHPB experiment

The length of the striker bar and that of the incident and transmission bar was kept at 0.3 m and 2 m respectively. All bars were made of prismatic stainless steel rods of 20 mm diameter. Two diametrically opposite strain gauges ($120\ \Omega$) were mounted in a half bridge configuration at two positions (quarter and mid-length) on the incident bar and at the mid-length of the transmission bar. Two gauges were bonded on the incident bar to ascertain that there was no attenuation in the incident or reflected wave. Figure 2 shows typical voltage signals obtained in one of the experiments. Strain data from the gauges is later processed to determine the constitutive behaviour of the material. As the strain rate in the specimen is directly proportional to the reflected strain pulse ε_R , the average specimen strain rate is given as

$$\dot{\varepsilon} = \frac{2C_b\varepsilon_R}{h} \quad (2.1)$$

where C_b is the elastic wave speed in the bar and h is the specimen length. Since the initial and final volume of the specimen remain constant, the average engineering stress σ_S and strain ε_S in the specimen is given by the following relation

$$\sigma_S(t) = \frac{A_b}{A_s} E_b \varepsilon_T(t) \qquad \varepsilon_S(t) = 2 \frac{C_b}{h} \int_0^t \varepsilon_R(t) \, dt \qquad (2.2)$$

where A_b is the cross sectional area of the bars and A_s is the cross sectional area of the specimen. E_b is the elastic modulus of the bar material and ε_T is the transmitted strain pulse.

3. Specimen preparation and nomenclature

Three sets of cylindrical disc specimens of varying aspect ratios of aluminium (Al 6063-T6) and mild steel (IS 1570) were fabricated from a single 11 mm diameter rods for both metals. This helped in avoiding slight property variations that might exist between different production batches. The chemical composition analysis of Al 6063-T6 and IS 1570 used in this study is given in Table 1.









Table 1. Chemical composition of Al 6063-T6 and IS 1570

Al 6063-T6									
Element	Fe	Si	Cu	Mn	Al	Zn	Ni	Mg	Ti
% wt.	0.3982	0.431	0.0069	0.014	98.55	0.0153	0.0058	0.5431	0.0056
IS 1570 (mild steel)									
Element	Fe	Si	Cu	Mn	Al	Cr	Mo	Ni	C
% wt.	99.02	0.1349	0.1001	0.4073	0.0113	0.0556	0.0083	0.0613	0.111

To avoid stress localization at the interfaces, it was ensured that specimen surface was flat and perpendicular to the sides. The machined specimens were first polished on a paper of grit designation 500, and then a progressively finer grit paper was used till a smooth surface was achieved with a grit paper of 800. Both the contact surfaces of the specimen as well as the incident and reflected bars were lubricated for each experiment with a thin layer special Molybdenum Disulphide grease to reduce frictional effects. In case of layered specimens, the specimen-to-specimen interfaces along with the specimen-bar interfaces were also lubricated for each experiment. The specimen diameter utilized in this study was 11 mm and their thicknesses were 11, 8.75 and 5.5 mm.

The stacking sequences for the specimens used in this study are shown in Table 2. The stacking scheme is divided into three specimen overall aspect ratios viz. 1, 0.75 and 0.5 which are further divided into smaller thicknesses of equal proportions as shown in Table 2. Specimens have been denoted with names according to their aspect ratio and the number of parts in which they are divided. For example, the specimen with 0.75 aspect ratio which is divided into 3 equal parts is named as 11-R-0.75-1/3, where 11 represents the specimen diameter, $R - x$ is the aspect ratio term and 1/3 denotes the number of partitions.

Table 2. Specimen stacking sequence utilized in this study

L/D ratio	Specimen stacking scheme			
$R = L/D = 1$				
	11R-1-1	11R-1-1/2	11R-1-1/3	11R-1-1/4
$R = L/D = 0.75$				
	11R-0.75-1	11R-0.75-1/2	11R-0.75-1/3	11R-0.75-1/4

3.1. Pulse shaping and dynamic force equilibrium

When the pulse shaper deforms plastically on impact, it filters out the high frequency components of the incident pulse which are responsible for the dispersive nature of the incident wave. Different stages of the pulse shaper deformation for a typical case can be seen in Fig. 3 (Naghdbadi *et al.*, 2012).

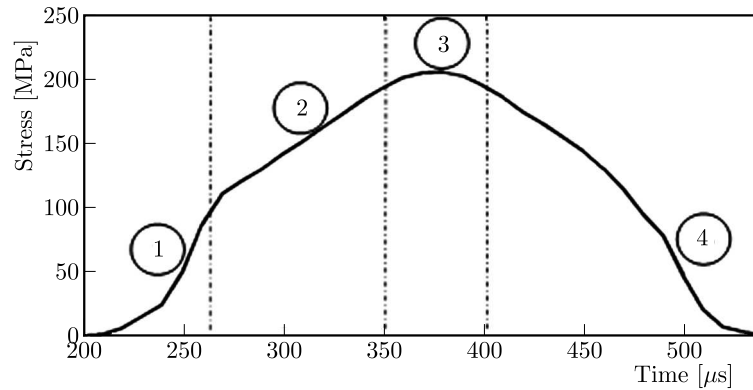


Fig. 3. A typical stress pulse obtained using a pulse shaper showing four stages of pulse shaper deformation

The initial stage of the process is dominated by elastic deformation of the pulse shaper on impact. Stage 2 represents plastic deformation of the pulse shaper. Stage 3 is the rigid mode and stage 4 is the elastic deformation during unloading of the pulse shaper (Naghdbadi *et al.*, 2012). Early literature (Ellwood *et al.*, 1982) shows that in order to obtain a constant strain rate deformation in the specimen it is beneficial to have an incident pulse with a nature similar to the anticipated stress-strain response of the specimen. This ensures that the stresses on both the faces of the specimen represent the average stress within the specimen which is an essential condition for any SHPB experiment. For the present study, a pulse shaper made of 2 mm thick discs of Al 6063 and IS 1570 were used. For each experiment in this study, it was verified that these conditions were satisfied so that governing equations (2.1) and (2.2) could be applied to determine the stress-strain history in the specimen. Experimental validation indicating that for all the four stacking sequences of the Al 6063 specimens force equilibrium is presented in Fig. 4.

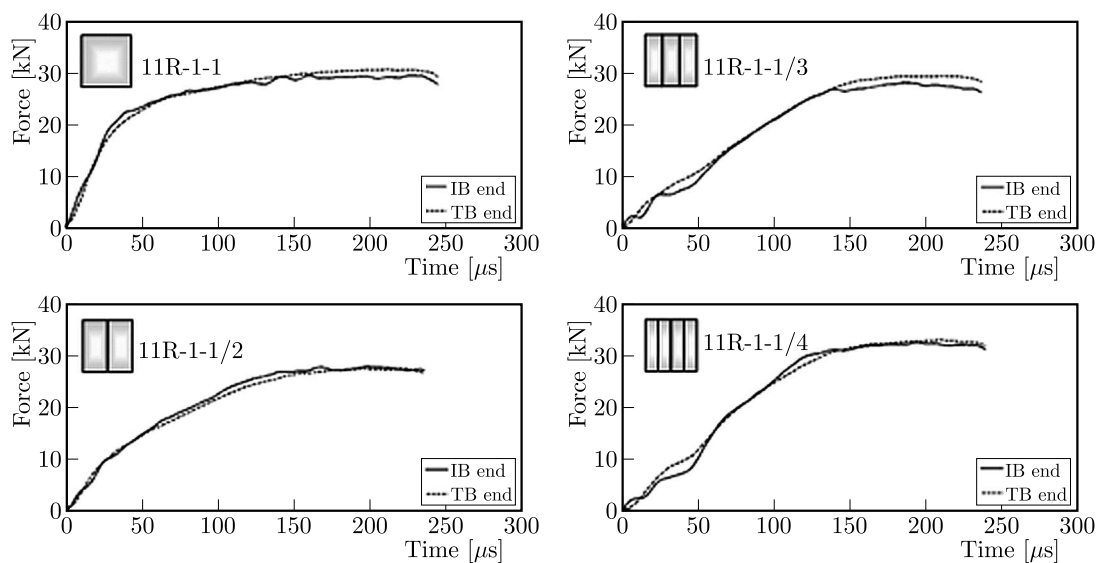


Fig. 4. Comparison of forces at the specimen interfaces, Incident Bar end (IB end) and Transmission Bar end (TB end) for all four stacking sequences

The influence of the pulse shaper on the strain pulses and force ratio can be clearly seen in Fig. 5. It shows (Fig. 5a) voltage signals, variation of forces and force ratio (Fig. 5b) respectively for a typical experiment without the pulse shaper. Here, although the pulse is trapezoidal in shape, the forces on the two specimen bar interfaces do not match, which is also evident by the variation of the force ratio. In comparison, when a pulse shaper was used (Figs. 5c and 5d) it could be observed that there was a marked reduction in loading magnitude as compared to the experiment without the pulse shaper, but the loading time (pulse width) increased remarkably. This seems to ensure that the forces on the specimen faces are in dynamic equilibrium, as can be seen from Fig. 5d. Also, a significant increase in the rise time and the loading time of the pulse was observed, thus ensuring that the mandatory SHPB conditions of constant strain rate and dynamic stress equilibrium were satisfied. Similar results were also obtained for the IS 1570.

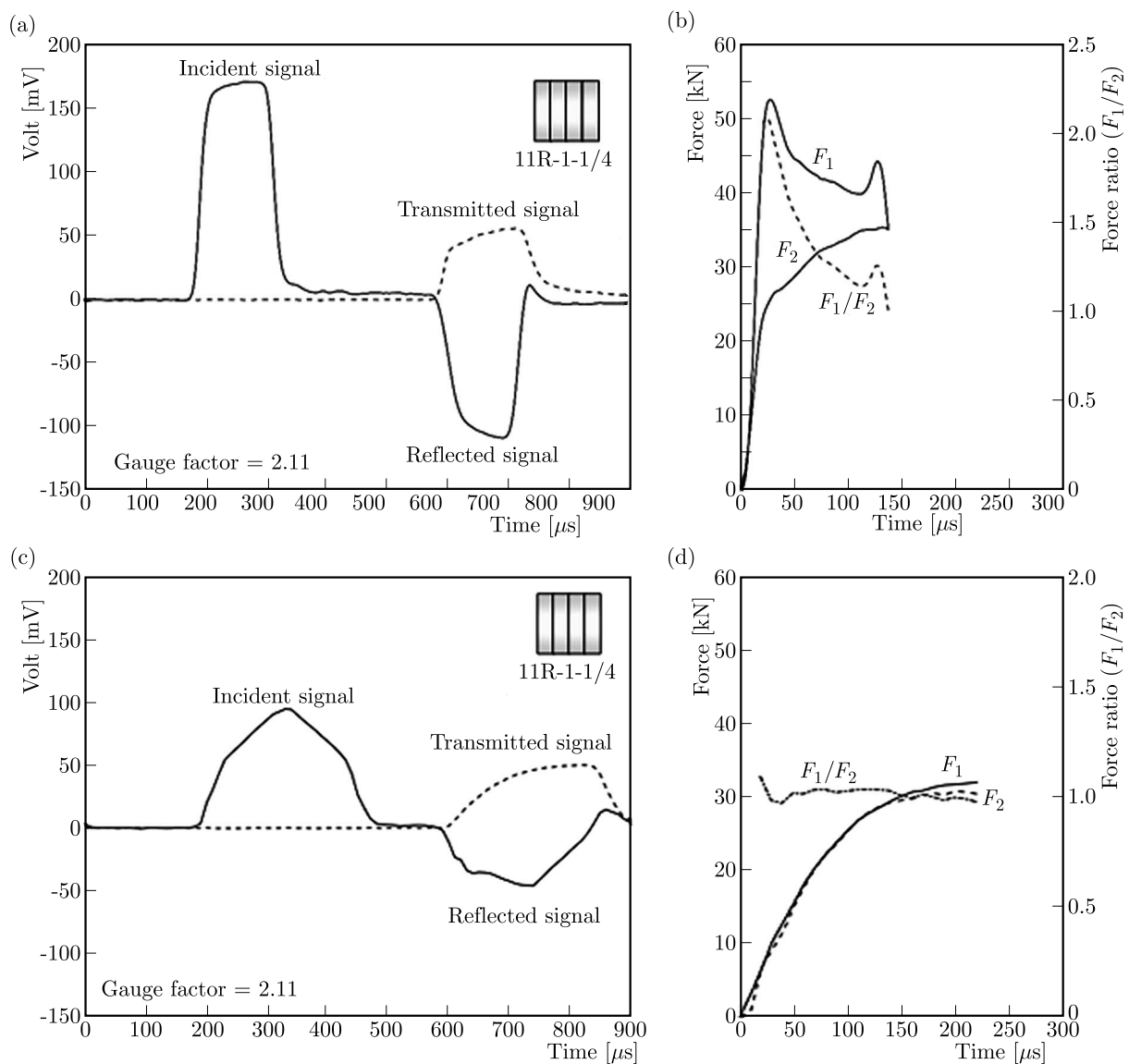


Fig. 5. (a) Voltage signals obtained without using a pulse shaper; (b) forces at specimen ends and the force ratio; (c) voltage signals obtained using the pulse shaper; (d) forces at specimen ends and the force ratio

4. Finite element simulations

Non-linear 3D finite element simulations have been performed on ABAQUS/Explicit to numerically study the effect of specimen stacking on its stress-strain response in an SHPB experiment. The physical dimensions of the incident bar, transmission bar and specimen were kept same for all cases as those of the actual SHPB setup. The model had a bar diameter of 20 mm and a length of 2000 mm. Since for a valid SHPB experiment the bars should remain elastic, a linear elastic model developed for isotropic elastic behaviour was used for the bars. The strain rate dependent behaviour of the specimen was modelled using the well-known Johnson-Cook model to evaluate its dynamic compressive response (Johnson and Cook, 1983)

$$\sigma_{fl} = (A + B\varepsilon_{pl}^n) \left[1 + C \ln \left(\frac{d\varepsilon_{pl}/dt}{\dot{\varepsilon}_0} \right) \right] \left[1 - \left(\frac{T - T_t}{T_m - T_t} \right)^m \right] \quad (4.1)$$

where A , B , n , C and m are material parameters. The J-C strength parameters used for aluminium and steel alloys are given in Table 3. The parameters A , B , n and C were evaluated from a series of experiments performed. The value of thermal softening exponent ($m = 0.89$) was taken from the literature (Ye *et al.*, 2016).

Table 3. Johnson-Cook parameters for Al 6063-T6 and IS 1570

J-C Parameters	A [MPa]	B [MPa]	n	C
Al 6063-T6	156.3	284.55	0.12	0.0146
IS 1570 (MS)	225	352.65	0.4073	0.022

To further improve the predictions of this numerical model, thermo-mechanical coupling effects were also incorporated. For this purpose, the increase in temperature ΔT was obtained from the following relation (Ye *et al.*, 2016)

$$\Delta T = \frac{\beta}{\rho C_p} \int \bar{\sigma} d\bar{\varepsilon}^{pl} \quad (4.2)$$

here β is the inelastic heat fraction, ρ and C_p are density and specific heat coefficients of the material. For simulations these parameters $C_p = 851$ J/kgK and $\beta = 0.9$ were incorporated from the literature (Sato *et al.*, 1999).

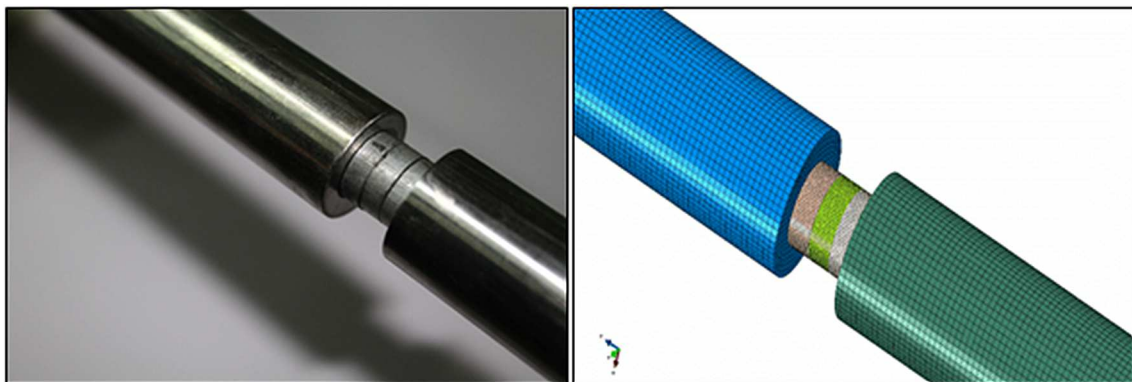


Fig. 6. Incident bar, specimen and transmission bar – experimental setup and FE model

The bars were meshed using 8 noded hexahedral brick elements (C3D8R), and the nodes along the axis of the bars were constrained radially. The total number of mesh elements generated on the incident and transmission bar were 29348 each, and the specimen with a much finer mesh (11R-1-1/3) had 23316 elements (Fig. 6). The interface between the specimen and bars was

modelled as surface-to-surface contact. A penalty contact algorithm which allowed for treatment of more general types of contact and to enforce interfacial friction was utilized in the numerical simulations. A coefficient of friction of 0.05 was given to the interface between the bars and the specimen (Hartley *et al.*, 2007). In the case of layered specimens, the specimen-to-specimen interface was given a coefficient of friction 0.03 (Hartley *et al.*, 2007; Zhong *et al.*, 2015).

The load was introduced in the form of the incident stress pulse at the free end of the incident bar. The strain data was measured on the nodes at the mid-points on the bar surfaces mimicking the actual experimental conditions. The SHPB equations were then employed to evaluate the true stress and strain data of the specimen under consideration.

5. Results and discussion

Dynamic compression tests were performed using the split Hopkinson pressure bar on stacked sequences of two selected materials viz. Al 6063-T6 and IS 1570 (mild steel) at different sets of strain rates. A single specimen of the aspect ratio 1 was sub-divided into 2, 3 and 4 equal parts, such that their individual aspect ratios l/d were 0.5, 0.33 and 0.25. On the same lines the specimens with the aspect ratio 0.75 and 0.5 were equally partitioned in 4 and 2 parts, respectively (Table 2). These specimens were then systematically evaluated under different sets of high strain loading conditions. Figures 7a-7c represent the true stress-true strain behaviour of Al 6063-T6 specimens with the aspect ratio 1, which are then further sub-divided into 2,3 and 4 layers of equal thickness, and evaluated under three different strain rates. The highest post yield stress is observed for the non-partitioned specimen at 500 s^{-1} and 1000 s^{-1} strain rates.

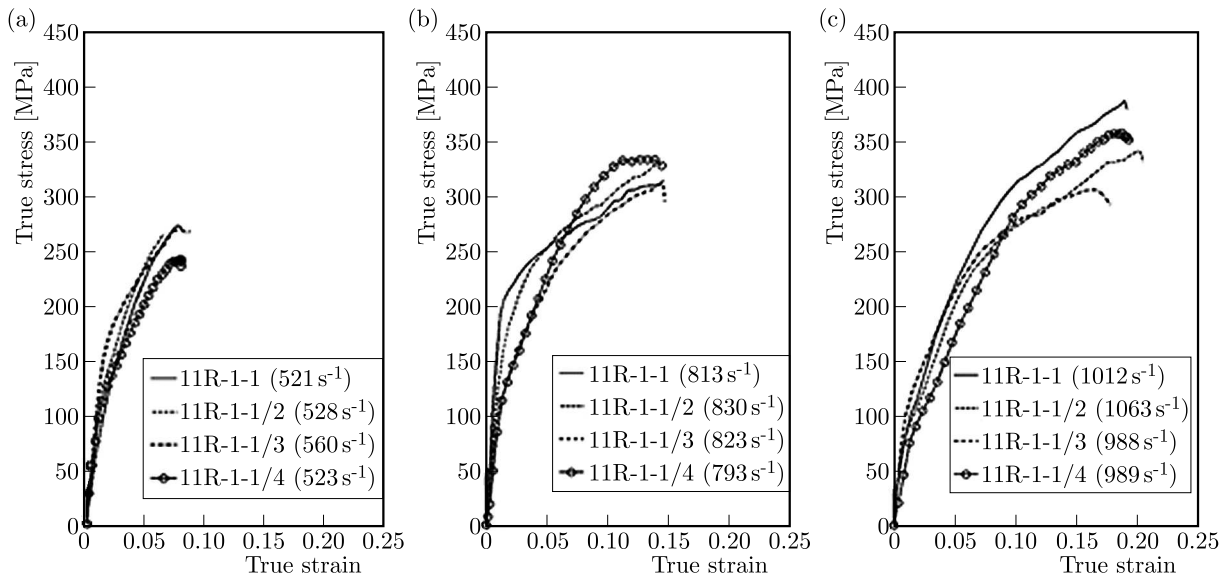


Fig. 7. (a), (b), (c) True stress versus true strain curves for different stacking sequences for Al 6063-T6 (11R-1-XX) at approximate strain rates of 500 s^{-1} , 800 s^{-1} and 1000 s^{-1}

However, at the strain rate of 800 s^{-1} , the specimen with 4 sub-divisions is observed to have the highest post yield stress. Figure 7 also reveals that there is a greater degree of similarity between the non-partitioned specimen and the specimen partitioned into half. Quantitatively, the peak stresses differ by 3% for 11R-1-1 and 11R-1-1/2 specimens and 9% for 11R-1-1/3 and 11R-1-1/4 specimens. With a further increase in the number of sub-divisions, this similarity reduces. When the aspect ratio was reduced to 0.75, it can be seen from Fig. 8 that the stress strain behaviour of the partitioned specimens was qualitatively closer to each other than that of the single specimen. This effect was found to be more pronounced at higher strain rates.

However, at a lower aspect ratio of 0.5, the plastic post yield stresses were both quantitatively and qualitatively closely matched, as can be seen in Fig. 9.

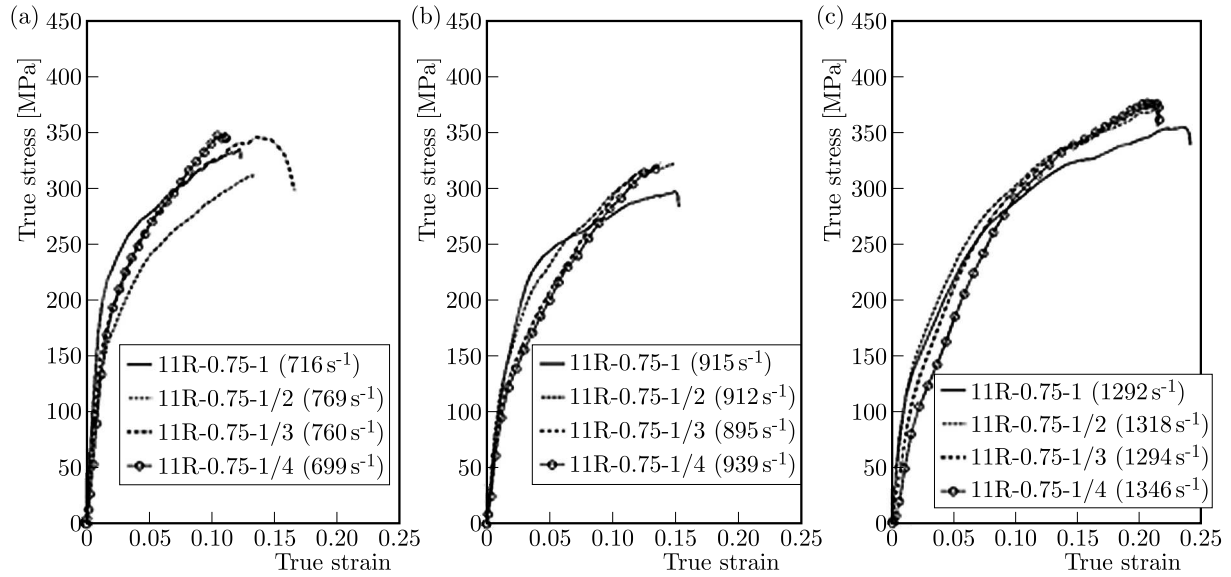


Fig. 8. True stress versus true strain curves for different stacking sequences for Al 6063-T6 (11R-0.75-XX) at approximate strain rates of (a) 700 s^{-1} , (b) 900 s^{-1} and (c) 1300 s^{-1}

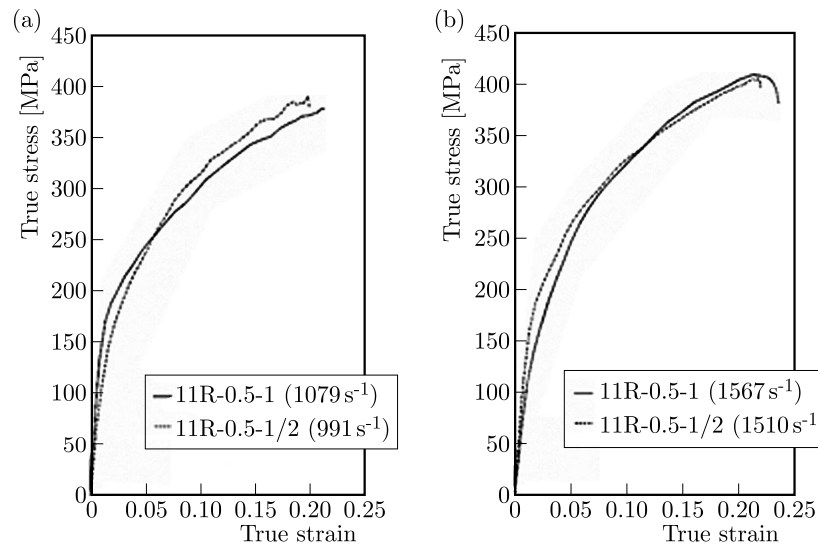


Fig. 9. True stress versus true strain curves for different stacking sequences for Al 6063-T6 (11R-0.5-XX) at approximate strain rates of (a) 1000 s^{-1} and (b) 1500 s^{-1}

It can be observed that the difference in peak post yield stresses were 0.2% and 0.9% at 1000 s^{-1} and 1500 s^{-1} , respectively. Experiments on the mild steel specimens were also performed at two different strain rates, 500 s^{-1} and 900 s^{-1} . It was also observed that non-partitioned single specimens showed a characteristic upper and lower yield points as is generally seen in the quasi-static tests of mild steel (Fig. 10). However, this behaviour was not observed when the specimen was sub-divided in two, three and four layers. The highest post yield stress was observed for the specimen partitioned in two halves. The magnitudes of peak post yield stresses obtained were 662 MPa and 725 MPa at 500 s^{-1} and 900 s^{-1} , respectively. The lowest peak post yield stress magnitudes were obtained for the specimen with three partitions as 602 MPa and 687 MPa. If the slope of the individual curves in the plastic region are carefully observed in Fig. 10a, it is revealed that for non-partitioned and half partitioned specimens, the slopes match closely, both qualitatively as well as quantitatively. The maximum difference is about 2%. Similarly,

the difference in the magnitude of slope for one-third partitioned and one-fourth partitioned specimens is nearly 1.5%. At higher strain rates, these magnitudes are found to be around 1.8% for single and halved specimens and 7% for one-third and one-fourth specimens, respectively. It is also observed that with an increase in the number of specimen partitions, the variation in the effective stiffness is more predominant in Al 6063 in comparison to IS 1570.

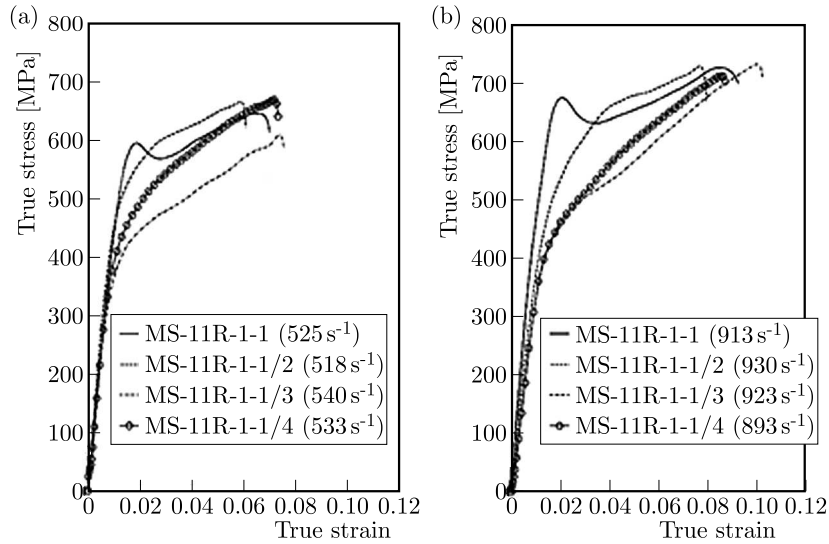


Fig. 10. True stress versus true strain curves for different stacking sequences for IS 1570 (mild steel) (MS-11R-0.5-XX) at approximate strain rates of (a) 500 s^{-1} and (b) 900 s^{-1}

Along with the experiments, finite element simulations were also performed for a different set of strain rates for Al 6063-T6 and IS 1570. Some of the results obtained are shown in Figs. 11 and 12 for Al 6063 and IS 1570, respectively. For Al 6063 it is observed that FE model incorporating the rate dependent Johnson-Cook model is able to correctly predict the true stress-strain response of the specimens for upto bi-partitions. However, when the same specimen is partitioned into tri and quad configurations, the J-C model and the experiments exhibit poor correlation.

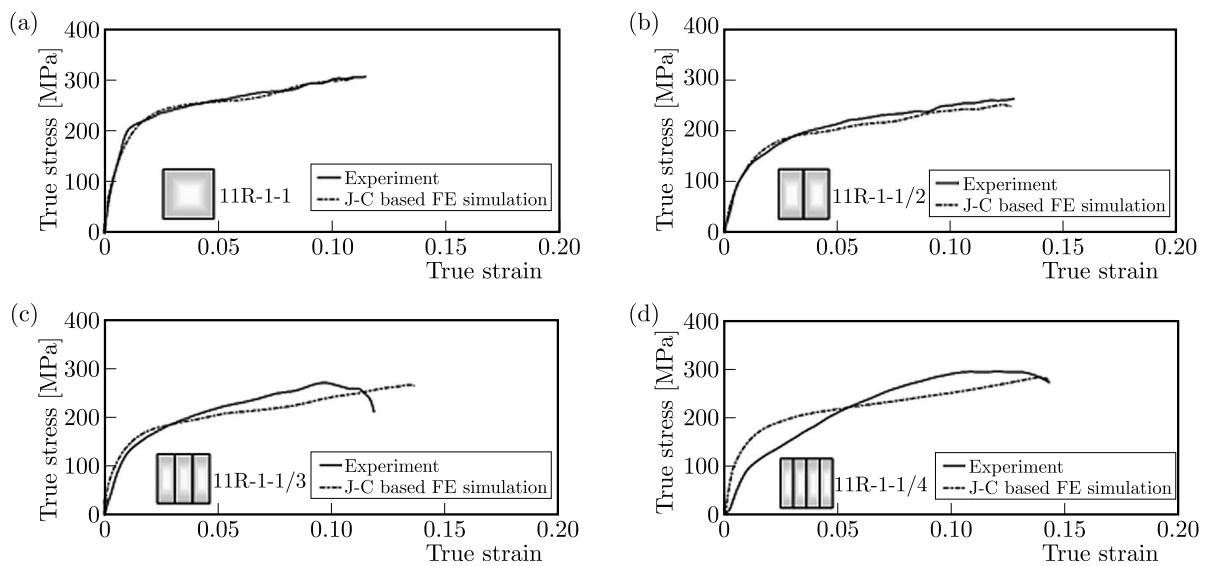


Fig. 11. (a)-(d) Comparison of experimental and FE simulation curves obtained for Al 6063-T6 (11R-1-XX) at an approximate strain rate of 800 s^{-1}

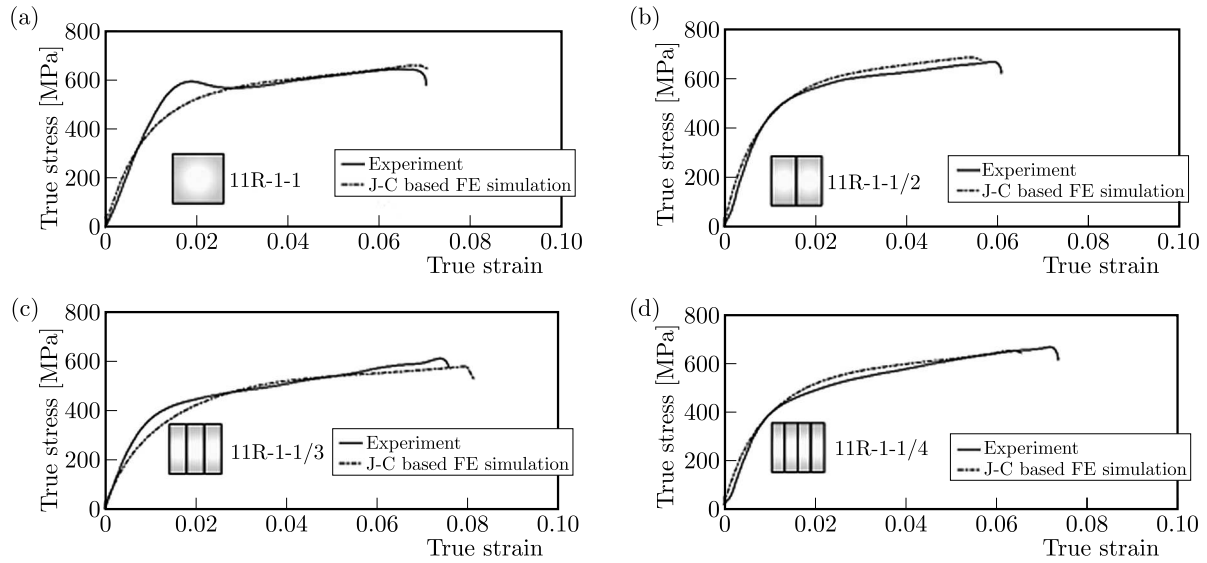


Fig. 12. (a)-(d) Comparison of experimental and FE simulation curves obtained for IS 1570 (MS-11R-1-XX) at an approximate strain rate of 500 s^{-1}

In Figs. 11c and 11d, it can be clearly seen that the Johnson-Cook model is not able to correctly capture the response observed in the experiments for tri and quad partitioned specimens. In the case of mild steel, it can be observed from Fig. 12 that the J-C based FE model show a good agreement with the experimental results for all one, two, three and four partition configurations of the specimen. However, in Fig. 12a, it is also visible that J-C model could not completely capture the specimen response around the yield point region. It should be also noted that the authors observed no meaningful difference between the model predictions, with and without thermomechanical coupling. One such a result from FE simulation using thermomechanical coupling can be observed in Fig. 13 which shows the transient cross sectional view of the quad configuration (11R-1-1/4) of aluminium specimen at a strain rate of 500 s^{-1} . Using FE simulations of Eq. (3.2), the maximum temperature gradient is found to be within 10 K.

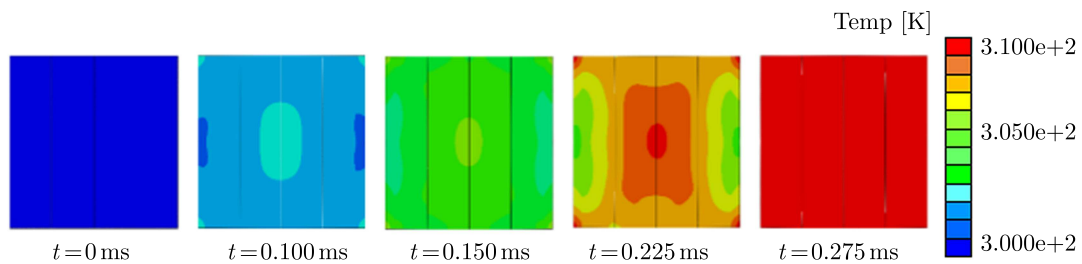


Fig. 13. Evolution of temperature in Al 6063-T6 specimen (11R-1-1/4) at a strain rate of 500 s^{-1}

In the authors' opinion, even though the overall specimen response can be measured accurately, it is extremely difficult to predict the interlayer dynamic coefficient of friction for the stacked specimens. The difference between the experimental results and the numerical predictions can be attributed to so hard to quantify, complex and evolving boundary conditions at the interfaces. From the results, it is clearly evident that the mild steel specimens showed a comparatively higher strain rate sensitivity than the aluminium alloy at different strain rates. All the different layered mild steel specimens show a response that is relatively similar in nature to each other for the given strain rate. A single specimen when tested in dynamic compression showed an upper and lower yield point which is characteristic of mild steel when tested under the quasi-static condition. However, this behaviour was only limited to the non-partitioned specimens only. The finite element analysis, in the case of aluminium alloy, shows a good agreement

with the experiments for specimens with zero and one partition. For the other two remaining cases, a clear difference in the slope, magnitude and the behaviour of the stress-strain curve is observed. In the case of FE simulations for IS 1570 mild steel specimens, a good correlation is achieved with the same material model for all the four cases. However, our simulations do not match the characteristic hump as can be seen in Fig. 13a.

The difference in the experimental and numerical predictions can be attributed to various factors like; (a) reliability of the value of dynamic coefficient of friction between the specimen-specimen and bar-specimen interfaces, (b) in experiments, even with the utmost care, it is impossible to create perfectly parallel surfaces of the specimen. While in the numerical model, perfectly parallel surfaces can be easily defined.

6. Conclusions

The present study involves experimental and numerical investigation of the behaviour of homolayered metallic media subjected to dynamic compressive loading. Two metallic alloys Al 6063-T6 and IS 1570 steel have been tested at different strain rates. The Al alloy under consideration exhibited a near tri-linear nature of the true stress-true strain curve when the specimen was partitioned into three and four parts. The above work can be concluded in the following points:

- This study has clearly shown that the dynamic response of homo layer stacking can be quite different than the monolithic layer specimen of the equivalent thickness.
- Design and selection of the pulse shaper is an important factor in evaluating the dynamic response of homostacked specimens. It is shown that by using a pulse shaper it is possible to apply the established technique like SHPB to characterize the stacked specimens.
- The current material model (Johnson-Cook) gives reasonably satisfactory match between numerical and experimental results for non-partitioned and bi-partitioned specimens. With an increase in the number of partitions, the similarity between the results decreases. Incorporating thermo-mechanical coupling does not yield any significant change in the model predictions. A better model capable of incorporating transient frictional boundary conditions and multiple wave reflections at the interfaces is required for evaluating further partitions.

References

1. CORRAN R.S.J., SHADBOLT P.J., RUIZ C., 1983, Impact loading of platesan experimental investigation, *International Journal of Impact Engineering*, **1**, 1, 3-22
2. ELLWOOD S., GRIFFITHS L.J., PARRY D.J., 1982, Materials testing at high constant strain rates, *Journal of Physics E: Scientific Instruments*, **15**, 280-282
3. Engineers and Builders, 2015, Standard tools and techniques for dynamic characterization of materials, Design book, <http://www.engineersandbuilders.com>
4. FLORES-JOHNSON E.A., SALEH M., EDWARDS L., 2011, Ballistic performance of multi-layered metallic plates impacted by a 7.62-mm APM2 projectile, *International Journal of Impact Engineering*, **38**, 12, 1022-1032
5. HARTLEY R.S., CLOETE T.J., NURICK G.N., 2007, An experimental assessment of friction effects in the split Hopkinson pressure bar using the ring compression test, *International Journal of Impact Engineering*, **34**, 1705-1728
6. JANKOWIAK T., RUSINEK A., LODYGOWSKI T., 2011, Validation of the Klepaczko-Malinowski model for friction correction and recommendations on Split Hopkinson Pressure Bar, *Finite Elements in Analysis and Design*, **47**, 10, 1191-1208

7. JENQ S.T., SHEU S.L., 1994, An experimental and numerical analysis for high strain rate compressional behaviour of 6061-O aluminium alloy, *Computers and Structures*, **52**, 1, 27-34
8. JOHNSON G.R., COOK W.H., 1983, A constitutive model and data for metal subjected to large strains, high strain rates and high temperatures, *Proceedings of the Seventh Symposium on Ballistics*, The Hague, Netherlands
9. KHAN A.S., HUANG S., 1992, Experimental and theoretical study of mechanical behaviour of 1100 aluminium in the strain rate range 10^{-5} - 10^4 s $^{-1}$, *International Journal of Plasticity*, **8**, 4, 397-424
10. KOLSKY H., 1949, An investigation of mechanical properties of materials at very high rates of loading, *Proceedings of the Physical Society, B*, **62**, 11, 676-700
11. LI P., SIVIOUR C.R., PETRINIC N., 2009, The effect of strain rate, specimen geometry and lubrication on responses of aluminium AA2024 in uniaxial compression experiments, *Experimental Mechanics*, **49**, 4, 587-593
12. NAGHDABADI R., ASHRAFI M.J., ARGHAVANI J., 2012, Experimental and numerical investigation of pulse shaped split Hopkinson pressure bar test, *Materials Science and Engineering A*, **539**, 285-293
13. NIA A.A., HOSEINI G.R., 2011, Experimental study of perforation of multi-layered targets by hemispherical-nosed projectiles, *Materials and Design*, **32**, 2, 1057-1065
14. PANKOW M., ATTARD C., WAAS A.M., 2009, Specimen size and shape effect in split Hopkinson pressure bar testing, *Journal of Strain Analysis for Engineering Design*, **44**, 8, 689-698
15. RADIN J., GOLDSMITH W., 1988, Normal projectile penetration and perforation of layered targets, *International Journal of Impact Engineering*, **7**, 2, 229-259
16. SATO Y.S., KOKAWA H., ENOMOTO M., JOGAN S., 1999, Microstructural evolution of 6063 aluminum during friction-stir welding, *Metallurgical and Materials Transactions A*, **30**, 9, 2429-2437
17. WALLEY S.M., RADFORD D.D., CHAPMAN D.J., 2006, The effect of aspect ratio on the compressive high rate deformation of three metallic alloys, *Journal de Physique IV*, **134**, 851-856
18. WOLDESENBET E., VINSON J.R., 1999, Specimen geometry effects on high strain rate testing of graphite/epoxy composites, *AIAA Journal*, **37**, 9, 1102-1106
19. WU X.J., GORHAM D.A., 1997, Stress equilibrium in the split Hopkinson pressure bar test, *Journal de Physique IV*, **7**, C3, 91-96
20. YE T., LI L., GUO P., XIAO G., CHEN Z., 2016, Effect of aging treatment on the microstructure and flow behavior of 6063 aluminum alloy compressed over a wide range of strain rate, *International Journal of Impact Engineering*, **90**, 72-80
21. ZHONG W.Z., RUSINEK A., JANKOWIAK T., ABED F., BERNIER R., SUTTER G., 2015, Influence of interfacial friction and specimen configuration in Split Hopkinson Pressure Bar system, *Tribology International*, **90**, 1-14

MECHANICAL NATURE OF A SINGLE WALLED CARBON NANOTUBE USING LEGENDRE'S POLYNOMIALS

PARUL TIWARI

*Centre for Advanced Computational Solutions, Lincoln University, New Zealand, and
Jaypee Institute of Information Technology, Noida, Uttar Pradesh, India; e-mail: parultiwari8922@gmail.com*

PRIYANKA NAGAR

Jaypee Institute of Information Technology, Noida-201309, Uttar Pradesh, India

This paper is concerned with the mechanical response of a single-walled carbon nanotube. Euler-Bernoulli's beam theory and Hamilton's principle are employed to derive the set of governing differential equations. An efficient variational method is used to determine the solution of the problem and Legendre's polynomials are used to define basis functions. Significance of using these polynomials is their orthonormal property as these shape functions convert mass and stiffness matrices either to zero or one. The impact of various parameters such as length, temperature and elastic medium on the buckling load is observed and the results are furnished in a uniform manner. The degree of accuracy of the obtained results is verified with the available literature, hence illustrates the validity of the applied method. Current findings show the usage of nanostructures in vast range of engineering applications. It is worth mentioning that completely new results are obtained that are in validation with the existing results reported in literature.

Keywords: Euler-Bernoulli's beam theory, nonlocal elasticity theory, Legendre's polynomial, aspect ratio, critical buckling load, Winkler and Pasternak elastic constants

1. Introduction

Nanotechnology has been continuously booming in the world wide research community for the last two decades as it offers numerous applications in the diversified field of biomaterials, communications, medicines and designing of efficient devices. Nanotubes, nanowires, nanotube resonators and nanoparticles are some nanomaterials in which beams and plates are widely used as main components at nano or micro length scale. One of the most fascinating elements in the periodic table is carbon that has several allotropes (diamond, fullerene, graphite, carbon nanotubes and graphene) according to its hybridization states. Carbon nanotubes were discovered by Iijima (1991) and formed by curling a graphitic sheet in a way which produced a class of materials that possess extraordinary mechanical and electrical properties (Dai *et al.*, 1996) and (Kim and Lieber, 1999). These nanotubes are used as nanobeams in microelectromechanical and nanoelectromechanical systems (Li *et al.*, 2003). These nanotubes are stronger and stiffer than any other materials because of high elastic modulus of graphite sheets. Minuscule size plays a considerable role in the analysis of mechanical nature of these nanotubes and, thus, it is hard to ignore.

Atomistic modeling, nanoscale continuum mechanics and continuum mechanics are three main methods used to define mechanical properties of carbon nanotubes. In atomistic modeling, the position of atoms are computed based on their interactive forces and end conditions (Lu and Bhattacharya, 2005). Atomistic modeling is very costly and time consuming. However, nano-scale continuum mechanics approach replaces the C-C bond by a continuum element and can be

used at nano-scale (Rafiee and Moghadam, 2014). Continuum mechanics states that the stress at each point of the body is a function of strain at the same point only. At nanoscale, size effects play a vital role in investigating the mechanical behavior as compared to that in macroscopic scale. But it is a well known fact that continuum beam theories are scale free, that is why these theories are not suitable for predicting small-scale effects of single walled carbon nanotubes. Therefore, to study the buckling behavior of carbon nanotubes the need for nonlocal continuum mechanics (Eringen, 1972, 1983) takes place. Non-classical (Nonlocal) elasticity theory has more information on forces between atoms than the classical elasticity theory. Thus it has been widely used for accurate and fast analysis of carbon nanotubes.

Initially, Peddieson *et al.* (2003) implemented nonlocal theory to nanotechnology. To investigate buckling behavior of carbon nanotubes, nonlocal continuum models were developed and used for general edge conditions by Wang Q. *et al.* (2006). Murmu and Pradhan (2009) employed a differential quadrature method alongwith the nonlocal Timoshenko beam theory. Challamel (2011) applied higher-order shear beam theories for buckling of nanobeams. Differential model of Eringen's theory is applied to formulate elastic beam theories by Reddy and El-Borgi (2014). Pradhan and Reddy (2011) used a differential transform technique to determine the buckling load of CNTs using different boundary conditions. Nagar and Tiwari (2017) applied successive differentiation approach to study characteristics of carbon nanobeams. Ansari *et al.* (2011) reported thermal buckling analysis of embedded single-walled carbon nanotube modeled through the Timoshenko beam model. Chirality effect was studied by Semmah *et al.* (2015) for zig-zag single walled carbon nanotubes. Chakraverty and Behera (2015) proposed a numerical technique to study vibration and buckling behavior of nanobeams using two types of elastic medium. Nejad and Hadi (2016) used theory of nonlocal elasticity to analyse bending behavior of bi-directional functionally graded beams. Norouzzadeh and Ansari (2017) predict the mechanical nature of nanobeams using the integral model of Eringen's theory. A review has been done for the modeling of carbon nanotubes using different models by Sakharova *et al.* (2017). Although several methods are used in literature to analyse the buckling behavior, authors find the importance of using the Rayleigh-Ritz method with Legendre's polynomials.

In the present paper, the buckling characteristics of single walled carbon nanotubes resting on a two-parameter elastic medium are analyzed using the Rayleigh-Ritz method, and Legendre's polynomials are used as shape functions. Nonlocal elasticity theory in conjunction with the Euler-Bernoulli beam theory (EBT) is used to obtain the governing equation of motion. A solution to the governing equation is obtained in the form of an eigen value problem for which a simple code is generated. Outputs of the problem are plotted graphically, and the interpretation of results is validated with those reported in literature (Wang C.M. *et al.*, 2006). The effect of change in temperature is also observed for different room environments. The impact of distinct parameters on the lowest buckling load is examined and graphs are used to draw conclusions.

2. Problem formulation

According to nonlocal elasticity theory (Eringen, 2002), the stress at a specific point in the system is considered as a function of the strain state at all points of the system. The nonclassical stress tensor σ at a point x over the volume V is determined by the following relation

$$\sigma(x) = \int_V K(D, \xi) \tau dV(x^*) \quad (2.1)$$

where τ is the local stress tensor, K is a nonclassical modulus of two parameters D and ξ . The nonlocal parameter is $\xi = (e_0 a)^2$ in which e_0 is the material specific constant, a is internal length parameter, l is length of the tube and D is Euclidean distance given as $|x^* - x|$. To solve

integral constitutive relation (2.1), its simplified differential form is given by Eringen (1972) in the following form

$$(1 - \xi l^2 \nabla^2) \boldsymbol{\sigma}(x) = \boldsymbol{\tau}(x) \quad (2.2)$$

where ∇^2 is the Laplace operator and $\boldsymbol{\tau}(x)$ is the local stress tensor defined by Hooke's law as follows

$$\boldsymbol{\tau}(x) = \mathbf{C}(x) : \boldsymbol{\varepsilon}(x) \quad (2.3)$$

where $\mathbf{C}(x)$ and $\boldsymbol{\varepsilon}(x)$ is the elasticity tensor of the order four and the local strain tensor, respectively, and “:” denotes the double dot product. It is to be noted that in absence of a , equation (2.2) reduces to the constitutive equation of classical elasticity. Governing equations are formulated using the Eringen (1972, 1983) theory and EBT nonlocal theory of elasticity. For the exceptional strength and stiffness of carbon nanotubes, they are constructed with a very high length to diameter ratio, approximately 1, 32 000 000 : 1.

Hamilton's principle is expressed by the following relation

$$\int_0^t [(\delta U_s + \delta U_p) - \delta U_k] dt = 0 \quad (2.4)$$

where δU_s , δU_p and δU_k are the variations in strain, potential energy and kinetic energy, respectively.

The displacement components as stated in the Euler-Bernoulli beam theory are such that the transverse shear stress at the boundaries of the surface of the beam is zero and nonzero at other places. The displacement field is defined as

$$u_x(x, z, t) = -z \frac{\partial u}{\partial x} \quad u_y(x, z, t) = 0 \quad u_z(x, z, t) = u(x, t) \quad (2.5)$$

where u is the transverse deflection of a point of the beam in the mid plane. The non-zero strain displacement or bending strain is defined as

$$\varepsilon_{xx} = -z \frac{\partial^2 u}{\partial x^2} \quad (2.6)$$

and the strain energy is

$$U_s = \frac{1}{2} \int_0^l \int_A \sigma_{xx} \varepsilon_{xx} dA dx \quad (2.7)$$

where σ_{xx} is the normal stress, l is the size of the beam and A is the cross-sectional area.

Using (2.6) into (2.7), the strain energy is given as

$$U_s = -\frac{1}{2} \int_0^l \int_A z \sigma_{xx} \frac{\partial^2 u}{\partial x^2} dA dx = -\frac{1}{2} \int_0^l M \frac{\partial^2 u}{\partial x^2} dx \quad (2.8)$$

where $M = \int_A z \sigma_{xx} dA$ is defined as the bending moment. For free harmonic motion, the natural frequency ω of vibration is given by $u = u_0(x) \sin(\omega t)$.

Therefore, the strain and kinetic energy of the beam are expressed as

$$U_s = -\frac{1}{2} \int_0^l M \frac{d^2 u_0}{dx^2} dx \quad U_k = \frac{1}{2} \int_0^l \rho A u^2 u_0^2 dx \quad (2.9)$$

where ρ is mass density of the beam.

The work done by external forces (potential energy) is defined as

$$U_p = \frac{1}{2} \left[\int_0^l F \left(\frac{du_0}{dx} \right)^2 dx + \int_0^l \rho_e u_0 dx \right] \quad (2.10)$$

where $F = F_m + F_\theta$ is the compressive force applied to the beam. Here, F_m and F_θ both are axial forces due to change in mechanical load and temperature, respectively, and F_θ is related with temperature θ as

$$F_\theta = -\frac{EA\gamma_x\theta}{1-2\nu} \quad (2.11)$$

where $\rho_e = k_1 u_0 - k_2 (d^2 u_0 / dx^2)$ is the elastic medium density and EA is tensile rigidity. Here, k_1 and k_2 are Winkler elastic modulus and Pasternak shear elastic modulus, respectively. According to the Winkler elastic modulus, the force on the foundation is directly proportional to deflection while the Pasternak model assumes the existence of shear interaction between the spring elements.

Using equations (2.9) and (2.10) in (2.4) and equating the coefficient of δu_0 to zero, equation (2.4) reduces to

$$\frac{d^2 M}{dx^2} + \left(F \frac{d^2}{dx^2} - k_1 + k_2 \frac{d^2}{dx^2} + \rho A \omega^2 \right) u_0 = 0 \quad (2.12)$$

The constitutive equations of the nonclassical Euler-Bernoulli beam is given as

$$-EI \frac{d^2 u_0}{dx^2} = M - \xi \frac{d^2 M}{dx^2} \quad (2.13)$$

where EI is defined as bending rigidity.

Using (2.12) and (2.13), the bending moment for nonlocal elasticity theory is written as

$$M = -EI \frac{d^2 u_0}{dx^2} + \xi \left(-\rho A \omega^2 u_0 - F \frac{d^2 u_0}{dx^2} + k_1 u_0 - k_2 \frac{d^2 u_0}{dx^2} \right) \quad (2.14)$$

Equating the maximum kinetic and potential energy, the dimensionless equation of motion for nonlocal EBT nanobeams is expressed as

$$\begin{aligned} \frac{EI}{l^2} (1 + \hat{F} \beta^2 + K_2 \beta^2) \left(\frac{d^2 U}{dX^2} \right)^2 + \frac{EI}{l^2} (-K_1 \beta^2 U - K_2 U + \alpha^2 \beta^2 U) \frac{d^2 U}{dX^2} \\ + \frac{EI}{l^2} \hat{F} \left(\frac{d^2 U}{dX^2} \right)^2 + \frac{EI}{l^2} (K_1 - \alpha^2) U^2 = 0 \end{aligned} \quad (2.15)$$

The dimensionless form of parameters is as follows

$$\begin{aligned} X = \frac{x}{l} \quad U = \frac{u_0}{l} \quad \beta = \frac{e_0 a}{l} \quad K_1 = \frac{k_1 l^4}{EI} \quad K_2 = \frac{k_2 l^2}{EI} \\ \hat{F} = \frac{F l^2}{EI} \quad \hat{F}_m = \frac{F_m l^2}{EI} \quad \hat{F}_\theta = \frac{F_\theta l^2}{EI} \quad \alpha^2 = \frac{\rho A \omega^2 l^4}{EI} \end{aligned} \quad (2.16)$$

3. Solution procedure

To solve equation (2.15), Rayleigh-Ritz method (R-R) is employed with a Legendre's polynomial as a shape function. This method is generally used for finding an approximate solution for different types of mechanical engineering problems and is often used to determine first eigen frequencies and eigenfunctions of continuous linear elastic systems. The approximate solution of eigenvalues and eigenfunctions of the continuous system is improved by using a large number of terms in the Ritz expansion and the error in the approximation of the eigenfunction being measured in a certain norm. The boundary function is chosen in such a way so that it satisfies the essential end conditions of the beam.

According to R-R method, the displacement function can be written as a sum of polynomials as

$$U(X) = \sum_{n=1}^N b_n \psi_n \quad (3.1)$$

where b_n are unknowns to be determined, ψ_n are orthonormal polynomials and N is the number of terms needed to find the results up to desired level of accuracy. Here we used a Legendre's polynomial as an orthonormal polynomial.

The Legendre polynomials are chosen in such a way that they bijectively map the interval $[0, 1]$ to $[-1, 1]$. This is to show that the polynomials are orthogonal on $[0, 1]$ to satisfy the end conditions $\psi_n(0) = \psi_n(1) = 0$, $n \geq 1$. To fulfill the conditions of orthogonality in the interval $[0, 1]$, modified form of the Legendre polynomial is used and is defined as

$$\psi_n(X) = \left[\frac{1}{n!} \frac{d^n}{dX^n} (X^2 - X)^n - (-1)^n \right] (X - 1) \quad (3.2)$$

Some of the modified Legendre polynomials over the interval $[0, 1]$ are as follows

$$\begin{aligned} \psi_1(X) &= -2X + 2X^2 & \psi_2(X) &= 6X - 12X^2 + 6X^3 \\ \psi_3(X) &= -12X + 42X^2 - 50X^3 + 20X^4 \\ \psi_4(X) &= 20X - 110X^2 + 230X^3 - 210X^4 + 70X^5 \\ \psi_5(X) &= -30X + 240X^2 - 770X^3 + 1190X^4 - 882X^5 + 252X^6 \end{aligned}$$

These modified Legendre polynomials can be used as a set of basis functions and satisfy the special properties $\psi_n(0) = \psi_n(1) = 0$, $n \geq 1$ at the boundaries. Putting $\hat{F}_m = -P$ and the inertia term α^2 to zero in equation (2.15), the following governing equations are obtained to analyze the critical buckling load

$$\left(1 - K_2 \beta^2 + \frac{\hat{F}_\theta l^2}{EI} + \frac{F_\theta l^2}{EI} \beta^2 \right) \left(\frac{d^2 U}{dX^2} \right)^2 - (K_1 \beta^2 U + K_2 U) \frac{d^2 U}{dX^2} K_1 U^2 = \hat{P} \left[\left(\frac{dU}{dX} \right)^2 + \beta^2 \left(\frac{d^2 U}{dX^2} \right)^2 \right] \quad (3.3)$$

where $\hat{P} = Pl^2/(EI)$.

Incorporating equation (3.1) into equation (3.2), solution of equation (3.3) is obtained by minimizing the buckling load with respect to unknown coefficients b_j , $j = 1, 2, \dots, n$. Thus, by putting $\partial \hat{P} / \partial b_j = 0$, the solution of equation (3.3) in matrix form is

$$\mathbf{S}\mathbf{Y} = \hat{\mathbf{P}}\mathbf{B}\mathbf{Y} \quad (3.4)$$

where $\mathbf{Y} = [b_1, b_2, \dots, b_n]^T$ is the transpose matrix of the unknown coefficients b_j , $j = 1, 2, \dots, n$ and the stiffness and buckling matrices are given by

$$S(i, j) = \int_0^1 \left[(1 + 2K_2\beta^2 + 2\hat{F}\beta^2) \ddot{\psi}_i \ddot{\psi}_j + 2\hat{F}\beta^2 \dot{\psi}_i \dot{\psi}_j + 2K_1 \psi_i \psi_j - (K_2 + K_1) \ddot{\psi}_i \psi_j - (K_2 + K_1) \psi_i \ddot{\psi}_j \right] dX \quad (3.5)$$

$$B(i, j) = \int_0^1 (2\dot{\psi}_i \dot{\psi}_j + 2\beta^2 \ddot{\psi}_i \ddot{\psi}_j) dX$$

where $i, j = 1, \dots, n$, $\dot{\psi}_i$ and $\ddot{\psi}_i$ represents derivatives of the first and second order of $\psi_i(X)$ with respect to X for all i and j . Equation (3.4) is an eigen value problem in which the smallest eigen value will provide the critical buckling load which is to be obtained by equating the determinant of the coefficient matrix to zero. Corresponding eigenvectors are used as shape functions and for finding the critical buckling loads and post buckling behavior of beams and columns.

4. Results and discussions

To obtain the numerical results, values of different parameters for a single-walled carbon nanotube according to (Benzair *et al.*, 2008) and (Murmu and Pradhan, 2009) are given in Table 1.

Table 1. Values of different parameters to determine buckling load (Benzair *et al.*, 2008) and (Murmu and Pradhan, 2009)

Parameter	Value
Modulus of elasticity	1 TPa
Thermal expansion coefficient	$-1.4 \cdot 10^{-6}$ for low temperature environment $1.0 \cdot 10^{-6}$ for high temperature environment
Poisson's ratio	0.19

Values in Table 2 show the critical buckling load for clamped-clamped end conditions for varying values of the aspect ratio and nonlocal scale parameter.

Table 2. Critical buckling load using the present approach and (Pradhan and Reddy, 2011) for the clamped-clamped (C-C) case

Aspect ratio (l/d)	Nonlocal parameter [nm^2] Pradhan and Reddy (2011)				Nonlocal parameter [nm^2] Present approach			
	$\xi = 0$	$\xi = 1.0$	$\xi = 1.5$	$\xi = 2.0$	$\xi = 0$	$\xi = 1.0$	$\xi = 1.5$	$\xi = 2.0$
10	9.6311	8.2298	6.3549	3.2367	9.6318	8.2314	6.3512	3.2369
12	5.3601	4.3316	3.3686	2.1855	5.3617	4.3325	3.3698	2.1865
14	3.1114	2.6010	2.1238	1.6296	3.1134	2.6025	2.1230	1.6362
16	2.1183	1.7992	1.5629	1.2102	2.1193	1.8001	1.5632	1.2050
18	1.7741	1.5201	1.2251	1.0135	1.7721	1.5124	1.2253	1.0090
20	1.6125	1.3459	1.1248	0.9905	1.6134	1.3462	1.1253	0.9963

It is observed from the numerical results that the critical buckling load decreases as the length to diameter ratio increases, and this effect is more significant for higher values of the nonclassical scale parameter. Figure 1a shows variation in the critical buckling strain (or load)

with the length-to-diameter ratio for C-C end conditions. Multiple graphs are plotted for different nonclassical parameter values.

It is to be noted that if the nonclassical parameter is neglected, the obtained results correspond to those that are obtained from the local theory. It is also observed from the graph that in order to set a lower buckling load, the value of the scale coefficient is to be increased. These observations are verified with (Pradhan and Reddy, 2011).

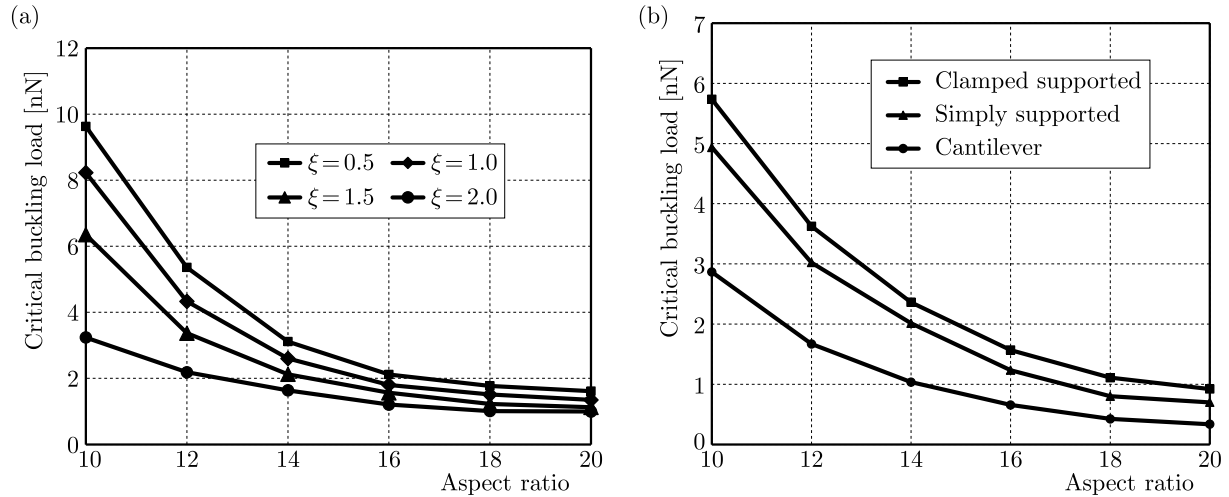


Fig. 1. (a) Variation in the critical buckling load with different values of the aspect ratio. (b) Impact of the aspect ratio on the critical buckling load

Figure 1b illustrates the impact of the length-to-diameter ratio on the lowest (critical) buckling load for various boundary conditions. The load value decreases for all boundary conditions as the aspect ratio increases. Moreover, clamped-simply supported end conditions provide a higher buckling load as compared to simply supported and cantilever beams. The graph shows that buckling solutions are highly influenced by the small scale coefficient. Buckling strain is high for a lower aspect ratio. The obtained results are in agreement with (Wang C.M. *et al.*, 2006).

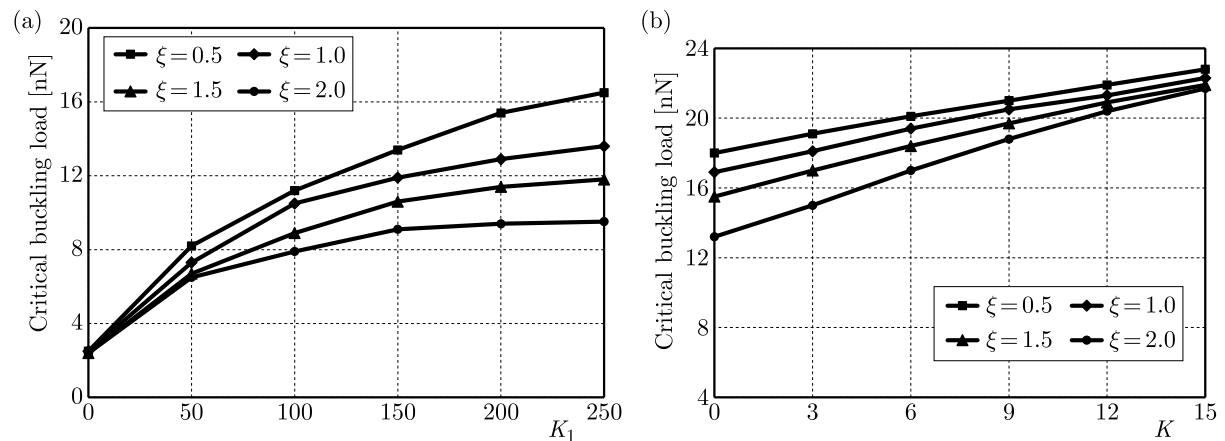


Fig. 2. (a) Distribution of the critical buckling load for different Winkler elastic moduli. (b) Impact of the Pasternak shear elastic modulus on the critical buckling load

Figure 2a represents the impact of the Winkler elastic constant. To study this effect, different physical values are taken as $\theta = 20$, $l/d = 15$ and $K_2 = 0$. Variations in the buckling load are shown for different scale coefficients, and the Winkler modulus is taken between 0-250. It is shown in the graph that the critical buckling load increases with the increment in the Winkler

modulus. For higher values of the scale coefficient, nonlinear behavior of the lowest buckling load for different values of the Winkler elastic medium is observed. The reason behind this effect is that the nanotube becomes rigid after increasing the value of the Winkler elastic medium constant.

Figure 2b demonstrates the change in the critical buckling load parameter with respect to the Pasternak shear modulus parameter for various values of nonlocal parameters. Different parameters are taken as $\theta = 20$, $l/d = 15$ and $K_1 = 0$ to study the effect of the elastic medium on buckling solutions. It is noticed that the increasing of the Pasternak elastic modulus increases the critical buckling load, and this increment is linear in nature due to the commanding nature of this foundation. It can be easily seen that the critical buckling loads in the Pasternak model are larger than in the Winkler model. The critical buckling loads of single walled carbon nanotubes for higher values of small scale coefficients are small compared to lower values of the scale coefficient. The obtained results are in validation with (Murmu and Pradhan, 2009).

Figure 3 shows the effect of temperature on the critical buckling load for two different environments (Murmu and Pradhan, 2010) and $K_2 = 3$. It is observed from the graph that if the nanobeam is placed in low temperature environment, the critical buckling strain increases as temperature increases. However, in high temperature environment, the critical buckling strain decreases with an increase in temperature. This is due to the fact that rigidity of the nanobeam in low temperature environment increases as temperature increases, and in high temperature environment the rigidity of a single walled carbon nanotube decreases as temperature increases. Similar interpretations were also presented in (Murmu and Pradhan, 2010) and (Chakraverty and Behera, 2015).

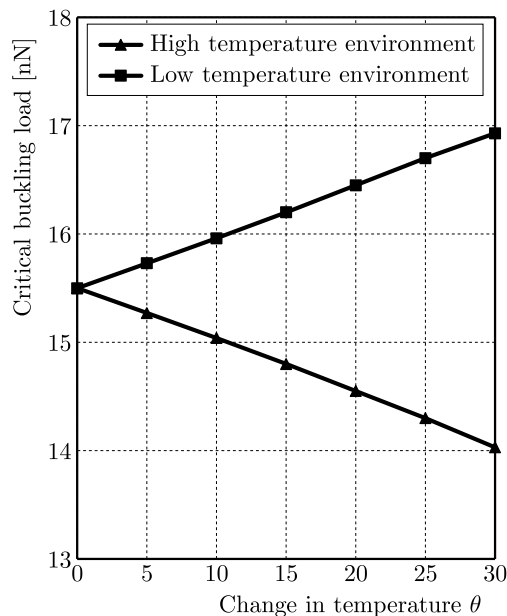


Fig. 3. Variation in the critical buckling load due to different temperature environments

5. Conclusion

In the present paper, considering the effect of temperature in conjunction with two foundation models, the mechanical analysis of single walled carbon nanotubes is studied. Legendre's polynomial is used as a characteristic polynomial along with the Rayleigh-Ritz method playing a significant contribution to this study. The orthogonality of these polynomials ensures the results to be found valid with a reasonable accuracy. For two-parameter models, the influence of phy-

sical parameters like the elastic coefficients, nonlocal parameter, aspect ratio and temperature is discussed graphically. Conclusions are drawn with the help of the obtained numerical results and are in fair agreement with those reported in literature. It is found that the critical buckling load increases as the nonlocal parameter increases. Moreover, it is also observed that in the case of the Pasternak foundation, the critical buckling load behaves linearly while for the Winkler foundation this behavior is nonlinear. Critical buckling loads behave nonlinearly for the Winkler elastic modulus because single walled carbon nanotubes become stiffer after an increment in the Winkler elastic modulus. The reason for linearity may be due to the commanding nature of the Pasternak type elastic foundation.

References

1. ANSARI R., GHOLAMI R., DARABI M.A., 2011, Thermal buckling analysis of embedded single-walled carbon nanotubes with arbitrary boundary conditions using the nonlocal Timoshenko beam theory, *Journal of Thermal Stresses*, **34**, 12, 1271-1281
2. BENZAI A., TOUNSI A., BESSEGHIER A., HEIRECHE H., MOULAY N., BOUMIA L., 2008, The thermal effect on vibration of single-walled carbon nanotubes using nonlocal Timoshenko beam theory, *Journal of Physics D: Applied Physics*, **41**, 22, 225404
3. CHAKRAVERTY S., BEHERA L., 2015, Vibration and buckling analyses of nanobeams embedded in an elastic medium, *Chinese Physics B*, **24**, 9, 097305
4. CHALLAMEL N., 2011, Higher-order shear beam theories and enriched continuum, *Mechanics Research Communications*, **38**, 5, 388-392
5. DAI H., HAFNER J.H., RINZLER A.G., COLBERT D.T., SMALLEY R.E., 1996, Nanotubes as nanoprobe in scanning probe microscopy, *Nature*, **384**, 6605, 147-150
6. ERINGEN A.C., 1972, Linear theory of nonlocal elasticity and dispersion of plane waves, *International Journal of Engineering Science*, **10**, 5, 425-435
7. ERINGEN A.C., 1983, On differential equations of nonlocal elasticity and solutions of screw dislocation and surface waves, *Journal of Applied Physics*, **54**, 9, 4703
8. ERINGEN A.C., 2002, *Nonlocal Continuum Field Theories*, Springer Science & Business Media
9. IJIMA S., 1991, Helical microtubules of graphitic carbon, *Nature*, **354**, 6348, 56-58
10. KIM P., LIEBER C.M., 1999, Nanotube nanotweezers, *Science*, **286**, 5447, 2148-2150
11. LI X., BHUSHAN B., TAKASHIMA K., BAEK C.W., KIM Y.K., 2003, Mechanical characterization of micro/nanoscale structures for MEMS/NEMS applications using nanoindentation techniques, *Ultramicroscopy*, **97**, 1-4, 481-494
12. LU Q., BHATTACHARYA B., 2005, The role of atomistic simulations in probing the small-scale aspects of fracture – a case study on a single-walled carbon nanotube, *Engineering Fracture Mechanics*, **72**, 13, 2037-2071
13. MURMU T., PRADHAN S.C., 2009, Buckling analysis of a single-walled carbon nanotube embedded in an elastic medium based on nonlocal elasticity and Timoshenko beam theory and using DQM, *Physica E: Low-Dimensional Systems and Nanostructures*, **41**, 7, 1232-1239
14. MURMU T., PRADHAN S.C., 2010, Thermal effects on the stability of embedded carbon nanotubes, *Computational Materials Science*, **47**, 3, 721-726
15. NAGAR P., TIWARI P., 2017, Recursive differentiation method to study the nature of carbon nanobeams: A numerical approach, *AIP Conference Proceedings*, **1897**, 1, 020009, AIP Publishing
16. NEJAD Z.M., HADI A., 2016, Eringen's non-local elasticity theory for bending analysis of bi-directional functionally graded Euler-Bernoulli nano-beams, *International Journal of Engineering Science*, **106**, 1-9

17. NOROUZZADEH A., ANSARI R., 2017, Finite element analysis of nano-scale Timoshenko beams using the integral model of nonlocal elasticity, *Physica E: Low-Dimensional Systems and Nanostructures*, **88**, 194-200
18. PEDDIESON J., BUCHANAN G.R., MCNITT R.P., 2003, Application of nonlocal continuum models to nanotechnology, *International Journal of Engineering Science*, **41**, 3, 305-312
19. PRADHAN S.C., REDDY G.K., 2011, Buckling analysis of single walled carbon nanotube on Winkler foundation using nonlocal elasticity theory and DTM, *Computational Materials Science*, **50**, 3, 1052-1056
20. RAFIEE R., MOGHADAM R.M., 2014, On the modeling of carbon nanotubes: A critical review, *Composites Part B: Engineering*, **56**, 435-449
21. REDDY J.N., EL-BORGI S., 2014, Eringen's nonlocal theories of beams accounting for moderate rotations, *International Journal of Engineering Science*, **82**, 159-177
22. SAKHAROVA N.A., ANTUNES J.M., PEREIRA A.F.G., FERNANDES J.V., 2017, Developments in the evaluation of elastic properties of carbon nanotubes and their heterojunctions by numerical simulation, *AIMS Materials Science*, **4**, 3, 706-737
23. SEMMAH A., TOUNSI A., ZIDOUR M., HEIRECHE H., NACERI M., 2015, Effect of the chirality on critical buckling temperature of zigzag single-walled carbon nanotubes using the nonlocal continuum theory, *Fullerenes, Nanotubes and Carbon Nanostructures*, **23**, 6, 518-522
24. WANG C.M., ZHANG Y.Y., RAMESH S.S., KITIPORNCHAI S., 2006, Buckling analysis of micro- and nano-rods/tubes based on nonlocal Timoshenko beam theory, *Journal of Physics D: Applied Physics*, **39**, 17, 3904
25. WANG Q., VARADAN V.K., QUEK S.T., 2006, Small scale effect on elastic buckling of carbon nanotubes with nonlocal continuum models, *Physics Letters A*, **357**, 2, 130-135

Manuscript received November 6, 2017; accepted for print May 28, 2018

BENDING, BUCKLING AND FREE VIBRATION OF A BEAM WITH UNSYMMETRICALLY VARYING MECHANICAL PROPERTIES

KRZYSZTOF MAGNUCKI, JERZY LEWIŃSKI

Institute of Rail Vehicles TABOR, Poznań, Poland

EWA MAGNUCKA-BLANDZI

Poznan University of Technology, Institute of Mathematics, Poznań, Poland

e-mail: ewa.magnucka-blandzi@put.poznan.pl

PIOTR KĘDZIA

Poznan University of Technology, Institute of Applied Mechanics, Poznań, Poland

The subject of the paper is a beam with unsymmetrically varying mechanical properties in the depth direction. The nonlinear hypothesis of plane cross section deformation is assumed. Based on Hamilton's principle, two differential equations of motion are obtained. The system of equations is analytically solved with a view to analyse the bending, buckling and free vibration problems of the beam. Moreover, the FEM model of the beam is developed and deflections, critical axial forces and natural frequencies of the beam are calculated. The results of these two methods are compared.

Keywords: FGM beam, mathematical modelling, numerical FEM calculations

1. Introduction

Elements with varying mechanical properties are applied in modern constructions. Kubiak (2005) presented dynamic buckling problems of thin-walled composite plates with varying width-wise material properties. Zhang *et al.* (2006) presented free vibration analysis of rectangular composite laminated plates. Zenkour (2006) analysed bending problems of rectangular functionally graded plates under a transverse uniform load. Birman and Byrd (2007) presented a review of the papers published since 2000 related to the modelling and analysis of functionally graded materials and structures. Kapuria *et al.* (2008) described the theoretical model of bending and free vibration of layered functionally graded beams and its experimental validation. Debowski *et al.* (2010) studied the dynamic stability problem of a metal foam rectangular plate under compression in the middle plane. Magnucka-Blandzi (2011) presented bending and dynamic stability results of studies of the sandwich beam with a metal foam core. Kubiak (2011) described an estimation problem of dynamic buckling for composite columns with open cross-sections. Thai and Vo (2012, 2013) presented bending, buckling, and vibration of functionally graded beams and plates with the use of nonlinear shear deformation theories. Mahi *et al.* (2015) presented bending and free vibration analysis of isotropic, functionally graded sandwich and laminated composite plates with the use of a new hyperbolic deformation theory. Kolakowski and Mania (2015) presented the dynamic response of thin functionally graded plates with a static unsymmetrical stable postbuckling path. Chen *et al.* (2015, 2016a,b) analysed static bending, elastic buckling and free vibrations problems of shear deformable functionally graded porous beams and sandwich beams with a functionally graded porous core. Jun *et al.* (2016) studied the free vibration problem of axially loaded laminated composite beams using a unified higher-order shear deformation theory and a dynamic stiffness method. Mojahedin *et al.* (2016) presented

the buckling problem of functionally graded circular plates with symmetrically and unsymmetrically varying mechanical properties based on a higher order shear deformation theory. Li and Hu (2016) analysed nonlinear bending and free vibration problems of nonlocal strain gradient beams made of a functionally graded material. Feyzi and Khorshidvand (2017) presented the axisymmetric post-buckling behaviour problem of saturated porous circular plates. Song *et al.* (2017) described vibration problems of functionally graded polymer composite plates reinforced with graphene nanoplatelets. Smyczynski and Magnucka-Blandzi (2018) presented a comparison of the study results of three-point bending of a sandwich beam with two binding layers with the use of two nonlinear hypotheses. Sayyad and Ghugal (2017) presented an extensive review of the papers devoted to bending, buckling and free vibration problems with special attention paid to the shear effects.

The subject of the study is a beam with unsymmetrically varying mechanical properties. A nonlinear hypothesis of deformation of the plane cross section of the beam is developed. Particular attention is paid to location of the neutral axis with consideration of the shear effect. Variability of the elastic modulus – Young's modulus in the depth direction of the beam is shown in Fig. 1.

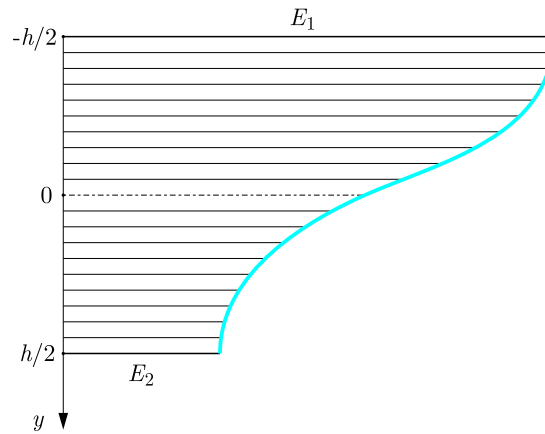


Fig. 1. Scheme of the elastic modulus variability in the depth direction of the beam

The values of elasticity moduli and mass density of the beam vary as follows

$$\begin{aligned} E(y) &= \frac{1}{2}E_1[1 + e_2 - (1 - e_2)\sin(\pi\eta)] & G(y) &= \frac{1}{2}G_1[1 + g_2 - (1 - g_2)\sin(\pi\eta)] \\ \rho(y) &= \frac{1}{2}\rho_1[1 + \tilde{\rho}_2 - (1 - \tilde{\rho}_2)\sin(\pi\eta)] \end{aligned} \quad (1.1)$$

where: $e_2 = E_2/E_1$, $g_2 = G_2/G_1 = (1 + \nu_1)/(1 + \nu_2)e_2$, $\tilde{\rho}_2 = \rho_2/\rho_1$ are dimensionless relative parameters, E_1 , E_2 – Young's moduli, ν_1 , ν_2 – Poisson's ratios, ρ_1 , ρ_2 – mass densities, $\eta = y/h$ – dimensionless coordinate ($-0.5 \leq \eta \leq 0.5$), h – depth of the beam.

The relationship between the relative density and Young's moduli ratio $\tilde{\rho}_2 = \sqrt{e_2}$ is assumed based on the papers by Chen *et al.* (2015, 2016b).

2. Analytical model of the beam

The nonlinear hypothesis is assumed for the purpose of modelling of the beam. A plane cross section before bending is no longer plane after bending of the beam (Fig. 2). This hypothesis is a generalization of the shear deformation theory for functionally graded structures.

Two coordinate systems are adopted – x, y and x_1, y_1 (Fig. 2). The x_1 axis is the neutral axis, therefore, the displacement $v(x_1, t)$ is equivalent with $v(x, t)$. The coordinate $y_1 = h(\eta + \eta_0)$,

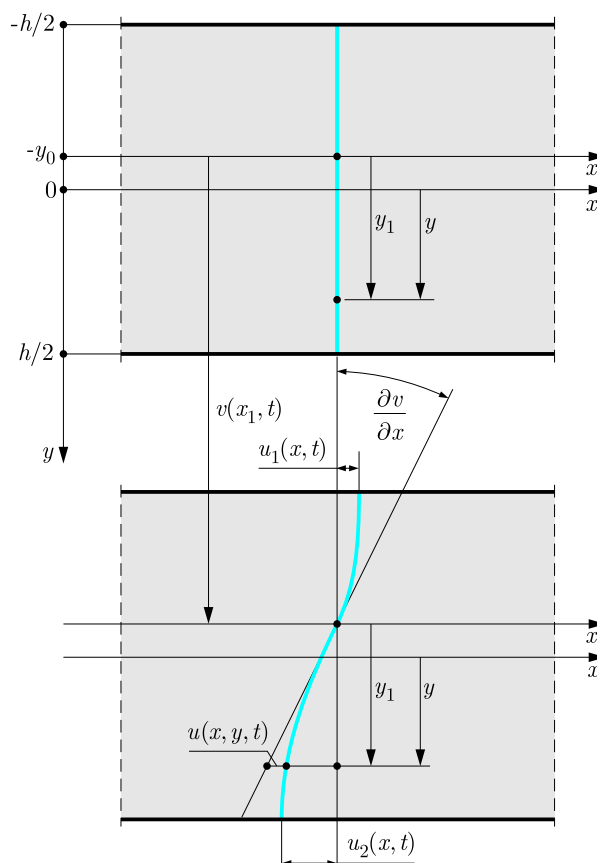


Fig. 2. Deformation of the plane cross section of the beam – the nonlinear hypothesis

where $\eta_0 = y_0/h$, therefore, based on the above hypothesis, the displacement is in the following form

$$u(x, y, t) = -h \left\{ (\eta + \eta_0) \frac{\partial v}{\partial x} - [\sin(\pi\eta) + \sin(\pi\eta_0)] \psi(x, t) \right\} \quad (2.1)$$

where: $v(x, t)$ – deflection, $\psi(x, t)$ – dimensionless function of the shear effect.

The shear effect displacements of upper and lower surfaces of the beam are as follows

$$u_1(x, t) = -h[1 - \sin(\pi\eta_0)]\psi(x, t) \quad u_2(x, t) = h[1 + \sin(\pi\eta_0)]\psi(x, t) \quad (2.2)$$

Then, the longitudinal strain

$$\varepsilon_x(x, y, t) = \frac{\partial u}{\partial x} = -h \left\{ (\eta + \eta_0) \frac{\partial^2 v}{\partial x^2} - [\sin(\pi\eta) + \sin(\pi\eta_0)] \frac{\partial \psi}{\partial x} \right\} \quad (2.3)$$

and the shear strain

$$\gamma_{xy}(x, y, t) = \frac{\partial u}{\partial y} + \frac{\partial v}{\partial x} = \pi \cos(\pi\eta) \psi(x, t) \quad (2.4)$$

The stresses – Hooke's law

$$\sigma_x(x, y, t) = E(y)\varepsilon_x(x, y, t) \quad \tau_{xy}(x, y, t) = G(y)\gamma_{xy}(x, y, t) \quad (2.5)$$

The simply supported beam with unsymmetrically varying mechanical properties of length L , depth h and width b is subjected to a uniformly distributed transverse load of intensity q or to axial compression force F_0 (Fig. 3).

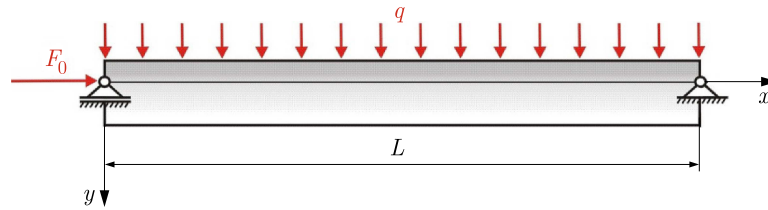


Fig. 3. Scheme of the beam and loads

The Hamilton principle

$$\int_{t_1}^{t_2} [T - (U_\varepsilon - W)] dt = 0 \quad (2.6)$$

where: T is the kinetic energy, U_ε – elastic strain energy, W – work of the load

$$T = \frac{1}{2} b h \rho_b \int_0^L \left(\frac{\partial v}{\partial t} \right)^2 dx \quad U_\varepsilon = \frac{1}{2} b \int_0^L \int_{-h/2}^{h/2} [E(y) \varepsilon_x^2 + G(y) \gamma_{xy}^2] dx dy \quad (2.7)$$

$$W = \int_0^L \left[q v(x) + \frac{1}{2} F_0 \left(\frac{\partial v}{\partial x} \right)^2 \right] dx$$

and the equivalent – mean mass density of the beam

$$\rho_b = \frac{1}{h} \int_{-h/2}^{h/2} \rho(y) dy = \frac{1}{2} (\rho_1 + \rho_2) = \frac{1}{2} \rho_1 (1 + \sqrt{e_2}) \quad (2.8)$$

Substitution of expressions (1.1)₁ and (1.1)₂ for the elasticity moduli and expressions (2.3) and (2.4) for strains into expression (2.7)₂, after integration along depth of the beam, gives elastic strain energy as a functional of the two unknown functions

$$U_\varepsilon = \frac{1}{4} E_1 b h^3 \int_0^L \left[C_{vv} \left(\frac{\partial^2 v}{\partial x^2} \right)^2 - 2 C_{v\psi} \frac{\partial^2 v}{\partial x^2} \frac{\partial \psi}{\partial x} + C_{\psi\psi} \left(\frac{\partial \psi}{\partial x} \right)^2 + C_{\psi 0} \frac{\psi^2(x, t)}{h^2} \right] dx \quad (2.9)$$

where

$$C_{vv} = \frac{1}{12} \left[1 - \frac{48}{\pi^2} \eta_0 + 12 \eta_0^2 + \left(1 + \frac{48}{\pi^2} \eta_0 + 12 \eta_0^2 \right) e_2 \right] \quad C_{\psi 0} = \frac{\pi^2}{4(1 + \nu_1)} (1 + g_2)$$

$$C_{v\psi} = \frac{1}{2\pi^2} \{ (4 - \pi^2 \eta_0) [1 - \sin(\pi \eta_0)] + (4 + \pi^2 \eta_0) [1 + \sin(\pi \eta_0)] e_2 \}$$

$$C_{\psi\psi} = \frac{1}{2} - \sin(\pi \eta_0) + \sin^2(\pi \eta_0) + \left[\frac{1}{2} + \sin(\pi \eta_0) + \sin^2(\pi \eta_0) \right] e_2$$

Based on Hamilton's principle (2.6) with consideration of expressions (2.7)₁, (2.7)₃ and (2.9), two differential equations of motion are obtained in the following form

$$b h \rho_b \frac{\partial^2 v}{\partial t^2} + \frac{1}{2} E_1 b h^3 \left(C_{vv} \frac{\partial^4 v}{\partial x^4} - C_{v\psi} \frac{\partial^3 \psi}{\partial x^3} \right) + F_0 \frac{\partial^2 v}{\partial x^2} = q \quad (2.10)$$

$$C_{v\psi} \frac{\partial^3 v}{\partial x^3} - C_{\psi\psi} \frac{\partial^2 \psi}{\partial x^2} + C_{\psi 0} \frac{\psi(x, t)}{h^2} = 0$$

The bending moment

$$M_b(x) = b \int_{-h/2}^{h/2} y \sigma_x(x, y) dy \quad (2.11)$$

Substituting expression (2.5) for the normal stress, after integration along depth of the beam, one obtains the following equation

$$C_{vv} \frac{d^2 v}{dx^2} - C_{v\psi} \frac{d\psi}{dx} = -2 \frac{M_b(x)}{E_1 b h^3} \quad (2.12)$$

It may be noticed that for static problems this equation is equivalent to equation (2.10)₁.

The position of the neutral axis is determined on the basis of the following condition – total axial force at the cross section

$$\int_{-h/2}^{h/2} \sigma_x(x, y) dy = 0 \quad (2.13)$$

Substituting expression (2.5) for the normal stress, after integration along depth of the beam, one obtains the following equation

$$C_{Nv} \frac{d^2 v}{dx^2} - C_{N\psi} \frac{d\psi}{dx} = 0 \quad (2.14)$$

where

$$C_{Nv} = (1 + e_2) \eta_0 - \frac{2}{\pi^2} (1 - e_2) \quad C_{N\psi} = \frac{1}{2} (1 - e_2) - (1 + e_2) \sin(\pi \eta_0)$$

Based on this condition, the position of the neutral axis $\eta_0 = y_0/h$ is obtained (Fig. 2).

3. Analytical solution of two differential equations of motion of the beam

The system of two differential equations (2.10) for the beam is approximately solved with the use of two assumed functions

$$v(x, t) = v_a(t) \sin\left(\pi \frac{x}{L}\right) \quad \psi(x, t) = \psi_a(t) \cos\left(\pi \frac{x}{L}\right) \quad (3.1)$$

where: $v_a(t)$, $\psi_a(t)$ are functions of time t , which in the case of static problems become parameters. These functions satisfy the conditions of a simply supported beam.

Substitution of functions (3.1) into equations (2.10) gives the following equations

$$\begin{aligned} \left\{ b h \rho_b \frac{d^2 v_a}{dt^2} + \frac{1}{2} \left(\frac{\pi}{L}\right)^4 E_1 b h^3 \left[C_{vv} v_a(t) - \frac{L}{\pi} C_{v\psi} \psi_a(t) \right] - \left(\frac{\pi}{L}\right)^2 F_0 v_a(t) \right\} \sin\left(\pi \frac{x}{L}\right) &= q \\ \left(\frac{\pi}{L}\right)^3 C_{v\psi} v_a(t) - \left(\frac{\pi}{L}\right)^2 \left[C_{\psi\psi} + \left(\frac{\lambda}{\pi}\right)^2 C_{\psi 0} \right] \psi_a(t) &= 0 \end{aligned} \quad (3.2)$$

where $\lambda = L/h$ is relative length of the beam.

From equation (3.2)₂, the function of time related to the shear effect is

$$\psi_a(t) = \frac{\pi}{L} k_{se} v_a(t) \quad (3.3)$$

where the dimensionless coefficient of the shear effect is

$$k_{se} = \frac{C_{v\psi}}{C_{\psi\psi} + \left(\frac{\lambda}{\pi}\right)^2 C_{\psi 0}} \quad (3.4)$$

It may be noticed that the value of this coefficient decreases with increasing relative length of the beam.

Equation (3.2)₁ with consideration of expression (3.3) is in the following form

$$\left[bh\rho_b \frac{d^2 v_a}{dt^2} + \frac{1}{2} \left(\frac{\pi}{L} \right)^4 E_1 bh^3 (C_{vv} - k_{se} C_{v\psi}) v_a(t) - \left(\frac{\pi}{L} \right)^2 F_0 v_a(t) \right] \sin\left(\pi \frac{x}{L}\right) = q \quad (3.5)$$

and after application of Galerkin's method is as follows

$$bh\rho_b \frac{d^2 v_a}{dt^2} + \frac{1}{2} \left(\frac{\pi}{L} \right)^4 E_1 bh^3 (C_{vv} - k_{se} C_{v\psi}) v_a(t) - \left(\frac{\pi}{L} \right)^2 F_0 v_a(t) = \frac{4}{\pi} q \quad (3.6)$$

This equation is the base for detailed studies of the bending, buckling and free vibration of the simply supported beam with unsymmetrically varying mechanical properties.

Condition (2.14) for calculation of the position of the neutral axis of the beam (Fig. 2) with consideration of functions (3.1) and (3.2)₁ and expression (3.3) takes form of a transcendental equation

$$\eta_0 - k_{se} \sin(\pi\eta_0) - \left(\frac{2}{\pi^2} - \frac{1}{2} k_{se} \right) \frac{1 - e_2}{1 + e_2} = 0 \quad (3.7)$$

It may be noticed that for large relative length of the beam ($\lambda \rightarrow \infty$, $k_{se} = 0$), the position of the neutral axis is determined as

$$\eta_0^{(lim)} = \eta_0^{k_{se}=0} = \frac{2}{\pi^2} \frac{1 - e_2}{1 + e_2} \quad (3.8)$$

Example. The following data of the beam are assumed: Poisson's ratios: $\nu_1 = \nu_2 = 0.33$, $e_2 = 0.010, 0.025, 0.050$, and relative length $\lambda = 4, 6, \dots, 14, \infty$. The dimensionless values η_0 (3.7) and $\eta_0^{(lim)}$ (3.8) of the position of the neutral axis of the beam are specified in Table 1.

Table 1. The dimensionless values η_0 of the position of the neutral axis

e_2	λ						
	4	6	8	10	12	14	∞
0.010	0.2019	0.2001	0.1995	0.1992	0.1990	0.1989	0.1986
0.025	0.1962	0.1943	0.1936	0.1933	0.1931	0.1930	0.1928
0.050	0.1870	0.1850	0.1843	0.1839	0.1838	0.1836	0.1833

The graph of the dimensionless values η_0 and $\eta_0^{(lim)}$ of the position of the neutral axis of the beam is shown in Fig. 4.

For the homogeneous beam ($e_2 = 1$), the neutral axis is located in the middle depth of the beam ($\eta_0 = 0$).

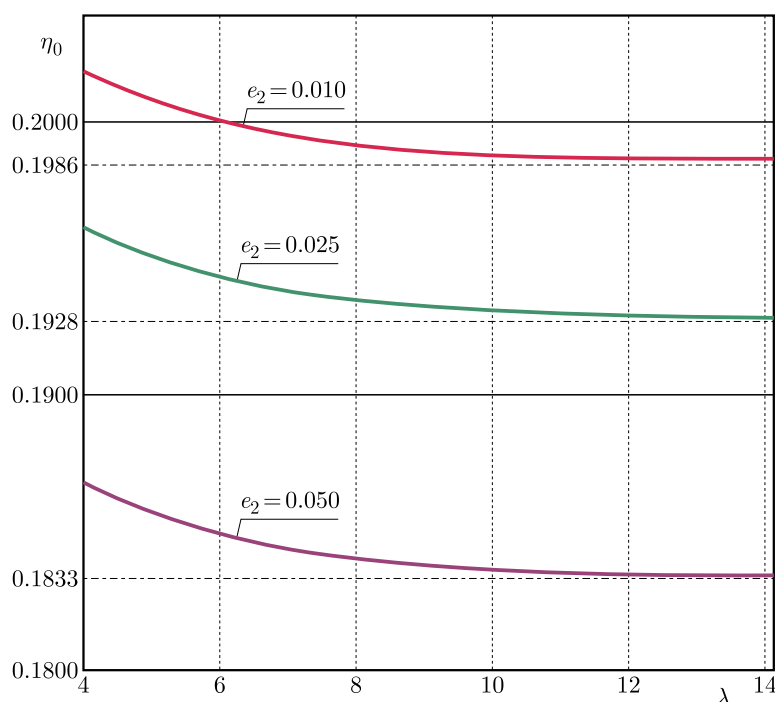


Fig. 4. The graph of dimensionless values η_0 for the position of the neutral axis of the beam

4. Bending of the beam, static problem – analytical solution

The simply supported beam with unsymmetrically varying mechanical properties is subjected to a uniformly distributed transverse load of intensity q (Fig. 3). On the basis of equation (3.6) for the static problem ($d^2v_a/dt^2 = 0$) and $F_0 = 0$, the relative maximum deflection is obtained

$$\tilde{v}_{max} = \frac{v_{max}}{L} = k_{vmax} \frac{q\lambda^3}{E_1 b} \quad (4.1)$$

where the dimensionless coefficient of the maximal deflection is

$$k_{vmax} = \frac{8}{\pi^5(C_{vv} + k_{se}C_{v\psi})} \quad (4.2)$$

In the case of large relative length of the beam ($\lambda \rightarrow \infty$, $k_{se} = 0$), this coefficient of the maximum deflection is

$$k_{vmax}^{(lim)} = \frac{8}{\pi^5 C_{vv}} \quad (4.3)$$

Example. The following data of the beam are assumed: Poisson's ratios: $\nu_1 = \nu_2 = 0.33$, $e_2 = 0.010, 0.050, \dots, 0.50, 1.0$, and relative length $\lambda = 5, 10, 15, 20, \infty$. The values of the dimensionless coefficient of the maximum deflection k_{vmax} and $k_{vmax}^{(lim)}$ are specified in Table 2.

The graph of the values of the dimensionless coefficient of the maximum deflection k_{vmax} and $k_{vmax}^{(lim)}$ is shown in Fig. 5.

For the homogeneous beam ($e_2 = 1$) of large relative length, the dimensionless coefficient of the maximum deflection $k_{vmax}^{(lim)} = 48/\pi^5$.

Table 2. The dimensionless coefficient $k_{v\max}$ of the maximum deflection

e_2	λ				
	5	10	15	20	∞
0.01	0.6215	0.5978	0.5934	0.5919	0.5899
0.05	0.5314	0.5084	0.5042	0.5027	0.5008
0.10	0.4550	0.4329	0.4288	0.4274	0.4256
0.25	0.3312	0.3116	0.3080	0.3067	0.3051
0.50	0.2431	0.2267	0.2237	0.2226	0.2213
1.0	0.1733	0.1610	0.1587	0.1579	0.1569

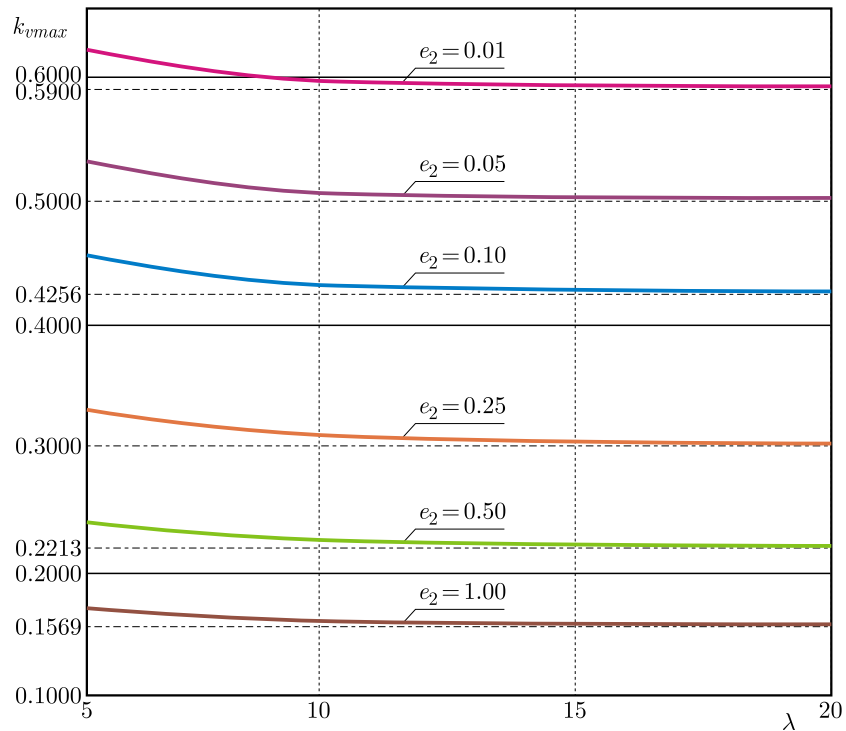


Fig. 5. The graph of the values of the dimensionless coefficient of the maximum deflection

5. Buckling of the beam, static problem – analytical solution

The simply supported beam with unsymmetrically varying mechanical properties is subjected to axial compression with the force F_0 (Fig. 3). On the basis of equation (3.6) for static problem ($d^2v_a/dt^2 = 0$) and $q = 0$, the critical force is obtained

$$F_{0,CR} = \left(\frac{\pi}{\lambda}\right)^2 k_{FCR} E_1 b h \quad (5.1)$$

where the dimensionless coefficient of the critical force is

$$k_{FCR} = \frac{1}{2}(C_{vv} - k_{se} C_{v\psi}) \quad (5.2)$$

In the case of large relative length of the beam ($\lambda \rightarrow \infty$, $k_{se} = 0$), this coefficient of the critical force is

$$k_{FCR}^{(lim)} = \frac{1}{2} C_{vv} \quad (5.3)$$

Example. The following data of the beam are assumed: Poisson's ratios: $\nu_1 = \nu_2 = 0.33$, $e_2 = 0.010, 0.050, \dots, 0.50, 1.0$, and relative length $\lambda = 25, 30, 35, 40, \infty$. The values of the dimensionless coefficient of the critical force k_{FCR} and $k_{FCR}^{(lim)}$ are specified in Table 3. The λ values in the buckling problem are larger than those for bending, since the critical loads for short beams would be very high and, therefore, elastic-plastic buckling would arise.

Table 3. The values of the dimensionless coefficient k_{FCR} and $k_{FCR}^{(lim)}$ of the critical force

e_2	λ				
	25	30	35	40	∞
0.01	0.022112	0.022126	0.022135	0.022141	0.022159
0.05	0.026038	0.026058	0.026070	0.026077	0.026102
0.10	0.030629	0.030655	0.030671	0.030681	0.030714
0.25	0.042698	0.042742	0.042769	0.042787	0.042844
0.50	0.058845	0.058916	0.058959	0.058987	0.059078
1.0	0.082985	0.083091	0.083155	0.083197	0.083333

The graph of the values of the dimensionless coefficient of the critical force k_{FCR} and $k_{FCR}^{(lim)}$ is shown in Fig. 6.

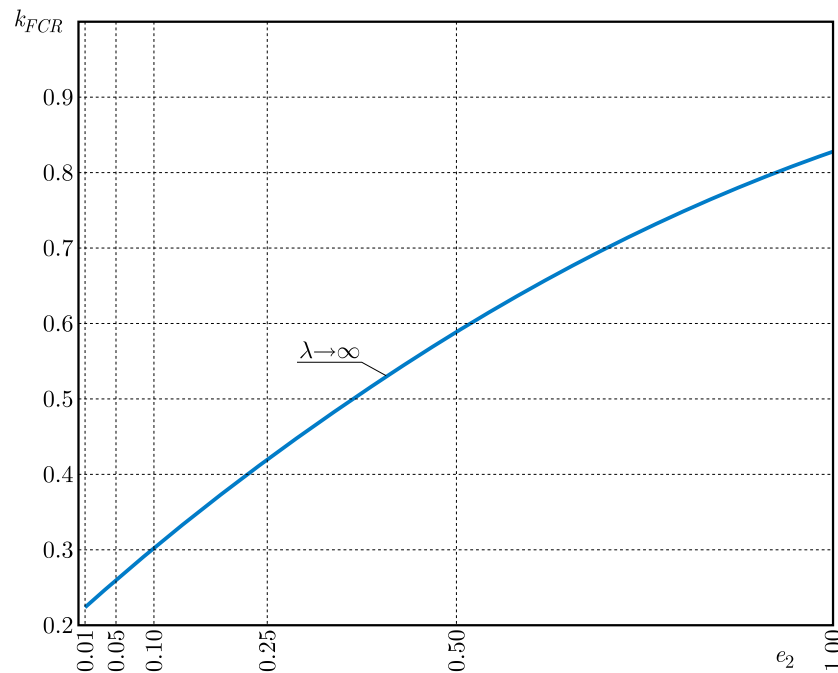


Fig. 6. The graph of the values of the dimensionless coefficient of the critical force

For the homogeneous beam ($e_2 = 1$) of large relative length, the dimensionless coefficient of the critical force $k_{FCR}^{(lim)} = 1/12$.

6. Free vibration of the beam, dynamic problem – analytical solution

The simply supported beam with unsymmetrically varying mechanical properties is not loaded ($q = 0$, $F_0 = 0$) (Fig. 3). Equation (3.6) for the dynamic problem is as follows

$$\rho_b \frac{d^2 v_a}{dt^2} + \frac{1}{2} \left(\frac{\pi}{L} \right)^4 E_1 h^2 (C_{vv} - k_{se} C_{v\psi}) v_a(t) = 0 \quad (6.1)$$

The equation is solved with the use of the assumed function

$$v_a(t) = v_a \sin(\omega t) \quad (6.2)$$

where: v_a is the amplitude of flexural vibration, ω – fundamental natural frequency.

Substituting this function into equation (6.1), after simple transformation, one obtains the fundamental natural frequency

$$\omega = \left(\frac{\pi}{\lambda}\right)^2 k_\omega \sqrt{\frac{E_1}{\rho_b h^2}} \quad (6.3)$$

where the dimensionless coefficient of the fundamental natural frequency is

$$k_\omega = \sqrt{\frac{1}{2}(C_{vv} - k_{se} C_{v\psi})} = \sqrt{k_{FCR}} \quad (6.4)$$

Taking into account expression (5.3), one formulates $k_\omega^{(lim)} = \sqrt{k_{FCR}^{(lim)}}$.

Example. The following data of the beam are assumed: Poisson's ratios: $\nu_1 = \nu_2 = 0.33$, $e_2 = 0.010, 0.050, \dots, 0.80, 1.0$, and relative length $\lambda = 5, 10, 15, 25, \infty$. The values of the dimensionless coefficient of the fundamental natural frequency k_ω and $k_\omega^{(lim)}$ are specified in Table 4.

Table 4. The values of the dimensionless coefficient k_ω and $k_\omega^{(lim)}$ of the natural frequency

e_2	λ				
	5	10	15	25	∞
0.01	0.14502	0.14787	0.14842	0.14870	0.14886
0.05	0.15683	0.16034	0.16101	0.16136	0.16156
0.10	0.16949	0.17376	0.17458	0.17501	0.17526
0.25	0.19866	0.20481	0.20601	0.20663	0.20699
0.50	0.23187	0.24011	0.24173	0.24258	0.24306
0.80	0.25984	0.26954	0.27146	0.27246	0.27303
1.0	0.27465	0.28497	0.28701	0.28807	0.28868

The graph of the values of the dimensionless coefficient of the fundamental natural frequency k_ω and $k_\omega^{(lim)}$ is shown in Fig. 7.

In the case of the homogeneous beam ($e_2 = 1$) of large relative length, the dimensionless coefficient of the critical force $k_{FCR}^{(lim)} = \sqrt{3}/6$.

7. Numerical calculations – FEM study

7.1. Numerical FEM model

The numerical analysis of the beam with unsymmetrically varying mechanical properties is carried out with the help of the SolidWorks software. The simulation assumed the same geometry parameters and mechanical properties as those used in the analytical calculations.

The beam is modelled using 3D finite elements in 20 layers, each with different mechanical properties satisfying expressions (1.1). Taking into account symmetry of the structure, a half of the beam is considered (Fig. 8).

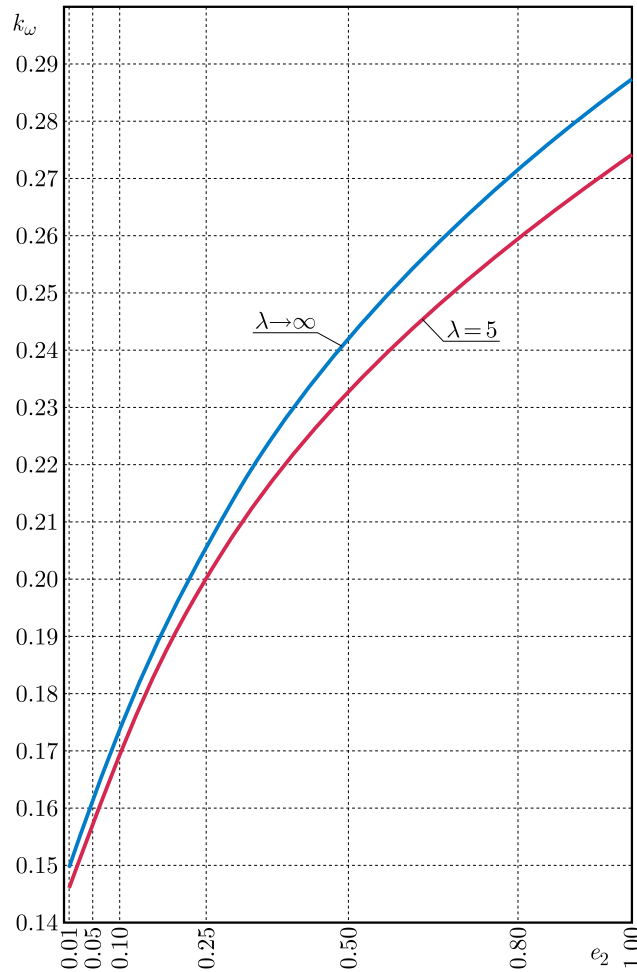


Fig. 7. The graph of the values of the dimensionless coefficient of the fundamental natural frequency

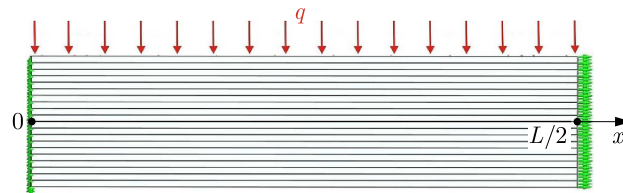


Fig. 8. Boundary conditions and load for the bending problem in the FEM study

Therefore, the following boundary conditions are adopted:

- for $x = 0$ – the simple support – $v(0)$ displacements in the y direction are zero;
- for $x = L/2$ – the middle of the beam – $u(L/2)$ displacements in the x direction are zero.

The numerical study of bending, buckling and free vibration is restrained to the xy -plane, similarly as in the case of the analytical approach.

SolidWorks calculations have been carried out for beams with a rectangular cross-section of depth $h = 80$ mm, width $b = 20$ mm, and length values $L = \lambda h$ ($400 \text{ mm} \leq L \leq 3200 \text{ mm}$).

7.2. Bending of the beam, static problem – numerical FEM solution

The beam is subjected to a uniformly distributed load of intensity q . A view to the bent half-beam is shown in Fig. 9.

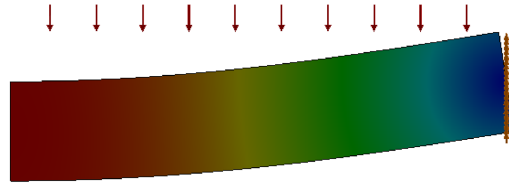


Fig. 9. Deflection of the beam (SolidWorks simulation)

Results of the study are maximum deflections v_{max} [mm]. Based on expressions (4.1) and (4.2), values of the dimensionless coefficient k_{vmax} are calculated. These values are specified in Table 5.

Table 5. The values of the dimensionless coefficient k_{vmax} of the maximum deflection (FEM study)

e_2	λ			
	5	10	15	20
0.01	0.6136	0.5950	0.5886	0.5875
0.05	0.5248	0.5050	0.5007	0.5000
0.10	0.4496	0.4295	0.4257	0.4250
0.25	0.3272	0.3090	0.3062	0.3050
0.50	0.2400	0.2250	0.2222	0.2216
1.0	0.1696	0.1595	0.1580	0.1569

Values of the relative difference between analytical and FEM solutions are below 2.2%. The highest difference occurs for small relative length values λ . For greater λ values, the difference decreases.

7.3. Buckling of the beam, static problem – numerical FEM solution

The half-beam under compression is shown in Fig. 10. Cross-sections and variation of mechanical properties of the beam are the same as in the case of bending. Therefore, the buckling is analysed only in the xy -plane, similarly as for bending and free vibration. In order to avoid lateral buckling the z -displacements in the whole xy -plane are zeroed.

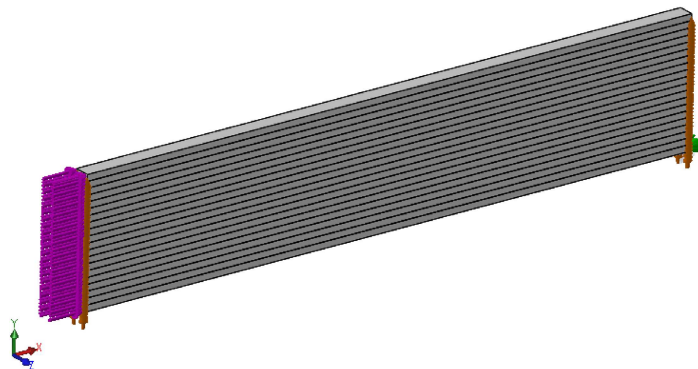


Fig. 10. Boundary conditions and load for the buckling problem in the FEM study

Buckling shape of the beam resulting from the numerical study is shown in Fig. 11.

Results of the study are critical force values $F_{0,CR}$ [N]. Based on expressions (5.1) and (5.2), values of the dimensionless coefficient k_{FCR} are calculated. These values are specified in Table 6.

Values of the relative difference between analytical and FEM solutions are below 4.6%.

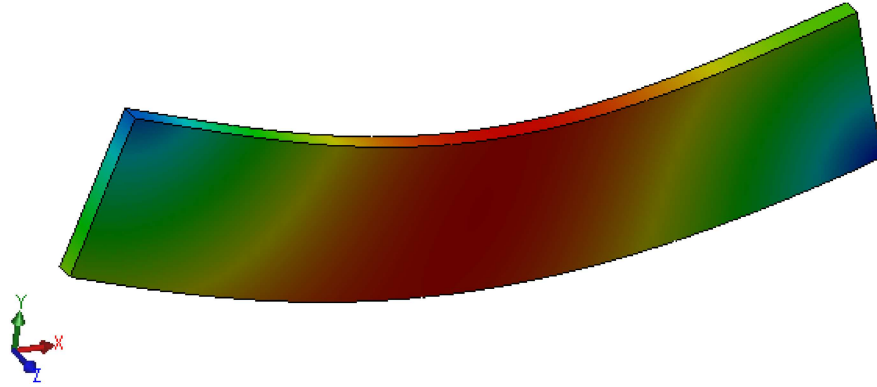


Fig. 11. Buckling shape of the beam (SolidWorks simulation)

Table 6. The values of the dimensionless coefficient k_{FCR} of the critical force (FEM study)

e_2	λ			
	25	30	35	40
0.01	0.0211	0.0213	0.0215	0.0216
0.05	0.0252	0.0255	0.0256	0.0258
0.10	0.0300	0.0302	0.0304	0.0306
0.25	0.0424	0.0429	0.0431	0.0435
0.50	0.0591	0.0598	0.0602	0.0607
1.0	0.0806	0.0811	0.0815	0.0817

7.4. Free vibration of the beam, dynamic problem – numerical FEM solution

Free vibrations are computed with the SolidWorks software for the FEM model composed of 10 layers of varying mechanical properties. A half-beam is adopted with the boundary conditions shown in Fig. 12.

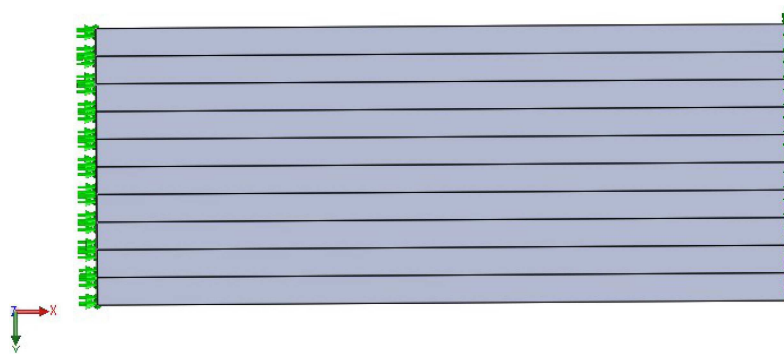


Fig. 12. Half-beam model used in the free-vibration calculation

The middle of the beam is placed in the left-hand side of the illustration. Hence, the x and z displacements are zeroed there. The right-hand part of the beam is simply supported and, therefore, the displacement y is blocked.

The SolidWorks simulation tool used to compute the free-vibration frequencies provides angular frequencies ω of particular vibration modes. Nevertheless, in order to compare the analytical and numerical results, the dimensionless coefficient of the natural frequencies should be calculated for each case specified in Table 4. Taking into account expressions (2.8) and (6.3), one obtains

$$k_\omega = \omega h \left(\frac{\lambda}{\pi} \right)^2 \sqrt{\frac{\rho_1(1 + \sqrt{e_2})}{2E_1}} \quad (7.1)$$

In the case of the example presented in Fig. 13, the following data are assumed: $e_2 = 0.01$, $b = 20$ mm, $h = 80$ mm, $L = 400$ mm. Such a data set corresponds to the upper row and left-hand column of Table 4. The angular frequency in this case is equal to $\omega = 5093$ rad/s, which gives $k_\omega = 0.14240$.

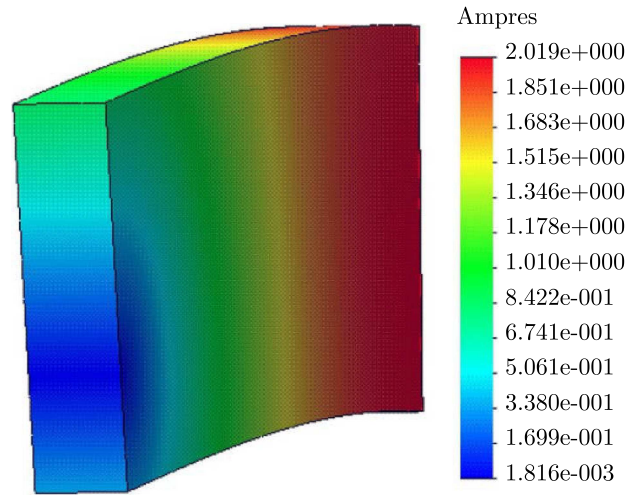


Fig. 13. An example result for $e_2 = 0.01$ and $\lambda = 5$

The results k_ω of all the considered cases are presented in Table 7.

Table 7. Values of the dimensionless coefficient k_ω of the natural frequency computed numerically

e_2	λ			
	5	10	15	25
0.01	0.14240	0.14609	0.14680	0.14714
0.05	0.15530	0.15987	0.16075	0.16119
0.10	0.16775	0.17326	0.17434	0.17489
0.25	0.19658	0.20426	0.20578	0.20655
0.50	0.22962	0.23955	0.24153	0.24254
0.80	0.25743	0.26893	0.27125	0.27243
1.0	0.27214	0.28435	0.28681	0.28805

They perfectly comply with the results of Table 4 obtained analytically. The relative difference values between analytical and FEM solutions are below 2%. The highest difference, equal to 1.8%, occurs for the example case mentioned above, whereas for the others they are significantly smaller.

8. Conclusions

The neutral axis of the studied beam deviates from the geometric centre of the rectangular cross section as a result of unsymmetrical properties of the material. The location of the neutral axis is affected by the shear effect (Fig. 4). This effect is meaningful in the case of short beams and disappears for longer ones. The values of deflection, critical load and free-vibration frequencies depend on the position of the neutral axis. Therefore, in the case of the analytical approach, the

position of the axis should be determined first of all. The values of deflection, critical load and free-vibration frequencies obtained analytically have been compared to those computed with the SolidWorks software. It may be noticed that the difference between both sets of the results does not exceed 5%.

References

1. BIRMAN V., BYRD L.W., 2007, Modeling and analysis of functionally graded materials and structures, *Applied Mechanics Reviews*, **60**, 195-216
2. CHEN D., KITIPORNCHAI S., YANG J., 2016a, Nonlinear free vibration of shear deformable sandwich beam with a functionally graded porous core, *Thin-Walled Structures*, **107**, 39-48
3. CHEN D., YANG J., KITIPORNCHAI S., 2015, Elastic buckling, and static bending of shear deformable functionally graded porous beam, *Composite Structures*, **133**, 54-61
4. CHEN D., YANG J., KITIPORNCHAI S., 2016b, Free and forced vibrations of shear deformable functionally graded porous beams, *International Journal of Mechanical Sciences*, **108-109**, 14-22
5. DEBOWSKI D., MAGNUCKI K., MALINOWSKI M., 2010, Dynamic stability of a metal foam rectangular plate, *Steel and Composite Structures*, **10**, 2, 151-168
6. FEYZI M.R., KHORSHIDVAND A.D., 2017, Axisymmetric post-buckling behaviour of saturated porous circular plates, *Thin-Walled Structures*, **112**, 149-158
7. JUN L., XIANG H., XIAOBIN L., 2016, Free vibration analyses of axially loaded laminated composite beams using a unified higher-order shear deformation theory and dynamic stiffness method, *Composite Structures*, **158**, 308-322
8. KAPURIA S., BHATTACHARYYA M., KUMAR A.N., 2008, Bending and free vibration response of layered functionally graded beams: A theoretical model and its experimental validation, *Composite Structures*, **82**, 390-402
9. KOLAKOWSKI Z., MANIA R.J., 2015, Dynamic response of thin FG plates with a static unsymmetrical stable postbuckling path, *Thin-Walled Structures*, **86**, 10-17
10. KUBIAK T., 2005, Dynamic buckling of thin-walled composite plates with varying width-wise material properties, *International Journal of Solids and Structures*, **45**, 5555-5567
11. KUBIAK T., 2011, Estimation of dynamic buckling for composite columns with open cross-sections, *Computers and Structures*, **89**, 21-22, 2001-2009
12. LI L., HU Y., Nonlinear bending and free vibration analyses of nonlocal strain gradient beams made of functionally graded material, *International Journal of Mechanical Sciences*, **107**, 77-97
13. MAGNUCKA-BLANDZI E., 2011, Dynamic stability and static stress state of a sandwich beam with a metal foam core using three modified Timoshenko hypothesis, *Mechanics of Advanced Materials and Structures*, **18**, 2, 147-158
14. MAHI A., BEDIA E.A.A., TOUNSI A., 2015, A new hyperbolic deformation theory for bending and free vibration analysis of isotropic, functionally graded, sandwich and laminated composite plates, *Applied Mathematical Modelling*, **39**, 2489-2508
15. MOJAHEDIN A., JABBARI M., KHORSHIDVAND A., ESLAMI M., 2016, Buckling analysis of functionally graded circular plates made of saturated porous material based on higher order shear deformation theory, *Thin-Walled Structures*, **99**, 83-90
16. SAYYAD A.S., GHUGAL Y.M., 2017, Bending, buckling and free vibration of laminated composite and sandwich beams: A critical review of literature, *Composite Structures*, **171**, 486-504
17. SONG M., KITIPORNCHAI S., YANG J., 2017, Free and forced vibrations of functionally graded polymer composite plates reinforced with graphene nanoplatelets, *Composite Structures*, **159**, 579-588

18. SMYCZYNSKI M.J., MAGNUCKA-BLANDZI E., 2018, Three-point bending of a sandwich beam with two binding layers – Comparison of two nonlinear hypotheses, *Composite Structures*, **183**, 96-102
19. THAI H.-T., VO T.P., 2012, Bending and free vibration of functionally graded beams using various higher-order shear deformation beam theories, *International Journal of Mechanical Sciences*, **62**, 57-66
20. THAI H.-T., VO T.P., 2013, A new sinusoidal shear deformation theory for bending, buckling, and vibration of functionally graded plates, *Applied Mathematical Modelling*, **37**, 3269-3281
21. ZENKOUR A.M., 2006, Generalized shear deformation theory for bending analysis of functionally graded plates, *Applied Mathematical Modelling*, **30**, 67-84
22. ZHANG Y., WANG S., LOUGHLAN J., 2006, Free vibration analysis of rectangular composite laminates using a layerwise cubic B-spline finite strip method, *Thin-Walled Structures*, **44**, 601-622

Manuscript received September 21, 2017; accepted for print June 7, 2018

COMPUTATIONAL OPTIMIZATION AND IMPLEMENTATION OF CONTROL SYSTEM FOR MECHATRONIC TREADMILL WITH BODY WEIGHT SUPPORT SYSTEM

GRZEGORZ GEMBALCZYK, SŁAWOMIR DUDA, EUGENIUSZ ŚWITOŃSKI

Silesian University of Technology, Department of Theoretical and Applied Mechanics, Gliwice, Poland

e-mail: grzegorz.gembalczyk@polsl.pl; slawomir.duda@polsl.pl; eugeniusz.switonski@polsl.pl

The purpose of this paper is to present a novel mechatronic system for gait re-education which consists of a body weight support system (BWS system) and a treadmill. This publication covers mainly issues related to the design and optimization process of a control algorithm dedicated for the unloading system. The proposed control system is based on a fuzzy logic controller coupled with a PID regulator. The optimization of parameters for regulators has been conducted based on numerical simulations in which a hybrid optimization method combining a genetic algorithm with a gradient algorithm has been used. The developed control system has been tested experimentally.

Keywords: gait reeducation, control system, optimization, fuzzy logic

1. Introduction

Half of all deaths are caused by cardiovascular diseases in the modern world. It is estimated that the number of deaths due to stroke can reach 7.69 mln people to 2030, and it will constitute one of more important medical problems. Strokes constitute the main reason for permanent disability in the adult population, particularly after turning 60. They are one of the main reasons for remaining in the condition of disability for a longer period of time. The restoration of possibility to move or keep balance in the upright position is significant for patient's proper functioning. The deficit connected with the lack of ability to walk pertains to almost 70% of patients who have experienced a stroke. Kinesiotherapy is the most common and obvious way of treatment after a stroke that should be started as soon as possible. The simplest form of exercises is walking in company of a physiotherapist using simple devices for support such as walkers or banisters. Mechatronic devices which support the process of kinesiotherapy after a stroke are in some sense "packed with the latest technological solutions". They affect training efficiency and, especially, improve the speed of walking, endurance and balance. Such devices support physiotherapists relieving them from hard physical work of supporting a patient and allowing them to concentrate on the essence of the exercises carried out to a greater degree (Koceska and Koceski, 2013; Kot and Nawrocka, 2012). These devices both implement the rehabilitation process and verify the progress of treatment. When analyzing rehabilitation devices for kinesiotherapy within a dozen years, it is possible to notice that unloading a patient is the most significant element subject to continuous modifications. It is possible to find in the market devices with a simple design that make it possible to unload a patient in a passive way as well as technologically advanced solutions with active body weight support systems. In the case of passive systems (unloading force regulated by a crank, counterweight, spring, etc.), the difference between the unloading force that is set and the one that is measured during exercises is much bigger (Frey *et al.*, 2006). Therefore, the exercises with devices equipped in body weight support systems with active control of the unloading force are more beneficial for patients. When comparing rehabilitation

devices equipped with active body weight support systems with one another, it is possible to notice that the unloading mechanism is an element connected with a still supporting structure (it does not keep up with a patient's movement) in most cases; and the patient's walk forces the manipulator (mechanic orthosis) or treadmill movement (Chen *et al.*, 2013; Pajor and Herbin, 2015). In the second case, training is recommended for people who have regained the ability to walk in a degree that makes it possible to move independently, but they still require support and improvement of the technique, speed and stamina (Mehrholtz *et al.*, 2014; Cao *et al.*, 2014; Querry *et al.*, 2008). The technologies of biofeedback and virtual reality are also used in the devices of this type (Koenig *et al.*, 2011; Lünenburger *et al.*, 2007, Jurkojć *et al.*, 2017).

A device in which the movement of a training person is limited only by the space of a supporting frame, on which a BWS system moves, has been created as a result of research at the Institute of Theoretical and Applied Mechanics financed by the National Centre for Research and Development (Duda *et al.*, 2016). The possibility of free side movements of a patient's pelvis plays a significant role in rehabilitation exercises that restore the proper pattern of walking, as research shows (Dragunas and Gordon, 2016; Mignardot *et al.*, 2017).

A new form of a mechatronic device for the re-education of walking has been currently developed.

It is a combination of a movable body weight support system with a treadmill. The thing that differentiates the proposed solution from those existing on the market results from coupling the movement of an exercising person with the movement of a treadmill tape. It is not the treadmill movement that forces patient's movement. It is the patient that forces treadmill movement. It is implemented by using a sensor measuring the inclination angle of a sling rope. Moreover, the device allows free side movements that are so important for proper rehabilitation. It is achieved thanks to drive in a direction that is transverse to the direction of walking. The invented mechatronic system for gait re-education includes four drives:

- two independently working drives of the body weight support system,
- the drive of a winch trolley making it possible for training a person to move in the direction that is perpendicular to the plane of the patient's movement,
- the drive of the treadmill tape.

This publication involves an attempt at developing and optimizing a control system of the body weight support system with a fuzzy logic controller. No such solutions have been found in literature. Systems used for unloading a patient with an automatically regulated force are usually described in a very general way. Most of all, there are no descriptions of systems steering winches equipped with two drives cooperating with each other. The minimization of mass and size constitutes an important construction condition in the case of unloading systems with mobile BWS systems that have been suspended to the ceiling in the current solutions (Hidler *et al.*, 2011; Duda *et al.*, 2016). However, it is connected with the limitation of a linear drive movement range. The right synchronization of the work of a winding drum with a linear actuator is necessary if one wants to make it possible for patients to do exercises with significant movements. Due to limited movement of such a linear actuator, the development of an optimal steering system constitutes an interesting engineering problem. This is why the problem of optimization of a system controlling the BWS system has been tackled in this article.

The most detailed description of a similar system was presented by Frey *et al.* (2006) describing the Lokolift device. A winding drum cooperates with a rope (passive) drive in that solution. In order to steer this winding drum, switches have been used which are activated at the moment when the movement of the linear actuator (instantaneous or mean) goes beyond the admissible range. Thus, the engine that propels the rope drum works only with the nominal speed or it does not work at all.

The Lokolift system is meant mainly for the cooperation with a patient training on the treadmill, and its whole construction is placed on the floor. Therefore, this device does not have

to meet restrictive criteria connected with the minimization of mass and dimensions, so the range of the linear actuator is not limited by any restrictive conditions. Taking into account the way devices for the re-education of walking develop and the beneficial influence of mobile body weight support systems on the stability of a patient's walk when training in reduced weight conditions, it is possible to expect further development of similar devices (Reinkensmeyer and Dietz, 2016; Riener *et al.*, 2010).

2. Description of the device

The device used for the re-education of walking presented in this paper is a mechatronic system in which the body weight support system, the system of compensating side inclinations and the training treadmill have been integrated (Fig. 1).

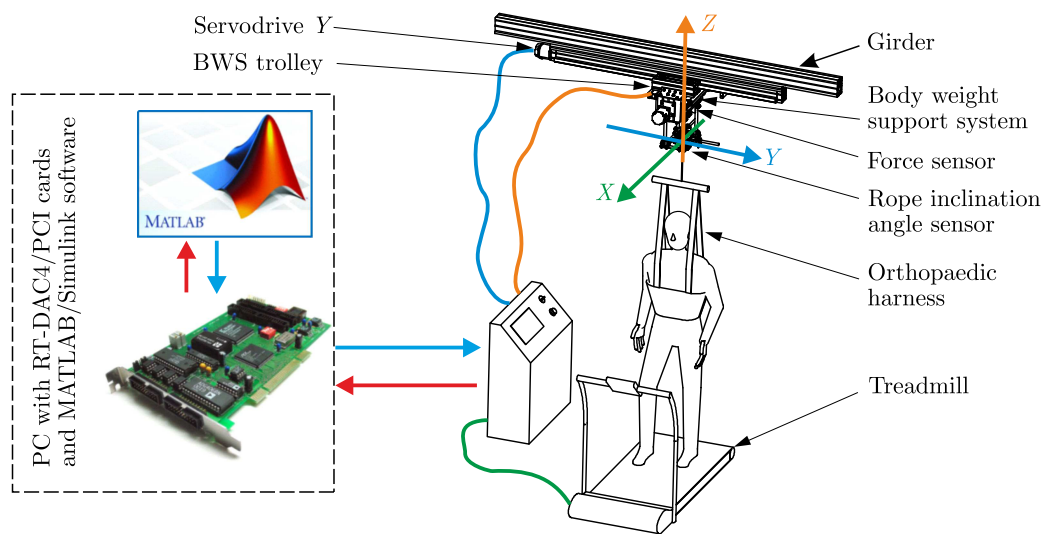


Fig. 1. Mechatronic device for gait re-education

A training person is pinned up in a special orthopaedic harness fastened to the rope of a winching device. The coupling between the mentioned subsystems and the patient is implemented through measurement systems, one measuring the unloading force and the other measuring linear movements resulting from the deflection of the line from the vertical axis (sensors) and particular mechanism drives (actuators). The encoders of servo drives are additional servers that the device is equipped with.

The transmission of measurement and control signals of the device takes place in the real time mode (Miądlicki and Pajor, 2015; Sapiński *et al.*, 2016) with the use of a computer equipped with 2 RT-DAC4/PCI cards and MATLAB/Simulink software. The calculation step of the real time is $T_0 = 0.01$ s. The servo drives of the winching device and compensation of side inclinations work in the speed control mode. Then, the generated steering signals retain the set rotational speed in a precise way.

Steering the treadmill, described in details in (Duda *et al.*, 2017), takes place by a modified original control panel. It has been achieved by parallel connection of an additional controller whose task involves simulation of the work of buttons placed on the panel that steers the treadmill. The electronic system has been built with the use of optocouplers steered with digital signals generated by the steering system in a PC Computer. The change of a signal from a high status to a low one and back to the high status has been obtained after 0.1 s. It is equivalent to the change of the treadmill speed obtained after pressing the button (faster or slowly) on

the control panel of the treadmill. This is also the reason for a relatively low sensitivity of the steering system to changes of walking parameters.

A tracking system with a PD controller has been implemented for controlling the movement of the BWS system trolley (servodrive Y) along a girder. Descriptions of such a system were presented in (Duda *et al.*, 2016; Raczka *et al.*, 2013). Controlling a BWS system requires the use of a more advanced active control system which is presented in Section 5.

3. Modelling the body weight support system

The processes of optimization of complex steering algorithms in which several or dozen parameters should be specified are usually carried out with offline methods. These methods are basically necessary in the case of tuning steering systems with devices meant for cooperation with people; for rehabilitation in particular. In order to carry out the optimization of a system controlling a BWS system it is necessary to develop a numerical model taking into account the coupling between the electric part, the mechanical one, and the patient. A model of a synchronous motor with permanent PMSM magnets (Permanent Magnet Synchronous Motor) described in (Mężyk *et al.*, 2016; Xu, 2012) has been used for building the numerical model of the device.

The body weight support system that is responsible for unloading the patient with the set force is the most important subsystem of the device presented in the article. In contrast to classic hoist devices, its driving system has been equipped with two independently working engines. The first one that is marked as $Z1$ is responsible for propelling the rope drum; the second one ($Z2$ linear actuator) is connected with the system of dynamic compensation. This system works on the drive basis of a Series Elastic Actuator type (SEA) (Pratt and Williamson, 1995; Robinson *et al.*, 1999). Figure 2 presents a detailed construction of the driving system. The

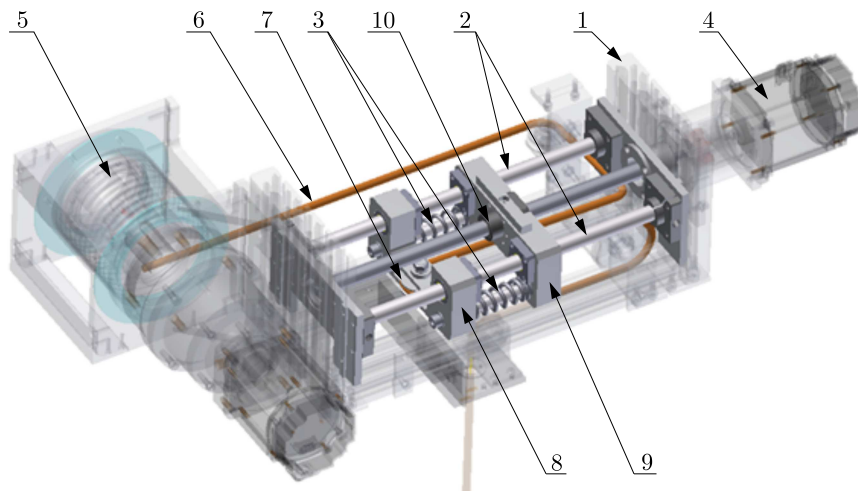


Fig. 2. The structure of the driving system of the body weight support system

construction of the BWS system has been developed on the basis of aluminium profiles creating supporting frame (1) to which the following have been fixed: track guides (2), compression springs (3), driving engine of the $Z2$ axis, winding drum with an engine (5), and a system of pulleys. The construction of the presented system makes it possible to change rope length (6) through a change of the location of the pulley (7). This pulley is fixed to the first steel trolley out of two (8) that move along tracking guides (2) and are separated with springs (3). This diminishes the consequences of impact loads appearing during operation. The movement of the second trolley (9) is implemented with a linear drive with ball screw (10) of a 5mm pitch whose rotation causes movement of a nut that is fastened to this trolley (9). The maximum range of the $Z2$ linear actuator movement is ca. 110 mm.

The developed physical model of the BWS system is shown in Fig. 3a, after including simplifying assumptions.

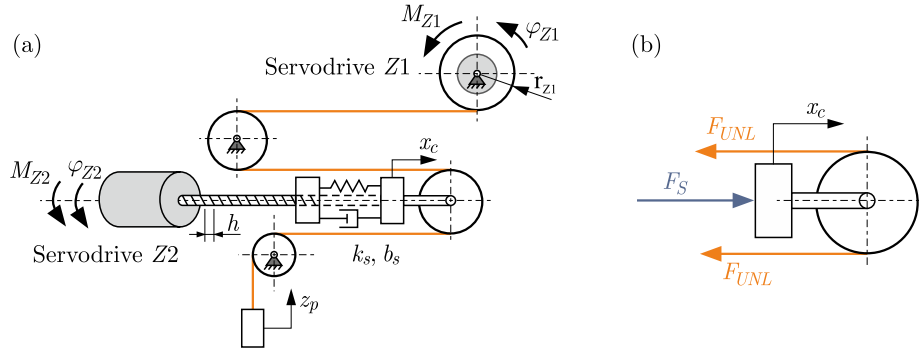


Fig. 3. (a) The physical model of the BWS system. (b) The forces which act on the actuator Z2

Three generalized coordinates connected with the rotation angles of rotators in the engines and the shift of the patient's centre of gravity have been accepted in the mathematical model of the presented system

$$\mathbf{q} = [\varphi_{Z1}, \varphi_{Z2}, z_p] \quad (3.1)$$

If one takes into account the fact that the resistance to movement and the trolley weight whose movement is marked with the x_c coordinate are negligibly small, then one can estimate the value of the unloading force influencing the patient (rope tension force) F_{UNL} , when considering the forces influencing this trolley (Fig. 3b)

$$F_{UNL} \approx \frac{F_s}{2} \quad F_s = k_s \left(\varphi_{Z2} \frac{h}{2\pi} - x_c \right) + b_s \left(\dot{\varphi}_{Z2} \frac{h}{2\pi} - \dot{x}_c \right) \quad (3.2)$$

where

$$x_c = \frac{z_p - \varphi_{Z1} i_{Z1} r_{Z1}}{2} \quad (3.3)$$

In the equation above, i_{Z1} specifies the planetary gear ratio between the rope drum and the Z1 engine. In the mathematical model of the BWS system, the mass of the propelling screw and the trolley propelled by it have been reduced to the moment of inertia of the Z2 engine shaft. The inertia of other pulleys, the winding drum, and the planetary gear has been reduced to the moment of inertia of the Z1 engine shaft. In such a case, the searched equations of motion have the following form

$$\begin{aligned} \ddot{\varphi}_{Z1} &= \frac{1}{I_{Z1}} (M_{Z1} - b_{Z1} \dot{\varphi}_{Z1} - F_{UNL} i_{Z1} r_{Z1}) \\ \ddot{\varphi}_{Z2} &= \frac{1}{I_{Z2}} \left(M_{Z2} - b_{Z2} \dot{\varphi}_{Z2} - 2F_{UNL} \frac{h}{2\pi} \right) \\ \ddot{z}_p &= \frac{1}{m_p} (F_{UNL} - m_p g) \end{aligned} \quad (3.4)$$

The coupling between the electric and mechanical part is implemented in such a way that the driving moment determined from the numerical model of the PMSM motor (M_{Z1} and M_{Z2}) has been implemented in the model of the mechanical part (3.4). The calculated angular acceleration ($\ddot{\varphi}_{Z1}$ and $\ddot{\varphi}_{Z2}$) has been, in turn, used in the engine model for calculating the rotation speed and the rotor rotation angle.

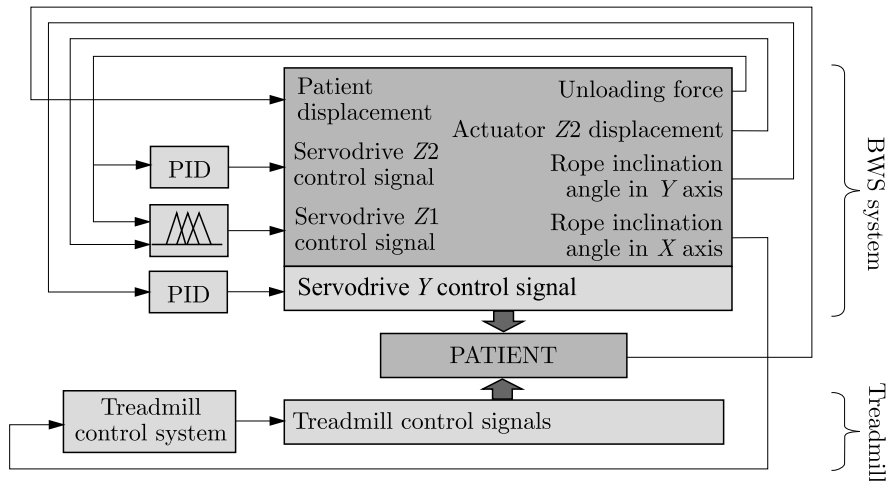


Fig. 4. A functional scheme of a mechatronic treadmill for locomotive training

Figure 4 shows a functional plan of the device in a block form in which the servo drives, the mechanical part (BWS system and treadmill), patient's movement, and the steering system have been included.

Parameters of the mathematical model have been determined on the basis of catalog data, experimental tests on the universal testing machine and in the estimation process. The estimation of parameters in the models of Z1 and Z2 servo drives has been carried out on the basis of catalogue data and experimental data in which the rotational speed of the engine in various strain conditions has been registered. The validation of the model developed for the BWS system (Fig. 3a) has been carried out with the use of a weight of 20 kg hung at the end of the rope. During the experiment, the rotational speed of 1000 (rotations/per minute) has been set on the Z1 engine; and the value of the unloading force has been measured at the same time. Analogical tests have been carried out with the use of the Z2 drive. The correlation coefficient has been calculated with R-Pearson's method (Gniłka and Mężyk, 2015), and it equals 0.87.

4. Modelling the patient's gait

A kinematic input has been used in further numerical research for simulation of the patient's movements. Thus, the third equation has been reduced in the system of equations of the BWS system movement, see Eq. (3.4).

The equations describing patient's movements z_p [m] (used to calculate the force F in accordance with equations (3.2) and (3.3)) have been described with mathematical functions whose formulas have been formulated on the basis of parameter measurements of walking of the disabled person. The results of the research of walk kinematics with participation of people after a stroke with paresis of the right side have been used in the model. The analysis of the walk kinematics has been carried out with the use of APAS software. Taking into account the fact that the BWS system should also guarantee a reliable work during doing other exercises in which vertical movements have a wide range (e.g. squats, climbing stairs), this input has been described by the system of equations

$$z_p = \begin{cases} 0 & \text{for } t < 2 \\ 0.016[\sin(2\pi(t - 2)) - \sin(4\pi(t - 2))] & \text{for } 2 \leq t < 5.166 \\ 0.2(t - 5.166) & \text{for } 5.166 \leq t < 6.166 \\ 0.2 & \text{for } t \geq 6.166 \end{cases} \quad (4.1)$$

5. Optimization of the control system

The results of a preliminary experimental study of the control systems of the presented body weight support system has shown that the use of the $Z2$ drive only is sufficient for ordinary walking on a treadmill (Duda and Gembalczyk, 2016). In the case when a rehabilitated person is supposed to do a different exercise which involves a significant change of the trunk (e.g. squats, standing up from a chair, climbing obstacles), it is necessary to start a winding drum- the $Z1$ drive.

In order to take advantage of the device potential fully and to guarantee a patient the biggest comfort of exercises done possible, one should develop and tune steering systems designated separately for every performed exercise or several main modes of the device operation.

From the point of view of physiotherapists, a simple system with few options is desired. Therefore, a universal steering system that will be able to steer a device independently of the patient's behaviour is an optimal solution for them. An attempt at developing a universal steering system of the BWS system has been made to meet these expectations taking into account economic aspects at the same time (energy efficiency). On the basis of earlier experience, the proposed steering system has been based on a PID controller coordinating with a fuzzy controller (Zhao *et al.*, 2007). The $Z2$ drive is steered in a feedback loop with the sensor of the unloading force, whereas the $Z1$ drive controller additionally uses movement measurement of the $Z2$ drive actuator. This solution is presented in the form of a scheme in Fig. 5.

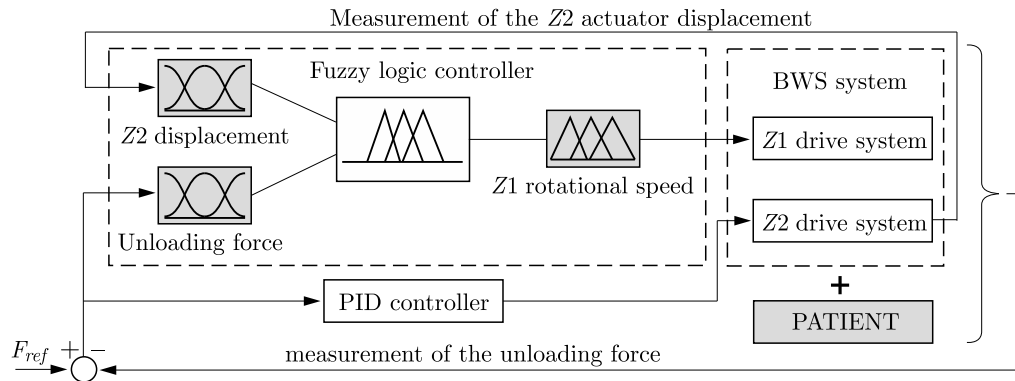


Fig. 5. Block diagram of the proposed control system

The basis of rules of the fuzzy controller has been prepared in such a way so that the $Z1$ drive is started only in the situation when the $Z2$ actuator moves away from the admissible working range or when the deviation of the relieving force is bigger than the accepted admissible deviation. The accepted set of rules is presented in the table. Seven membership functions have been defined for every input and output signal of the fuzzy controller. The symbol of $Z2$ disp means movement of the actuator in the $Z2$ drive, whereas ΔUNL is the value of the unloading force error

$$\Delta UNL(t) = F_{ref} - F_{UNL}(t) \quad (5.1)$$

The signs from “— — —” to “+ + +” represent the value from the lowest to the highest one. The “nom” index means that the variable value is placed within the accepted admissible range, where the operation of $Z1$ is not required. The assumed admissible range for moving the $Z2$ actuator is 10 mm ($Z2D_{nom} = \pm 10$ mm), and the admissible deviation of the unloading force 20 N ($\Delta UNL_{nom} = \pm 20$ N). Moreover, the following ranges of the input signals have been accepted

$$\Delta UNL \in \langle -100; 100 \rangle \text{ [N]} \quad Z2_{disp} \in \langle -50; 50 \rangle \text{ [mm]} \quad (5.2)$$

Table 1. The basis of fuzzy logic controller rules

		Displacement of the Z2 actuator ($Z2_{disp}$)						
		---	--	-	nom	+	++	+++
Unloading force	$\Delta UNL---$	0	0	Z1+	Z1++	Z1+++	Z1+++	Z1+++
	$\Delta UNL--$	0	0	0	Z1+	Z1++	Z1+++	Z1+++
	$\Delta UNL-$	0	0	0	0	Z1+	Z1++	Z1+++
	$\Delta UNLnom$	Z1--	Z1--	Z1-	0	Z+	Z1++	Z1++
	$\Delta UNL+$	Z1---	Z1--	Z1-	0	0	0	0
	$\Delta UNL++$	Z1---	Z1---	Z1--	Z1-	0	0	0
	$\Delta UNL+++$	Z1---	Z1---	Z1---	Z1--	Z1-	0	0

The optimal values of the PID controller settings and the range of the accepted membership functions of input signals in the fuzzy controller have been searched for in the process of optimization. Both controllers have been optimized separately due to the accepted assumptions. The input has been limited only to simulation of walking itself during the selection of the PID controller settings. The simulation time has been limited to $t < 5.166$ in Eq. (4.1). The settings of the PID controller have been the optimized variables, whereas the goal function has been connected with the minimization of the unloading force error

$$FC_{PID} = \int_0^{5.166} |\Delta UNL(t)| dt \rightarrow \min \quad (5.3)$$

The optimization of the fuzzy controller has been started with the acceptance of the relevant convention of generating membership functions. The coordinates of four additional points P_1 - P_4 are calculated for each input in the proposed approach. The relevant membership functions are created in the next step on their basis. The values of these points are calculated with the use of the factors of proportionality included in the vector of the decision variables $x(n)$, and their detailed description is included in equations (5.4). The decision variables describe the proportion of the section division between the final value of the range and the previous section point. They can assume values in the range from 0 to 1. The maximum values of P_{max} and the admissible P_{nom} result from the accepted assumptions

$$\begin{aligned} P_1 &= x(1)(P_{max} - P_{nom}) & P_2 &= x(2)(P_{max} - P_{nom}) \\ P_3 &= x(3)(P_{max} - P_2) & P_4 &= x(4)(P_{max} - P_3) \end{aligned} \quad (5.4)$$

Two types of the membership functions have been used in the fuzzy controller, the triangular and trapezoid ones. The visualisation of the developed convention is pictured in Fig. 6.

The presented solution has been used for description of the membership functions for both inputs so values of 8 variables have been looked for in the process of optimization.

The ranges of the membership functions of the output signal (values of the set rotational speed of the Z1 engine) have been accepted as constants in accordance with Fig. 7.

Both the unloading force and movement of the Z1 drive should be taken into account during fuzzy controller optimization in the goal function. Due to the limit switches that are used in the device, the most important criterion connected with the position of the Z2 actuator is that none of the trolleys goes beyond the working range. This criterion is included in the form of a penalty function. Moreover, it is important to ensure fluent regulation of the unloading force in order to ensure the biggest patient's comfort. It is achieved by limiting the second derivative of this value in terms of time. The minimization of such a component also affects the energy efficiency

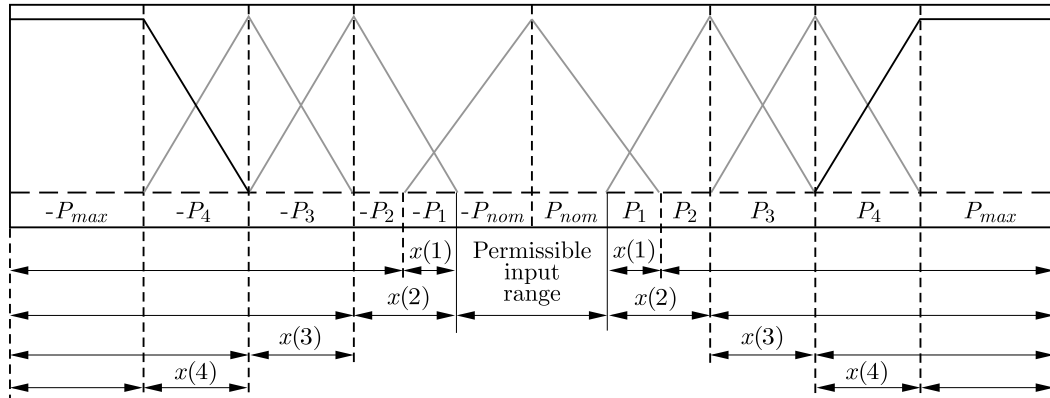


Fig. 6. Visualization of the developed method of describing the input membership functions

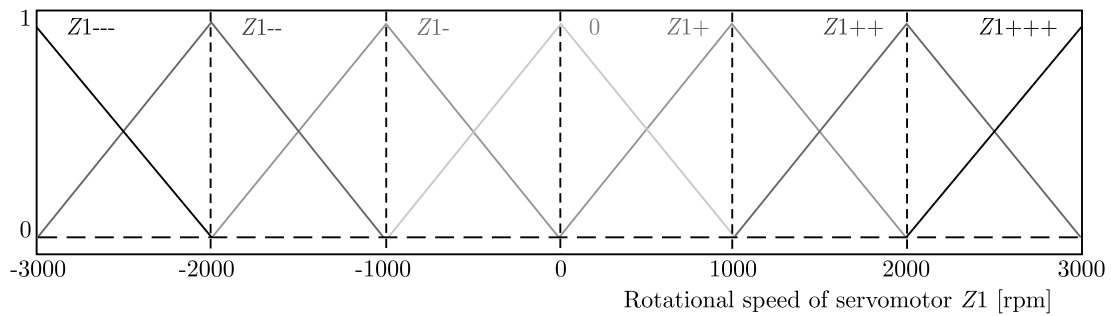


Fig. 7. Output membership function for rotational speed of the servomotor Z1

of the device. The inclusion of all the aspects discussed above has allowed for formulating a multi-objective goal function with the internal penalty function

$$\begin{aligned}
 FC_{fuzzy} = & (1 - w_1 - w_2) \int_0^T |\Delta UNL(t)| dt + w_1 \int_0^T \frac{d^2 |\Delta UNL(t)|}{dt^2} dt \\
 & + w_2 \int_0^T |\omega_{Z1}(t)| dt + \int_0^T |\Delta UNL(t)| P(t) dt \rightarrow \min
 \end{aligned} \quad (5.5)$$

where

$$P(t) = \begin{cases} 0 & \text{if } Z2_{disp} < 40 \text{ mm} \\ 10^4 & \text{if } Z2_{disp} > 40 \text{ mm} \end{cases} \quad (5.6)$$

The optimization of both controllers has been carried out with the use of the Optimization Toolbox module that is implemented in the MATLAB software making use of a hybrid optimization method combining a genetic algorithm with a gradient algorithm for continuous optimization with limitations (*fmincon* function). The best individual created in the genetic algorithm constitutes the starting point for calculations with the gradient method in the calculations carried out. The research carried out has shown that it is most advantageous to use the PD controller for steering the Z2 drive with the following settings:

$$P = 57,13 \quad I = 0 \quad D = 0.755$$

The case in which the weight factor $w_1 = 0.005$, $w_2 = 0.02$ has been considered the best one after analysis of the set of paretooptimal solutions obtained during the optimization of the fuzzy controller. The obtained distribution of the membership functions and a graphic interpretation of the output signal (as a surface) are shown in the three consecutive figures.

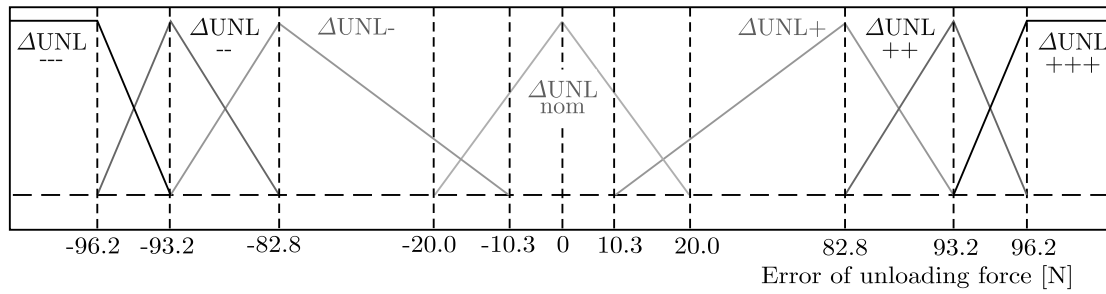


Fig. 8. Input membership function for unloading the force error

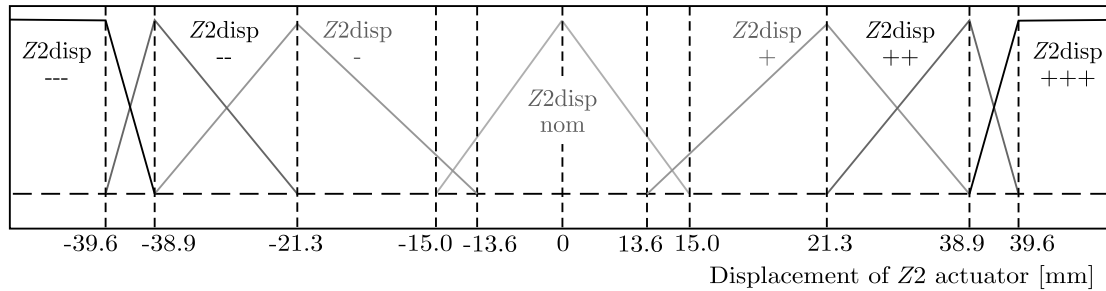


Fig. 9. Input membership function for displacement of the Z2 actuator

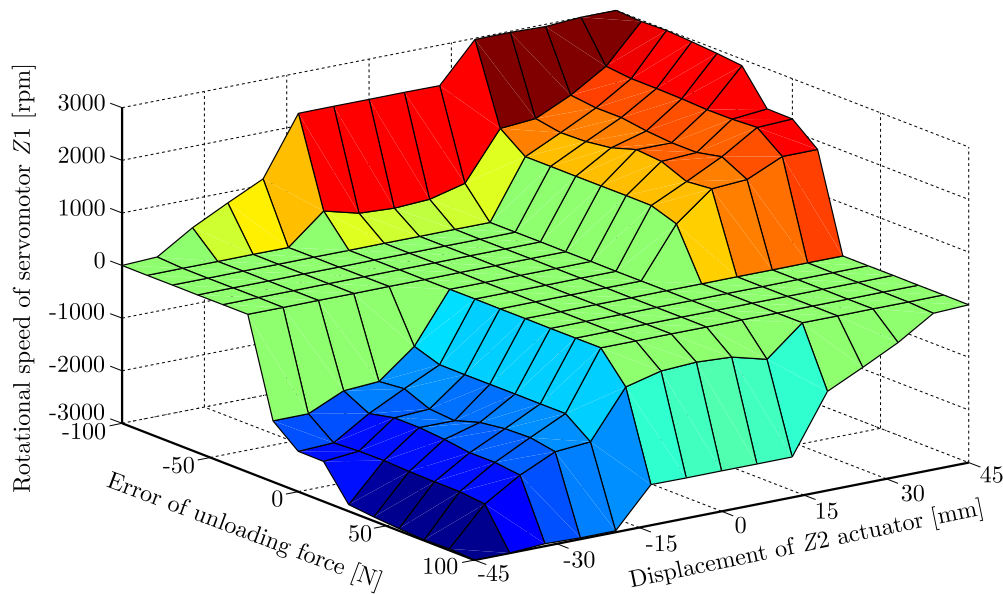


Fig. 10. Surface of the fuzzy logic controller output signal

6. Results of experimental research

In order to verify the developed algorithm controlling the drives of the unloading system, a series of experiments has been conducted. In the presented results, the operation of the BWS drive systems has been tested during walking on a treadmill with a constant speed 2 km/h, but the set value of the unloading force has been changed and equaled to 50, 120, 180, 300 and 180 N, respectively.

The charts show the registered value of the unloading force (Fig. 11), rotational speed of the servomotor Z2 (Fig. 12), displacement of the actuator in the Z2 drive system (Fig. 13) and the rotational speed of the servomotor Z1 (Fig. 14).

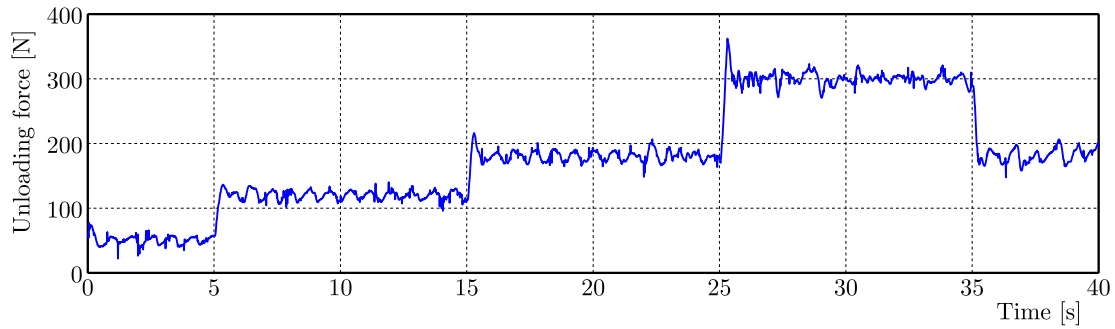


Fig. 11. Registered value of the unloading force as a function of time

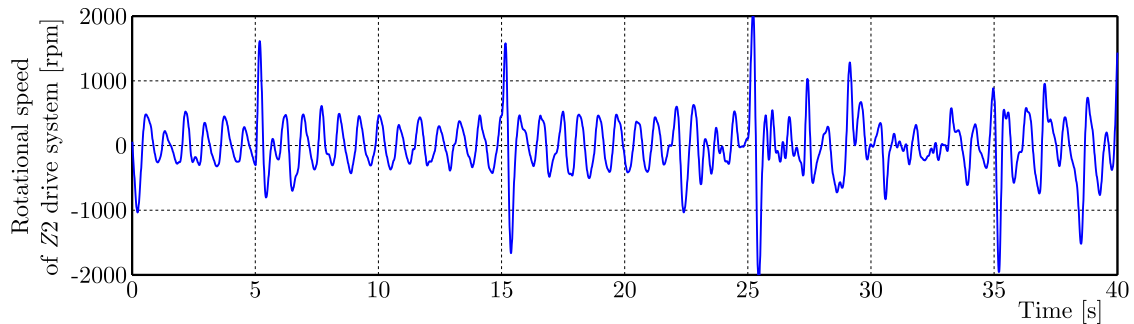


Fig. 12. Registered value of the Z2 servomotor rotational speed as a function of time

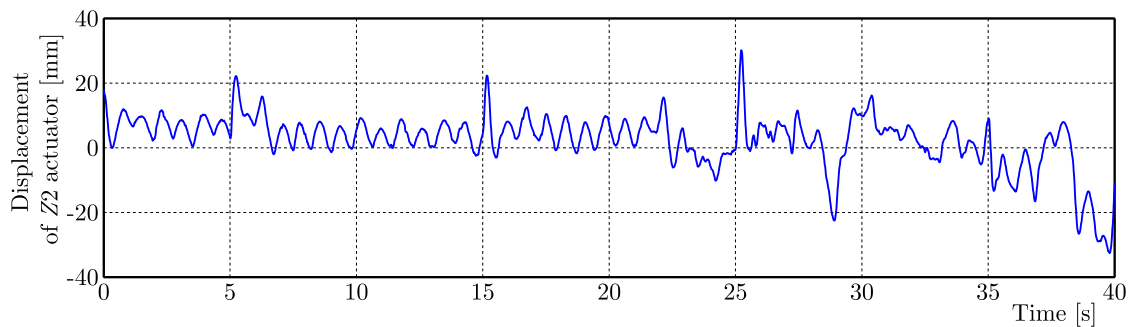


Fig. 13. Registered linear displacement of the Z2 actuator as a function of time

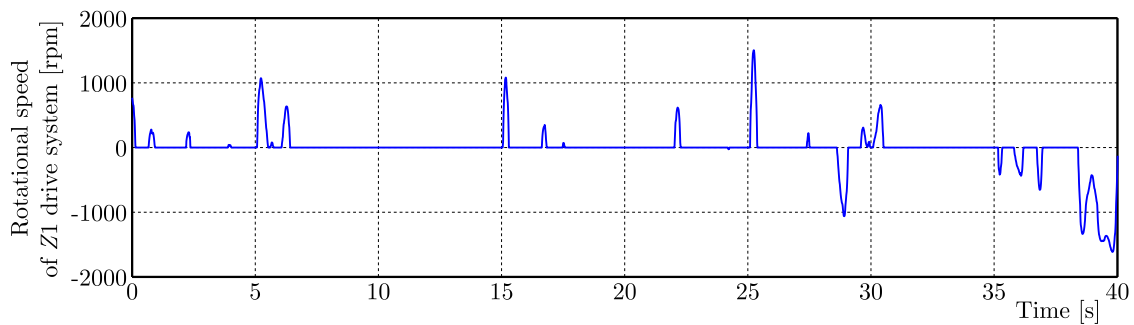


Fig. 14. Registered value of the Z1 servomotor rotational speed as a function of time

7. Conclusions

The paper presents a mechatronic device supporting the process of walking re-education in which the body weight support system cooperates with the training treadmill, and has the possibility of making follow-up movements with side movements of the patient.

The use of a fuzzy controller makes it possible to develop a universal steering system that ensures the maintenance of a constant unloading force value and synchronizes the operation of

the winding drum with the SEA drive type independently of the exercise done. The proposed solution is particularly beneficial for physiotherapists supervising a patient because it requires introduction of the unloading force value only. It is a particularly important advantage as the simplicity of handling is expected.

As the charts show, the drive of the Z1 winding drum is started only in the situation when the Z2 actuator is close to the limit switches; it is not, however, used during normal walking on the treadmill. It is an advantage in economic terms. Testing the device by a healthy person only is a certain limitation of the conducted research; however, it is a beneficial situation for the verification of the steering system operation as the exercising person can move in a more dynamic way.

References

1. CAO J., XIE S.Q., DAS R., ZHU G.L., 2014, Control strategies for effective robot assisted gait rehabilitation: the state of art and future prospects, *Medical Engineering and Physics*, **36**, 12, 1555-1566
2. CHEN G., CHAN C.K., GUO Z., YU H., 2013, A review of lower extremity assistive robotic exoskeletons in rehabilitation therapy, *Critical Reviews in Biomedical Engineering*, **41**, 4-5, 343-363
3. DRAGUNAS A.C., GORDON K.E., 2016, Body weight support impacts lateral stability during treadmill walking, *Journal of Biomechanics*, **49**, 13, 2662-2668
4. DUDA S., GAŚIOREK D., GEMBALCZYK G., KCIUK S., MEŻYK A., 2016, Mechatronic device for locomotor training, *Acta Mechanica et Automatica*, **10**, 4, 310-315
5. DUDA S., GEMBALCZYK G., 2016, Experimental study on the fuzzy-PID hybrid control algorithm for unloading system in mechatronic device for gait re-education, *Proceedings of VII European Congress on Computational Methods in Applied Sciences and Engineering*, 6567-6573
6. DUDA S., GEMBALCZYK G., SWITONSKI E., 2017, Design study and development of mechatronic treadmill for gait reeducation, *Engineering Dynamics and Life Sciences. Proceedings of 14th International Conference Dynamical Systems Theory and Applications 2017*, 183-191
7. FREY M., COLOMBO G., VAGLIO M., BUCHER R., JÖRG M., RIENER R., 2006, A novel mechatronic body weight support system, *Neural Systems and Rehabilitation Engineering*, **14**, 3, 311-321
8. GNIŁKA J., MEŻYK A., 2017, Experimental identification and selection of dynamic properties of a high-speed tracked vehicle suspension system, *Eksploatacja i Niezawodność – Maintenance and Reliability*, **19**, 1, 108-113
9. HIDLER J., BRENNAN D., BLACK I., NICHOLS D., BRADY K., 2011, ZeroG: Overground gait and balance training system, *Journal of Rehabilitation Research and Development*, **48**, 4, 287-298
10. JURKOJC J., WODARSKI P., BIENIEK A., GZIK M., MICHNIK R., 2017, Influence of changing frequency and various sceneries on stabilometric parameters and on the effect of adaptation in an immersive 3D virtual environment, *Acta of Bioengineering and Biomechanics*, **19**, 3, 129-137
11. KOCESKA N., KOCESKI S., 2013, Review: robot devices for gait rehabilitation, *International Journal of Computer Applications*, **62**, 13, 1-8
12. KOENIG A., OMLIN X., BERGMANN J., ZIMMERLI L., BOLLIGER M., MÜLLER F., 2011, Controlling patient participation during robot assisted gait training, *Journal of Neuroengineering and Rehabilitation*, **8**, 14-25
13. KOT A., NAWROCKA A., 2012, Balance platform system dynamic properties, *Journal of Vibroengineering*, **14**, 1, 178-182
14. LÜNENBURGER L., COLOMBO G., RIENER R., 2007, Biofeedback for robotic gait rehabilitation, *Journal of Neuroengineering and Rehabilitation*, **4**, 1

15. MEHRHOLZ J., POHL M., ELSNER B., 2014, Treadmill training and body weight support for walking after stroke, [In:] *Cochrane Database of Systematic Reviews*, **1**, John Wiley & Sons, Ltd
16. MEŻYK A., KLEIN W., FICE M., PAWLAK M., BASIURA K., 2016, Mechatronic model of continuous miner cutting drum driveline, *Mechatronics*, **37**, 12-20
17. MIĄDLICKI K., PAJOR M., 2015, Real-time gesture control of a CNC machine tool with the use Microsoft Kinect sensor, *International Journal of Scientific and Engineering Research*, **6**, 538-543
18. MIGNARDOT J.B., LE GOFF C.G., VAN DEN BRAND R., 2017, A multidirectional gravity-assist algorithm that enhances locomotor control in patients with stroke or spinal cord injury, *Science Translational Medicine*, **9**
19. PAJOR M., HERBIN P., 2015, Exoskeleton of upper limb – model using real movement parameters (in Polish), *Modelowanie Inżynierskie*, **26**, 57, 40-46
20. PRATT G.A., WILLIAMSON M.M., 1995, Series elastic actuators, *IEEE International Conference on Intelligent Robots and Systems*, 399-406
21. QUERRY R.G., PACHECO F., ANNASWAMY T., GOETZ L., WINCHESTER P.K., TANSEY K.E., 2008, Synchronous stimulation and monitoring of soleus H reflex during robotic body weight-supported ambulation in subjects with spinal cord injury, *Journal of Rehabilitation Research and Development*, **45**, 1, 175-186
22. RACZKA W., SIBIELAK M., KOWAL J., KONIECZNY J., 2013, Application of an SMA spring for vibration screen control, *Journal of Low Frequency Noise, Vibration and Active Control*, **32**, 1-2, 117-131
23. REINKENSMeyer D.J., DIETZ V., 2016, *Neurorehabilitation Technology*, Springer, International Publishing
24. RIENER R., LÜNENBURGER L., MAIER I.C., COLOMBO G., DIETZ V., 2010, Locomotor training in subjects with sensori-motor deficits: an overview of the robotic gait orthosis lokomat, *Journal of Healthcare Engineering*, **1**, 2, 197-216
25. ROBINSON D.W., PRATT J.E., PALUSKA D.J., PRATT G.A., 1999, Series elastic actuator development for a biomimetic walking robot, *Proceedings of IEEE/ASME International Conference on Advanced Intelligent Mechatronics*, 561-568.
26. SAPIŃSKI B., ROSÓŁ M., WĘGRZYŃSKI M., 2016, Investigation of an energy harvesting MR damper in a vibration control system, *Smart Materials and Structures*, **25**, 12, 125017, 1-15
27. SNAMINA J., KOWAL J., ORKISZ P., 2013, Active suspension based on low dynamic stiffness, *Acta Physica Polonica A*, **123**, 6, 1118-1122
28. XU W.J., 2012, Permanent magnet synchronous motor with linear quadratic speed controller, *Energy Procedia*, **14**, 364-369
29. ZHAO C.S., ZHU S.J., HE Q.W., 2007, Fuzzy-PID control method for two-stage vibration isolation system, *Journal of Theoretical and Applied Mechanics*, **45**, 1, 171-177

ROBUST NEURAL NETWORKS CONTROL OF OMNI-MECANUM WHEELED ROBOT WITH HAMILTON-JACOBI INEQUALITY

ZENON HENDZEL

Rzeszow University of Technology, Faculty of Mechanical Engineering and Aeronautics, Rzeszów, Poland
e-mail: zenhen@prz.edu.pl

This paper presents a novel approach to the problem of controlling mechanical objects of unspecified description, considering variable operating conditions. The controlled object is a mobile robot with mecanum wheels (MRK_M). To solve the control task, taking into account compensation for nonlinearity and the object variable operating conditions, the Lyapunov stability theory is applied, including the Hamilton-Jacobi (HJ) inequality. A neural network with basic sigmoid functions is used to compensate for the nonlinearity and variable operating conditions of the robot. A simulation example is provided in order to evaluate the analytical considerations. The simulation results obtained confirmed high accuracy of the predicted robot motion in variable operating conditions.

Keywords: mechatronics, mobile robot, mecanum wheels, Hamilton-Jacobi inequality

1. Introduction

The motivation for analytical considerations of the behaviour of a mobile robot with Swedish wheels (Canudas de Wit *et al.*, 1996), referred to in the literature as mecanum wheels (Becker *et al.*, 2014; Abdelrahman *et al.*, 2014; Hendzel and Rykała, 2015) comes from the fact that there is a relatively small amount of literature in this area, especially with regards to the impact of resistance to motion and variable operating conditions on the quality of motion and its control in real time. Most often, control synthesis for these objects is carried out based on kinematics equations (Siegwart *et al.*, 2011; Tai *et al.*, 2011). Kinematics control does not take into account nonlinearity of the robot and variable operating conditions. The literature offers solutions which take into consideration dynamic equations of motion (Han *et al.*, 2009; Park *et al.*, 2010; Tsai *et al.*, 2010) typically in a simplified form not including, for example, resistance to motion. The work of (Lin and Shih, 2013) includes control synthesis for a mobile robot with mecanum wheels based on the Lagrange equations using an adaptive control algorithm. The current paper presents a new approach to the problem of controlling a mobile robot with mecanum wheels as a mechanical object of unspecified description, considering variable operating conditions. To solve the mobile robot control task, the Lyapunov stability theory is applied, including the HJ inequality. The method of synthesis of robust neural networks control proposed in this paper aims at extending the existing solutions with a particular emphasis on its application in the field of control methods for intelligent mobile wheeled robots. In Section 2, kinematic and dynamic equations for MRK_M motion are formulated. Section 3 provides a theoretical basis of dissipation of nonlinear systems and L_2 stability. In Section 4, the assumed structure of the neural network is discussed, and its description is given. The synthesis of robust neural networks control of MRK_M, including the HJ inequality, is provided in Section 5. Section 6 contains a simulation example and simulation results of the adopted solution.

2. Mobile wheeled robot

When describing motion of mobile wheeled robots, we are interested in the issues of kinematics and dynamics of such systems (Żylski, 1996). From the perspective of controlling these objects in the areas of both kinematics and dynamics, we solve reverse tasks. To describe kinematics of a mobile robot with mecanum wheels, the model shown in Fig. 1 is adopted. In this figure, x , y and z are the axes of the fixed system. The basic units of this model are: frame 5 and the driving units. The driving unit consists of wheels 1, 2, 3, 4, which are mounted on semi-axes and set in motion by a drive module associated with a given wheel. The points A_1, A_2, A_3, A_4 lie in their centres of symmetry. These wheels rotate around their own axes which do not change their position relative to the frame. The rollers are placed on the periphery of the wheels, and they are set at an angle of $\alpha = \pi/4$ radians, relative to the axis of the driving wheel. Figure 1c shows appropriate geometric dimensions and characteristic points of the system. Point S is the centre of mass of the frame, point H is the point lying on the axis A_1A_2 halfway between these points. Point B , like point H , is the point belonging to the frame. The angle β is the angle of temporary rotation of the frame. Figures 1a and 1b exemplify the angular velocity vectors of wheel 2, ω_2 and roller ω_{r2} , respectively. To describe kinematics of any point in the system, it is useful to give the kinematics equation. Knowing the geometry of the system and applying classical methods used in mechanics, the description of the kinematics of the analysed system is as follows

$$\begin{aligned} \dot{x}_s \cos(\beta - \alpha) + \dot{y}_s \sin(\beta - \alpha) - \dot{\beta}(l \cos \alpha + l_1 \sin \alpha) &= \omega_1(R + r) \cos \alpha \\ \dot{x}_s \cos(\beta + \alpha) + \dot{y}_s \sin(\beta + \alpha) + \dot{\beta}(l \cos \alpha + l_1 \sin \alpha) &= \omega_2(R + r) \cos \alpha \\ \dot{x}_s \cos(\beta + \alpha) + \dot{y}_s \sin(\beta + \alpha) - \dot{\beta}(l \cos \alpha + l_1 \sin \alpha) &= \omega_3(R + r) \cos \alpha \\ \dot{x}_s \cos(\beta - \alpha) + \dot{y}_s \sin(\beta - \alpha) + \dot{\beta}(l \cos \alpha + l_1 \sin \alpha) &= \omega_4(R + r) \cos \alpha \end{aligned} \quad (2.1)$$

The adopted description will enable determination of the reverse kinematics task, which will be the set motion trajectory for the S point of the robot in the control system.

When describing the dynamics of complex systems such as mobile wheeled robots, especially robots with mecanum wheels, Lagrange's equations with multipliers or Maggi's equations can be used (Giergiel *et al.*, 2002). To determine the dynamic equations of MRK_M motion, Maggi's equations are used (Żylski, 1996) with an additional disturbance element, which are convenient for synthesis of control. In the analysed case, take the general form

$$\mathbf{M}(\mathbf{q})\ddot{\mathbf{q}} + \mathbf{C}(\mathbf{q}, \dot{\mathbf{q}})\dot{\mathbf{q}} + \mathbf{F}(\boldsymbol{\omega}) + \boldsymbol{\tau}_d(t) = \mathbf{u} \quad (2.2)$$

where the vector of disturbances meets the restriction $\|\boldsymbol{\tau}_d(t)\| < b$, $b = \text{const} > 0$, matrices \mathbf{M} , \mathbf{C} and vectors \mathbf{F} , \mathbf{u} take the following form

$$\begin{aligned} \mathbf{M}(\mathbf{q}) &= \begin{bmatrix} a_1 \sin \beta + a_2 \cos(\beta - \alpha) & a_2 \sin(\beta - \alpha) - a_1 \cos \beta & -a_3 \\ a_2 \cos(\beta + \alpha) - a_8 \sin(\beta - \alpha) & a_2 \sin(\beta + \alpha) - a_8 \cos(\beta - \alpha) & -a_4 \\ a_1 \cos \beta + a_2 \cos(\beta - \alpha) & a_2 \sin(\beta - \alpha) + a_1 \sin(\beta - \alpha) & a_3 \end{bmatrix} \\ \mathbf{C}(\mathbf{q}, \dot{\mathbf{q}}) &= \begin{bmatrix} -a_2 \sin(\beta - \alpha)\dot{\beta} & a_2 \cos(\beta - \alpha)\dot{\beta} & 0 \\ -a_2 \sin(\beta + \alpha)\dot{\beta} & a_2 \cos(\beta + \alpha)\dot{\beta} & 0 \\ -a_2 \sin(\beta - \alpha)\dot{\beta} & a_2 \sin(\beta - \alpha)\dot{\beta} & 0 \end{bmatrix} \\ \mathbf{F}(\boldsymbol{\omega}) &= \begin{bmatrix} a_5 \text{sgn} \omega_1 \\ a_6 \text{sgn} \omega_3 \\ a_7 \text{sgn} \omega_4 \end{bmatrix} & \mathbf{q} &= \begin{bmatrix} x_s \\ y_s \\ \beta \end{bmatrix} & \mathbf{u} &= \begin{bmatrix} M_1 \\ M_3 \\ M_4 \end{bmatrix} & \boldsymbol{\tau}_d(t) &= \begin{bmatrix} \tau_{d1} \\ \tau_{d3} \\ \tau_{d4} \end{bmatrix} \end{aligned} \quad (2.3)$$

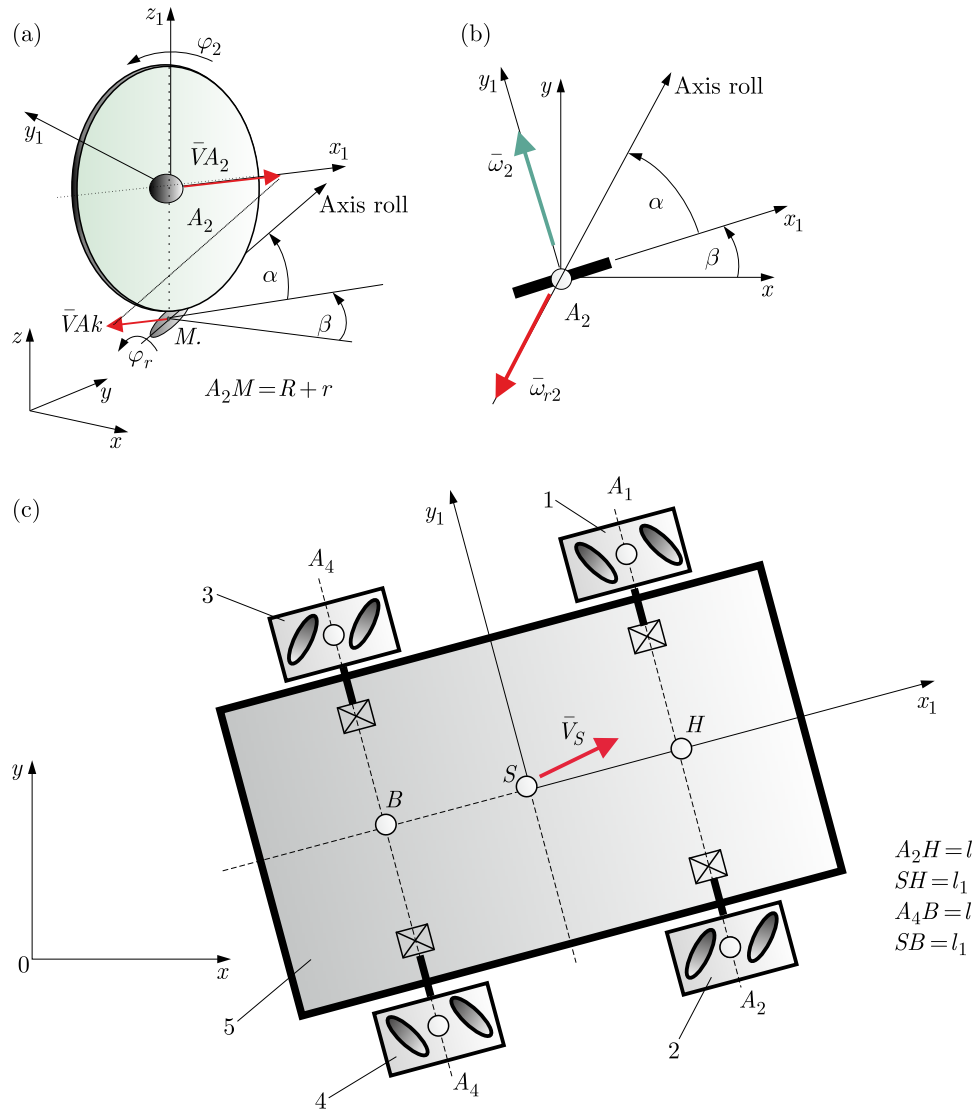


Fig. 1. MRK_M model

Since the analysed robot has 3 degrees of freedom and four drive modules, it is an object of an “over actuated” type, the missing moment M_2 is determined on the basis of the power balance of the drive systems

$$M_2 = M_3 + M_4 - M_1 \quad (2.4)$$

The vector $\mathbf{a} = [a_1, \dots, a_8]^T$ contains parameters resulting from the geometry, mass distribution and the robot resistance to motion. We further assume that the trajectory of the robot motion $\mathbf{q}_d(t) \in \mathbb{R}^3$ and its derivatives are known. Equation (2.2) allows solving the direct and inverse dynamics tasks. The direct task will be used in simulation of the controlled object, and the inverse task in the feedback system will be used to determine the values of the driving moments of the mobile robot wheels, i.e. the control vector.

3. Continuous dissipative systems and L_2 gain

From the perspective of control theory, the dissipation and L_2 gain properties of dynamic non-linear systems are important in the control synthesis of these systems in the context of the

input-output relationship. Further considerations will focus on finite energy signals. This approach to control synthesis is important when considering the effects of disturbances in closed control systems.

Definition 2.1 (Abu-Khalaf and Lewis, 2006; van der Schaft, 1992, 2000). For a given continuous function $f(t) : [0, \infty) \rightarrow \mathbb{R}^n$, its norm L_p , $\|f(t)\|_{L_p}$ is defined as

$$\|f(t)\|_{L_p} = \left(\int_0^\infty \|f(t)\|_p^p dt \right)^{1/p} \quad (3.1)$$

and for $p = 2$ we have

$$\|f(t)\|_{L_2} = \left(\int_0^\infty \|f(t)\|^2 dt \right)^{1/2} \quad (3.2)$$

In order to define dissipation of the system, let us consider the description of the dynamic system in the form

$$\dot{\mathbf{x}}_o = \mathbf{f}_x(\mathbf{x}_o) + \mathbf{b}(\mathbf{x}_o)\mathbf{d}(t) \quad \mathbf{z}(t) = \mathbf{g}(\mathbf{x}_o) \quad (3.3)$$

where $\mathbf{x}_o(t) \in \mathbb{R}^n$ is the state vector, $\mathbf{f}_x(\mathbf{x}_o) \in \mathbb{R}^n$, $\mathbf{b}(\mathbf{x}_o) \in \mathbb{R}^{n \times m}$, $\mathbf{g}(\mathbf{x}_o) \in \mathbb{R}^p$ and $\mathbf{d}(t) \in \mathbb{R}^m$ is the disturbances signal, and $\mathbf{z}(t) \in \mathbb{R}^p$ is the system output signal, which can be interpreted as a tracking control error, additionally $\mathbf{f}_x(0) = \mathbf{0}$ and $\mathbf{x}_o = \mathbf{0}$ is the system equilibrium point.

Definition 2.2 (Abu-Khalaf, Lewis, 2006; Fariwata *et al.*, 2000; Nash, 1951; Slotine and Li, 1991; van der Schaft, 1992). The dynamic system described by equation (3.3) with the supplied rate $w(\mathbf{d}, \mathbf{z})$ is dissipative if there exists a function $V(\mathbf{x}_o) \geq 0$ which is interpreted as a storage function, such that there is a dissipation inequality

$$V(\mathbf{x}_o(t_1)) - V(\mathbf{x}_o(t_0)) \leq \int_{t_0}^{t_1} w(\mathbf{d}(t), \mathbf{z}(t)) dt \quad (3.4)$$

Generally, it can be stated that the dynamic system is dissipative if it loses cumulative energy during operation until the state of the system reaches the equilibrium point.

Definition 2.3 (Abu-Khalaf and Lewis, 2006; Basar and Bernard, 1995; Lewis *et al.*, 2012). Dynamic system (3.3) has L_2 gain less than or equal to γ , for $\gamma \geq 0$, if the following inequality is true

$$\|\mathbf{z}(t)\|_{L_2} \leq \gamma \|\mathbf{d}(t)\|_{L_2} \quad (3.5)$$

This means that the analysed system has $L_2 < \gamma$ gain if there exists $0 \leq \hat{\gamma} < \gamma$ such that equation (3.5) is true for $\hat{\gamma}$. As has been demonstrated (van der Schaft, 2000), if the level of energy supplied to the system is defined as $w(\mathbf{d}(t), \mathbf{z}(t)) = \gamma^2 \|\mathbf{d}(t)\|^2 - \|\mathbf{z}(t)\|^2$ and the system is dissipative, then the dynamic system has gain L_2 , i.e. it is stable. The determination of dissipativity of the system and, hence, the stability of the analysed nonlinear L_2 system requires demonstrating that the function $V(\mathbf{x}_o)$ is bounded from below. Demonstrating this condition requires solving the optimization problem, which comes down to solving the HJ equation or HJ inequality (Basar and Bernard, 1995), written as

$$\dot{V}(\mathbf{x}_o) = \frac{\partial V(\mathbf{x}_o)}{\partial \mathbf{x}_o} [\mathbf{f}_x(\mathbf{x}_o) + \mathbf{b}(\mathbf{x}_o)\mathbf{d}(t)] \leq \frac{1}{2}(\gamma^2 \|\mathbf{d}(t)\|^2 - \|\mathbf{z}(t)\|^2) \quad (3.6)$$

Satisfying this inequality leads to the solution $V(\mathbf{x}_o) \geq 0$ for every $\mathbf{d}(t) \in \mathbb{R}^m$ and $\mathbf{z}(t) = \mathbf{g}(\mathbf{x}_o)$. Determining the system gain L_2 as

$$J = \sup_{\mathbf{d} \neq 0} \frac{\|\mathbf{z}(t)\|_{L_2}}{\|\mathbf{d}(t)\|_{L_2}} \quad (3.7)$$

this equation can be interpreted as an indicator of the system resistance to interference. The smaller it is, the more the designed control system is robust to disturbance, provided that inequality (3.6) is satisfied, i.e. for

$$\dot{V}(\mathbf{x}_o) \leq \frac{1}{2}(\gamma^2 \|\mathbf{d}(t)\|^2 - \|\mathbf{z}(t)\|^2) \quad (3.8)$$

$J \leq \gamma$ occurs. To solve the robust neural network control of MRK_M motion, we will apply HJ inequality (3.8) with the evaluation of the control by (3.7).

4. Neural network structure

Due to nonlinearity as well as complexity of the structure of dynamic equations of motion of mobile wheeled robots and the need to include a mathematical model in motion control algorithms for these objects, the application of artificial neural networks theory is an alternative and attractive approach to solve these tasks. From the perspective of control theory, the possibilities of approximation of nonlinear mappings are the most important properties of neural networks. These properties will be used in synthesis of neural networks control for the implementation of MRK_M tracking motion (Hendzel, 2007). In the real-time control, linear networks are used due to weights, with the structure shown in Fig. 2.

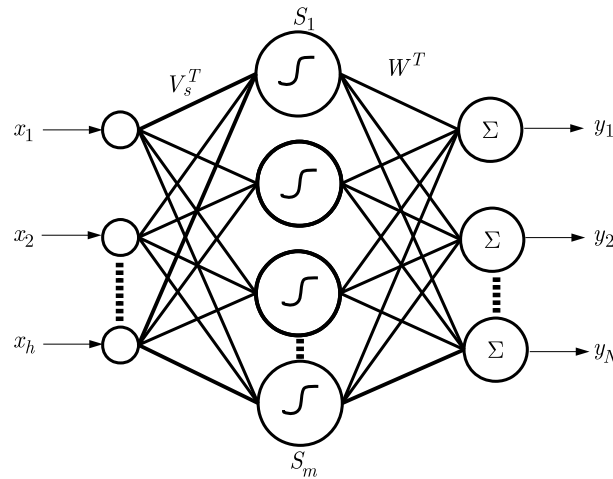


Fig. 2. Neural network structure

The input layer weight matrix \mathbf{V}_s is a constant matrix generated randomly. The network input-output mapping from Fig. 2 has the form (Lewis *et al.*, 1999)

$$y_i = \sum_{j=1}^m \left[w_{ij} S \left(\sum_{k=1}^h v_{jk} x_k + v_{j0} \right) + w_{i0} \right] \quad i = 1, 2, \dots, N \quad (4.1)$$

Assuming the element of the input vector to be $\mathbf{x}_0 \equiv \mathbf{1}$ and the vector of threshold values $[v_{10}, v_{20}, \dots, v_{m0}]^T$ as the first column of the matrix \mathbf{V}_s^T , we get

$$\mathbf{y} = \mathbf{W}^T \mathbf{S}(\mathbf{V}_s^T \mathbf{x}) = \mathbf{W}^T \varphi_x(\bar{\mathbf{x}}) \quad (4.2)$$

where $\bar{\mathbf{x}} = \mathbf{V}_s^T \mathbf{x}$, $\mathbf{S} = [1, S_1(\cdot), S_2(\cdot), \dots, S_m(\cdot)]^T$ is a vector describing neuron functions, whose first element is equal to 1, and the vector $[w_{10}, w_{20}, \dots, w_{N0}]^T$ is the first column of the matrix \mathbf{W}^T in order to account for the threshold value of linear neurons in the network output layer.

5. Synthesis of robust neural networks control of MRK_M motion

The purpose of the synthesis of the control algorithm is to determine the control rule and the rule for adaptation of network weights, for which the trajectory of the selected point S of the robot, Fig. 1, will coincide with the set trajectory (Hendzel and Szuster, 2012, 2015; Szuster and Hendzel, 2018), despite the occurrence of variable operating conditions of the robot. To this end, the tracking error $\mathbf{e} \in \mathbb{R}^3$, the generalized error \mathbf{s} and the auxiliary vector \mathbf{v} are defined as

$$\mathbf{e} = \mathbf{q}_d - \mathbf{q} \quad \mathbf{s} = \dot{\mathbf{e}} + \mathbf{\Lambda} \mathbf{e} \quad \mathbf{v} = \dot{\mathbf{q}}_d + \mathbf{\Lambda} \mathbf{e} \quad (5.1)$$

where $\mathbf{\Lambda}$ is a diagonal matrix, positively defined. Then equation (2.2) can be transformed into

$$\mathbf{M}(\mathbf{q})\dot{\mathbf{s}} = -\mathbf{u} - \mathbf{C}(\mathbf{q}, \dot{\mathbf{q}})\mathbf{s} + \mathbf{M}\dot{\mathbf{v}} + \mathbf{C}(\mathbf{q}, \dot{\mathbf{q}})\mathbf{v} + \mathbf{F}(\boldsymbol{\omega}) + \boldsymbol{\tau}_d(t) \quad (5.2)$$

If we define the nonlinear function

$$\mathbf{f}(\mathbf{x}_r) = \mathbf{M}(\mathbf{q})\dot{\mathbf{v}} + \mathbf{C}(\mathbf{q}, \dot{\mathbf{q}})\mathbf{v} + \mathbf{F}(\boldsymbol{\omega}) \quad (5.3)$$

where $\mathbf{x}_r = [\mathbf{v}^T, \dot{\mathbf{v}}^T, \dot{\mathbf{q}}^T, \mathbf{q}^T, \boldsymbol{\omega}^T]^T$, then equation (5.2) will be written as

$$\mathbf{M}(\mathbf{q})\dot{\mathbf{s}} = -\mathbf{u} - \mathbf{C}(\mathbf{q}, \dot{\mathbf{q}})\mathbf{s} + \mathbf{f}(\mathbf{x}_r) + \boldsymbol{\tau}_d(t) \quad (5.4)$$

In practice, an approximation of the control compensating for the robot nonlinearity $\mathbf{f}(\mathbf{x}_r)$ is applied. For the approximation of the nonlinearity, the neural network described in Section 4 is used, assuming $\mathbf{x} = \mathbf{x}_r$, $\mathbf{y} = \mathbf{f}(\mathbf{x}_r)$. The nonlinear function $\mathbf{f}(\mathbf{x}_r)$ is written as

$$\mathbf{f}(\mathbf{x}_r) = \mathbf{W}^T \boldsymbol{\varphi}_x(\bar{\mathbf{x}}) + \boldsymbol{\varepsilon} \quad (5.5)$$

where $\boldsymbol{\varepsilon}$ is the approximation error. The estimate the function $\mathbf{f}(\mathbf{x}_r)$ is written as

$$\hat{\mathbf{f}}(\mathbf{x}_r) = \hat{\mathbf{W}}^T \boldsymbol{\varphi}_x(\bar{\mathbf{x}}) \quad (5.6)$$

where $\hat{\mathbf{W}}$ is an estimate of weight of the ideal neural network. In addition, it is assumed that ideal network weights are fixed, $\mathbf{W} = \text{const}$. Using equation (5.6), we adopt the control rule in the following form

$$\mathbf{u} = \hat{\mathbf{W}}^T \boldsymbol{\varphi}_x(\bar{\mathbf{x}}) + \frac{1}{2} \left(1 + \frac{1}{\gamma^2} \right) \mathbf{s} \quad (5.7)$$

It should be noted that the second component of equation (5.7) has an interpretation of the PD type controller since the second component of (5.7) can be written as

$$K_D \mathbf{s} = K_D \dot{\mathbf{e}} + K_D \mathbf{\Lambda} \mathbf{e} \quad (5.8)$$

where $K_D = 0.5(1 + 1/\gamma^2)$. Substituting (5.7) and (5.5) for (5.4), we obtain

$$\mathbf{M}(\mathbf{q})\dot{\mathbf{s}} + \mathbf{C}(\mathbf{q}, \dot{\mathbf{q}})\mathbf{s} + \frac{1}{2} \left(1 + \frac{1}{\gamma^2} \right) \mathbf{s} = \tilde{\mathbf{f}}(\mathbf{x}_r) + \boldsymbol{\tau}_d(t) \quad (5.9)$$

where $\tilde{\mathbf{f}}(\mathbf{x}_r)$ is a function of the approximation error $\mathbf{f}(\mathbf{x}_r)$, which is

$$\tilde{\mathbf{f}}(\mathbf{x}_r) = \mathbf{f}(\mathbf{x}_r) - \hat{\mathbf{f}}(\mathbf{x}_r) = \mathbf{W}^T \boldsymbol{\varphi}_x(\bar{\mathbf{x}}) - \widehat{\mathbf{W}}^T \boldsymbol{\varphi}_x(\bar{\mathbf{x}}) + \boldsymbol{\varepsilon} = \widetilde{\mathbf{W}}^T \boldsymbol{\varphi}_x(\bar{\mathbf{x}}) + \boldsymbol{\varepsilon} \quad (5.10)$$

where $\widetilde{\mathbf{W}} = \mathbf{W} - \widehat{\mathbf{W}}$ is the error of estimation of neural network weights. Using equation (5.10), equation (5.9) is written as follows

$$\mathbf{M}(\mathbf{q})\dot{\mathbf{s}} + \mathbf{C}(\mathbf{q}, \dot{\mathbf{q}})\mathbf{s} + \frac{1}{2}\left(1 + \frac{1}{\gamma^2}\right)\mathbf{s} = \widetilde{\mathbf{W}}^T \boldsymbol{\varphi}_x(\bar{\mathbf{x}}) + \boldsymbol{\varepsilon} + \boldsymbol{\tau}_d(t) \quad (5.11)$$

In order to apply the considerations described in Section 3, the designations in equation (3.3) are interpreted as

$$\begin{aligned} \dot{\mathbf{x}}_o &= \dot{\mathbf{s}} & \mathbf{x}_o &= \mathbf{s} & \mathbf{b}(\mathbf{x}_o) &= \mathbf{M}(\mathbf{q})^{-1} \\ \mathbf{g}(\mathbf{x}_o) &= \mathbf{s} & \mathbf{d}(t) &= \boldsymbol{\varepsilon} + \boldsymbol{\tau}_d(t) \\ \mathbf{f}_x(\mathbf{x}_o) &= \mathbf{M}(\mathbf{q})^{-1} \left[-\frac{1}{2}\left(1 + \frac{1}{\gamma^2}\right)\mathbf{s} - \mathbf{C}(\mathbf{q}, \dot{\mathbf{q}})\mathbf{s} + \widetilde{\mathbf{W}}^T \boldsymbol{\varphi}_x(\bar{\mathbf{x}}) \right] \end{aligned}$$

In order to synthesize the neural network control of MRK_M motion, the Lyapunov stability theory is used. As a candidate for the Lyapunov function, the following function has been selected

$$V(\mathbf{s}) = \frac{1}{2}\mathbf{s}^T \mathbf{M}(\mathbf{q})\mathbf{s} + \frac{1}{2} \text{tr}(\widetilde{\mathbf{W}}^T \mathbf{P}^{-1} \widetilde{\mathbf{W}}) \quad (5.12)$$

where $\mathbf{P} = \mathbf{P}^T > \mathbf{0}$ is a design matrix. The derivative of the function $V(\mathbf{s})$ relative to time along the trajectory of system (5.11) is

$$\dot{V}(\mathbf{s}) = \mathbf{s}^T \mathbf{M}(\mathbf{q})\dot{\mathbf{s}} + \frac{1}{2}\mathbf{s}^T \dot{\mathbf{M}}(\mathbf{q}, \dot{\mathbf{q}})\mathbf{s} + \text{tr}(\widetilde{\mathbf{W}}^T \mathbf{P}^{-1} \dot{\widetilde{\mathbf{W}}}) \quad (5.13)$$

Substituting from equation (5.11) the expression $\mathbf{M}(\mathbf{q})\dot{\mathbf{s}}$ and taking advantage of the fact that $0.5[\dot{\mathbf{M}}(\mathbf{q}, \dot{\mathbf{q}}) - 2\mathbf{C}(\mathbf{q}, \dot{\mathbf{q}})]$ is a zero matrix (for $\beta(t) = 0$), the following is obtained

$$\dot{V}(\mathbf{s}) = -\mathbf{s}^T \frac{1}{2}\left(1 + \frac{1}{\gamma^2}\right)\mathbf{s} + \text{tr}\{\widetilde{\mathbf{W}}^T [\mathbf{P}^{-1} \dot{\widetilde{\mathbf{W}}} + \boldsymbol{\varphi}_x(\bar{\mathbf{x}})\mathbf{s}^T]\} + \mathbf{s}^T [\boldsymbol{\varepsilon} + \boldsymbol{\tau}_d(t)] \quad (5.14)$$

Selecting the following as the rule for adaptation of neural network weights

$$\dot{\widetilde{\mathbf{W}}} = -\mathbf{P} \boldsymbol{\varphi}_x(\bar{\mathbf{x}})\mathbf{s}^T \quad (5.15)$$

equation (5.14) will be transformed into

$$\dot{V}(\mathbf{s}) = -\frac{1}{2\gamma^2}\mathbf{s}^T \mathbf{s} - \frac{1}{2}\mathbf{s}^T \mathbf{s} + \mathbf{s}^T [\boldsymbol{\varepsilon} + \boldsymbol{\tau}_d(t)] \quad (5.16)$$

Let D denote transformed equation (3.8)

$$D = \dot{V}(\mathbf{s}) - \frac{1}{2}\gamma^2 \|\boldsymbol{\varepsilon} + \boldsymbol{\tau}_d(t)\|^2 + \frac{1}{2}\|\mathbf{s}\|^2 \quad (5.17)$$

and then, on the basis of (5.16), equation (5.17) will be transformed into

$$D = -\frac{1}{2\gamma^2}\mathbf{s}^T \mathbf{s} - \frac{1}{2}\mathbf{s}^T \mathbf{s} + \mathbf{s}^T [\boldsymbol{\varepsilon} + \boldsymbol{\tau}_d(t)] - \frac{1}{2}\gamma^2 \|\boldsymbol{\varepsilon} + \boldsymbol{\tau}_d(t)\|^2 + \frac{1}{2}\|\mathbf{s}\|^2 \quad (5.18)$$

Because $-0.5\mathbf{s}^T \mathbf{s} + 0.5\|\mathbf{s}\|^2 = 0$, equation (5.18) will take the form

$$\mathbf{s}^T [\boldsymbol{\varepsilon} + \boldsymbol{\tau}_d(t)] - \frac{1}{2\gamma^2}\mathbf{s}^T \mathbf{s} - \frac{1}{2}\gamma^2 \|\boldsymbol{\varepsilon} + \boldsymbol{\tau}_d(t)\|^2 = -\frac{1}{2}\left\|\frac{1}{\gamma}\mathbf{s} + \gamma[\boldsymbol{\varepsilon} + \boldsymbol{\tau}_d(t)]\right\|^2 \leq 0 \quad (5.19)$$

From inequality (5.19) it follows that $D \leq 0$ and, based on equation (5.17), we get

$$\dot{V}(\mathbf{s}) \leq \frac{1}{2}\gamma^2 \|\boldsymbol{\varepsilon} + \boldsymbol{\tau}_d(t)\|^2 - \frac{1}{2}\|\mathbf{s}\|^2 \quad (5.20)$$

Determining $\mathbf{z}(t) = \mathbf{s}(t)$, $\mathbf{d}(t) = \boldsymbol{\varepsilon} + \boldsymbol{\tau}_d(t)$, we have thus shown that condition (3.8) is satisfied, i.e. inequality $J \leq \gamma$ is satisfied for the structure adopted as control rule (5.7) and, furthermore, that the analysed system is stable according to the definition in (2.3).

5.1. Caution

In the proposed control synthesis, based on the Lyapunov stability theory, there is a component of the form $\mathbf{s}^T 0.5[\dot{\mathbf{M}}(\mathbf{q}, \dot{\mathbf{q}}) - 2\mathbf{C}(\mathbf{q}, \dot{\mathbf{q}})]\mathbf{s}$ which takes a value of zero if the matrix in brackets is an obliquely symmetrical matrix. This situation takes place in the analysed case only for the configuration of the robot frame $\beta(t) = 0$. In the case where $\dot{\beta}(t) \neq 0$, the indicated equation does not take place. Then, when determining the expression $\varepsilon_1 = 0.5[\dot{\mathbf{M}}(\mathbf{q}, \dot{\mathbf{q}}) - 2\mathbf{C}(\mathbf{q}, \dot{\mathbf{q}})]\mathbf{s}$, the last component of equation (5.14) needs to be modified to the form $\mathbf{s}^T[\boldsymbol{\varepsilon} + \boldsymbol{\tau}_d(t) + \varepsilon_1]$ and, consequently, equation (5.20) will be $\dot{V}(\mathbf{s}) \leq 0.5\gamma^2\|\boldsymbol{\varepsilon} + \boldsymbol{\tau}_d(t) + \varepsilon_1\|^2 - 0.5\|\mathbf{s}\|^2$, and the expression ε_1 needs to be interpreted as a structural interference.

The next Section presents a simulation example, the purpose of which is to confirm the solutions arrived at in the analytical considerations and to obtain quantitative solutions.

6. Simulation example

In the example, simulation of the suggested solution has been carried out for the movement of the selected point S of the mobile robot on the trajectory set in the form of a loop, consisting of five characteristic stages of motion: moving on a rectilinear track, starting, moving at a fixed speed when, $V_s^* = 0.4 \text{ m/s}$, moving on a circular path with the radius $R = 0.7 \text{ m}$, exit from the curve taking into account a transitional period, then moving on the rectilinear track at a fixed speed and braking. For the assumed stages of motion, Figure 3 shows the trajectory set for the point S with the assumed orientation angle of the robot, assuming the initial conditions of motion: $x_s(0) = 1 \text{ m}$, $y_s(0) = 5 \text{ m}$, $\beta(0) = 0$.

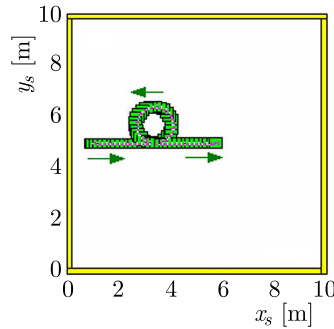


Fig. 3. The trajectory set for motion of the point S and the robot orientation

During motion, there is no change in the orientation angle of the robot frame $\beta(t)$. Figure 4 presents a solution to the task of inverse kinematics. For the time $t \geq 7.5 \text{ s}$, there is a movement of the point S of the robot on a circular trajectory with the radius $R = 0.7 \text{ m}$.

Table 1. Values of a_i parameters of a mobile robot

a_1	a_2	a_3	a_4	a_5	a_6	a_7	a_8
0.044	11.5708	2.4558	2.4545	3.001	3.001	3.001	0.0622

Then, the self-rotation angle of wheel 2 increases and the self-rotation angle of wheel 1 decreases resulting from the structure of the robot, as shown in Fig. 4a. The change of these values is shifted in time. The change in motion is confirmed by a change in the angular velocity of the wheels, see Fig. 4b, and the course of angular accelerations of the wheels, see Fig. 4c. When the point S turns an angle $\pi/2 \text{ rad}$ then the angular velocities and angular accelerations have the same values, which is followed by a change in the values and turns of vectors of these kinematics parameters. The obtained parameters of motion of the driving wheels constitute the

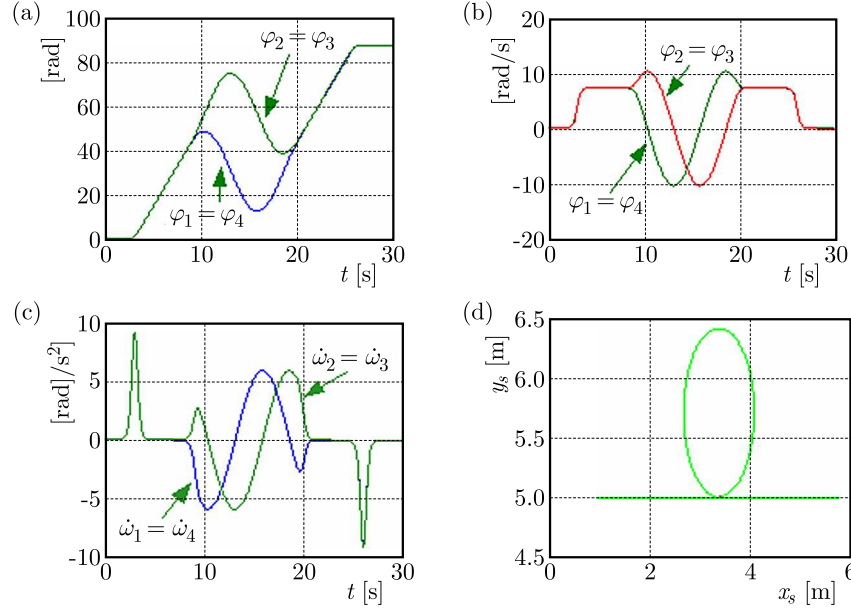


Fig. 4. The parameters set for the movement of the robot wheel and the path of the point S :
 (a) values of self-rotation angles of the driving wheels, φ_1, φ_4 and φ_2, φ_3 , (b) angular velocity of self-rotation of the driving wheels ω_1, ω_4 and ω_2, ω_3 , (c) angular accelerations $\dot{\omega}_1, \dot{\omega}_4, \dot{\omega}_2, \dot{\omega}_3$,
 (d) set trajectory for the point S

set trajectory of motion for the control system. For simulation of the control system, values of the robot parameters have been adopted as specified in Table 1 and the remaining data are: $\mathbf{A} = \text{diag}[2, 2, 2]$, $K_D = 0.5(1 + 1/\gamma)$, $\mathbf{P} = \text{diag}[100, \dots, 100]$, $\gamma = 0.2$, $\boldsymbol{\tau}_d = \mathbf{0}$. In order to check the robustness of the proposed solution, it has been also assumed that for the time $t \geq 15$ s there is a parametric disturbance $\mathbf{a} + \Delta\mathbf{a}$ where $\Delta\mathbf{a} = [0, 0, 0, 0, 1, 1, 1, 0]^T$, associated with the change of the rolling friction of the robot wheels. The neural network adopted in simulation to compensate for the robot nonlinearity and the variable operating conditions consist of 6 sigmoidal bipolar neurons whose first layer weights are generated by a random number generator from the range $[-0.1, 0.1]$. A separate neural network for each element is used for approximation of the nonlinear function $\mathbf{f}(\mathbf{x}_r) \in \mathbb{R}^3$. The calculations are made by adopting the Euler method of integration with the time discretization step 0.01 s. In the process of initializing the neural network, zero initial values of the output layer weights are assumed. In order to evaluate quality of the generated robust control and implementation of tracking motion, the following quality indicators have been adopted, restricted to the assessment of motion only for wheels 1 and 2:

- maximum value of the angle of rotation error $e_1 = (\varphi_{1d} - \varphi_1)$ [rad], $e_2 = (\varphi_{2d} - \varphi_2)$ [rad], $e_{\max(\cdot)} = \max |e_{(\cdot)}|$ [rad], $\varphi_{1d}, \varphi_{2d}$ are the set angles of wheel rotation, Fig. 4a,
- maximum value of the angular velocity error $\dot{e}_{\max(\cdot)} = \max |\dot{e}_{(\cdot)}|$ [rad/s],
- root-mean-squared error for wheel rotation angles, $\varepsilon_1 = \sqrt{(1/n) \sum_{k=1}^n e_{1k}^2}$, $\varepsilon_2 = \sqrt{(1/n) \sum_{k=1}^n e_{2k}^2}$ [rad], where k is the number of subsequent discrete measurements, $n = 3001$ – total number of discrete measurements,
- root-mean-squared error for tracking the given angular velocity $\dot{\varepsilon}_1 = \sqrt{(1/n) \sum_{k=1}^n \dot{e}_{1k}^2}$, $\dot{\varepsilon}_2 = \sqrt{(1/n) \sum_{k=1}^n \dot{e}_{2k}^2}$ [rad/s],
- generalised root-mean-squared error: $s_1 = \dot{e}_1 + \lambda e_1$, $s_2 = \dot{e}_2 + \lambda e_2$, $\nu_1 = \sqrt{(1/n) \sum_{k=1}^n s_{1k}^2}$, $\nu_2 = \sqrt{(1/n) \sum_{k=1}^n s_{2k}^2}$ [rad/s], mean-squared error of distance d_k , $\rho = \sqrt{(1/n) \sum_{k=1}^n d_k^2}$ [m], where $d_k = \sqrt{(x_{Sk} - x_{dSk})^2 + (y_{Sk} - y_{dSk})^2}$ [m], $k = n$ is the distance between the set

(x_{dS}, y_{dS}) , Fig. 4d and implemented (x_S, y_S) locations of the selected point S of the mobile robot in the xy plane during motion,

- maximum distance $d_{max} = \max(d_k)$ [m].

Implementing adopted control algorithm (5.7), patterns of control errors have been obtained as shown in Fig. 5.

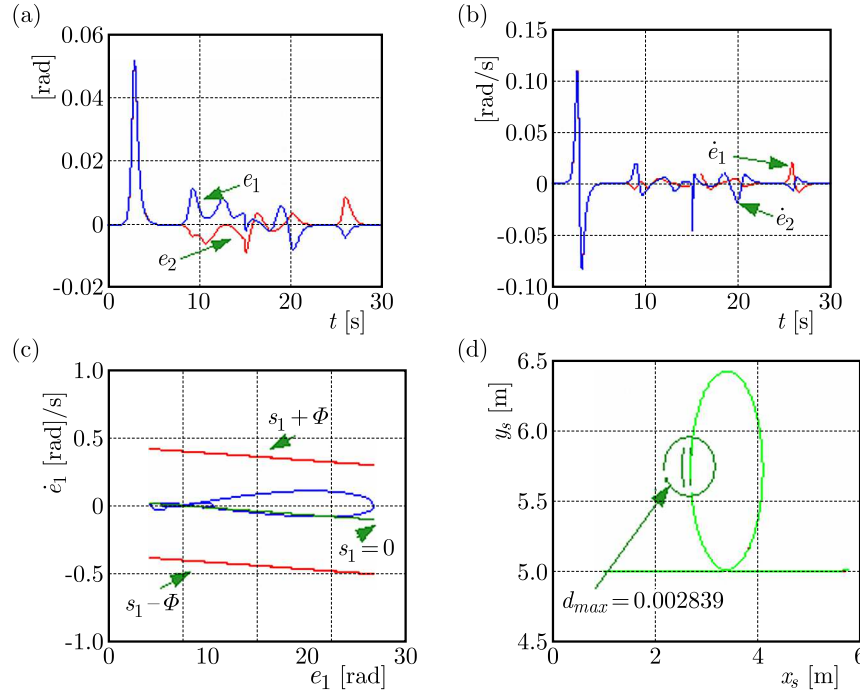


Fig. 5. Results for the obtained errors: (a) patterns of errors of tracking the rotation angles of wheels 1 and 2, (b) patterns of errors of tracking the angular velocity of wheels 1 and 2, (c) pattern of error in the phase plane for the generalized error s_1 , (d) implementation of the set trajectory for the point S

The quantitative assessment of the solution is given in Tables 2 and 3.

Table 2. Values of the quality indicators for the robust neural networks control

Indicator	$e_{i\max}$ [rad]	ε_i [rad]	$\dot{e}_{i\max}$ [rad/s]	$\dot{\varepsilon}_i$ [rad/s]	ν_i [rad/s]
wheel 1, $i = 1$	0.05139	0.007379	0.1087	0.01529	0.02125
wheel 2, $i = 2$	0.05184	0.007703	0.1097	0.01578	0.02205

Table 3. Values of the indicators d_{max} , ρ for the robust neural networks control

Indicator	d_{max} [m]	ρ [m]
Value	0.002839	0.0004151

Having analysed the changes in the individual indicators of the quality of motion implementation in the presence of variable operating conditions, it can be concluded that a high accuracy in the implementation of the adopted method of solution has been obtained. However, Fig. 6 presents patterns of control signals in the presence of variable operating conditions of the object, resulting from the assumed resistance to motion in the form of a change in the rolling friction. The neural networks compensation of the robot nonlinearity plays a predominant role in the control structure, as shown in Fig. 6b, in comparison with the PD control, Fig. 6c. The observed parametric disturbance is particularly visible for driving wheel 2.

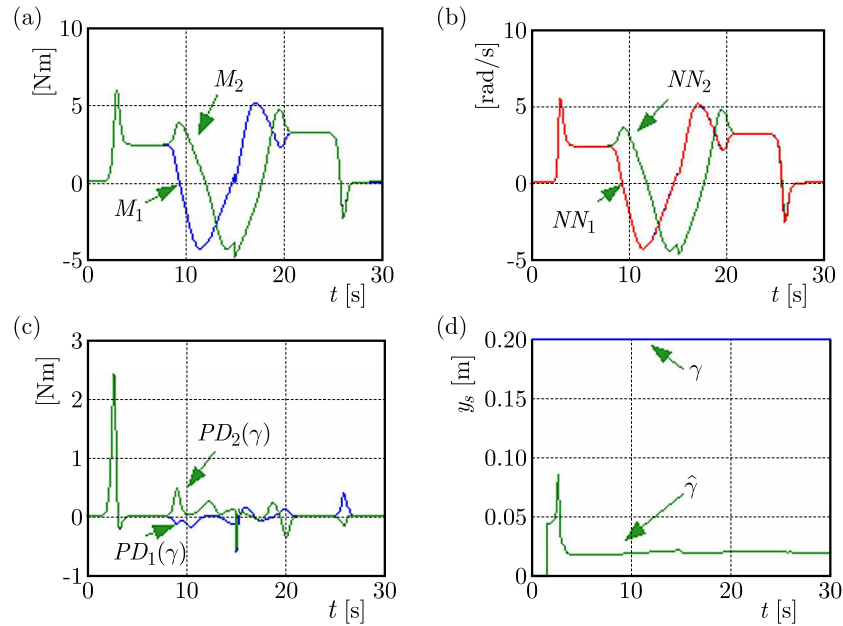


Fig. 6. Results of simulation of the neural networks control system: (a) total control, (b) $NN_{(.)}$ neural networks control, (c) PD control (γ), (d) evaluation of the system robustness $\hat{\gamma} \leq \gamma$

The limitation of the signals shown in Fig. 6 confirms stability of the adopted solution in accordance with Lyapunov's interpretation of stability. Figure 6d presents the results of the solution for the robust neural networks control of MRK_M motion which changes over time, with equation (3.7) constituting the evaluation of this control method. As indicated by the patterns shown in Fig. 6d, the analysed system has gain $L_2 < \gamma$, for $\gamma = 0.2$, and the condition $0 \leq \hat{\gamma} < \gamma$ is met, thus equation (3.5) is satisfied.

7. Summary

This paper presents a novel approach to the problem of controlling mechanical objects of unspecified description considering variable operating conditions. In order to solve the task of controlling a mobile robot with mecanum wheels taking into account the compensation for nonlinearity and variable operating conditions of the object, Lyapunov's stability theory has been applied including the HJ inequality. A neural network with basic sigmoid functions has been used to compensate for the nonlinearity and variable operating conditions of the robot. Additionally, there is a $PD(\gamma)$ controller in the control structure, i.e. the structure of moments driving the wheels. The gain values of the $PD(\gamma)$ controller have been determined based on the HJ inequality, thus formulating an algorithm which is stable and interference-resistant from the perspective of input-output signals.

References

1. ABDELRAHMAN M., ZEIDIS I., BONDAREV O., ADAMOV B., BECKER F., ZIMMERMANN K., 2014, A description of the dynamics of a four wheel mecanum mobile system as a basis for a platform concept for special purpose vehicles for disabled persons, *58-th Ilmenau Scientific Colloquium*
2. ABU-KHALAF M., LEWIS F.L., 2006, *Nonlinear H_2/H_∞ Constrained Feedback Control*, Springer Verlag, London

3. BASAR T., BERNARD P., 1995, *H_∞ Optimal Control and Related Minimax Design Problems*, Birkhäuser
4. BECKER F., BONDAREV O., ZEIDIS I., ZIMMERMANN K., ABDELRAHMAN M., ADAMOV B., 2014, An approach to the kinematics and dynamics of a four-wheeled mecanum vehicles, *Scientific Journal of IfToMM „Problems of Mechanics”*, special issue, **2**, 55, 27-37
5. CANUDAS DE WIT C., SICILIANO B., BASTIN G., 1996, *Theory of Robot Control*, Springer-Verlag, London
6. FARIWATA S.S., FILEV D., LANGARI R., 2000, *Fuzzy Control*, John Wiley & Sons, Ltd, England
7. GIERGIEL M., HENDZEL Z., ŻYLSKI W., 2002, *Modelling and Control of Mobile Robots* (in Polish), PWN, Warszawa
8. HAN K.-L., CHOI O.-K., KIM J., KIM H., LEE J.S., 2009, Design and control of mobile robot with mecanum wheel, *ICROS-SICE International Joint Conference*, Fukuoka International Congress Center, Japan, 2932-2937
9. HENDZEL Z., 2007, An adaptive critic neural network for motion control of a wheeled mobile robot, *Nonlinear Dynamics*, **50**, 4, 849855, DOI 10.1007/s11071-007-9234-1
10. HENDZEL Z., RYKAŁA Ł., 2015, Description of kinematics of a mobile wheeled robot with wheels of the mecanum type (in Polish), *Modelowanie Inżynierskie*, **57**, 26, 5-12
11. LEWIS F.L., JAGANNATHAN S., YESILDIREK A., 1999, *Neural Network Control of Robot Manipulators and Nonlinear Systems*, Taylor & Francis, London
12. LEWIS F.L., VRABIE D.L., SYROMS V.L., 2012, *Optimal Control*, 3rd ed., Wiley & Sons, New Jersey
13. LIN L.-C., SHIH H.-Y., 2013, Modeling and adaptive control of an omni-mecanum-wheeled robot, *Intelligent Control and Automation*, **4**, 166-179
14. NASH J., 1951, Non-cooperative games, *Annals of Mathematics*, **2**, 286-295
15. PARK J., KIM S., KIM J., KIM S., 2010, Driving control of mobile robot with mecanum wheel using fuzzy inference system, *International Conference on Control, Automation and Systems*, Gyeonggi-do, 2519-2523
16. SIEGWART R., NOURBAKHSI I.R., SCARAMUZZA D., 2011, *Introduction to Autonomous Mobile Robots*, 2nd Edition, MIT Press, London
17. SLOTINE J.-J.E., LI W., 1991, *Applied Nonlinear Control*, Prentice Hall, NJ
18. SZUSTER M., HENDZEL Z., 2018, *Intelligent Optimal Adaptive Control for Mechatronic Systems*, Springer International Publishing AG
19. TSAI C.-C., WU H.-L., 2010, Nonsingular terminal sliding control using fuzzy wavelet networks for mecanum- wheeled omni-directional vehicles, *IEEE International Conference on Fuzzy Systems*, 1-6
20. TSAI C.-C., TAI F.-C., LEE Y.-R., 2011, Motion controller design and embedded realization for mecanum wheeled omni-directional robots, *Proceedings of the 8th World Congress on Intelligent Control and Automation*, Taiwan, 546-551
21. VAN DER SCHAFT A.J., 1992, L2-gain analysis of nonlinear systems and nonlinear state feedback H_{∞} control, *IEEE Transactions on Automatic Control*, **37**, 6, 770-784
22. VAN DER SCHAFT A.J., 2000, *L2-Gain and Passivity Techniques in Nonlinear Control*, Springer Verlag, London
23. ŻYLSKI W., 1996, *Kinematics and Dynamics of Wheeled Mobile Robots* (in Polish), Rzeszow University of Technology Publishing Press, Rzeszow

IMPLICATIONS OF INERTIA FOR HYDROELASTIC INSTABILITY OF HERSCHEL-BULKLEY FLUIDS IN PLANE POISEUILLE FLOW

SHAPOUR JAFARGHOLINEJAD

*Department of Mechanical Engineering, Ardabil Branch, Islamic Azad University, Ardabil, Iran, and
Young Researchers and Elite Club, Ardabil Branch, Islamic Azad University, Ardabil, Iran*

MOHAMMAD NAJAFI

*Department of Mechanical and Aerospace Engineering, Science and Research Branch, Islamic Azad University, Tehran,
Iran; e-mail: m.najafi.srbu@gmail.com*

This study investigates the effects of inertia on the hydroelastic instability of a pressure-driven Herschel-Bulkley fluid passing through a two-dimensional channel lined with a polymeric coating. The no-viscous hyperelastic polymeric coating is assumed to follow the two-constant Mooney-Rivlin model. In this work, analytical basic solutions are determined for both the polymeric gel and the fluid at very low Reynolds numbers. Next, the basic solutions are subjected to infinitesimally-small, normal-mode perturbations. After eliminating the nonlinear terms, two 4-th order differential equations are obtained. The equations with appropriate boundary conditions are then numerically solved using the shooting method. The results of the solution show that the inertia terms in the perturbed equations destabilize the pressure-driven Herschel-Bulkley fluid flow. The investigation reveals that the elastic parameter has a stabilizing effect on the flow. Also, based on the obtained results, the yield stress, depending on the power-law index, has a stabilizing or destabilizing effect on the flow. Since in this work the inertia terms are included in the pertinent governing equations, therefore, the results of this study are much more realistic and reliable than previous works in which inertia terms were absent. In addition, unlike the previous works, the present study considers both the shear-thinning and shear-thickening types of fluids. Hence, the results of this work embrace all the fluids which obey the Herschel-Bulkley model.

Keywords: inertia, instability, Herschel-Bulkley fluid, Mooney-Rivlin solid

1. Introduction

In general, most fluids flowing at very low Reynolds numbers, like creep flow, when passing through deformed channels sustain a type of instability called hydroelastic instability. This type of instability is much more intense when dealing with a non-Newtonian fluid passing through a channel coated with a highly-compliant material. In some industries, this instability phenomenon is of potential importance for enhancement of mixing in microfluidic devices. That is, due to vanishingly-small Reynolds numbers in such devices, they suffer from a very weak mixing because of the laminar nature of the creeping flow. To improve this poor mixing, the channel inner surface can be covered with a layer of a soft polymeric gel. By this way, when the fluid flows through the channel, certain waves may become unstable at the fluid-solid interface which eventually cause flow turbulence leading to a great improvement of the mixing performance which, in turn, advances the flow heat and mass transfer. The degree in improvement of the mixing, however, highly depends on the rheological properties of both the solid gel and fluid. Basically, most of what is available in the literature with regard to the hydroelastic instability assumes Newtonian fluids, which is not realistic, at least, when dealing with mixing enhancement in microfluidic

devices. In the previous years, the fluid viscous effects on hydroelastic instability in the creeping planar Poiseuille flow have been investigated by a few researchers in the field.

Kramer (1960) concentrated on advancing the concept of boundary layer stabilization, in particular, hydroelastic instability for many non-Newtonian fluids flowing through channels. In his works, he drew a conclusion that the stability of boundary layers could be affected by compliant coatings. In that sense, he was able to experience a considerable drag reduction for underwater moving bodies which were covered with some types of compliant coatings.

Gad-el-Hak (2002), Babenko and Kozlov (1972) and Fu and Joseph (1970) reported that although compliant materials can stabilize different types of instabilities, they might cause other types of instabilities such as hydro- and aero-elastic instabilities. In fact, it was noticed by researchers that stable fluid flows inside rigid channels became unstable in deformable channels.

Regarding fluid flows in microchannels, fluid mixing in such channels, in practice, is hardly possible according to reports of Jensen (1999), Franjione and Ottino (1992) and Chien *et al.* (1986). In laminar flow domains, microscale dimensions lead to very low Reynolds numbers. Therefore, the concept of instability for such tiny devices becomes a prime concern when one is to advance the mixing effect in order to enhance the transfer of heat and mass as demonstrated by Kandlikar *et al.* (2005) and Ottino (1989).

Today, it is realized that rheological properties of both Newtonian and non-Newtonian fluids and coating materials used are very important for design purposes to reach fluid stability (Jafargholinejad, 2015; Muralikrishnan and Kumaran, 2002; Davies and Carpenter, 1997). Recently, Pourjafar *et al.* (2015) studied stability of power-law fluids in the creeping plane Poiseuille flow and analysed the effect of wall compliance on the stability of such fluids. In a study by Jafargholinejad *et al.* (2015), linear instability of viscoplastic fluids in the plane Poiseuille flow was investigated in the absence of inertia. Based on their results, the yield stress was found to have a stabilizing or a destabilizing effect on the pressure-driven flow of Herschel-Bulkley fluids, depending on the power-law exponent. However, Jafargholinejad *et al.* (2015) did not include the inertia terms and did not consider both the shear-thinning and shear-thickening fluids in their work.

Based on the above literature survey, to the best of the authors' knowledge, there is no published work on hydroelastic instability which takes into account the effects of inertia terms on both the shear-thinning and shear-thickening fluids.

The current study investigates the effect of inertia terms on the hydroelastic instability of pressure-driven Herschel-Buckley fluids flowing at very low Reynolds numbers through a two-dimensional channel lined with a polymeric solid gel. The no-viscous polymeric gel is assumed to follow the hyperelastic Mooney-Rivlin model since its solid model fits the rheological data for soft polymeric gels and provides more realistic results. In this study, very low laminar Reynolds numbers (creeping flow condition) are considered to simulate microfluidic fields industrial applications. Also, by varying the value of n , the power-law index, from $n < 1.0$ to $n > 1.0$, this study, unlike the previous works, considers the hydroelastic instability for both the shear-thinning as well as the shear-thickening fluids obeying the Herschel-Buckley non-Newtonian model.

2. Physical description of the problem and governing equations

Figure 1 illustrates a pressure-driven laminar, isothermal and viscoplastic fluid flowing (with no gravity effect) between two rigid parallel plates of $2R$ height and HR thickness coated with a compliant polymeric material. Both, the fluid and solid are assumed to have the same density and they are incompressible. The dashed curves in the figure illustrate a typical sinusoidal perturbation imposed on the fluid-solid interface. The origin of both the Lagrangian axes (X, Y) and the Eulerian axes (x, y) is set at the fluid-solid interface (Fig. 1).

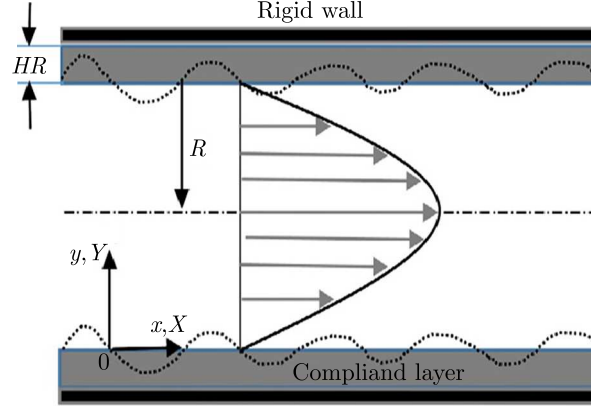


Fig. 1. Schematic of a channel lined with a compliant coating

The equations of motion for the solid are (Lai 2010)

$$\det(\mathbf{F}) = 1 \quad \rho_s \frac{\partial^2 \mathbf{w}}{\partial t^2} \bigg|_X = \nabla_X \cdot \mathbf{P} \quad (2.1)$$

In Eq. (2.1)₂, the subscript X denotes the differentiation in the Lagrangian frame of reference, ρ_s denotes density of the solid, \mathbf{F} – deformation gradient tensor, \mathbf{w} – current position of solid particles, and \mathbf{P} is the Piola-Kirchhof stress tensor which is defined by

$$\mathbf{P} = \boldsymbol{\sigma}(\mathbf{F}^{-1})^T \quad (2.2)$$

where $\boldsymbol{\sigma} = -p\boldsymbol{\delta} + \boldsymbol{\tau}$ is the Cauchy stress tensor with $\boldsymbol{\tau}$ being the deviatoric part of the stress tensor. In dimensionless form, the stress tensor for the Mooney-Rivlin solid can be written as

$$\boldsymbol{\sigma} = -p_s\boldsymbol{\delta} + \mathbf{B} + \frac{C_2}{C_1}\mathbf{B}^{-1} \quad (2.3)$$

where p is pressure, $\boldsymbol{\delta}$ – identity tensor, $\mathbf{B} = \mathbf{F}\mathbf{F}^T$ is the Cauchy Green strain tensor, and C_1 and C_2 are material constants (also known as the Mooney-Rivlin constants). Here, $C_2/C_1 = \beta$, where β is the elastic parameter. It needs to be mentioned that in this work C_1 (Mooney-Rivlin 1st parameter) is used for making all the stress terms dimensionless. Now, the momentum equation, in dimensionless form, for the solid side becomes

$$\text{Re}_s \frac{\partial^2 \mathbf{w}}{\partial t^2} \bigg|_X = \nabla_X \cdot \mathbf{P} \quad (2.4)$$

where $\text{Re}_s = \rho_s(C_1 R^2 / \eta^2)$ is referred to as the solid fictitious Reynolds number. Here, η is the apparent viscosity of the fluid. It is noted here that η/C_1 is used to make ‘time’ dimensionless and R is used for scaling the length.

For the fluid side, the conservation of mass equation is incorporated into the Cauchy equations of motion, and the resulting equations become (Lai *et al.*, 2010)

$$\rho_f \frac{D\mathbf{v}}{Dt} = -\nabla p + \nabla \cdot \boldsymbol{\tau} \quad \nabla \cdot \mathbf{v} = 0 \quad (2.5)$$

where ρ_f is the fluid density and D/Dt is the material substantial derivative. Here, \mathbf{v} denotes the velocity vector, p is the isotropic pressure, and $\boldsymbol{\tau}$ denotes the deviatoric stress tensor. In this

study, it is assumed that the working fluid follows the Herschel Bulkley model; that is (Bird, 1987)

$$\boldsymbol{\tau}_f = \left(T_y |\boldsymbol{\Pi}_{2D}|^{\frac{-1}{2}} + m \left| \frac{1}{2} \boldsymbol{\Pi}_{2D} \right|^{\frac{n-1}{2}} \right) 2\mathbf{D} \quad (2.6)$$

where T_y denotes the yield stress, $\boldsymbol{\Pi}_{2D}$ denotes the second invariant of the rate-of-deformation tensor, m denotes the consistency index, n is the power-law exponent, $2\mathbf{D} = \nabla \mathbf{v}^T + \nabla \mathbf{v}$ – rate-of-deformation tensor, and the superscript T denotes the velocity-gradient tensor ($\nabla \mathbf{v}$) transpose.

In dimensionless form, continuity equation (2.5)₂ remains unchanged, but the momentum equation (2.5)₁ becomes

$$\text{Re}_f \frac{D\mathbf{v}}{Dt} = -\nabla p + \nabla \cdot \boldsymbol{\tau} \quad (2.7)$$

where Re_f denotes the fluid Reynolds number which is defined as $\text{Re}_f = \rho_f (C_1 R^2 / \eta^2)$.

Now, to find the base-state solution for the solid (assuming that both the velocity and shear stress are continuous at the fluid-solid interface), the following basic deformation and stress tensors in Lagrangian form are employed

$$w_X(X, Y) = X + \frac{1}{1-\beta} \left[\frac{1}{2} G(Y^2 - H^2) + (\tau_y - G)(Y + H) \right] \quad w_Y(Y) = Y \quad (2.8)$$

where G and H are the pressure gradient and the coating thickness in dimensionless form, respectively. Therefore, the basic stress tensor for the solid becomes (Jafargholinejad *et al.*, 2015)

$$\boldsymbol{\sigma} = \begin{bmatrix} -p_s + 1 + \left(\frac{\partial w_X}{\partial Y} \right)^2 + \beta & \frac{\partial w_X}{\partial Y} (1 - \beta) \\ \frac{\partial w_X}{\partial Y} (1 - \beta) & -p_s + 1 + \beta \left(1 + \left(\frac{\partial w_X}{\partial Y} \right)^2 \right) \end{bmatrix} \quad (2.9)$$

Assuming that the fluid-solid interface is flat, then, in dimensionless form, the basic stress and basic velocity equations can be written as (Jafargholinejad *et al.*, 2015)

$$\boldsymbol{\sigma} = \begin{bmatrix} -p_f & \tau_y + \mu \left(\frac{\partial v_x}{\partial y} \right)^n \\ \tau_y + \mu \left(\frac{\partial v_x}{\partial y} \right)^n & -p_f \end{bmatrix} \quad v_x = -\frac{n}{n+1} \left(-\frac{G}{\mu} \right)^{\frac{1}{n}} [(1-y)^{\frac{n+1}{n}} - 1] \quad (2.10)$$

3. Stability analysis

Knowing the base-state solutions, they are now subjected to infinitesimally-small, time dependent, normal-mode perturbations in order to make linear stability analysis. Through the normal-mode concepts (Drazin and Reid, 2004), the flow variables are expressed in terms of the sum of infinitesimal perturbation and the base-state solution, therefore

$$f(x, y, t) = \bar{f} + f' = \bar{f} + \hat{f}(y) e^{ikx + \alpha t} \quad (3.1)$$

where (\bullet') denotes perturbation to the base-state, $(\hat{\bullet})$ is the perturbation amplitude, $(\bar{\bullet})$ denotes the basic flow, k is the wave number of perturbation (a real number), α – the growth rate (a complex number), and t – time.

To come up with a set of relations in terms of the perturbation variables, the perturbed variables are incorporated into the governing equations. After determining the appropriate boundary conditions and linearizing them, the intended set of equations are obtained.

Now, based on what is described above, the solid and fluid side stability equations are derived. For the solid side, Eq. (3.1) is substituted into the appropriate governing equations for each field variable, and the resulting equations are linearized to obtain the following ordinary differential equation

$$\begin{aligned} \text{Re}_s\{\alpha^2[1 + 2k - ik^2(1 + Q^2) + kdQ]\} + S_0 w_Y(Y) + S_1 d^2 w_Y(Y) \\ + S_2 d^2 w_Y(Y) + S_3 d^3 w_Y(Y) + S_4 d^4 w_Y(Y) = 0 \end{aligned} \quad (3.2)$$

where

$$\begin{aligned} S_0 &= \left(k^2 + ik^2 \frac{\partial \bar{p}_s}{\partial Y}\right) dQ + ik^4 Q^2 + ik^2 Q(dQ) - ik^4 - ik^2 \frac{\partial^2 \bar{p}_s}{\partial Y^2} \\ &\quad - k(d^3 Q) + \beta[ik^4(1 + Q^2) - k^3(dQ) + 2ik^2(dQ)^2 + ik^2 Q(d^2 Q) + k(d^3 Q)] \\ S_1 &= (2k^3 + 2ik^2 dQ)Q + k \frac{\partial^2 \bar{p}_s}{\partial X \partial Y} - 3k(dQ) + \beta[3k(d^2 Q) - 2ik^2 Q(dQ) - 2k^3 Q] \\ S_2 &= -3kdQ + 2ik^2 + ik^2 Q^2 + \beta[-ik^2 Q^2 + 3k(dQ) - 2ik^2] \\ S_3 &= 2kQ(\beta + 1) \quad S_4 = i(\beta - 1) \end{aligned} \quad (3.3)$$

where $Q = (1 - \beta)^{-1}(GY + \tau_y - G)$.

It is noted here that, in the special case when $\text{Re}_s = 0$, Eqs. (3.3) reduce to the analogous equation reported earlier by Jafargholinejad *et al.* (2015).

Now, for the fluid side, the linearized form of the second invariant of the rate-of-deformation tensor in the perturbed state can be written as

$$(\Pi_{2D})^{\frac{n-1}{2}} = \lambda^{n-1} \left[1 + \left((n-1) \frac{d\hat{v}_x}{\lambda} + i(n-1)k \frac{\hat{v}_y}{\lambda} \right) e^{ikx + \alpha t} \right] \quad (3.4)$$

where $\lambda = d\bar{v}_x/dy$. The equations governing the perturbations for the fluid side can be shown as

$$ik\hat{v}_x + d\hat{v}_y = 0 \quad (3.5)$$

and

$$\begin{aligned} \text{Re}_f \left[\left(\frac{1}{ik} \frac{d^2 \hat{v}_y}{dy^2} + ik\hat{v}_y \right) v_x(y) - \frac{1}{ik} d\lambda + \alpha \left(\hat{v}_y - \frac{1}{k^2} \right) \right] + F_0 \hat{v}_y + F_1 d\hat{v}_y \\ + F_2 d^2 \hat{v}_y + F_3 d^3 \hat{v}_y + F_4 d^4 \hat{v}_y = 0 \end{aligned} \quad (3.6)$$

where

$$\begin{aligned} F_0 &= \lambda^{n-1} (3k^2 \mu n^2 - 2k^2 \mu n - k^2 \mu n^3) (d\lambda)^2 + \lambda^n (k^2 \mu n - k^2 \mu n^2) d^2 \lambda + \lambda^{n+1} (-k^4 \mu n) \\ F_1 &= \lambda^{n-1} [-\mu n k^2 (n-1)(n-2)(d\lambda)^2] + \lambda^n [-\mu n k^2 (n-1)(d\lambda)^2] + \lambda^{n+1} (-\mu n k^4) \\ F_2 &= -4k^2 T_y d\lambda + \lambda^n (-2k^2 \mu n^2 + 6k^2 \mu n - 4k^2 \mu) d\lambda \\ F_3 &= -4k^2 T_y d\lambda + \lambda^n [-2\mu k^2 (n-1)(n-2)d\lambda] \\ F_4 &= \lambda (4k^2 T_y) + \lambda^{n-1} (3\mu n^2 - 2\mu n - \mu n^3) (d\lambda)^2 + \lambda^n (\mu n^2 + \mu n) d^2 \lambda + \lambda^{n+1} (4k^2 \mu - 2k^2 \mu n) \end{aligned} \quad (3.7)$$

In the above equations, d stands for the conventional total derivative d/dy . For Newtonian fluids (i.e., for $n = 1$), this equation (Eqs. (3.7)) reduces to the Orr-Sommerfeld equation, as it should. In the special case of $n \neq 1$ and $\text{Re}_f = 0$, Eq. (3.7) reduces to the form reported by Jafargholinejad *et al.* (2015).

4. Boundary conditions

To come up with right boundary conditions, the method of solution must be identified. In the present work, the Eulerian-Lagrangian type of framework is employed. That is, the Eulerian framework is used for the Herschel-Bulkley fluid variables, and the Lagrangian approach is used for the Mooney-Rivlin hyperelastic coating. Regarding the hyperelastic solid side, the no-slip condition is assumed at the channel inside walls. For the fluid side, however, the varicose mode perturbation is considered at the channel centreline. That is, the oscillation of the upper and lower fluid-solid interface goes out of phase, hence, based on Fig. 1, an even function of y is assumed. Therefore, at the channel centreline the following boundary conditions can be used

$$\hat{v}_y \Big|_{y=1} = 0 \quad d\hat{v}_x \Big|_{y=1} = 0 \Rightarrow d^2\hat{v}_y \Big|_{y=1} = 0 \quad (4.1)$$

with the assumption of no deformation for the outer side of the channel rigid wall

$$\hat{w}_Y \Big|_{Y=-H} = 0 \quad \hat{w}_X \Big|_{Y=-H} = 0 \Rightarrow d\hat{w}_Y \Big|_{Y=-H} = 0 \quad (4.2)$$

For the Eulerian variables, keeping the first-order terms of the Taylor series expansion, the following conditions can be written

$$\begin{aligned} \Phi \Big|_{\text{perturbed interface}} &= \Psi \Big|_{\text{perturbed interface}} \\ \Phi \Big|_{y=0} + \hat{w}_X \frac{\partial \Phi}{\partial x} \Big|_{y=0} + \hat{w}_Y \frac{\partial \Phi}{\partial y} \Big|_{y=0} &= \Psi \Big|_{\text{perturbed interface}} \end{aligned} \quad (4.3)$$

where Φ and Ψ refer to arbitrary variables at the interface for the fluid and solid sides, respectively.

At $y = Y = 0$, the linearized form of the boundary conditions becomes

$$\hat{v}_y \Big|_{y=0} = \alpha \hat{w}_Y \Big|_{Y=0} \quad \hat{v}_x \Big|_{y=0} + \lambda_0 \hat{w}_Y \Big|_{Y=0} = \alpha \hat{w}_X \Big|_{Y=0} \quad (4.4)$$

and

$$\begin{aligned} n\mu \left(\frac{du_0}{dy} \right)^{n-1} \left[\frac{d\hat{v}_x}{dy} + ik\hat{v}_y \right] + \hat{w}_Y G + ik\hat{w}_Y \left(\frac{df}{dy} \right)^2 - ik\hat{w}_Y - \frac{df}{dy} \frac{d\hat{w}_Y}{dY} - \frac{d\hat{w}_X}{dY} \\ + \beta \left(2ik\hat{w}_Y + \frac{df}{dy} \frac{d\hat{w}_Y}{dY} + \frac{d\hat{w}_X}{dY} \right) = 0 \end{aligned} \quad (4.5)$$

and

$$\begin{aligned} -\hat{p}_f + \hat{p}_s - ik\hat{w}_Y \left[\mu \left(\frac{du_0}{dy} \right)^n + \tau_y \right] + 2\mu \left(\frac{du_0}{dy} \right)^{n-1} \frac{d\hat{v}_y}{dy} + 2\tau_y \left(\frac{du_0}{dy} \right)^{-1} \frac{d\hat{v}_y}{dy} \\ + ik\hat{w}_Y \frac{df}{dy} - 2\frac{d\hat{w}_Y}{dY} - k^2 T \hat{w}_Y + \beta \left(-2ik\hat{w}_Y - 2\frac{df}{dy} \frac{d\hat{w}_X}{dY} - ik\hat{w}_Y \frac{df}{dy} \right) = 0 \end{aligned} \quad (4.6)$$

where $\lambda_0 = (dv_x/dy)|_{y=0}$ and $T = \gamma/(C_1 R)$, and where T is dimensionless interfacial tension and γ is interfacial tension.

5. Numerical method and results

To make the stability analysis, Eqs. (3.3) for the solid side and Eqs. (3.7) for the fluid side and their pertinent boundary conditions are to be solved. To do so, a computer code is developed which uses the shooting method. A similar method like the one utilized in the present study, was

used by Lee and Finlayson (1986) as well as Gkanis and Kumar (2005). It has also been used in the author's earlier works and produced reliable results even for the Mooney-Rivlin solids. The proposed code takes Eqs. (3.3) and (3.7) for the solid and fluid sides respectively together with the pertinent boundary conditions (Eqs. (4.1)-(4.7) as the input. The code begins solution at one end of the proposed boundary and shoots to the other end using an initial value solver iteratively to the point that the boundary condition at the other end is converged to its precise value. It has to be mentioned here that the developed code is verified for Newtonian data for a channel lined with a neo-Hookean gel under creeping flow conditions, see Gkanis and Kumar (2005) for details.

To solve Eqs. (3.3) and (3.7) simultaneously, two 4th-order boundary-value problems (Eqs. (3.3) and (3.7)) are treated like initial-value problems since the fluid and solid boundary conditions are coupled at the interface. Next, each 4th-order differential equation is transformed to a system of four 1st-order, linear and homogenous ordinary differential equations having a total of four unknown coefficients. To solve these ordinary differential equations, four boundary conditions are required for each, the fluid and the solid. Noting that there are only two explicit boundary conditions available (two for the fluid, Eqs. (4.1), and two for the solid, Eqs. (4.2)), the other two orthogonal boundary conditions have to be guessed for the fluid side and for the solid side to solve the problem. These unknown constants can be determined by constructing a matrix which contains the interfacial boundary conditions (Eqs. (4.5)-(4.7)). The computer code uses the developed shooting technique, takes the above mentioned matrix and other inputs like the Reynolds numbers, power-law index, surface tension, elastic parameter, and wall thickness, and by varying the channel pressure gradient, it calculates the real value of α and the growth rate of perturbations. Now, at the critical pressure gradient $real(\alpha) = 0$, the flow is stable for $real(\alpha) < 0$ and unstable flow is experienced for $real(\alpha) > 0$. Regarding the shooting technique, it actually uses the methods developed for solving initial value problems. The idea is to write the boundary value problem in vector form and to begin solution at one end of the boundary value problem and shoot to the other end with an initial value solver until the boundary condition at the other end converges to its precise value.

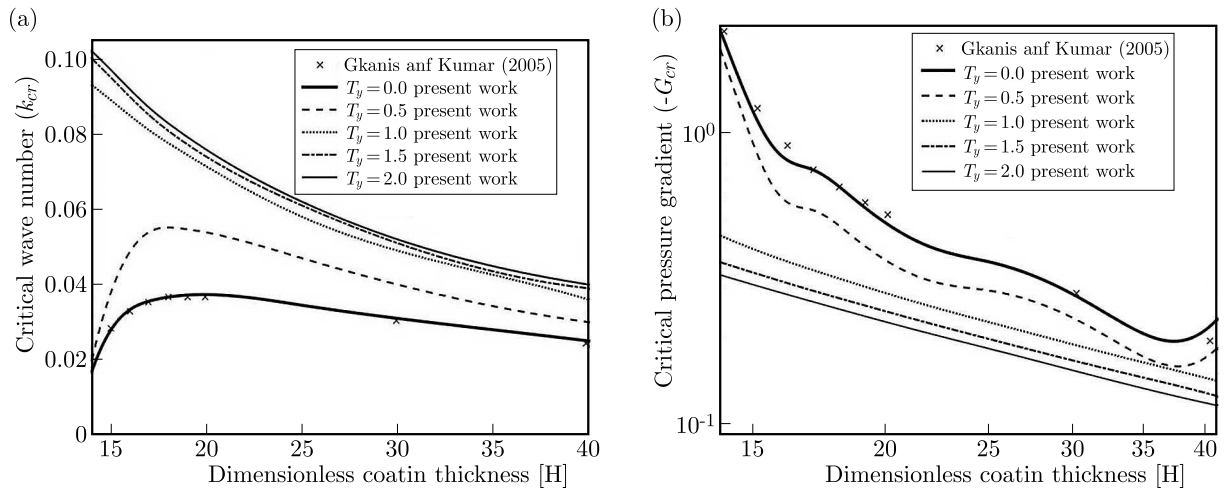


Fig. 2. Comparison between the present results for Newtonian fluids (solid line) and the numerical data reported by Gkanis and Kumar (2005), (symbols) at $Re = 0$ for: (a) the critical pressure gradient, and (b) the critical wave number

Figures 2a and 2b illustrate the effects of the yield stress on the critical wave number and the critical pressure gradient at different compliant coating thicknesses, respectively. The figures also compare the plots of the present work obtained from the developed code for when the fluid becomes Newtonian (i.e. $n = 1$ and $T_y = 0$ in Eq. (2.6)) with the Newtonian data of Gkanis

and Kumar (2005). This comparison actually verifies the present results as they coincide with the data of Gkanis and Kumar (2005) in both Figs. 2a and 2b. In Fig. 2a, as it can be seen, at any given coating thickness the critical wave number is increased as the yield stress increases, meaning that the fluid when at short wavelengths extracts energy from the flow and becomes unstable. Based on this figure, as the yield stress increases, the peak of the plot disappears, meaning that, unlike Newtonian fluids, for viscoplastic fluids, as the coating thickness increases, a monotonic drop in the critical wave number takes place. Again, unlike Newtonian fluids, at very small coating thicknesses, large wave numbers become unstable. Based on what can be seen in Fig. 2b, the yield stress actually destabilizes the flow. That is, the critical pressure gradient decreases as the fluid yield stress increases.

Figure 3 shows the variation of the critical pressure gradient versus the power-law index for very small Reynolds numbers. As it can be seen in this figure, an increase in the Reynolds number causes the fluid flow to be more unstable. In other words, the inertia terms have a destabilizing effect on the fluid flow under the creeping condition. Based on this figure, as the Reynolds number increases, the critical pressure gradient in the flow decreases which means the fluids become more and more unstable. Therefore, a better mixing process takes place in microchannels lined with flexible gels. However, at a given Reynolds number, this instability effect diminishes as a shear-thinning fluid approaches Newtonian behaviour.

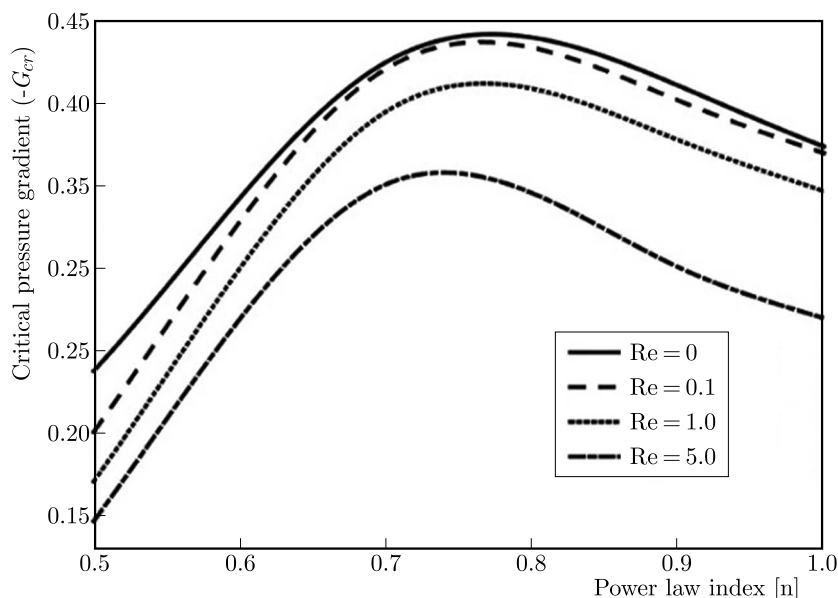


Fig. 3. Effect of the Reynolds number on the critical pressure gradient vs. the power-law index n for different small Reynolds numbers for $T_y = 0.2$, $\beta = 1$, $H = 40$, and $T = 0.5$

Figure 4 shows the variation of the critical pressure gradient versus the yield stress for four Reynolds numbers. As it can be seen in this figure, increasing the Reynolds number has a destabilizing effect on the flow. This figure also shows that at a given Reynolds number, increasing the yield stress decreases the critical pressure gradient, meaning that the flow becomes unstable with an increase in the yield stress. Based on this figure, at any given Reynolds number, as the yield stress increases, the fluid becomes more and more unstable, which is a positive effect regarding the mixing process. Figure 4 also shows that, as the yield stress decreases, higher Reynolds numbers show higher instability.

Figure 5 shows the critical pressure gradient variation versus the Reynolds number for different power-law indices including both the shear-thinning and shear-thickening fluids. It can be seen in this figure that the inertia terms have a destabilizing effect on both the shear-thinning and shear-thickening fluids. From this figure, it can be concluded that for the Reynolds numbers

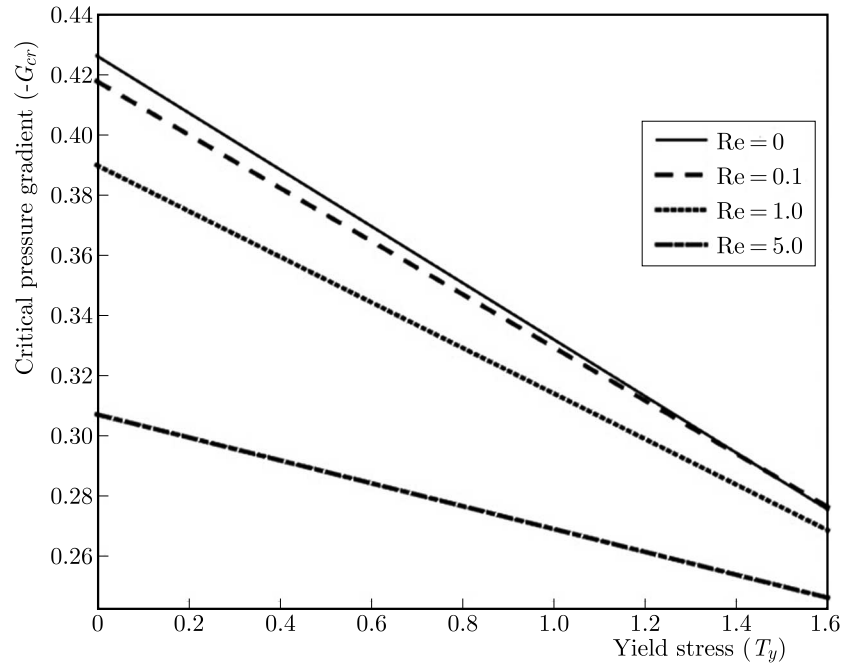


Fig. 4. Critical pressure gradient variation vs. the yield stress for different small Reynolds numbers for $H = 40$, $T = 0.5$, $\beta = 1$, and $n = 0.9$

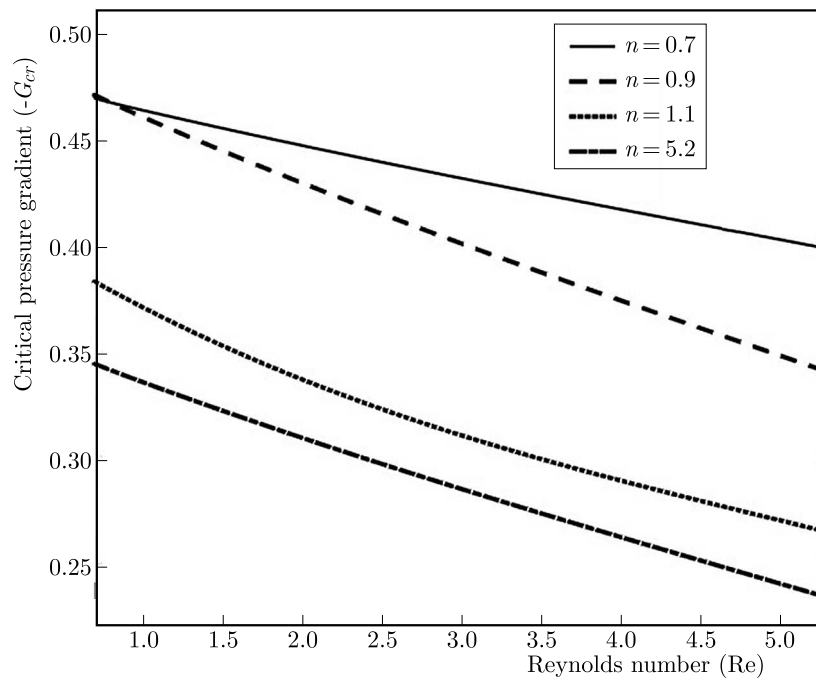


Fig. 5. Critical pressure gradient variation vs. the Reynolds number for $H = 40$, $T_y = 0.5$, $T = 0.5$, and $\beta = 1$

considered here, the shear-thinning fluids are the most stable ones as they need the largest critical pressure gradient to become unstable. Based on this figure, for both the shear-thinning ($n < 1$) and shear-thickening ($n > 1$) fluids, instability increases as the Reynolds number increases. This result is actually in line with the other results shown in the previous figures.

Figure 6 shows the effect of the yield stress on the critical pressure gradient for a coating obeying the Mooney-Rivlin model. The elastic parameter is unity and $Re = 5$. Based on the trend of the plots in Fig. 6, in the presence of inertia, the increase of the yield stress has a

destabilizing effect on the non-zero Reynolds numbers flow. The figure also shows that as the power-law index increases, the fluid becomes more and more stable up to $n \simeq 0.75$, after which the fluid becomes unstable with a very low slope. This figure actually shows how the power-law exponent plays the key role in the hydroelastic instability phenomenon. To see the effect of this key role here, note that a decrease of the fluid viscosity is due to an increase of the shear rate, and noting that the fluid viscosity is actually controlled by the power-law index, then, the shear stress at the fluid-solid interface is also controlled by the index n . Therefore, the diffusive transfer of energy from the basic flow to the imposed perturbations is increased when the power-law index is decreased.

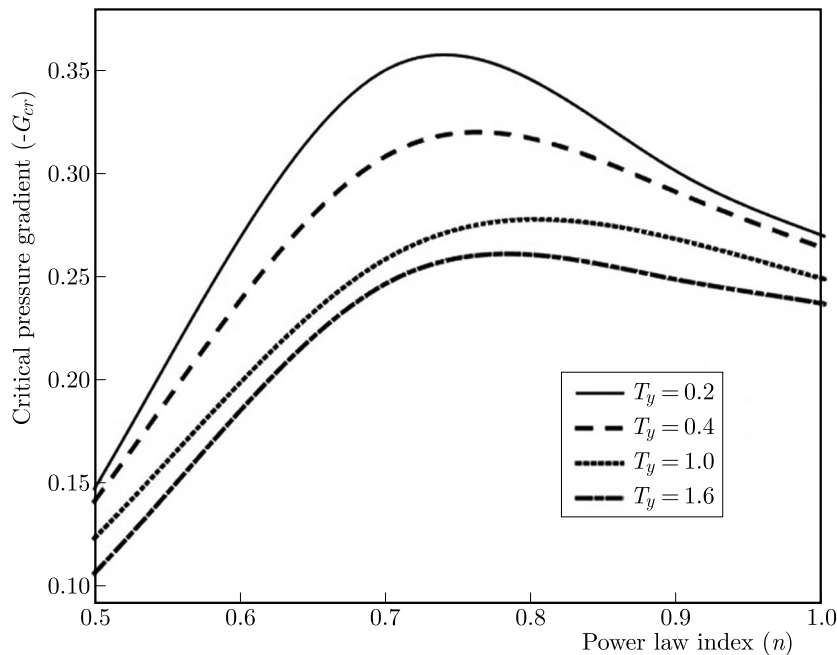


Fig. 6. Critical pressure gradient variation vs. the power-law index n for $H = 40$, $\beta = 1$, $T = 0.5$, and $Re = 5$

Figure 7 shows the critical pressure gradient variation vs. the power-law index for different elastic parameters β . This figure shows that the neo-Hookean solid ($\beta = 0$) is the least stable model regardless of the magnitude of the index n . Moreover, based on the figure, with an increase in the elastic parameter, the curves are shifted to more stable states. It is also noticed in this figure that in the presence of the inertia terms, for any given elastic parameter, the fluid shear-thinning can have a stabilizing or destabilizing effect on the flow depending on the magnitude of the index n . An important effect of β is that this parameter controls the first-normal-stress-difference at the fluid-solid interface. This parameter also affects the pressure discontinuity at the interface. Both effects, however, compete with the fluid shear stress (which initiates the instability) in affecting the hydroelastic instability, thereby, influencing the overall instability trend, as it can be seen in Fig. 7.

6. Conclusions

The aim of the present study has been to investigate the effects of inertia on the stability of the Poiseuille flow of the Herschel-Bulkley fluids passing through a two-dimensional channel. The channel is assumed to be coated with a hyperelastic polymeric material which obeys the two-constant Mooney-Rivlin model. This study is actually an extension of the authors' previous work in which the inertia terms were excluded from the governing equations, hence the effect of

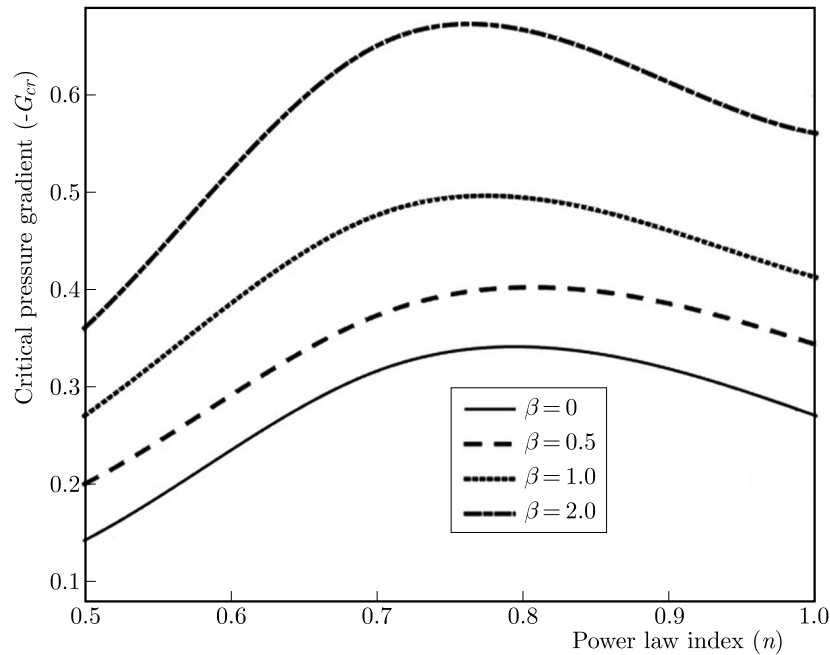


Fig. 7. Critical pressure gradient variation vs. the power-law index for $H = 40$, $T_y = 0.5$, $T = 0.5$, and $Re = 1$

inertia on the fluid flow stability was never determined. In addition, here, unlike the previous works, the effect of the power-law index n on both the shear-thinning and shear-thickening fluids flow are investigated. The above two new contributions in this work enable the results of this study not only to embrace a larger group of fluids, but also to be more realistic and reliable than ever before.

After determining appropriate governing equations for both the polymeric coating and the non-Newtonian fluid used, the base-state solutions have been obtained. Next, the solutions were subjected to infinitesimally-small disturbances after which the non-linear terms were eliminated. The equations after being reduced to two forth-order ordinary differential equations were solved numerically. A shooting technique numerical code was developed to solve (after some lengthy mathematical manipulations) the two fourth-order ordinary differential equations with appropriate boundary conditions. Having solved these equations numerically, the effects of the Reynolds number, yield stress and the elastic parameter on the growth rate of the unstable modes were investigated.

Based on the obtained results, it has been found that the inertia, in general, played a destabilizing role in the flowing fluids. It was determined that by increasing the Reynolds number, the flow became more unstable regardless of the yield stress values. It was also found that considering inertia in the governing equations did not affect the yield stress. Also, as the results showed, for extremely shear-thinning fluids, the yield stress was slightly stabilizing the flow, and for a wide range of power-law indices (close to unity), the yield stress was predicted to have a destabilizing effect on the pressure-driven flow in channels lined with the compliant coating. Based on the numerical results obtained in this work, it was noted that the elastic parameter strongly affected the hydroelastic stability. That is, Mooney-Rivlin coating became more stable than the neo-Hookean coating regardless of the values of the Reynolds number and the yield stress. The above findings of this study now help the investigators in the field to determine how to optimize the mixing efficiency when dealing with the hydroelastic instability of non-Newtonian fluids flowing in channels lined with polymeric gels. The more realistic and meaningful results of this work will definitely affect the microfluidic field research activities.

References

1. BABENKO V.V., KOZLOV L.F., 1972, Experimental investigation of hydrodynamic stability on rigid and elastic damping surfaces, *Journal of Hydraulic Research*, **10**, 383-408
2. BIRD R.B., ARMSTRONG R.C., HASSAGER O., 1987, *Dynamics of Polymeric Liquids*, **1**, John Wiley, New York
3. CHIEN W.L., RISING H., OTTINO J.M., 1986, Laminar and chaotic mixing in several cavity flows, *Journal of Fluid Mechanics*, **170**, 355-377
4. DAVIES C., CARPENTER P.W., 1997, Instabilities in a plane channel flow between compliant walls, *Journal of Fluid Mechanics*, **352**, 205-243
5. DRAZIN P.G., REID W.H., 2004, *Hydrodynamic Stability*, 2nd edit., Cambridge University Press
6. FRANJIONE J.G., OTTINO J.M., 1992, Symmetry concepts for the geometric analysis of mixing flows, *Philosophical Transactions of the Royal Society A*, **338**, 301-323
7. FU T.S., JOSEPH D.D., 1970, Linear stability of asymmetric flow in channels, *Physics of Fluids*, **13**, 217-222
8. GAD-EL-HAK M., 2002, Compliant coatings for drag reduction, *Progress in Aerospace Sciences*, **38**, 77-99
9. GKANIS V., KUMAR S., 2005, Stability of pressure-driven creeping flows in channels lined with a nonlinear elastic solid, *Journal of Fluid Mechanics*, **524**, 357-375
10. JAFARGHOLINEJAD S., 2015, Hydroelastic instability of Herschel-Bulkley fluids in channel flows, Ph.D. dissertation, Islamic Azad University
11. JAFARGHOLINEJAD S., NAJAFI M., SADEGHY K., 2015, Hydroelastic instability of viscoplastic fluids in planar channel flow, *Journal of the Society of Rheology, Japan*, **43**, 5, 157-164
12. JENSEN K.F., 1999, Micromechanical systems: status, challenges and opportunities, *AIChE Journal*, **45**, 2051-2054
13. KRAMER M.O., 1960, Boundary-layer stabilization by distributed damping, *Journal of the Aerospace Sciences*, **27**, 1, 69-69
14. KRAMER M.O., 1960, Boundary layer stabilization by distributing damping, *Journal of the American Society for Naval Engineers*, **72**, 25-33
15. KANDLIKAR S.G., WILLISTEIN D.A., BORRELLI J., 2005, Experimental evaluation of pressure drop elements and fabricated nucleation sites for stabilizing flow boiling in microchannels, *Third International Conference on Microchannels and Minichannels, ASME Paper, ICMM2005-75197*, Toronto, Canada
16. LAI W.M., RUBIN D., KREMPL E., 2010, *Introduction to Continuum Mechanics*, 4th Ed., Elsevier
17. LEE K.C., FINLAYSON B.A., 1986, Stability of plane Poiseuille and Couette flow of a Maxwell fluid, *Journal of Non-Newtonian Fluid Mechanics*, **21**, 1, 65-78
18. MURALIKRISHNAN R., KUMARAN V., 2002, Experimental study of the instability of the viscous flow past a flexible surface, *Physics of Fluids*, **14**, 2, 775-780
19. OTTINO J.M., 1989, *The Kinematics of Mixing: Stretching, Chaos, and Transport*, Cambridge University Press
20. POURJAFAR M., HAMEDI H., SADEGHY K., 2015, Stability of power-law fluids in creeping plane Poiseuille: the effect of wall compliance, *Journal of Non-Newtonian Fluid Mechanics*, **216**, 22-30

INFLUENCE OF PULSE SHAPER GEOMETRY ON WAVE PULSES IN SHPB EXPERIMENTS

ROBERT PANOWICZ, JACEK JANISZEWSKI, KRZYSZTOF KOCHANOWSKI

Military University of Technology, Warsaw, Poland

e-mail: robert.panowicz@wat.edu.pl

Results of numerical analysis of the influence of pulse shaper geometry on wave signals in the split Hopkinson pressure bar experiment are presented. Five pulse shapers, i.e. square, ring, cross, star and disk ones have been analysed. It has been assumed that the disc pulse shaper is the reference geometry to assess the remaining types of pulse shapers. The results of numerical analyses have shown that pulse shapers with shapes different than disk are highly capable of minimizing high-frequency Pochhammer-Chree oscillations and, thus, reduce dispersion of waves propagating in the bar. The greatest damping ability has been observed while using the ring pulse shaper at both low and high impact velocities of the striker.

Keywords: SHPB, pulse shaping technique, high-strain-rate testing, numerical analysis

1. Introduction

The Split Hopkinson Pressure Bar (SHPB) technique requires satisfying some fundamental conditions, i.e., one-dimensional wave propagation in bars, no friction between the specimen and the bars, negligibly low influence of inertia and nearly uniformly specimen deformation at a constant strain rate under dynamically equilibrated stresses (Chen and Song, 2011). The condition regarding the nearly uniformly specimen deformation under dynamically equilibrated stresses is satisfied when stresses on external contact surfaces of the specimen are equal.

The waveform of the phenomenon results in the fact that at the initial moment of loading the sample through the incident bar, the condition regarding the uniform deformation of the specimen under dynamically equilibrated stresses cannot be satisfied. This condition is satisfied after some time, depending on the shape of the incident pulse and on the pulse rising time as well as geometrical parameters of the specimen and its properties (Frantz and Follansbee, 1984; Follansbee, 1985; Gorham, 1991). Currently, the pulse shaper technique is widely used to shape the incident pulse. The technique is based on placing a small coaxial disk (pulse shaper) between the strike and the incident bar. This disk is made of a soft material compared to the striker and bars material, and deforms plastically when the striker hits it.

Frantz and Follansbee (1984) and Follansbee (1985) showed that with an increase in the shaper thickness, the pulse rise time increases and the amplitude of Pochhammer-Chree high-frequency oscillations (Pochhammer, 1876; Chree, 1886) decreases. As a result, the dispersion is reduced and the dynamic equilibrium in the specimen is achieved much faster.

In most cases, during experimental tests, different thickness and diameter of shapers made of copper were used to increase the rise time of the incident pulse to reduce dispersion as well as to achieve the state of dynamic equilibrium faster, see e.g. (Chen *et al.*, 2003; Naghdabadi *et al.*, 2012).

In SHPB, thin disks are used for wave shapers. This is due to, among others, the fact that it is easy to produce them with the use of machining methods or by punching them from metal sheets. For this reason, elements with more complex geometry, such as rings, crosses, stars, are

not used. Hence, the idea of examining the influence of various shapes of pulse shapers on wave pulses registered in SHPB experiments.

The article presents results of numerical analyses for 5 types of geometry of the pulse shapers presented in Fig. 1.

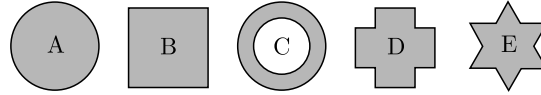


Fig. 1. Geometry of the analyzed pulse shapers

2. Numerical modelling

The model contains all main components of the arrangement: a pulse shaper, slide bearings and a barrel. In simulation, dimensions of all elements of SHPB are the same as in the experiments (Panowicz *et al.*, 2017).

The Johnson-Cook constitutive model with the Gruneisen hydrodynamic equation of state has been used to describe the behavior of the copper shaper and a titanium specimen (Hallquist, 2006). The Ti6Al4V specimen (3.7 mm length, 4 mm diameter) and copper pulse shaper materials constants have been taken from literature (Grazka and Janiszewski, 2012; Ozel and Sima, 2010).

The authors used the Finite Element Method with a central difference time integration scheme implemented in explicit LS-Dyna to carry out numerical simulations (Hallquist, 2006).

In order to assess the correctness of the numerical model, validation with experimental tests for two striker impact velocities ($V = 15.3$ m/s and 11.8 m/s) and two shaper thicknesses ($d = 0.101$ and 0.201 mm) has been carried out to obtain high compliance.

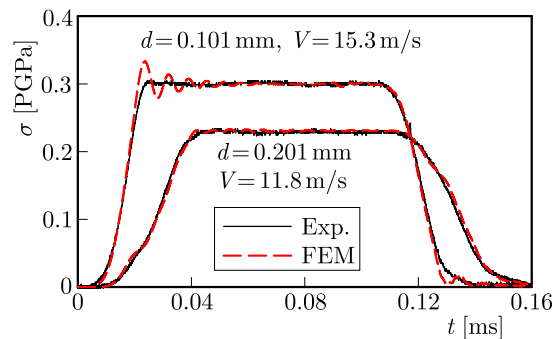


Fig. 2. Comparison of incident wave profiles obtained from numerical (FEM) and experimental (Exp.) analyses, in which shapers with different thicknesses d were used; the striker hits the bar with velocity V

3. Results and discussion

Numerical analysis of the geometry influence of the pulse shaper with thickness of 0.1 mm has been carried out for frequently used striker impact velocities, i.e. 10 and 15 m/s. The results are presented in the form of incident and reflect waves pulses shown in Figs. 3 and 4, respectively.

Based on the obtained results, the influence of the pulse shapers geometry on waves pulses profiles has been confirmed, however, it is little, especially in the test with velocity of 10 m/s (Figs. 3a,b and 4a,b). This effect is also manifested in the course of both the rising and falling time of wave profiles. In relation to the standard geometry of the pulse shaper – the disk (geometry A, Fig. 1), the profiles of the rising and falling time of the incident wave, for the remaining types of pulse shapers, have a characteristic inflection occurring at about 2/3 of the wave amplitude. The rise time of the wave profile to the point of inflection is shorter in relation

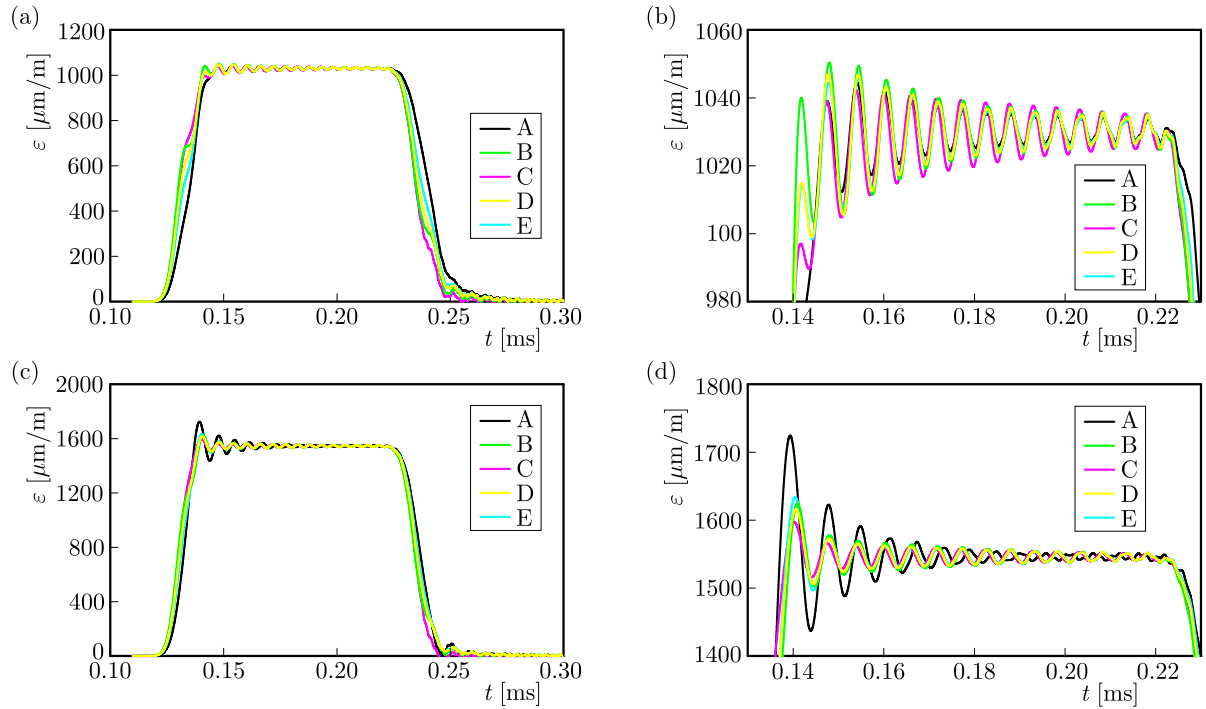


Fig. 3. Incident pulses for different striker velocity: (a), (b) $V = 10$ m/s, (c), (d) $V = 15$ m/s, (a) and (c) all signals, (b) and (d) zoom

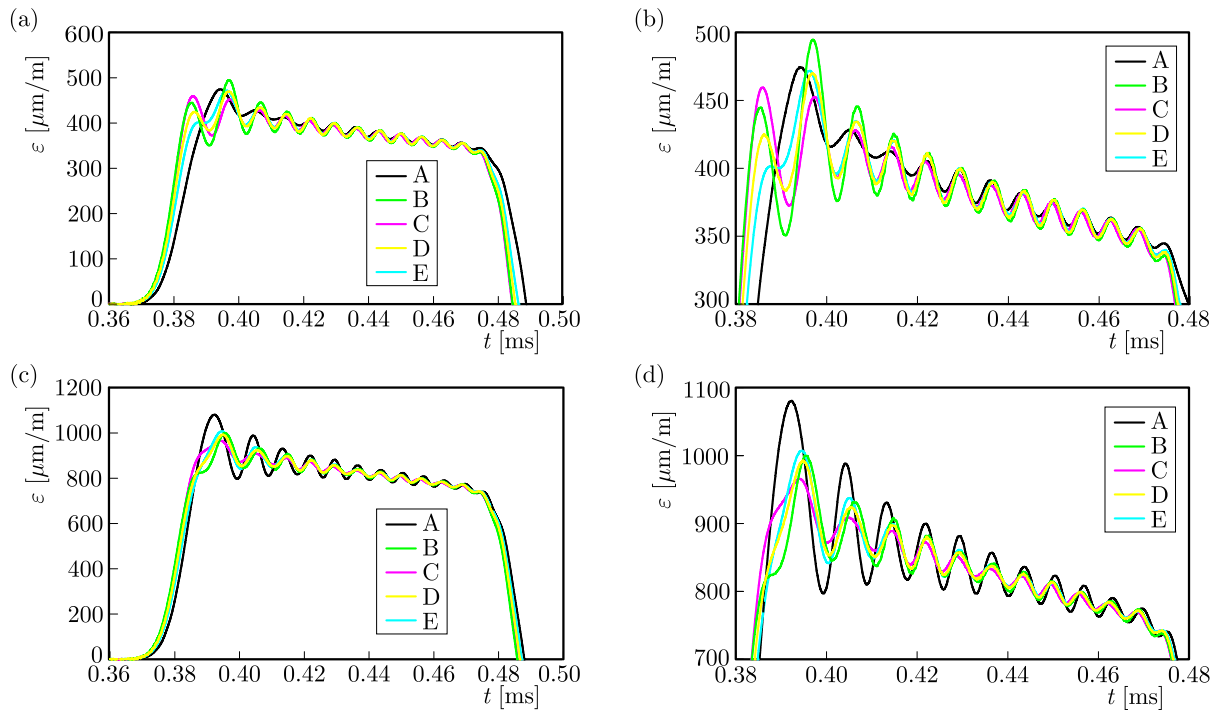


Fig. 4. Reflected pulses for different striker velocity: (a), (b) $V = 10$ m/s, (c), (d) $V = 15$ m/s, (a) and (c) all signals, (b) and (d) zoom

to the rise time when the classical shaper is used (geometry A, Fig. 1). This is due to a faster process of deformation and work hardening of the pulse shapers.

Small differences can also be observed in the area of the occurrence of Pochhammer-Chree high-frequency oscillations. The highest oscillation amplitude for the striker velocity of 10 m/s

was found for the square geometry, and the smallest for the ring geometry. In turn, for the striker impact velocity equal to 15 m/s, the largest oscillation amplitude occurs in the case when the pulse shaper of the disk type is used, and the smallest for the ring type. Therefore, it can be concluded that the pulse shaper with ring (Fig. 1c) geometry has the highest ability to suppress high-frequency components of the pulses and, thus, to minimize dispersion of waves propagating in the SHPB bar.

It should be noted that the effect of the pulse shaper geometry is revealed with an increase of the striker impact velocity. At the striker velocity equal to 15 m/s, the high damping ability is demonstrated by pulse shapers with geometry different than the disk (Fig. 1a). It follows that, especially for high striker velocities, the use of a classical pulse shaper with disk geometry is not appropriate. It is also observed in the reflected wave profile (Fig. 4c,d) on which the largest oscillations amplitudes are found for the disk pulse shaper (geometry A). Too large oscillation amplitudes visible on the wave profile delay the attainment of the specimen dynamic stress equilibrium state and, thus, make it impossible to meet the basic methodological requirement of the SHPB technique.

4. Conclusion

A method frequently used in the SHPB technique for forming an incident wave propagating in the input bar is the use of a pulse shaper with disk geometry. The numerical analysis presented in the article shows, however, that it is advantageous to use pulse shapers with shapes different than disks. It has been found that they have a high ability to minimize high-frequency Pochhammer-Chree oscillations and, thus, reduce dispersion of waves propagating in the bar. For example, a ring pulse shaper has a greater ability to suppress oscillations than a disk pulse shaper at both low and high striker impact velocities. The ring pulse shaper also allows reaching the equilibrium stress state in the test specimen faster. This feature is really desirable, especially while testing high-strength materials with low plastic properties.

Acknowledgements

The support of Military University of Technology grants PBS 23-937 and 23-941 is gratefully acknowledged.

References

1. CHEN W., SONG B., 2011, *Split Hopkinson (Kolsky) Bar: Design, Testing and Applications*, Berlin, Springer
2. CHEN W., SONG B., FREW D.J., FORRESTAL M.J., 2003, Dynamic small strain measurements of a metal specimen with a split Hopkinson pressure bar, *Experimental Mechanics*, **43**, 1
3. CHREE C., 1886, Longitudinal vibrations of a circular bar, *Quarterly Journal of Pure and Applied Mathematics*, **21**, 287-298
4. FOLLANSBEE P.S., 1985, *The Hopkinson Bar in Mechanical Testing and Evaluations*, ASM Handbook, 9th ed. ASM Int., Materials Park Ohio
5. FRANTZ C.E., FOLLANSBEE P.S., 1984, Experimental techniques with the split Hopkinson pressure bar, *Proceedings of the 8th International Conference on High Energy Rate Fabrication*, San Antonio, Texas, TX, 229-236
6. FREW D.J., FORRESTAL M.J., CHEN W., 2002., Pulse shaping techniques for testing brittle materials with a split Hopkinson pressure bar, *Experimental Mechanics*, **42**, 93-106

7. GORHAM D.A., 1991, The effect of specimen dimensions on high strain rate compression measurements of copper, *Journal of Physics, D: Applied Physics*, **24**, 8, 1489-1492, <https://doi.org/10.1088/0022-3727/24/8/041>
8. GRAZKA M., JANISZEWSKI J., 2012, Identification of Johnson-Cook equation constants using finite element method, *Engineering Transactions*, **60**, 215-223
9. HALLQUIST J.O., 2006, *Ls-Dyna. Theoretical Manual*, California: Livermore Software Technology Corporation
10. NAGHDABADI R., ASHRAFI M.J., ARGHAVANIC J., 2012, Experimental and numerical investigation of pulse-shaped split Hopkinson pressure bar test, *Materials Science and Engineering A*, **539**, 285-293
11. NEMAT-NASSER S., ISAACS J.B., STARRETT J.E., 1991, Hopkinson techniques for dynamic recovery experiments, *Proceedings of the Royal Society*, **435**, 371-391
12. OZEL T., SIMA M., 2010, Finite element simulation of high speed machining Ti-6Al-4V alloy using modified material models, *Transactions of NAMRI/SME*, **38**, 49-56
13. PANOWICZ R., JANISZEWSKI J., TRACZYK M., 2017, Strain measuring accuracy with splitting-beam laser extensometer technique at split Hopkinson compression bar experiment, *Bulletin of the Polish Academy of Sciences Technical Sciences*, **65**, 2, 163-169, <https://doi.org/10.1515/bpasts-2017-0020>
14. POCHHAMMER L., 1876, On the propagation velocities of small oscillations in an unlimited isotropic circular cylinder, *Journal für die reine und angewandte Mathematik*, **81**, 324-326

Manuscript received March 22, 2018; accepted for print May 9, 2018

INFORMATION FOR AUTHORS

Journal of Theoretical and Applied Mechanics (JTAM) is devoted to all aspects of solid mechanics, fluid mechanics, thermodynamics and applied problems of structural mechanics, mechatronics, biomechanics and robotics. Both theoretical and experimental papers as well as survey papers can be proposed.

We accept articles in English only. The text of a *JTAM* paper should not exceed **12 pages of standard format A4** (11-point type size, including abstract, figures, tables and references), short communications – **4 pages**.

The material for publication should be sent to the Editorial Office via electronic journal system: <http://www.ptmts.org.pl/jtam/index.php/jtam>

Papers are accepted for publication after the review process. Blind review model is applied, which means that the reviewers' names are kept confidential to the authors. The final decision on paper acceptance belongs to the Editorial Board.

After qualifying your paper for publication we will require L^AT_EX or T_EX or Word document file and figures.

The best preferred form of figures are files obtained by making use of editorial environments employing vector graphics:

- generated in CorelDraw (*.cdr), AutoCad and ArchiCad (*.dwg) and Adobe Illustrator (*.ai). We require original files saved in the standard format of the given program.
- generated by calculation software (e.g. Mathematica) – we need files saved in *.eps or *.pdf formats.
- made in other programs based on vector graphics – we ask for *.eps, *.wmf, *.svg, *.psfiles.

Any figures created without application of vector graphics (scans, photos, bitmaps) are strongly encouraged to be supplied in *.jpg, *.tif, *.png formats with resolution of at least 300 dpi.

Requirements for paper preparation

Contents of the manuscripts should appear in the following order:

- Title of the paper
- Authors' full name, affiliation and e-mail
- Short abstract (**maximum 100 words**) and 3-5 key words (**1 line**)
- Article text (equations should be numbered separately in each section; each reference should be cited in the text by the last name(s) of the author(s) and the publication year)
- References in alphabetical order. See the following:
 1. Achen S.C., 1989, A new boundary integral equation formulation, *Journal of Applied Mechanics*, **56**, 2, 297-303
 2. Boley B.A., Weiner J.H., 1960, *Theory of Thermal Stresses*, Wiley, New York
 3. Canon W., 1955, Vibrations of heated beams, Ph.D. Thesis, Columbia University, New York
 4. Deresiewicz H., 1958, Solution of the equations of thermoelasticity, *Proceedings of Third U.S. National Congress of Applied Mechanics*, 287-305
- Titles of references originally published not in English, should be translated into English and formulated as follows:
 5. Huber M.T., 1904, Specific work of strain as a measure of material effort (in Polish), *Czasopismo Techniczne*, **XXII**, 3, 80-81

All the data should be reported in **SI units**.

Contents

Głębocki R., Jacewicz M. — Simulation study of a missile cold launch system	901
Arslan O. — Inclined surface cracks in a graded half-plane subjected to frictional sliding contact	915
Brzeziński K. — XFEM simulation of the influence of cracking introduced by pre-loading on the strengthening of a cement treated mixture	927
Hedayati R., Sadighi M. — Low-velocity impact behaviour of open-cell foams	939
Chen H.Y., Zhang K., Bai Y.X., Ma Y., Deng H.Z. — Model construction and experimental verification of the equivalent elastic modulus of a double-helix wire rope	951
Felhi H., Trabelsi H., Taktak M., Chaabane M., Haddar M. — Effects of viscoelastic and porous materials on sound transmission of multilayer systems	961
Gesualdo A., Iannuzzo A., Minutolo V., Monaco M. — Rocking of freestanding objects: theoretical and experimental comparisons	977
Goyal R., Kumar S., Sharma V. — Microstructural considerations on SH-wave propagation in a piezoelectric layered structure	993
Abbasi S., Pirnia A., Taghavi-Zenouz R. — Investigation of inlet distortion effects on axial compressor performance based on streamline curvature method	1005
Topczewska K. — Analytical model for investigation of the effect of friction power on thermal stresses in friction elements of brakes	1017
Allam M.N.M., Tantawy R., Zenkour A.M. — Thermoelastic stresses in functionally graded rotating annular disks with variable thickness	1029
Alacali S., Arslan G. — Assessment of the strength reduction factor in predicting the flexural strength	1043
Tomczyk A., Seweryn A., Doroszko M. — Monotonic behaviour of typical Al-Cu-Mg alloy pre-strained at elevated temperature	1055
Jade N., Venkatesham B. — Free vibrational analysis of rectangular ducts with different joint conditions	1069
Zheng T., Qiang X.-Q., Teng J.-F., Feng J.-Z. — Numerical loss analysis in a compressor cascade with leading edge tubercles	1083
Nasirzadeh R., Behjat B., Kharazi M. — Finite element study on thermal buckling of functionally graded piezoelectric beams considering inverse effects	1097
Gao J., Li P. — Life prediction for LY12CZ notched plate based on the continuum damage mechanics and the genetic algorithm and radial basis function method	1109
Mohammadi M., Hematiyan M.R., Shiah Y.C. — An efficient analysis of steady-state heat conduction involving curved line/surface heat sources in two/three-dimensional isotropic media	1123
Iqbal D., Tiwari V. — Structural response of multilayered aluminum and steel specimens subjected to high strain rate loading conditions	1139
Tiwari P., Nagar P. — Mechanical nature of a single walled carbon nanotube using Legendre's polynomials	1153
Magnucki K., Lewiński J., Magnucka-Blandzi E., Kędzia P. — Bending, buckling and free vibration of a beam with unsymmetrically varying mechanical properties	1163
Gembalczyk G., Duda S., Świtoński E. — Computational optimization and implementation of control system for mechatronic treadmill with body weight support system	1179
Hendzel Z. — Robust neural networks control of omni-mecanum wheeled robot with Hamilton-Jacobi inequality	1193
Jafargholinejad S., Najafi M. — Implications of inertia for hydroelastic instability of Herschel-Bulkley fluids in plane Poiseuille flow	1205
<u>Short Research Communication</u>	
Panowicz R., Janiszewski J., Kochanowski K. — Influence of pulse shaper geometry on wave pulses in SHPB experiments	1217